Circulation submésoéchelle et comportements des prédateurs marins supérieurs : Apport de l'analyse multi-échelles et multi-capteurs

J. Sudre

▶ **To cite this version:**

J. Sudre. Circulation submésoéchelle et comportements des prédateurs marins supérieurs : Apport de l'analyse multi-échelles et multi-capteurs. Océan, Atmosphère. Université Paul Sabatier - Toulouse III, 2013. Français. NNT : . tel-00929804

HAL Id: tel-00929804
https://theses.hal.science/tel-00929804

Submitted on 13 Jan 2014

HAL is a multi-disciplinary open access archive for the deposit and dissemination of scientific research documents, whether they are published or not. The documents may come from teaching and research institutions in France or abroad, or from public or private research centers.

L'archive ouverte pluridisciplinaire **HAL**, est destinée au dépôt et à la diffusion de documents scientifiques de niveau recherche, publiés ou non, émanant des établissements d'enseignement et de recherche français ou étrangers, des laboratoires publics ou privés.

THÈSE

En vue de l'obtention du

DOCTORAT DE L'UNIVERSITÉ DE TOULOUSE

Délivré par *l'Université Toulouse III - Paul Sabatier*
Discipline ou spécialité : *Océanographie Physique - Traitement du signal - Comportement Animal*

Présentée et soutenue par *Joël SUDRE*
Le *Date de la soutenance*

Titre : *Circulation submésoéchelle et comportements des prédateurs marins supérieurs: Apport de l'analyse multi-échelles et multi-capteurs*

JURY
Nom
Nom
Nom
Nom
... (préciser la qualité de chacun des membres)

Ecole doctorale : *"SCIENCES DE L'UNIVERS, DE L'ENVIRONNEMENT ET DE L'ESPACE" SDU2E*
Unité de recherche : *Laboratoire d'Etudes en Géophysique et Océanographie Spatiales (UMR5566)*
Directeur(s) de Thèse : *Véronique Garçon et Hussein Yahia*
Rapporteurs : *Noms des rapporteurs (s'ils ne font pas partie des membre du jury)*

Table des matières

Introduction 1

Introduction générale 3

Chapitre 1 Du corps noir...aux satellites 15

1 Les données utilisées 17
1.1 Introduction . . . 18
1.2 Approche théorique de l'électromagnétisme . . . 19
1.2.1 Ondes électromagnétiques . . . 19
1.2.2 Bande de fréquences des ondes électromagnétiques . . . 22
1.2.3 Le corps noir . . . 24
1.2.4 Le corps gris . . . 25
1.2.5 La fenêtre atmosphérique . . . 26
1.3 Données satellitaires . . . 27
1.3.1 Altimétrie radar à visée nadir . . . 27
a Principe de la mesure . . . 27
b Historique et principales missions . . . 32
c Données utilisées . . . 33
1.3.2 Diffusiométrie . . . 39
a Principe de la mesure . . . 39
b Historique et principales missions . . . 42
c Données utilisées . . . 43
1.3.3 Température de surface de la mer . . . 50
a Principe de la mesure . . . 50
b Historique et principales missions . . . 54
c Données utilisées . . . 54
1.3.4 Couleur de l'océan . . . 60
a Principe de la mesure . . . 60
b Historique et principales missions . . . 63

c Données utilisées 63
1.4 Données *in-situ* de courant 67
1.4.1 Données Eulériennes 67
a ADCP de coque 68
b Données des réseaux d'observation TAO, PIRATA, RAMA 69
1.4.2 Données Lagrangiennes 72
a Bouées dérivantes de surface 72
b Bouées dérivantes de subsurface 73
1.5 Pré-traitement des données 76

Chapitre 2 La dynamique mésoéchelle 77

2 La dynamique mésoéchelle 79
2.1 Introduction 80
2.1.1 Aperçu de nos connaissances actuelles 80
2.2 Estimation des courants à l'échelle globale 82
2.2.1 Courants géostrophiques 82
2.2.2 Courants d'Ekman 83
2.3 Article : Global surface currents : a high-resolution product for investigating ocean dynamics, Sudre and Morrow, 2008 87
2.3.1 Résumé de l'article (version française) 87
2.3.2 Article publié dans *Ocean Dynamics* 88
2.3.3 Améliorations souhaitables de l'estimation des courants au quart de degré à l'échelle globale 107
2.4 Article : On the global estimates of geostrophic and Ekman surface currents, Sudre et al., 2013 107
2.4.1 Résumé de l'article (version française) 107
2.4.2 Article publié dans *Limnology and Oceanography : Fluids and Environments* 108
2.5 Compléments sur la composante d'Ekman 129
2.6 Comparaison des courants de l'article [*Sudre et Morrow*, 2008] et de l'article [*Sudre et al.*, 2013] 138
2.7 Conclusions 140

Chapitre 3 La dynamique submésoéchelle **143**

3 La dynamique submésoéchelle **145**
3.1 Introduction . . . 147
3.2 La turbulence pleinement développée . . . 152
3.3 Spectre de singularités et description canonique de la cascade multiplicative . . . 156
3.4 Le FMM et la formulation microcanonique de la cascade multiplicative . . . 157
3.5 Formulation microcanonique de la cascade multiplicative et ondelettes optimales . . . 160
3.6 Spectres de singularités des données d'acquisition en Océanographie . . . 162
3.7 Histogrammes conditionnels des coefficients d'ondelettes . . . 163
3.8 Article : Motion analysis in oceanographic satellite images using multiscale methods and the energy cascade, H. Yahia *et al.*, 2010 163
3.8.1 Résumé de l'article (version française) . . . 163
3.8.2 Article publié dans *Pattern Recognition* . . . 165
3.9 Article : Inferring Information across Scales in Acquired Complex Signals, S. K. Maji *et al.*, 2012 . . . 180
3.9.1 Résumé de l'article (version française) . . . 180
3.9.2 Article publié dans *European Conference on Complex Systems 2012* . . . 180
3.10 Détermination de la norme . . . 199
3.11 Validation de la dynamique turbulente à haute résolution . . . 200
3.11.1 Méthodes de validation . . . 200
3.11.2 Validation de la dynamique à haute résolution obtenue à partir de la TSM MODIS/AQUA . . . 205
3.11.3 Validation de la dynamique turbulente obtenue à partir de la TSM OSTIA . . . 212
3.12 Conclusions . . . 217

Chapitre 4 De l'inanimé au vivant **219**

4 Impact de dynamique océanique sur le monde marin du vivant **221**
4.1 Introduction . . . 222
4.2 Les exposants de Lyapunov . . . 224
4.2.1 Définition mathématique des exposants de Lyapunov . . . 224

4.2.2 Exemple sur exposants de Lyapunov : les campagnes BATS Val / Submesoscale Biogeochemistry Cruise Logistics . . . 225
4.3 Les systèmes d'upwellings de bord est . . . 231
4.4 Impact de la dynamique océanique sur les prédateurs marins supérieurs . . . 232
4.4.1 La dynamique océanique du Canal du Mozambique . . . 233
4.4.2 Zone d'alimentation des Frégates du Pacifique (Fregata minor) 236
4.4.3 Capacités d'orientation des tortues vertes (Chelonia mydas) et impact des courants marins sur leurs déplacements . . 239
4.5 Article : The Role of Geomagnetic Cues in Green Turtle Open Sea Navigation, S. Benhamou *et al.*, 2011 . . . 245
4.5.1 Résumé de l'article . . . 245
4.5.2 Article publié dans *PLoS ONE* . . . 246
4.6 Conclusions . . . 258

Conclusions et perspectives **261**

Conclusions et perspectives générales **263**

Références **271**

Les Annexes **295**

Annexe A : Article soumis **297**

A Annexe A : Article soumis **299**

Annexe A : Article soumis **300**
A.1 Article soumis : Ocean Turbulent Dynamics at Super Resolution : A True Picture, Sudre et al. . . . 300
A.1.1 Abstract . . . 300
A.1.2 Article soumis dans *Nature Geoscience* . . . 300

Annexe B : Articles cités dans ce manuscrit **319**

B Annexe B : Articles cités dans ce manuscrit dont je suis co-auteurs **321**

B.1 Article : Homing in green turtles Chelonia mydas : oceanic currents act as a constraint rather than as an information source, C. Girard *et al.*, 2006 323
B.1.1 Abstract 323
B.1.2 Article publié dans *Marine Ecology Progress Series* 323
B.2 Article : Marine Turtles Use Geomagnetic Cues during Open-Sea Homing, P. Luschi *et al.*, 2007 333
B.2.1 Abstract 333
B.2.2 Article publié dans *Current Biology* 333
B.3 Article : Comparative study of mixing and biological activity of the Benguela and Canary upwelling systems, V. Rossi *et al.*, 2008 . . 342
B.3.1 Abstract 342
B.3.2 Article publié dans *Geophysical Research Letters* 342
B.4 Article : Top marine predators track Lagrangian coherent structures, E. Tew Kai *et al.*, 2009 348
B.4.1 Abstract 348
B.4.2 Article publié dans *Proceedings of the National Academy of Sciences* 348
B.5 Article : Surface mixing and biological activity in the four Eastern Boundary Upwelling Systems, V. Rossi *et al.*, 2009 355
B.5.1 Abstract 355
B.5.2 Article publié dans *Nonlinear Processes in Geophysics* . . . 355

Annexe C : Articles dans le domaine de l'optique adaptative 369

C Annexe C : Articles dans le domaine de l'optique adaptative (Science de l'univers : Astronomie) 371
C.1 Article : A multiscale approach to phase reconstruction for Adaptive Optics, Maji S. K. *et al.*, 2011 372
C.1.1 Abstract 372
C.1.2 Article publié dans *IEEE NASA/ESA Conference on Adaptive Hardware and Systems (AHS-2012)* 372
C.2 Article : Towards Multiscale Reconstruction of Perturbated Phase from Hartmann-Shack Acquisitions, Maji S. K. *et al.*, 2012 377
C.2.1 Abstract 377
C.2.2 Article publié dans *IEEE NASA/ESA Conference on Adaptive Hardware and Systems (AHS-2012)* 377

Publications **387**

Liste des publications, conférences internationales **389**

Table des figures

1 *Illustration d'une "current chart" dans le Canal du Mozambique de M. Maury ; © avec l'aimable autorisation de Mme Jackie Grace (Grace Galleries, LLC).* 6

1.1 *Illustration du tenseur électromagnétique dans le cas simple d'une onde électromagnétique sinusoïdale.* 20
1.2 *Illustration des caractéristiques d'une onde électromagnétique pour le cas simple de l'onde simple sinusoïdale.* 20
1.3 *Représentation de la fenêtre atmosphérique de transmission (en blanc sur cette représentation). (http://e-cours.univ-paris1.fr/modules/uved/envcal/html/rayonnement/index.html). ©Université Paris 1* 26
1.4 *Illustration du principe de l'altimétrie. (http://www.aviso.oceanobs.com). ©CNES.* 29
1.5 Représentation des formes d'ondes en fonction du temps. ©CNES. 30
1.6 *Représentation d'une forme d'onde réelle (courbe verte) et de sa courbe théorique (courbe rouge). L'axe des abscisses représente le temps, celui des ordonnées la puissance reçue de l'écho.* 31
1.7 *Représentation d'un paquet d'onde obtenu avec 90 formes d'onde réelles (courbe bleue) et de sa courbe théorique (courbe rouge) en fonction du temps (axe des abcisses) et de la puissance reçue (axe des ordonnées).* 31
1.8 *Vue d'artiste des différentes missions altimétriques. ©CNES.* . . . 33
1.9 *Illustration des traces du satellite TOPEX/POSEIDON. ©CNES.* . . 34
1.10 SLA et sa MDT associée utilisées dans l'article [*Sudre et Morrow*, 2008]. 36
1.11 SLA et sa MDT associée au Sud-Ouest de l'Océan Indien utilisées dans l'article [*Sudre et Morrow*, 2008]. 37
1.12 MADT globale et au Sud-Ouest de l'Océan Indien utilisées dans l'article [*Sudre et al.*, 2013]. 38

1.13 *Illustration de la résolution spatiale d'un diffusiomètre à visée latérale.* . . . 41
1.14 *Illustration de la couverture spatiale de QuikSCAT (antenne à balayage conique). ©[Spencer et al., 2000].* . . . 42
1.15 Tension de vent provenant du produit QuikSCAT du CERSAT utilisée dans les articles [*Sudre et Morrow*, 2008] et [*Sudre et al.*, 2013]. 47
1.16 Tension de vent provenant du produit du NCDC. . . . 48
1.17 Tension de vent provenant du produit DASCAT MWF du CERSAT. 49
1.18 *Illustration de profils de température idéalisés de la couche de surface de l'océan durant (a) la nuit ou le jour avec des conditions de vent fort et (b) le jour avec des conditions de vent faible et une forte insolation provoquant une stratification thermique de la couche de surface. ©Journal of Climate AMS.* . . . 51
1.19 TSM provenant du produit TSM MODIS/Aqua. . . . 58
1.20 TSM du produit OSTIA. . . . 59
1.21 *Illustration du signal mesuré par un capteur satellitaire. L'épaisseur des flux montre l'importance de la part atmosphérique dans le signal mesuré (jusqu'à 90%). ©[Pottier, 2006].* . . . 61
1.22 Concentration en chlorophylle-a du produit MODIS/Aqua. . . . 66
1.23 *Illustration de l'ensemble des sections disponibles de l'archive du JASADCP. ©JASADCP.* . . . 69
1.24 *Illustration de la configuration standard des bouées ATLAS. ©TAO project office NOAA/PMEL.* . . . 71
1.25 *Illustration des positions des mouillages sur les réseaux TAO/TRITON, PIRATA et RAMA. ©TAO project office NOAA/PMEL.* 72
1.26 *Illustration des positions des 1051 bouées en activité du GDP pour le 30 Septembre 2013. ©M. Pazos et R. Lumpkin.* . . . 73
1.27 *Illustration des positions des flotteurs ARGO ayant délivré des données dans les 30 derniers jours avant le 1 Octobre 2013. ©ARGO.* 75
1.28 *Illustration du cycle d'une bouée ARGO. ©ARGO.* . . . 75

2.1 Obtention des paramètres h_E et r_E. . . . 130
2.2 *Moyenne de la tension de vent provenant du produit QuikSCAT du CERSAT calculée pour la période du 01 Janvier 2000 au 31 Décembre 2008.* . . . 131
2.3 Régression linéaire du paramètre h_E dans l'hémisphère Nord. La droite représente la régression linéaire du nuage de points (noirs) et le point rouge représente la valeur moyenne de ce nuage. . . . 133

2.4 Régression linéaire du paramètre h_E dans l'hémisphère Sud. La droite représente la régression linéaire du nuage de points (noirs) et le point rouge représente la valeur moyenne de ce nuage. . . . 134
2.5 Régression linéaire du paramètre r_E dans l'hémisphère Nord. La droite représente la régression linéaire du nuage de points (noirs) et le point rouge représente la valeur moyenne de ce nuage. . . . 135
2.6 Régression linéaire du paramètre r_E dans l'hémisphère Sud. La droite représente la régression linéaire du nuage de points (noirs) et le point rouge représente la valeur moyenne de ce nuage. . . . 136
2.7 Valeurs de régression des paramètres h_E et r_E. 137
2.8 Corrélations obtenues entre les deux produits satellitaires au quart de degré et les bouées dérivantes de surface. 139

3.1 *Illustration des échelles spatio-temporelles dans l'océan selon Dickey et al. [2006]. ©Sung Yong Kim et Eric Terrill (OSTST 2011).* . . 147
3.2 *Spectre de singularité obtenu pour les données de TSM à trois différentes résolutions :* $1/12°$ *en bleue,* $1/6°$ *en rouge et* $1/3°$ *en vert. Ce spectre a été calculé à partir de 960 sous-images de* 256×256 *pixels extraites de la base globale TSM MODIS/Aqua correspondant à la période du 01 Janvier 2006 au 31 Décembre 2008 (Ces sous-images ont été sélectionnées pour avoir moins de 5% de données manquantes).* 162
3.3 Histogrammes conditionnels $E(\log_2|\alpha_c| \mid \log_2|\alpha_p|)$ des coefficients d'ondelettes correspondant à l'ondelette Battle-Lemarié d'ordre 3 calculée avec 41 coefficients centraux et utilisée pour le calcul numérique de l'analyse multirésolution. L'axe horizontal correspond aux coefficients d'ondelette père et l'axe vertical aux coefficients d'ondelette enfant. 164
3.4 *Exposants de singularité, pour la date du 02 août 2007, dérivés à partir des données de TSM MODIS/Aqua. Les fronts de transition représentés par les courbes claires sur cette image représentent les zones où les gradients de température sont importants dans l'océan en délimitant les structures océaniques cohérentes à différentes échelles. Le carré noir représente la sous-zone de la figure 3.6.* 201
3.5 *Dynamique océanique du produit GEKCO, pour la date du 02 août 2007, superposée à la topographie dynamique absolue. Le carré noir représente la sous-zone de la figure 3.6.* 202

3.6 *Dynamique océanique turbulente obtenue par l'analyse multirésolutions au moyen des données GEKCO à basse résolution et des exposants de singularité à haute résolution pour propager la dynamique turbulente à travers les échelles. Du fait de la très haute densité du champ de vecteurs résultant, l'image montre uniquement les valeurs à l'intérieur du sous-domaine carré des figures 3.4 et 3.5.* 203
3.7 *Déplacement des 373 bouées Lagrangiennes droguées à* $15\ m$ *sur la période du 01 janvier 2006 au 31 décembre 2009.* 204
3.8 Nombre de positions de bouées Lagrangiennes collocalisées avec les données de courant pour la période de validation du 01 Janvier 2006 au 31 Décembre 2009. 207
3.9 Différence de la norme calculée entre les positions des bouées Lagrangiennes collocalisées avec les données des courants pour la période de validation du 01 Janvier 2006 au 31 Décembre 2009. 208
3.10 Produit scalaire calculé entre les positions des bouées Lagrangiennes collocalisées avec les données des courants pour la période de validation du 01 Janvier 2006 au 31 Décembre 2009. . . 209
3.11 *Nombre de positions de bouées Lagrangiennes collocalisées avec les données de courant pour la période de validation du 01 Janvier 2006 au 31 décembre 2009.* 210
3.12 Validation de la norme et du produit scalaire entre les positions des bouées Lagrangiennes collocalisées avec les données des courants lissées pour la période de validation du 01 Janvier 2006 au 31 Décembre 2009. 211
3.13 *Nombre de positions de bouées Lagrangiennes collocalisées avec les données de courant pour la période de validation du 01 Janvier 2006 au 31 Décembre 2009.* 212
3.14 Différence de la norme calculée entre les positions des bouées Lagrangiennes collocalisées avec les données des courants pour la période de validation du 01 Janvier 2006 au 31 Décembre 2009. 213
3.15 Produit scalaire calculé entre les positions des bouées Lagrangiennes collocalisées avec les données des courants pour la période de validation du 01 Janvier 2006 au 31 Décembre 2009. . . 214

3.16 *Dynamique océanique turbulente obtenue par l'analyse multirésolutions au moyen des données GEKCO à basse résolution et des exposants de singularité à haute résolution du produit MODIS/Aqua pour propager la dynamique turbulente à travers les échelles (dynamique obtenue pour le 02 Août 2007).* 215
3.17 *Dynamique océanique turbulente obtenue par l'analyse multirésolutions au moyen des données GEKCO à basse résolution et des exposants de singularité à haute résolution du produit OSTIA pour propager la dynamique turbulente à travers les échelles (dynamique obtenue pour le 02 Août 2007).* 216

4.1 Position du mouillage BATS. ©BIOS. 227
4.2 LCSs obtenues par la méthode FSLE et par la méthode FTLE à partir des courants GEKCOs, au cours de la campagne BATS Val / Submesoscale Biogeochemistry Cruise Logistics en 2011. 228
4.3 LCSs obtenues par la méthode FSLE et par la méthode FTLE à partir des courants GEKCOs en utilisant la composante géostrophique avec ou sans la composante d'Ekman au cours de la campagne BATS Val / Submesoscale Biogeochemistry Cruise Logistics en 2012. La ligne noire (sur les images à gauche) représente le transit du navire et les points noires la position des stations. Le cadre violet sur la figure (b) indique la position du zoom de la figure 4.4. Le fond de carte représente la topographie dynamique absolue. ©Erik Fields. 229
4.4 LCSs obtenues par la méthode FSLE (Gauche) et la méthode FTLE (Droite) en utilisant la composante géostrophique uniquement (en haut) et en association avec la composante d'Ekman des courants GEKCOs (en bas). En rouge LCSs FSLE / LCSs FTLE calculées chronologiquement, en bleu anti-chronologiquement. 230
4.5 Climatologie moyenne des LCSs calculées par la méthode FSLE anti-chronologique dans le Canal du Mozambique de Janvier 2001 à Décembre 2006. ©[*Tew Kai*, 2009]. 233
4.6 Bathymétrie dans le Canal du Mozambique avec le schéma de circulation générale superposé. SEC : Courant Sud-Equatorial, SEMC : Courant Sud-Est Malgache, NEMC : Courant Nord-Est Malgache, EACC : Courant Côtier Est Africain, AC : Courant des Aiguilles, MCE : Tourbillons du Canal du Mozambique, SEME : dipôle formé par la branche Sud-Est du Courant Malgache. . . . 235

4.7 Photo de la Frégate du Pacifique (Fregata minor), ©Christer Sundstrom. 236

Liste des tableaux

1.1 *Tableau de la classification des ondes du spectre électromagnétique. Source : UIT.* 23
1.2 *Tableau de la classification des ondes THF du spectre électromagnétique utilisées en télédétection. Source : UIT.* 23
1.3 *Tableau des missions (ou séries de missions) en vol actuellement ayant à bord un capteur susceptible de produire de la TSM.* 55
1.4 *Tableau des missions planifiées ayant à bord un capteur susceptible de produire de la TSM.* 55
1.5 *Tableau des missions ayant eu à leur bord au moins un capteur susceptible de produire de la couleur de l'eau.* 63
1.6 *Tableau des missions en activité ayant à leur bord au moins un capteur susceptible de produire de la couleur de l'eau.* 64
1.7 *Tableau des missions planifiées ayant à leur bord au moins un capteur susceptible de produire de la couleur de l'eau.* 64

Introduction

Introduction générale

L'océan, cette mince pellicule d'eau salée aux dimensions verticales mille fois inférieures aux dimensions horizontales, couvre 71% de la surface de la Terre. D'une profondeur moyenne de $3800\ m$, représentant $1/1700^{ime}$ du rayon terrestre, il est une composante essentielle d'un système global (atmosphère, glace, océan, biosphère continentale) qui régit les évolutions du climat sur des périodes allant de la saison à quelques centaines d'années et même plus !
Au même titre que l'atmosphère, l'océan est une énorme machine thermique. Le soleil le réchauffe dans les zones tropicales, et la chaleur ainsi stockée dans l'eau est restituée vers l'atmosphère aux plus hautes latitudes, ce qui le refroidit. C'est ainsi que sont engendrés les courants océaniques profonds et de surface qui transportent cette chaleur de l'équateur vers les pôles.

La compréhension de cet environnement marin a été gouvernée par l'évolution des techniques permettant de naviguer sur les océans afin de les explorer. Des motivations d'ordre économique ont également prévalu ; ce point est illustré par le développement des marines marchandes et de la volonté d'expansion politique dont les flottes de guerre constituent l'un des éléments privilégiés sur des territoires éloignés. La nécessité de comprendre cet environnement hostile a poussé les navigateurs à consigner dans leurs carnets de bord l'ensemble des observations dont ils étaient témoins. Ces observations étaient nombreuses et variées allant de la description de phénomènes physiques (météorologiques, océanographiques, etc.) jusqu'à la description de nouvelles espèces en passant par l'état de santé des marins.

La connaissance de cet environnement était sporadique, régionale et le plus souvent concentrée aux saisons où la navigation s'effectuait sans trop de risque pour l'équipage. Le but de la navigation n'était pas d'étudier l'océan

mais d'en éviter ses dangers au cours des traversées.

Les prémices de l'océanographie moderne

Un exemple significatif relatif à l'émergence de l'océanographie moderne se trouve dans la prise en compte des courants pour la navigation entre l'ancien et le nouveau continent.
A la suite de la découverte de l'Amérique, de sa colonisation, et de la récente création des États-Unis, les échanges commerciaux entre l'Europe et le nouveau monde s'intensifièrent. Le courrier en partance des États-Unis mettant deux fois moins de temps pour arriver que celui en retour, Benjamin Franck-lin (1706 - 1786), nommé Maître des postes en 1736, reçut de nombreuses plaintes relatives à la lenteur d'acheminement des plis. En recherchant les raisons de ces retards il se pencha sur les carnets de bord des navires effectuant les liaisons. Après consultation attentive et de nombreuses discussions avec les capitaines de navires, il mit en relation les températures de l'océan (observations effectuées systématiquement sur tous les navires au moyen de thermomètres immergés en surface) avec la lenteur de certains trajets en direction du nouveau continent. Les trajets s'effectuant au Nord dans les eaux chaudes étaient deux fois moins rapides que ceux plus au Sud dans les eaux froides. De ces observations, il conçut la notion de régime d'écoulement des eaux chaudes vers l'Est et fit ainsi la première description physique du Gulf Stream. Les navires effectuant la liaison Europe - États-Unis reçurent ainsi l'ordre de naviguer dans les eaux froides, et ceux faisant la liaison inverse durent naviguer dans les eaux chaudes. Le courrier fut acheminé par la suite avec les mêmes délais dans les deux sens.
Cet exemple illustre l'importance de l'observation et des outils de mesure en océanographie.

La naissance de l'océanographie moderne

Bien que l'on attribue au Comte italien Luigi Ferdinando Marsili (1658 - 1730), membre de l'Académie Royale des Sciences de Paris, le premier livre d'océanographie avec son ouvrage *"L'histoire physique de la mer"*, et que la France crée en 1752, l'Académie de Marine (société savante composée d'hydrographes, de marins, de naturalistes et d'astronomes qui participent aux explorations maritimes), l'océanographie moderne prend sa naissance au

milieu du XIX^{e} siècle par les écrits de Matthew Fontaine Maury (1806 - 1873) et en particulier son ouvrage *"Physical Geography of the Sea"* publié en 1855. M. F. Maury est considéré comme le père de l'océanographie moderne et de la météorologie navale ; un paragraphe particulier de cet ouvrage (le premier du chapitre VIII) en témoigne :
"We here set out with the postulate that the sea, as well obedient to order. As the air, has its system of circulation, and that this system, whatever it be, and wherever its channels lie, whether in the waters at or below the surface, is in obedience to physical laws. The sea, by the circulation of its waters, doubtless has its offices to perform in the terrestrial economy ; and when we see the currents in the ocean running hither and thither, we feel that they were not put in motion without a cause. On the contrary, we know they move in obedience to some law of Nature, be it recorded down in the depths below, never so far beyond the reach of human ken ; and being a law of Nature, we know who gave it, and that neither chance nor accident had any thing to do with its enactment. Nature grants us all that this postulate demands, repeating it to us in many forms of expression ; she utters it in the blade of green grass which she causes to grow in climates and soils made kind and genial by warmth and moisture that some current of the sea or air has conveyed far away from under a tropical sun. She murmurs it out in the cooling current of the north ; the whales of the sea tell of it and all its inhabitants proclaim it."
Cet extrait montre que la notion de circulation océanique (mouvement des masses d'eau) est intimement liée à celle de forçage ; forçage physique sur toute la couche océanique qui en surface est relié plus particulièrement à celle du forçage atmosphérique.

A cette époque on naviguait à l'estime : la vitesse et la direction des courants marins se déduisaient de la dérive effectuée par le navire entre sa position actuelle et celle qu'il aurait dû avoir sans la présence des courants, et ce en fonction de sa position précédente.
Par la compilation de ces données consignées dans les journaux de bord par les navires, M. F. Maury a établi les premières cartes des courants mondiaux ; la figure 1 illustre ce point pour le Canal du Mozambique.

H.M.S. Challenger

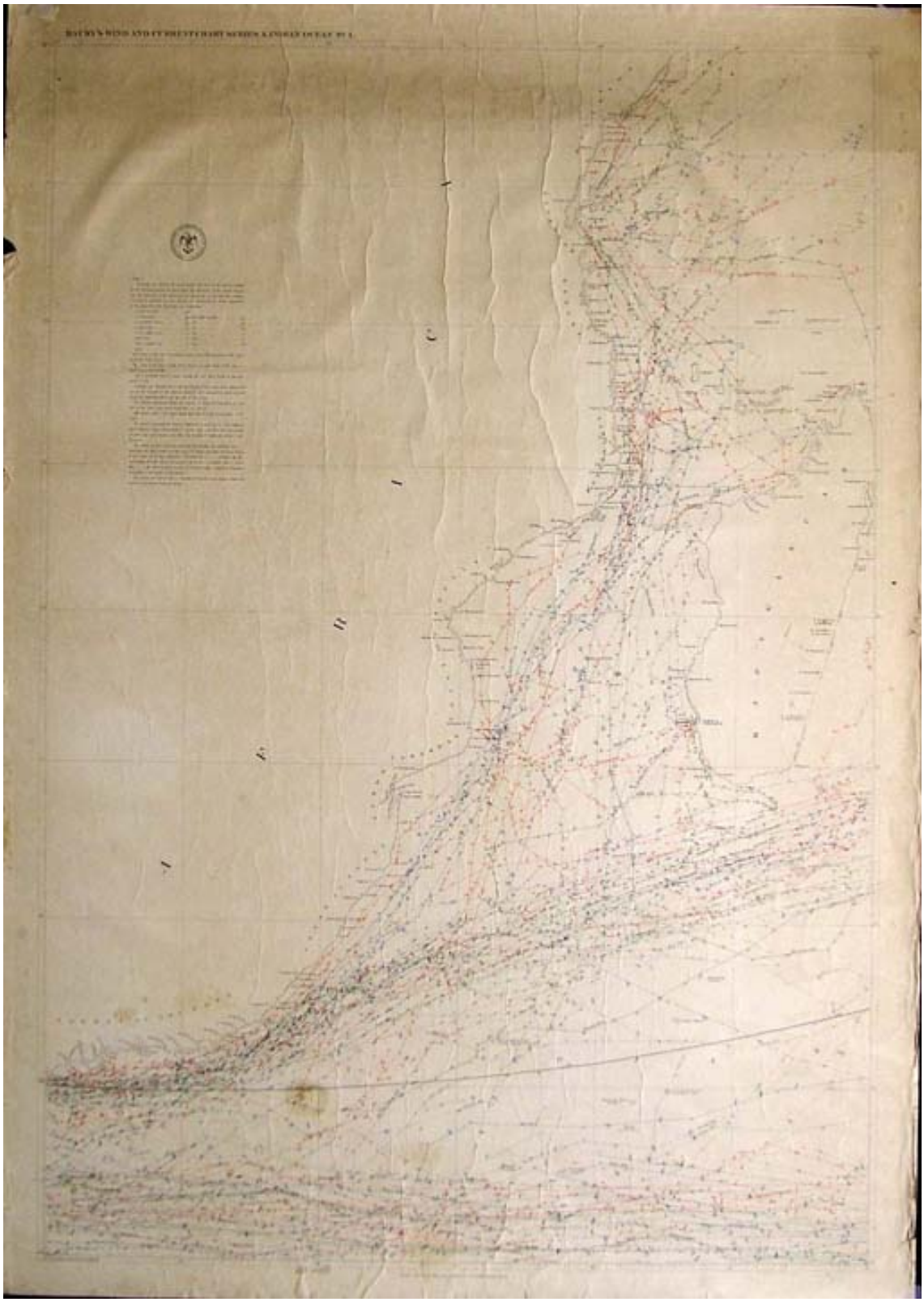

FIGURE 1 – *Illustration d'une "current chart" dans le Canal du Mozambique de M. Maury ; © avec l'aimable autorisation de Mme Jackie Grace (Grace Galleries, LLC).*

Jusqu'en 1870, les navires ("instrument" de prédilection pour observer les océans) étaient construits et armés pour la navigation lointaine avec pour objectifs le commerce, la conquête, la stratégie militaire ou l'exploration de nouveaux territoires. La première expédition dédiée à l'étude scientifique de l'océan est celle du H.M.S. Challenger. En 1870, la *Royal Society of London* eut l'autorisation d'utiliser ce navire de la *Royal Navy* pour mettre en place la plus célèbre expédition océanographique. Pendant deux ans (1870 - 1872), le H.M.S. Challenger (le cinquième du nom) fut complètement modifié et armé pour relever le défi d'un tour du monde permettant mesures et prélèvements tous les 200 milles marins. Entre décembre 1872 et mai 1876, le H.M.S. Challenger parcourut 127 633 km sur les océans Atlantique, Austral, Indien et Pacifique avec comme capitaine George Stong Nares et environ 200 hommes d'équipage. A sa tête, pour les travaux scientifiques, Charles Wyville Thomson et William Benjamin Carpenter, assistés par John Murray, Henry Nottidge Mosely, Alphonse Renard, John Buchanan et l'artiste John James Wild, leurs objectifs ayant été de déterminer :

- le relevé bathymétrique en chaque station,
- la composition des échantillons de sédiments prélevés,
- la composition de l'eau de mer à différentes profondeurs,
- l'évaluation des espèces benthiques, à mi profondeur et en surface récupérées aux moyens de chaluts et de dragues,
- la température observée à différentes profondeurs de la surface jusqu'au grand fond,
- les conditions atmosphériques et météorologiques en chaque station.

Certaines stations furent dédiées à l'estimation de l'écoulement à différentes profondeurs. Cependant l'espoir de W. B. Carpenter de découvrir les mécanismes régissant la circulation océanique n'aboutirent pas, en dépit des acquisitions de température, salinité et densité de l'eau de mer. A la suite de cette campagne, un rapport en 50 volumes mentionnait entre autres que l'océan n'était pas plus profond au centre des bassins et que la composition du sédiment était principalement de deux types (précipités chimiques et résidus organiques). Cette campagne permit aussi la découverte et l'identification de 715 nouveaux genres et 4417 nouvelles espèces.

A la suite de cette grande expédition maritime, en 1880 et 1883 deux navires français, le *Travailleur* et le *Talisman*, furent affrétés par le Muséum

National d'Histoire Naturelle de Paris pour la recherche océanographique et plus particulièrement l'étude des espèces marines. Actuellement certains spécimens récoltés aux moyens de ces deux navires océanographiques figurent encore parmi les collections du Muséum ! Puis les campagnes océanographiques se sont multipliées dans le monde entier (les États-Unis en 1888, l'Allemagne en 1899, les Pays-Bas en 1900) avec comme ambition de mieux connaître la faune et la flore de ce milieu. L'océanographie moderne est donc née du désir des biologistes curieux de savoir si la vie existait dans les grandes profondeurs et des navigateurs désireux de comprendre le fonctionnement de la circulation océanique.

The "steady" Ocean

Pendant près d'un siècle, on accumula les connaissances de l'environnement marin et de la circulation océanique. La circulation moyenne des bassins fut découverte par Sverdrup en 1947, puis l'intensification des courants de bord Ouest par Stommel en 1948, la redécouverte du sous-courant équatorial par Ray Montgomery en 1952 (qui originellement revient à Buchanan en 1885). En 1958, la circulation abyssale fut décrite par *Stommel* [1958] et la théorie de la circulation thermohaline découle des travaux de *Stommel et Arons* [1959a,b]. La méthode usuelle pour déduire la vitesse et la direction des courants étaient la méthode de l'hydrostatique et de la géostrophie. Les courants étaient déduits des observations de la salinité et de la température à différentes profondeurs et positions. Comme les prélèvements se faisaient sur des stations régulièrement très espacées, la circulation océanique était perçue comme régulière, stable, moyenne avec une variabilité quasi nulle. Les variations entre deux stations étaient attribuées à leur différence de position et non à une différence dans le temps. De plus la variation d'une même station à deux instants donnés était attribuée à l'erreur sur la mesure et non à sa variabilité propre, bien que cette notion fut clairement abordée dans les travaux de Nansen et d'Ekman.

La découverte spectaculaire de la variabilité mésoéchelle

Dans les années cinquante, la communauté océanographique prit conscience de l'existence des différentes branches du Gulf-Stream [*Fuglister*, 1951b], de ses méandres [*Fuglister et Worthington*, 1951] et de sa variabilité saisonnière [*Fuglister*, 1951a]. Puis en 1955, Swallow, à l'aide de

bouées dérivantes de subsurface suivies par acoustique, mit définitivement un terme au dogme du "steady ocean" en démontrant que la variabilité spatio-temporelle n'était pas une exception mais la règle générale de la dynamique océanique. Le concept de la dynamique océanique passa abruptement d'un océan ayant une vitesse moyenne de $10 \pm 1 cm.s^{-1}$ à celle de $1 \pm 10 cm.s^{-1}$ pour reprendre l'expression de [*Munk*, 2000a]. Pendant plus de 100 ans, toute la variabilité mésoéchelle est passée au travers de la maille du filet créée par des points d'échantillonnage trop espacés horizontalement sur les sections des campagnes océanographiques.

A partir des années 1950, la stratégie d'échantillonnage dut être complètement repensée pour prendre en compte la variabilité spatio-temporelle. Les campagnes océanographiques via les grands programmes nationaux et internationaux se sont focalisées sur la variabilité saisonnière et la dynamique mésoéchelle. L'étude des structures mésoéchelles, leurs processus de génération, leurs déplacements au sein de la circulation à grande échelle, leurs interactions, leurs relations avec la bathymétrie, le vent, etc., est encore de nos jours un sujet d'étude et de controverse, comme nous le verrons dans le chapitre 2 de ce manuscrit.

Simultanément à cette nouvelle description de la dynamique océanique, la technologie a connu une (r)évolution profonde dans la deuxième partie du XX^{e} siècle. L'arrivée de l'électronique, de l'informatique et de nouveaux matériaux a ouvert les portes à de nouvelles branches de l'océanographie par la conception et l'amélioration de nouvelles méthodes et instruments d'observation *in situ* :

- les sondeurs et les sonars qui permettent de mesurer la profondeur, de connaître le relief des fonds marins, et les premières strates de sédiment,
- les bathysondes permettant d'obtenir des profils de température, de conductivité, de pression, d'oxygène, de concentration de phytoplancton, et plus souvent associées à une "rosette" prélevant des échantillons d'eau de mer à différentes profondeurs,
- les sondes perdables (XBT et XCTD), permettant d'obtenir des profils sans l'arrêt du navire,
- les "poissons remorqués" permettant de faire des profils horizontaux à profondeurs variables,

- les sondes autonomes (exemple : bouées dérivantes),
- les célérimètres qui mesurent la vitesse du son,
- les marégraphes déterminant la hauteur de mer et la hauteur des marées,
- les granulomètres mesurant la quantité de particules et leur distribution en terme de taille,
- les instruments de tomographie permettant de mesurer la température sur des centaines de kilomètres,
- les bennes et les carottiers qui récoltent le sédiment,
- les dragues qui raclent horizontalement les fonds marins,
- les pénétromètres et les flûtes sismiques permettant l'étude de la dynamique des fonds marins,
- les courantomètres, les ADCP qui mesurent la vitesse et la direction des courants,
- les mouillages instrumentés qui permettent l'obtention de séries temporelles de divers paramètres,
- les planeurs sous-marins qui sont de véritables sous-marins téléguidés,
- les robots sous-marins (ROV et AUV) qui filment et photographient en 2D et depuis 2006 en 3D,
- tous les instruments de prélèvement des organismes vivants (filets à plancton, chambres benthiques, biocapteurs),
- les engins habités, etc.

L'essor technologique actuel autorise toujours le développement et la conception de nouvelles méthodes d'observation et de nouveaux capteurs *in situ*. Ayant participé au montage épique de sa bouée de surface sur le port de Marseille par un fort Mistral, je ne peux que citer ici le "YOYO". Ce profileur eulérien développé par le LODYC (Laboratoire d'Océanographie Dynamique et de Climatologie, actuellement LOCEAN) dans le cadre du projet européen MAST III "YOYO 2001 : L'Odyssée de l'Océan", transitait le long d'un câble tendu entre 1000 mètres de profondeur et la surface avec une autonomie de 400 cycles de montée-descente [*Provost et Du Chaffaut*, 1996, 1998]. Ce véhicule était muni de plusieurs capteurs bio-optiques, biologiques, physiques et chimiques, en particulier, l'analyseur chimique de sels nutritifs ANAIS développé au LEGOS permettant de mesurer simultanément les nitrate, silicate et phosphate [*Vuillemin et al.*, 1999; *Thouron et al.*, 2003]. La miniaturisation et la faible consommation d'énergie étant cruciales pour embarquer ce type de capteur sur des instruments autonomes (ayant une faible quantité

d'énergie pour une longue autonomie), le LEGOS, après le succès du prototype ANAIS s'est orienté vers la conception et réalisation de micro-éléctrodes en utilisant des mèthodes électrochimiques [*Lacombe et al.*, 2008; *Jońca et al.*, 2011].

Cet essor technologique a été accompagné par un développement significatif des capacités de calcul et de stockage des ordinateurs. L'émergence des sciences et technologie de l'information a eu de profondes implications en océanographie notamment en modélisation, en utilisation de données satellitaires, et en traitement des signaux d'océanographie. La multidisciplinarité est aujourd'hui nécessaire pour comprendre le fonctionnement de la "machine océan" dont les processus physiques influencent très fortement toute son activité biologique à toutes les échelles.

Un Océan sous pression...

L'océan est à tous les niveaux de plus en plus impacté par l'activité anthropique [*Amara*, 2010]. Les preuves scientifiques abondent pour montrer qu'il est vulnérable, surexploité, et que l'accroissement de l'élévation des concentrations de gaz à effet de serre, cause du changement climatique, a un impact profond sur l'environnement marin [*Guinotte et Fabry*, 2008]. Conséquence d'une surexploitation par la pêche, les prédateurs marins peu à peu disparaissent ce qui modifie toute la chaîne alimentaire marine.

Par l'augmentation des émissions de CO_2 anthropique, le niveau de la mer augmente [*Nerem et al.*, 2006; *Becker et al.*, 2012], l'océan se réchauffe [*Cheung et al.*, 2013], devient plus acide [*Orr et al.*, 2005] et perd de l'oxygène [*Helm et al.*, 2011]. Tous ces processus sont clairement responsables de changement dans l'écosystème et dans la biodiversité marine [*Pörtner*, 2008] ; cependant leurs impacts sur le fonctionnement de l'écosystème marin et sur la mise à disposition des ressources restent peu clairs. La "santé" de l'océan en regard des pressions anthropiques est un enjeu capital qui doit être évalué. Cette nécessaire estimation implique la compréhension des mécanismes qui le régissent aussi bien que leurs implications dans les processus comme la production primaire et secondaire, le cycle des sels nutritifs, la minéralisation, la bioturbation, la stabilisation sédimentaire, mais aussi, dans l'interaction entre les espèces comme la prédation ou la compétition qui régit toute la

chaîne trophique [*Boyen et al.*, 2012]. Il est impératif actuellement pour mieux comprendre les écosystèmes marins de prendre en compte la dynamique océanique à toutes les échelles car elle est la clef de voûte du fonctionnement de l'océan.

Objectif et plan de thèse

Notre travail est centré sur l'étude de différentes méthodes en évaluation de la dynamique océanique à mésoéchelle et submésoéchelle. Les satellites permettent une observation de la dynamique océanique, et fournissent des données de plus en plus précises spatialement, temporellement et spectralement : ils fournissent des observations synoptiques à des fréquences d'observations temporelles croissantes dans des plages spectrales toujours plus étendues. L'utilisation systématique de ces données est au centre de mon travail.

L'ensemble des observations spatiales et des données *in situ* utilisées dans le cadre de cette étude, et qui sont nécessaires pour la validation de la dynamique océanique, est présenté de façon détaillée dans le premier chapitre.

Les données altimétriques et diffusiométriques vont être exploitées dans le chapitre 2 afin d'estimer les courants marins à l'échelle globale. Les composantes géostrophique et d'Ekman de ces courants seront développées et mathématiquement définies pour obtenir un produit de courants de surface (nommé GEKCO). Global, avec une résolution spatiale au quart de degré et une périodicité quotidienne, ce produit sera ensuite validé par diverses données de courants provenant d'instruments *in situ*.

L'utilisation combinée du produit GEKCO (chapitre 2) et des données de température de surface de la mer à super-résolution ($\sim 4\ km$) est présentée au chapitre 3 pour obtenir une nouvelle évaluation de la dynamique océanique à super-résolution. Les méthodes mises en oeuvre dans ce chapitre utilisent l'Océanographie Physique, le traitement non-linéaire du signal et la très récente "Science de la complexité" ; les résultats sont validés dans le Sud-Est de l'Océan Indien.

Le chapitre 4 est consacré à différentes études de la dynamique océanique et des outils associés permettant d'évaluer son impact sur la chaîne trophique en particulier sur ces premiers maillons et sur le comportement de prédateurs marins supérieurs.

Chapitre 1
Du corps noir...aux satellites

Chapitre 1

Les données utilisées

Sommaire

1.1 Introduction 18

1.2 Approche théorique de l'électromagnétisme 19

1.2.1 Ondes électromagnétiques 19

1.2.2 Bande de fréquences des ondes électromagnétiques 22

1.2.3 Le corps noir 24

1.2.4 Le corps gris 25

1.2.5 La fenêtre atmosphérique 26

1.3 Données satellitaires 27

1.3.1 Altimétrie radar à visée nadir 27

1.3.2 Diffusiométrie 39

1.3.3 Température de surface de la mer 50

1.3.4 Couleur de l'océan 60

1.4 Données *in-situ* de courant 67

1.4.1 Données Eulériennes 67

1.4.2 Données Lagrangiennes 72

1.5 Pré-traitement des données 76

1.1 Introduction

Les moyens d'acquérir des observations en vue d'étudier notre environnement sont nombreux et variés. Le plus simple étant d'utiliser nos propres sens pour d'effectuer une mesure directe sur le lieu d'étude.
Ce type d'observation *in situ* permet l'acquisition d'informations très localisées spatio-temporellement avec une précision difficile à estimer qui est due aux limitations de nos capacités sensorielles, et du biais provenant de notre propre interprétation. Ce type d'observation *in situ* est toujours employé en écologie pour étudier le déplacement des espèces, le comptage de leur individus dans une zone d'étude et/ou de connaître leur groupe d'appartenance. Pour éliminer le biais dû au "facteur humain", on met en place des protocoles stricts pour générer des observations à la fois analysables et reproductibles. Les limitations de nos sens et notre aptitude à développer des "outils" de remplacement pour dépasser nos propres limites sensitives, nous ont permis de construire des instruments de mesure afin d'avoir une observation plus précise, plus répétitive, plus rigoureuse etc..
Pour un domaine d'observation aussi vaste que l'océan, il est nécessaire, si l'on s'intéresse à sa dynamique de surface, d'utiliser des moyens d'observation synoptiques et précis. L'avènement de l'ère satellitaire a permis cette observation synoptique de la surface de l'océan ainsi que son environnement associé avec une fréquence d'échantillonnage quasi quotidienne. Cette (r)évolution majeure a été rendu possible par le développement considérable de l'électronique, des instruments de mesure, et la maîtrise de l'électromagnétisme : "*toute observation est basée sur la détection d'un signal ou d'une source de rayonnement*". Cette source peut-être une émission naturelle provenant de l'océan, de l'atmosphère, des terres émergées et même stellaire, ou peut-être générée par un capteur pour analyser sa "déformation". Ce qui nous permet donc de quantifier notre observation est, soit une énergie électromagnétique, soit l'intensité des ondes électromagnétiques. Nous allons donc commencer par rappeler les principes physiques en acquisition des phénomènes en insistant sur le cas particulier des observations satellitales qui occupent une place privilégiée dans nos travaux.

1.2 Approche théorique de l'électromagnétisme

L'énergie électromagnétique est le moyen par lequel une information est transmise de l'objet observé jusqu'au capteur qui l'analyse. Cette information va donc contenir toutes les caractéristiques de l'onde électromagnétique telles que : sa fréquence, son intensité, sa polarisation etc. Les caractéristiques de l'onde électromagnétique sont modifiées par les milieux, en particulier lors de la traversée de l'atmosphère. Nous commençons donc par rappeler les principales caractéristiques du rayonnement électromagnétique.

1.2.1 Ondes électromagnétiques

Une onde électromagnétique est produite par le déplacement d'une charge électrique. Ce déplacement va générer une modification du champ électrique environnant la particule, ce qui va, à son tour, induire une perturbation dans le champ magnétique. De la même façon, une variation d'intensité d'un des deux champs va entraîner une variation de l'autre. Le bilan est qu'une onde d'énergie (constituée d'un champ magnétique et électrique) va se déplacer dans l'espace : on le nomme le tenseur électromagnétique. La figure 1.1 représente le schéma classique du tenseur électromagnétique se déplacement dans un *medium* homogène et isotrope et pour une onde simple sinusoïdale.

Une onde électromagnétique est caractérisée par sa longueur d'onde ou sa fréquence, son intensité ou son amplitude, ainsi que sa direction de propagation. La longueur d'onde est la distance entre deux crêtes (ou creux) successives, généralement représentée par la lettre grecque λ et mesurée en mètre (m). La fréquence est le nombre de crêtes passant par un point fixe en une seconde, et son unité est le Hertz (Hz). L'amplitude est la hauteur de la crête mesurée à partir du point médian. Elle est proportionnelle à l'énergie transportée par cette onde (voir figure 1.2).

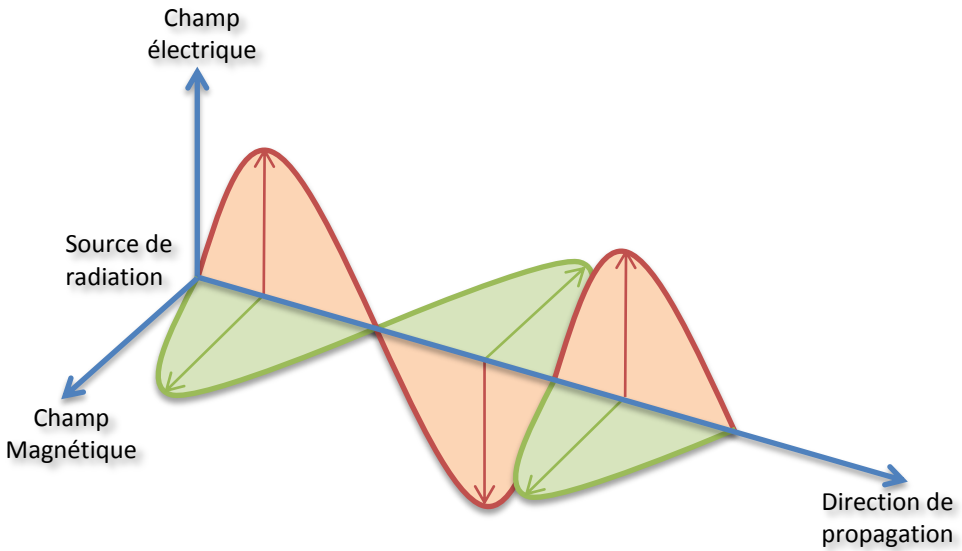

FIGURE 1.1 – *Illustration du tenseur électromagnétique dans le cas simple d'une onde électromagnétique sinusoïdale.*

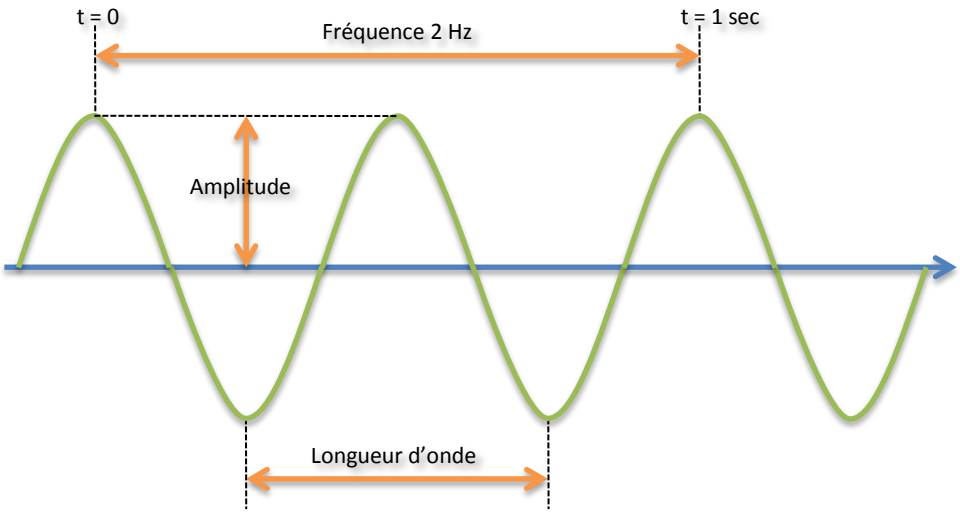

FIGURE 1.2 – *Illustration des caractéristiques d'une onde électromagnétique pour le cas simple de l'onde simple sinusoïdale.*

Dans le cas le plus général, la propagation du tenseur électromagnétique est décrit par les équations Maxwell :

$$\begin{cases} \nabla \times \mathbf{E} &= -\dfrac{\partial \mathbf{B}}{\partial t} \\ \nabla \times \mathbf{H} &= -\dfrac{\partial \mathbf{D}}{\partial t} + J \\ \mathbf{B} &= \mu_0 \mu_r \mathbf{H} \\ \mathbf{D} &= \varepsilon_0 \varepsilon_r \mathbf{E} \\ \nabla \cdot \mathbf{E} &= 0 \\ \nabla \cdot \mathbf{B} &= 0 \end{cases} \tag{1.1}$$

avec :

- **E** : champ électrique,
- **D** : champ de déplacement,
- **H** : champ magnétique,
- **B** : champ d'induction,
- μ_0, ε_0 : perméabilité et permittivité du vide,
- μ_r, ε_r : perméabilité et permittivité relative.

A partir des équations de Maxwell, on obtient les équations de propagation de chacune des composantes du tenseur électromagnétique par exemple le champ électrique :

$$\nabla^2 \mathbf{E} - \mu_0 \varepsilon_0 \mu_r \varepsilon_r \frac{\partial^2 \mathbf{E}}{\partial t^2} = 0 \tag{1.2}$$

Cette équation d'onde peut s'écrire dans le cas d'un champ sinusoïdal :

$$\nabla^2 \mathbf{E} + \frac{\omega^2}{c_r^2 \mathbf{E}} = 0 \tag{1.3}$$

avec :

- $c_r = \frac{c}{\sqrt{\mu_r \varepsilon_r}}$,
- ω : fréquence angulaire.

En résolvant l'équation différentielle ci-dessus, on obtenons :

$$\mathbf{E} = \mathbf{A} e^{i(\mathbf{k}r - \omega t + \phi)} \tag{1.4}$$

avec :

- A : vecteur amplitude de l'onde, (l'amplitude étant la norme de A, la polarisation étant définit ses composantes),
- ϕ : phase,
- k : vecteur d'onde se propageant dans le *medium* ($k = 2\pi\sqrt{\varepsilon_r}/\lambda$, λ étant la longueur d'onde tel que : $\lambda = 2\pi c/\omega$ où c est la vitesse de la lumière dans le vide (note : on définit la fréquence d'onde par ν où $\nu = \omega/2\pi$).

Il est possible d'obtenir des informations sur les propriétés du *medium* traversé par la radiation. Les instruments d'observation vont enregistrer certaines de ces informations pour obtenir des observations de l'échantillon du *medium*. On peut citer par exemple, la quantification de l'énergie de l'onde au moyen de la constante de Planck ($h = 6.626 \times 10^{-34}\ Js^{-1}$), celle-ci étant égale à $Q = h\nu$, l'intensité de l'onde, sa polarisation, sa cohérence (dans le cas d'une onde électromagnétique issue de plusieurs ondes monochromatiques dans une bande de fréquence), la vitesse de groupe, la vitesse de phase, l'effet Doppler, etc. Le sujet de cette thèse n'étant pas l'électromagnétisme toutes ces caractéristiques ne seront pas détaillées, on donne cependant à la fin de la section 1.2 les références nécessaires.

1.2.2 Bande de fréquences des ondes électromagnétiques

Les radiations électromagnétiques couvrent un large éventail de longueurs d'ondes, se déployant des rayons gamma ($\lambda \sim< 10^{-10}\ m$) jusqu'aux ondes radio ($\lambda \sim> 1\ m$) : le spectre électromagnétique. Ce spectre est communément segmenté en différente plages dont les frontières les séparant sont assez mal définies. Le tableau 1.1 récapitule ces principales plages utilisées en télécommunication et dont la classification a été faite par l'Union Internationale des Télécommunications (UIT), agence spécialisée des Nations Unies dont le siège se trouve à Genève (http://www.itu.int/fr/pages/default.aspx).

Le tableau 1.2 décrit les ondes THF (Tremendously High Frequency) qui sont utilisées usuellement en télédétection.

Nous nous intéressons à présent aux caractéristiques de la source de radiation électromagnétique. Pour cela, nous allons tout d'abord nous placer dans

Nom de la bande	Fréquence en Hz	λ en m
Ondes TLF (Tremendously Low Frequency)	$0-3$	$10^{8}-\infty$
Ondes ELF (Extremely Low Frequency)	$3-3.10^{1}$	$10^{7}-10^{9}$
Ondes SLF (Super Low Frequency)	$3.10^{1}-3.10^{2}$	$10^{6}-10^{7}$
Ondes ULF (Ultra Low Frequency)	$3.10^{2}-3.10^{3}$	$10^{5}-10^{6}$
Ondes VLF (Very Low Frequency)	$3.10^{3}-3.10^{4}$	$10^{4}-10^{5}$
Ondes LF (Low Frequency)	$3.10^{4}-3.10^{5}$	$10^{3}-10^{4}$
Ondes MF (Medium Frequency)	$3.10^{5}-3.10^{6}$	$10^{2}-10^{3}$
Ondes HF (High Frequency)	$3.10^{6}-3.10^{7}$	$10-10^{2}$
Ondes VHF (Very High Frequency)	$3.10^{7}-3.10^{8}$	$1-10$
Ondes UHF (Ultra High Frequency)	$3.10^{8}-3.10^{9}$	$10^{-1}-1$
Ondes SHF (Super High Frequency)	$3.10^{9}-3.10^{10}$	$10^{-2}-10^{-1}$
Ondes EHF (Extremely High Frequency)	$3.10^{10}-3.10^{11}$	$10^{-3}-10^{-2}$
Ondes THF (Tremendously High Frequency)	$3.10^{11}-3.10^{17}$	$10^{-9}-10^{-3}$

TABLE 1.1 – *Tableau de la classification des ondes du spectre électromagnétique. Source : UIT.*

Nom de la bande	Fréquence en Hz	λ en m
Rayons Infrarouges extrêmes (EIR)	$3,00.10^{10}-2,00.10^{10}$	$1,50.10^{-7}-1,00.10^{-3}$
Rayons Infrarouges lointaines (FIR)	$2,00.10^{10}-5,00.10^{10}$	$6,00.10^{-7}-1,50.10^{-7}$
Rayons Infrarouges moyennes (MIR)	$5,00.10^{10}-1,00.10^{11}$	$3,00.10^{-7}-6,00.10^{-7}$
Rayons Infrarouges Proches (NIR)	$1,00.10^{11}-3,84.10^{11}$	$0,78.10^{-6}-3,00.10^{-7}$
Rayons Visibles	$3,84.10^{11}-7,89.10^{11}$	$7,80.10^{-7}-3,80.10^{-7}$
Rayons Ultraviolets	$8,49.10^{11}-3.10^{12}$	–
Rayons X mous	$3,00.10^{14}-3,00.10^{15}$	–
Rayons X durs	$3,00.10^{15}-3,00.10^{16}$	–
Rayons gamma mous	$3,00.10^{16}-3,00.10^{17}$	–
Rayons gamma durs*	$3,00.10^{17}-\infty$	–

*Notons que les rayons gamma durs ne font plus partie de la bande THF.

TABLE 1.2 – *Tableau de la classification des ondes THF du spectre électromagnétique utilisées en télédétection. Source : UIT.*

le cadre idéal où l'objet émetteur de la source de radiation a une température supérieure au zéro absolu.

1.2.3 Le corps noir

Le corps noir est le modèle physique théorique utilisé pour représenter les émissions électromagnétiques d'un objet en fonction de sa température. Il absorbe toutes les radiations incidentes provenant de toutes les directions. Pour une température et une longueur d'onde données, aucun objet ne peut émettre plus que le corps noir, et celui-ci transforme toute la chaleur qu'il reçoit en énergie de rayonnement selon la loi de Planck :

$$L_\lambda = \frac{2\pi hc^2}{\lambda^5[\exp^{(\frac{hc}{kT\lambda})} - 1]}\ W.m^{-2}.sr^{-1}.\mu m^{-1} \tag{1.5}$$

avec :

- L_λ : luminance énergétique monochromatique en $W.m^{-2}.sr^{-1}.\mu m^{-1}$,
- λ : longueur d'onde fixée dans un angle solide d'un stéradian pour une surface de $1\ m^2$ où le corps noir rayonne en μm,
- h : constante de Planck ($6,6256.10^{-34}\ W.s^2$),
- k : constante de Boltzmann ($1,3805.10^{-23}\ W.s.K^{-1}$),
- T : température du corps noir en Kelvin,
- c : vitesse de la lumière ($2,9979.10^8\ m.s^{-1}$).

Il est à noter que plus la longueur d'onde est petite (ou plus la fréquence est grande), plus l'énergie par photon est grande. Si on s'intéresse à la puissance totale émise ou luminance totale (L_{Tcn}) du corps noir, il est nécessaire d'intégrer l'équation 1.5 sur toutes les longueurs d'ondes et dans toutes les directions. En faisant cela, on obtient la loi de Stefan-Boltzmann qui s'exprime selon l'équation :

$$L_{Tcn} = \sigma T^4\ W.m^{-2} \tag{1.6}$$

où σ représente la constante de Stefan-Boltzmann ($5.6710^{-8} Wm^{-2}K^{-4}$). Il est possible alors d'en déduire la longueur d'onde pour le rayonnement maximal en posant $\frac{\mathrm{d}L_\lambda}{\mathrm{d}\lambda} = 0$ pour obtenir λ_{max}. Par ce cheminement nous obtenons la loi de déplacement de Wien :

$$\lambda_{max} = \frac{2898.3}{T}\ \mu m.K \tag{1.7}$$

Il est simple de déduire que plus la température est haute, plus la longueur d'onde pour le maximum d'émission est petite. Malheureusement, toute cette théorie n'est pas applicable aux corps naturels car ils ne sont pas des corps noirs. Ils émettent et absorbent à des taux inférieurs à ceux du corps noir. Pour cela il est nécessaire d'introduire la notion de corps gris.

1.2.4 Le corps gris

On définit l'émissivité comme le rapport entre la luminance du corps réel et celle du corps noir placé dans les mêmes conditions de température et de longueur d'onde. La luminance totale d'un corps gris (L_{Tcg}) est :

$$L_{Tcg} = e\sigma T^4 W.m^{-2} \tag{1.8}$$

où e est l'émissivité qui est comprise entre zéro et un et qui est sans dimension. Cette émissivité est une propriété physique qui dépend de la nature et de la surface des matériaux dont le corps gris est composé. Elle peut aussi être directionnelle dans le sens où le corps que l'on cherche à observer peut rayonner différemment suivant l'angle d'observation. (Cette notion est primordiale pour les diffusiomètres).

Si on désire observer notre planète et plus précisément l'océan depuis l'espace, il est nécessaire de se demander quelles luminances sont accessibles depuis l'espace. En effet le problème majeur est que le rayonnement que l'on cherche à observer doit traverser l'atmosphère. L'atmosphère étant constituée de molécules, celles-ci vont absorber une partie du rayonnement provenant à la fois de l'espace (rayonnement solaire et stellaire) mais aussi de la surface terrestre (rayonnement océanique et continental). L'atmosphère se comporte donc comme un filtre fonctionnant dans les deux sens. Si la vie existe sur notre planète c'est que l'atmosphère nous protège en absorbant la plupart des rayonnements nocifs pour la vie en provenance de l'espace, mais aussi en retenant une partie de la chaleur rayonnée par la terre elle-même, ce qui nous permet d'avoir des températures propices à la vie. Il est aussi important de considérer

que les molécules qui constituent l'atmosphère ont aussi leurs propres luminances.

1.2.5 La fenêtre atmosphérique

La fenêtre atmosphérique est le domaine du spectre électromagnétique où l'atmosphère est presque transparente. La plupart des radiations terrestres dont les longueurs d'ondes appartiennent à la fenêtre atmosphérique sont très peu absorbées par l'atmosphère et se perdent dans l'espace. Ce sont ces mêmes longueurs d'ondes qui peuvent être utilisées pour observer la terre depuis l'espace. La figure 1.3 représente la fonction de transmission (ou transmittance) de l'atmosphère en fonction de la longueur d'onde du signal.

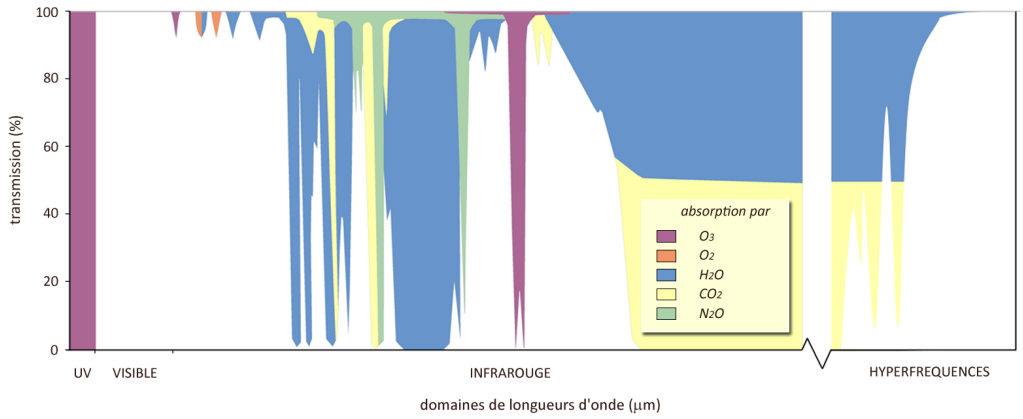

FIGURE 1.3 – *Représentation de la fenêtre atmosphérique de transmission (en blanc sur cette représentation). (http://e-cours.univ-paris1.fr/modules/uved/envcal/html/rayonnement/index.html). ©Université Paris 1*

De nombreuses autres propriétés fondamentales associées aux ondes électromagnétiques ainsi que celles de la fenêtre atmosphérique n'ont pas été abordées dans cette sous-partie. Cependant il n'est pas nécessaire de les mentionner pour la compréhension de ce document. Si le lecteur désire approfondir ses connaissances sur ce sujet, celui-ci pourra le faire en consultant le "*Manual of remote sensing : Theory, instruments and techniques*" de [*Reeves et al.*, 1975]. Ce manuel étant difficile à compulser du fait de son ancienneté, la seconde édition de l'ouvrage "*Fundamentals of remote sensing*" de *Joseph* [2005] est tout à fait appropriée. Enfin pour les francophiles, on pourra consulté "*Introduction à l'étude de la télédétection aérospatiale et de son vocabulaire*" de *Paul* [1991].

1.3 Données satellitaires

Nous allons tout d'abord présenter la donnée altimétrique dans la sous-partie 1.3.1, puisque cette donnée océanographique globale de haute précision, est depuis 1992, avec le lancement de TOPEX/POSEIDON, le fer de lance du LEGOS. La topographie dynamique provenant de l'altimétrie permet d'obtenir en utilisation conjointe avec la diffusiométrie des produits de dynamique océanique à mésoéchelle qui seront présentés dans le chapitre 2. Nous allons donc décrire dans la seconde sous-partie (1.3.2) les capteurs diffusiométriques.
La sous-partie 1.3.3 va nous permettre d'exposer une des plus anciennes données satellites, puisque qu'en 1967 les premiers satellites dédiés à la météorologie ont embarqué des capteurs permettant d'observer la Température de Surface de la Mer (TSM). Enfin la dernière sous-partie passera en revue le principe de la mesure, ainsi que les différents capteurs permettant d'observer depuis l'espace le premier maillon de la chaîne trophique marine : Le phytoplancton ou la couleur de l'océan.

1.3.1 Altimétrie radar à visée nadir

Au cours des années 1960 est apparue l'idée de concevoir un capteur embarqué sur un satellite qui aurait la capacité de mesurer le niveau des océans de manière globale et à des fins scientifiques [*Kaula*, 1966]. C'est en 1969 sous l'égide de la NASA, au congrès de Williamstown que la faisabilité d'un tel instrument est évoquée. Quelques années plus tard, en 1973, à bord de SKYLAB, la NASA teste le premier capteur altimétrique.

a Principe de la mesure

Un altimètre est un radar dont la visée est verticale (orienté vers la terre) qui émet une onde électromagnétique. Ce capteur actif[1], qui envoie son signal vers la surface terrestre, reçoit le signal rétrodiffusé renvoyé par la cible. Par la connaissance de la vitesse de propagation de l'onde ainsi que du temps entre

1. Un capteur actif est un dispositif qui va émettre un signal et va en analyser l'écho pour en déterminer une mesure.

son émission et sa réception, il est possible de mesurer la distance entre le capteur et sa cible par la relation :

$$D = \frac{v.t}{2} \tag{1.9}$$

avec :

- D : distance entre le capteur et sa cible en m,
- v : vitesse de propagation de l'onde $m.s^{-1}$,
- t : temps entre l'émission et la réception de l'onde en s.

Pour avoir une précision centimétrique voire millimétrique de cette distance D, il est nécessaire de connaître avec exactitude la position du satellite sur sa trajectoire. Les satellites embarquent pour cela plusieurs systèmes permettant leur positionnement avec une extrême précision (http://ilrs.gsfc.nasa.gov, http://ids-doris.org, http://www.schriever.af.mil/GPS/) :

- positionnement par le système télémétrique LASER [*Pearlman et al.*, 2002],
- positionnement par le système Doppler Orbitography and Radiopositioning Integrated by Satellite (DORIS) [*Jayles et al.*, 2006],
- positionnement par les satellites du Global Positionning System (GPS) [*Remondi*, 1985].

La principale difficulté pour obtenir D est d'estimer la vitesse de propagation de l'onde électromagnétique dans les media qu'elle va traverser ainsi que la déformation de son écho par la cible. De plus, si l'objectif est d'obtenir non pas la distance D mais le niveau de la mer ou la topographie dynamique, il est crucial d'avoir une surface de référence (figure 1.4).

Les ondes electromagnetiques couramment utilisées pour l'altimétrie radar sont les bandes C et Ku qui ont respectivement des fréquences de $\sim 5,3\ Ghz$ et $\sim 13,6\ Ghz$ et qui se situent dans les micro-ondes (ondes SHF du tableau 1.1). Les bandes S ($\sim 3,2\ Ghz$) et K_a ($\sim 35\ Ghz$) sont aussi employées.

Les "formes d'onde altimétriques" sont les courbes représentant l'évolution de la puissance du signal reçue par le capteur en fonction du temps. La figure 1.5(a) nous montre ces formes d'ondes dans le cas idéal d'une surface plane, et la figure 1.5(b) dans le cas plus complexe d'une surface hétérogène ayant des discontinuités dues à la topographie de la cible. Il est à noter que par l'analyse

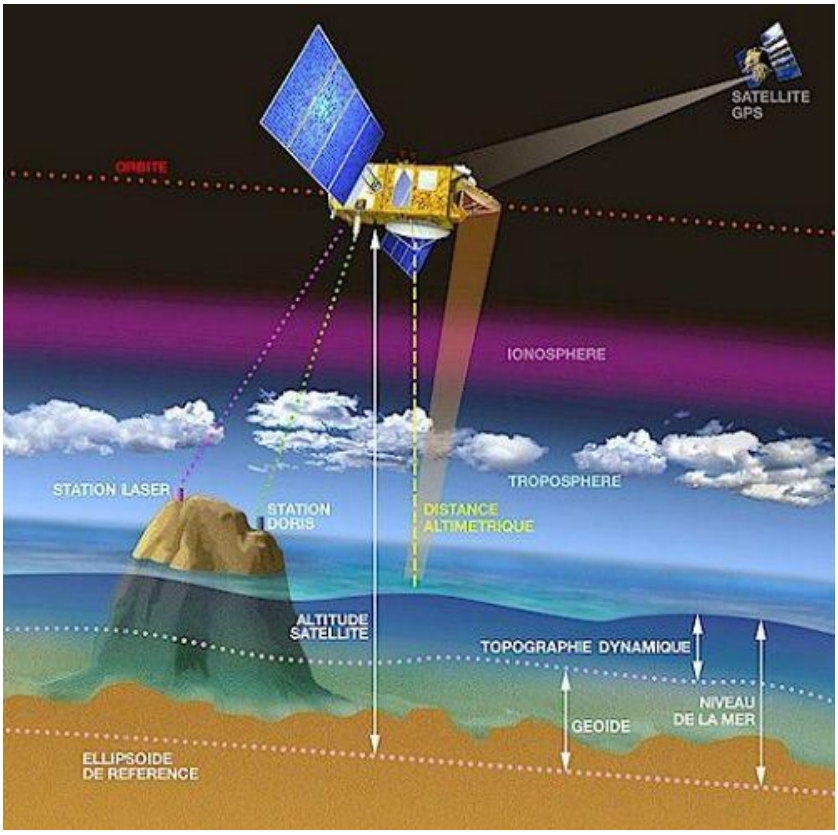

FIGURE 1.4 – *Illustration du principe de l'altimétrie. (http://www.aviso.oceanobs.com).* ©*CNES.*

de l'écho radar, il est possible de déduire la hauteur des vagues provenant d'une cible océanique.

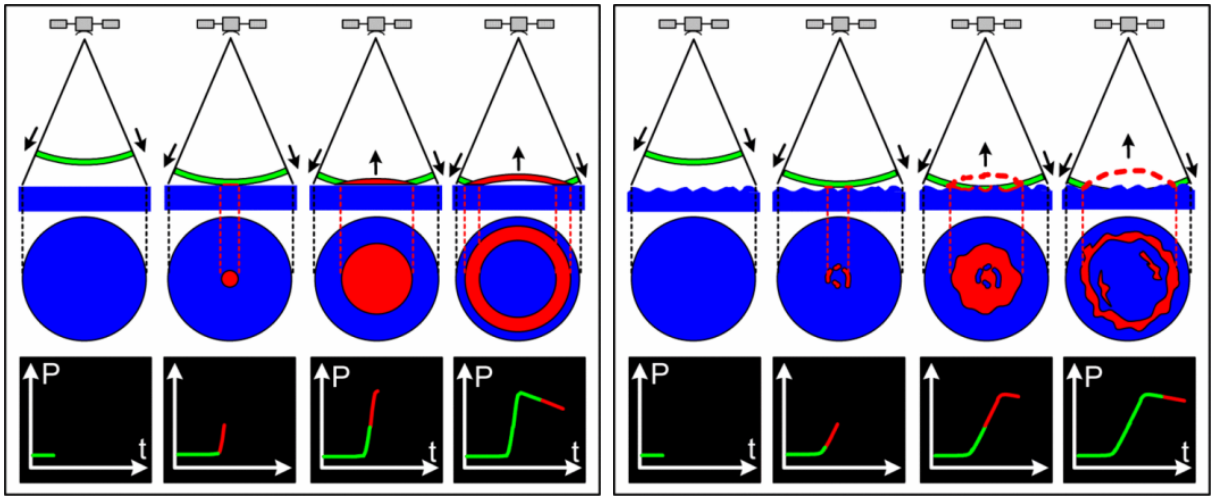

(a) Le cas idéal d'une surface plane.

(b) Le cas réel d'une surface topographiquement hétérogène.

FIGURE 1.5 – Représentation des formes d'ondes en fonction du temps. ©CNES.

Si l'on observe la forme d'onde plus attentivement (figure 1.6), on constate que le signal obtenu (courbe verte) est extrêmement bruité et assez éloigné du modèle mathématique le caractérisant (courbe rouge) : le modèle de Brown. Il est donc nécessaire si l'on veut pouvoir utiliser ces formes d'onde d'en prendre plusieurs et de les moyenner. Cette somme de formes d'onde se nomme communément (dans le jargon de la télédétection) : un paquet d'onde. La figure 1.7 représente ce paquet d'onde dans le cas concret d'une moyenne obtenu à partir de 90 ondes.

Le milieu du front de montée (le point médian de la puissance de l'écho) va finalement permettre de calculer le retard de l'écho en retour et ainsi d'en déduire le temps mis par l'impulsion pour parcourir la distance aller-retour entre le satellite et la cible qui est dans le cas présent la surface terrestre (voir équation 1.9). La distance ou 'range' est ainsi la mesure la plus élémentaire de l'altimètre. Cette distance doit toutefois être estimée en tenant compte d'un certain nombre de corrections [*Fu et al.*, 1994], [*Cheney et al.*, 1994] :

- les corrections instrumentales (dues au fonctionnement de l'altimètre et au rayonnement naturel),
- les corrections atmosphériques sur les allongements de trajet du signal causés par la propagation dans différentes couches de l'atmosphère (ionosphère, troposphère, etc.),

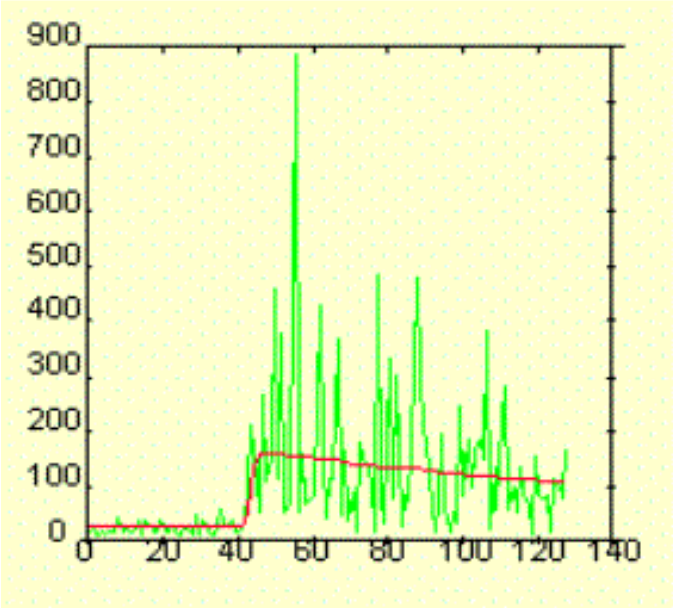

FIGURE 1.6 – *Représentation d'une forme d'onde réelle (courbe verte) et de sa courbe théorique (courbe rouge). L'axe des abscisses représente le temps, celui des ordonnées la puissance reçue de l'écho.*

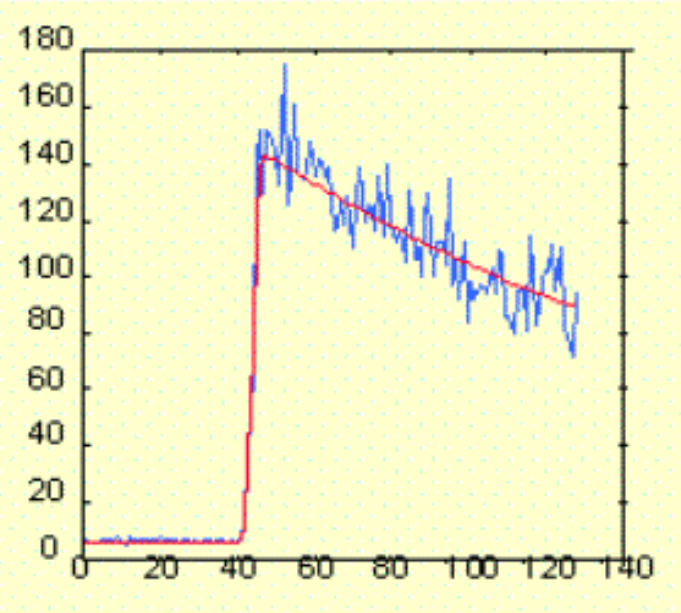

FIGURE 1.7 – *Représentation d'un paquet d'onde obtenu avec 90 formes d'onde réelles (courbe bleue) et de sa courbe théorique (courbe rouge) en fonction du temps (axe des abscisses) et de la puissance reçue (axe des ordonnées).*

- les corrections géophysiques (les marées, l'état de mer, etc.).

Le calcul du niveau de la mer se fait donc en effectuant la différence entre l'altitude du satellite (calculée à partir de l'ellipsoïde) et la distance altimétrique D corrigée.

b Historique et principales missions

Les premières missions embarquant un altimètre sont avant tout des missions pluridisciplinaires comme GEOS-3 (1975), SEASAT (1978), GEOSAT (1985) et ERS-1 (1991). En 1992, une coopération franco-américaine lance le premier satellite dédié exclusivement à l'altimétrie spatiale. Il s'agit de la première mission à long terme de mesure topographique des océans qui prend fin en 2006. Le satellite issu de cette fructueuse coopération embarquait alors un altimètre américain (TOPographic EXperiment) et un altimètre européen (POSEIDON), dont les principales missions consistaient à étudier la circulation océanique, le transport de chaleur dans les océans, à modéliser les marées et surveiller les variations du niveau moyen des océans à l'échelle mondiale. L'Europe poursuivit ses efforts dans la lignée de ERS-1 avec les missions ERS-2 (1995) puis ENVISAT (2002), dédiées à l'étude de l'environnement et plus précisément au changement climatique. Quant à Cryosat-2 (2010) qui est aussi un satellite altimétrique de l'agence spatiale européenne (ESA), il est plutôt dédié à l'observation des glaces polaires. Du côté américain, une mission à visée militaire voit le jour par le lancement du satellite Global Follow On (GFO), en 1998. Les données de ce satellite ont ensuite été rendues publiques. Les prouesses de TOPEX/POSEIDON ont permis à la communauté franco-américaine de concevoir dans les années 2000, une nouvelle génération d'altimètres. Notamment en 2001 avec la mission JASON-1, placé sur la même orbite que TOPEX/POSEIDON afin de pérenniser les mesures et ainsi d'approfondir nos connaissances des différents phénomènes océanographiques (figure 1.8) sur une période temporelle plus étendue. En 2011, la Chine a lancé son premier capteur altimétrique embarqué sur le satellite HY-2 dont la mission est l'étude de l'environnement marin.

Qu'en est-il du futur de l'altimétrie ?

En vue de toujours améliorer la précision de la mesure, la bande Ka est mise à l'épreuve avec le lancement de SARAL (2013). En 2014 le satellite Sentinel-

FIGURE 1.8 – *Vue d'artiste des différentes missions altimétriques. ©CNES.*

3 devrait être lancé avec pour mission inscrite au programme du GMES, la surveillance de la Terre et l'océanographie opérationnelle. Dans un avenir plus lointain plusieurs options sont avancées, soit les missions altimétriques vont se diriger vers des instruments à large fauchée SWOT (2019), soit vers une constellation d'au moins trois satellites JASON-3 (2014), HY-2B, Sentinel-3C, JASON-CS séries. Nous allons voir dans la sous-partie suivante pourquoi il est nécessaire de prendre une de ces deux options au travers des produits altimétriques actuels.

c Données utilisées

A la différence des instruments imageurs (que nous allons voir dans les sous-parties suivantes), les altimètres sont tous actuellement des capteurs à visée nadir, qui acquièrent une unique mesure à un instant donné, le long de leurs traces au sol. Cette particularité est représentée sur la figure 1.9 pour le satellite TOPEX/POSEIDON. L'inter-trace est, si on se place par exemple à l'équateur, de 315 km. Il est donc difficile avec un seul altimètre d'étudier des processus physiques qui ont une dimension inférieure puisque ces processus à l'équateur passent "sous la maille du filet" et ne seront pas détectés. Il en est de même pour la résolution temporelle qui est d'environ dix jours pour ce

satellite.
Il est donc nécessaire de combiner plusieurs informations altimétriques provenant de plusieurs satellites pour obtenir des cartes avec une résolution spatio-temporelle adéquate à l'observation des processus physiques à mésoéchelles [*Le Traon et al.*, 1998]. Le développement de ce type de produits combinés est effectué par le projet Data Unification and Altimeter Combinaison System du Segment Sol multimissions d'ALTimétrie, d'Orbitographie et de localisation précise (SSALTO/DUACS) [*Ducet et al.*, 2000; *Pascual et al.*, 2006]. Une description complète de toute cette gamme de produits développée par SSALTO/DUACS se trouve en suivant le lien : (http://www.aviso.oceanobs.com/fr/donnees/boite-a-outils/manuels-d-utilisation-des-donnees-aviso/index.html).

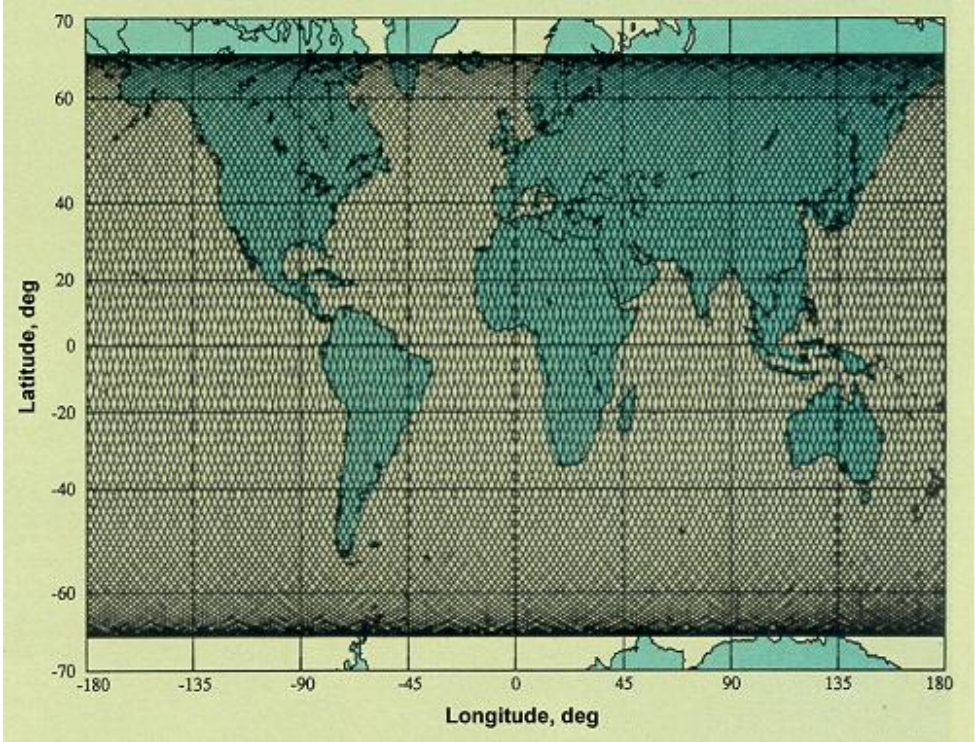

FIGURE 1.9 – *Illustration des traces du satellite TOPEX/POSEIDON. ©CNES.*

Les produits utilisés en altimétrie pour l'obtention des courants géostrophiques qui vont être abordés dans le chapitre 2, sont les cartes de topographie dynamique absolue (MADT), sur grille Mercator avec une résolution de $1/3° \times 1/3°$. Ces produits sont disponibles en temps quasi-réel (NRT) ainsi qu'en temps différé et leurs archives couvrent la période de 1992 à nos jours. Le manuel utilisateur de ces données peut être téléchargé à cette adresse : http://www.aviso.oceanobs.com/fileadmin/documents/data/tools/

hdbk_duacs.pdf.

En accord avec la figure 1.4, cette MADT est une hauteur de mer calculée par rapport au géoïde. Elle peut être décomposée en une topographie dynamique moyenne (MDT) et une anomalie de hauteur de mer (SLA). Les figures 1.10, 1.11, 1.12 illustrent ces données pour le 01/08/2007 en global et sur la zone Sud-Ouest de l'Océan Indien que nous allons suivre tout au long de ce document.

Nous pouvons identifier sur la SLA ou sur la MADT plusieurs zones océaniques où les zones frontales ainsi que la variation d'amplitude sont extrêmement marquées : les courants de bord Ouest (Gulf Stream, Kiroshio, etc.), le courant du Brésil avec au Sud le courant des Malouines, le courant des Aiguilles avec sa rétroflexion, le courant circumpolaire.

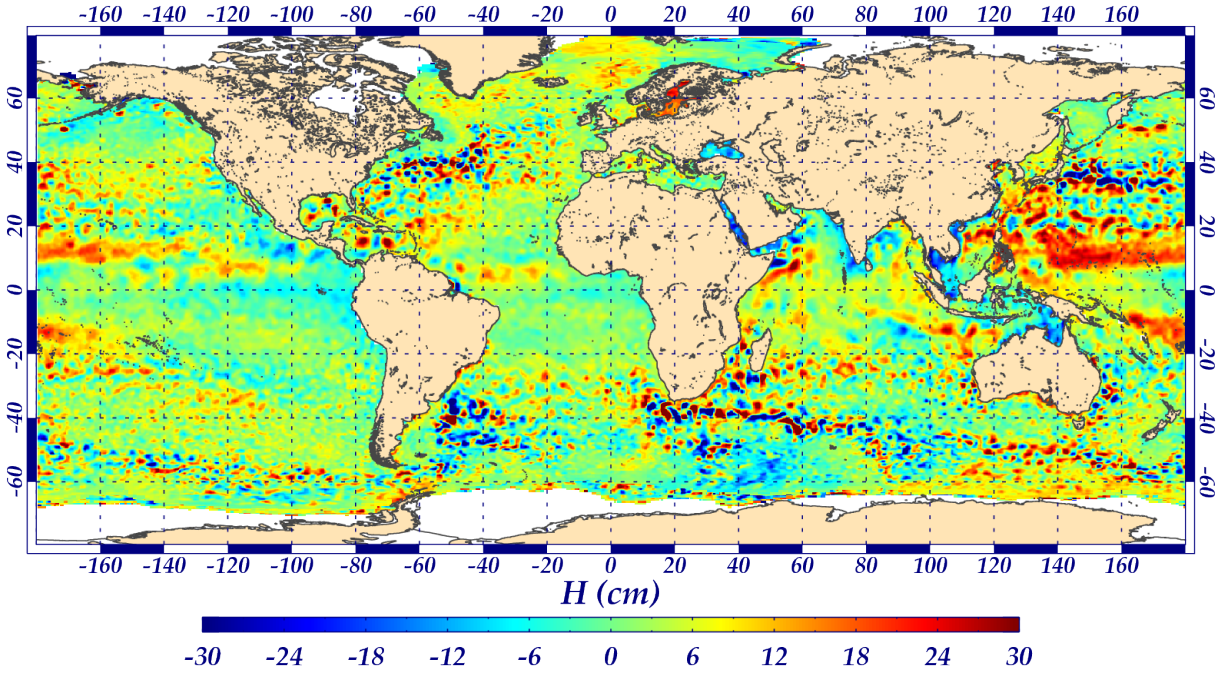

(a) SLA globale pour le 01/08/2007.

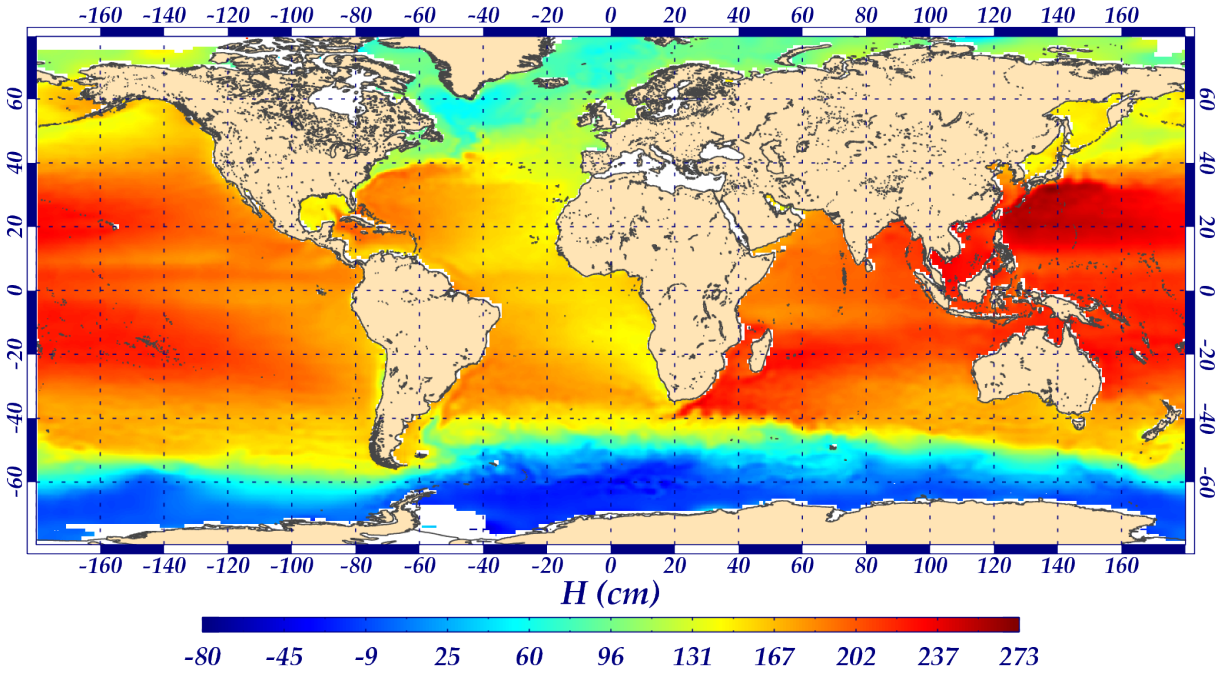

(b) MDT de *Rio et Hernandez* [2004] globale pour le 01/08/2007.

FIGURE 1.10 – SLA et sa MDT associée utilisées dans l'article [*Sudre et Morrow*, 2008].

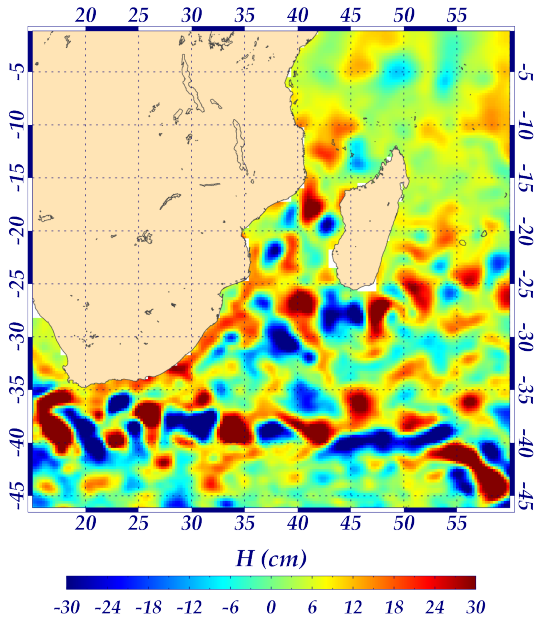

(a) SLA au Sud-Ouest de l'Océan Indien pour le 01/08/2007.

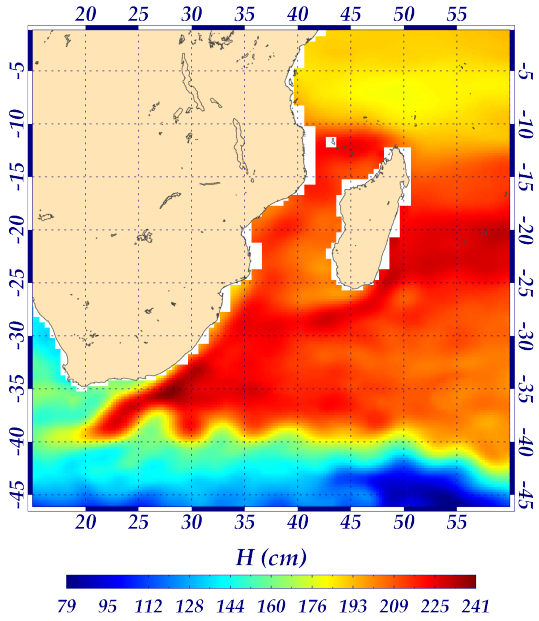

(b) MDT de *Rio et Hernandez* [2004] au Sud-Ouest de l'Océan Indien pour le 01/08/2007.

FIGURE 1.11 – SLA et sa MDT associée au Sud-Ouest de l'Océan Indien utilisées dans l'article [*Sudre et Morrow*, 2008].

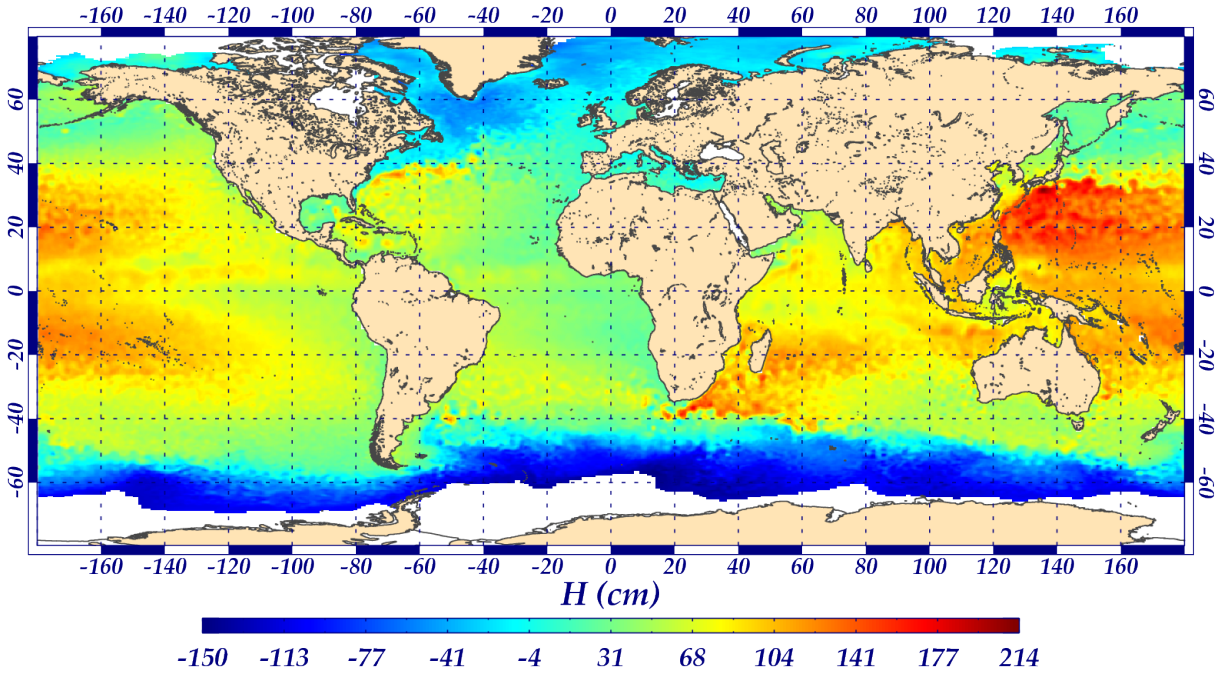

(a) MADT globale pour le 01/08/2007.

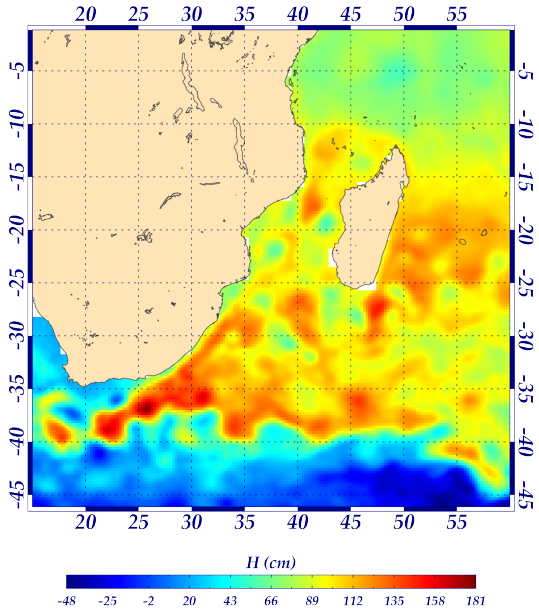

(b) MADT au Sud-Est de l'Océan Indien pour le 01/08/2007.

FIGURE 1.12 – MADT globale et au Sud-Ouest de l'Océan Indien utilisées dans l'article [*Sudre et al.*, 2013].

1.3.2 Diffusiométrie

Avant l'ère satellitaire, les observations des vents à la surface des océans étaient irrégulières dans le temps, parfois approximatives et la plupart du temps provenaient de navires et de quelques bouées ancrées. La diffusiométrie a vu le jour au cours de la seconde guerre mondiale. Au cours de cette guerre, les premiers radars, employés pour détecter la présence d'objets, avaient des échos qui étaient fortement bruités par les nombreux signaux parasites provenant de la réponse du vent sur la surface océanique, ce phénomène n'était alors pas connu. Il fallut attendre la fin des années soixante pour mettre en relation la réponse des radars avec le vent [*Bradley*, 1971]. C'est encore à bord du SKYLAB de la NASA en 1973 que le premier diffusiomètre spatial montra la faisabilité d'obtenir la direction et la vitesse du vent sur les océans [*Moore et al.*, 1975].
Dans la sous-partie suivante le principe de la mesure des diffusiomètres est explicité, cependant d'autres capteurs comme le SAR ou les capteurs polarimétriques passifs permettent aussi d'avoir le champ complet du vent (vitesse et direction). Les altimètres que nous avons vu précédemment et les radiomètres micro-ondes permettent uniquement d'obtenir l'intensité du vent et non sa direction.

a Principe de la mesure

Lorsque le vent souffle sur l'océan, des vagues de capillarité (de quelques centimètres) se forment à sa surface. Ces structures ont une orientation privilégiée et vont modifier les propriétés de rugosité de la surface océanique. Une réponse anisotrope en fonction de l'angle de visée va donc être générée par la surface océanique et le coefficient de rétrodiffusion d'une onde lorsqu'elle vient frapper la surface va en être fonction. Les diffusiomètres sont donc des radars ajustés pour mesurer précisément le coefficient de rétrodiffusion σ^0 de l'océan.

De la même façon que les altimètres, les diffusiomètres envoient des 'pulses' micro-ondes (en bande C ou en bande Ku) et mesurent l'intensité de la rétrodiffusion ainsi que le temps entre l'émission et la réception. Ces deux informations permettent d'obtenir l'intensité du coefficient σ_0 et la localisation du point de la mesure sur la surface océanique. Le coefficient de rétrodiffusion

(défini comme la puissance réémise par unité de flux incident et par unité de surface de la cible) s'exprime ainsi :

$$\sigma_0 = \frac{(4\pi)^3 D^4}{G_0^2 \lambda^2 A_w} \left[\frac{P_r}{P_t}\right] \tag{1.10}$$

avec :

- σ_0 : coefficient de rétrodiffusion par unité de flux incident et par unité de surface de la cible en dB,
- D : distance mesurée,
- G_0 : gain maximum de l'antenne,
- λ : longueur d'onde,
- A_w : surface pondérée,
- P_r : puissance de réception,
- P_t : puissance de transmission.

Le gain d'antenne est dépendant du diagramme de radiation. Ce gain est la partie la plus complexe du signal à obtenir pour estimer une calibration absolue du capteur. Pour cela, il est nécessaire de faire des calibrations du capteur en vol au moyen de cibles dont le coefficient de rétrodiffusion est parfaitement connu [*Ulaby et al.*, 1982].

Pour estimer la direction du vent, le diffusiomètre se base sur le fait que les vagues sont allongées dans la direction perpendiculaire au vent. Pour évaluer cette direction, il est nécessaire d'avoir plusieurs mesures co-localisées avec différent angles d'azimut. Ceci est réalisé en utilisant plusieurs antennes avec des orientations différentes par rapport à la direction de déplacement du satellite [*Naderi et al.*, 1991] ou par l'utilisation d'une antenne à balayage conique [*Wu et al.*, 1994]. L'onde délivrée par chaque antenne est caractérisée par une direction de propagation par rapport à la verticale.
A la différence des altimètres qui ont une visée nadir, les diffusiomètres ont une visée latérale avec un angle d'incidence θ. De plus, la direction du champ électromagnétique par rapport au plan d'incidence doit être connue, ce que l'on nomme la polarisation. Il existe quatre configurations de polarisation habituellement utilisées en télédétection radar : HH, VV, VH et HV. La première lettre indique la polarisation de l'onde émise, quant à la seconde celle de l'onde reçue (H est une polarisation horizontale et V une polarisation verticale). Actuellement seules les configurations HH et VV sont utilisées pour les diffusiomètres. En faisant varier l'angle θ, le diffusiomètre (à la différence des altimètres) va

permettre d'échantillonner plusieurs cibles contiguës. La figure 1.13 représente la résolution spatiale d'échantillonnage qui peut être décomposée en une résolution radiale (R_r dans la direction de l'onde émise) et une direction azimutale (R_a dans la direction du déplacement du satellite).

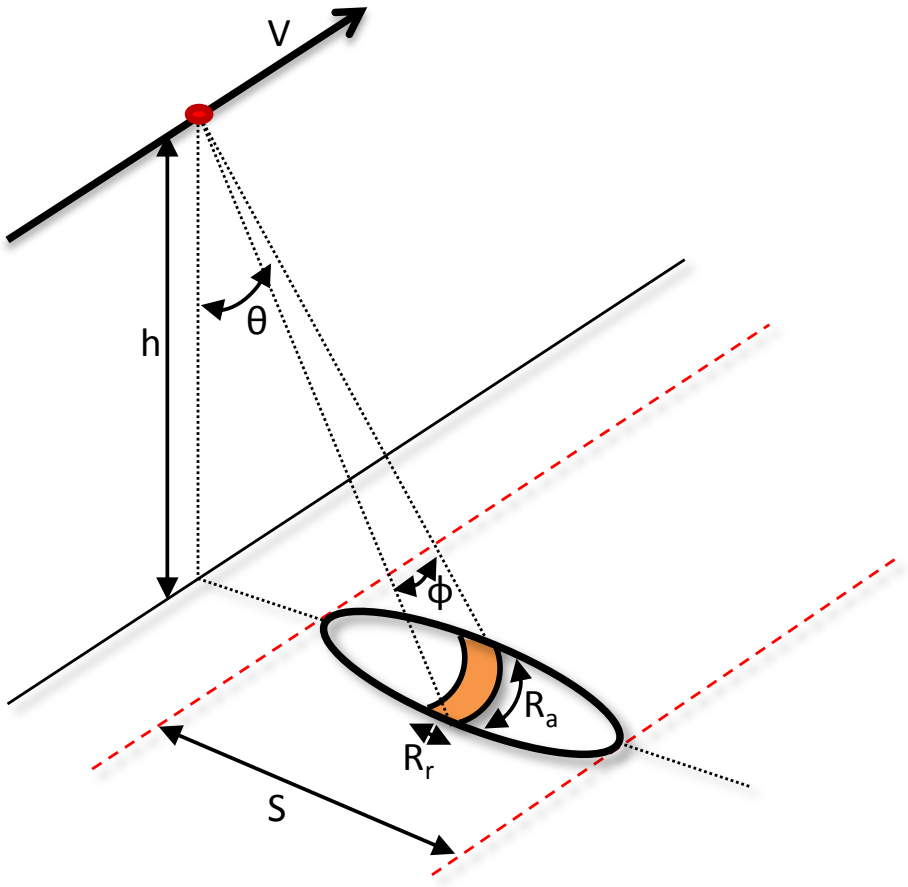

FIGURE 1.13 – *Illustration de la résolution spatiale d'un diffusiomètre à visée latérale.*

La R_r va dépendre de la durée de l'impulsion de l'onde. La R_a peut s'exprimer selon *Ulaby et al.* [1982] :

$$R_a = \frac{h.\Phi}{\cos\theta} \tag{1.11}$$

avec :

- R_a : résolution azimutale en m,
- h : hauteur du capteur en m,
- Φ : largeur du faisceau d'ouverture de l'antenne en m,

- θ : angle d'incidence en rad.

Il est à noter que Φ est directement proportionnel à λ et inversement proportionnel à la longueur de l'antenne. Donc plus l'antenne est longue, plus R_a sera petite. Malheureusement la longueur de l'antenne ne peut dépasser quelques mètres. Cette principale difficulté peut être palliée en utilisant des radars à ouverture de synthèse (SAR) qui ont une résolution pouvant atteindre $\sim 30\ m$. La contrepartie est que l'on va réduire la couverture spatiale d'échantillonnage à une centaine de kilomètres. Pour cette raison, les SARs sont encore peu utilisés pour des études globales ou à l'échelle d'un bassin océanique. Pour les diffusiomètres en bande C et en bande Ku, R_a est de $\sim 50\ km$ et $\sim 25\ km$, respectivement. Quant à la couverture spatiale elle est de $\sim 200\ km$ à $\sim 750\ km$ voire $\sim 1600\ km$ pour QuikSCAT (antenne à balayage conique voir figure 1.14).

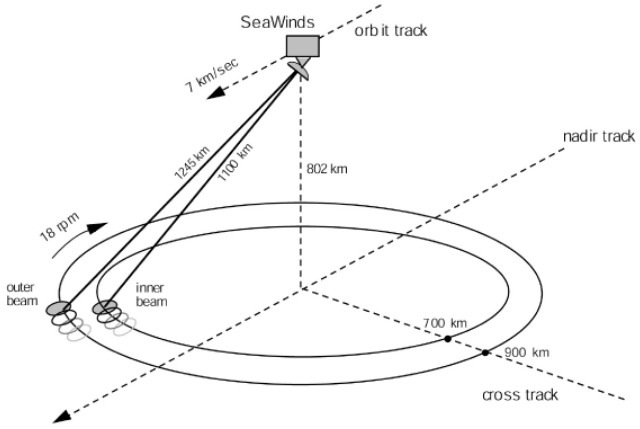

FIGURE 1.14 – *Illustration de la couverture spatiale de QuikSCAT (antenne à balayage conique). ©[Spencer et al., 2000].*

b Historique et principales missions

A la suite de la mission SKYLAB qui avait embarqué à son bord le premier diffusiomètre (S-193), l'instrument qui prit sa suite fût lancé en 1978 à bord du satellite SEASAT-A. Ce diffusiomètre (SASS) démontra que le vent (direction et vitesse) pouvait être mesuré avec une précision suffisante pour une exploitation scientifique de la donnée [*Grantham et al.*, 1977]. Cependant ce capteur n'utilisait que deux antennes de chaque côté, ce qui ne permit pas de lever l'ambiguité sur les quatre directions possibles pour le vent.
Le premier capteur possédant 3 antennes a été lancé sur le satellite European Remote Sensing 1 (ERS-1) en 1991 [*Attema*, 1991]. Puis ce fût le tour du diffu-

siomètre de la NASA (NSCAT), lancé à bord du satellite japonais ADEOS-Midori en Août 1996. Ce capteur connu une vie assez courte due à la fin prématurée du satellite par une panne de courant en Juin 1997. Entre-temps l'Organisation européenne pour l'exploitation des satellites météorologiques (EUMETSAT) envoya son second satellite (ERS-2) avec pour mission de succéder à ERS-1.
Malgré sa durée de vie très courte, NSCAT permit avec sa couverture spatiale sans précédent et sa précision dans la détermination de la direction et de l'intensité du vent, de couvrir une large variété d'études scientifiques comme l'estimation des pluies tropicales, la prédiction météorologique, etc.. Pour combler cette perte significative, les américains mirent sur pied une mission en seulement 12 mois. Cette rapidité à mettre en orbite un nouveau satellite donna le nom à la mission quick scatterometer (QuikSCAT) avec son capteur SeaWinds [*Wu et al.*, 1994] lancé en Juin 1999. En décembre 2002, un nouveau satellite ADEOS-II vu le jour et connu une destinée aussi tragique que celle de son prédécésseur car seulement 11 mois après son lancement en octobre 2003, il s'arrêta de transmettre les données du capteur SeaWinds embarqué.
Du côté Européen, une série de trois satellites de météorologie opérationnelle (MetOp) fût programmée avec un lancement pour MetOp-A en 2005 [*Figa-Saldaña et al.*, 2002] dont la fenêtre de tir fût décalée en octobre 2006. Cette série de satellites, avec comme diffusiomètre embarqué ASCAT, a pour but d'alimenter les modèles numériques prédictifs de météorologie. Le succés de la coopération entre EUMETSAT, l'ESA ainsi que la NOAA et le CNES, a permis de mettre en orbite le second satellite : MetOp-B avec une fenêtre de tir initialement prévue pour le 23 Mai 2012 qui a été reportée au 19 Septembre 2012. Quant à MetOp-C, son lancement est prévu pour 2016.
Dans la lignée de QuikSCAT, deux capteurs ont récemment été lancés par l'Inde et la Chine. Du côté Indien, c'est à bord du satellite Oceansat-2 que le capteur ISRO scatterometer a été embarqué en Septembre 2009 pour une mission d'une durée de vie de cinq ans. Quant au satellite chinois HY-2A dont la durée de la mission est de trois ans, une de ses charges utiles est un diffusiomètre (HY-2A scatterometer). Cet année, le satellite HY-2B devrait être mis en orbite très prochainement avec, à son bord, la même charge utile.

c Données utilisées

Dans un contexte de changement et de variabilité climatique, la possibilité d'obtenir avec précision les vents au moyen de diffusiomètres est extrêmement

précieuse. En alimentant les modèles de prédiction météorologique, cela permet, entre autres, de quantifier avec précision la trajectoire des tempêtes et cyclones, d'évaluer les phénomènes de sur-côtes ainsi que les inondations littorales. Ces informations sont d'un point de vue sociétal cruciales car elles permettent de minimiser les dommages ainsi que les pertes humaines. La vision globale et à long terme de la connaissance des vents permet aussi de mettre sous surveillance constante des phénomènes climatiques majeurs comme El Niño. Cela permet également des avancées significatives dans d'autres disciplines scientifiques comme la glaciologie, l'évaluation de l'humidité des sols et l'évolution de la végétation et des zones désertiques.
D'un point de vue plus économique, l'appauvrissement des ressources fossiles continentales pousse les entreprises pétrolifères à extraire le pétrole et le gaz naturel dans des zones "offshores" qui sont de plus en plus éloignées des côtes. La connaissance des vents (et des vagues) dans les sites d'implantation devient cruciale pour la conception des plates-formes de forage mais aussi pour la sécurité des employés. L'évaluation des vents à la surface de l'océan est aussi de première importance pour minimiser l'impact environnemental de certains désastres comme le déversement de pétrole à la surface océanique (marées noires, dégazages).

Dans le contexte de cette thèse, les produits que nous avons utilisés ne sont pas directement les produits de vents classique à $10\ m$ mais les tensions de vent déduites à la surface de l'océan.

Trois produits ont été exploités :

- le produit global de QuikSCAT (QSCAT MWF) qui a une résolution de $1/2° \times 1/2°$ qui est fourni par le Centre ERS d'Archivage et de Traitement (CERSAT ; http://cersat.ifremer.fr/content/download/2427/16800/file/mutwqscat.pdf). Ce produit est délivré soit en moyenne quotidienne, soit en moyenne hebdomadaire sur une période allant de Juillet 1999 à Novembre 2009 [*Bentamy et al.*, 1999],
- le produit journalier sur grille régulière au $1/4° \times 1/4°$, issu de la fusion des observations de plusieurs capteurs et délivré par le National Climatic Data Center (NCDC ; http://www.ncdc.noaa.gov/oa/rsad/air-sea/seawinds.html). La période temporelle couverte par ce produit s'étend de Juillet 1987 à nos jours [*Zhang et al.*, 2006],

- le produit global de Metop/ASCAT (DASCAT MWF) qui à une résolution au quart de degré est aussi fourni par le CERSAT (ftp://ftp.ifremer.fr/ifremer/cersat/products/gridded/MWF/L3/ASCAT/Daily/Doc/DailyAscatWind-Doc.pdf). Ce produit est délivré en moyenne quotidienne sur une période allant de Mars 2007 à nos jours [*Bentamy et Fillon*, 2012],

Pour obtenir les tensions de vent à partir du vent à $10\ m$, les produits du CERSAT utilisent la "bulk formulation" (qui a été préconisée par la communauté WOCE) :

$$(\tau_x, \tau_y) = \rho C_D \mathbf{W}(u, v) \tag{1.12}$$

avec :

- $|\tau| = \rho C_D W^2$: intensité de la tension,
- τ_x et τ_y : composantes zonale et méridienne de la tension,
- C_D : coefficient de traînée, formulé selon *Smith* [1988],
- ρ : densité de l'air à la surface de l'océan ($\rho = 1.225\ kg.m^{-3}$),
- $\mathbf{W}(u, v)$: vitesse du vent avec u et v ses composantes zonale et méridienne.

Le produit du NCDC utilise un rapport entre les vents satellitaires et les vents des réanalyses (NRA-2) du modèle du National Centers for Environmental Prediction (NCEP) :

$$\begin{cases} \tau_{xs} = -\left[\dfrac{W_s}{W_m}\right]^2 \tau_{xm} \\ \tau_{ys} = -\left[\dfrac{W_s}{W_m}\right]^2 \tau_{ym} \end{cases} \tag{1.13}$$

avec :

- τ_{xs} et τ_{ys} : composantes zonale et méridienne de la tension acquise par le satellite,
- τ_{xm} et τ_{ym} : composantes zonale et méridienne de la tension du modèle NCEP,
- W_s : norme de la vitesse du vent à $10m$ satellitaire,
- W_m : norme de la vitesse du vent à $10m$ du modèle NCEP.

Les figures 1.15, 1.16 et 1.17 illustrent ces trois produits pour la date du 01/08/2007. Si la structure générale et l'intensité globale entre ces produits sont bien respectées, on notera cependant de différences notables :

- des structures atmosphériques,
- des zones côtières,
- de certaines zones très localisées.

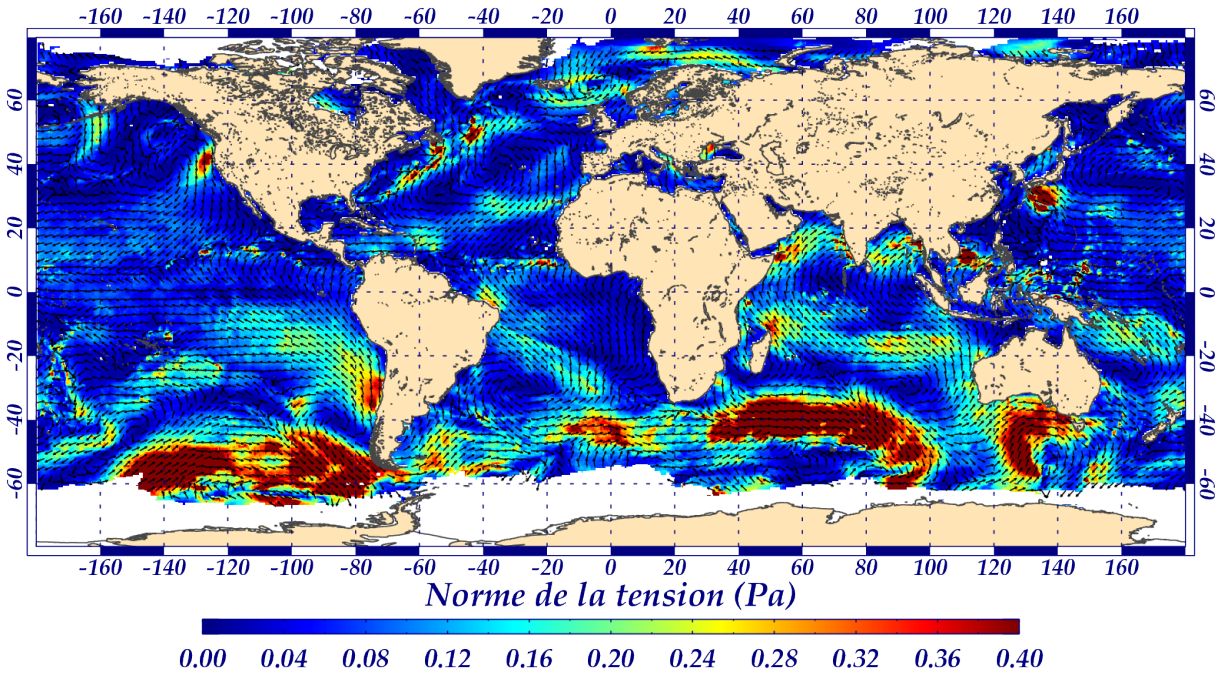

(a) Tension de vent globale pour le 01/08/2007.

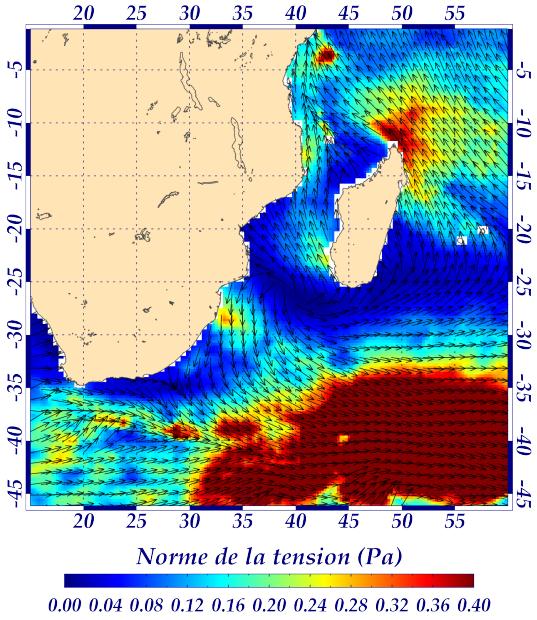

(b) Tension de vent au Sud-Ouest de l'Océan Indien pour le 01/08/2007.

FIGURE 1.15 – Tension de vent provenant du produit QuikSCAT du CERSAT utilisée dans les articles [*Sudre et Morrow*, 2008] et [*Sudre et al.*, 2013].

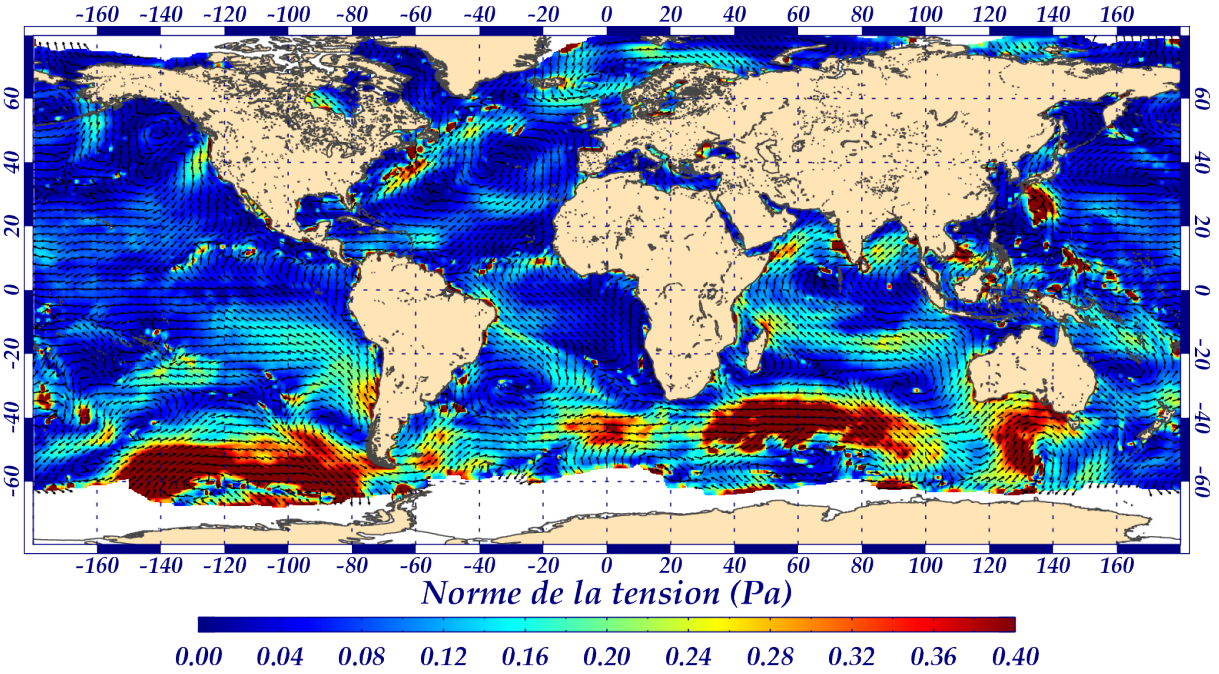

(a) Tension de vent globale pour le 01/08/2007.

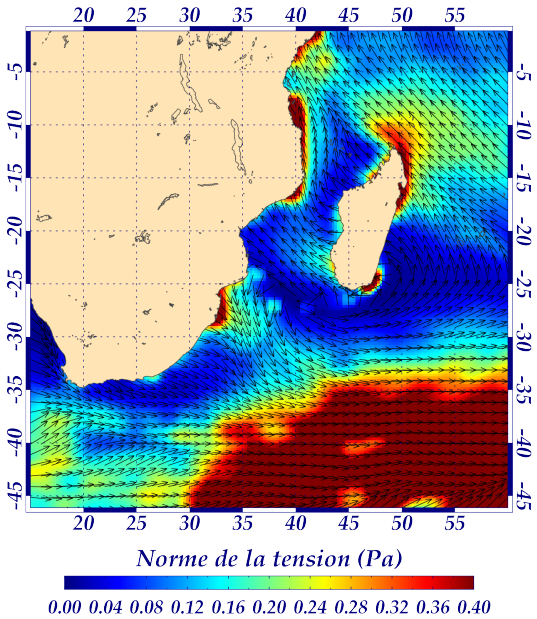

(b) Tension de vent au Sud-Ouest de l'Océan Indien pour le 01/08/2007.

FIGURE 1.16 – Tension de vent provenant du produit du NCDC.

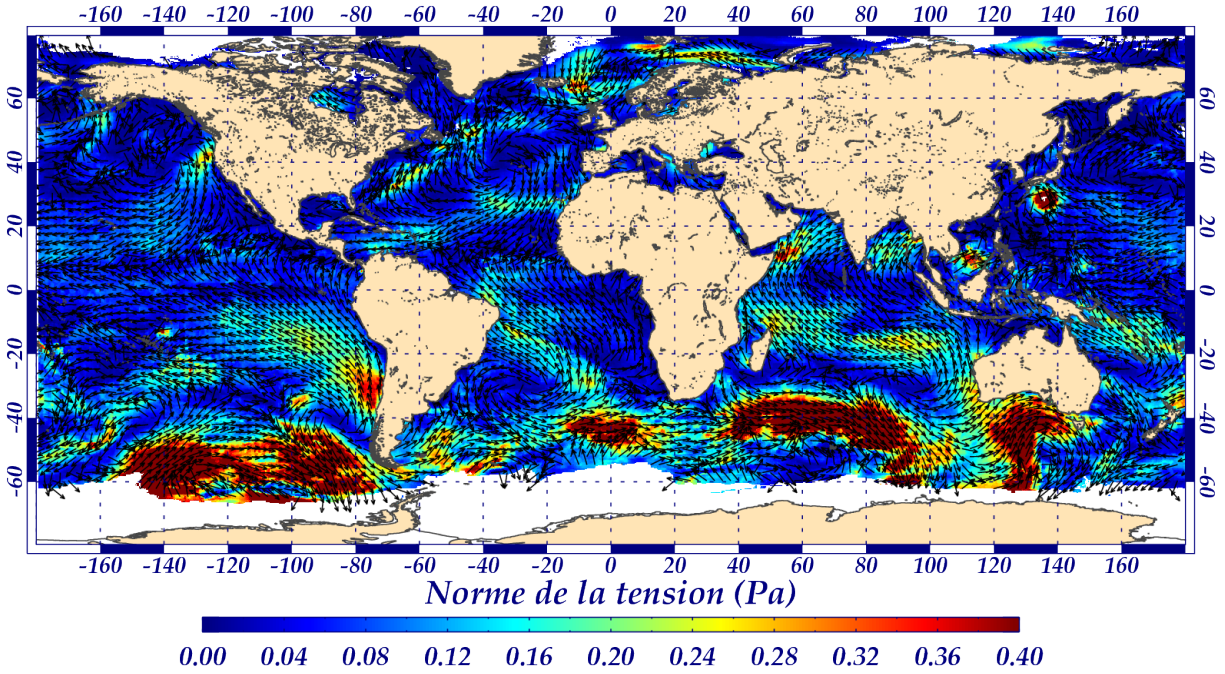

(a) Tension de vent globale pour le 01/08/2007.

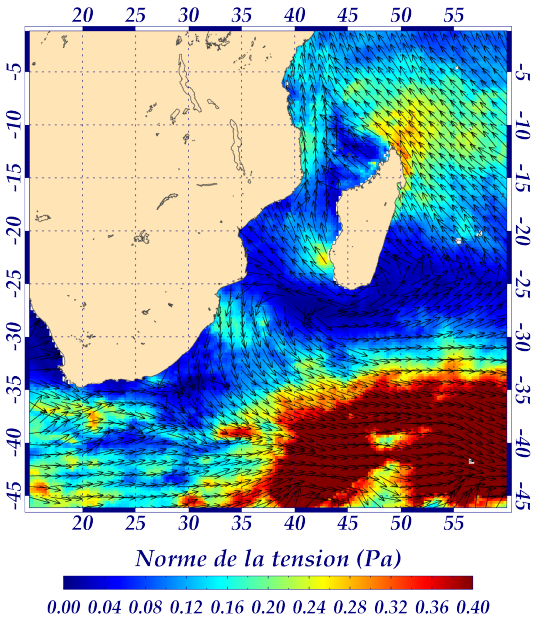

(b) Tension de vent au Sud-Ouest de l'Océan Indien pour le 01/08/2007.

FIGURE 1.17 – Tension de vent provenant du produit DASCAT MWF du CERSAT.

1.3.3 Température de surface de la mer

En 1858, Gaspard-Félix Tournachon à bord de son ballon monté réalise la première photographie aérienne de Paris. "Nadar" a ainsi ouvert la voie à la télédétection aérienne. Historiquement, cette idée fût de plus en plus employée pour la reconnaissance de sites lors de la guerre civile américaine, puis connut son essor lors de la première guerre mondiale en Europe. La télédétection spatiale pour l'observation de la surface terrestre débuta en 1966 avec le programme "Earth Resources Technology Satellites Program", dont le nom changea quelques années plus tard en Landsat (1975). En 1972 ce programme, qui hérita des avancées du programme Nimbus (lancement de Nimbus-1 en 1964) pour la météorologie spatiale, lança le premier satellite dédié à l'observation des surfaces terrestres : Earth Resources Technology Satellite 1 (ERTS-1) renommé par la suite Landsat-1. Une des charges utiles de ce satellite était un "MultiSpectral Scanner" (MSS) à quatre bandes dont l'objectif était d'obtenir des images radiométriques de la terre.

a Principe de la mesure

Avant de voir le principe de la mesure de la température de surface de la mer (TSM), il est nécessaire de définir ce terme. La TSM est la température des premiers microns ($\sim 10-20\ \mu m$) de la surface de l'océan. Cette couche océanique est soumise aux réchauffements diurnes, aux refroidissements nocturnes, aux vents, etc. [*Katsaros*, 1980; *Robinson et al.*, 1984; *Schluessel et al.*, 1990; *Soloviev et Schluessel*, 1996; *Fairall et al.*, 1996; *Donlon et al.*, 1999; *Gentemann et al.*, 2003]. Cette température est un paramètre très difficile à déterminer car la structure de la température des premiers mètres de la couche de surface est complexe et variable, ce qui pose un important problème affectant directement l'interprétation de la mesure de TSM par télédétection. On peut décomposer la couche de surface en différentes sous-couches. La première sous-couche est l'interface océan-atmosphère (de l'épaisseur d'une à deux molécules), sa température ne peut pas être déterminée. Sous cette interface, on trouve une couche d'une épaisseur de $\sim 10-20\ \mu m$ que l'on nomme la peau de l'océan. C'est précisément dans cette seconde sous-couche que les radiations infrarouges pénétrant dans l'océan s'atténuent et qui vont nous permettre de déterminer la TSM. En dessous de la peau de l'océan, on trouve la "sous-peau" de l'océan qui va jusqu'à une profondeur de $1\ mm$, qui est la profondeur d'atténuation

des micro-ondes, sa température va donc être déterminée par des capteurs travaillant dans cette gamme de fréquences. Au-delà, on se trouve dans la couche proche de la surface. Chacune de ces couches a donc une température spécifique qui est représentée à la figure 1.18 extraite de l'article de [*Donlon et al.*, 2002] et qui varie différemment en fonction du réchauffement diurne, du refroidissement nocturne, et du vent.

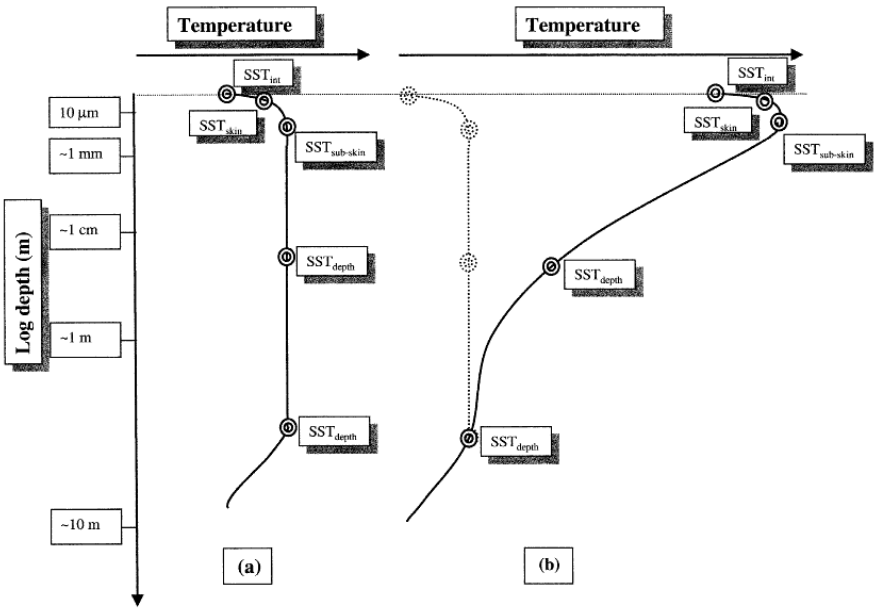

FIGURE 1.18 – *Illustration de profils de température idéalisés de la couche de surface de l'océan durant (a) la nuit ou le jour avec des conditions de vent fort et (b) le jour avec des conditions de vent faible et une forte insolation provoquant une stratification thermique de la couche de surface. ©Journal of Climate AMS.*

A la différence des altimètres et des diffusiomètres qui ont la propriété de générer l'émission d'une onde électromagnétique vers la cible pour en analyser son écho, les radiomètres, les spectromètres et les spectroradiomètres qui vont nous servir à mesurer la TSM, sont des capteurs passifs, qui se contentent d'observer le rayonnement émis par la cible. Ces capteurs sont le plus souvent des imageurs, qui vont balayer la cible sur une distance variable que l'on nomme la fauchée. Deux méthodes d'acquisition de la fauchée sont classiquement utilisées sur ce type de capteur :

- soit l'instrument possède un seul détecteur et le balayage orthogonal va être effectué par un miroir (méthode opto-mécanique),
- soit l'instrument possède une rampe (ou matrice) de détecteurs (Charge Coupled Devices - CCD) qui opère de la même façon que les appareils photos numériques.

Dans les deux cas, l'image va être construite par acquisitions successives au fur et à mesure du déplacement du satellite sur son orbite. La fauchée est décomposée en parcelles élémentaires qui sont des images élémentaires : les pixels.
Si on considère β, la taille du pixel en steradian et h la hauteur du satellite par rapport à sa cible, on peut en déduite l'empreinte au sol r telle que :

$$r = \beta h \tag{1.14}$$

Si on désire pixels contiguës, il est nécessaire d'ajuster la vitesse de balayage du capteur pour obtenir une ligne de pixels de la taille de la fauchée à la vitesse de déplacement du satellite. De plus, l'empreinte au sol va être déformée (en taille et/ou en forme) en fonction du roulis, du tangage, du lacet, de l'altitude, de la vitesse trop rapide ainsi que des accélérations du satellite. Ainsi la valeur moyenne du contenu de chaque pixel (la température) va d'être altérée si l'empreinte au sol est modifiée.

Quelle est la différence entre un radiomètre, un spectromètre et un spectroradiomètre ?

Un radiomètre est un instrument de mesure qui va quantifier l'intensité de la radiation électromagnétique d'une bande de fréquences dans le spectre. Un radiomètre est souvent identifié par la portion de bande spectrale qu'il couvre comme par exemple les radiomètres micro-ondes ou infrarouge.

Un spectromètre est un instrument qui détecte, mesure et analyse le contenu spectral de la radiation électromagnétique. Il va donc discriminer le spectre pour en analyser le contenu.

Le spectroradiomètre est l'association des deux instruments précédents. A savoir que cet instrument est un radiomètre qui va quantifier l'intensité de plusieurs bandes de fréquences. C'est l'instrument multispectral le plus adapté pour l'observation à haute résolution des paramètres comme la température de surface et la couleur de l'eau.

Comment obtient-on théoriquement la TSM ?

La luminance quittant le haut de l'atmosphère est la somme de deux sources de radiation :

- la luminance provenant de la surface de l'océan (atténuée par les molécules actives aux longueurs d'onde observées et par la brume),
- la luminance émise par les constituants de l'atmosphère.

Ceci peut être traduit mathématiquement par l'équation suivante [*Anding et Kauth*, 1970] :

$$L_\lambda = L_\lambda^g(T)\tau(\lambda) + L_\lambda^a \tag{1.15}$$

avec :

- L_λ : luminance quittant de haut de l'atmosphère,
- $L_\lambda^g(T)$: luminance du corps gris de la surface de l'océan,
- $\tau(\lambda)$: transmittance de l'atmosphère,
- L_λ^a : luminance émise par l'atmosphère.

Pour pouvoir éliminer les effets de l'absorption et de l'émission de la vapeur d'eau, *Smith et al.* [1970] préconisent l'utilisation d'une méthode statistique alors que *Anding et Kauth* [1970] préconisent l'utilisation de deux bandes spectrales (dans l'infrarouge). [*Prabhakara et al.*, 1974] ont utilisé avec succès ce second modèle avec les données de Nimbus-3 et 4. De nos jours, la méthode de *Anding et Kauth* [1970] est la plus employée, la seule différence est que l'on préfère utiliser les températures de brillance plutôt que la luminance.
La température de brillance est une mesure descriptive de la température d'un corps noir hypothétique ayant une radiance identique à la radiance observée aux même longueurs d'ondes. La température de brillance est obtenue en appliquant l'inverse de la fonction de Planck (voir équations : 1.5 et 1.8) à la radiance mesurée.
La TSM peut-être calculée soit à partir des ondes infrarouges, soit à partir des micro-ondes. Ces deux moyens d'obtention présentent chacun des avantages et des inconvénients mais dans les deux cas il est nécessaire de calibrer la température obtenue avec des données *in-situ*.
La TSM obtenue à partir des infrarouges est calculée soit dans des longueurs d'ondes $\sim 4\ \mu m$ ou $\sim 10\ \mu m$. Les longueurs d'ondes $\sim 4\ \mu m$ sont uniquement utilisées pour le calcul de la TSM de nuit, car la radiation solaire contamine trop le signal diurne. Les longueurs d'ondes $\sim 10\ \mu m$ permettent d'obtenir la TSM de jour comme de nuit (faible contamination par les radiations solaires). Ces deux bandes présentent une sensibilité particulière à la présence de nuages, à la rétrodiffusion des aérosols ainsi qu'à la présence de vapeur

d'eau dans l'atmosphère. De ce fait, les mesures de la TSM dans l'infrarouge nécessitent une attention particulière dans le traitement de la correction atmosphérique et ne peuvent se faire uniquement qu'en absence de nuage. Malgré ces inconvénients majeurs, la résolution et la précision des mesures de TSM dans l'infrarouge sont très élevées ($250\ m$ de résolution et une erreur de RMS inférieure à ~ 0.76 avec un biais nul).
Pour les micro-ondes, les mesures de la TSM ont une résolution et une précision plus faibles ($\sim\ 25\ km$, une erreur de RMS de 0.90 et un biais de 0.26) ce qui est dû à la faible émission de Planck dans ces longueurs d'ondes [*Wick et al.*, 2002]. Cette TSM doit donc être nécessairement calibrée par des données *in-situ* pour avoir une précision suffisante ; cependant elle présente l'avantage d'être insensible à la présence de nuage.

b Historique et principales missions

Comme nous l'avons vu précédemment, la TSM peut être obtenue par différent capteurs (radiomètres imageurs, spectromètres imageurs, ou spectro-radiomètres), il y a donc une constellation importante de satellites qui ont à leurs bords ce type de capteurs depuis les années soixante. Le tableau 1.3 synthétise la plupart de ces missions satellitaires, qu'elles soient dédiées à la météorologie ou à l'océanographie, mais ayant toutes la possibilité de fournir une mesure de la TSM.

Le tableau 1.4 permet d'avoir un aperçu des futures missions satellitaires qui auront la capacité de fournir des données de TSM dans un proche avenir.

c Données utilisées

Les missions satellitaires permettant d'avoir une information de la TSM sont nombreuses et variées, avec des répétitivités, des résolutions, des précisions et des séries temporelles différentes. Afin d'estimer les courants à haute résolution (chapitre 3), deux jeux de données ont été sélectionnés pour leurs longues périodes temporelles, leurs répétitivités journalières, leurs hautes résolutions ainsi que leurs excellentes calibrations avec des données *in-situ*.
Le premier jeu de données provient du capteur MOderate Resolution Imaging Spectroradiometer (MODIS) embarqué sur le satellite américain Aqua. Ce cap-

Mission s.=séries	Date de lancement	Instruments
POES s.	01/04/1960	AVHRR
GOES s.	16/10/1975	ABI, Imager, Sounder
Meteosat s.	23/11/1977	MVIRI, SEVIRI
Meteor s.	24/10/1985	IKFS-2, MSU-MR, MTVZA
INSAT s.	02/07/1992	VHRR
GOMS/electro s.	31/10/1994	MSU-GS
FY-2 s.	10/06/1997	IVISSR
TRMM	27/11/1997	TMI, VIRS
OCEANSAT s.	27/05/1999	MSMR
Terra	18/12/1999	MODIS
NMP s.	21/11/2000	ALI, Hyperion
Envisat	01/03/2002	AATSR
Aqua	04/05/2002	AIRS, AMSR-E, MODIS
HY-1 s.	15/05/2002	COCTS , IRAS
KALPANA-1	12/09/2002	VHRR
Coriolis	06/01/2003	Windsat
MTSAT s.	26/02/2005	IMAGER JAMI
EPS s.	19/10/2006	AVHRR, HIRS, IASI
FY-3 s.	27/05/2008	MVIRS, VIRR
SAC s.	22/05/2010	NIRST D/Aquarius
COMS s.	26/06/2010	MI
HY-2 s.	11/08/2011	RAD
NPP	01/09/2011	VIIRS
GCOM s.	18/05/2012	AMSR-2

TABLE 1.3 – *Tableau des missions (ou séries de missions) en vol actuellement ayant à bord un capteur susceptible de produire de la TSM.*

Mission s.=séries	Date estimée	Instruments
FY-4 s.	2013	MCSI
Sentinel-3 s.	2014	SLSTR
GCOM-C s.	2014	SGLI
JPSS s.	2016	MIS, VIIRS
MTG-I s.	2016	FCI

TABLE 1.4 – *Tableau des missions planifiées ayant à bord un capteur susceptible de produire de la TSM.*

teur possède quatre bandes dans l'infrarouge entre $3,7\ \mu m$ et $4\ \mu m$ et deux autres canaux à $11,03\ \mu m$ et $12,02\ \mu m$. Sa période de revisite est de deux jours avec une fauchée de 2330 km et une résolution de $1000\ m$ pour ces six canaux. Les données utilisées sont de niveau 3, journalières, "binnées" sur une grille à aire égale de $1/24° \times 1/24°$ où chaque pixel va représenter une valeur de TSM. Le retraitement correspondant à ces données est le R2009 (http://oceancolor.gsfc.nasa.gov/REPROCESSING/Aqua/R2009/).
L'équation de calcul de la TSM, à partir des températures de brillance, dérive de l'algorithme 1.15, auquel il a été adjoint une correction pour prendre en compte les modifications de la masse atmosphérique aux grands angles d'incidence, ainsi qu'une forme non-linéaire pour prendre en compte les variations de température atmosphérique entre les hautes et basses latitudes [*Walton*, 1988]. L'algorithme suivant montre les équations appliquées pour le calcul de la TSM pour les bandes spectrales $11\ \mu m$ et $12\ \mu m$:

$$\begin{cases} dTb \leq 0.5 \\ TSM = a_{00} + a_{01} \cdot Tb_{11} + a_{02} \cdot dTb \cdot btsm + a_{03} \cdot dTb \cdot \dfrac{1}{(\cos\theta - 1)} \\ \\ 0.5 < dTb < 0.9 \\ TSM_a = a_{00} + a_{01} \cdot Tb_{11} + a_{02} \cdot dTb \cdot btsm + a_{03} \cdot dTb \cdot \dfrac{1}{(\cos\theta - 1)} \\ TSM_b = a_{10} + a_{11} \cdot Tb_{11} + a_{12} \cdot dTb \cdot btsm + a_{13} \cdot dTb \cdot \dfrac{1}{(\cos\theta - 1)} \\ TSM = TSM_a + \dfrac{dTb - 0.5}{0.9 - 0.5} \cdot (TSM_b - TSM_a) \\ \\ dTb \geq 0.9 \\ TSM = a_{10} + a_{11} \cdot Tb_{11} + a_{12} \cdot dTb \cdot btsm + a_{13} \cdot dTb \cdot \dfrac{1}{(\cos\theta - 1)} \end{cases} \tag{1.16}$$

avec :

- dTb : $dTb = Tb_{11} - Tb_{12}$,
- Tb_{11} : température de brillance à $11\ \mu m$ en $°C$,
- Tb_{12} : température de brillance à $12 \mu m$ en $°C$,
- $btsm$: ligne de base de la TSM provenant d'une source de TSM de référence bi-linéairement interpolée pour le pixel considéré (TSM de référence : Reynolds (OISST) [*Reynolds et al.*, 2002]),
- θ : angle zénithal du capteur,

- a_{ij} ($i = 0, 1$ et $j = 0, 1, 2, 3$) : coefficients de pondération permettant de faire correspondre les TSM provenant du satellite avec des TSM provenant de données *in-situ*. (Ces coefficients sont évolutifs dans le temps).

Sous l'égide du "Global Ocean Data Assimilation Experiment" (GODAE), le "Group for High-Resolution Sea Surface Temperature" (GHRSST) a pour but de produire des données de TSM à la meilleure précision possible, sans donnée manquante et à toutes les échelles de temps (du décennal jusqu'à la donnée horaire). Le GHRSST a aussi pour objectif de distribuer ses produits en temps quasi-réel pour des tâches opérationnelles. Dans ce cadre, plusieurs équipes internationales dont le Met office (service de la météorologie britannique) fournissent leurs propres produits pour générer chaque jour un "GHRSST Multi-product Ensemble" (GMPE). Le produit "Operational Sea Surface Temperature and Sea Ice Analysis" (OSTIA) en est un élément. Ce second produit, que nous allons utiliser, fusionne, au moyen d'une variante de l'interpolation optimale [*Martin et al.*, 2007], des données provenant du projet GHRSST (niveau3) avec des observations *in-situ* pour déterminer une TSM de niveau 4, journalière, globale avec une résolution de $1/20° \times 1/20°$ ($\sim 5\ km$) [*Donlon et al.*, 2012].

Les deux figures 1.19 et 1.20 présentent les deux produits de TSM.

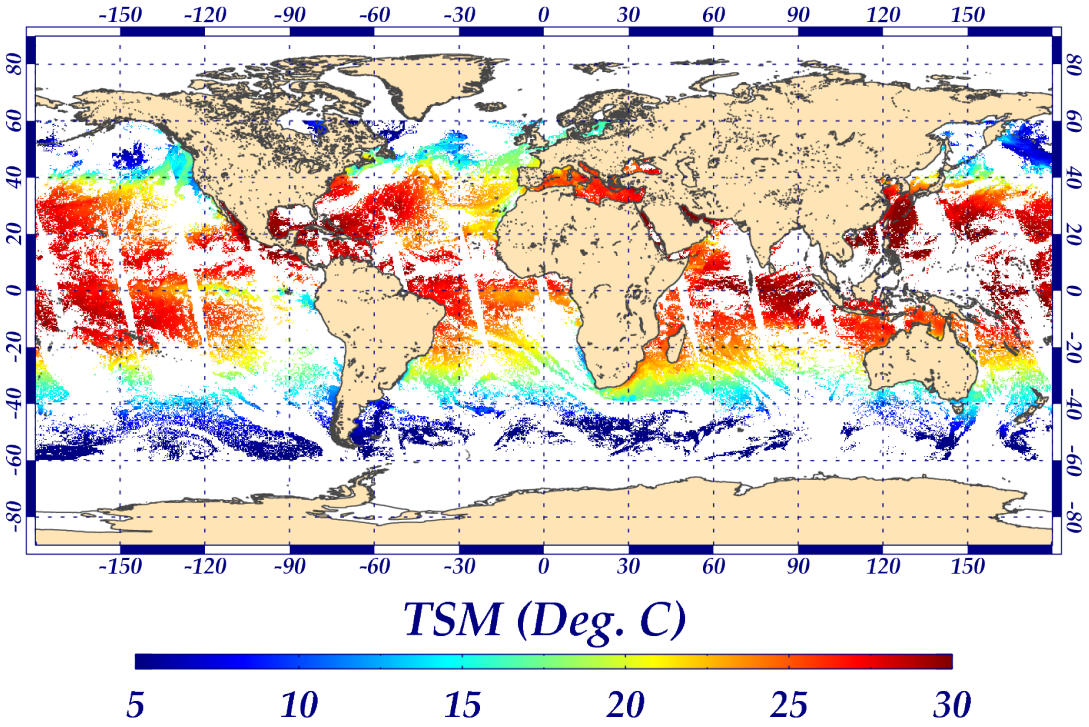

(a) TSM globale pour le 01/08/2007.

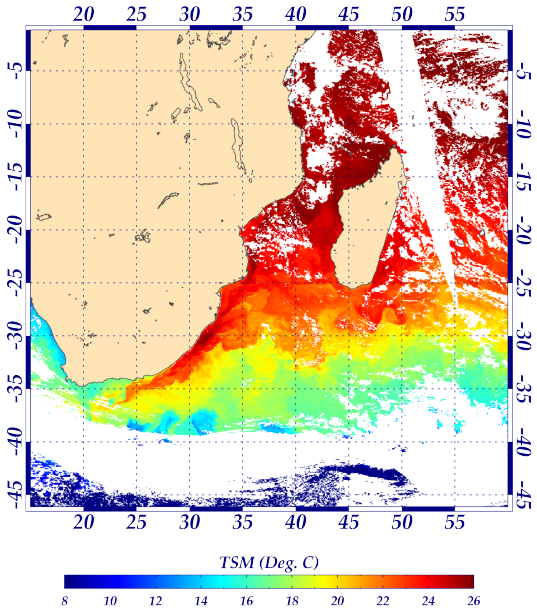

(b) TSM au Sud-Ouest de l'Océan Indien pour le 01/08/2007.

FIGURE 1.19 – TSM provenant du produit TSM MODIS/Aqua.

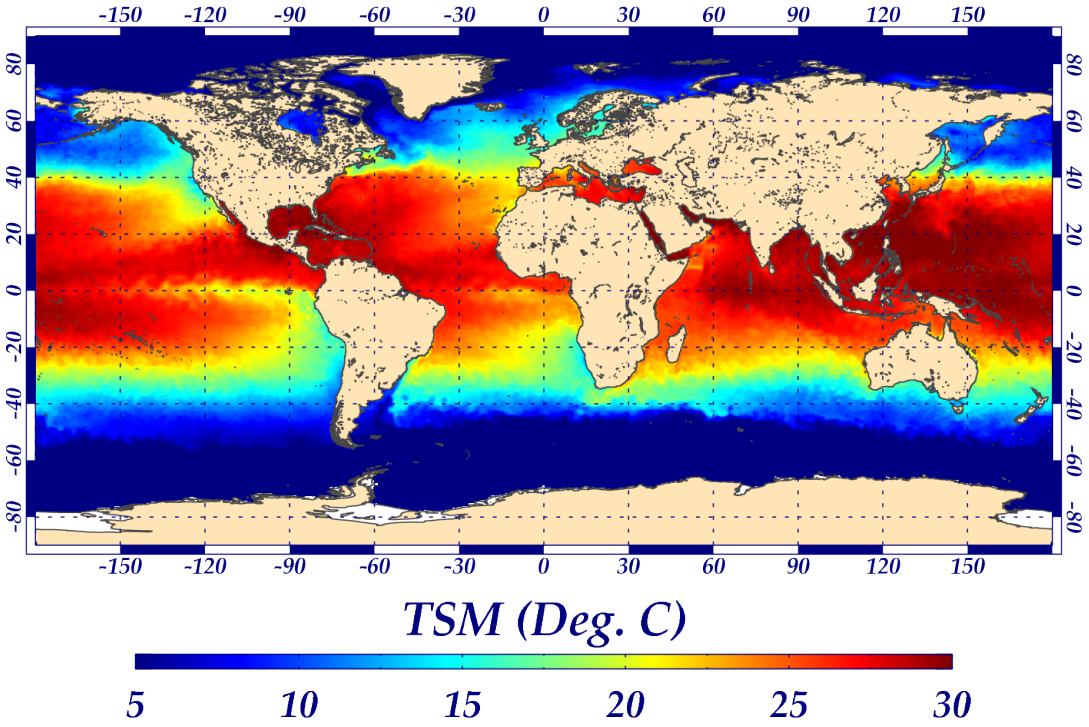

(a) TSM globale pour le 01/08/2007.

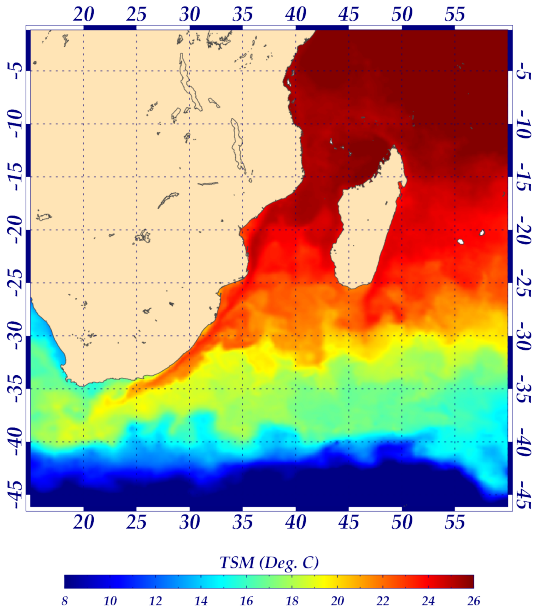

(b) TSM au Sud-Ouest de l'Océan Indien pour le 01/08/2007.

FIGURE 1.20 – TSM du produit OSTIA.

1.3.4 Couleur de l'océan

En 1978, la première mission expérimentale Nimbus-7 embarqua à son bord le capteur de la NASA "Coastal Zone Color Scanner" (CZCS), un spectroradiomètre ayant la capacité de mesurer des bandes spectrales dans le visible. Cette mission expérimentale programmée à l'origine pour avoir une durée de vie d'un an, permit jusqu'en 1986 de fournir une série temporelle de mesure globale. Elle a surtout démontré la possibilité d'observer à partir de l'espace la distribution du phytoplancton océanique à l'échelle globale. Ses données ont été utilisées dans de nombreuses études, dans le but de mieux comprendre le rôle de l'océan dans les cycles biogéochimiques.
Après 1986, il fallu attendre dix ans pour avoir une autre source de mesure de la couleur de l'eau avec le lancement de IRS-P3 par l'Organisation Spatiale de la Recherche Indienne (ISRO) et du capteur "Modular Optoelectronic Scanning Spectrometer" (MOS) du centre national de l'aéronautique et de l'espace Allemand (DLR), lancé en mars 1996.

a Principe de la mesure

A la différence de la TSM qui est issue du rayonnement thermique propre de l'océan dans l'infrarouge, la couleur de l'eau est déterminée par les interactions du rayonnement solaire (centré dans le visible) avec l'eau ainsi que les constituants qui s'y trouvent en suspension. Un objet quelconque est visible uniquement parce qu'il réfléchit les ondes électromagnétiques comprises entre $380\ nm$ et $780\ nm$ (le spectre de la lumière blanche) qui est perceptible par l'oeil humain. Tout objet qui a une couleur particulière va absorber, transmettre ou disperser toutes les ondes électromagnétiques provenant d'une source de rayonnement sauf celles que nous percevons comme sa combinaison de couleur, qui elles vont être réfléchies à différentes intensités.
L'énergie solaire pénétrant dans l'océan va être en partie absorbée et en partie diffusée. La proportion entre absorption et diffusion va dépendre essentiellement de la nature et de la quantité de particules contenues dans l'eau. La partie diffusée par les substances en suspension est déviée dans une nouvelle direction qui peut être celle de la surface et ainsi quitter le milieu aquatique. Cette lumière diffusée quittant l'océan va déterminer la couleur de l'eau en fonction de ses caractéristiques spectrales. Ainsi le phytoplancton, les particules inorganiques ou organiques, la matière organique dissoute vont avoir leurs propres

caractéristiques spectrales.
La chlorophylle contenue dans le phytoplancton absorbe les rayonnements dans le rouge ($620 - 700\ nm$), dans le bleu ($446 - 500\ nm$) et réfléchit les rayonnements dans le vert ($500 - 578\ nm$). La caractéristique spectrale de l'eau pure correspond au bleu profond. Ainsi plus la concentration en phytoplancton dans les couches de surface de l'océan est importante et plus les caractéristiques spectrales de l'eau contenant du phytoplancton vont tendre vers le bleu-vert (i.e. propriété d'additivité des ondes électromagnétiques). La couleur de l'eau va donc correspondre à une partie du rayonnement solaire réfléchie par l'océan.

Comment déterminer mathématiquement la réflection solaire depuis l'espace ?

La réflectance diffuse pour une longueur d'onde donnée (λ) des couches océaniques supérieures $R_{rs}(\lambda)$ est le rapport entre l'éclairement ascendant issu de la surface de l'océan (L_W) et l'éclairement descendant y pénétrant (E_d) [*Jerlov*, 1976] (voir figure 1.21) :

$$R_{rs}(\lambda) = \frac{\pi \cdot L_W}{E_d} \tag{1.17}$$

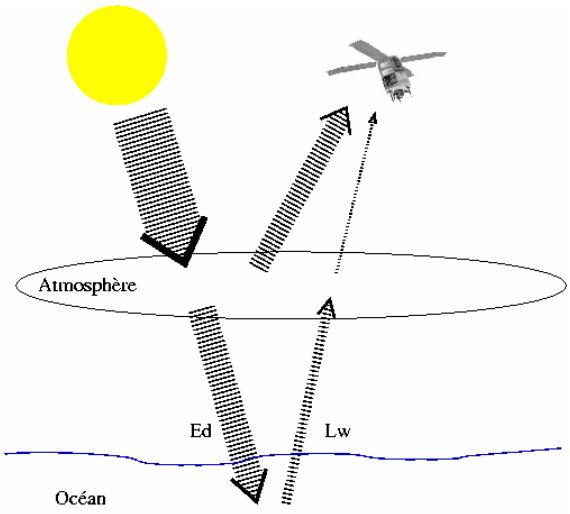

FIGURE 1.21 – *Illustration du signal mesuré par un capteur satellitaire. L'épaisseur des flux montre l'importance de la part atmosphérique dans le signal mesuré (jusqu'à 90%). ©[Pottier, 2006].*

Cette réflectance peut aussi être exprimée selon *Morel et Prieur* [1977] comme :

$$R_{rs}(\lambda) = F_{L,\beta}\frac{b_b(\lambda)}{a(\lambda)} \tag{1.18}$$

avec :

- $F_{L,\beta}$: coefficient de proportionnalité qui est fonction de la luminance et de la forme de l'indicatrice totale de diffusion β [*Antoine*, 1998],

- $a(\lambda)$: coefficient d'absorption de la couche de surface océanique pour la longueur d'onde considérée,
- b_b : coefficient de rétrodiffusion de la couche de surface océanique pour la longueur d'onde considérée.

Les ondes électromagnétiques étant additives en amplitude, il est possible de décomposer les coefficients d'absorption et de rétrodiffusion en une somme de coefficients dépendant des N composantes constituant les couches de surface océanique (i.e. l'eau pure, le phytoplancton, l'ensemble des particules ne contenant pas de chlorophylle, les substances dissoutes). On obtient :

$$R_{rs}(\lambda) = F_{L,\beta} \sum_{i=1}^{N} \frac{b^*_{b,i}(\lambda) \cdot [i]}{a^*_i(\lambda) \cdot [i]} \tag{1.19}$$

avec :

- N : nombre de constituants de la couche de surface océanique,
- $[i]$: concentration du constituant i,
- $F_{L,\beta}$: coefficient de proportionnalité,
- $a^*_i(\lambda)$: coefficient normalisé d'absorption par unité de concentration du constituant i pour la longueur d'onde considérée,
- $b^*_{b,i}(\lambda)$: coefficient normalisé de rétrodiffusion par unité de concentration du constituant i pour la longueur d'onde considérée.

La luminance marine L_W nécessaire pour calculer la réflectance permettant d'accéder à la concentration d'un constituant est une partie de la luminance totale reçue par le capteur pour une longueur d'onde donnée pour chaque pixel. La luminance totale peut être décomposée de la manière suivante : $L_T = L_R + L_A + L_{RA} + L_{WC} + L_G + t \cdot L_W$ avec :

- L_R : luminance issue de la dispersion moléculaire (Rayleigh),
- $L_A + L_{RA}$: luminance issue des aérosols (cette correction utilise deux canaux du proche infrarouge),
- L_{WC} : luminance issue du "panneau de recouvrement blanc", estimée à partir d'une relation statistique avec la vitesse du vent,
- L_G : luminance issue de la réflection solaire directe ou diffuse,
- t : transmittance diffuse de l'atmosphère.

D'importants efforts doivent être mis en oeuvre pour parfaitement calibrer le signal total mesuré par le capteur et le corriger des perturbations atmo-

Mission	Date d'activité	Instruments
IRS-P3	21/03/1996 - 31/05/2004	MOS
ADEOS	17/08/1996 - 29/06/1997	OCTS & POLDER
OrbView-2	01/08/1997 - 14/02/2011	SeaWiFS
ROCSAT-1	27/01/1999 - 16/06/2004	OCI
IRS-P4	26/05/1999 - 08/08/2010	OCM
KOMPSAT-1	20/12/1999 - 31/01/2008	OSMI
SAC-C	21/11/2000 $\sim$ 2009	MMRS
SZ-3	25/03/2002 - 15/09/2002	SZ-3
HY-1A	15/05/2002 - 01/04/2004	COCTS & CZI
ADEOS-II	14/12/2002 - 24/10/2003	GLI & POLDER-2

TABLE 1.5 – *Tableau des missions ayant eu à leur bord au moins un capteur susceptible de produire de la couleur de l'eau.*

sphérique car la luminance marine ne représente que $\sim 10\%$ de ce signal. Ceci représente la principale faiblesse de la télédétection de la couleur de l'eau.

b Historique et principales missions

Dix années après le lancement de CZCS, vingt et un satellites furent lancés à partir de 1996 avec à leur bord, un capteur permettant de déduire la couleur de l'eau. Le tableau 1.5 et le tableau 1.6 recensent ces missions avec le nom de chaque satellite ainsi que son(ses) capteur(s) permettant une mesure de la couleur de l'eau. Le tableau 1.7 donne un aperçu des futures missions satellitaires qui vont embarquer un capteur pouvant fournir des données de couleur de l'eau dans un proche avenir.

c Données utilisées

Le capteur MODIS que nous avons décrit pour les données de TSM possède 36 bandes spectrales dont 9 sont utilisées pour la couleur de l'eau. L'algorithme empirique, qui permet d'obtenir la concentration de chlorophylle-a à partir des radiances ($443\ \mu m$, $489\ \mu m$ et $547\ \mu m$) pour le retraitement des données que nous avons utilisés (R2009 - http://oceancolor.gsfc.nasa.gov/REPROCESSING/Aqua/R2009/) est le Ocean Color 3 version 6 (OC3MV6), [*Meister et al.*, 2005; *Franz et al.*, 2007; *Kwiatkowska et al.*, 2008] :

Mission	Date de lancement	Instruments
Terra (EOS-AM1)	18/12/1999	MODIS
ENVISAT	01/03/2002	MERIS
Aqua (EOS-PM1)	04/05/2002	MODIS
Parasol	18/12/2004	POLDER-3
HY-1B	11/04/2007	COCTS & CZI
FY-3A	27/05/2008	MERSI
JEM-EF	18/09/2009	HICO
Oceansat-2	23/09/2009	OCM-2
COMS	26/06/2010	GOCI
FY-3B	05/11/2010	MERSI
NPP	28/10/2011	VIIRS

TABLE 1.6 – *Tableau des missions en activité ayant à leur bord au moins un capteur susceptible de produire de la couleur de l'eau.*

Mission	Date estimée	Instruments
EnMAP	2013	HSI
Sentinel-3A	2014	OLCI
GCOM-C	2015	SGLI
HY-1C/D	2014	COCTS & CZI
SABIA-MAR	2015	Multi-spectral Optical Camera
Meteor-3M(3)	2015	OC Scanner & Coastal Zone Scanner
JPSS-1	2015	VIIRS
Sentinel-3B	2017	OLCI
HY-1E/F	2017	COCTS & CZI
KMGS-B	2018	GOCI-II
PACE	2019	OES
ACE	>2020	OES
GEO-CAPE	>2020	Coastal Ocean Color Imaging Spec.

TABLE 1.7 – *Tableau des missions planifiées ayant à leur bord au moins un capteur susceptible de produire de la couleur de l'eau.*

$$\log_{10}(\mathbf{Chl}_a) = 0.2424 - 2.7423 \cdot R + 1.8017 \cdot R^2 + 0.0015 \cdot R^3 - 1.2280 \cdot R^4$$
$$\text{avec} \tag{1.20}$$
$$R = \log_{10}\left(\frac{\max(R_{rs}443, R_{rs}489)}{R_{rs}547}\right)$$

où R est le rapport de bande maximal et $R_{rs}X$ désigne la réflectance relative de la longueur d'onde X. Il est à noter que cet algorithme est calibré à partir d'un jeu de donnée *in-situ* qui évolue au cours du temps, et que les coefficients (0.2424, -2.7423, 1.8017, 0.0015 et -1.2280) reflètent les valeurs de cette calibration et sont valables uniquement pour le retraitement utilisé au cours de cette thèse.

La figure 1.22 représente une image globale pour le 01/08/2007 ainsi qu'un zoom de la concentration en chlorophylle-a obtenue à partir du produit MODIS/Aqua de niveau 3 "binnée", dont la résolution est de $1/24° \times 1/24°$ sur une grille régulière.

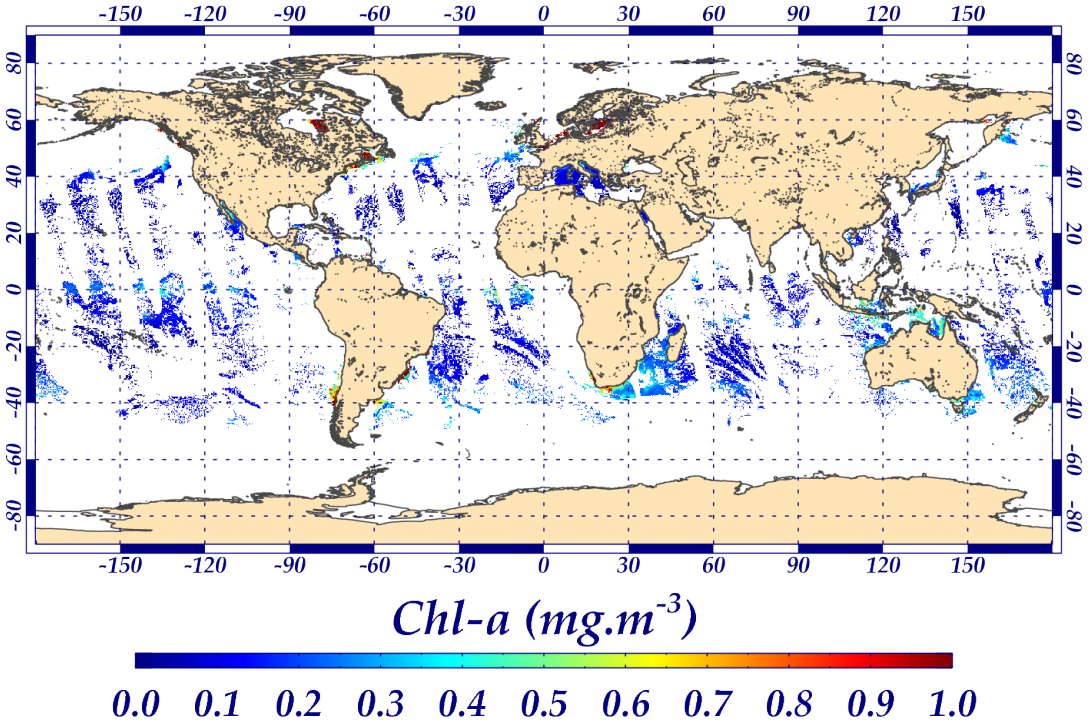

(a) Concentration en chlorophylle-a globale pour le 01/08/2007.

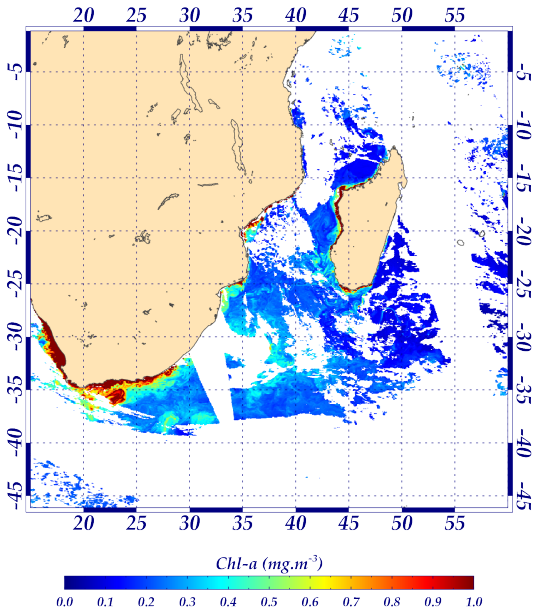

(b) Concentration en chlorophylle-a au Sud-Ouest de l'Océan Indien pour le 01/08/2007.

FIGURE 1.22 – Concentration en chlorophylle-a du produit MODIS/Aqua.

1.4 Données *in-situ* de courant

Les mesures de vitesse et de direction des courants de surface *in-situ* ont été utilisées pour estimer soit la qualité des données obtenues, soit la calibration de la profondeur de couche d'Ekman (voir le chapitre 2, partie 2.5). Il existe de nombreux instruments permettant d'obtenir des courants de surface *in-situ*, de manière Eulérienne ou Lagrangienne.
Pour la méthode Eulérienne, nous avons privilégié les données issues des "Acoustic Doppler Current Profiler" de coque (ADCP), et des réseaux d'observations tropicaux. Cette sélection a été faite en raison de l'homogénéité des bases, des séries temporelles étendues et bien évidemment de la possibilité d'obtenir des courants de surface à une profondeur équivalente aux profondeurs des courants obtenus via les données satellitaires.
Pour la méthode Lagrangienne, deux jeux de données ont été sélectionnés pour ces mêmes raisons : les données de bouées dérivantes munies d'une ancre flottante à $15m$ de profondeur et les flotteurs ARGO lors de leurs trajets de surface.

Dans cette partie, nous commencerons par introduire la technique pour mesurer les vitesses de chaque instrument, puis nous nous intéressons aux données utilisées.

1.4.1 Données Eulériennes

Les deux jeux de données considérés sont par nature très différents l'un de l'autre. Les données issues des ADCP de coque estiment les courants horizontaux dans une profondeur allant de $20\ m$ à $300\ m$ avec un échantillonage temporel, horizontal et vertical de l'ordre de ~ 5 minutes, $\sim 2\ km$ et $10\ m$ respectivement. Ces ADCP sont orientés vers le bas et sont directement incorporés dans la coque du navire. Les données provenant des réseaux d'observations sont acquises par des ADCP orientés vers la surface sur des lignes de mouillage fixes et placés à une profondeur de $300 - 400\ m$ au dessous de la surface. La mesure représente donc une série temporelle en un point fixe. L'orientation vers la surface présente un inconvénient car la surface de l'eau rétrodiffuse le signal et peut bruiter la mesure dans les 40 premiers mètres. Pour cette raison, certaines lignes de mouillage des réseaux tropicaux sont aussi équipées de courantomètres proches de la surface. Au cours de cette thèse, ces deux

moyens d'acquisition ont été utilisés à partir du moment qu'une observation était disponible à la profondeur de $25\ m$. De plus, seules les données ayant une qualification de "bonne" ou "probablement bonne", par les institutions les délivrant, ont été considérées.

a ADCP de coque

Les ADCP sont des instruments de mesure permettant de déterminer la vitesse du courant marin. En réalité, ils évaluent la vitesse de déplacement de la matière en suspension dans le milieu, celle-ci ayant une vitesse de déplacement négligeable devant la vitesse du courant. Pour cela, une onde acoustique est envoyée dans le milieu à une fréquence F_e et une vitesse C. Cette onde est diffusée par la matière en suspension en mouvement (avec une vitesse V vers la source d'émission) et son écho est réceptionné par l'instrument avec une fréquence F_r différente de F_e par effet Doppler.
Dans le cas d'un ADCP immobile, la relation entre ces paramètres est la suivante :

$$F_r = F_e \left(1 + \frac{V}{C}\right). \tag{1.21}$$

Dans le cas d'un ADCP de coque sur un navire en mouvement, il y a un double effet Doppler et l'équation 1.21 devient (avec $F_r^{'}$ la fréquence reçue) :

$$V = C \cdot \frac{(F_r^{'} - F_e)}{2F_e}. \tag{1.22}$$

Si le temps est pris en compte, il est possible de déterminer la distance D entre la source de l'émission et la position de la matière en suspension. Ce principe étant identique à la détermination de la hauteur par un altimètre, la relation est identique à l'équation 1.9. En analysant la réception du signal en fonction du temps (phases de réception), il est aussi possible d'obtenir la vitesse de déplacement de plusieurs couches adjacentes (cellules). La taille des cellules et la portée moyenne vont être inversement proportionnelles à la fréquence d'émission. Les fréquences typiques de ces transducteurs s'échelonnent de 38 à $1200\ kHz$ ce qui permet d'obtenir des cellules de 24 à $0,5\ m$ avec une portée moyenne de 1500 à $20\ m$ [*Lurton*, 2010]. La fréquence va donc être déterminante pour l'échantillonnage de la colonne d'eau que l'on souhaite effectuer et va être un compromis entre portée moyenne et taille des cellules [*Hummon et Firing*,

2003].

Les données d'ADCP de coque que nous avons utilisées sont distribuées par le "Joint Archive for Shipboard ADCP" (JASADCP). Le JASADCP est un groupement de plusieurs institutions, le "National Oceanographic Data Center" (NODC), le "National Coastal Data Development Center" (NCDDC) et l'Université d'Hawaii (HU) ; il a été initié dans les années 1990 pour centraliser, documenter, homogénéiser et assurer la qualité de l'archive des données ADCP de coque. Une autre de ses missions est de rendre disponible à la communauté scientifique cette archive croissante depuis 1985 (http://ilikai.soest.hawaii.edu/sadcp/intro.html).
L'archive actuelle catalogue les campagnes à la mer de 59 navires de différentes nationalités et répresente plus de 1500 campagnes s'échelonnant de 1985 à nos jours. La figure 1.23 représente l'ensemble des sections disponibles dans l'archive du JASADCP.

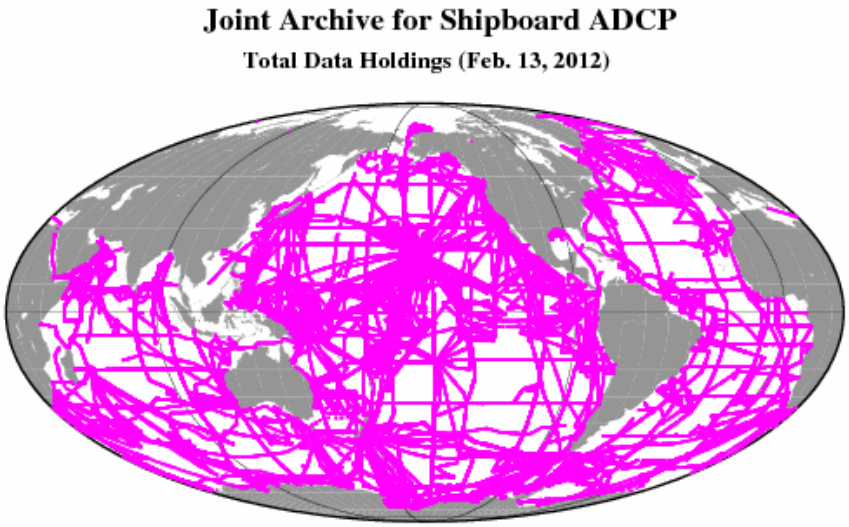

FIGURE 1.23 – *Illustration de l'ensemble des sections disponibles de l'archive du JASADCP. ©JASADCP.*

b Données des réseaux d'observation TAO, PIRATA, RAMA

Les données de courant de surface délivrées par les réseaux d'observation tropicaux dans l'Océan Pacifique, l'Océan Atlantique et plus récemment de l'Océan Indien proviennent de bouées ancrées et sont constituées de séries temporelles discontinues dont les périodes d'enregistrement sont d'une durée

variable. Ces données sont issues soit d'ADCP, soit de courantomètres à rotor ou à effet Doppler placés en subsurface sur les lignes de mouillages. Le principe de fonctionnement des courantomètres à effet Doppler est identique à celui des ADCPs, mis à part qu'ils enregistrent les courants à une seule profondeur (cellule d'acquisition unique). Les courantomètres à rotor sont des instruments associant la mesure de la direction à celle de la vitesse. La direction est évaluée au moyen d'un compas et d'une dérive permettant d'orienter l'instrument dans le sens du courant. Le module de la vitesse est acquis au moyen d'un capteur tournant qui enregistre le déplacement de la masse d'eau pendant un intervalle de temps :

$$V = \frac{C \cdot N}{T} + V_0 \tag{1.23}$$

avec :

- V : module de la vitesse,
- C : coefficient de proportionnalité dépendant du capteur utilisé,
- N : nombre de tours du rotor,
- T : intervalle de temps,
- V_0 : seuil de démarrage (dû au frottement du système pivots-crapaudines du capteur).

Dans la décennie du programme TOGA (Tropical Ocean-Global Atmosphere), la mise sous surveillance constante de l'Oscillation Australe et ses phénomènes associés El Niño/La Niña est apparue comme une nécessité aux impacts sociétaux majeurs [*McPhaden et al.*, 2010]. La connaissance et la prévision de ces phénomènes réclamant une observation combinée de l'océan et de l'atmosphère au niveau de tout l'Océan Pacifique tropical, le programme TOGA initia la création du réseau d'observation TAO (Tropical Atmosphere Ocean) [*Hayes et al.*, 1991]. Ce réseau, constitué de mouillages ancrés ayant une plateforme ATLAS (voir figure 1.24) en surface, délivre en temps réel un jeu de paramètres environnementaux (atmosphérique et océanique : http://www.pmel.noaa.gov/tao/proj_over/sensors.shtml). Initialement, ces mouillages n'étaient pas équipés pour estimer les courants, cependant au fur et à mesure de leurs remplacements et de leurs entretiens, certaines zones de ces lignes de mouillage ont été pourvues d'ADCPs et de courantomètres [*Plimpton et al.*, 2004]. En 2000, le réseau TAO est devenu, via sa fusion avec le réseau japonais "Triangle Trans-Ocean Buoy

Network" du Japan Agency for Marine-Earth Science and Technology (JAMSTEC), le réseau TAO/TRITON constitué de 69 mouillages.

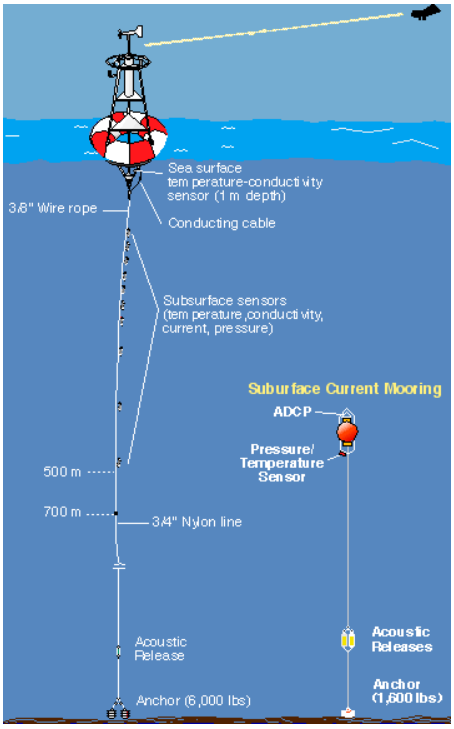

FIGURE 1.24 – *Illustration de la configuration standard des bouées ATLAS. ©TAO project office NOAA/PMEL.*

Dans le cadre du programme international CLIVAR ("CLImatic VARiability and predictability"), et dans la lignée du projet TAO/TRITON, le programme expérimental PIRATA ("Pilot Research morred Array in the Tropical Atlantic" qui depuis 2008 est devenu "Prediction and Research Moored Array in the Tropical Atlantic") a été mis en place en 1997 dans l'Océan Atlantique tropical [*Servain et al.*, 1998] (http://www.brest.ird.fr/pirata/index.php). Il en est de même pour le programme RAMA (Research Moored Array for Africa-Asian-Autralian Monsoon Analysis and Prediction) dont les objectifs scientifiques sont plus axés sur l'analyse et la surveillance de la mousson [*McPhaden et al.*, 2009]. Ce dernier programme est en cours de déploiement avec 65% de ses mouillages actuellement opérationnels (http://www.pmel.noaa.gov/tao/rama/). La figure 1.25 représente l'ensemble des mouillages de ces trois réseaux d'observation de la zone tropicale. Afin d'avoir une information sur les courants au niveau de la singularité équatoriale, les mouillages de la ligne équatoriale sont privilégiés pour l'installation des capteurs estimant les courants.

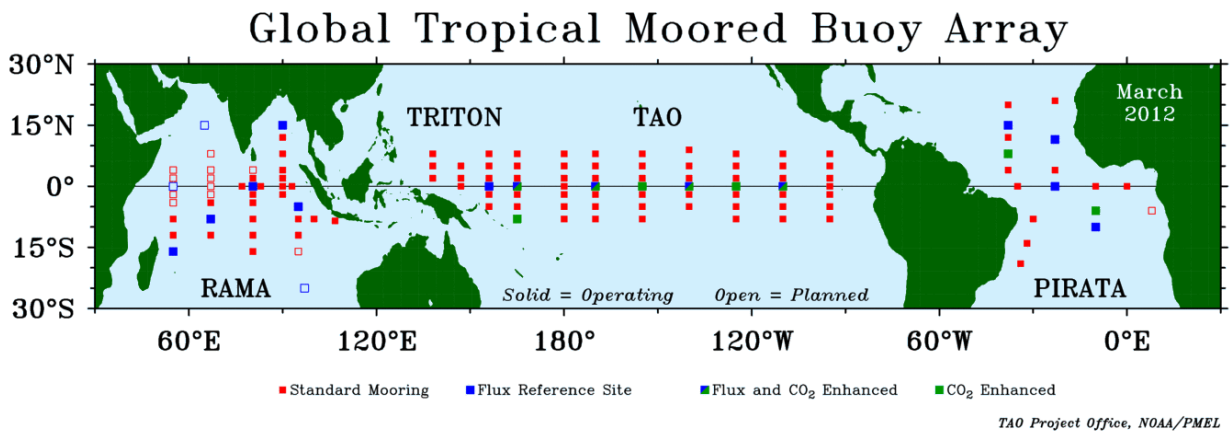

FIGURE 1.25 – *Illustration des positions des mouillages sur les réseaux TAO/TRITON, PIRATA et RAMA. ©TAO project office NOAA/PMEL.*

1.4.2 Données Lagrangiennes

Les bouées dérivantes, version moderne de "la bouteille à la mer", permettent de suivre le déplacement des masses d'eau de selon un schéma Lagrangienne. Elles enregistrent des paramètres physiques de la masse d'eau les environnant et transmettent ces informations en temps réel (pour les bouées de surface) via les réseaux de communication satellites. La localisation spatio-temporelle de la bouée est aussi enregistrée permettant ainsi d'obtenir entre deux positions sa vitesse moyenne de déplacement. Ces bouées peuvent dériver soit en surface, soit au moyen d'un ballast à une certaine profondeur déterminée par l'équilibre en densité entre la bouée et la masse d'eau.

a Bouées dérivantes de surface

En 1982 le "World Climate Research Program" (WRCP) reconnut la nécessité pour les recherches oceanographiques et climatiques de développer des bouées dérivantes avec des caractéristiques standardisées et facilement déployables. Le développement de ces nouveaux capteurs commença sous l'égide du Surface Velocity Program (SVP) du TOGA et du WRCP. En 1992 fût proposé le modèle d'une bouée de surface sphérique équipée d'une drogue semi-rigide la contraignant à suivre la masse d'eau à $15\ m$ de profondeur [*Sybranly et Niiler*, 1992]. Le premier déploiement en masse de ces bouées SVP commença en 1988 avec comme objectif de cartographier la circulation de surface de l'Océan Pacific tropical. Puis sous l'impulsion du WOCE et de Atlantic Climate Change Program

(ACCP), ce déploiement fut étendu à l'échelle globale [*Niiler*, 2001; *Lumpkin et Garzoli*, 2005].
En Septembre 2005, le nombre nominal de 1250 bouées, réparties sur l'ensemble du globe, a été atteint pour obtenir une résolution de $5° \times 5°$. La température et la salinité de surface, les courants de la couche de mélange, la pression atmosphérique ainsi que les vents acquis sont actuellement mis à disposition par le Global Drifter Program (GDP), qui assure aussi la maintenance de ce réseau d'observation *in-situ* (voir figure 1.26).

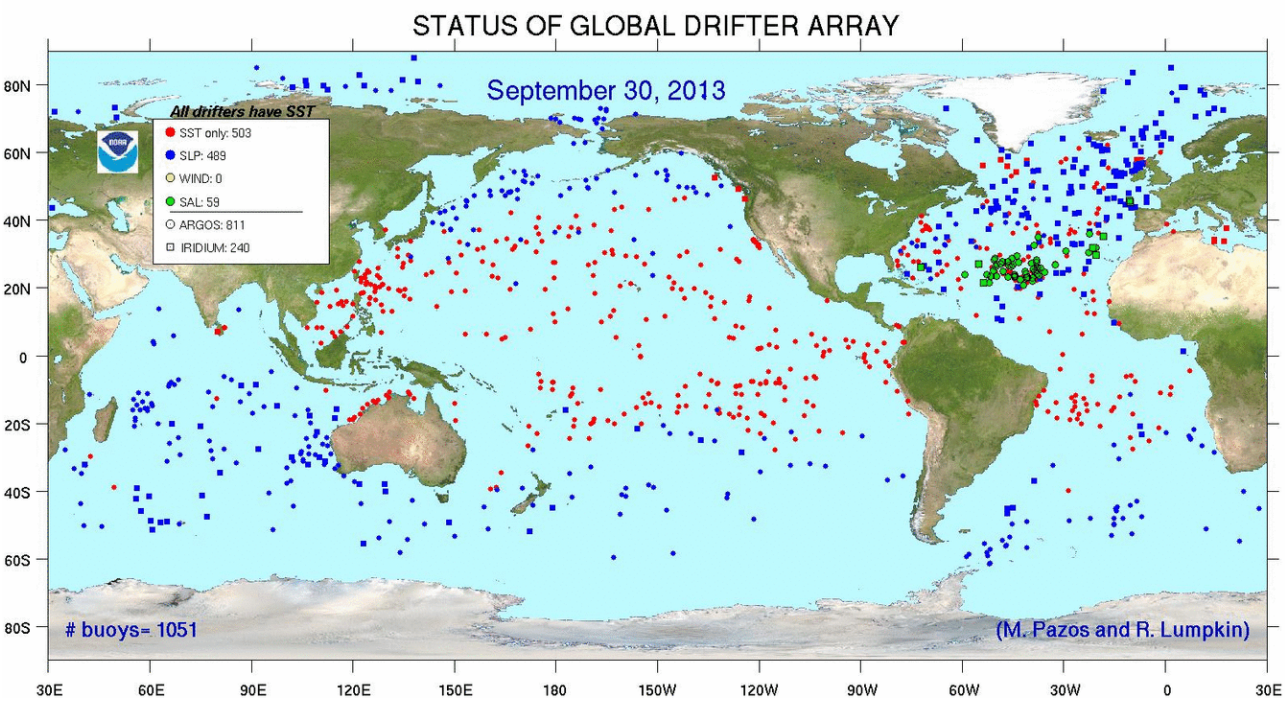

FIGURE 1.26 – *Illustration des positions des 1051 bouées en activité du GDP pour le 30 Septembre 2013. ©M. Pazos et R. Lumpkin.*

Au cours de cette thèse nous avons utilisé l'ensemble de l'archive disponible des données de bouées du GDP (http://www.aoml.noaa.gov/phod/dac/index.php).

b Bouées dérivantes de subsurface

Les déplacements des masses d'eau au dessous de la couche de surface n'étant pas accessibles par l'observation satellitaire, seules les observations *in-situ* permettent d'échantillonner ces profondeurs. Collecter le déplacement des couches intermédiaires, est de première importance dans le contexte du changement climatique global où nous nous trouvons actuellement. Afin d'ali-

menter les modèles climatiques, de mieux comprendre et prédire l'évolution de ces masses d'eau, il est nécessaire d'avoir un réseau autonome d'observation les surveillant. Pour répondre à cette attente scientifique et sous l'impulsion de WOCE du WRCP, un capteur a été développé dans les années 1990 par Russ Davis et Doug Webb, le : "Autonomous Lagrangian Circulation Explorer" (ALACE) [*Davis et al.*, 1992].
Au moyen d'un système de ballast, cette bouée dérivante a la capacité de modifier sa flottaison et donc de plonger, de se déplacer avec la masse d'eau en subsurface [*Stommel*, 1955; *Swallow*, 1955], puis de revenir à la surface pour transmettre sa position. Ainsi par sa position au moment de son immersion et de celle à son retour en surface, il est possible via la connaissance du temps de son trajet d'estimer son déplacement en subsurface. Sa spécificité de déplacement sur la verticale a rapidement conduit à l'idée d'échantillonner, en plus des déplacements horizontaux, les caractéristiques physiques de la masse d'eau. Ainsi cette seconde génération de bouées de subsurface, appelées SOLO ("Sounding Oceanographic Lagrangian Observer"), a été équipée d'une CTD ("Conductivity, Temperature, Depth") permettant d'enregistrer des profils de température et de salinité [*Davis et al.*, 2001].
A partir de 1998 les équipes internationales collaborant à GODAE et CLIVAR ont mis une forte priorité pour l'extension de ce concept à l'ensemble du globe et ont créé le programme ARGO (http://www.argo.net/index_flash.html). Le déploiement global a commencé en 2000 et en Novembre 2007, l'objectif d'avoir plus de 3000 flotteurs a été atteint (voir figure 1.27), avec un replacement de 800 flotteurs par an afin de ré-ensemencer les zones de divergence. L'autonomie de ces flotteurs est actuellement de 150 cycles d'une durée de 8 à 10 jours et le profil "standard" échantillonne les 2000 premiers mètres (voir figure 1.28). Actuellement trois modèles sont utilisés :

- le PROVOR développé par KANNAD en France en étroite collaboration avec l'IFREMER,
- l'APEX produit par Teledyne Webb Research aux États-Unis,
- le SOLO construit par le Scripps Institution of Oceanography aux États-Unis.

Au cours de cette thèse, nous avons utilisé les estimations de courant moyen de surface analysées et distribuées par *Xie et Zhu* [2008, 2009] sur la période

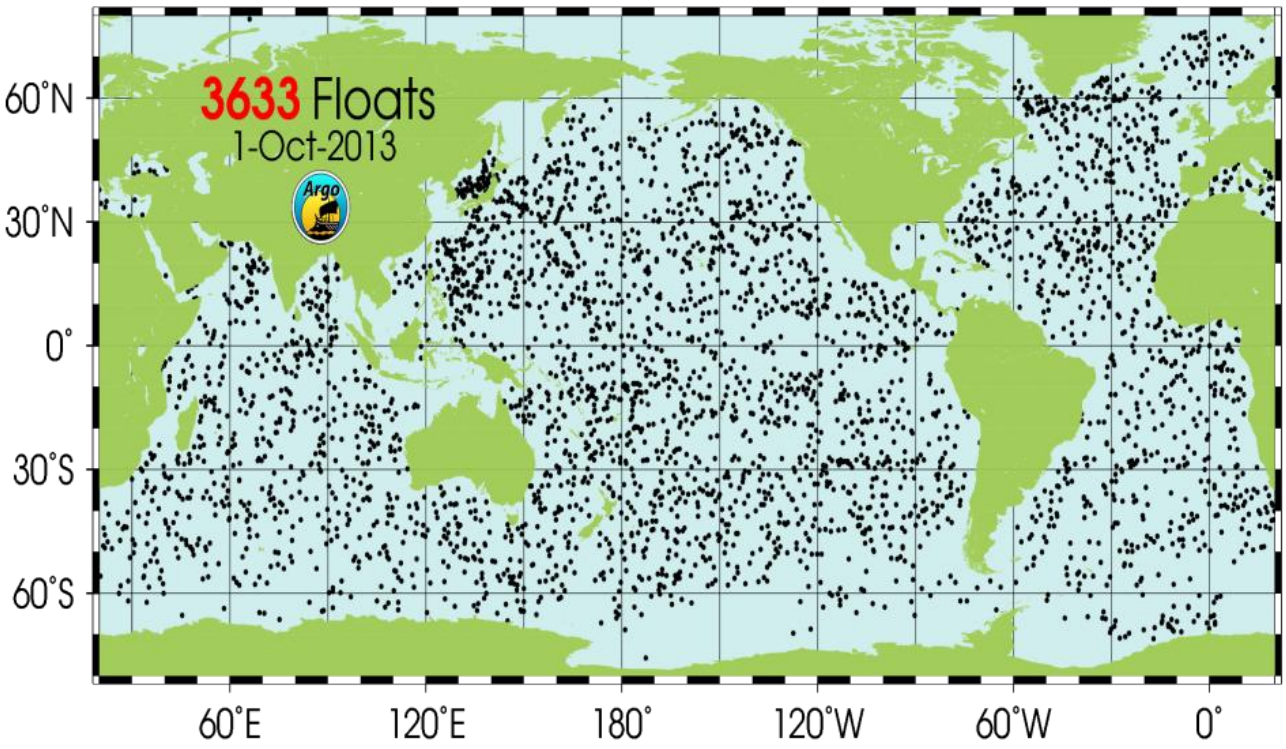

FIGURE 1.27 – *Illustration des positions des flotteurs ARGO ayant délivré des données dans les 30 derniers jours avant le 1 Octobre 2013. ©ARGO.*

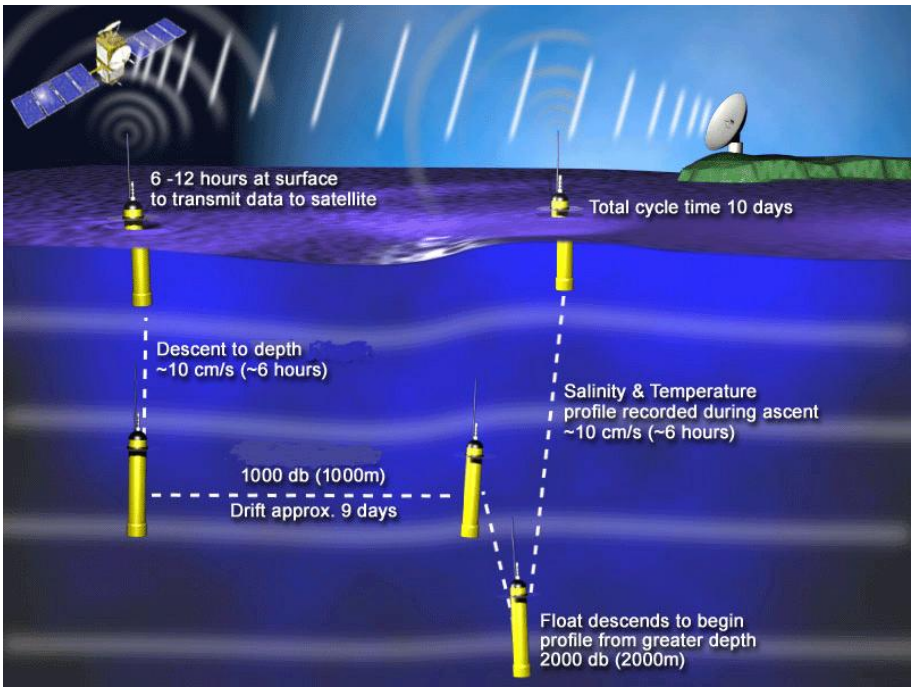

FIGURE 1.28 – *Illustration du cycle d'une bouée ARGO. ©ARGO.*

allant de 2000 à 2008. Ce courant moyen de surface est déterminé entre la position initiale et finale de la bouée ARGO lors de son déplacement en surface.

1.5 Pré-traitement des données

Comme nous l'avons vu dans les sections précédentes les données satellitaires possèdent des résolutions spatio-temporelles hétérogènes, il est donc nécessaire si l'on veut fusionner les informations déduites de ces données de choisir une résolution spatio-temporelle identique à toutes les données. Ceci est effectué au moyen d'une classique méthode d'interpolation bilinéaire où la valeur du point considérée est calculée à partir de la somme des quatre valeurs les plus proches pondérées par l'aire des surfaces opposées, le tout étant renormalisé par l'aire totale.

Afin d'éliminer les courants inertiels, si nécessaire, dans les données de bouées Lagrangiennes de surface droguées à $15\ m$, un lissage des déplacements a été effectué avec un noyau de 17 points, ce qui représentent un lissage du déplacement sur 4.25 jours, et correspond à la période d'inertie ($T = 12/\sin(f)$) d'une particule se déplaçant à $\sim 6.75°$ de latitude. Cette valeur ayant été calculée empiriquement pour éliminer simplement ces courants sans trop affecter les déplacements moyens de l'ensemble du jeu de données.

Chapitre 2
La dynamique mésoéchelle

Chapitre 2

La dynamique mésoéchelle

Sommaire

2.1 Introduction 80

2.1.1 Aperçu de nos connaissances actuelles 80

2.2 Estimation des courants à l'échelle globale 82

2.2.1 Courants géostrophiques 82

2.2.2 Courants d'Ekman 83

2.3 Article : Global surface currents : a high-resolution product for investigating ocean dynamics, Sudre and Morrow, 2008 . 87

2.3.1 Résumé de l'article (version française) 87

2.3.2 Article publié dans *Ocean Dynamics* 88

2.3.3 Améliorations souhaitables de l'estimation des courants au quart de degré à l'échelle globale 107

2.4 Article : On the global estimates of geostrophic and Ekman surface currents, Sudre et al., 2013 107

2.4.1 Résumé de l'article (version française) 107

2.4.2 Article publié dans *Limnology and Oceanography : Fluids and Environments* 108

2.5 Compléments sur la composante d'Ekman 129

2.6 Comparaison des courants de l'article [*Sudre et Morrow*, 2008] et de l'article [*Sudre et al.*, 2013] 138

2.7 Conclusions 140

2.1 Introduction

2.1.1 Aperçu de nos connaissances actuelles

L'océan est le siège de mouvements complexes à toutes échelles spatiales agissant sur des échelles de temps extrêmement variées. Les structures océaniques à grande échelle spatiale comme les gyres se révèlent sur des échelles de temps allant de plusieurs mois à plusieurs années et fournissent sur le long terme la dynamique océanique moyenne [*Maximenko et al.*, 2009]. Ces structures, composantes principales de la circulation océanique globale de surface, sont générées, en première approximation, par la rotation de la Terre, la circulation atmosphérique à l'échelle planétaire, et les gradients de pression horizontaux dûs aux variations de la hauteur de mer [*Sverdrup*, 1947]. Elles sont restreintes par des conditions aux limites précises via la forme des bassins entraînant la formation de courants de bord étroits et intenses à l'Ouest et des branches de plus faible intensité à l'Est [*Stommel*, 1948]. Cette circulation globale est aussi conditionnée par la profondeur des seuils sous-marins contrôlant les échanges entre les différents bassins.
Au sein de cette circulation de surface moyenne et globale se développe une circulation secondaire complexe où la variabilité en terme d'énergie cinétique est d'un ordre supérieur à celle de la circulation moyenne [*Fu et al.*, 2010]. Bien qu'il soit difficile d'en donner une définition précise, on peut situer la mésoéchelle comme une classe de phénomènes à forte énergie avec des échelles spatio-temporelles typiques de l'ordre de 50 à $500\ km$ et de 10 à $100\ jours$. Les jets étroits, les méandres, les anneaux et les fronts sont des représentants de cet aspect de la dynamique océanique. Cependant, les structures océaniques les plus représentatives de cette activité sont les tourbillons. Qu'ils soient cyclonique ou anticlyclonique, ils sont caractérisés par des diamètres de O($100km$), et des durées de vie moyennes de 32 semaines, pouvant dépasser l'année. D'une profondeur pouvant atteindre couramment $2000\ m$ et d'une vitesse de rotation supérieure à $20\ cm.s^{-1}$, ces structures ont une translation moyenne d'environ $550\ km$ et la majorité d'entre elles se déplace vers l'Ouest, à l'exception de celles issues du Gulf Stream, du Kiroshio et du Courant Circumpolaire Antarctique [*Chelton et al.*, 2011]. Estimés à plus de 3500 à un instant donné, ils sont répartis non seulement dans les zones de courants intenses mais aussi sur l'ensemble du globe. Ces tourbillons, qui sont des vortex que l'on peut préci-

sément caractériser comme des circulations persistantes fermées sont générés par divers processus physiques parmi lesquels on trouve :

- les instabilités baroclines issues du cisaillement vertical du courant moyen qui sous certaines conditions peuvent convertir leur énergie potentielle en énergie tourbillonnaire potentielle et cinétique,
- les instabilités barotropes issues du cisaillement horizontal provenant le plus souvent de jets,
- l'association combinée des deux instabilités précédentes,
- les fluctuations du vent (tourbillons orographiques),
- les variations de la topographie ou des obstacles topographiques, qui viennent modifier la circulation moyenne.

Ces structures cohérentes représentent une concentration de la vorticité dans un domaine restreint de l'écoulement. A la suite de leur création elles vont être advectées pendant toute leur durée de vie par l'écoulement moyen [*Mcwilliams*, 1984]. N'étant pas isolées les une des autres, de nombreuses interactions vont se produire entres elles et également avec l'écoulement moyen et toutes les autres structures présentes sur leur cheminement. Ces nombreuses interactions vont générer d'autres structures comme des filaments d'étirement, des plumes, ou d'autres structures cohérentes ayant des échelles spatiales inférieures. Ces structures de sous mésoéchelle, bien qu'extrêmement importantes d'un point de vue dynamique, ont des durées de vie beaucoup plus courtes allant de la journée à la dizaine de jours et des dimensions spatiales de 1 à 50 km. Ce processus d'échange et de transfert d'énergie, que l'on nomme la cascade d'enstrophie, va s'effectuer des grandes structures spatiales vers les structures de moindres dimensions, et va se produire jusqu'à l'échelle de dissipation. De même, il existe une cascade inverse, qui va se produire des structures de la petite échelle vers les structures de la grande échelle et qui est désignée sous l'appellation de cascade d'énergie inverse. Au cours de ce processus, l'énergie emmagasinée dans la fine échelle est (ré)absorbée par les structures peuplant la grande échelle.
Il existe donc toute une hiérarchie de structures et de processus associés intervenant dans le développement et le maintien de la dynamique océanique qui est ainsi turbulente, et les effets non linéaires dominent nettement ceux provenant de la viscosité.

Les satellites permettent d'observer indirectement une partie de la dynamique océanique, en fonction de leurs résolutions spatiale et temporelle. Toutes les structures océaniques citées précédemment ont une signature satellitaire identifiable, ainsi il est possible de suivre leurs évolutions de positions et leurs intensités. Si on s'intéresse à la dynamique océanique à grande échelle et à mésoéchelle, une résolution au quart de degré est nécessaire et la plupart du temps suffisante, cependant toute la dynamique présente dans l'océan ne sera pas représentée.
L'échelle horizontale des tourbillons à mésoéchelle est de l'ordre de 50 à 200 km, et le rayon de déformation de Rossby barocline est de l'ordre de 20 à 50 km, ces structures océaniques sont donc en équilibre géostrophique et vont avoir une signature identifiable au niveau dynamique lors du calcul des courants géostrophiques.

2.2 Estimation des courants à l'échelle globale

2.2.1 Courants géostrophiques

Le principe de base permettant de déterminer la circulation océanique à partir du champ de densité est l'équilibre géostrophique et hydrostatique. A condition de se tenir éloigné des côtes (profondeur infinie), de l'équateur (où le paramètre de Coriolis va être nul) et dans le cas d'un fluide incompressible (condition de Boussinesq), on peut déterminer u et v, les composantes zonale et méridienne de la vitesse (w, la composante sur l'axe des profondeurs étant nul à l'équilibre géostrophique) :

$$\begin{cases} u &= & -\dfrac{1}{f \cdot \rho} \cdot \dfrac{\partial p}{\partial y} \\ v &= & \dfrac{1}{f \cdot \rho} \cdot \dfrac{\partial p}{\partial x} \\ 0 &= & -\dfrac{\partial \cdot p}{\partial \cdot z} - g \cdot \rho \end{cases} \tag{2.1}$$

avec :

- p : pression,
- ρ : densité de l'eau de mer,

- f : paramètre de Coriolis défini par $f = 2\Omega\sin(\phi)$, où Ω est la vitesse angulaire de rotation de la terre et ϕ la latitude.

Si on multiplie la topographie dynamique obtenue à partir des satellites altimétriques par $\rho \cdot g$ (où g est l'accélération standard de la pesanteur), il en résulte la pression dynamique à la surface de l'océan. Ainsi il est possible d'obtenir une approximation de la vitesse géostrophique par la mesure de l'altimétrie en injectant ce calcul dans l'équation 2.1 qui devient :

$$\begin{cases} u &= -\dfrac{g}{f} \cdot \dfrac{\partial h}{\partial y} \\ v &= \dfrac{g}{f} \cdot \dfrac{\partial h}{\partial x} \end{cases} \tag{2.2}$$

Il convient de préciser qu'il est nécessaire pour pouvoir utiliser ces équations d'avoir une profondeur de référence où les composantes de la vitesse horizontale sont connues. De plus, les équations 2.2 de l'approximation géostrophique font intervenir le paramètre de Coriolis au dénominateur, ce qui entraîne une impossibilité de les utiliser dans la zone proche de l'équateur. Les articles des sections 2.3 et 2.4 traitent ce sujet en proposant deux méthodes pour obtenir la dynamique océanique dans la zone équatoriale.

2.2.2 Courants d'Ekman

Une part importante de la variabilité de la dynamique océanique dans la couche de surface à mésoéchelle peut être étudiée, en première approximation, au moyen de la géostrophie. Cependant cette variabilité ne tient pas compte des processus agéostrophiques, en particulier ceux issus de l'impact des vents à la surface de l'océan. Pour appréhender cet impact, il est nécessaire d'introduire un second type de courant dont la génération provient de la friction du vent à la surface de l'océan.

De 1893 à 1896, à bord de la goélette "Fram", Fridtjof Wedel-Jarlsberg Nansen, homme d'état, diplomate Norvégien ayant fortement contribué à la Société des Nations (prix Nobel de la paix en 1922), et explorateur polaire, conduit une expédition en Arctique visant à étudier l'existence d'un courant marin transpolaire qui entraîne une dérive de la banquise. A la suite de

cette expédition, il publie, en novembre 1896, un récit en six volumes de cette extraordinaire aventure humaine, en consignant toutes les observations effectuées à bord du Fram ainsi que sur la banquise. L'année suivante ce récit est traduit en anglais et en français sous les titres respectifs "Farthest North" et "Vers le pôle". Ce zoologue de formation, reconverti en océanographe suite à l'expédition du Fram, fait part de ces observations sur la dérive des glaces de la banquise au professeur Wilhelm Friman Koren Bjerknes de l'Université d'Oslo. Intrigué par cette dérive (dont la vitesse estimée de $O(2\%)$ de la vitesse du vent et avec une direction variant de $20°$ à $40°$ à droite de la direction du vent), "Vilhelm" Bjerknes propose à un de ses étudiants, Vagn Walfrid Ekman d'expliquer analytiquement cette dérive. En 1902, Ekman met en évidence au moyen des observations des courants océaniques estimés, l'effet du vent sur la surface de la mer. En particulier, il démontre l'existence de courants qui "forment quelque chose comme un escalier en colimaçon, en descendant vers les profondeurs". Ce principe de l'océanographie est actuellement reconnu comme la spirale d'Ekman, et permet de déduire, dans la couche d'Ekman (h_E), l'intensité et la direction des courants de dérive, à une profondeur donnée. Ces courants sont issus de l'équilibre entre les forces de friction et de l'effet de rotation de la terre (Coriolis). Cette spirale d'Ekman n'a été observée que bien plus tard en 1975 par *Hunkins* [1975], avec des mesures de courant en bordure de banquise.

Formulation analytique des courants de dérive d'Ekman par les vents

Dans le cas d'un état stationnaire ($\frac{du}{dt} = 0$), dans les approximations de Boussinesq (qui permettent de négliger la variation de densité entre deux fluides) et en présence de frottement, l'équation du mouvement devient :

$$\begin{cases} -fu + F_y - \dfrac{1}{\rho_0}\dfrac{\partial p}{\partial y} &= 0 \\ fv + F_x - \dfrac{1}{\rho_0}\dfrac{\partial p}{\partial x} &= 0 \end{cases} \tag{2.3}$$

avec F_x et F_y les composantes de la force de frottement qui peuvent s'écrire :

$$\begin{cases} F_x = \dfrac{1}{\rho_0}\dfrac{\partial \tau_x}{\partial z} = A_z\dfrac{\partial^2 u}{\partial z^2} \\ F_y = \dfrac{1}{\rho_0}\dfrac{\partial \tau_y}{\partial z} = A_z\dfrac{\partial^2 v}{\partial z^2} \end{cases} \tag{2.4}$$

où τ_x et τ_y sont les composantes zonale et méridienne de la tension de frottement (ou stress), A_z est le coefficient de viscosité moléculaire (viscosité turbulente dans le cas d'un écoulement turbulent).

Il convient de préciser que dans le développement de l'équation 2.3, deux forces sont génératrices de courant (la force de pression et la force de friction). Cependant il est possible de séparer les solutions de ce système linéaire en deux composantes : la composante de la vitesse géostrophique (voir équation 2.1) et la composante de la vitesse de dérive par les vents. On obtient pour ces dernières composantes, les équations dites d'Ekman en introduisant la tension du vent $\tau(\tau_x, \tau_y)$:

$$\begin{cases} -fu_E + \dfrac{1}{\rho_0}\dfrac{\partial \tau_y}{\partial z} &= 0 \\ fv_E + \dfrac{1}{\rho_0}\dfrac{\partial \tau_x}{\partial z} &= 0 \end{cases} \tag{2.5}$$

L'obtention d'une solution au système d'équations ci-dessus, nécessite la connaissance des profils des composantes de la tension du vent de la surface ($z = 0$) jusqu'à la profondeur h_E où l'effet du vent devient négligeable. Ceci représente le principal écueil pour déduire les courants de dérive par cette formulation. Il est donc nécessaire, si on veut estimer les courants de dérive, d'utiliser un modèle statistique permettant une paramétrisation de la profondeur de la couche d'Ekman et de la viscosité turbulente.

Approche statistique de la paramétrisation de la couche d'Ekman et du coefficient de traînée

Les données *in situ* récoltées par les bouées dérivantes de surface (cf 1.4.2 a) permettent d'avoir une estimation des courants de surface comprenant essentiellement les courants géostrophiques, les courants agéostrophiques (les courants de dérive en étant la composante principale, ainsi que les courants inertiels). *Niiler et Paduan* [1995] montrent au moyen de 63 bouées dérivant dans le Pacifique Nord-Est, qu'il existe une forte corrélation entre le déplacement des bouées dérivantes et le vent sur des périodes allant de 5 à 20 $jours$, ainsi qu'une différence de profondeur notable entre la profondeur de couche de mélange observée (60 m) et la profondeur de couche estimée, au moyen d'un modèle de régression par la tension du vent ($34 - 38$ m).
Dans la littérature, plusieurs algorithmes ont été testés pour convertir le for-

çage des vents en courants de dérive à différentes profondeurs, et dans différentes régions océaniques. On peut citer :

- dans l'Atlantique Nord Tropical [*Chereskin et Roemmich*, 1991],
- dans l'Océan Indien en Mer d'Arabie [*Chereskin et al.*, 1997],
- dans le Pacifique Tropical [*Ralph et Niiler*, 1999].

Différents auteurs ont développé des méthodes de séparation de la composante de la vitesse géostrophique dérivée par l'altimétrie et de la composante de la vitesse de dérive obtenue par les bouées dérivantes [*Ralph et Niiler*, 1999; *Reverdin et al.*, 2003; *Niiler et al.*, 2003]. Le modèle de régression retenu ici pour l'obtention des courants de dérive par l'effet des vents est celui développé par [*Van Meurs et Niiler*, 1997] et [*Lagerloef et al.*, 1999]. Sous forme complexe sa formulation est :

$$\mathbf{U}_E = Be^{i\theta}\tau \tag{2.6}$$

avec :

- $i = \sqrt{-1}$,
- $\tau(\tau_x, \tau_y)$: tension du vent,
- $\mathbf{U}_E(u_E, v_E)$: courant d'Ekman (ou de dérive par l'effet des vents),
- B : amplitude,
- θ : angle de rotation par rapport à la direction du vent.

Lagerloef et al. [1999] en se basant sur un modèle de régression linéaire multiple empirique et en utilisant des bouées dérivantes à $15\ m$ de profondeur sur l'ensemble du Pacifique Tropical ($25°N$,$25°S$) , ont estimé les paramètres B et θ tels que :

$$\begin{cases} B &= \dfrac{1}{\rho}(r^2 + f^2 h_e^2)^{-\frac{1}{2}} \\ \theta &= \arctan\left(\dfrac{f h_e}{r}\right) \end{cases} \tag{2.7}$$

avec :

- ρ : densité standard de l'eau de mer ($\rho = 1025 kg \cdot m^{-3}$) ,
- r : paramètre de friction,
- f : paramètre de Coriolis (exprimé en fonction de la latitude),
- h_E : profondeur de la couche d'Ekman.

Dans l'article présenté ci-après, cette approche a été étendue à l'ensemble du globe conjointement à l'estimation des courants géostrophiques.

2.3 Article : Global surface currents : a high-resolution product for investigating ocean dynamics, Sudre and Morrow, 2008

2.3.1 Résumé de l'article (version française)

Un produit de courants de surface global avec une résolution au 1/4° a été développé par le Centre de Topographie des Océans et de l'Hydrosphère. Ce courant de surface est une combinaison du courant d'Ekman estimé à partir du produit de vent issu du satellite QuikSCAT, de l'anomalie du courant géostrophique dérivée de l'altimétrie et du courant géostrophique moyen dérivé d'une climatologie. Dans la bande équatoriale, les courants ont été ajustés en suivant la méthode proposée par [*Lagerloef et al.*, 1999]. Ce produit de courants satellitaires a été comparé à plusieurs types d'observation *in situ* du courant. Une validation globale a été effectuée en utilisant des bouées Lagrangiennes de surface et des observations de courants d'ADCP de coque. Cette comparaison montre un très bon accord dans les bandes subtropicales et de moyennes latitudes. Les corrélations zonales et méridiennes entre les courants satellitaires dérivés et les courants issus des bouées dérivantes se situent autour de 0.7 sur la plupart du globe. Ces corrélations sont réparties en bandes zonales. Dans les régions de courant de bord Ouest, cette corrélation dépasse 0.8. Dans la bande équatoriale, la corrélation avec les bouées dérivantes diminue jusqu'à une valeur minimale de 0.51. La comparaison avec les courantomètres des mouillages du réseau TAO/TOGA montre qu'à l'équateur la variabilité à basse fréquence des courants est bien capturée par ce produit de courants de surface satellitaires. Cependant le signal à haute fréquence ($< 20\ jours$) n'est pas bien reproduit, ce qui est particulièrement le cas de la composante méridienne dû à la présence des ondes d'instabilités tropicales. Par l'utilisation d'un forçage journalier par les vents issus de QuikSCAT, nous montrons une amélioration significative du produit de courants satellitaires, en particulier, dans les régions de forts vents d'Ouest à hautes latitudes ainsi que dans l'Océan Tropical Indien.

2.3.2 Article publié dans *Ocean Dynamics*

Référence : Sudre J. and R. Morrow, 2008 : Global surface currents : a high-resolution product for investigating ocean dynamics, *Ocean Dynamics*, **58**, 101-118, DOI 10.1007/s10236-008-0134-9.

Ocean Dynamics (2008) 58:101–118
DOI 10.1007/s10236-008-0134-9

Global surface currents: a high-resolution product for investigating ocean dynamics

Joel Sudre · Rosemary A. Morrow

Received: 15 June 2007 / Accepted: 23 March 2008 / Published online: 14 May 2008
© Springer-Verlag 2008

Abstract A global 1/4° resolution product of surface currents has been developed by the Centre de Topographie des Océans et de l'Hydrosphère. The surface current is calculated from a combination of Ekman currents derived from wind estimates from QuikSCAT satellite, geostrophic current anomalies derived from altimetry, and a mean geostrophic current derived from climatology. In the equatorial band, the currents are adjusted following the methodology proposed by Lagerloef et al. (J Geophys Res, 104(C10):22313–22326, 1999). These satellite-derived currents have been compared to different types of in situ current observations. A global validation is performed using Lagrangian surface drifting buoys and acoustic Doppler current profiler current observations along ship tracks. The comparison shows a very good agreement in the subtropical and mid-latitude bands. The correlation between the satellite-derived currents and the drifter currents in zonal mean bands is around 0.7 for most of the world oceans, both for the zonal and the meridional components. This correlation rises up to 0.8 in the regions of strong boundary currents. In the equatorial band, the correlation with the surface drifting buoys is reduced. A direct comparison with the TOGA/TAO moored current meter data at the equator shows that the low frequency currents are captured by the satellite current product, but there is a substantial high-frequency signal (<20 days), which is not reproduced. This is especially the case for the meridional component and is mainly related to the tropical instability waves. We also show that using daily QuikSCAT wind forcing improves the satellite current product, particularly in the high-latitude westerly wind belt and in the tropical Indian Ocean.

Keywords Ocean surface currents · Satellite altimetry · Scatterometry winds · In situ currents

Responsible Editor: John Wilkin

J. Sudre (✉) · R. A. Morrow
CTOH/LEGOS,
18 av. E. Belin,
31401 Cedex 9 Toulouse, France
e-mail: joel.sudre@legos.obs-mip.fr

1 Introduction

High-resolution ocean surface currents are of great importance for many oceanographic applications. From a practical perspective, they are necessary for monitoring the surface advection of oil spills (e.g., Wahl et al. 1996) or the role of horizontal advection on plankton dynamics (Garçon et al. 2001) for interpreting ocean in situ measurements with respect to meandering fronts or eddies (Morrow et al. 2003) or interpreting the trajectories of migrating sea mammals, birds, or turtles (e.g., Girard et al. 2006). Long-term, high-resolution observations of the ocean surface circulation are also fundamental for climate studies, for example, for quantifying the role of horizontal advection on the surface heat budget in different regions (Caniaux et al. 2005; Picaut et al. 2002; Chaigneau et al. 2004), for investigating the onset and evolution of El Niño events (e.g., Lagerloef et al. 2003), or for the ocean response to the North Atlantic Oscillation (e.g., Esselborn and Eden 2001).

Global coverage of the surface circulation is relatively new. Global surface geostrophic currents have been determined from satellite altimetry data over the last 10–15 years, excluding the tropical band where the Coriolis force approaches zero (e.g., Ducet et al. 2000). These geostrophic currents are derived from gridded altimetric data, and the mapping process smooths out small-scale

features that are less than a 70- to 250-km wavelength (depending on latitude) or 15-day period. Ducet et al. (2000) note that in the high-latitude bands, up to 40% of the eddy kinetic energy (EKE) may be missing from the gridded altimetric data. In the tropical band, specific algorithms can be adapted using the β-plane geostrophic approximation, which involves the second derivative of surface height (Lukas and Firing 1984; Picaut et al. 1989; Lagerloef et al. 1999). The second derivative is valid over space scales of >100 km and timescales greater than 15–30 days (Picaut et al. 1989), providing relatively smoothed geostrophic velocities at the equator.

The ageostrophic component of the surface current field is more difficult to access. The Ekman component of this ageostrophic circulation can be calculated from the wind stress forcing fields. Algorithms to convert the surface wind forcing to Ekman currents at different depths have been tested in various regions, for example, in the Arabian Sea (Chereskin et al. 1997), at 11°N in the north Atlantic (Chereskin and Roemmich 1991), and in the tropical Pacific (Ralph and Niiler 1999). A global Ekman component based on the Ralph and Niiler (1999) algorithm has also been recently developed (Niiler et al. 2003). We will apply this global formulation in the following analysis. Ageostrophic currents associated with frontogenesis or other small-scale ageostrophic dynamics are not included in these Ekman currents.

The global surface circulation has also been derived from in situ near-surface drifting buoys (Niiler 2001). This is a recent development because, up until the 1990s, global drifter-based circulation studies were limited by the sparse drifter coverage in the southern hemisphere. Regional studies with better data coverage have considered the surface circulation in the tropical Pacific, where drifters have been deployed since the late 1970s (e.g., Reverdin et al. 1994; Ralph and Niiler 1999), in the tropical Indian (e.g., Molinari et al. 1990), and in the North Atlantic (e.g., Reverdin et al. 2003; Brambilla and Talley 2006). The near-surface drifters, drogued at 15 m depth to avoid wind slippage, follow the near-surface ocean currents in a Lagrangian sense. Their Lagrangian drift responds to ocean movements at a wide range of space and timescales, and include both ageostrophic and geostrophic movements. Unlike satellite-derived geostrophic and Ekman currents, the surface drifter data distribution is not homogeneous. The majority of drifters are deployed along shipping lanes, and they tend to accumulate in convergent regions, especially along fronts. These sampling effects can result in biases in the mean field or in box averages. Despite their different sampling capabilities, various authors have developed techniques to separate the satellite-derived geostrophic and Ekman components from these drifter trajectories (Ralph and Niiler 1999; Reverdin et al. 2003; Niiler et al. 2003).

In this paper, we present a high-resolution satellite-derived global surface current product, developed at the Centre de Topographie des Océans et de l'Hydrosphère (CTOH) at LEGOS, Toulouse. The product is based on geostrophic currents calculated from satellite altimetry and a mean sea surface height field, and Ekman currents from scatterometry. The data processing in the tropical band follows the pioneering work of the Ocean Surface Current Analyses Real time (OSCAR) project, who developed a tropical Pacific surface current product with specific algorithms adapted for equatorial regions (Lagerloef et al. 1999; Bonjean and Lagerloef 2002). The CTOH product is global and maintains a high spatial resolution (1/4°), whereas OSCAR geostrophic currents are spatially smoothed to obtain their final 1° product. Although adequate for the tropics, our analyses show that it is important to maintain the 1/4° spatial resolution at mid- to high latitudes where the Rossby radius scales are small and where any small-scale changes will be amplified by the geostrophic currents, which are based on the first derivative of the sea level field.

The CTOH satellite near-surface currents are validated by a statistical comparison with various in situ data sets (global surface drifters, ship acoustic Doppler current profiler (ADCP), TAO current meter mooring data). The CTOH product is also briefly compared to the OSCAR project (http://www.oscar.noaa.gov). The CTOH product provides separate time series of the three current components: the mean and variable geostrophic currents and the wind-driven Ekman currents. This separation allows us to compare the relative contributions of wind versus internal ocean forcing (Section 4). We also investigate using daily wind forcing for the Ekman currents for the period 1999–2006 when QuikSCAT daily winds are available (Section 7). This improves the surface currents in the high-latitude westerly wind belt in both hemispheres and in the tropical Indian Ocean. The daily wind product does of course increase the data storage for users by a factor of seven.

The CTOH surface current data product is available for the period 1992–1999 using gridded altimetric data and ERS scatterometry winds, and for the period 1999–2006 using altimetry and QuikSCAT winds (http://www.legos.obs-mip.fr/observations/ctoh). This validation paper will concentrate on the QuikSCAT wind period 1999–2006.

2 Data

2.1 Sea surface height

The mapped sea level anomaly (MSLA) from the Data Unification and Altimeter Combination System (DUACS) are combined with the mean dynamic topography RIO05 (Rio et al. 2005) to obtain a time-variable sea surface height (SSH)

data product. The MSLA product for the 1999–2006 period merges altimetric measurements from five altimeter missions (Topex/Poseidon, ERS1&2, Geosat Follow-on, Envisat, Jason-1). A complete description of the DUACS processing is given on the AVISO web site (http://www.jason.oceanobs.com/documents/donnees/duacs/handbook_duacs.pdf).

The mean dynamic topography (MDT) is the mean sea surface height that is due to the permanent ocean circulation, with the marine geoid removed. The MDT product used hereafter is derived from the RIO05 product (Rio et al. 2005), which is based on multiple in situ and satellite data sets, including GRACE gravity data. More information about the MDT used in the CTOH current product can be found at (http://www.jason.oceanobs.com/html/donnees/produits/auxiliaires/mdt_uk.html).

In the following sections, the geostrophic currents are calculated from the SSH field that represents the sum of the MSLA and the MDT. We use the weekly DUACS SSH data that has a spatial resolution of 1/3° projected onto a Mercator grid. We convert this spatial resolution onto a 1/4° regular grid using a standard bilinear interpolation algorithm. We have also calculated velocities on the original 1/3° Mercator grid and validated them with our global in situ data; the statistical validation of the 1/3° or 1/4° product is nearly identical. The 1/4° resolution is often requested by our users, being more easily compared to other satellite data products (e.g., 1/4° resolution SST) or model outputs, and so this resolution product is validated here.

2.2 Wind stress

QuikSCAT was launched by the National Aeronautics and Space Administration on 19 June 1999 (http://winds.jpl.nasa.gov/missions/quikscat/index.cfm). The mission carries a Ku-band microwave scatterometer (SeaWinds) that measures near-surface wind stress and direction under all weather and cloud, and has daily coverage over 92% of the global ice-free oceans. We use the QuikSCAT mean wind field (QSCAT MWF) global 1/2° resolution product, which provides daily and weekly wind stress fields and is processed and distributed by the Centre ERS d'Archivage et de Traitement (CERSAT; http://www.ifremer.fr/cersat/en/documentation/manuals.htm). As for the altimetric products, a bilinear interpolation is performed on the daily and weekly QSCAT MWF products to obtain a similar resolution on a 1/4° regular grid.

2.3 Acoustic Doppler current profiles

The Joint Archive for Shipboard ADCP (JASADCP) is responsible for the acquisition, review, documentation, archival, and distribution of shipboard ADCP data sets. The growing JASADCP now totals nearly 1,000 cruises available on this web site: http://ilikai.soest.hawaii.edu/wadcp/index.html.

For the period between 1 January 2000 and 31 December 2005, a total number of 313 cruises have been extracted from the JASADCP database. These data at 20-m depth will be used to validate the CTOH currents. The trajectories of these cruises are shown in Fig. 1a. We use 93,719 ADCP profiles from these cruises over the global oceans.

2.4 Current meter data from the TAO/TRITON moorings

Current meter data are available on a selected number of TAO/TRITON moorings anchored along the equator (McPhaden et al. 1998). We selected three moored ACDP current meter time series at 110° W, 140° W, and 170° W (Fig. 1a). We only use the near-surface data at 10-m depth, as there is strong vertical current shear, especially in the eastern Pacific (McPhaden and Taft 1988). The data are available from the TAO website (http://www.pmel.noaa.gov/tao/).

2.5 Lagrangian drifting buoy data

Global Lagrangian float data are available from the international Global Drifter Programme (GDP; http://www.aoml.noaa.gov/phod/dac/gdp.html). We collected buoy observations from 3,101 buoys at 15-m depth over the global ocean. Only the buoy data with drogues are used. The buoy locations are shown in Fig. 1b, corresponding to the period from 1 January 2003 to 31 December 2005.

To compare our satellite current velocities to the Lagrangian float velocities, it is necessary to eliminate the inertial movements from the buoy displacements. The inertial period varies with latitude, but we chose to smooth our buoy positions over 72 h (longer than the inertial period) to provide buoy observations that are coherent with our geostrophic currents. This also tends to smooth out any short-period ageostrophic signals, which are neither observed by the altimetric measurements nor the weekly averaged wind-forced currents. Next, the speed due to the displacement of the buoys was obtained at each point by calculating the distance between two consecutive six hourly positions and dividing by time. The direction of the vector speed is also calculated between two consecutive points. Finally, the velocity vector was broken up into its zonal and meridional components.

3 Methodology

The satellite surface currents we used, $U_t(u_t,v_t)$, are the sum of the gridded geostrophic velocities, $U_g(u_g,v_g)$,

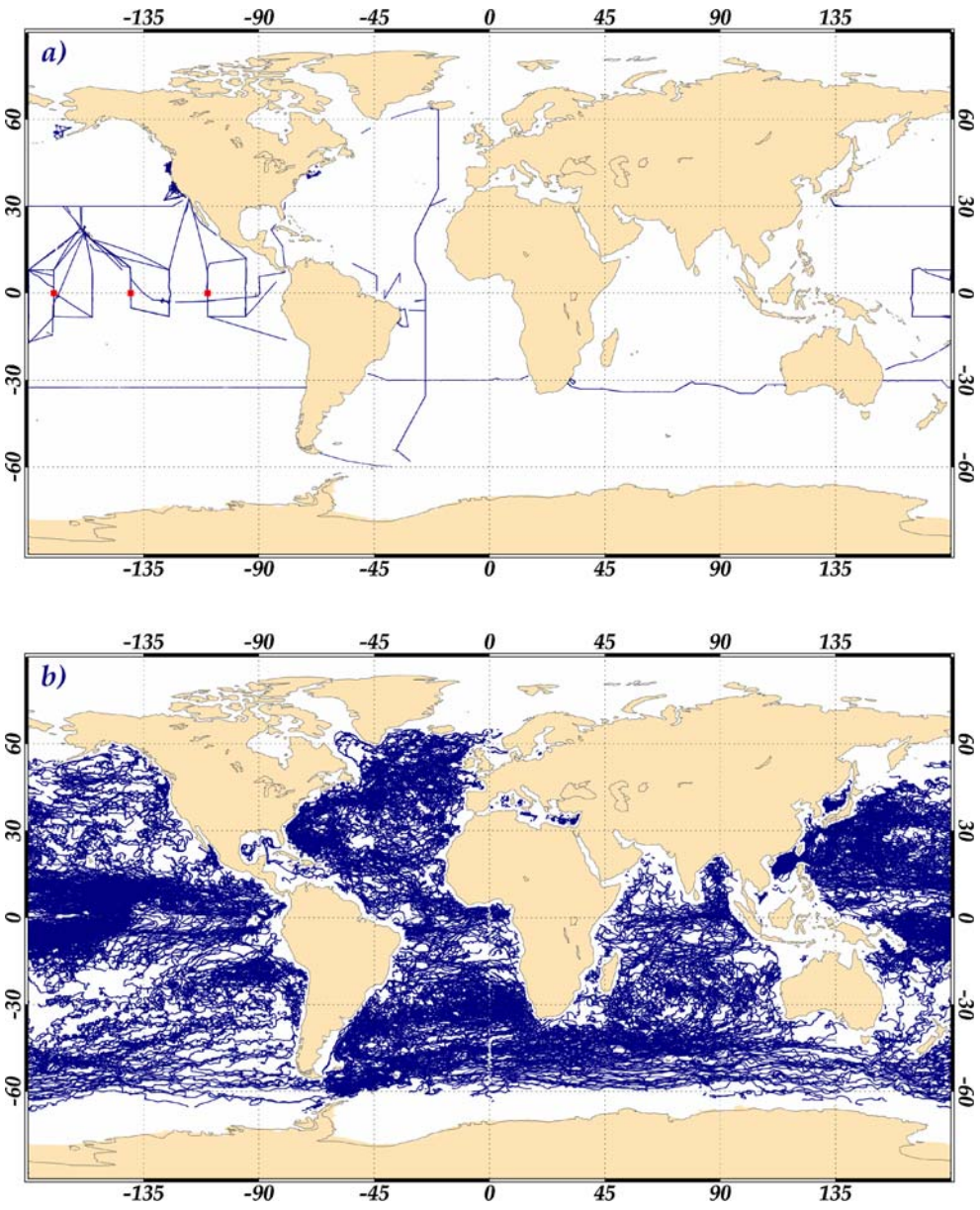

Fig. 1 **a** Position of the 313 cruise tracks with ADCP data at 20-m depth for the 5-year period from January 2000 to December 2005, used to validate the satellite current product. The three TAO/TRITON current meter positions in the equatorial Pacific are marked with *squares*. **b** Positions of the GDP Lagrangian drifters used to validate the currents for the 3-year period, January 2003–December 2005

and the Ekman currents at 15-m depth, $U_e(u_e,v_e)$:

$$u_t = u_g + u_e, \qquad v_t = v_g + v_e \tag{1}$$

3.1 Global surface geostrophic currents

Firstly, we calculate the total SSH as the sum of the altimetric MSLA and the RIO05 MDT. The SSH gradients ($\partial h/\partial y$, $\partial h/\partial x$) are calculated linearly from the surrounding grid points using a finite difference formulation. Outside the equatorial band (5° S–5° N), the surface currents are calculated from these SSH gradients, assuming a geostrophic balance.

There is a singularity near the equator because f vanishes, which requires special attention. Different studies have shown that a β-plane geostrophic approximation involving the second derivative of surface height provides good agreement with the observed velocity field in the equatorial band (Lukas and Firing 1984; Picaut et al. 1989). We follow such an approach within the equatorial band (5° S–5° N) to estimate a geostrophic velocity $\mathbf{U}_\beta(\mathbf{u}_\beta, \mathbf{v}_\beta)$ on the β plane as

$$u_\beta = -\frac{g}{\beta}\frac{\partial^2 h}{\partial y^2}, v_\beta = \frac{g}{\beta}\frac{\partial^2 h}{\partial x \partial y} \tag{2}$$

In this approximation, β is a constant for the equatorial region given by $\beta = 2\Omega/r = 2.3\times10^{-11}$ m^{-1} s^{-1}.

The second derivatives in the β-plane geostrophic velocity tend to amplify any noise. To reduce this effect, we have calculated a smoother β term based on a linear regression over nine points (i.e., over 1°), as suggested by Picaut et al. (1989). To ensure a smooth transition from the

β-plane calculation in the equatorial band to the normal f-plane calculation elsewhere, Lagerloef et al. (1999) defined a weighting function within the equatorial band as

$$\mathbf{U}_g = W_f \mathbf{U}_f + W_\beta \mathbf{U}_\beta \tag{3}$$

where $W_\beta = 1$ and W_f=0 at the equator, $W_\beta \to 0$ and $W_f \to 1$ at 5° N and 5° S. We have defined the W_β and W_f weighting functions as

$$W_\beta = C.\exp\left[-\left(\frac{\theta}{\theta_s}\right)^2\right], W_f = 1 - \exp\left[-\left(\frac{\theta}{\theta_s}\right)^2\right] \tag{4}$$

where θ is the latitude, θ_s is a latitudinal length scale equal to 2.2°, and C is a constant amplitude scaling, set to 0.7. This amplitude constant was tuned to provide a better fit to the equatorial current meter data (see Section 6). Finally, some very large currents occurred near coastal regions where the standard open ocean altimetric corrections are not well adapted. To remove these erroneous currents, we eliminated all zonal or meridional currents larger than 3 m s^{-1}.

3.2 Global surface Ekman currents at 15-m depth

In the following, we calculate Ekman currents at 15-m depth rather than at the surface to compare directly with in situ surface drifters, which are drogued at 15-m depth to reduce the effects of wind slippage. Both Van Meurs and Niiler (1997) and Lagerloef et al. (1999) propose a two-parameter regression model between the Ekman currents at 15-m depth and the surface wind stress:

$$(u_e + iv_e) = B\, e^{i\theta}(\tau_x + i\tau_y) \tag{5}$$

where the amplitude B~0.3 m s^{-1} Pa^{-1} and θ is the turning angle relative to the wind direction: 55° to the right (left) of the wind in the northern (southern) hemisphere at 15-m depth. Wind stress (τ_x, τ_y) is in N m^{-2}.

At the equator, there is a clear discontinuity and strong divergence in the Ekman currents, as we have imposed that currents north (respectively south) of the equator will be oriented 55° to the right (respectively left). To ensure a smoother transition at the equator, Lagerloef et al. (1999) propose the same two-parameter regression model as in Eq. 5, but within the tropical band (25° S–25° N), the amplitude, B, and the turning angle relative to the wind direction, θ, vary with latitude:

$$B = \frac{1}{\rho}\left(r^2 + f^2 h_{md}^2\right)^{-1/2}, \theta = \arctan\left(\frac{f h_{md}}{r}\right) \tag{6}$$

Here, the wind mixing depth scale is h_{md}, and r is a frictional parameter. As we approach the equator ($f \to 0$), the turning angle, θ, also approaches zero, and the current at 15-m depth become orientated in the same direction as the wind. Toward 10–25° N and 10–25° S, the amplitude B approaches 0.3 and the turning angle approaches 55°, leading to a smooth transition with the extra-tropics. In the tropical Pacific, Lagerloef et al. (1999) have performed a regression analysis and find values of r=2.15×10^{-4} m s^{-1} and h_{md}=32.5 m, which remain fairly constant over the tropical band. We have applied these values in our global tropical band analysis.

4 Results

The global standard deviation of the surface CTOH current amplitude is presented in Fig. 2. The standard deviation is computed from January 2000 to January 2006. The standard deviation map is close to that calculated from the geostrophic component alone, which has been discussed globally by Ducet et al. (2000), and in the North Atlantic by Brachet et al. (2004). Large current variability is evident within the strong boundary currents, such as the Kuroshio, whose root-mean square (RMS) over the 6-year period is 45 cm s^{-1}, the East Australian Current (33 cm s^{-1}), or the Leeuwin Current (22 cm s^{-1}). The fine detail of these currents can also be observed in the zonal bands associated with the north and south equatorial currents, the Rossby wave bands at 10°N in the eastern Pacific, and the seasonally reversing currents in the Indian Ocean (Somalia Current, South Java Current, etc.). The contribution of the Ekman currents is small, less than 5 cm s^{-1} for most of the global ocean. Some currents, such as the Somalia current or the equatorial currents, exhibit significant Ekman variability reaching 25 cm s^{-1}.

Having separate geostrophic and Ekman components also allows us to quantify the relative role of the surface Ekman currents versus the geostrophic velocity over the global oceans. Figure 3 shows the ratio of the standard deviation of Ekman currents compared to geostrophic currents for the period from January 2000 to January 2006. Geostrophic variability prevails when this ratio is less than 1; a ratio higher than 1 occurs in areas where the wind-driven currents dominate. For most of the world ocean, the geostrophic component dominates (where the maps are white) as expected. However, the Ekman variability becomes important in the high-latitude areas, particularly in the westerly wind belts around 40–50° N and S and in the eastern basins where the geostrophic circulation is weak. The Ekman currents also dominate over shallow plateaux at high latitude where the wind forcing is strong and the geostrophic variability is weak. This occurs, for example, over the Kerguelen Plateau around 70° E and 50° S, the Campbell Plateau at 50° S south of New Zealand, north of

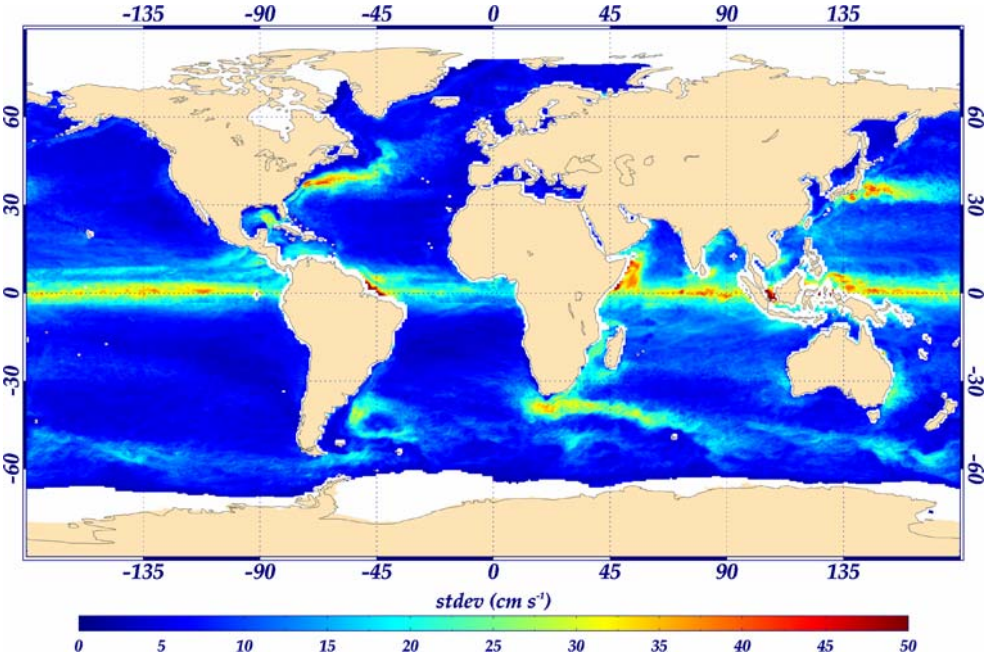

Fig. 2 Standard deviation of the CTOH currents for the global ocean, calculated over the period 2000–2006

Iceland at 20° W and 70° N, or in the shallow Sea of Okhotsk, east of Russia, where North Pacific Intermediate Waters form (Hill et al. 2002). Open-ocean regions include the Arabian Sea, where the seasonal monsoonal winds prevail, inducing strong-wind-forced surface currents (Subrahmanyam and Robinson 2000), and the NE Atlantic and NW Mediterranean Sea. Deep-water formation in the NW Mediterranean partly depends on an accurate wind-driven circulation, which is crucial for destabilizing the winter surface layer (Schott et al. 1996).

5 Comparison with in situ data

In this section, we validate our satellite surface current product by comparing the near-surface current vectors with in situ observations. For each in situ current vector, we interpolate the zonal and meridional components of the satellite CTOH product onto the in situ point, taking into account the position and time. We used a spatial bilinear interpolation and a temporal linear interpolation of the satellite data onto each in situ data point. To present the

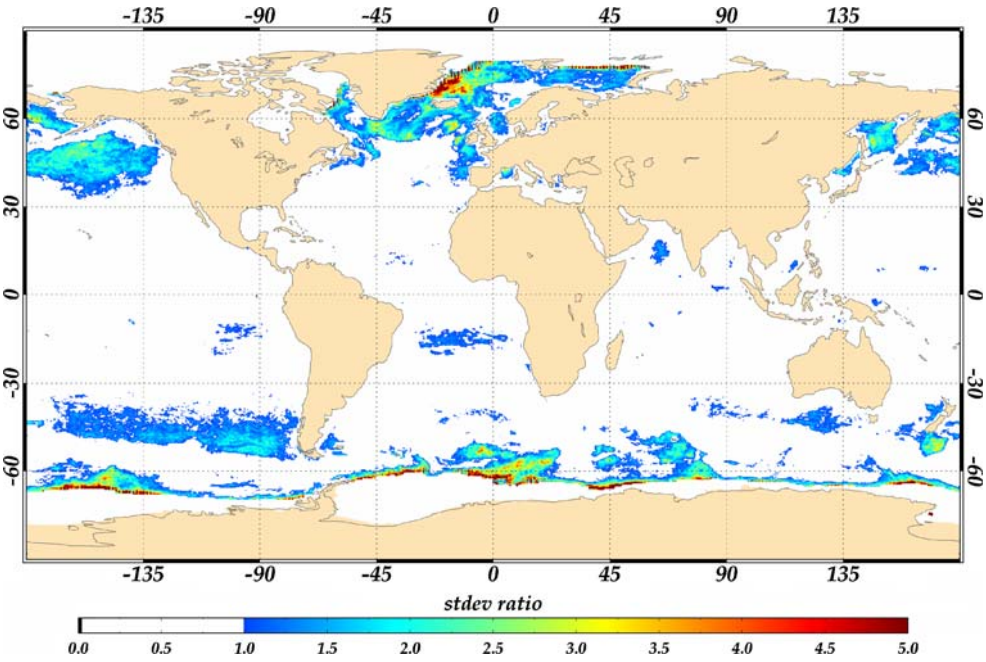

Fig. 3 Ratio of the standard deviation of the Ekman current component versus the standard deviation of the geostrophic current component (standard Ekman/standard geostrophy), calculated over the period 2000–2006. Regions where the Ekman current variability exceeds the geostrophic currents are *shaded in color*

global results of our comparisons, we have binned the global in situ data into 5°×5° resolution boxes from January 2003 to December 2005. Such a resolution represents a good compromise between a small number of in situ data in some areas and the surface of the global ocean.

5.1 Global ADCP data

The ADCP currents are available along selected ship tracks (Fig. 1a). Although there are fewer ADCP current observations than drifter currents, their advantage is in providing Eulerian observations from a precise measurement location, without the Lagrangian averaging. Their disadvantage is in providing a "snapshot" of near-surface currents, compared with the weekly averaged satellite currents. We note that inertial oscillations may also be present in the ADCP currents. Their standard deviation values in 5°×5° bins are quite similar to the satellite CTOH standard deviation values (not shown). In general, the vector correlations (Crosby et al. 1993) with the CTOH currents exceed 1.0 in the mid- to high latitudes (zonal and meridional correlations > 0.7) and in the tropical Atlantic and eastern Pacific (Fig. 4a). The correlations are reduced in low-eddy-energy regions. The good correlation between the Eulerian ADCP currents at 20-m depth and the satellite-derived currents reinforces that the two data sets are capturing similar dynamics at mid- to high latitudes. This is also shown for the example in the southeast Indian Ocean in Fig. 4b, when the ship ADCP currents from the TIP2000 research cruise (Fieux et al. 2005) are superimposed on the CTOH near-surface currents. Here, the vector correlation is ~1.2 (Fig. 4a). The mesoscale velocity structure is very well captured by the satellite current product, although the small-scale ADCP current structure is missing (Fig. 4b).

5.2 Global Lagrangian drifting buoy data

Figure 5a shows the number of Lagrangian drifting buoy observations per 5°×5° bin over the 3-year period from 2003–2005. The data are limited to 65° N and 65° S, with a higher density of observations in the Atlantic Ocean, and the North and the equatorial Pacific Ocean. The Northern Indian Ocean, and the far North and South Pacific Oceans are notably undersampled, as are many coastal regions. Figure 5b shows the standard deviation of the Lagrangian buoy speeds on the same grid. This figure should be compared with the 1/4° resolution standard deviation of the satellite CTOH speeds shown in Fig. 2. These two maps show similar features: large current variability exceeding 30 cm s^{-1} in the region with strong western boundary currents (Gulf Stream, Kuroshivo, Agulhas Current, etc.). As our CTOH currents include specific algorithms for the equatorial band, we note that the strong standard deviation exceeding 40 cm s^{-1} along the equatorial Pacific and Indian in the Lagrangian data is also replicated in Fig. 2. In both data sets, there is weaker equatorial current variability in the Atlantic Ocean compared to the Indian and Pacific oceans. The reduction in variability in the eastern basins is also clear in the buoy data. Isolated patches of stronger standard deviation are often in regions with low-buoy data coverage.

Figure 6a shows the geographical variations of the correlation between the zonal drifter velocities and the zonal CTOH velocities; Fig. 6b shows the same for the meridional correlations. If we consider that the drifter observations are independent after 5 days, then the 95% statistical significance level of the correlation ranges from 0.1 to 0.2, the higher values being in the data sparse regions of Fig. 5a. The zonal correlations are statistically significant, being greater than 0.7 in regions where the standard deviation of the CTOH currents is greater than 5 cm s^{-1}. The zonal and meridional correlations are greater than 0.8 in the strong western boundary currents. In the band of high westerly winds from 40–60° N and 40–60° S, the meridional correlation increases in response to the larger meridional component of the Ekman currents at these latitudes. In the tropical band, the zonal correlations are quite good, especially in the stronger NECC and SECC; however, the meridional components are poorly represented.

To quantify the differences between the two data sets, we have calculated scatterplots of the CTOH satellite near-surface currents versus the drifting buoy currents in their zonal and meridional components (Fig. 7). The global analysis (Fig. 7a) shows a higher zonal correlation (r=0.83) compared to the meridional correlation (r=0.71), with a small mean difference and a RMS difference of 10–12 cm s^{-1}. However, the regional analysis reveals important differences. There is a very good intercomparison between the satellite CTOH currents and the drifter currents at mid- to high latitudes, and examples are given for the North Atlantic, Southern Indian, and Southern Oceans (Fig. 7b–d). Here, zonal and meridional correlations are between 0.8–0.85. In the Southern Ocean, the meridional correlations are stronger than the zonal correlations. Although the mean geostrophic flow is mainly zonal here, the meridional velocity component is energetic, associated with strong meanders and eddies, and there is a stronger meridional Ekman component with respect to the dominant zonal winds. It is encouraging that the satellite near-surface currents are so strongly correlated here.

The weakest performance for the satellite CTOH currents is in the equatorial band (10° N–10° S; Fig. 7e). Here, the zonal correlation remains quite good (r=0.82), but the meridional correlation is poor (r=0.51), with large RMS differences between the two data sets (15–20 cm s^{-1}).

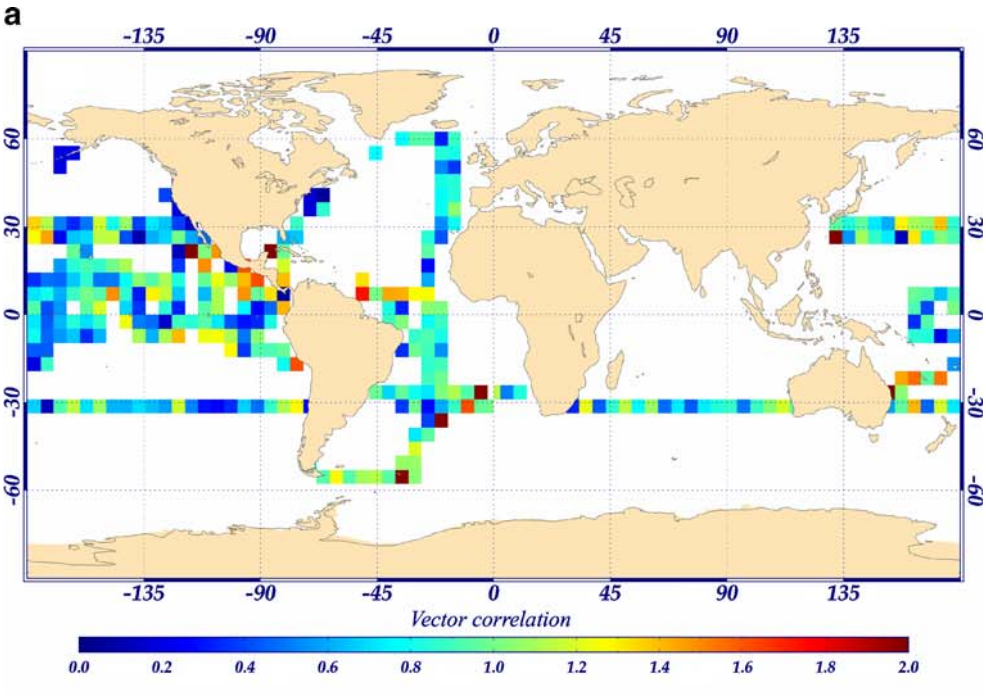

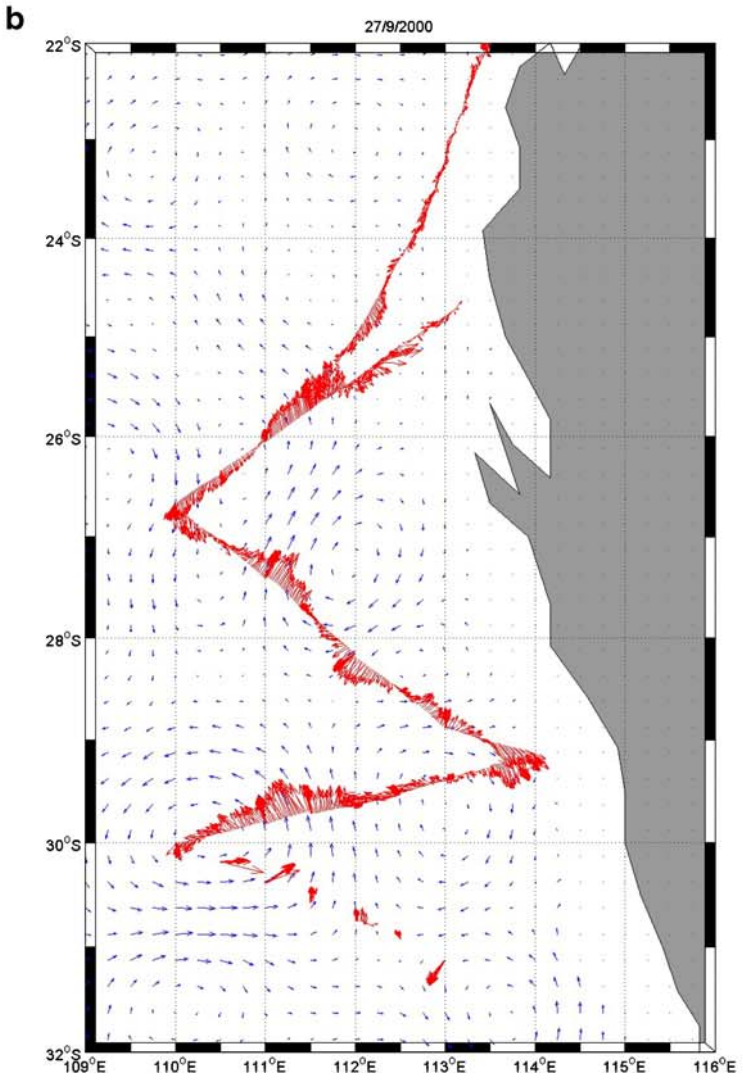

Fig. 4 **a** Vector correlations between the CTOH satellite currents and the ADCP currents, available during the period 2000–2005. **b** Ship ADCP currents at 31 m (*red arrows*) overlaid on CTOH near surface currents (*blue arrows*) in September 2000 in the southeast Indian Ocean

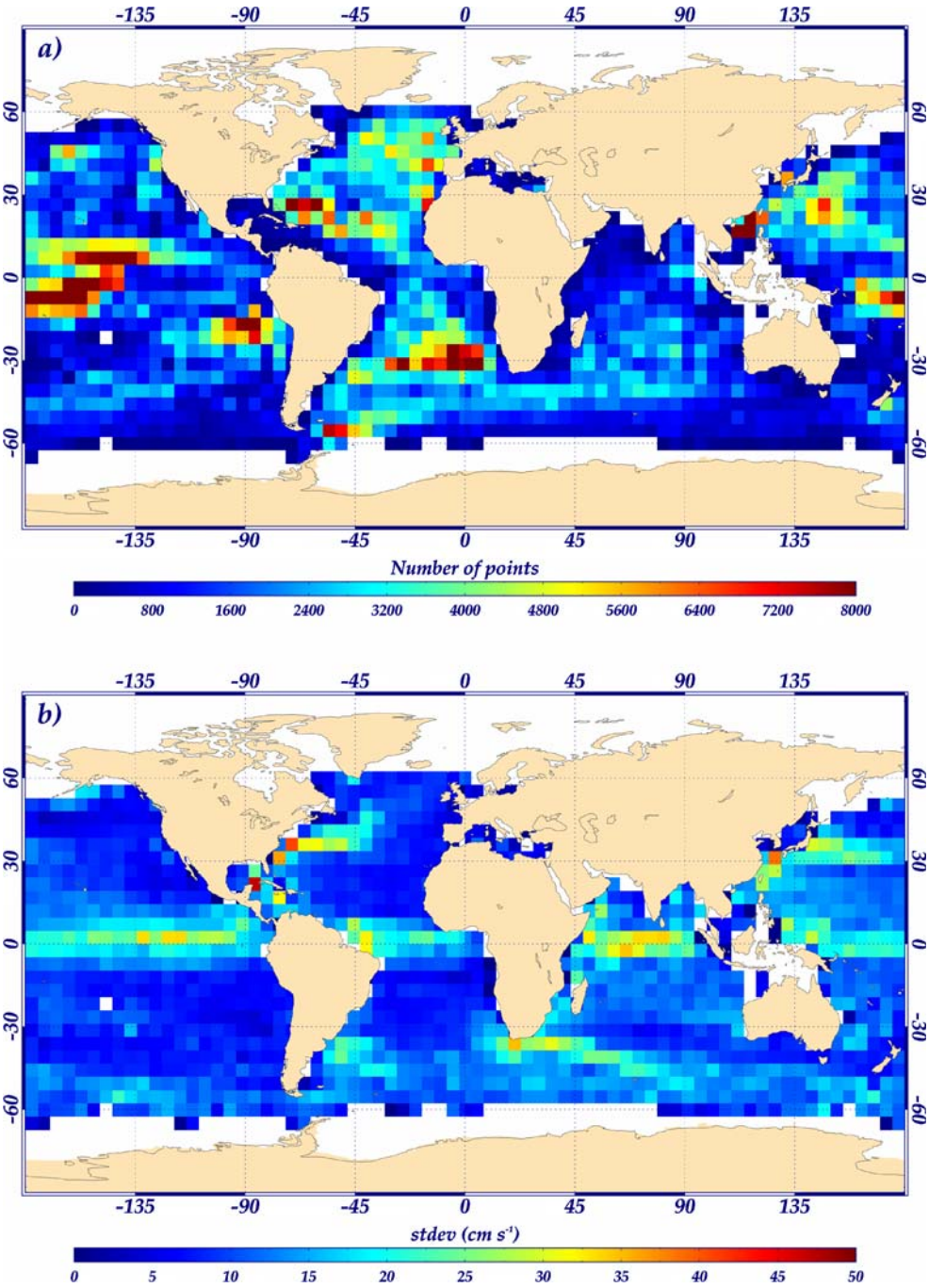

Fig. 5 **a** Number of GDP Lagrangian drifter current observations per 5° bin in the global ocean for the 3-year period 2003–2005. **b** Standard deviation of the Lagrangian drifter current speeds for the period 2003–2005

The poor performance of the meridional component here explains why the global meridional correlation drops to 0.7. A more detailed analysis of the equatorial band will be discussed in the following sections.

In terms of amplitude, the two data sets have similar current speeds in the energetic regions. In the low-energy regions (with a standard deviation less than 15 cm s^{-1}, in Fig. 2), the drifter currents are a factor of 1.3 stronger than the satellite currents, possibly due to smaller-scale or higher-frequency signals, which are not sampled by the satellite data coverage.

5.3 TAO/TRITON 10-m current meter data

In this section, time series based on three moored current meter records from the TOGA/TAO array in the equatorial Pacific are compared to the satellite CTOH currents (Fig. 8). The sites are along the equator at 0° N and at 110° W, 140° W, and 170° W. These sites span the equatorial Pacific and include regions where the zonal and meridional comparisons with the surface drifters were low. Note that the geostrophic component of our satellite CTOH currents has been scaled by an amplitude factor of 0.7 at the

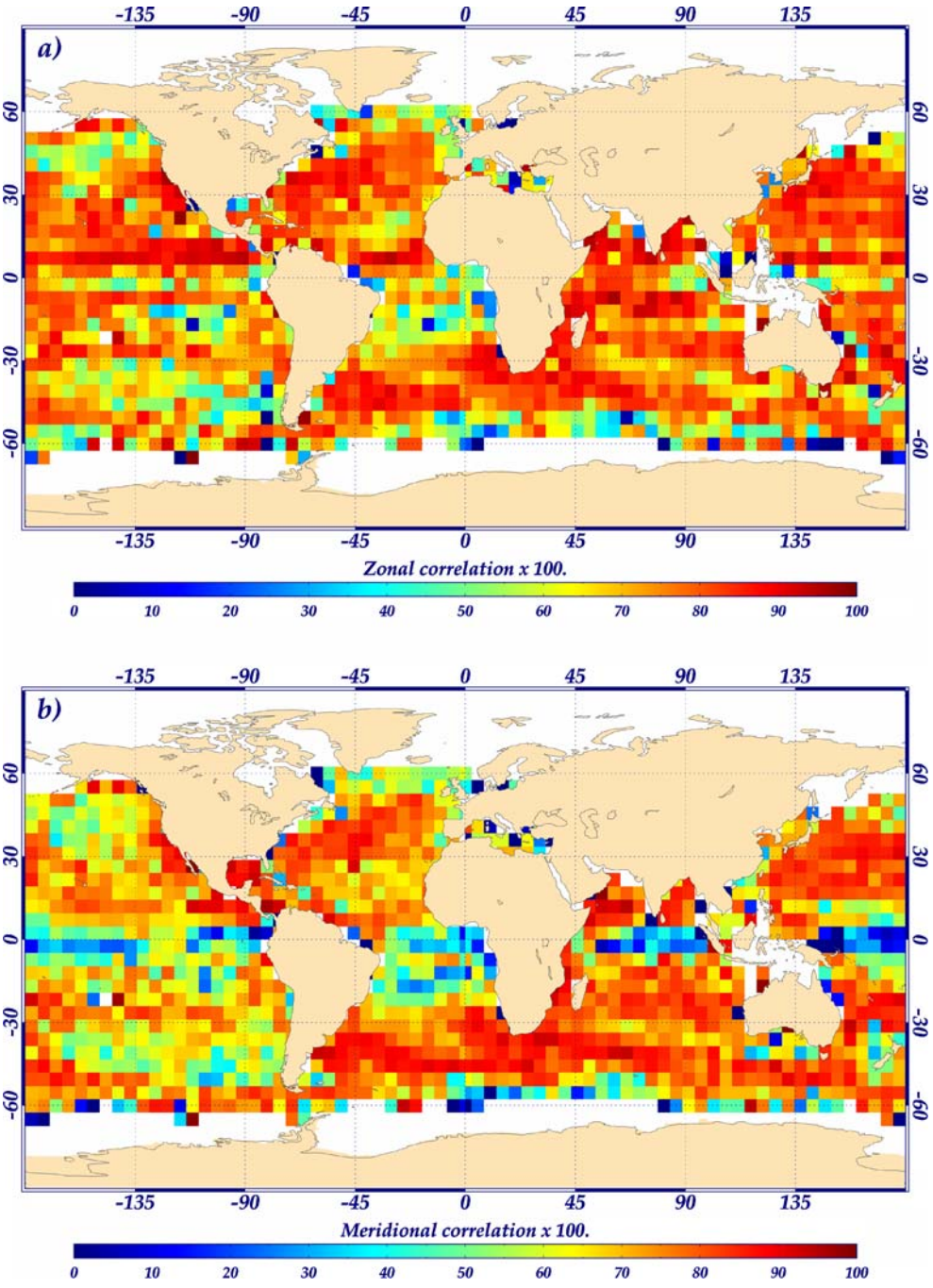

Fig. 6 **a** Correlations between the zonal component of the CTOH satellite currents and the zonal component of the GDP Lagrangian drifter currents for the 3-year period 2003–2005. **b** Meridional correlations

equator (Eq. 6), which improves the amplitude of the currents at the equator. The current meter data have also been smoothed by a 10-day running mean to construct the weekly current meter time series used in our comparisons.

The zonal correlation varies from 0.44 to 0.52, whereas the meridional correlation is low (between 0.11–0.27). The zonal correlations are above the significance level (0.16 at 110° W; 0.14 at 140° W and 170° W), whereas the meridional correlation at 170° W is not. We note that there is a distinct high-frequency signal in the meridional current meter data (<20 days), which is not sampled at all by the weekly satellite product. However, the CTOH currents do show a stronger 20- to 60-day signal than is apparent in the current meter observations for both the zonal and meridional components. This may be an aliasing problem, given that our altimetry data with their 20-day Nyquist frequency are at the limit of correctly observing the ~20-day tropical instability waves (Qiao and Weisberg 1995).

In the eastern Pacific at 140° W and 110° W, the satellite CTOH currents at the nominal 15 m depth are mainly westward at both sites (Fig. 8c,e), whereas the deeper in situ currents at 30 m depth show a stronger eastward

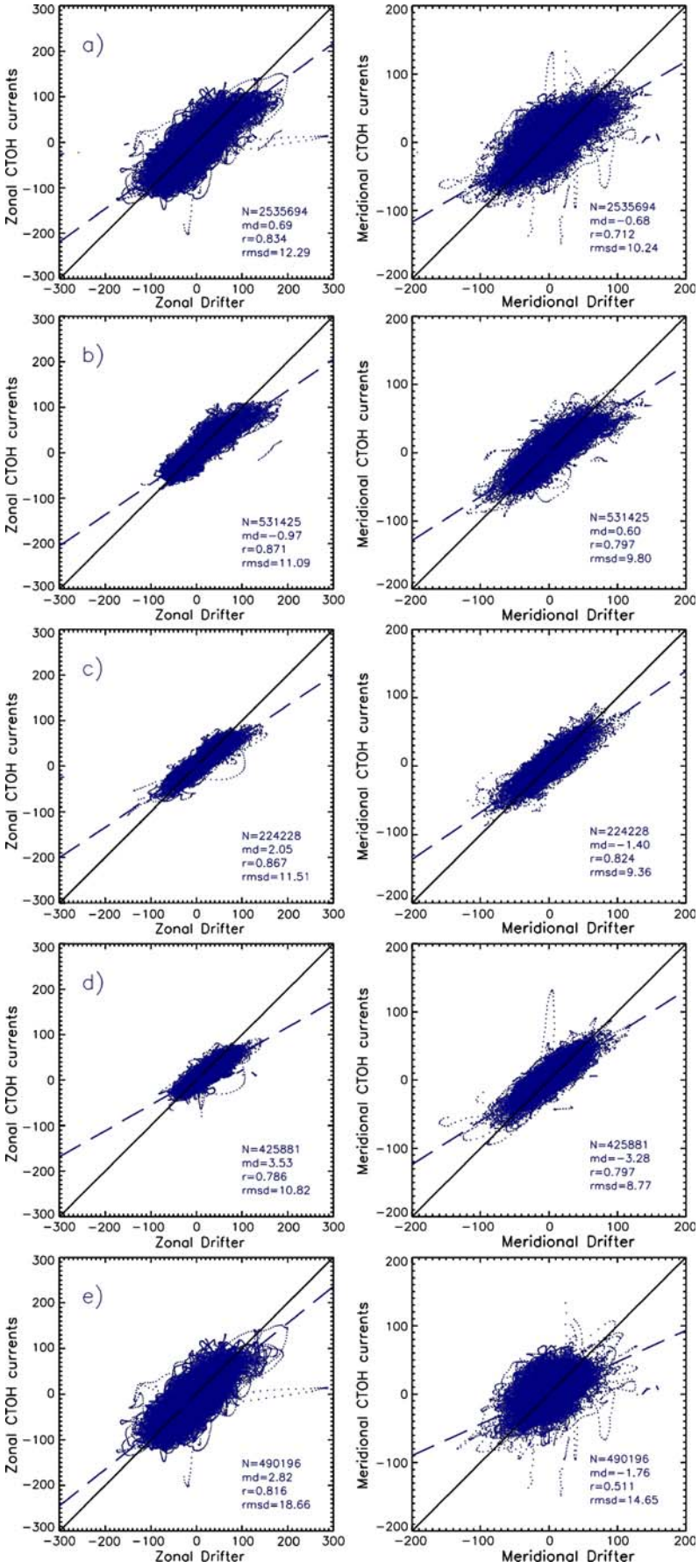

Fig. 7 Scatterplots of drifter velocity components versus CTOH satellite velocities. *Left panels* zonal components. *Right panels* Meridional components. Different regions are shown: **a** global, 65° N–65° S; **b** North Pacific, 10–60° N, 120–300° E; **c** South Indian, 10–50° S, 20–110° E; **d** Southern Ocean, 40–65° S; **e** tropical band 10° N–10° S. Statistics are *N* number of points, *md* mean difference, *r* correlation, *rmsd* RMS difference

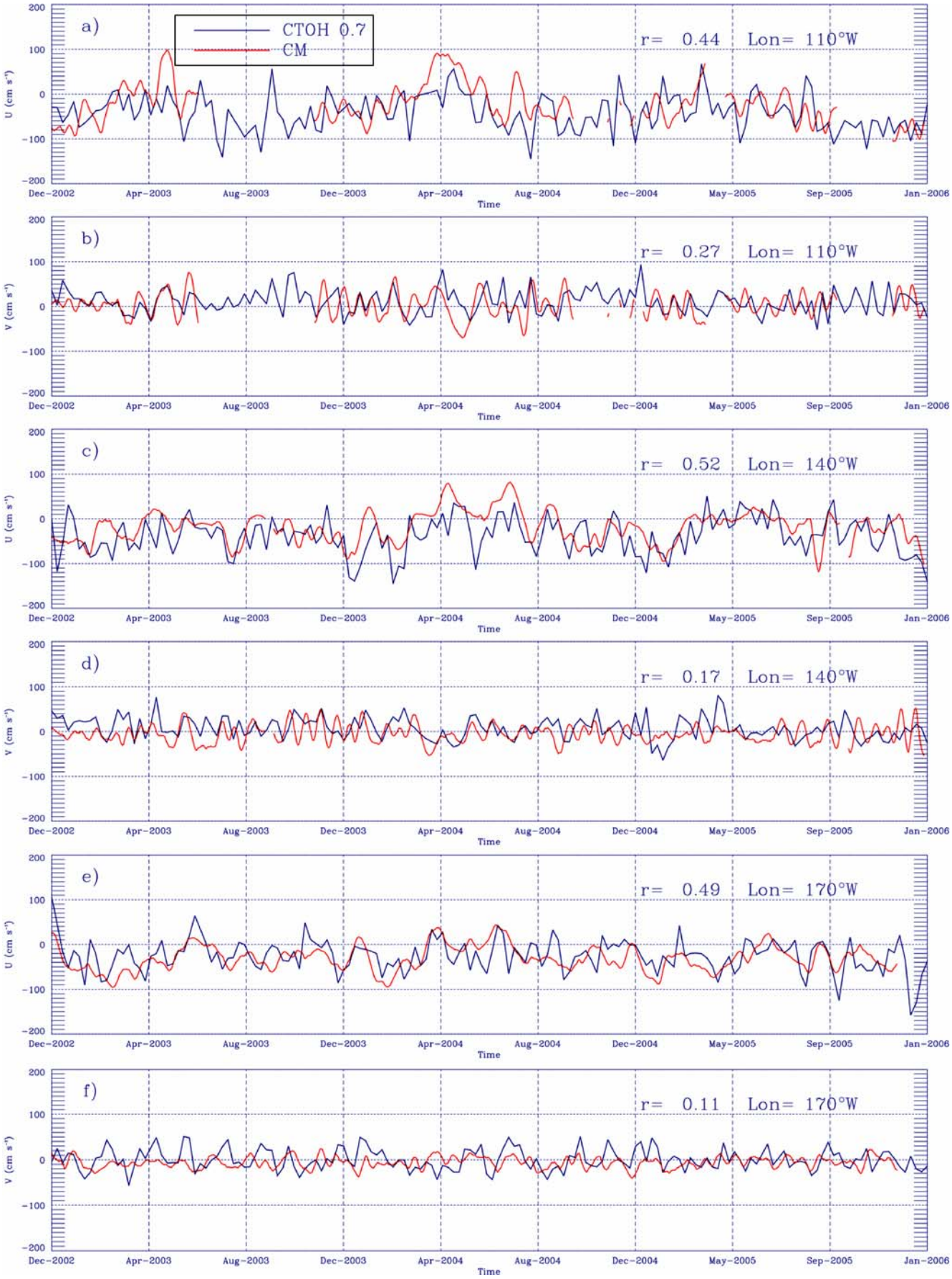
a)
CTOH 0.7
CM
r= 0.44 Lon= 110°W
U (cm s⁻¹)
b)
r= 0.27 Lon= 110°W
V (cm s⁻¹)
c)
r= 0.52 Lon= 140°W
U (cm s⁻¹)
d)
r= 0.17 Lon= 140°W
V (cm s⁻¹)
e)
r= 0.49 Lon= 170°W
U (cm s⁻¹)
f)
r= 0.11 Lon= 170°W
V (cm s⁻¹)
200
100
0
−100
−200
Dec−2002
Apr−2003
Aug−2003
Dec−2003
Apr−2004
Aug−2004
Dec−2004
May−2005
Sep−2005
Jan−2006
Time

◀ **Fig. 8** Comparison of TAO/TRITON currents (*red line*) with CTOH currents scaled by a factor of 0.7 (*blue line*) along the equator. **a** Zonal and **b** meridional currents at 0° N, 110° W; **c** zonal and **d** meridional currents at 0° N, 140° W; **e** zonal and **f** meridional currents at 0° N, 170° W

current, which is evident during February to May at 110° W and occurs later during April to June at 140° W (not shown). Despite this strong vertical shear associated with the seasonal strengthening of the equatorial undercurrent (Lukas and Firing 1984), the satellite CTOH currents are correctly capturing the surface layer's zonal flow.

In this region, with faster oceanic adjustment and rapid equatorial waves, the difference between the in situ data sets and the weekly averaged satellite data becomes important. The in situ meridional variations are dominated by monthly and shorter timescale signals, dominated by the tropical instability wave signal with a 20-day period (e.g., Legeckis 1977; Qiao and Weisberg 1995). The satellite product cannot resolve these fluctuations adequately (Seidel and Giese 1999), and their strong signal may be aliased into the lower frequency band. The same problem was reported for the OSCAR satellite current product by Bonjean and Lagerloef (2002) and Johnson et al. (2007).

6 Comparison with other satellite current products

A number of satellite near-surface current products exist and are distributed over the Internet. We have performed similar validation statistics on the widely used OSCAR near-surface current product. The OSCAR global product uses only Topex–Poseidon and Jason-1 altimeter sea level anomalies for the geostrophic anomaly component. Their mean dynamic topography is also different, based on an earlier version of the RIO05 product (Rio and Hernandez 2004) with less in situ data and no GRACE gravity data. Their wind-forced current component is from scattermometry winds.

The OSCAR methodology calculates the total surface current based on a quasi-linear, quasi-steady formulation of the surface momentum equations. Within the equatorial band (8° N–8° S), the OSCAR methodology resolves the equations based on a fit of 12 orthogonal polynomials to represent the total near-surface velocity (Bonjean and Lagerloef 2002). The product is calculated on a 1° spatial resolution, and the model approximations resolve low-frequency signals (Johnson et al. 2007).

Figure 9 shows the zonal average of the zonal and meridional correlations for each satellite current product, co-located onto the drifter velocity positions. Outside the equatorial band of 10° N–5° S, the CTOH near-surface currents show a consistent higher correlation with the drifting buoy velocities compared to the OSCAR product. The lower correlation for OSCAR at mid- to high latitudes is affected by its 1° spatial resolution and the limited spatial distribution of the T/P and Jason altimetric observations, which misses much of the mesoscale eddy energy at these latitudes. The misfit increases toward 60° latitude as the Rossby radius decreases. In the equatorial band, OSCAR

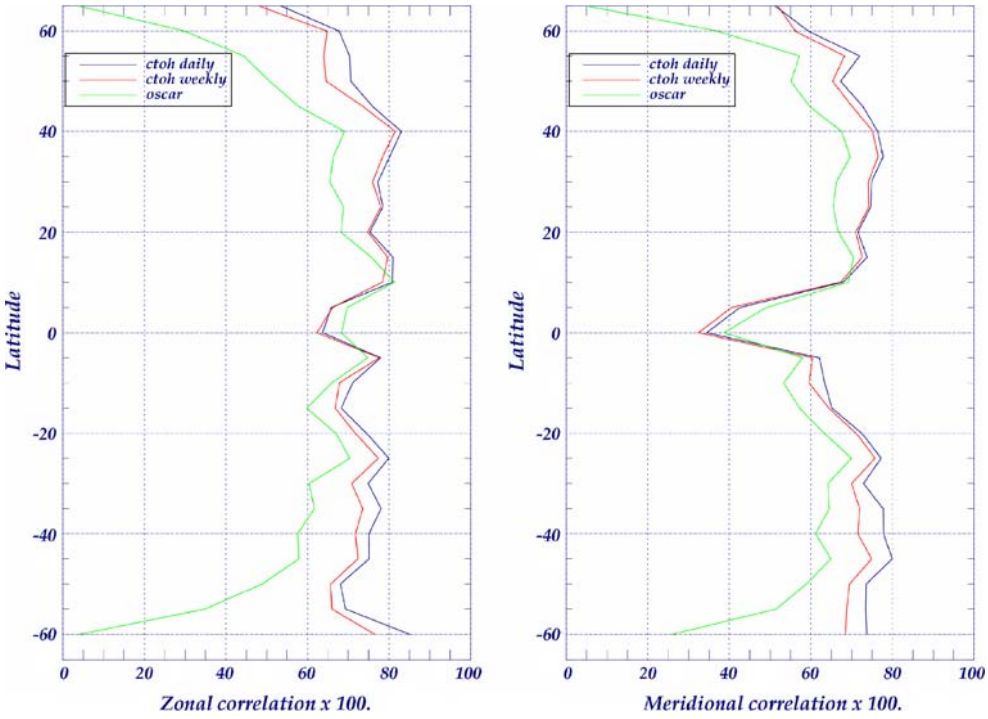

Fig. 9 Zonal averages of the zonal correlations (*left*) and the meridional correlations (*right*) of the surface drifters versus the global OSCAR currents (*green line*); the CTOH currents forced by weekly winds (*red line*) or forced by daily winds (*blue line*)

provides a higher correlation for both the zonal and meridional velocity components, confirming that the OSCAR methodology is better adapted here. These results are confirmed by a statistical comparison of the two satellite products with the equatorial current meter velocities in Table 1. The OSCAR product shows higher zonal and meridional correlations along the equator compared to the CTOH currents. The RMS difference is also lower at all current meter sites for the smoother OSCAR currents. This confirms a separate validation by Bonjean and Lagerloef (2002) that their improved equatorial algorithm is better adapted to the tropical Pacific than the Lagerloef et al (1999) algorithm used in our product.

7 Daily wind forcing of Ekman currents

In theory, the geostrophic currents will be established after a 2- to 3-day adjustment time. However, the present configuration of satellite altimetry missions does not allow us to resolve timescales less than a week to 10 days, so our geostrophic current calculations are limited to these longer timescales. The QuikSCAT and ERS wind products we use are also based on weekly gridded winds. It is possible that higher frequency winds may have an impact on the circulation, especially in the equatorial and high latitude zones. To test this hypothesis, we have computed the Ekman currents using the daily QuikSCAT gridded product over the same 3-year period (2003–2005) instead of the weekly product. The daily wind-forced Ekman and CTOH current product is compared to the weekly product, and both are interpolated and compared to the global GDP drifter data over the same period.

Figures 9 and 10 show the improvements in the zonal and meridional correlations when we include daily wind-forced Ekman currents in our satellite product and compare these satellite currents with the GDP drifter currents. Using daily winds rather than weekly winds always improves the correlation, although the impact is small for the subtropical currents, for example, in the North Atlantic. However, there is a substantial improvement in the northeast Pacific (north of 30–40° N) and in the Southern Ocean (south of 30° S). These improvements are in regions where the Ekman currents prevail over the geostrophic flow (Fig. 3). In addition, there is a stronger meridional Ekman current in these regions of strong zonal winds due to the fact that our 15-m Ekman currents are at a 55° angle with respect to the wind. Thus, the zonal average in Fig. 9 exhibits an improved meridional correlation (by 0.05–0.1) at higher latitudes. This is a good confirmation that using better wind sampling and our simple Ekman calculation is producing realistic surface current fields in comparison to the independent surface drifter observations.

Using the daily wind forcing makes a minor improvement to the meridional currents in the equatorial band. There is little impact on the zonal currents, which already showed better agreement with the in situ data. The improved meridional component is most evident in the tropical Indian Ocean, with a minor improvement in the western tropical Pacific near New Guinea.

At all latitude bands, the Ekman currents will take a few days to adjust to changes in the daily wind forcing, which is not taken into account in our algorithm. However, we still observe a real improvement in the correlation with surface drifters in the regions where the Ekman currents become important. This suggests that the winds are persistent enough in these zones that the Ekman adjustment does occur. It also highlights that wind forcing in the 2- to 7-day band has an important impact on high-latitude surface currents and in certain tropical zones.

Table 1 Statistical comparison of the CTOH and OSCAR satellite near-surface velocity products with the TOGA/TAO moored current meter vectors at 10-m depth for the period 2003–2005

CM Site	170°W		140°W		110°W	
Component	Zonal	Meridional	Zonal	Meridional	Zonal	Meridional
Correlations						
CTOH-CM	0.49	0.10	0.52	0.17	0.44	0.27
OSCAR-CM	0.69	0.22	0.70	0.47	0.82	0.60
Confidence level	(0.13)	(0.13)	(0.13)	(0.13)	(0.16)	(0.16)
RMS difference						
CTOH-CM	28.8	22.7	34.9	26.4	42.1	25.4
OSCAR-CM	20.4	12.8	25.8	17.3	24.5	21.8

The significance level is in brackets

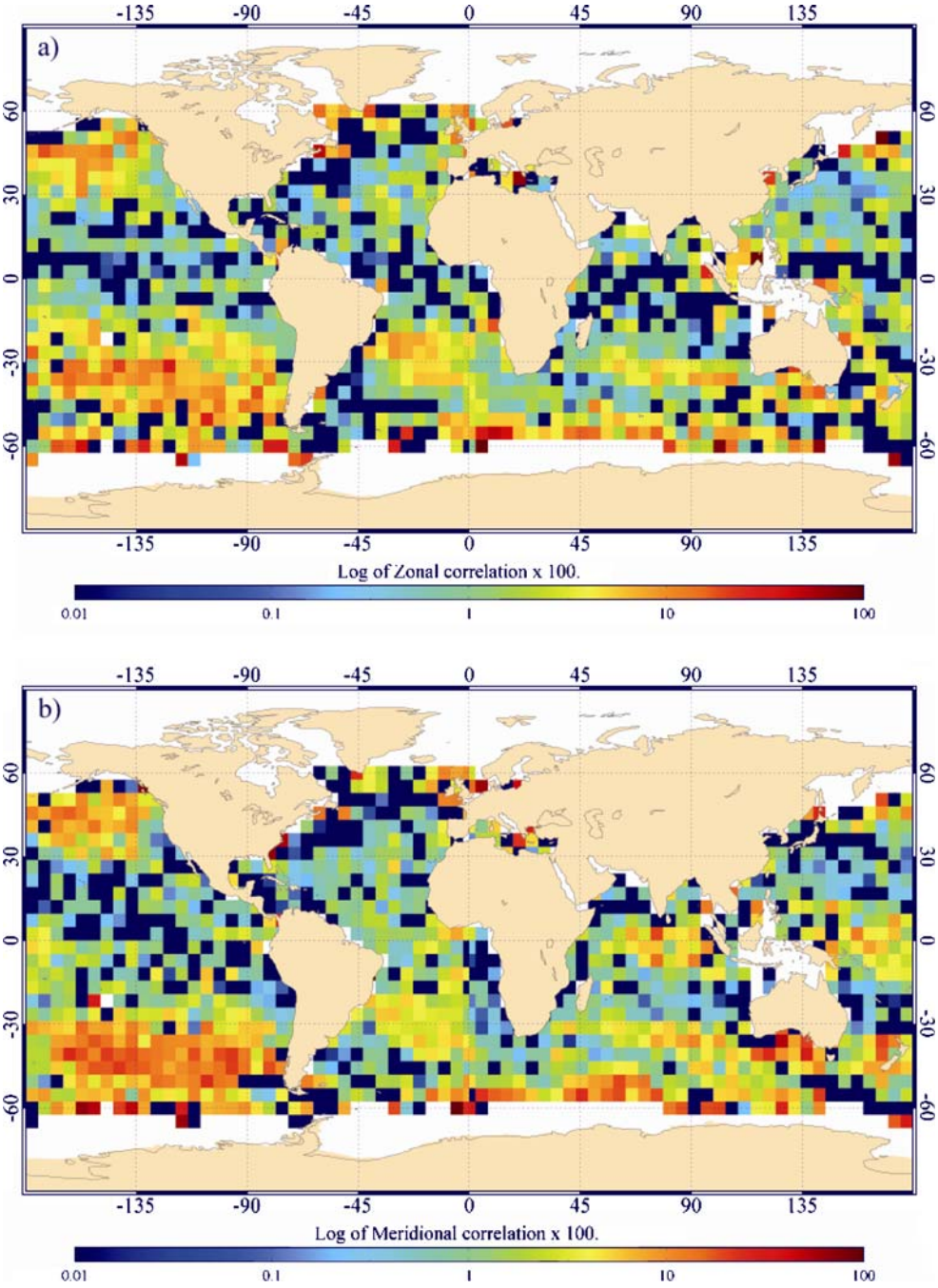

Fig. 10 Difference in correlation when daily winds are used to force the CTOH currents rather than the weekly winds, on a log scale. In detail, we **a** calculate the correlation between daily forced CTOH zonal currents and the drifter zonal currents, and then subtract the correlation between the weekly forced CTOH zonal currents and the drifter zonal currents. **b** Same for the meridional current components

8 Discussion—quality of the data product, and conclusions

The validation we have presented has shown the high quality of the satellite-based surface currents over the global ocean. In the subtropical to high-latitude bands, the satellite-based currents show very good correlations with the surface drifter data (around 0.7–0.8 on a zonal basin-wide average), with even higher correlations in regions of strong geostrophic currents (0.8 to 0.9). This is a very good result, considering we are comparing different measurement techniques (Eulerian vs Lagrangian), based on different spatio-temporal averages and highlights the very good quality of the altimetric geostrophic velocities. We note that the buoy data have been filtered over 72 h, and the weekly satellite data are at best resolving ocean processes greater than 20 days and 70–100 km. Therefore, the good correlation is based on the meso-scale and large-scale dynamical fields. The important sub-mesoscale circulation at shorter space and timescales is damped in the filtered buoy data and not included in the satellite observations.

The satellite CTOH currents are close to the buoy speed in energetic regions, but they underestimate the drifter velocities in low-energy areas. Indeed the satellite-derived

currents cannot detect sub-mesoscale oceanic structures with dimensions smaller than 70–100 km wavelength (Ducet et al. 2000) or ageostrophic motions that are not Ekman induced. Brachet et al. (2004) and Le Traon and Dibarboure (2002) have shown 30–40% of the high-latitude EKE variability may be missed in the gridded altimetric products. This missing small-scale variability may still be present in the Lagrangian buoy data, which maintain temporal scales >72 h, and is certainly present in the ADCP data.

In the high-latitude band and especially in regions where the Ekman currents dominate the flow, there is a marked improvement when we use the daily wind-forced Ekman current product. As mentioned earlier, the Ekman adjustment time is around 2–3 days, but despite this, we observe a real improvement in our comparisons between the daily satellite currents and the surface drifter observations. This suggests that the wind forcing in the 2- to 7-day synoptic band is important for the surface currents. We note that the 1/2° QuikSCAT surface winds are also effective in providing smaller space-scale forcing, which is important for ocean surface current studies. Recent publications have shown how the wind stress is affected by the mesoscale structure of the SST field, responding to ocean eddies (White and Annis 2003) and frontal movements (Chelton et al. 2001). Our surface current product from the period 1992–1999 based on the weekly ERS winds at 1° resolution does not have the same spatial–temporal resolution of the surface Ekman currents. A final point for the daily Ekman currents concerns the data storage: The daily 1/4° grid global data files represent 6.2 Go of compressed data per year, compared to ~1 Go per year for the weekly files. The trade-off between better and higher latitude currents and data storage requirements should be considered by users (http://www.legos.obs-mip.fr/observations/ctoh).

Our Ekman currents are based on a fairly simple empirical two-parameter model. We have also tested a different two-parameter model based on the wind-friction velocity, $u*$, and the Coriolis parameter, f : $U = Au*/f^{1/2}$ (Ralph and Niiler 1999; Niiler 2001). This new formulation gave large turning angles between 55–90° in the mid- to high latitudes. In comparison, Rio and Hernandez (2004) have tested an Ekman model in the global ocean and tuned their model parameters (amplitude, turning angle, Ekman depth, eddy viscosity) to fit the ageostrophic component of the drifter currents. They found turning angles of only 20–60° in the Southern Ocean and 50–70° in the tropics (whereas our method reduces the turning angle from 55° to 0°). Given the large uncertainty between these different formulations, we have chosen to maintain the simple two-parameter model proposed by Van Meurs and Niiler (1997), setting a fixed angle at $\theta = 55$ for our Ekman currents.

However, further improvements of this Ekman formulation will be necessary in the future. For example, in the presence of a stratified ocean, Price and Sundermeyer (1999) found that the Ekman spiral becomes flatter, and much of the wind-driven transport is trapped in the upper Ekman layer, in the warm diurnal layer. In this case, the in situ currents at 15-m depth can be stronger than those modeled by our simple Ekman model, which may explain part of the discrepancy between amplitudes of the satellite and in situ currents in the lower eddy energy regions. Rio and Hernandez (2004) considered 6-month averages of summer and winter conditions, and found significant spatial and seasonal variability in their tuned Ekman model parameters. This seasonal variability in the stratification needs to be further explored to develop improved near-surface Ekman currents.

The CTOH surface current product is also dependant on the quality of the mean dynamic topography based on the Rio et al. (2005) analysis. Neither the altimetry-derived currents nor the MDT product are accurate in the coastal zone (<25 km from the coast). An improved version, updated with more recent hydrographic data and a longer time series of GRACE data, is planned (M.H. Rio, personal communication). Other MDT products exist (e.g., Niiler et al. 2003), which should also be tested for future version of the surface current product.

The weakness of the CTOH satellite-based product for reproducing the current structure along the equator has also been discussed. We have adopted algorithms for the equatorial zone that are based largely on the Lagerloef et al. (1999) empirical formulism. The OSCAR surface current project uses a different formulation based on the resolution of quasi-linear and quasi-steady momentum equations, as detailed by Bonjean and Lagerloef (2002). Their 5-day products have a lower spatial resolution (1°) and have been specifically adapted for the equatorial region. A recent study by Johnson et al. (2007) carefully characterized the spatial and temporal resolution of their surface current product, in comparison with the available in situ data (surface drifters, TAO current meter arrays, etc.). Whereas our intercomparison between the two products was based on correlation statistics including a mix of all frequency bands, the analysis of the OSCAR currents separate the frequency bands into 10- to 20-day, 20- to 40-day, 40- to 80-day, and >80-day components (Johnson et al. 2007). They found that the OSCAR product provided reasonably accurate surface currents at periods >40 days and with meridional wavelengths >8°. Both satellite surface products show a high correlation with the zonal surface drifter velocities in the northern tropical band, especially around the North Equatorial Current at 10°N, with lower correlations in the southern tropical band. The OSCAR product clearly shows improved near-surface circulation in

the 5° S–10° N band, whereas the finer resolution CTOH product is better adapted at the mid- to high latitudes.

Neither product correctly captures the meridional current system in the 10° N–10° S band. These meridional velocities are dominated by tropical instability waves, with wavelengths of ~1,000 km and periods of ~15–20 days (Qiao and Weisberg 1995; Halpern et al. 1988). These timescales are less than the Nyquist frequency of the Topex–Poseidon–Jason altimeter missions, which are themselves the most frequently repeating missions. In addition, the satellite ground-tracks have steeper angles at low latitudes, providing better sampling of the zonal currents, with larger errors in the meridional currents (Morrow et al. 1994; Johnson et al. 2007). This combination of fast timescales and larger meridional errors means that Tropical Instability Waves cannot be well resolved by the present generation of satellite altimeters. In the future, high-resolution satellite altimetry products will also be available, such as the Altika or WATER projects. In the meantime, we have greatly improved our estimates of the zonal velocities in the equatorial band. The problem of resolving high-resolution and accurate meridional surface currents in the 10° N–10° S band remains.

Acknowledgment We are grateful to the CERSAT team for providing the validated and calibrated wind data, and to CNES/AVISO Altimetry for the MSLA and MDT data. The authors would like to thank the TAO/TRITON project, the Joint Archive for Shipboard ADCP, and the Global Drifter Program for the current meter data, ADCP data, and Lagrangian float data, respectively. Special thanks go to Dr. Véronique Garçon, Dr. Christophe Maes, and Dr. Gérard Eldin for their fruitful discussions and careful reading of the manuscript. Anonymous reviewers provided us with helpful comments that significantly improved the manuscript.

References

Bonjean F, Lagerloef GSE (2002) Diagnostic model and analysis of the surface currents in the tropical Pacific Ocean. J Phys Oceanogr 32:2938–2954

Brachet S, Le Traon PY, Le Provost C (2004) Mesoscale variability from a high-resolution model and from altimeter data in the North Atlantic Ocean. J Geophys Res 109:C12025

Brambilla E, Talley LD (2006) Surface drifter exchange between the North Atlantic subtropical and subpolar gyres. J Geophys Res 111(C7):C07026

Caniaux G, Brut A, Bourras D, Giordani H, Paci A, Prieur L, Reverdin G (2005) A 1 year sea surface heat budget in the northeastern Atlantic basin during the POMME experiment: 1. Flux estimates. J Geophys Res 110:C07S02

Chaigneau A, Morrow R, Rintoul S (2004) Seasonal and interannual evolution of the mixed layer in the Antarctic Zone, south of Tasmania. Deep-Sea Res I 51:2047–2072

Chelton DB, Esbensen SK, Schlax MG, Thum N, Freilich MH, Wentz FJ, Gentemann CL, McPhaden MJ, Schopf PS (2001) Observations of coupling between surface wind stress and sea surface temperature in the Eastern Tropical Pacific. J Clim 14:1479–1498

Chereskin TK, Roemmich D (1991) A comparison of measured and wind-derived Ekman transport at 11°N in the Atlantic ocean. J Phys Oceanogr 21:869–878

Chereskin TK, Wilson WD, Bryden HL, Ffield A, Morrison J (1997) Observations of the Ekman balance at 8°30 N in the Arabian Sea during the southwest monsoon. Geophys Res Lett 24:2541–2544

Crosby DS, Breaker LC, Gemmill WH (1993) A proposed definition for vector correlation in geophysics: Theory and Application. J Atmos Ocean Technol 10:355–367

Ducet N, Le Traon P-Y, Reverdin G (2000) Global high resolution mapping of ocean circulation from TOPEX/POSEIDON and ERS-1/2. J Geophys Res 105:19477–19498

Esselborn S, Eden C (2001) Sea surface height changes in the North Atlantic Ocean related to the North Atlantic Oscillation. Geophys Res Lett 28:3473–3476

Fieux M, Molcard R, Morrow R (2005) Leeuwin Current and Eddies off Western Australia. Deep Sea Res I 52:1617–1635

Garçon V, Oschlies A, Doney S, McGillicuddy D, Waniek J (2001) The role of mesoscale variability on plankton dynamics in the North Atlantic. Deep Sea Res II 48:2199–2226

Girard C, Sudre J, Benhamou S, Roos D, Luschi P (2006) Homing in green turtles *Chelonia mydas*: oceanic currents act as a constraint rather than as an information source. Mar Ecol Prog Ser 322:281–289

Halpern D, Knox RA, Luther DS (1988) Observations of 20-day period meridional current oscillations in the upper ocean along the Pacific Equator. J Phys Oceanogr 18:1514–1534

Hill KL, Weaver AJ, Freeland HJ, Bychkov A (2002) Evidence of change in the Sea of Okhotsk: Implications for the North Pacific. Atmos Ocean 41(1):49–63

Johnson ES, Bonjean F, Lagerloef GSE, Gunn JT, Mitchum GT (2007) Validation and error analysis of OSCAR sea surface currents. J Atmos Ocean Technol 24:688–701

Lagerloef GSE, Mitchum GT, Lukas RB, Niiler PP (1999) Tropical Pacific near-surface currents estimated from altimeter, wind and drifter data. J Geophys Res 104(C10):22313–22326

Lagerloef GSE, Lukas R, Bonjean F, Gunn JT, Mitchum GT, Bourassa M, Busalacchi AJ (2003) El Niño Tropical Pacific Ocean surface current and temperature evolution in 2002 and outlook for early 2003. Geophys Res Lett 30(10):1514

Legeckis R (1977) Long waves in the eastern equatorial Pacific Ocean: a view from a geostationary satellite. Science 197:1179–1181

Le Traon PY, Dibarboure G (2002) Velocity mapping capabilities of present and future altimeter missions: the role of high frequency signals. J Atmos Ocean Technol 19:2077–2088

Lukas R, Firing E (1984) The geostrophic balance of the Pacific Equatorial Undercurrent. Deep-Sea Res I 31:61–66

McPhaden MJ, Taft BA (1988) Dynamics of seasonal and intra-seasonal variability in the eastern equatorial Pacific. J Phys Oceanogr 18(11):1713–1732

McPhaden MJ, Busalacchi AJ, Cheney R, Donguy J-R, Gage KS, Halpern D, Ji M, Julian P, Meyers G, Mitchum GT, Niiler PP, Picaut J, Reynolds RW, Smith N, Takeuchi K (1998) The Tropical Ocean Global Atmosphere Observing System: a decade of progress. J Geophys Res 103(C7):14,169–14,240

Molinari RL, Olson D, Reverdin G (1990) Surface current distributions in the tropical Indian Ocean derived from compilations of surface buoy trajectories. J Geoph Res 95:7217–7238

Morrow RA, Coleman R, Church JA, Chelton DB (1994) Surface eddy momentum flux and velocity variances in the Southern Ocean from Geosat altimetry. J Phys Oceanogr 24:2050–2071

Morrow RA, Fang F, Fieux M, Molcard R (2003) Anatomy of three warm-core Leeuwin Current eddies. Deep Sea Res II 50:2229–2243

Niiler PP (2001) The world ocean surface circulation. In: Church J, Siedler G, Gould J (eds) Ocean circulation and climate-observing and modeling the global ocean. Academic, San Diego, CA

Niiler PP, Maximenko NA, McWilliams JC (2003) Dynamically balanced absolute sea level of the global ocean derived from near-surface velocity observations. Geosphys Res Lett 30 (22):2164

Picaut J, Hayes SP, McPhaden MJ (1989) Use of the geostrophic approximation to estimate time-varying zonal currents at the equator. J Geophys Res 94:3228–3236

Picaut J, Hackert E, Busalacchi AJ, Murtugudde R, Lagerloef GSE (2002) Mechanisms of the 1997–1998 El Niño-La Niña, as inferred from space-based observations. J Geophys Res 107:C5

Price JF, Sundermeyer MA (1999) Stratified Ekman layers. J Geophys Res 104:20467–20494

Qiao L, Weisberg RH (1995) Tropical instability wave kinematics: observations from the tropical instability wave experiment. J Geophys Res 100(C5):8677–8693

Ralph EA, Niiler PP (1999) Wind-driven current in the tropical pacific. J Phys Oceanogr 29:2121–2129

Reverdin G, Frankignoul C, Kestenare E, McPhaden MJ (1994) Seasonal variability in the surface currents of the equatorial Pacific. J Geophys Res 99:20323–20344

Reverdin G, Niiler PP, Valdimarsson H (2003) North Atlantic Ocean surface currents. J Geophys Res 108(C1):3002

Rio M-H, Hernandez F (2004) A mean dynamic topography computed over the world ocean from altimetry, in situ measurements, and a geoid model. J Geophys Res 109 (C1):2032

Rio M-H, Schaeffer P, Hernandez F, Lemoine J-M (2005) The estimation of the ocean Mean Dynamic Topography through the combination of altimetric data, in-situ measurements and GRACE geoid: from global to regional studies. Proceedings of GOCINA workshop, Luxembourg, April 2005

Schott FA, Visbeck U Send, Fischer J, Stramma L, Desaubies Y (1996) Observations of deep convection in the Gulf of Lions, northern Mediterranean, during winter 1991/92. J Phys Oceanogr 26:505–524

Seidel HF, Giese BS (1999) Equatorial currents in the Pacific Ocean 1992–1997. J Geophys Res 104:7849–7863

Subrahmanyam B, Robinson IS (2000) Sea surface height variability in the Indian Ocean from Topex/Poseidon altimetry and model simulations. Mar Geod 23:167–195

Van Meurs P, Niiler PP (1997) Temporal variability of the large-scale geostrophic surface velocity in the northeast Pacific. J Phys Oceanogr 27:2288–2297

Wahl T, Skøelv A, Pedersen JP, Seljelv L-G, Andersen JH, Follum OA, Anderssen T, Dahle Strøm G, Bern T-I, Hovland Espedal H, Hamnes H, Solberg R (1996) Radar satellites: a new tool for pollution monitoring in coastal waters. Coast Manag 24:61–71

White WB, Annis JL (2003) Coupling of extratropical mesoscale eddies in the ocean to westerly winds in the atmospheric boundary layer. J Phys Oceanogr 33:1095–1107

2.3.3 Améliorations souhaitables de l'estimation des courants au quart de degré à l'échelle globale

L'estimation des courants de surface présentée dans l'article précédent a été distribuée à l'ensemble de la communauté scientifique via le CTOH. Quelques utilisateurs nous ont contacté à propos de ces estimations pour obtenir des informations complémentaires sur l'interprétation de la dynamique océanique de leurs zones d'études ou sur les estimations des courants. Il est apparu au cours de ces échanges que certaines améliorations de l'estimation des courants étaient souhaitables, en particulier :

- une estimation des courants géostrophiques en zone côtière,
- une meilleure estimation de la composante méridienne des courants en zone équatoriale,
- une climatologie de la zone équatoriale plus proche des observations,
- une prise en compte de la variation spatiale de la profondeur de couche d'Ekman et du coefficient de traînée, pour une estimation plus proche des observations des courants d'Ekman,
- l'obtention de courants d'Ekman suite à l'arrêt définitif du satellite QuikSCAT et de son diffusiomètre SeaWinds en Novembre 2009.

L'ensemble de ces points nous a conduit naturellement à reconsidérer l'obtention des courants géostrophiques et de dérive par les vents au cours de cette thèse ; le point central de celle-ci réside dans l'obtention de la dynamique océanique à différentes échelles de résolution.

2.4 Article : On the global estimates of geostrophic and Ekman surface currents, Sudre et al., 2013

2.4.1 Résumé de l'article (version française)

La connaissance des courants de surface est d'une importance cruciale en océanographie car ils transportent dynamiquement sur de longues distances la quantité de mouvement, la chaleur, la salinité ainsi que les traceurs passifs. Ces courants régulent ainsi les conditions climatiques à la fois à l'échelle locale

et globale, et ils contribuent aux déplacements Lagrangiens de tout le matériel flottant allant des ressources aux pollutions marines.
Au cours de ces dernières décennies, la connaissance de ces courants de surface a bénéficié de la possibilité conjointe d'observer par télédétection la hauteur de mer et la tension de vent. En combinant ces deux paramètres physiques, il est possible d'accéder aux composantes géostrophiques et de dérive par les vents des courants de surface de manière journalière, à l'échelle globale, et avec une résolution horizontale fine au quart de degré. Dans cette étude, l'obtention des courants de surface a été améliorée par la prise en compte de la dépendance spatio-temporelle des paramètres principaux impliqués dans la détermination de la composante d'Ekman et dans le traitement géostrophique de la singularité équatoriale. L'estimation résultante des courants géostrophiques et d'Ekman (GEKCO) a été validée au moyen d'observations indépendantes aussi bien en Lagrangien qu'en Eulérien. La comparaison statistique des courants de surface obtenus avec les données *in situ* sur l'ensemble du globe pour la période 2000-2008 est significative à l'exception de la composante méridienne le long de l'équateur qui nécessite un traitement du modèle dynamique plus approfondi ainsi que des mesures satellites plus précises. Au delà de cette nécessaire étape de validation, différentes applications ont été menées pour montrer l'approche interdisciplinaire que permet l'obtention de ces courants.

2.4.2 Article publié dans *Limnology and Oceanography : Fluids and Environments*

Référence : Sudre J., Maes C. and Garçon V., On the global estimates of geostrophic and Ekman surface currents, *Limnology and Oceanography : Fluids and Environments*, 03 1-20, 2013, DOI 10.121521573689-2071927.

Limnology and Oceanography
FLUIDS & ENVIRONMENTS

ORIGINAL ARTICLE

On the global estimates of geostrophic and Ekman surface currents

Joël Sudre,[1] **Christophe Maes,**[2] **and Véronique Garçon**[1]

Abstract

Surface currents in oceanic environments are of crucial importance because they transport momentum, heat, salt, and tracers over large distances that regulate both the local and large-scale climate conditions, and because they contribute to the Lagrangian displacement of floating material, ranging from living resources to marine pollution. In recent decades, the understanding of surface currents has benefited from the opportunity of observing sea level and wind stress via satellite-derived measurements. Combining these parameters into geostrophic and wind-driven components provides an estimate of surface currents with a quarter-degree horizontal resolution at a global scale and at a daily time scale. In the present study, improvements are made on the consideration of the time dependence of the main parameters implied in the determination of the Ekman wind-driven component, and on the treatment of the equatorial singularity. The resulting Geostrophic and Ekman Current Observatory (GEKCO) estimates were validated with independent observations from both Lagrangian and Eulerian perspectives. The statistics of comparison were significant over the globe for the 2000–2008 period. The only exception was the estimation of meridional current along the equator, which requires further developments of the dynamic model and, probably, more accurate measurements. Applications using our GEKCO surface current estimates in cross-disciplinary approaches from physical oceanography to marine ecology are presented and discussed.

Keywords: drifter buoys, Lagrangian trajectory applications, ocean circulation and dynamics, physical oceanography

Introduction

[1] Before the modern era of satellite observation, ocean surface currents were mainly estimated using data from historical ship drift (Richardson 1989). Since 1978, satellite-tracked drifters (issued from the National Oceanic and Atmospheric Administration's Atlantic Oceanographic and Meteorological Laboratory [AOML] Surface Velocity Program, now known as the Global Drifter Program) have been deployed in all ocean basins and have allowed computation of oceanic currents at global scales (Niiler et al. 2003; Lumpkin and Pazos 2007). These efforts take a long time to sample the global ocean in order to estimate the mean climatology of surface currents; furthermore, the analysis of variability remains problematic due to the coarse spatiotemporal sampling, which leaves some regions largely unexplored (e.g., Arctic and Antarctic). Moreover some key regions, such as equatorial divergence areas, are mostly undersampled because of the nature of

[1]CNRS/LEGOS, 18 av. E. Belin, 31401 Toulouse Cedex 9, France

[2]IRD/LEGOS, 18 av. E. Belin, 31401 Toulouse Cedex 9, France

Correspondence to Joël Sudre, joel.sudre@legos.obs-mip.fr

© 2013 by the Association for the Sciences of Limnology and Oceanography, Inc.

Downloaded by guest on March 1, 2013

surface drifters. Repeated satellite observations of sea level offer the opportunity to study mesoscale eddies through the geostrophic approximation over the ocean (Chelton et al. 2011). Combined with wind stress fields also observed from space, ocean surface circulation can be determined by a steady balance between geostrophic and Ekman dynamics (Lagerloef et al. 1999).

[2] The transport of heat and freshwater by ocean currents is crucial in climate variability and varies at both regional and global scales. In the Pacific Ocean, the zonal displacement of the western Pacific warm pool has strong implications in ocean atmosphere interactions associated with El Niño/Southern Oscillation (ENSO) at the interannual time scale (Picaut et al. 1996). The horizontal convergence of currents at the eastern edge of the warm pool results in a front of surface salinity (Maes et al. 2006) and a significant chlorophyll *a* gradient that is accurately monitored by satellite remote sensing (Maes et al. 2010). Surface current anomalies can lead ENSO or sea-surface temperature anomalies by a few months, representing a potential way to predict the arrival of the warming conditions in the eastern Pacific associated with ENSO (Lagerloef et al. 2003). At seasonal time scales, the mean surface divergence also links the equatorial band to the subtropical dynamic a few years later as part of the subtropical cells (Johnson 2001).

[3] In the euphotic zone, the surface currents associated with mesoscale structures strongly influence ocean biogeochemistry via advection, lateral stirring, frontal instabilities, and eddy pumping (Garçon et al. 2001). The latter process supplies nutrients to the upper layers and thus fuels phytoplankton growth and the subsequent marine food chain. The relationship between the ocean dynamics and biogeochemical variability is rather complex and not fully understood. For instance, the Agulhas current sustains long-lived and intense bloom events in the subtropical convergence zone south of Africa (Llido et al. 2005). By contrast, in the four major eastern boundary upwelling systems, the horizontal mixing counteracts the nutrient Ekman pumping, which remains nevertheless the dominant process (Rossi et al. 2008). Over the oceans, physical processes influence plankton dynamics (Abraham 1998) up to the ecology of the marine megafauna (Tew Kai et al. 2009; Robel et al. 2011).

[4] Quantifying ocean currents at global scale with a high level of accuracy is of significant cross-disciplinary interest. This relates to the aforementioned role of ocean currents as an initiator and moderator of climate variability and the influence on biological properties, including the behavior of marine animals. Whereas a number of approaches offer a comprehensive view of ocean motion at unprecedented spatial and temporal scales (e.g., Dohan and Maximenko 2010), they also include several discrepancies (e.g., amplitude of the mean current along the equator and the variability of meridional current within the tropical band, especially at the frequency of the tropical instability waves; Johnson et al. 2007; Sudre and Morrow 2008). The aim of this study is to improve estimates of the wind-driven currents via standard Ekman formalism and to tackle the specific singularity of the equator. The proposed Geostrophic and Ekman Current Observatory (GEKCO) is described methodologically, along with the different data sets required. The results presented include a broad overview of the mean and variability of the currents and a cross-validation using independent data sets. The implications of these results for ocean dynamics and cross-disciplinary applications are discussed.

Methods

[5] Oceanic currents result from movements of fluid particles in response to internal forces (pressure gradients and Coriolis forces), external forces (gravity force), and frictional forces (dominated in the surface ocean by wind stress). Steady ocean currents derive from balances between these different forces. A primary balance is between the horizontal pressure gradient and the Coriolis force, resulting in "geostrophic flow." Historically, the surface geostrophic flow was deduced by in situ observations of the geopotential anomaly determined from density profiles (resulting from temperature and salinity data). At the surface, it is also necessary to account for the wind-driven currents (or Ekman currents) that result from the balance between the frictional stress due to the wind and the Coriolis force. Theoretically,

© 2013 by the Association for the Sciences of Limnology and Oceanography, Inc. / e-ISSN 2157-3689

Downloaded by guest on March 1, 2013

the wind-driven component of mass transport in the surface (Ekman) layer is perpendicular to the mean wind stress, to the left of the wind stress in the southern hemisphere and to the right in the northern one. At the surface, the current associated with this transport deviates from the wind direction by 45°, and the amplitude decreases down to the Ekman layer depth following a spiral. In the tropical Pacific, Ralph and Niiler (1999) highlighted that 78% of the variance of ocean current as observed by Lagrangian drifters drogued at 15-m depth could be explained by the geostrophic and Ekman currents (63% and 15%, respectively). This important result provides the basis for estimating ocean surface currents at global scale computed from satellite altimetry and surface vector winds. In the following, we define zonal and meridional currents (u, v) as the sum of geostrophic (u_g, v_g) and Ekman (u_e, v_e) components. A user-friendly program for computing the oceanic currents at specified worldwide locations is available from the authors (www.legos.obs-mip.fr/sudre/mesoscale-oceanic-current-extracting-program).

The Geostrophic Component

[6] The geostrophic balance assumes that momentum advection and frictional forces are small. Outside the equatorial band (where the Coriolis force vanishes), geostrophic velocities are given by

$$u_g = -\frac{g}{f}\frac{\partial h}{\partial y} \tag{1a}$$

and

$$v_g = \frac{g}{f}\frac{\partial h}{\partial x}, \tag{1b}$$

where y and x are the latitude and longitude positions, f is the Coriolis parameter, g is the acceleration due to gravity (9.807 m s^{-2}), and h is the map of absolute dynamic topography (MADT) that results from the elevation of the sea surface height referenced by the geoid. The latter field represents the product from the Data Unification and Altimeter Combination System available on the AVISO (Archiving, Validation and Interpretation of Satellite Oceanographic data) website (www.aviso.oceanobs.com/en/data/productsinformation/duacs). This product provides a daily and global projection onto a Mercator grid (resolution of 1/3°). Our geostrophic component based on Eqs. 1a and 1b are determined on a regular grid at 1/4° resolution using bilinear interpolation.

[7] Eqs. 1a and 1b are singular at the equator, where $f = 0$, and are problematic nearby because the Coriolis force is small. However, both equatorial theory and several studies based on observations (Moore and Philander 1978) suggest the use of the second derivative of the meridional pressure field on an equatorial β-plane ($f = \beta y$, where β is a constant). When applied to the MADT, the equations for each component of the so-called "semigeostrophic" current (u_{sg}, v_{sg}) become

$$u_{sg} = -\frac{g}{\beta}\frac{\partial^2 h}{\partial y^2} \tag{2a}$$

and

$$v_{sg} = \frac{g}{\beta}\frac{\partial^2 h}{\partial x^2}, \tag{2b}$$

where $\beta = 2.3 \times 10^{-11}$ m^{-1}s^{-1}. A condition to use Eqs. 2a and 2b at the equator is that the first meridional derivative of h needs to be null. A correction factor is then introduced to the MADT in order to force that condition, following the procedure detailed by Picaut and Tournier (1991). Away from the equator, the continuity between Eqs. 1a and 2a (Eqs. 1b and 2b, respectively) is ensured by applying a classical spline function within the 2°N–2°S band. Outside of this band, the estimates of current remain purely geostrophic.

The Ekman Component

[8] The Ekman regression model of the wind-driven current, following van Meurs and Niiler (1997) and Lagerloef et al. (1999), represents the following linear steady momentum balance,

$$fh_e u_e + r_e v_e = \tau_y/\rho \tag{3a}$$

and

$$r_e u_e - fh_e v_e = \tau_x/\rho, \tag{3b}$$

where $\tau(\tau_x, \tau_y)$ is the wind stress field, $\rho = 1025$ kg m^{-3} is the water density, and h_e and r_e are, respectively, the thickness of the Ekman layer and the linear drag coeffi-

© 2013 by the Association for the Sciences of Limnology and Oceanography, Inc. / e-ISSN 2157-3689

Downloaded by guest on March 1, 2013

cient that represents the vertical viscosity terms as a body force on the Ekman components. These latter parameters need to be determined before estimating the Ekman current, but they are largely unknown for the real ocean. For instance, Lagerloef et al. (1999) derived (h_e, r_e) based on an empirical multiple linear regression using the Lagrangian surface drifters, but these parameters were constant spatially and temporally. Extending this approach from the Pacific to other basins, Sudre and Morrow (2008) pointed out that improvement for the Ekman component was needed to account for the strong variability of the Ekman layer. This is a very complex problem that could be addressed, pragmatically, by estimating (h_e, r_e) from observations. Indeed, once the geostrophic component has been removed from the current observed by surface drifters, the residual is assumed to represent the Ekman current. Based on the equilibrium as stated by Eq. 3a and 3b, the (h_e, r_e) parameters could be expressed as

$$h_e = \frac{1}{f}\frac{\tau_y u_e - \tau_x v_e}{\rho\left(u_e^2 + v_e^2\right)} \tag{4a}$$

and

$$r_e = \frac{\tau_x u_e + \tau_y v_e}{\rho\left(u_e^2 + v_e^2\right)}. \tag{4b}$$

In the next step, we determined linear regressions between (h_e, r_e) and the wind stress modulus regionally over the global ocean, and we used these slopes to estimate u_e and v_e through Eqs. 3a and 3b. To avoid discontinuity and to treat regions poorly sampled by surface drifters, we kept only the latitude dependence of these relationships when they are averaged by basin. Fig. 1 illustrates how the complete methodology applies: for each parameter, the value was determined by considering the input of observed wind stress (Fig. 1A) and the climatological slope based on the aforementioned linear regression (Fig. 1B, C, respectively, for h_e and r_e). The resulting thickness of the Ekman layer and linear drag coefficient are displayed per basin on Fig. 1, D and E. In the Pacific and Atlantic, the equatorial Ekman layers reach values $\sim$30 m, which is well known in these regions. Outside of the equatorial band, values decrease to $<$10 m toward polar regions.

Ancillary Data

[9] To evaluate the Ekman current, we used the mean wind field data from the ku-band microwave scatterometer (SeaWinds) onboard the *QuikSCAT* satellite, distributed by the Centre ERS d'Archivage et de Traitement (CERSAT). The global daily product at 1/2° resolution is processed by a bilinear interpolation on a 1/4° regular grid and is available from 19 July 1999 to 21 November 2009.

[10] To evaluate the Ekman layer depth and the drag coefficient, we used a set of 6951 drifters drogued at 15-m depth over the global ocean during the period from 18 July 1999 to 31 March 2009 from the Global Drifter Program at AOML. To obtain the drifter velocity, we first smoothed the positions over a 72-h window to filter the inertial movements from drifter displacements. Second, the speed and direction (referenced to the north) of each drifter were calculated at each point considering two consecutive positions at six hourly intervals.

[11] To validate the time variability with independent data, we used direct observations of equatorial currents by Acoustic Doppler Current Profiler (ADCP) moorings at several discrete locations within the Pacific, Atlantic, and Indian oceans known as the TAO/TRITON, PIRATA, and RAMA arrays, respectively. Due to the backscatter from the ocean surface in the upper 30–40 m, additional current meters were included in some moorings near the surface. In the following, we used both types of observation independently as soon as observations were available at the minimum depth of 25 m in order to validate our surface currents. Only the data qualified as good or probably good (meaning that pre/post deployment calibrations have been applied) were considered hereafter.

[12] Two other sources of independent data of surface current were provided by hull-mounted ADCP and by the estimates of surface drifting in Argo floats. These data sets are very different, the former providing estimates of the horizontal current at a depth range of between 20 and 300 m every $\sim$5 min, whereas the latter

© 2013 by the Association for the Sciences of Limnology and Oceanography, Inc. / e-ISSN 2157-3689

Downloaded by guest on March 1, 2013

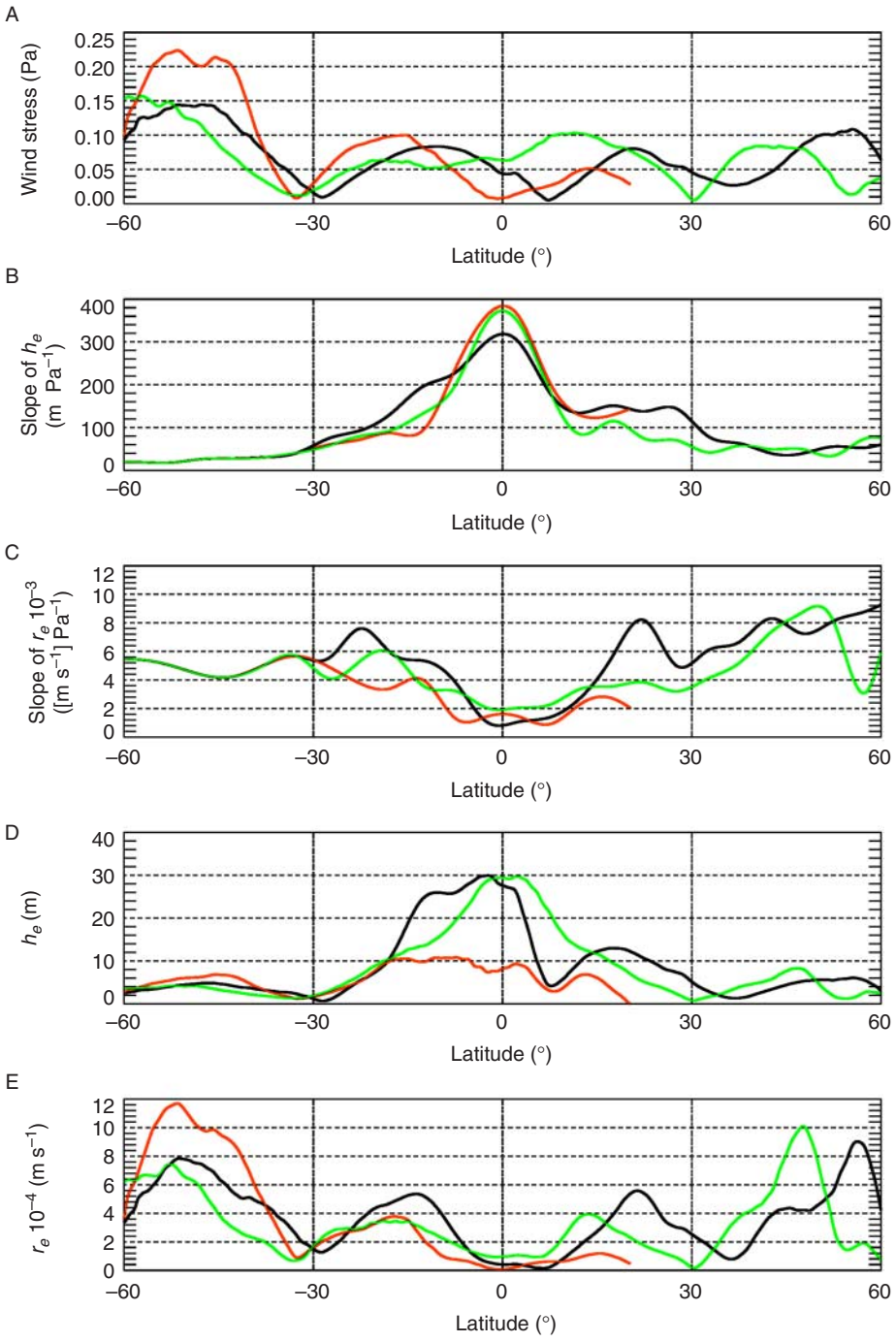

Fig. 1 Meridional section of wind stress (A), slope of the thickness of the Ekman layer (h_e) (B), slope of the linear drag coefficient (r_e) (C), and h_e and r_e per basin (D and E, respectively). Red, green, and black lines indicate Indian, Pacific, and Atlantic basins, respectively.

relies on the evaluation of surface current from the displacement of the float during the time at the surface required for satellite communication each ~10 d cycle. The ADCP current at the 20-m depth (qualified as good data only), represented 265 cruises operated on research vessels between 21 July 1999 and 22 July 2009 from the Joint Archive for Shipboard ADCP (Hummon and Firing 2003). Since the 2000s, the emergence of the Argo program offers a unique data set with global coverage that represents an alternative to the traditional drifters. We used the estimates analyzed and distributed by Xie and Zhu (2008, 2009) over the period 2000–2008. Each current evaluation based on Argo floats is considered an independent datum, and the GEKCO estimates were determined by considering the mean current between the initial and the final positions of the Argo float during its surface time. Furthermore, the geographical deployment of the Argo floats offers a complementary view for several regions that remain poorly sampled, and the error estimate in surface currents ($<5\,\mathrm{cm\,s^{-1}}$) is equivalent to the accuracy of surface drifters (Xie and Zhu 2009). In order to provide statistics comparable with those from the drifters, the data and statistics were compiled with a global repartition by $5° \times 5°$ bins.

[13] Different references for the climatology of mean currents were also considered. The drifter-derived climatology is based on the analysis described by Lumpkin and Garraffo (2005)

© 2013 by the Association for the Sciences of Limnology and Oceanography, Inc. / e-ISSN 2157-3689

Downloaded by guest on March 1, 2013

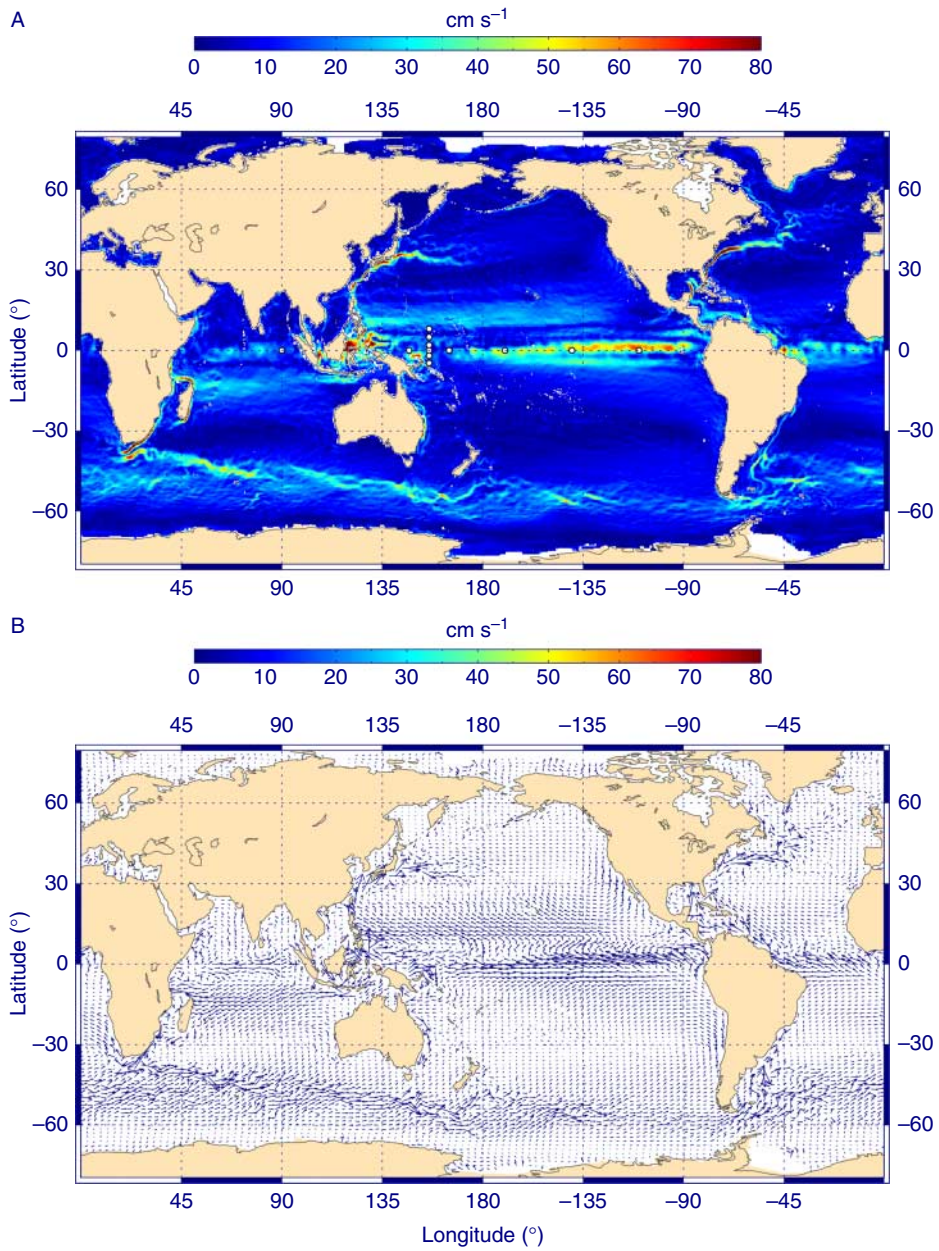

Fig. 2 Amplitude (A) and vector representation (B) of the total surface current (in cm s^{-1}) averaged for the 2000–2008 period and based on the present combination of geostrophic and wind-driven estimates. The white dots on the first panel mark the positions of the TAO/TRITON moorings.

in which the final global results were smoothed via optimum interpolation assuming a Gaussian autocorrelation function with an isotropic e-folding scale of 150 km. More locally, meridional sections of ADCP shipboard zonal mean currents were compiled by Johnson et al. (2002) in the Pacific, primarily during the 1990s. In the Atlantic Ocean, we considered the section of zonal current at 18-m depth and along 10°W as described in the compilation of 18 cross-equatorial shipboard current profiling sections by Kolodziejczyk et al. (2009).

Results

[14] To understand the role of the ocean dynamics, the currents supplying and transporting heat, freshwater and biogeochemical properties need to be thoroughly investigated. The scope of the present paper is to offer a global survey of the major ocean currents rather than to describe the details of the different regional aspects of the surface circulation. As mentioned previously the near-surface circulation is driven primarily by the wind stress and forced into closed circulation cells by the continental boundaries. The main features that emerge from the annual mean circulation (Fig. 2) pertain to the strength of the tropical circulations, especially in the Atlantic and Pacific oceans, which share features because of the prevailing trade winds. The expected intensified currents near the western boundary are the Gulf Stream and the Kuroshio currents in the northern hemisphere of the Atlantic and Pacific oceans, respectively, but they also include the Brazil-Malvinas confluence region and the East Australian Current in the southern hemisphere. Around the

© 2013 by the Association for the Sciences of Limnology and Oceanography, Inc. / e-ISSN 2157-3689

Downloaded by guest on March 1, 2013

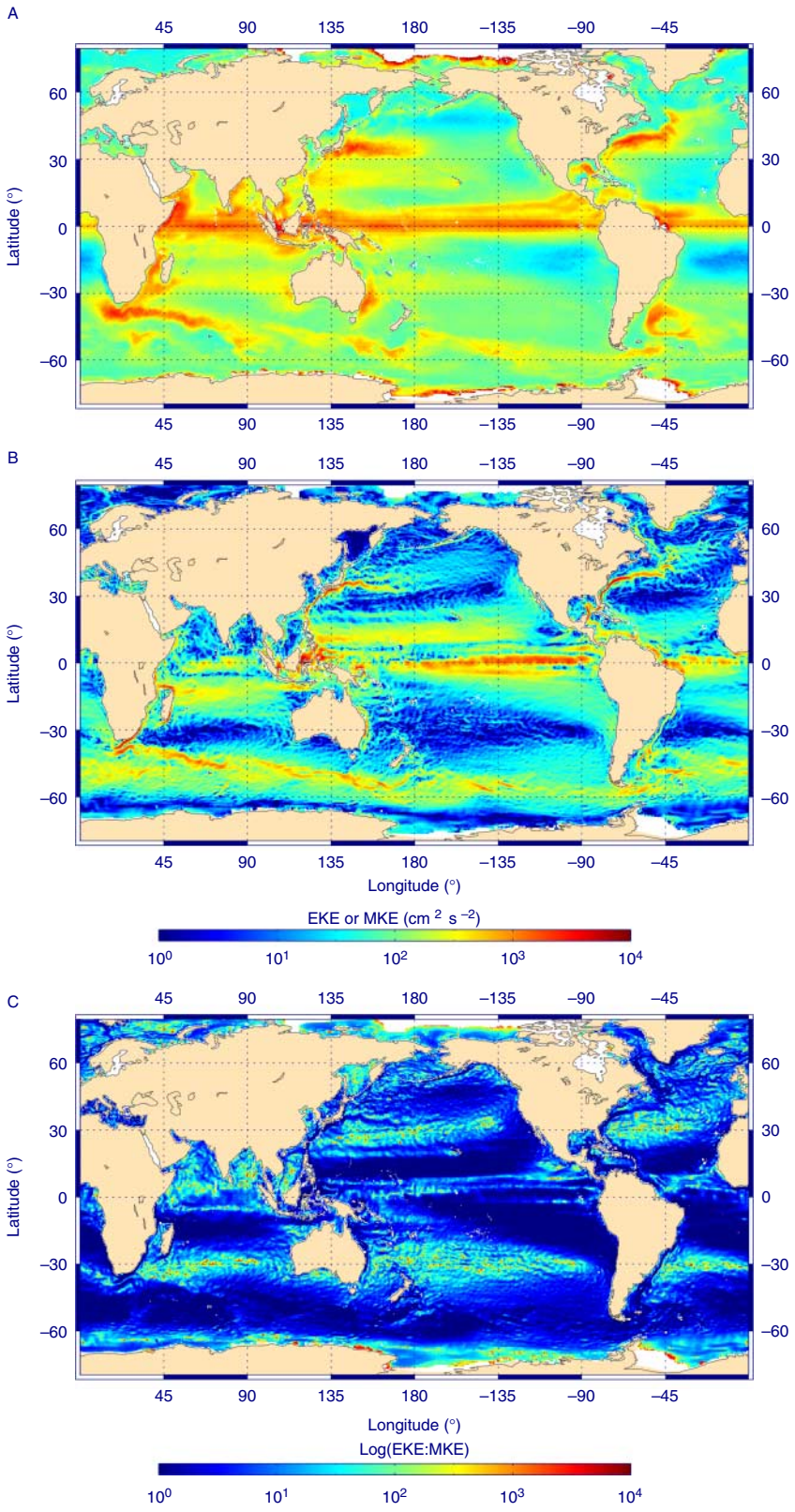

Fig. 3 Time-mean average of the eddy kinetic energy (EKE, in $cm^2\ s^{-2}$; A), mean kinetic energy (MKE, in $cm^2\ s^{-2}$; B), and EKE:MKE ratio (C). All the fields are plotted with the same logarithmic scale.

Antarctic continent, the Antarctic Circumpolar Current (ACC) provides the most significant interocean conduit by which waters of the three major basins interact. Rather than a broad flow, the ACC is composed of a number of high-energy jets separated by zones of weak currents, or even reversed westward flow. In the southern tip of Africa, the Agulhas current system that forms the western boundary system of the South Indian Ocean lies between the ACC and the subtropical convergence zone (near 40°S). The most prominent feature of this system is the retroflection of the Agulhas current in a tight loop with eastward flow as a return current (Fig. 2B). The high variability in the mesoscale activity resulting from this unstable loop configuration is important not only for the circulation in the Indian sector but also for the exchange of properties carried by the different eddies that detach and drift northward into the South Atlantic Ocean.

[15] The mean currents, as well as their variability, are of importance for energy transfer processes related to the general ocean circulation. In the ocean, the mesoscale activity lies roughly on spatial scales of 30–1000 km and time scales of 10–300 days. The eddy kinetic energy (EKE) is well suited to map this variability and can be defined by

$$\mathrm{EKE} = \frac{1}{2}(u'^2 + v'^2), \qquad (5)$$

where u' and v' are the velocity anomalies defined as the difference of current with the annual mean currents $(\bar{u}, \bar{v})$, as shown in Fig. 2A. Fig. 3A shows the averaged EKE

© 2013 by the Association for the Sciences of Limnology and Oceanography, Inc. / e-ISSN 2157-3689

Downloaded by guest on March 1, 2013

during the 2000–2008 period. The highest values ($>3000\,cm^2\,s^{-2}$) were typically found along the equatorial band and the extension of the major western boundary currents. The reversal twice a year of the Somali current due to the monsoon is responsible for the strong EKE in the western North Indian Ocean. Another pronounced high variability area is associated with the path of the ACC and is related to the meandering structures, including the Agulhas retroflection. Weaker peaks in EKE were observed in the subtropical region in each basin. Many local structures could be identified with specific dynamic regimes such as the loop current in the Gulf of Mexico, the north equatorial retroflection in the equatorial western Atlantic, and the pathway of south equatorial current around the southern part of Madagascar and into the Mozambique Channel.

[16] The relationship of EKE to large ocean circulation (which feeds EKE by barotropic and baroclinic instability) may be probed by examining the distribution of mean kinetic energy (MKE), defined as

$$\mathrm{MKE} = \frac{1}{2}(\bar{u}^2 + \bar{v}^2). \tag{6}$$

Similarly to EKE, values of MKE (Fig. 3B) exhibited maxima $> 3000\,cm^2\,s^{-2}$ in the major western boundary current regions, the ACC, and the tropics. However, these structures were thin, a result that is consistent with the idea that EKE is generated in areas of strong shear in mean flow. The ratio of EKE:MKE (Fig. 3C) shows areas where the ocean dynamics were stable (the ratio ranges between 1 and 10), as well as more turbulent (areas where this ratio exceeds 100). The former includes the pathway of the major western boundary currents, where the reduced EKE:MKE ratio is aligned along regions of enhanced MKE (Fig. 3B). It also includes the Labrador Current, the Alaskan stream flowing along the Aleutian Islands, the East Kamchatka Current, and the Norwegian Atlantic Current with its coastal extension. The five regions of high EKE:MKE values are approximately centered around 30° in the subtropics and cover each entire basin from east to west. In most of these areas, a ratio >1000 was found. High values of EKE:MKE were also found at regional scale such as the Bay of Bengal, Arabian Sea, South China Sea, Okhotsk Sea, and the Nordic Seas.

[17] The comprehensive global coverage of ocean currents in both space and time is an advantage inherent to satellite-derived fields, which also makes exhaustive validation with independent observations challenging. We used ADCP current meters, either hull mounted on ships or fixed on anchored mooring at different ocean sites, and estimates of currents derived from surface displacement of Argo floats. Each data set is characterized by heterogeneous samplings, both in time and in space, reflecting in part the dichotomous nature between their Lagrangian versus Eulerian dimension. Table 1 presents the statistics for zonal and meridional components in the three tropical regions where hull-mounted ADCP data density is reasonable. Similar standard deviations were found between in situ observations and GEKCO values in all regions. Not surprisingly, lower correlations characterized the meridional component (~0.5) compared with the zonal ones (~0.7), but both correlations were statistically significant. In order to focus on the variability, we used the

Table 1 A — Comparisons for the zonal component (u) between the data observed by shipboard ADCP and the GEKCO model estimates. N represents the number of collocated points to evaluate the mean, standard deviation (SD), root mean square difference (RMS dif), and correlation ($p > 95\%$ level of confidence). B — Same comparisons for the meridional component (v). The separation between the western and eastern parts of the Pacific (WPAC and EPAC, respectively) is located at 155°W. ATL, Atlantic basin.

A	u	N	Mean	SD	RMS dif	Correlation
WPAC	ADCP	5021	−4.46	29.87	23.37	0.70
	GEKCO		−8.73	29.42		
EPAC	ADCP	6915	−9.46	35.62	26.55	0.73
	GEKCO		−17.49	33.15		
ATL	ADCP	1636	−6.36	25.45	20.28	0.67
	GEKCO		−7.66	24.01		
B	v	N	Mean	SD	RMS dif	Correlation
WPAC	ADCP	5021	−0.26	19.12	18.72	0.45
	GEKCO		−0.43	16.18		
EPAC	ADCP	6915	−1.13	25.86	23.42	0.50
	GEKCO		4.09	17.20		
ATL	ADCP	1636	−3.38	23.97	22.22	0.46
	GEKCO		−0.20	16.93		

© 2013 by the Association for the Sciences of Limnology and Oceanography, Inc. / e-ISSN 2157-3689

Downloaded by guest on March 1, 2013

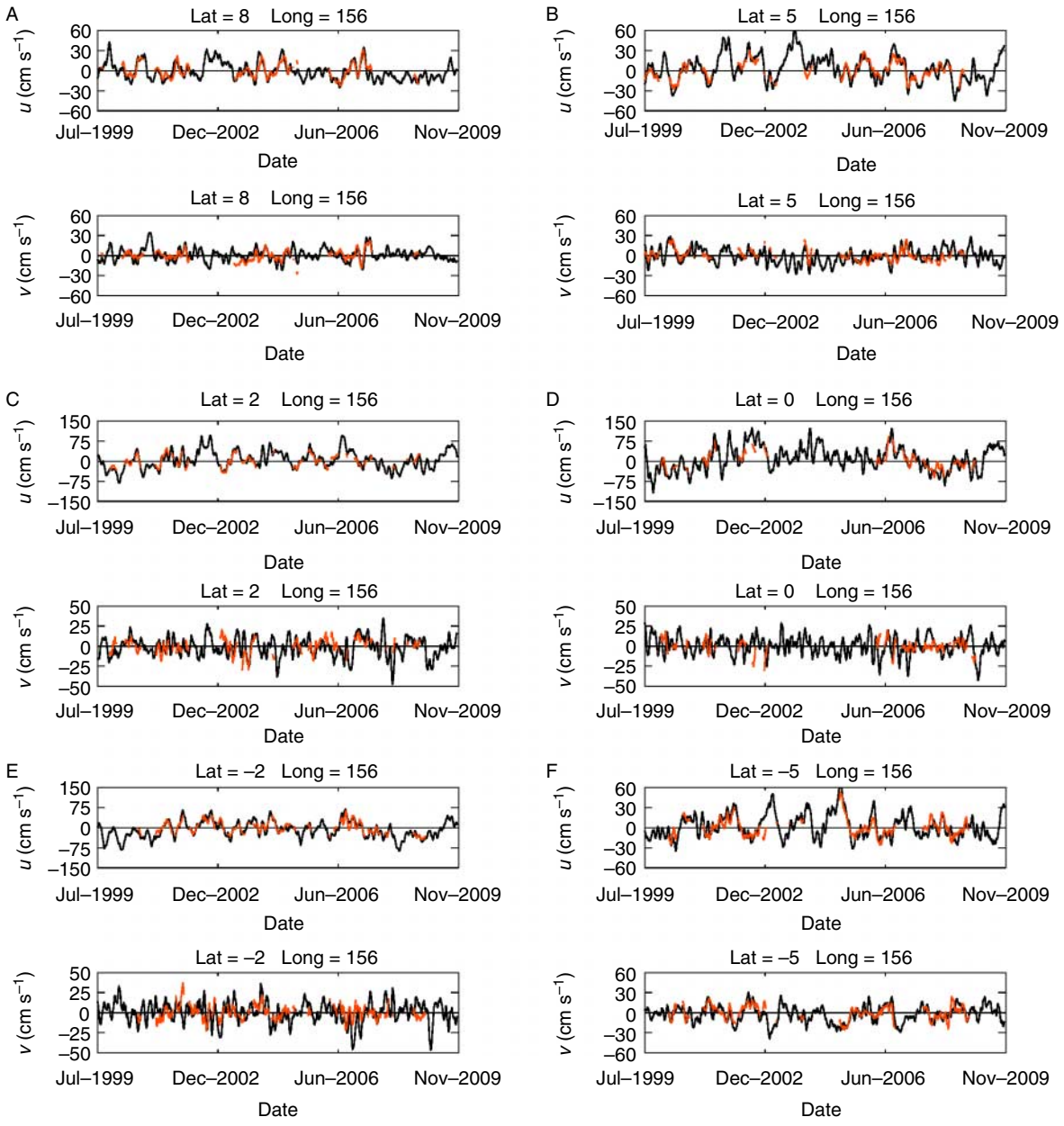

Fig. 4 Time series of the zonal (u, top) and meridional (v, bottom) components (in cm s^{-1}) along 156°E in the western Pacific Ocean as observed by ADCP moorings (red) and as estimated by GEKCO (black): A — (8°N, 156°E); B — (5°N, 156°E); C — (2°N, 156°E); D — (0°N, 156°E); E — (2°S, 156°E); and F — (5°S, 156°E). Note that the y-axis scales are different between the zonal and meridional components. Each time series was filtered at 30 days.

time series of current anomalies observed by current meter moorings corresponding to an Eulerian view of ocean dynamics. Unfortunately, time series are often interrupted by instrument failures or vandalism on the mooring lines, which prevents data recovery and produced gaps of $\geq$6 months. We considered only time series containing $\geq$3 full years of data in total. Note that each time series was normalized with its own mean value to focus only on the variability. Figs. 4 and 5 show the comparisons for the zonal and meridional components of moorings along 156°E (between 8°N and 5°S) and along the equator from 147°E to 110°W in the Pacific Ocean and 90°E in the Indian Ocean. Typical anomalies of the order of $O(1.0\,\mathrm{m\,s^{-1}})$ for the zonal

© 2013 by the Association for the Sciences of Limnology and Oceanography, Inc. / e-ISSN 2157-3689

Downloaded by guest on March 1, 2013

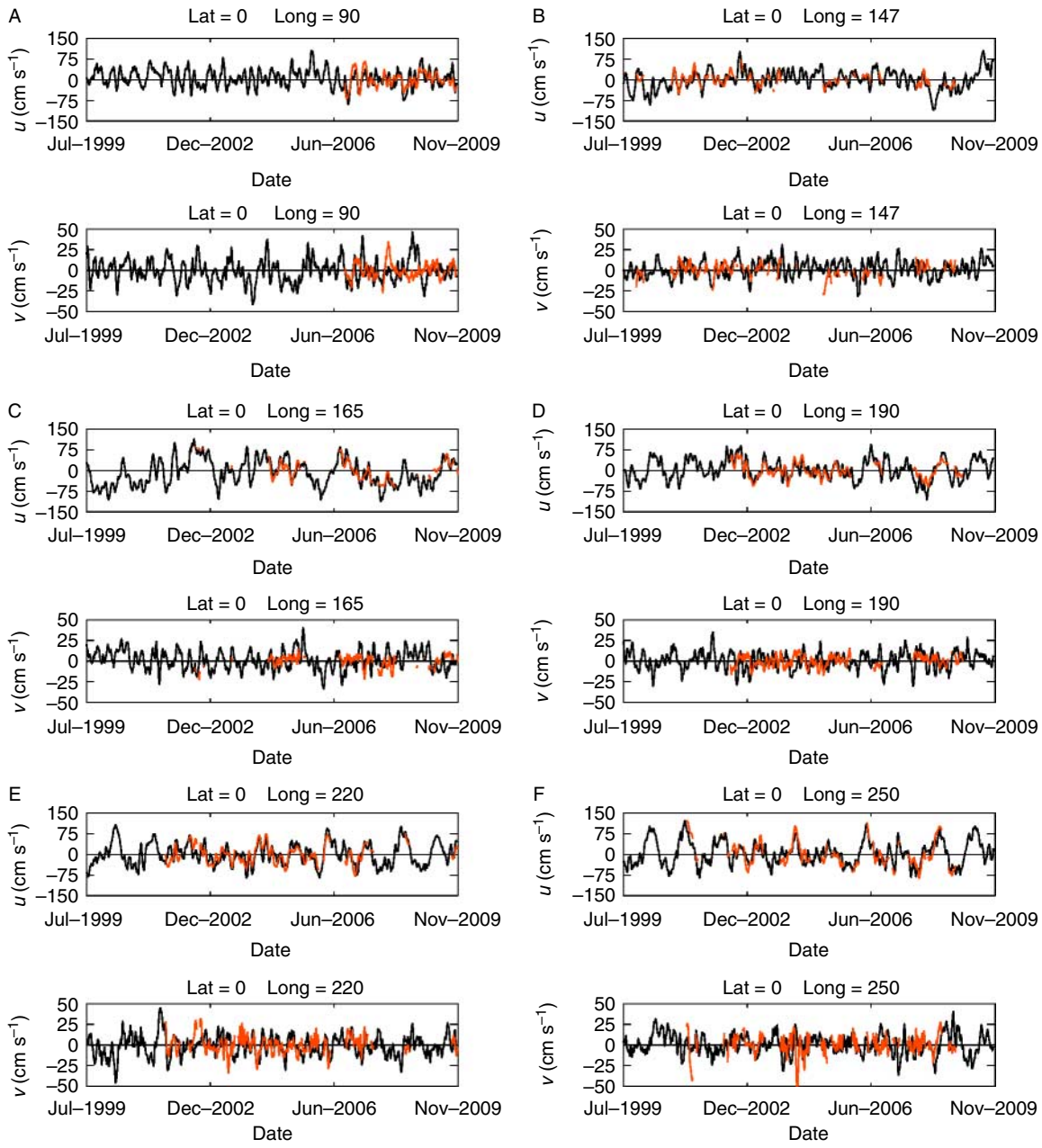

Fig. 5 Time series of the zonal (u, top) and meridional (v, bottom) components (in cm s^{-1}) for different equatorial positions (lat, long for each panel) along the Indian and Pacific oceans: A — (0°N, 90°E); B — (0°N, 147°E); C — (0°N, 165°E); D — (0°N, 190°E); E — (0°N, 220°E); and F — (0°N, 250°E). ADCP mooring indicated in red and GEKCO in black. Note that the y-axis scales are different between the zonal and the meridional components. Each time series was filtered at 30 days.

component were particularly well estimated by GEKCO, especially along the equator. For example, the time series at 165°E (Fig. 5C) exhibited positive anomalies between early 2001 and the end of 2007, which could be associated with zonal displacement of the warm pool toward the central Pacific with the development of the 2001–2002 El Niño event. Typical anomalies of $O(0.2\ \mathrm{m\ s^{-1}})$ characterized the meridional component within the 2°N–2°S band with an amplitude ratio of 5 compared with the zonal one. The GEKCO estimate showed a similar ratio even if the correlations for most equatorial sites were not significant for the meridional component. Conversely,

© 2013 by the Association for the Sciences of Limnology and Oceanography, Inc. / e-ISSN 2157-3689

Downloaded by guest on March 1, 2013

Table 2 A — Comparisons for the zonal component (u) between the observed data by moored ADCP and the GEKCO model estimates along the equatorial Indian and Pacific oceans. N represents the number of collocated points to evaluate the mean, standard deviation (SD), root mean square difference (RMS diff), and correlation (ns = $p <$ 95% level of confidence). B — Same comparisons for the meridional component (v).

A						
	u	N	Mean	SD	RMS dif	Correlation
0°N–090°E	ADCP	1061	5.65	27.81	24.41	0.68
	GEKCO		10.73	31.65		
0°N–147°E	ADCP	1441	−2.60	20.99	33.17	0.66
	GEKCO		25.49	22.21		
0°N–165°E	ADCP	1117	−10.45	34.45	29.64	0.88
	GEKCO		10.48	43.44		
0°N–170°W	ADCP	1759	−26.26	26.45	22.70	0.81
	GEKCO		−34.75	35.90		
0°N–140°W	ADCP	1818	−13.95	32.86	40.02	0.76
	GEKCO		−47.72	35.01		
0°N–110°W	ADCP	1581	−18.11	45.15	40.95	0.83
	GEKCO		−50.56	35.10		
B						
	v	N	Mean	SD	RMS dif	Correlation
0°N–090°E	ADCP	1061	−2.25	9.24	19.48	ns
	GEKCO		5.94	14.16		
0°N–147°E	ADCP	1441	−3.17	7.82	17.67	ns
	GEKCO		10.56	8.76		
0°N–165°E	ADCP	1117	−5.08	6.84	13.10	ns
	GEKCO		−6.27	11.44		
0°N–170°W	ADCP	1759	−5.77	6.56	12.11	ns
	GEKCO		−5.69	10.03		
0°N–140°W	ADCP	1818	−3.18	10.06	14.60	0.26
	GEKCO		4.02	11.04		
0°N–110°W	ADCP	1581	4.22	11.73	16.82	ns
	GEKCO		10.20	12.31		

for the zonal component (Table 2), the correlations, ranging from 0.67 to 0.90, were significant for all sites (Table 3A). Away from the equator, the amplitudes of zonal and meridional currents were quite similar (Fig. 4), and correlations were significant for both components (Table 3).

[18] These ADCP data considered only a few locations in the tropics, leaving large parts of the global ocean unvalidated. Moreover, strictly speaking, the surface drifters were not completely independent from the present estimates. Instead, the estimates of currents derived from surface displacement of Argo floats were used as an independent data set. A total of 482,370 observations between 2000 and 2008 were considered with the global repartition by $5° \times 5°$ bins, as shown in Fig. 6A. The best coverage was found in the North Indian and North West Pacific oceans, whereas the Southern Ocean remains, not surprisingly, the least-sampled region. Because of the 10-day interval between each current estimate, we considered all data as independent estimates in each bin. The statistical significance level (at 95%) of the correlation ranges from 0.1 for well-documented bins ($N > 400$) to 0.2 ($N > 100$) for the least-sampled ones. Fig. 6 (B, C), shows the correlation between the estimated currents from Argo floats and GEKCO. Globally, statistics were significant for both zonal and meridional components, and higher values were obtained in many regions that were also characterized by high levels of kinetic energy (Fig. 3). Whereas a few bins were not significant for the zonal component, the lower values and the least significant bins were located along the equatorial band for the meridional com-

© 2013 by the Association for the Sciences of Limnology and Oceanography, Inc. / e-ISSN 2157-3689

Downloaded by guest on March 1, 2013

Table 3 A — Comparisons for the zonal component (u) between the observed data by moored ADCP and the GEKCO model estimates along 156°E. N represents the number of collocated points to evaluate the mean, standard deviation (SD), root mean square difference (RMS diff), and correlation ($p >$ 95% level of confidence). B — Same comparisons for the meridional component (v).

A						
	u	N	Mean	SD	RMS dif	Correlation
8°N–156°E	ADCP	1685	−4.47	10.86	11.92	0.86
	GEKCO		−14.47	12.75		
5°N–156°E	ADCP	1814	15.17	12.17	8.08	0.89
	GEKCO		11.13	15.25		
2°N–156°E	ADCP	1414	−7.88	21.41	15.64	0.90
	GEKCO		3.99	23.67		
0°N–156°E	ADCP	1102	−11.47	29.13	31.77	0.87
	GEKCO		11.96	41.55		
2°S–156°E	ADCP	1786	−8.92	21.86	27.76	0.90
	GEKCO		16.35	26.30		
5°S–156°E	ADCP	1870	−6.64	13.56	13.45	0.83
	GEKCO		2.70	17.24		
B						
	v	N	Mean	SD	RMS dif	Correlation
8°N–156°E	ADCP	1685	2.59	7.69	7.30	0.65
	GEKCO		4.20	9.15		
5°N–156°E	ADCP	1814	3.56	7.77	7.47	0.67
	GEKCO		3.22	9.95		
2°N–156°E	ADCP	1414	5.24	8.94	12.57	0.37
	GEKCO		11.13	10.79		
0°N–156°E	ADCP	1102	−3.48	8.26	14.40	ns
	GEKCO		−7.73	12.02		
2°S–156°E	ADCP	1786	−1.76	8.58	25.47	0.28
	GEKCO		−23.09	13.65		
5°S–156°E	ADCP	1870	−3.64	10.26	8.57	0.73
	GEKCO		−7.07	11.32		

ponent. This results from the estimates close to the equatorial singularity in the 5°-width bins in latitude. Averaged globally, the mean correlations were equal to 0.68 and 0.62 for the zonal and meridional component, respectively.

[19] As mentioned earlier, comparisons with independent data revealed noticeable differences in mean currents. We compared the mean values over the 2000–2008 period with the drifter data and a few sections in latitude of zonal current based on the ADCP data. We focused on the equatorial band where the currents were strong and characterized by fine meridional structures. All the fields exhibited similar westward and eastward currents both in amplitude and latitudinal width (Fig. 7). However differences as high as 20 cm s^{-1} were noted, and in some cases, one estimate deviated significantly from the others. As an example, a large structure of eastward current at 165°E between the equator and 7°N was observed in the GEKCO estimates, whereas the ridge between the South Equatorial Current and the North Equatorial Counter Current was expected (Fig. 7A). We diagnosed the presence of this structure in absolute dynamic topography from which the geostrophic zonal current was derived. Compared with the Pacific Ocean, the latitudinal structures in the Atlantic equatorial ocean were even finer and were consistent among the different estimates.

Discussion

[20] Satellites are the primary sources of observations for the GEKCO surface ocean currents, providing an

© 2013 by the Association for the Sciences of Limnology and Oceanography, Inc. / e-ISSN 2157-3689

Downloaded by guest on March 1, 2013

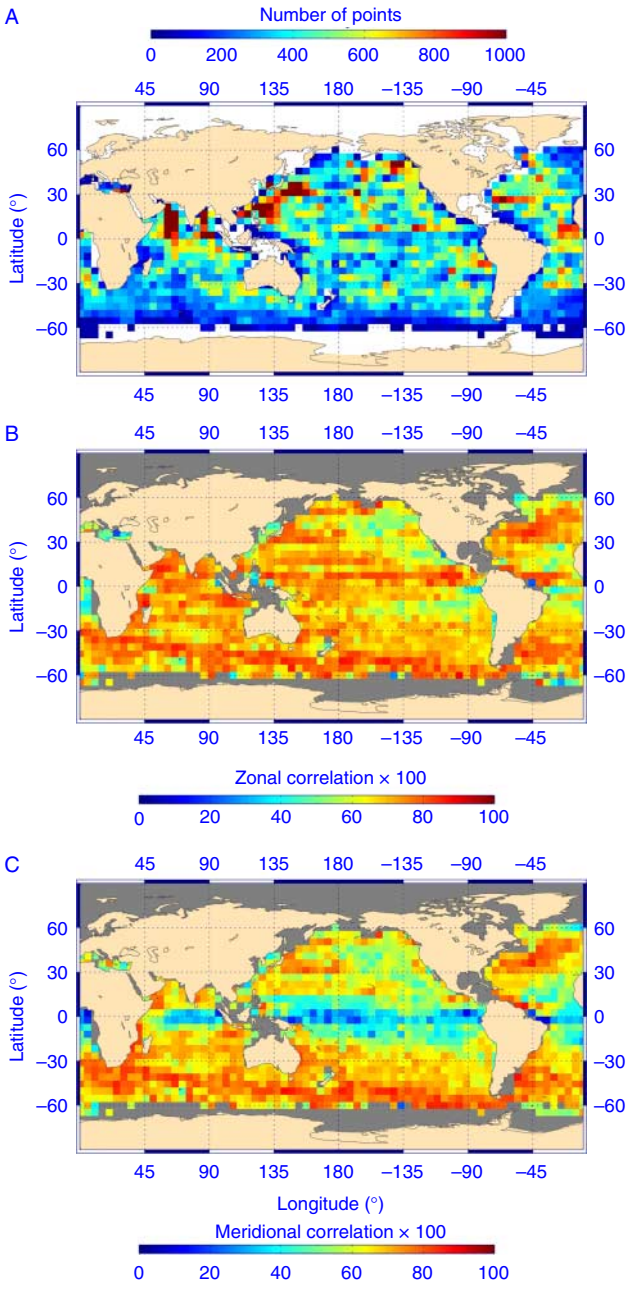

Fig. 6 A — Number of points by 5° × 5° bins used in the statistical comparison between the currents estimated by the Argo float displacement and GEKCO. B and C — Correlations for the zonal component (B) and the meridional component (C). Only correlations that were significant at the 95% level of confidence are plotted.

unprecedented spatiotemporal coverage at global scale over the last 20 years. The geostrophic component of the current is derived directly from the dynamic topography observed from space, whereas the wind-driven component is based on the conjoint use of wind stress and a physically based statistical model calibrated on 15-m drogued drifter data. The approach is essentially similar to the form proposed by Lagerloef et al. (1999) but differs in the present study by considering a time dependence of the (h_e, r_e) parameters (Eqs. 4a, 4b) implied in the Ekman motion instead of using constant values. Both approaches rely on accurate observations of current provided by the Global Drifter Program data developed since 1979 (Niiler and Paduan 1995; Lumpkin and Pazos 2007). Recently, Grodsky et al. (2011) reported a spurious temporal trend that has introduced errors in drifter currents. The origin of the problem was related to the contamination of the drogue-on data set by undrogued data, especially during the 2004–2008 period. The validation with independent data sets provides confidence about the reliability of the GEKCO estimates. As recommended by Grodsky et al. (2011), the use of drogue-on data could be achieved only by considering the first 90 days of data from each drifter. We choose to focus on the Indian Ocean because it represents a sector where data exhibit strong variations between the northern part that remains well sampled and the southern part where the total number of points for the comparison is much lower (Fig. 8A, B). The results are presented in terms of correlation between the currents (u, v) estimated by the drifters and GEKCO (Fig. 8C–F). In the North Indian Ocean, correlations were relatively unchanged or slightly better when using the 90-day drifter data; this result confirms the recommendations from Grodsky et al. (2011). In the South Indian Ocean, correlations were higher in most bins with the full data set, which suggests that the present determination has been only modestly affected by the bias in the full drifter data set. This latter point is reinforced by the averaged correlations over the entire Indian Ocean, which were not significantly different between the two data sets (0.79 vs. 0.77 and 0.77 vs. 0.75 between the full set and the 90-day set for the zonal and meridional component, respectively). This result suggests that the GEKCO estimates could be used in further studies to improve the drogue presence detection in the full drifter data set.

[21] The determination of GEKCO is based on the assumption that the near-surface velocity field can be decomposed into a geostrophic component and a wind-driven part. In the tropical Pacific, Ralph and

© 2013 by the Association for the Sciences of Limnology and Oceanography, Inc. / e-ISSN 2157-3689

Downloaded by guest on March 1, 2013

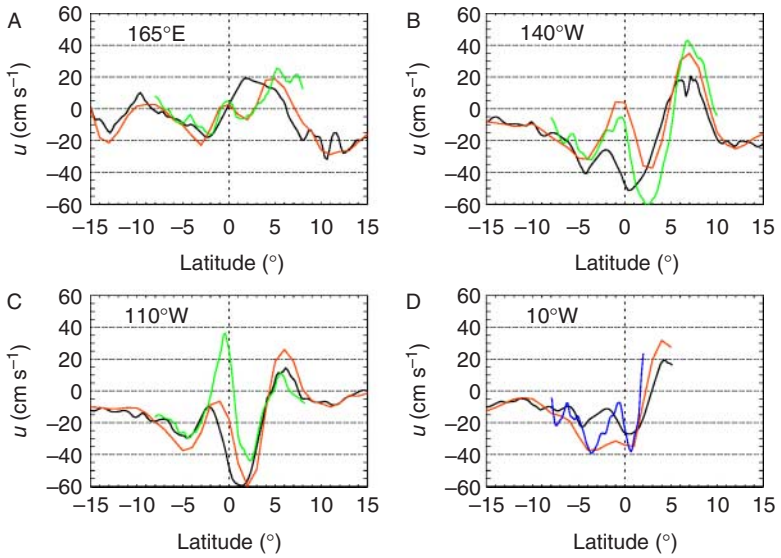

Fig. 7 Meridional sections of the mean zonal component (in cm s^{-1}) at 165°E, 140°W, 110°W, and 10°W for the drifter climatology (red) and the present estimates (in black). Additional estimates are given by Johnson et al. (2002) for the Pacific (green) and by Kolodziejczyk et al. (2009) for the Atlantic Ocean (blue).

Niiler (1999) reported that almost 80% of the variance of current measured by the drifter is accounted for by such a balance. Their results also support the observation that the strongest ageostrophic currents occurred in regions of the strongest winds. The strength of surface current also depends upon the turbulent processes that transport vertically the wind momentum, and several experiments confirm that the transport of water due to the winds is consistent with Ekman layer theories (Price et al. 1987; Chereskin and Roemmich 1991; Wijffels et al. 1994). Direct observations also show that the wind-driven transport is strongly surface trapped and that the long-term mean current exhibits a spiral-like structure. Consistent with such Ekman dynamics, we found that the deviation of the surface current at 15-m depth from the wind equals 52° ± 4° within the tropical Pacific Ocean. In comparison, Ralph and Niiler (1999) reported a deviation of 55° ± 5° by using a Ekman balance that specified the turbulent stress as a linear function of depth. The relative importance of each component in the present estimate of mean surface currents could be evaluated by considering a meridional section across the Atlantic Ocean (Fig. 9). Comparisons with drifter climatology (Lumpkin and Garraffo 2005) ensure that the present estimates along this section agree well with observational evidence. All across the basin, the total current results from a composition of geostrophic and wind-driven components with quite similar amplitudes, the dominance of the zonal wind-driven current being more important in the northern and southern subtropical regions where trade winds are established. For the meridional component, the balance is different and results in a more systematic compensation between the wind-driven and the geostrophic current. On each side of the equator, the wind-driven part exceeds the geostrophic component, resulting in a net deficit of water mass that is partially compensated by the vertical upwelling. Southward of 40°S, the positive meridional component could be associated with the northward Ekman flux in response to the strong and permanent westerly winds, whereas the eastward zonal current represents the signature of the ACC that encircles the Antarctic continent.

Biological Implications

[22] Compared with terrestrial environments, theoretical and predictive models of marine ecosystems that account for the complex food-web interactions also need to consider the fluid dynamics of oceanic environments. For example, the relationships among marine biota, biogeochemistry, and global climate are of utmost importance to determine the consequences of global change. In the ocean, the spatiotemporal distribution of phytoplankton and zooplankton populations results from changes in their environment generated by turbulent processes (Abraham 1998). Primary production is usually partitioned into the locally regenerated production and the new production resulting from mixing, stirring, and upwelling of nutrients into the euphotic zone (e.g., Dugdale and Goering 1967). The surface currents represent one key element to understand and describe these complex relationships. They are also needed for studies of top predators, the upper trophic level of the marine food web. Two examples illustrate such connectivities: horizontal surface stirring observed during iron

© 2013 by the Association for the Sciences of Limnology and Oceanography, Inc. / e-ISSN 2157-3689

Downloaded by guest on March 1, 2013

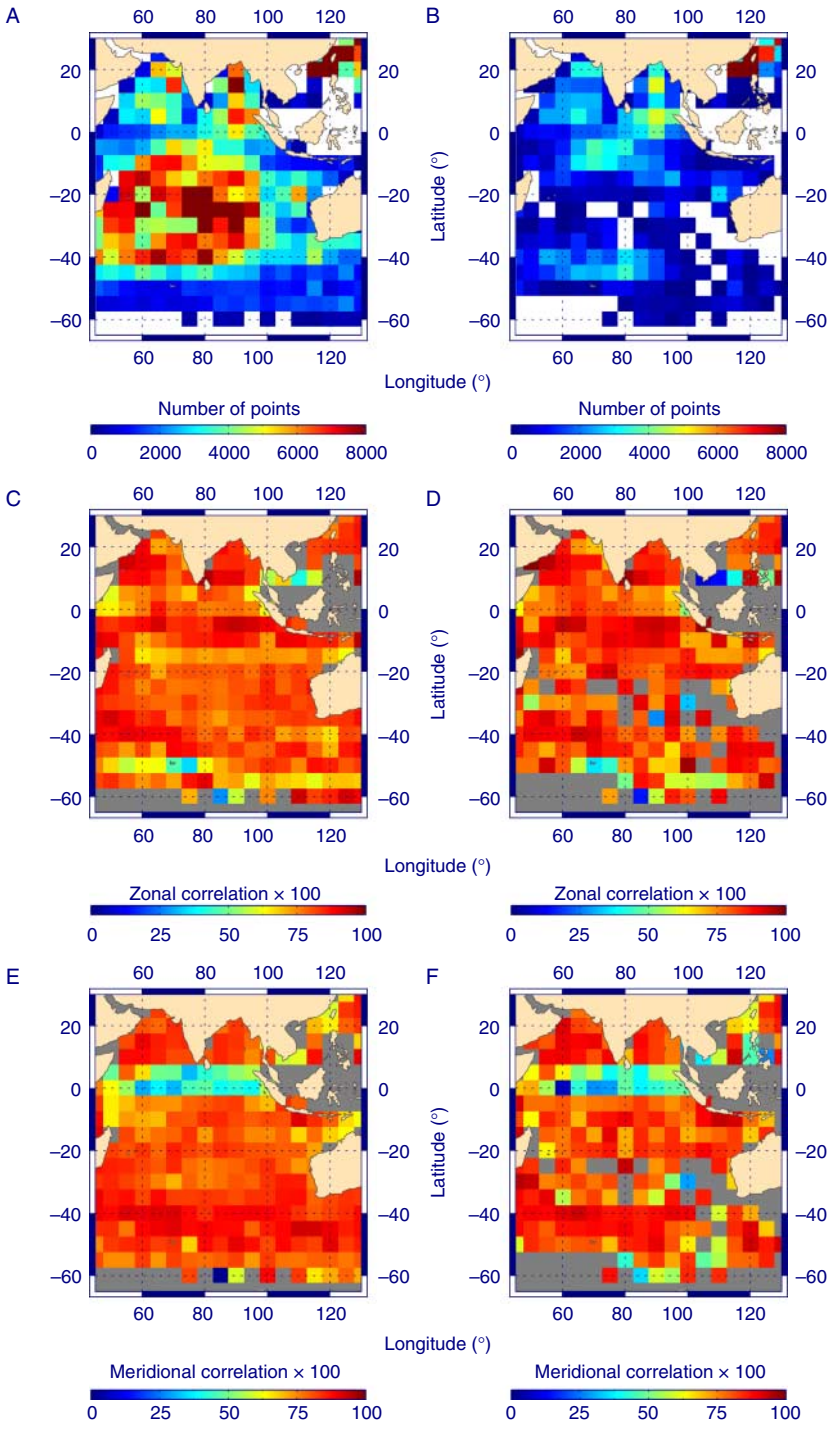

Fig. 8 Comparison between the total set of Lagrangian surface drifters (A, C, E) and the set of 90-day drifters data only (B, D, F) within the Indian Ocean representing number of points by 5° × 5° bins used in the statistical comparison between the currents estimated by the Argo float displacement and GEKCO (A and B), and correlations for the zonal component (C and D) and the meridional component (E and F). Only correlations that were significant at the 95% level of confidence are plotted.

fertilization experiments; and the deconvolution between the surface current and the observed displacements of animals.

[23] In the open ocean, remotely sensed ocean color images reveal the signature of phytoplankton blooms and provide evidence for their dispersal by horizontal stirring. In order to test John Martin's (1990) iron hypothesis, several mesoscale iron enrichment experiments have been conducted in different biogeochemical provinces (de Baar et al. 2005). During the Southern Ocean Iron Release Experiment (SOIREE), Abraham et al. (2000) and Boyd and Law (2001) argued that the ribbonlike bloom was produced from the enriched patch six weeks after the iron fertilization took place. They also proposed that stirring was the major process to control bloom development and phytoplankton mixing. Based on the estimate of surface currents, Lagrangian coherent structures (LCSs) can be determined to help the interpretation of the SOIREE observations. This can be done by estimating a direct measure of the local stirring through the computation of the finite-size Lyapunov exponent (FSLE). The FSLE represents the inverse time for which a couple of particles reach a prescribed spatial separation. When the time sequence is forward (backward), the computation of FSLE depicts LCSs associated with the convergence (divergence) of the flow. Typically, the initial distance is set to 0.025°, and the prescribed separation distance is set to 1°, in order to focus on mesoscale structures (d'Ovidio et al. 2004; Rossi et al. 2008).

[24] Currents and backward FSLE maps placed in the same time sequence

© 2013 by the Association for the Sciences of Limnology and Oceanography, Inc. / e-ISSN 2157-3689

Downloaded by guest on March 1, 2013

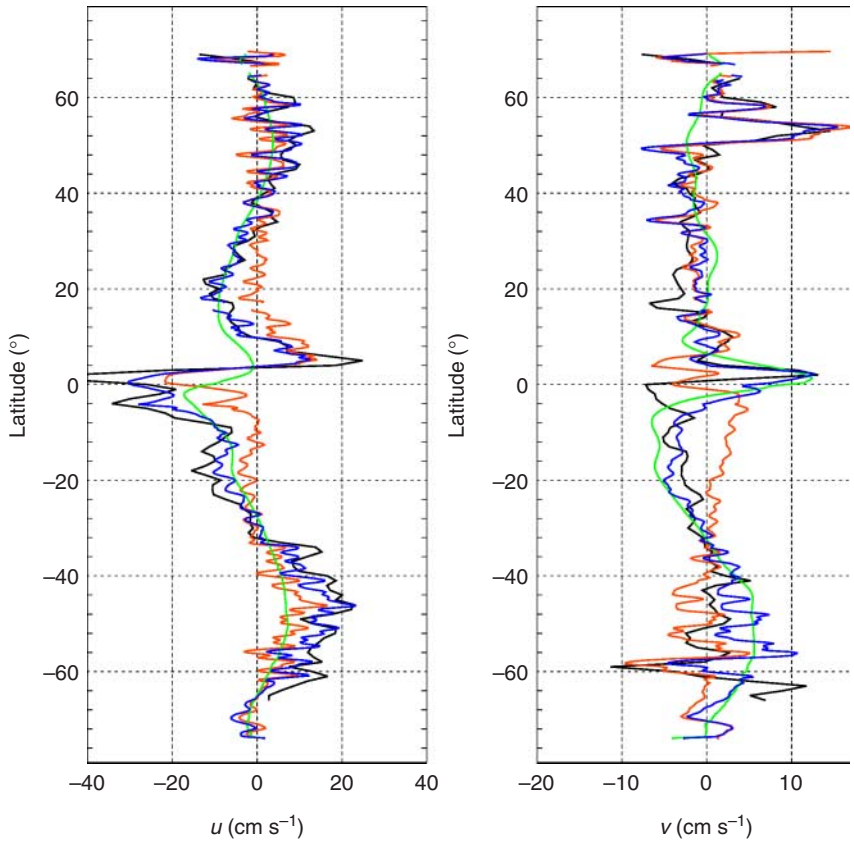

Fig. 9 Meridional section between 80°S and 80°N across the Atlantic Ocean along 23°W for the zonal (A) and meridional (B) components issued from the surface drifter climatology (black) given by Lumpkin and Garraffo (2005) and the total present current (blue), the latter resulting from the combination of the geostrophic (red) and wind-driven (green) components of GEKCO.

of the SOIREE images as shown by Abraham et al. (2000) are displayed in Fig. 10. The enlarged area centered around the SOIREE zone is characterized by a general eastward flow created by different currents of $\sim 30\,\mathrm{cm\,s^{-1}}$ and by a permanent presence of LCSs with high values of $\sim 0.2\,\mathrm{d^{-1}}$ corresponding to a 5-d time scale. Within the SOIREE area and near the released point of iron enrichment, backward FSLEs evolve from weak values ($< 0.01\,\mathrm{d^{-1}}$), corresponding to the absence of LCSs on 23 March 1999 (Fig. 10F). The FSLE diagnostics provide complementary elements to highlight the dynamic scenario of the SOIREE experiment. At the iron release, owing to the presence of a relatively deep mixed layer (Boyd and Law 2001) and the absence of LCSs in flow structure, the iron concentration remained high enough to allow the future development of the phytoplankton bloom. Then, associated with the ongoing appearance of the bloom, the flow was stirred by northward-propagating LCSs due to the intensification of the surface currents (Fig. 10F). Finally, we confirmed that the ribbonlike bloom as observed by chlorophyll satellite images (Abraham et al. 2000) represented the chlorophyll signature associated with the stirring of the LCSs. Fig. 10H shows that this LCS is deformed and advected northeastward by the mean flow close to the border of the SOIREE domain. Because the evolution of LCSs in a turbulent flow is by essence unpredictable, fertilization experiments should be considered with caution because adverse consequences remain possible (Neufeld et al. 2002).

[25] The use of satellites for precise localization (telemetry) combined with surface currents can be used to qualify the mechanical action of currents on the displacement of marine animals (Luschi et al. 2001; Girard et al. 2006). This approach aims to distinguish the tracking path (what the animal did) from the motor path (what the animal intended to do) to test homing ability (Luschi et al. 2007), to analyze in detail, for instance, a turtle's navigational performance (Benhamou et al. 2011) and to understand spatiotemporal foraging (Fossette et al. 2010). The interpretation of the behaviors and movements of individual animals requires that the trajectories of each displacement be examined from a Lagrangian perspective. Determining errors is rather difficult because of the heterogeneous and nonstationary regime of the flow. Nevertheless, in any particular region of the ocean, an estimate of such errors can be determined by considering the trajectory of an independent Lagrangian drifter. The displacement of any drifter in the ocean is due only to the motion. If we manage to compute a "current-corrected" track by using both the geostrophic and Ekman components, the only error on the drifter dis-

© 2013 by the Association for the Sciences of Limnology and Oceanography, Inc. / e-ISSN 2157-3689

Downloaded by guest on March 1, 2013

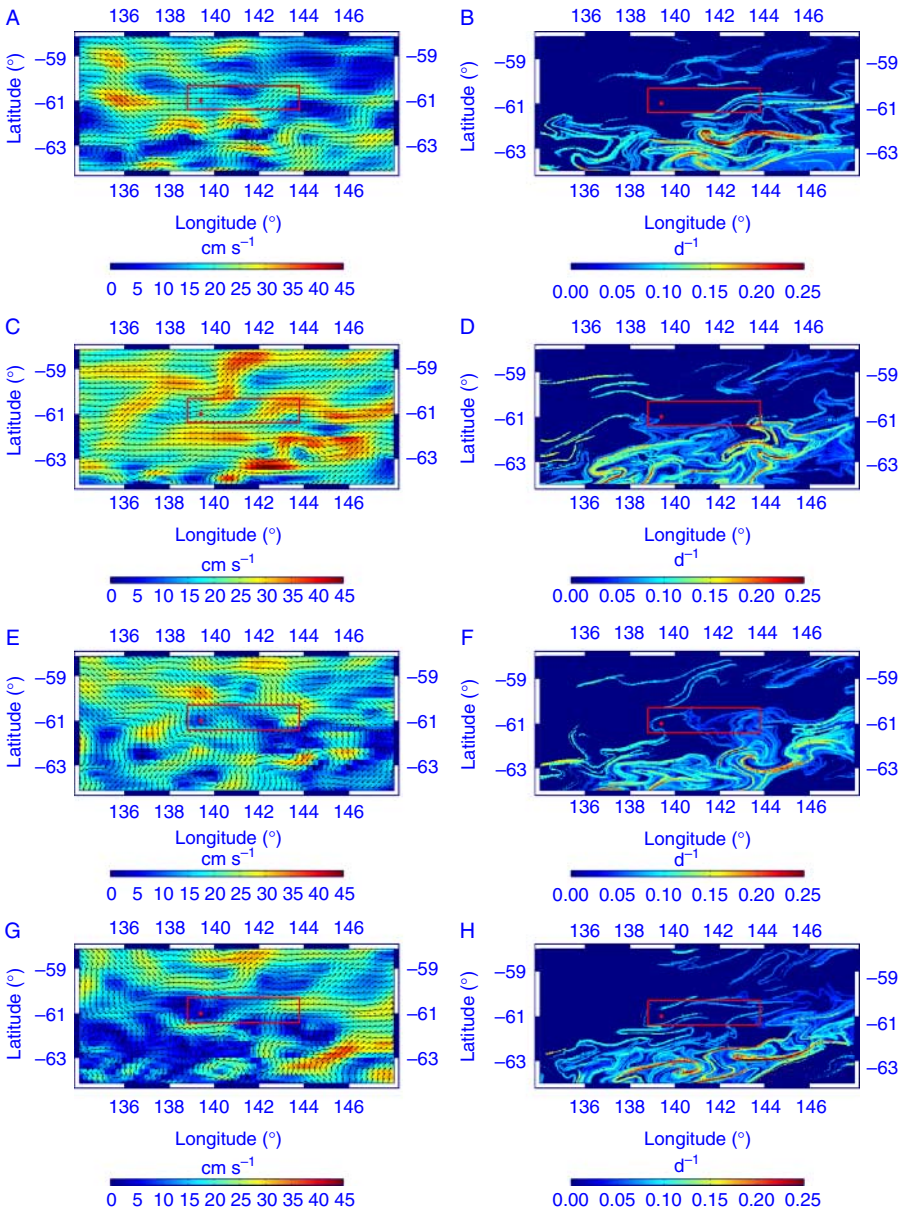

Fig. 10 Images of GEKCO (left) and FSLE (right) fields during the SOIREE experiment for 14 February 1999 (A and B), 10 March 1999 (C and D), 23 March 1999 (E and F), and 6 April 1999 (G and H). The red square indicates the area as shown in Abraham et al. (2000), where the red dot indicates the start of the SOIREE experiment on 9 February 1999.

placement will be due to errors in the currents. When dealing with marine animals, these errors will superimpose on the animals' motions.

[26] As an example, we estimated this correction for a drifter deployed in the northern part of the Mozambique Channel. Fig. 11 displays the original drifter trajectory (black curve), on which we superimposed the current-corrected tracks by using only geostrophy (blue curve) and geostrophy plus the Ekman component (red curve). We interpreted the differences between both current-corrected trajectories as a combination of errors resulting from the GEKCO estimate and of errors from physical small-scale processes that are inherently recorded in the trajectory of any individual drifter. Moreover, consideration of the wind-driven component reveals the importance of the wind influence on long-term displacements. If our GEKCO estimates were perfect representations of the oceanic total currents, the red curve should not move from the initial release point. This methodology also has biological implications. Typically, when applied to green turtle displacement, this correction provided information on ground-related movement compared with water-mass–related movement (Girard et al. 2006; Benhamou et al. 2011). In such cases, better current estimates will provide an improved assessment of the mechanical impact of ocean currents on turtle behavior. For studies integrating spatial analysis of the movement of marine animals, we recommend the systematic deployment of additional drifters when the animals are tagged and then released. Such types of studies are crucial for the long-term monitoring of migratory populations and for the management of efforts needed for future restoration (Myers and Worm 2003).

© 2013 by the Association for the Sciences of Limnology and Oceanography, Inc. / e-ISSN 2157-3689

Downloaded by guest on March 1, 2013

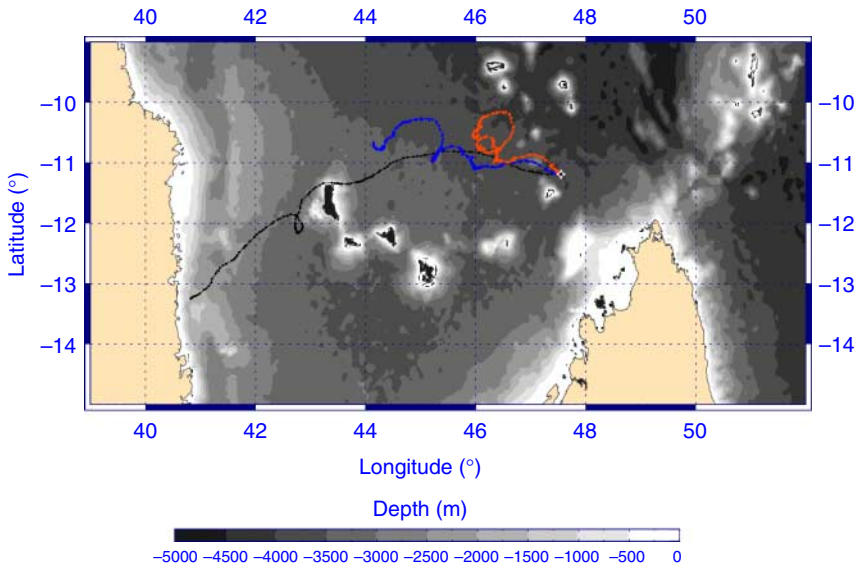

Fig. 11 Trajectory of a Lagrangian surface drifter at the entrance of the Mozambique Channel between 1 and 13 April 2008 (black line; dots mark the 293 hourly positions). The blue line shows the "corrected trajectory" by the geostrophic component, and the red line shows the corrections by the geostrophic and wind-driven currents. The white star marks the released point of the drifter. The background field represents the bottom topography.

Significance to Aquatic Environments

[27] A fundamental goal of physical oceanography is to provide a first-order description of the global ocean circulation. Such information can be used to model ocean currents and thus understand the displacement of matter, ranging from marine algae to turtles, and from plastic debris to oil spills. This study used the GEKCO model, which includes both geostrophic and Ekman current components of oceanic currents from remote-sensing altimeter and scatterometer data sets, to provide a global survey of the major ocean currents rather than a detailed description of the different regional surface circulations. The GEKCO estimates facilitated the evaluation of ocean surface velocity at a spatial resolution of 0.25° (~28 km) from 82°N to 82°S, retrospectively to October 1992. The estimates were validated against different data sets, and examples of applications to a diverse set of scientific problems were provided in which an improved understanding of ocean currents was required. GEKCO was able to model the relationships between ocean currents and phytoplankton blooms during the SOIREE iron fertilization experiment, which in this case were related to mass transport via Lagrangian coherent structures. GEKCO also enabled the separation of ground-related movements from water-mass–related movements of the displacement of marine turtles. In such cases, caution must be used in the interpretation of the difference of these two movements because of cumulative effects of different error sources.

Acknowledgments We are sincerely grateful to the different data providers, mainly including the CERSAT and the CNES/AVISO teams, the Global Drifter Program, the TAO/TRITON, PIRATA, and RAMA arrays, the Joint Archive for Shipboard ADCP, and the ARGO surface current estimates by J. Xie and J. Zhu. Improvements and comments provided by the two anonymous reviewers as well as editors Dr. André Visser and Dr. Joe Ackerman are greatly appreciated. Special thanks go to Mayra Pazos and staff at AOML for their work on drifters, to Dr. Cristóbal López and Dr. Emilio Hernández-García for providing their code for the FSLE computation, and to Dr. Simon Benhamou and Dr. Phil Wallhead for their careful critical reading.

References

Abraham, E. R. 1998. The generation of plankton patchiness by turbulent stirring. Nature **391**: 577–580, doi:10.1038/35361.

Abraham, E. R., C. S. Law, P. W. Boyd, S. J. Lavender, M. T. Maldonado, and A. R. Bowie. 2000. Importance of stirring in the development of an iron-fertilized phytoplankton bloom. Nature **407**: 727–730, doi:10.1038/35037555.

Benhamou, S., J. Sudre, J. Bourjea, S. Ciccione, A. De Santis, and P. Luschi. 2011. The role of geomagnetic cues in green turtle open sea navigation. PLoS ONE **6**: e26672, doi:10.1371/journal.pone.0026672.

Boyd, P. W., and C. S. Law. 2001. The Southern Ocean Iron Release Experiment (SOIREE)—introduction and summary. Deep Sea Res. Part II Top. Stud. Oceanogr. **48**: 2425–2438, doi:10.1016/S0967-0645(01)00002-9.

Chelton, D. B., M. G. Schlax, and R. M. Samelson. 2011. Global observations of nonlinear mesoscale eddies. Prog. Oceanogr. **91**: 167–216, doi:10.1016/j.pocean.2011.01.002.

Chereskin, T. K., and D. Roemmich. 1991. A comparison of measured and wind-derived Ekman transport at 11°N in the Atlantic

© 2013 by the Association for the Sciences of Limnology and Oceanography, Inc. / e-ISSN 2157-3689

Downloaded by guest on March 1, 2013

Ocean. J. Phys. Oceanogr. **21**: 869–878, doi:10.1175/1520-0485(1991)021<0869:ACOMAW>2.0.CO;2.

de Baar, H. J. W., et al. 2005. Synthesis of iron fertilization experiments: From the Iron Age in the Age of Enlightenment. J. Geophys. Res. **110** (C9): C09S16, doi:10.1029/2004JC002601.

Dohan, K., and N. Maximenko. 2010. Monitoring ocean currents with satellite sensors. Oceanography **23**: 94–103, doi:10.5670/oceanog.2010.08.

d'Ovidio, F., V. Fernández, E. Hernández-García, and C. López. 2004. Mixing structures in the Mediterranean Sea from finite-size Lyapunov exponents. Geophys. Res. Lett. **31**: L17203, doi:10.1029/2004GL020328.

Dugdale, R. C., and J. J. Goering. 1967. Uptake of new and regenerated forms of nitrogen in primary productivity. Limnol. Oceanogr. **12**: 196–206, doi:10.4319/lo.1967.12.2.0196.

Fossette, S., V. J. Hobson, C. Girard, B. Calmettes, P. Gaspar, J.-Y. Georges, and G. C. Hays. 2010. Spatio-temporal foraging patterns of a giant zooplanktivore, the leatherback turtle. J. Mar. Syst. **81**: 225–234, doi:10.1016/j.jmarsys.2009.12.002.

Garçon, V. C., A. Oschlies, S. C. Doney, D. McGillicuddy, and J. Waniek. 2001. The role of mesoscale variability on plankton dynamics in the North Atlantic. Deep Sea Res. Part II Top. Stud. Oceanogr. **48**: 2199–2226, doi:10.1016/S0967-0645(00)00183-1.

Girard, C., J. Sudre, S. Benhamou, D. Roos, and P. Luschi. 2006. Homing in green turtles *Chelonia mydas*: Oceanic currents act as a constraint rather than as an information source. Mar. Ecol. Prog. Ser. **322**: 281–289, doi:10.3354/meps322281.

Grodsky, S. A., R. Lumpkin, and J. A. Carton. 2011. Spurious trends in global surface drifter currents. Geophys. Res. Lett. **38**: L10606, doi:10.1029/2011GL047393.

Hummon, J. M., and E. Firing. 2003. A direct comparison of two RDI shipboard ADCPs: A 75-kHz ocean surveyor and a 150-kHz narrow band. J. Atmos. Ocean. Technol. **20**: 872–888, doi:10.1175/1520-0426(2003)020<0872:ADCOTR>2.0.CO;2.

Johnson, E. S., F. Bonjean, G. S. E. Lagerloef, J. T. Gunn, and G. T. Mitchum. 2007. Validation and error analysis of OSCAR sea surface currents. J. Atmos. Oceanic Technol. **24**: 688–701, doi:10.1175/JTECH1971.1.

Johnson, G. C. 2001. The Pacific Ocean subtropical cell surface limb. Geophys. Res. Lett. **28**: 1771–1774, doi:10.1029/2000GL012723.

Johnson, G. C., B. M. Sloyan, W. S. Kessler, and K. E. McTaggart. 2002. Direct measurements of upper ocean currents and water properties across the tropical Pacific during the 1990s. Prog. Oceanogr. **52**: 31–61, doi:10.1016/S0079-6611(02)00021-6.

Kolodziejczyk, N., B. Bourlès, F. Marin, J. Grelet, and R. Chuchla. 2009. Seasonal variability of the Equatorial Undercurrent at 10°W as inferred from recent in situ observations. J. Geophys. Res. **114** (C6): C06014, doi:10.1029/2008JC004976.

Lagerloef, G. S. E., R. Lukas, F. Bonjean, J. T. Gunn, G. T. Mitchum, M. Bourassa, and A. J. Busalacchi. 2003. El Niño tropical Pacific Ocean surface current and temperature evolution in 2002 and outlook for early 2003. Geophys. Res. Lett. **30**: 1514–1518, doi:10.1029/2003GL017096.

Lagerloef, G. S. E., G. T. Mitchum, R. B. Lukas, and P. P. Niiler. 1999. Tropical Pacific near-surface currents estimated from altimeter, wind, and drifter data. J. Geophys. Res. **104** (C10): 23313–23326, doi:10.1029/1999JC900197.

Llido, J., V. Garçon, J. R. E. Lutjeharms, and J. Sudre. 2005. Event-scale blooms drive enhanced primary productivity at the Subtropical Convergence. Geophys. Res. Lett. **32**: L15611, doi:10.1029/2005GL022880.

Lumpkin, R., and Z. Garraffo. 2005. Evaluating the decomposition of tropical Atlantic drifter observations. J. Atmos. Ocean. Technol. **22**: 1403–1415, doi:10.1175/JTECH1793.1.

Lumpkin, R., and M. Pazos. 2007. Measuring surface currents with Surface Velocity Program drifters: The instrument, its data and some recent results. Pp. 39–67. *In* A. Griffa, A. D. Kirwan, A. J. Mariano, T. Ozgokmen, and T. Rossby [eds.], Lagrangian Analysis and Prediction of Coastal and Ocean Dynamics (LAPCOD). Cambridge University Press, doi:10.1017/CBO9780511535901.003.

Luschi, P., S. Akesson, A. Broderick, F. Glen, B. Godley, F. Papi, and G. Hays. 2001. Testing the navigational abilities of ocean migrants: Displacement experiments on green sea turtles (*Chelonia mydas*). Behav. Ecol. Sociobiol. **50**: 528–534, doi:10.1007/s002650100396.

Luschi, P., S. Benhamou, C. Girard, S. Ciccione, D. Roos, J. Sudre, and S. Benvenuti. 2007. Marine turtles use geomagnetic cues during open-sea homing. Curr. Biol. **17**: 126–133, doi:10.1016/j.cub.2006.11.062.

Maes, C., K. Ando, T. Delcroix, W. S. Kessler, M. J. McPhaden, and D. Roemmich. 2006. Observed correlation of surface salinity, temperature and barrier layer at the eastern edge of the western Pacific warm pool. Geophys. Res. Lett. **33**: L06601, doi:10.1029/2005GL024772.

Maes, C., J. Sudre, and V. Garçon. 2010. Detection of the eastern edge of the equatorial Pacific warm pool using satellite-based ocean color observations. Sci. Online Lett. Atmos. **6**: 129–132, doi:10.2151/sola.2010-033.

Martin, J. H. 1990. Glacial-interglacial CO_2 change: The iron hypothesis. Paleoceanography. **5**: 1–13, doi:10.1029/PA005i001p00001.

Moore, D. W. H., and S. G. Philander. 1978. Modeling of the tropical oceanic circulation. Pp. 319–361. *In* E. D. Goldberg [ed.], The Sea. Wiley-Interscience.

Myers, R. A., and B. Worm. 2003. Rapid worldwide depletion of predatory fish communities. Nature **423**: 280–283, doi:10.1038/nature01610.

Neufeld, Z., P. H. Haynes, V. Garçon, and J. Sudre. 2002. Ocean fertilization experiments may initiate a large scale phytoplank-

© 2013 by the Association for the Sciences of Limnology and Oceanography, Inc. / e-ISSN 2157-3689

ASLO Association for the Sciences of Limnology and Oceanography DUKE UNIVERSITY PRESS

Downloaded by guest on March 1, 2013

ton bloom. Geophys. Res. Lett. **29**: 1534–1538, doi:10.1029/2001GL013677.

Niiler, P. P., N. A. Maximenko, and J. C. McWilliams. 2003. Dynamically balanced absolute sea level of the global ocean derived from near-surface velocity observations. Geophys. Res. Lett. **30**: 2164–2168, doi:10.1029/2003GL018628.

Niiler, P. P., and J. D. Paduan. 1995. Wind-driven motions in the Northeast Pacific as measured by Lagrangian drifters. J. Phys. Oceanogr. **25**: 2819–2830, doi:10.1175/1520-0485(1995)025<2819:WDMITN>2.0.CO;2.

Picaut, J., M. Ioualalen, C. Menkes, T. Delcroix, and M. J. McPhaden. 1996. Mechanism of the zonal displacements of the Pacific warm pool: Implications for ENSO. Science **274**: 1486–1489, doi:10.1126/science.274.5292.1486.

Picaut, J., and R. Tournier. 1991. Monitoring the 1979–1985 equatorial Pacific current transports with expendable bathythermograph data. J. Geophys. Res. **96** (Suppl.): 3263–3277.

Price, J. F., R. A. Weller, and R. R. Schudlich. 1987. Wind-driven ocean currents and Ekman transport. Science **238**: 1534–1538, doi:10.1126/science.238.4833.1534.

Ralph, E. A., and P. P. Niiler. 1999. Wind-driven currents in the tropical Pacific. J. Phys. Oceanogr. **29**: 2121–2129, doi:10.1175/1520-0485(1999)029<2121:WDCITT>2.0.CO;2.

Richardson, P. L. 1989. Worldwide ship drift distributions identify missing data. J. Geophys. Res. **94** (C5): 6169–6176, doi:10.1029/JC094iC05p06169.

Robel, A. A., M. S. Lozier, S. F. Gary, G. L. Shillinger, H. Bailey, and S. J. Bograd. 2011. Projecting uncertainty onto marine megafauna trajectories. Deep Sea Res. Part I Oceanogr. Res. Pap. **58**: 915–921, doi:10.1016/j.dsr.2011.06.009.

Rossi, V., C. López, J. Sudre, E. Hernández-García, and V. Garçon. 2008. Comparative study of mixing and biological activity of the Benguela and Canary upwelling systems. Geophys. Res. Lett. **35**: L11602, doi:10.1029/2008GL033610.

Sudre, J., and R. Morrow. 2008. Global surface currents: A high-resolution product for investigating ocean dynamics. Ocean Dyn. **58**: 101–118, doi:10.1007/s10236-008-0134-9.

Tew Kai, E., V. Rossi, J. Sudre, H. Weimerskirch, C. Lopez, E. Hernandez-Garcia, F. Marsac, and V. Garçon. 2009. Top marine predators track Lagrangian coherent structures. Proc. Natl. Acad. Sci. USA. **106**: 8245–8250, doi:10.1073/pnas.0811034106.

van Meurs, P., and P. P. Niiler. 1997. Temporal variability of the large-scale geostrophic surface velocity in the northeast Pacific. J. Phys. Oceanogr. **27**: 2288–2297, doi:10.1175/1520-0485(1997)027<2288:TVOTLS>2.0.CO;2.

Wijffels, S., E. Firing, and H. Bryden. 1994. Direct observations of the Ekman balance at 10°N in the Pacific. J. Phys. Oceanogr. **24**: 1666–1679, doi:10.1175/1520-0485(1994)024<1666:DOOTEB>2.0.CO;2.

Xie, J., and J. Zhu. 2008. Estimation of the surface and mid-depth currents from Argo floats in the Pacific and error analysis. J. Mar. Syst. **73**: 61–75, doi:10.1016/j.jmarsys.2007.09.001.

Xie, J., and J. Zhu. 2009. A dataset of global ocean surface currents for 1999–2007 derived from Argo float trajectories: Comparison with surface drifter and TAO measurements. Atmos. Oceanol. Sci. Lett. **2**: 97–102.

Received: 24 February 2012
Amended: 28 June 2012
Accepted: 20 October 2012

© 2013 by the Association for the Sciences of Limnology and Oceanography, Inc. / e-ISSN 2157-3689

ASLO Association for the Sciences of Limnology and Oceanography

DUKE UNIVERSITY PRESS

Downloaded by guest on March 1, 2013

2.5 Compléments sur la composante d'Ekman

A la suite de la lecture de l'article [*Sudre et al.*, 2013] quelques personnes nous ont sollicité pour avoir de plus amples informations sur la méthode d'obtention ainsi que sur les valeurs déduites de la profondeur de la couche d'Ekman (h_E) et du coefficient de traînée (r_E) dans différentes zones de l'océan. Il nous semble donc utile ici de proposer aux lecteurs de cette thèse un complément sur ce sujet.

En considérant uniquement la force de Coriolis et la force de friction due aux vents, l'équation de la quantité de mouvement à l'équilibre peut s'écrire de la façon suivante :

$$(ifh_E + r_E)\mathbf{U}_E = \frac{\tau}{\rho} \tag{2.8}$$

avec :

- $i = \sqrt{-1}$,
- ρ : densité standard de l'eau de mer ($\rho = 1025kg \cdot m^{-3}$),
- $\tau(\tau_x, \tau_y)$: tension du vent,
- $\mathbf{U}_E(u_E, v_E)$: courant d'Ekman (ou de dérive par l'effet des vents),
- h_E : profondeur de la couche d'Ekman,
- r_E : coefficient de traînée qui représente le terme de la composante verticale de la viscosité turbulente dans l'expression de la force de frottement.

Il est donc nécessaire si l'on veut connaître les composantes du courant d'Ekman d'avoir au préalable une estimation des paramètres h_E et r_E. Pour ce faire, il est possible d'exprimer ces deux paramètres de la façon suivante :

$$\begin{cases} h_E &= \frac{1}{f}\frac{\tau_y u_E - \tau_x v_E}{\rho(u_E^2 + v_E^2)} \\ r_E &= \frac{\tau_x u_E + \tau_y v_E}{\rho(u_E^2 + v_E^2)} \end{cases} \tag{2.9}$$

avec :

- f : paramètre de Coriolis,
- ρ : densité standard de l'eau de mer ($\rho = 1025kg \cdot m^{-3}$),
- $\tau(\tau_x, \tau_y)$: tension du vent,
- $U_E(u_E, v_E)$: courant d'Ekman (ou de dérive par l'effet des vents).

Afin d'avoir une estimation des composantes de la vitesse des courants d'Ekman $\mathbf{U}_E$, on peut faire l'approximation suivante en utilisant les vitesses de

courant obtenues par les bouées dérivantes de surface d'une part et la vitesse des courants géostrophiques d'autre part :

$$\mathbf{U}_E = \mathbf{U}_b - \mathbf{U}_g \tag{2.10}$$

Autrement dit, dans le cas présent, la vitesse des courants d'Ekman est considérée comme le résidu entre la vitesse de la bouée dérivante et la vitesse des courants géostrophiques, en chaque point où la vitesse d'une bouée dérivante est connue. Il est à noter qu'il est nécessaire de filtrer au préalable les courants inertiels des vitesses des bouées de surface (par un filtrage du déplacement de la bouée). Si on introduit cette approximation dans l'équation 2.9, on peut ainsi obtenir les paramètres h_E et r_E pour chaque position spatio-temporelle des bouées dérivantes de surface. Afin de présenter ces deux paramètres, la figure 2.1 synthétise les valeurs moyennes obtenues pour toute la période considérée (18 Juillet 1999 - 31 Mars 2009) ainsi que le nombre de points de bouées dérivantes de surface considérées et la norme de la tension de vent moyenne.

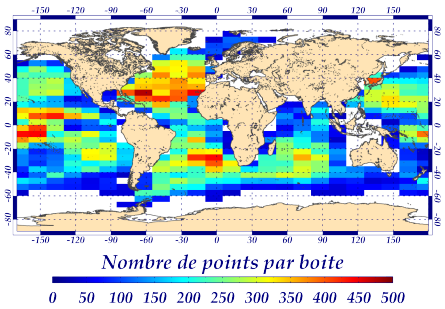

(a) Nombre de points de bouées dérivantes de surface considérés pour estimer les paramètres h_E et r_E.

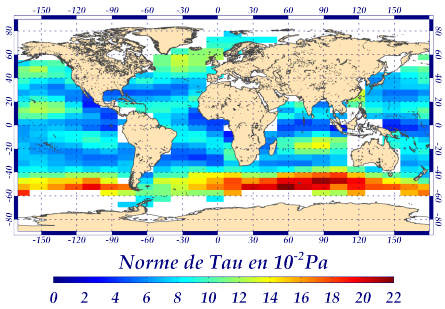

(b) Norme de la moyenne des tensions de vents sous les positions des bouées dérivantes.

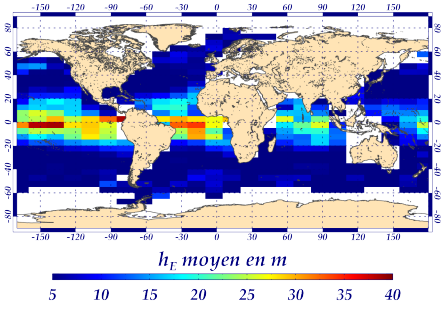

(c) h_E moyenne obtenue.

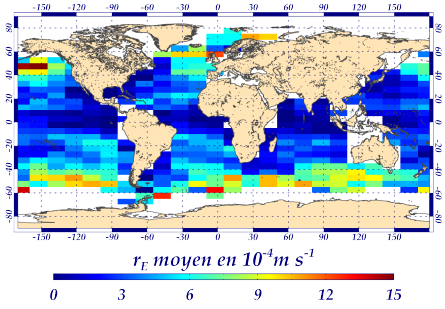

(d) r_E moyen obtenu.

FIGURE 2.1 – Obtention des paramètres h_E et r_E.

Afin d'obtenir des paramètres h_E et r_E variables au cours du temps et de l'espace en fonction de la tension du vent, il est nécessaire de définir une relation linéaire entre ces paramètres et la tension du vent obtenue à un instant donné (tension du vent qui est, dans notre cas, estimée indirectement via les données diffusiométriques). Etant donné que nous avons la connaissance de h_E et r_E en chaque point de bouée dérivante de surface et que nous avons aussi la connaissance de $\mathbf{U}_E$ par l'approximation de l'équation 2.10, une régression linéaire entre h_E, r_E et la tension du vent (τ) est calculée pour chacun de ces points. Cette relation va ainsi permettre d'estimer directement, sans avoir recours à la vitesse des courants d'Ekman, les paramètres h_E et r_E en fonction de τ. Ce faisant, ces deux paramètres seront recalculés systématiquement pour chaque point de l'espace et du temps par cette relation pour obtenir *in fine*, la vitesse des courants d'Ekman avec une profondeur de couche d'Ekman et un coefficient de traînée variables spatio-temporellement.

Afin de prouver la légitimité de cette démarche, les graphes des figures 2.3, 2.4, 2.5 et 2.6 présentent certaines régressions obtenues sur des zones de $5°$ de latitude par $15°$ de longitude. La taille des zones a été obtenue en considérant le nombre de points de bouées dérivantes disponibles sur la période de calcul (18 Juillet 1999 - 31 Mars 2009) ainsi que les zones de régime océanique éolien (voir figure 2.2).

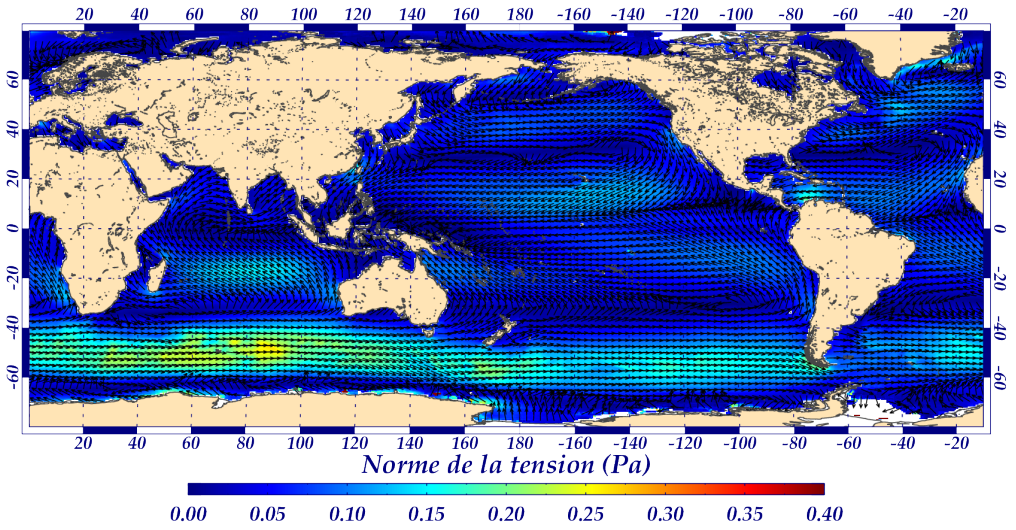

FIGURE 2.2 – *Moyenne de la tension de vent provenant du produit QuikSCAT du CERSAT calculée pour la période du 01 Janvier 2000 au 31 Décembre 2008.*

A l'analyse des différents graphes des figures citées ci-dessus, on peut remarquer que la régression linéaire se justifie parfaitement pour le paramètre r_E dans toutes les zones. Cependant pour le paramètre h_E, la zone comprise entre $10°$N et $10°$S est plus sujette à caution au vu de la dispersion des points. Cette dispersion provient essentiellement des valeurs des composantes de $\mathbf{U}_g$ qui est parfois mal estimée dans la zone équatoriale, mais aussi du fait que la composante méridienne de la tension de vent est faible dans la Zone de Convergence InterTropicale (ITCZ).

Au vu du nombre peu élevé de points de bouées dérivantes de surface pour estimer les valeurs des régressions linéaires de h_E et r_E dans certaines régions (voir figure 2.1(a)), l'obtention des valeurs (pente et constante) des régressions linéaires a été recalculée en fonction de la latitude et par bassin océanique. Une attention particulière a été effectuée pour éviter les discontinuités entre les bassins ainsi qu'une interpolation au quart de degré pour être homogène avec les données d'entrées (voir figure 2.7).

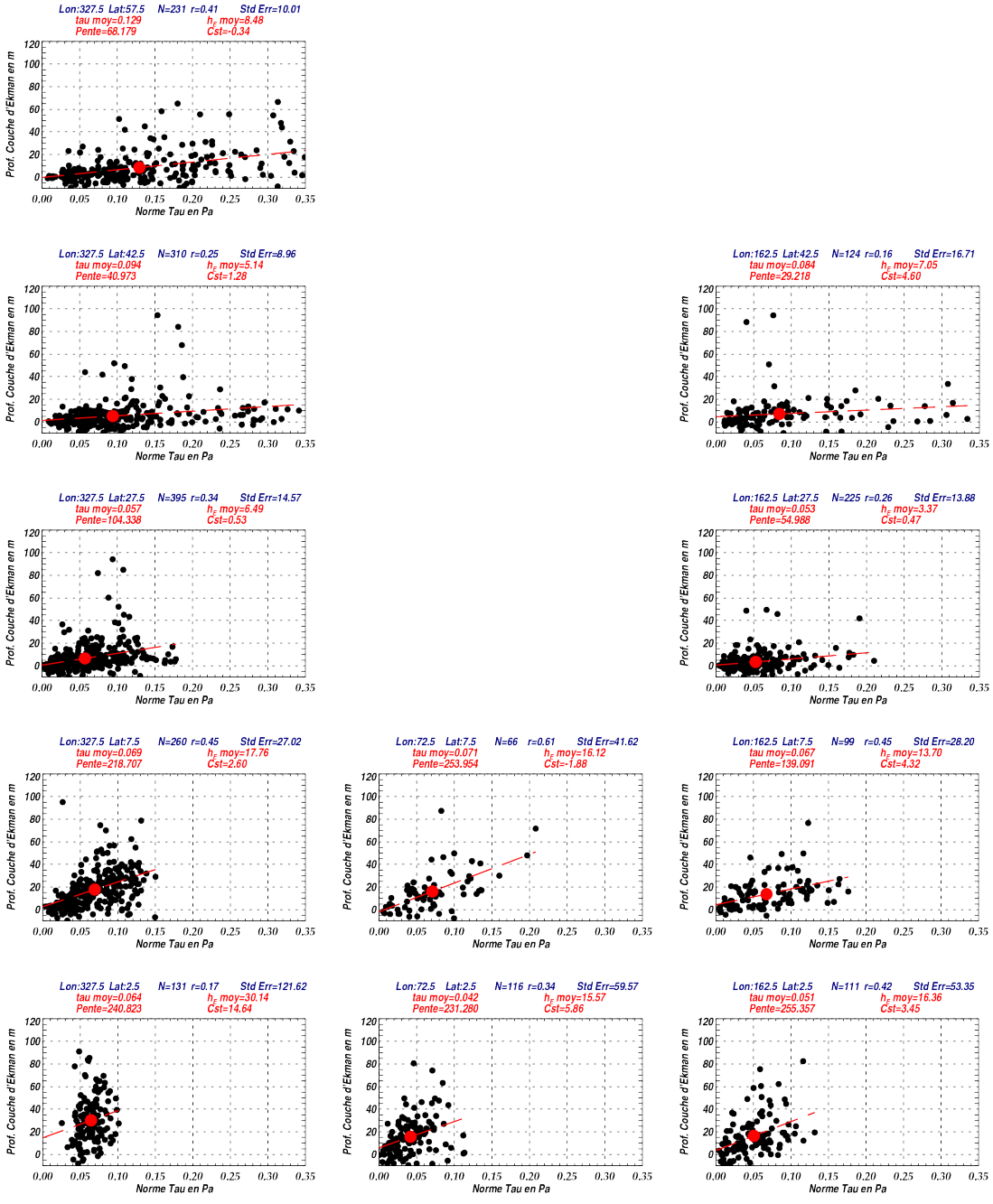

(a) Bassin Atlantique (b) Bassin Indien (c) Bassin Pacifique

FIGURE 2.3 – Régression linéaire du paramètre h_E dans l'hémisphère Nord. La droite représente la régression linéaire du nuage de points (noirs) et le point rouge représente la valeur moyenne de ce nuage.

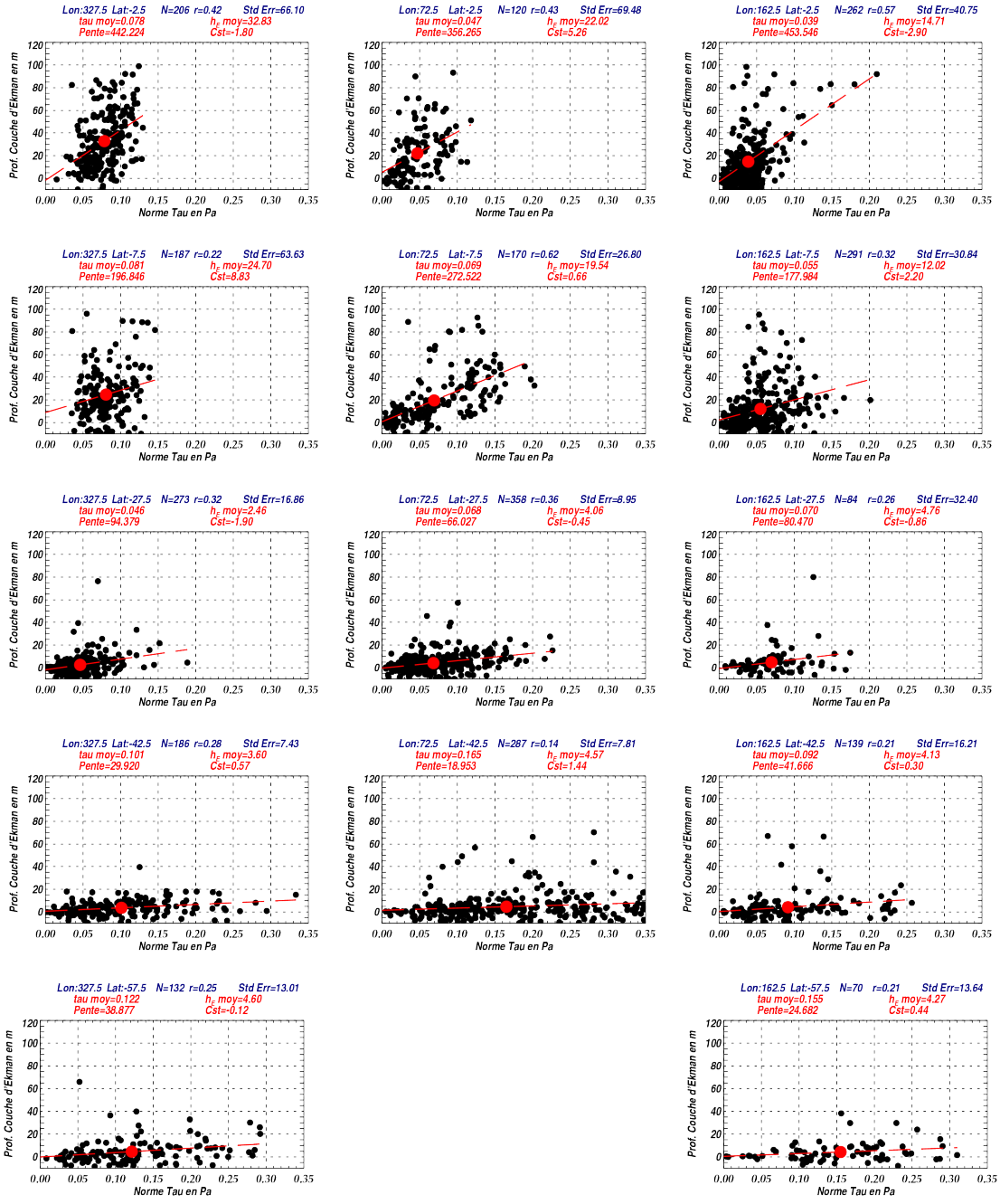

(a) Bassin Atlantique (b) Bassin Indien (c) Bassin Pacifique

FIGURE 2.4 – Régression linéaire du paramètre h_E dans l'hémisphère Sud. La droite représente la régression linéaire du nuage de points (noirs) et le point rouge représente la valeur moyenne de ce nuage.

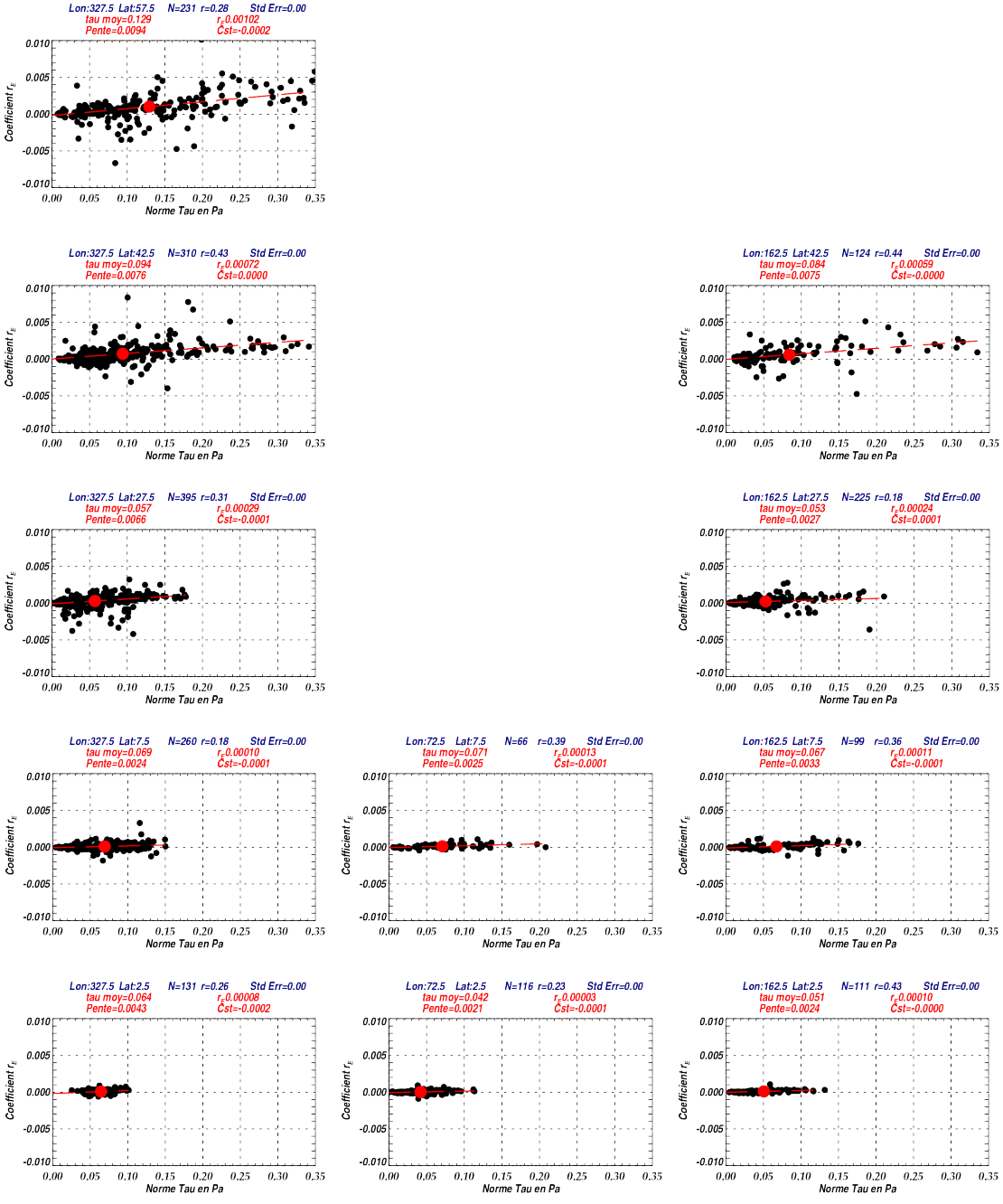

(a) Bassin Atlantique (b) Bassin Indien (c) Bassin Pacifique

FIGURE 2.5 – Régression linéaire du paramètre r_E dans l'hémisphère Nord. La droite représente la régression linéaire du nuage de points (noirs) et le point rouge représente la valeur moyenne de ce nuage.

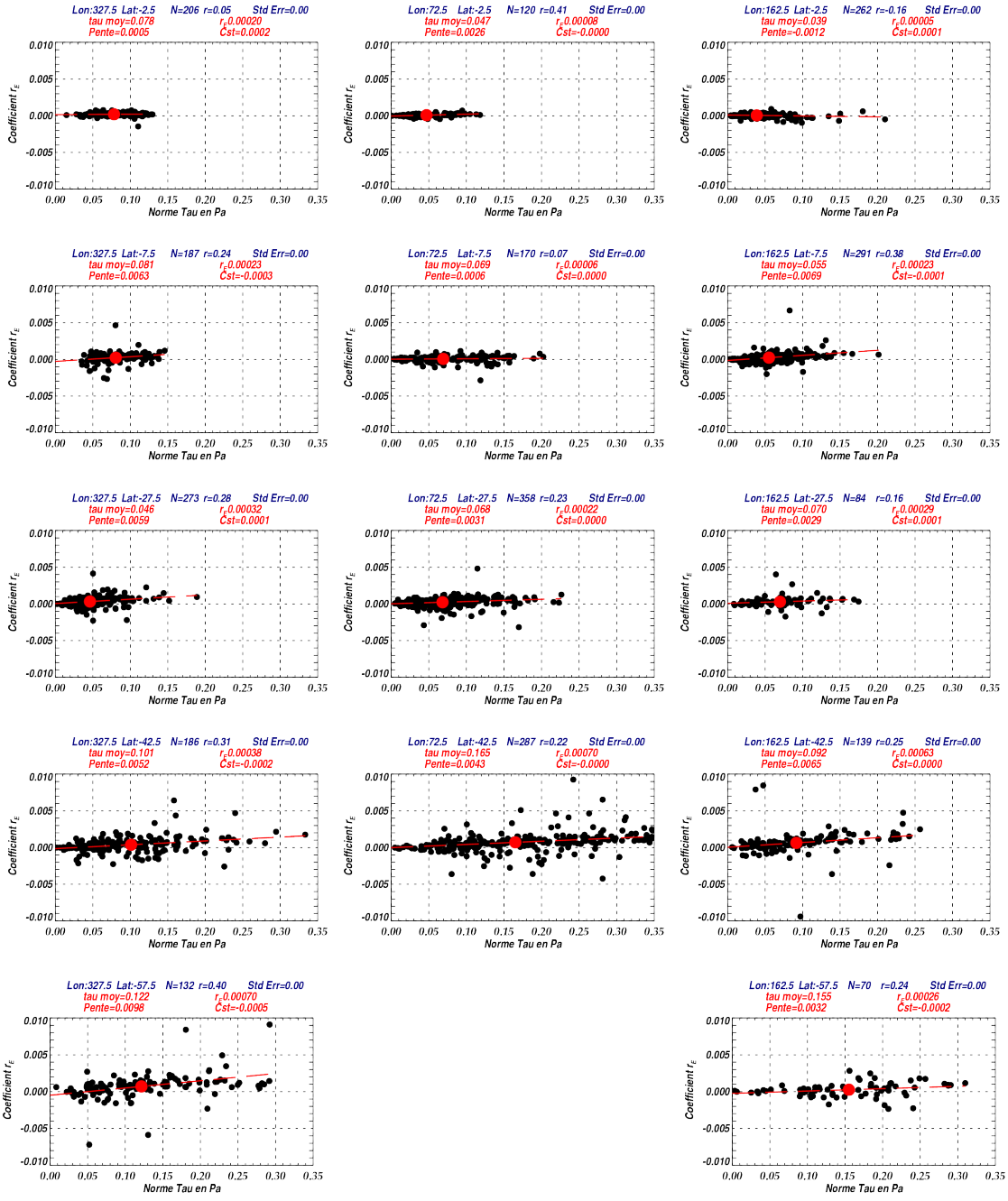

(a) Bassin Atlantique (b) Bassin Indien (c) Bassin Pacifique

FIGURE 2.6 – Régression linéaire du paramètre r_E dans l'hémisphère Sud. La droite représente la régression linéaire du nuage de points (noirs) et le point rouge représente la valeur moyenne de ce nuage.

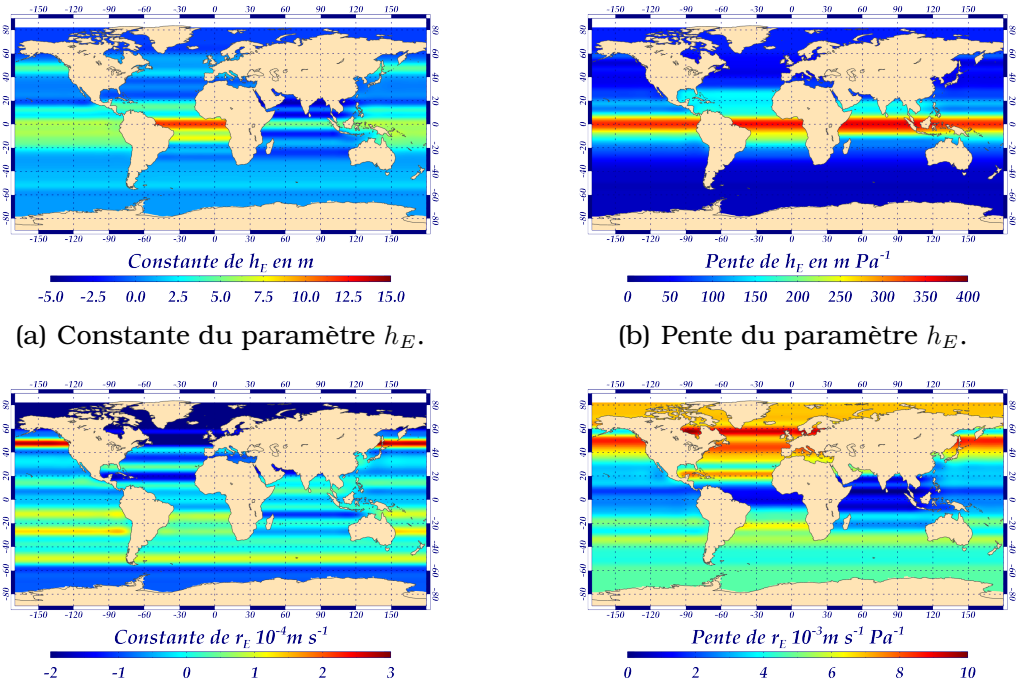

(a) Constante du paramètre h_E.

(b) Pente du paramètre h_E.

(c) Constante du paramètre r_E.

(d) Pente du paramètre r_E.

FIGURE 2.7 – Valeurs de régression des paramètres h_E et r_E.

2.6 Comparaison des courants de l'article [*Sudre et Morrow*, 2008] et de l'article [*Sudre et al.*, 2013]

Les divers points qui nous ont incité à reconsidérer la méthode d'obtention des courants géostrophiques et d'Ekman ont été énoncés dans la sous-section 2.3.3. L'article [*Sudre et al.*, 2013], qui a été publié dans *Limnology and Oceanography : Fluids and Environments*, avait pour but d'attirer des communautés scientifiques autres que les océanographes physiciens sur l'existence ainsi que sur l'utilisation des cartes journalières de courant au quart de degré. En ce sens, cet article ne répond pas à la question de première importance qui est : *"Est-ce que les différentes modifications de l'algorithme d'obtention qui ont été apportées par cette nouvelle méthode ont réellement amélioré la base de données résultante ?"*.

L'utilisation des bouées dérivantes de surface offre un jeu de données unique de par la répartition spatiale de son échantillonnage et de sa série temporelle. Il est donc difficile de se passer de la validation des courants par ces données *in situ*, même si l'on peut trouver discutable de valider les courants d'Ekman obtenus dans l'article [*Sudre et al.*, 2013] par un jeu de données dont certaines bouées ($\sim 90\%$) ont été utilisées pour paramétrer les régressions linéaires des paramètres h_E et r_E. On peut donc critiquer cette validation. Cependant il est impossible actuellement d'avoir pour la validation des courants de surface un autre jeu de données aussi étendu spatio-temporellement. Il est facile de comparer le nombre de points de bouées de ce jeu de données (voir figure 2.8(a)) avec celui des flotteurs Argo qui ont été utilisés pour la validation dans l'article [*Sudre et al.*, 2013] (voir figure 6A).

Pour cette validation, l'ensemble de l'archive temporelle des bouées dérivantes de surface a été utilisé sur toute la période disponible des données QuikSCAT (Juillet 1999 à Novembre 2009 - voir chapitre 1 section 1.3.2). Suite à l'article de *Grodsky et al.* [2011] qui a démontré que certaines bouées avaient perdu leur drogue sans que cela soit reporté dans les "flags" du jeu délivré par le Global Drifter Program (GDP), le jeu de données de bouées de surface utilisées pour cette validation a été réduit aux trois premiers mois de la période

après la mise à l'eau de ces bouées. Ce jeu de données a aussi été filtré des courants inertiels qui ne sont pas présents dans les données de courant dérivées des données satellitaires. La comparaison des figures 2.8(b) et 2.8(c) (pour la composante zonale) ainsi que les figures 2.8(d) et 2.8(e) (pour la composante méridienne), nous indiquent que les corrélations ont été améliorées :

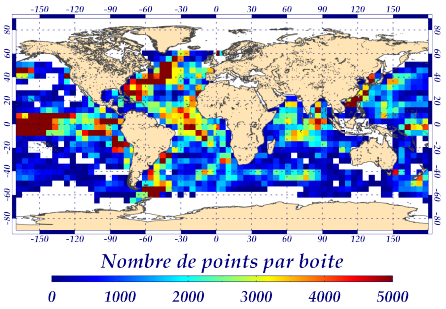

(a) Nombre de points de bouées dérivantes de surface considérés pour calculer les corrélations avec les courants satellitaires.

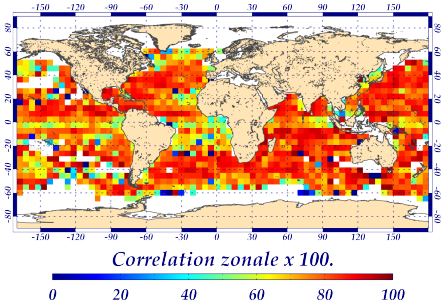

(b) Corrélation zonale entre les bouées dérivantes et le produit de courant de l'article [*Sudre et Morrow*, 2008].

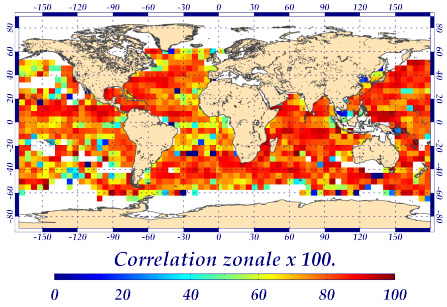

(c) Corrélation zonale entre les bouées dérivantes et le produit de courant de l'article [*Sudre et al.*, 2013].

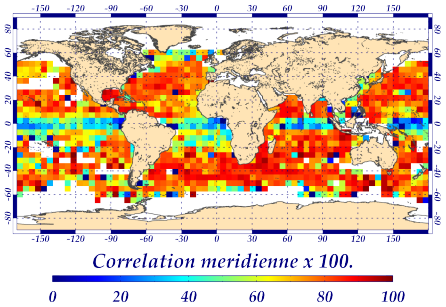

(d) Corrélation méridienne entre les bouées dérivantes et le produit de courant de l'article [*Sudre et Morrow*, 2008].

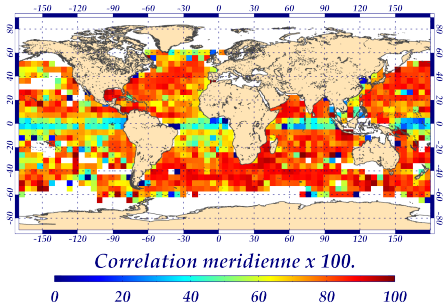

(e) Corrélation méridienne entre les bouées dérivantes et le produit de courant de l'article [*Sudre et al.*, 2013].

FIGURE 2.8 – Corrélations obtenues entre les deux produits satellitaires au quart de degré et les bouées dérivantes de surface.

- sur toutes les zones côtières. Cette amélioration provient directement de l'amélioration du produit MADT. En effet une attention particulière a été

portée pour affiner les filtrages nécessaires à l'altimétrie dans ces zones où le signal altimétrique est fortement contaminé par la présence des côtes,
- sur la zone équatoriale. Les progrès proviennent essentiellement du perfectionnement de la correction altimétrique par la méthode développée par *Picaut et Tournier* [1991]. Ceci a eu pour conséquence l'obtention d'une climatologie sur la période $2000 - 2008$ plus proche des observations,
- dans les zones $20°$ et $40°$ Nord et Sud, l'amélioration sensible a été obtenue par la prise en compte de la variation spatio-temporelle de la profondeur de couche d'Ekman et du coefficient de traînée.

2.7 Conclusions

Cette nouvelle base de données journalières de courants de surface au quart de degré a donc répondu aux objectifs qui avaient été énoncés précédemment. Cependant, un écueil de cette base de données dont la série temporelle va de Juillet 1999 à Novembre 2009 est de ne pas pouvoir être utilisable en temps quasi-réel. De ce fait, il est impossible d'utiliser cette base de manière opérationnelle lors d'une campagne à la mer ou pour répondre à des études récentes. De la même manière, il est difficile de répondre avec cette base à des questions scientifiques impliquant une variabilité décennale des courants de surface. Il a donc été nécessaire de trouver d'autres produits de tension de vent satellitaire pour étendre la période temporelle sur toute la période où l'altimétrie est disponible (1992 à nos jours). Ainsi nous avons mis en place deux nouvelles versions des courants GEKCO dont l'algorithmique est identique mais dont le signal diffusiométrique est différent :

- pour les études nécessitant la période temporelle la plus étendue, l'utilisation du produit "blended" du NCDC permet d'avoir une série temporelle d'Octobre 1992 à Octobre 2011 (soit 19 ans d'archives),
- pour les études nécessitant des courants de surface en temps quasi-réel, l'utilisation du produit DASCAT MWF du CERSAT est à privilégier. Cette dernière base est mise à jour quotidiennement et une carte des courants géostrophique et d'Ekman peut être obtenue au jour J-2 (les courants géostrophiques pouvant être obtenus au jour J-1).

Amélioration souhaitable des bases GEKCOs

La composante méridienne dans la zone équatoriale (et à moindre importance la composante zonale) est toujours faiblement corrélée avec les valeurs *in situ* des données de bouées dérivantes de surface. Cette estimation imparfaite des courants est due à la présence de nombreuses structures à mésoéchelle dans la zone équatoriale générées par la diffusion horizontale qui a une forte influence sur la dynamique équatoriale. Cette diffusion à grande échelle est associée aux "ondes d'instabilité barotrope" dont la période est de $\sim$20 jours pour le système des courants équatoriaux. Ces ondes sont difficilement détectables par l'altimétrie du fait de leur repliement de spectre ("aliasing") qui ne permet pas de distinguer ces signaux à hautes fréquences. Cependant les ondes d'instabilité barotrope sont très facilement détectables sur les données de TSM ou de couleur de l'eau, il est donc possible par des méthodes en traitement d'image et en particulier en utilisant des techniques de fusion et d'inférence multi-échelle que nous allons voir dans le chapitre 3 d'obtenir les courants issus de ces structures océaniques. La zone équatoriale n'étant pas la zone d'étude de cette thèse, ces résultats ne seront pas présentés dans ce document mais feront l'objet d'une étude ultérieure.

Bilan de l'utilisation des bases de données courants par la communauté scientifique

Notre intérêt se porte à la fois sur la diffusion scientifique des résultats et aussi sur la valorisation des bases de données que nous mettons à disposition pour la communauté scientifique. Cette valorisation peut être évaluée par le nombre d'extractions et de publications qui les citent qui ont été effectuées sur ces bases pour des études scientifiques diverses et variées.
Pour la période 2009 - 2012, plus de 200 extractions ont été exécutées sur la base de données de courants de surface au quart de degré. Ces demandes d'utilisation ont été effectuées à la fois par des scientifiques français, européens (en particulier Italiens, Espagnols, Portugais, Britanniques) et internationaux (majoritairement Nord Américains, Chiliens, Japonais, Indiens, Indonésiens, Coréens du Sud, Sénégalais), pour des études sur :

- la description et la variabilité de la circulation océanique sur des zones de courants spécifiques, et des zones d'upwelling,
- les interactions des courants et des tourbillons à mésoéchelle,
- le calcul de diagnostics lagrangiens (exposants de Lyapunov en temps - FTLE - ou en taille finis -FSLE-),

- la validation de modèles numériques,
- l'impact de la mousson indienne sur les courants,
- l'impact des tempêtes sur les courants océaniques,
- la distribution et l'advection de la chlorophylle, des sédiments et des sels nutritifs,
- le forçage physique sur la productivité biologique, et sur l'habitat d'organismes pélagiques,
- le déplacement d'animaux appartenant à la chaîne trophique supérieure (cétacés, phoques, tortues,...).

Certaines extractions ont été aussi demandées pour des supports de cours et des applications pour de la vulgarisation scientifique sur les courants marins.

Chapitre 3
La dynamique submésoéchelle

Chapitre 3

La dynamique submésoéchelle

Sommaire

3.1 Introduction . . . 147

3.2 La turbulence pleinement développée . . . 152

3.3 Spectre de singularités et description canonique de la cascade multiplicative . . . 156

3.4 Le FMM et la formulation microcanonique de la cascade multiplicative . . . 157

3.5 Formulation microcanonique de la cascade multiplicative et ondelettes optimales . . . 160

3.6 Spectres de singularités des données d'acquisition en Océanographie . . . 162

3.7 Histogrammes conditionnels des coefficients d'ondelettes . . . 163

3.8 Article : Motion analysis in oceanographic satellite images using multiscale methods and the energy cascade, H. Yahia *et al.*, 2010 . . . 163

3.8.1 Résumé de l'article (version française) . . . 163

3.8.2 Article publié dans *Pattern Recognition* . . . 165

3.9 Article : Inferring Information across Scales in Acquired Complex Signals, S. K. Maji *et al.*, 2012 . . . 180

3.9.1 Résumé de l'article (version française) . . . 180

3.9.2 Article publié dans *European Conference on Complex Systems 2012* . . . 180

3.10 Détermination de la norme . . . 199

3.11 Validation de la dynamique turbulente à haute résolution . . . 200

3.11.1 Méthodes de validation . . . 200

3.11.2 Validation de la dynamique à haute résolution obtenue à partir de la TSM MODIS/AQUA 205
3.11.3 Validation de la dynamique turbulente obtenue à partir de la TSM OSTIA 212
3.12 Conclusions 217

3.1 Introduction

Alors que le chapitre 2 avait pour but l'obtention de la dynamique océanique liée aux processus à mésoéchelle, ce chapitre s'intéresse à une catégorie de processus dont les structures océaniques associées ont des dimensions inférieures (de ∼100 m à 50 km, c'est à dire recouvrant une plage plus importante du *domaine inertiel* - voir infra -), et des durées de vie allant de quelques heures à quelques jours. Ces processus à submésoéchelle s'inscrivent entre les processus à plus grande échelle (mésoéchelle) et ceux à plus fine échelle (échelle de dissipation) dont ils sont distincts (figure 3.1).

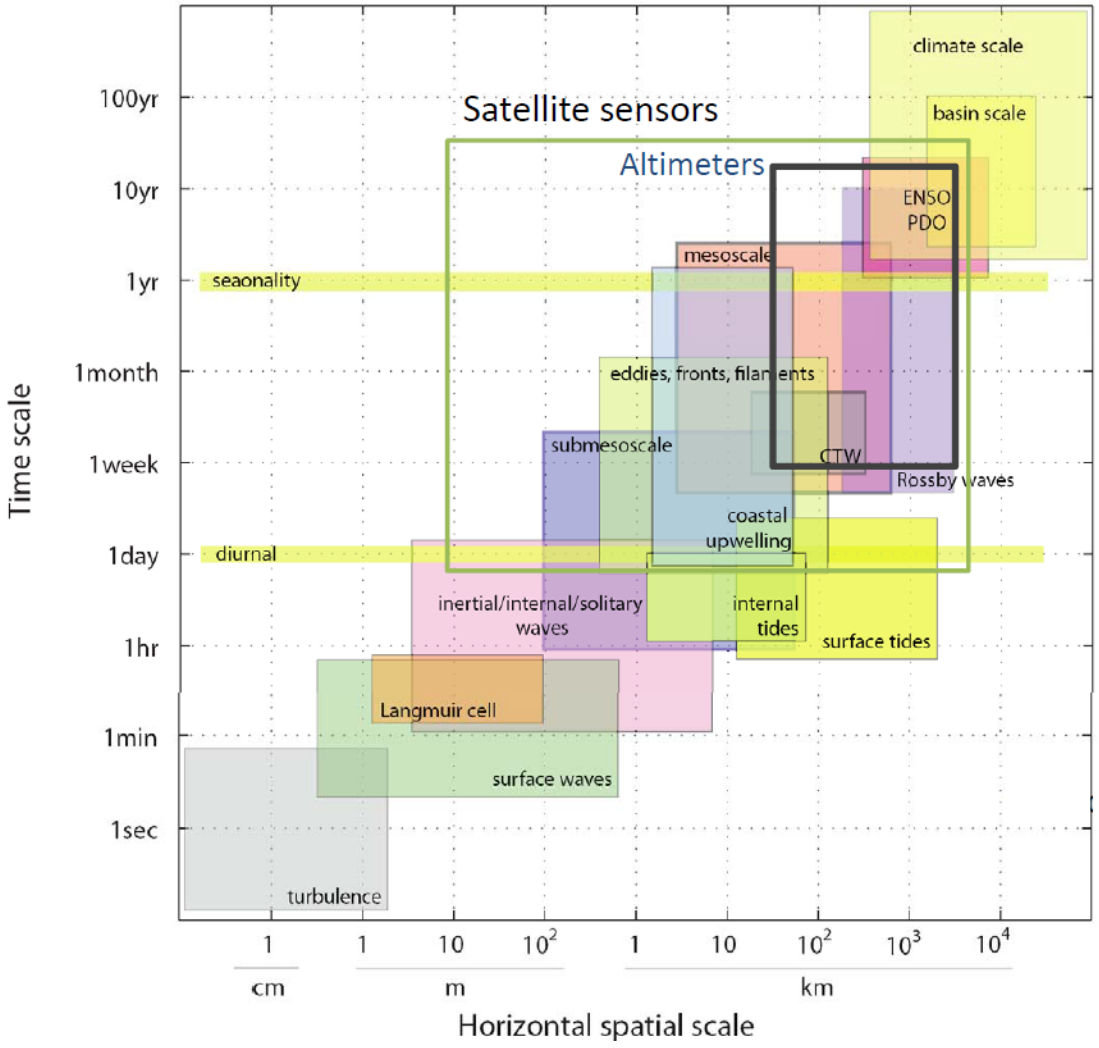

FIGURE 3.1 – *Illustration des échelles spatio-temporelles dans l'océan selon Dickey et al. [2006]. ©Sung Yong Kim et Eric Terrill (OSTST 2011).*

Comme indiqué sur la figure 3.1, les altimètres ne permettent pas d'identifier et de caractériser la majorité des structures océanographiques issues des processus à submésoéchelle. Seules les structures les plus importantes en terme de dimensions et de durée de vie vont être présentes et peuvent être révélées au moyen de diagnostics Lagrangiens comme les exposants de Lyapunov en taille finie [*Rossi et al.*, 2009]. Il est donc nécessaire si on veut déterminer la dynamique océanique provenant de cette échelle d'utiliser des capteurs satellitaires ayant la résolution suffisante pour en capturer les structures. Comme nous l'avons vu au chapitre 1, les capteurs délivrant des données de TSM et de couleur de l'océan ont une résolution permettant l'acquisition de la dynamique océanique provenant de la submésoéchelle. Cependant à la différence de l'altimétrie qui permet d'obtenir par l'utilisation des équations de la géostrophie une information quasi directe de la dynamique océanique, il est nécessaire d'utiliser, ici, des méthodes de traitement du signal plus complexes qui ont la capacité de prendre en compte les effets de la turbulence pleinement développée aux distances submésoéchelles.

L'analyse de l'information du mouvement contenu dans des séquences temporelles d'images acquises par télédétection constitue un domaine important tant sur le plan théorique que sur le plan applicatif en vision par ordinateur (la vision par ordinateur que l'on peut aussi qualifier de vision artificielle ou vision numérique, est une sous branche de l'intelligence artificielle). En océanographie, (tout comme en observation de la terre), l'apparition des données de télédétection a profondément bouleversé le domaine [*Munk*, 2000b], en particulier pour la compréhension de la dynamique océanique. Cependant, la plupart des approches en vision par ordinateur pour l'analyse du mouvement ne prennent pas en compte les caractéristiques clés de la dynamique océanique en turbulence pleinement développée qui sont l'intermittence et l'imprédictibilité, bien que celles-ci contribuent de manière importante à la forme et aux déplacements des structures cohérentes acquises. De plus, les artefacts spécifiques aux images de télédétection ("Sun glint", données manquantes, etc.) peuvent dans certains cas limiter l'application de ces approches.

Parmi les algorithmes existants pour analyser le mouvement d'un fluide représenté par une séquence temporelle d'images, on peut citer :

- la méthode "Particle Image Velocity" (PIV), basée sur des méthodes de corrélation, tente d'estimer un champ de vecteurs qui est supposé être constant sur une petite fenêtre spatiale de l'image centrée sur différents pixels. La corrélation est alors exprimée en définissant des critères de similarité qui peuvent être facilement implémentés dans l'espace de Fourier [*Adrian*, 2005],
- la méthode "Maximun Cross Correlation" (MCC), basée sur une méthode du calcul du maximum de corrélation sur une série d'images temporellement proches. Cette méthode consiste à prendre une sous-image et à chercher sur l'image suivante (temporellement) toutes les sous-images possibles. Une corrélation croisée est ensuite effectuée pour déterminer la sous-image qui obtient la plus forte corrélation avec la sous-image initiale. Il est à noter que cette méthode ne permet pas d'obtenir un champ de vecteurs dense [*Emery et al.*, 2003; *Crocker et al.*, 2007],
- la méthode de "corrélation - relaxation - catalogage" qui a été développée pour des données de TSM. Cependant pour cette méthode, l'hypothèse de voisinage utilisée ne correspond pas à la réalité turbulente de l'écoulement représenté par les images de TSM, ce qui a rendu cette méthode inappropriée dans un contexte opérationnel mais aussi du fait qu'elle nécessite une connaissance *a priori* du mouvement [*Wu*, 1995],
- les méthodes basées sur l'hypothèse de conservation de la luminance associée à différents types de contraintes de régularité représentent une vaste classe d'algorithmes qui a été fortement développée au cours des dernières années. Elles consistent à minimiser l'énergie d'une fonctionnelle définie sur le domaine de l'image et composée de deux termes :
  - une partie de la fonctionnelle exprime la conservation de la luminance durant le mouvement qui devient sous une forme différentielle une contrainte de mouvement apparent,
  - une autre partie de la fonctionnelle exprime le terme de régularisation qui contraint spatialement l'ensemble des solutions possibles.

  Ce type d'algorithme communément nommé "flot optique" a été extrêmement employé au cours des dernières années. Bien qu'il soit difficile d'en faire une bibliographie exhaustive, on peut tout de même citer les travaux précurseurs de *Horn et Schunck* [1981] qui se sont intéressés au cas de fluides turbulents et irréguliers. Un nombre considérable de travaux a été entrepris à la suite de ces travaux précurseurs, pour palier les limitations inhérentes de cette approche. Certains se sont axés sur l'amoindrisse-

ment de l'hypothèse sur les petits déplacements, par l'utilisation d'une extension du formalisme à la représentation multi-échelles des données [*Heitz et Bouthemy*, 1993; *Lai et Vemuri*, 1998; *Cohen et Herlin*, 1999; *Kornprobst et al.*, 1999; *Chefd'Hotel et al.*, 2001], d'autres ont modifié le terme de régularisation de la fonctionnelle pour permettre des solutions plus irrégulières du champ de vecteurs obtenu [*Alvarez et al.*, 2000; *Weickert et Schnörr*, 2001; *Mémin et Pérez*, 2002]. De notables extensions de cette approche ont aussi tenté de mieux approximer l'écoulement du fluide en dérivant de nouvelles lois de conservation provenant des équations de continuité [*Zhou et al.*, 2000]. Ce dernier type d'algorithme exploitant ces lois de conservation a pu être exploité dans un contexte opérationnel, mais ils ont nécessité un important effort de pré-traitement des données océaniques [*Vigan et al.*, 2009a,b]. Une autre branche des modèles de conservation de la luminance a aussi été développée en prenant l'hypothèse de régularisation sur la divergence et le rotationnel ("div-curl method") du signal analysé. Pour cette autre méthode, le terme de régularisation est modifié en introduisant dans celui-ci des dérivées d'ordre supérieur liées aux phénomènes divergents et rotatifs de l'écoulement [*Suter*, 1994; *Yuan et al.*, 2007].

  Toutes ces méthodes de "flot optique" basées sur la conservation de la luminance pour des écoulements turbulents et associées à des phénomènes complexes sur l'acquisition des données de télédétection possèdent des limitations certaines. En effet si la fréquence d'acquisition des images dans la séquence temporelle est grande, la variation de la luminance d'une image à l'autre est hautement imprévisible et la condition de régularité ne peut pas être vérifiée en particulier pour des signaux représentant un écoulement avec un nombre de Reynolds très grand [*Frisch*, 1995].

- D'autres méthodes en traitement du signal ont aussi été proposées en prenant en compte des estimations paramétriques basées sur la discrétisation de la vorticité [*Cottet et Koumoutsakos*, 2000; *Cuzol et Mémin*, 2005]. Elles ont été étendues pour mieux satisfaire les équations de Navier-Stokes, par l'estimation d'un champ de vecteurs possédant une loi d'évolution *a priori* [*Nogawa et al.*, 1997; *Papin et al.*, 2000; *Cuzol et Mémin*, 2009].

Les signaux naturels, provenant des capteurs agissant dans la bande spectrale du visible ou de l'infra-rouge, sont tous des signaux complexes. Ils ont

des causes très diverses mais ils présentent des caractéristiques d'organisation similaires qui peuvent s'appréhender par des propriétés communes en ce qui concerne : la distribution statistique de l'information qu'ils contiennent et la localisation de cette information dans les acquisitions des phénomènes [*Turiel et al.*, 1998; *Pont et al.*, 2009]. L'un des buts de cette "Science de la Complexité", dont nous assistons aujourd'hui à l'élaboration, consiste à déterminer quantitativement les paramètres permettant de rendre compte de ces organisations statistiques communes. Il existe une classe bien définie de phénomène complexe dont l'organisation statistique de la complexité interne est connue : la turbulence pleinement développée. Celle-ci joue un rôle essentiel dans les travaux présentés dans cette thèse, puisque la turbulence pleinement développée est précisément le régime de la dynamique océanique [*Parisi et Frisch*, 1985]. C'est à l'origine pour ce type de phénomène qu'a été développée depuis Kolmogorov [*Frisch*, 1995; *Arneodo et al.*, 1995; *Arnéodo et al.*, 1995] une description basée sur des lois de puissance observées sur les fonctions de structure. Cette description conduit à une première approche de la complexité, qualifée de "canonique" [*Turiel et al.*, 2006, 2008; *Pont et al.*, 2011b] et permet de comprendre le phénomène fondamental de *cascade multiplicative* associée à la turbulence. La distribution des exposants de ces lois de puissance, appelés "exposants d'échelle" (*scaling exponents*) permet de déterminer, par transformation de Legendre, le *spectre de singularités* à partir d'un grand nombre d'observations ("grand ensemble"). L'étude de ce spectre permet de déterminer des caractéristiques globales de la complexité, et constitue une trace de l'existence d'une structuration multiéchelles, de nature multifractale, dans le système dont on a un grand ensemble de réalisations et par voie de conséquence l' *existence* d'une cascade multiplicative. Un flot turbulent est chaotique d'un point de vue spatial et temporel. Ceci a pour conséquence des difficultés considérables en simulation numérique. Autre conséquence, il existe un continuum d'échelles actives, le *domaine inertiel*, dans lequel interviennent les phénomènes de cascades multiplicatives. Ces phénomènes décrivent l'injection de l'énergie, depuis l'échelle de forçage L jusqu'à l'échelle de dissipation visqueuse l. Les équations de Navier-Stokes, qui décrivent le champ de vitesses $\mathbf{u}(\mathbf{x},t)$ du flot à l'instant t :

$$\left\{\begin{array}{lcl} \dfrac{\partial \mathbf{u}}{\partial t} + (\mathbf{u}\cdot\nabla)\mathbf{u} & = & -\nabla p + \nu\Delta\mathbf{u} \\ \nabla\cdot\mathbf{u} & = & 0 \end{array}\right. \tag{3.1}$$

se réécrivent, en utilisant des variables adimensionnelles : $\mathbf{x} \to \mathbf{x}/L$, $\mathbf{u} \to \mathbf{u}/U$ et $t \to tU/L$ (L, U étant respectivement une longueur et vitesse caractéristiques) :

$$\frac{\partial \mathbf{u}}{\partial t} + (\mathbf{u} \cdot \nabla)\mathbf{u} = -\nabla p + \frac{\Delta \mathbf{u}}{\mathrm{Re}} \tag{3.2}$$

où $\mathrm{Re} = \frac{UL}{\nu} = \frac{\text{terme de convection}}{\text{terme visqueux}}$ est le *nombre de Reynolds* de l'écoulement. La *turbulence pleinement développée* - Fully Developed Turbulence ou FDT - apparaît aux grands nombres de Reynolds : $\mathrm{Re} \to +\infty$. Les propriétés statistiques des fluctuations à courte portée sont alors *universelles* dans des conditions données de frontière et de forçage.

3.2 La turbulence pleinement développée

Le nombre de Reynolds associé à l'écoulement océanique est caractéristique de la FDT (de l'ordre de 10^{11}). L'observation au moyen de capteurs optiques ayant une résolution kilométrique des structures océaniques, montre qu'à cette échelle de résolution une multitude de structures sont identifiables ayant des dimensions horizontales de l'ordre du kilomètre (voir figures 1.20 et 1.22). Ces structures sont essentiellement présentes dans la couche de surface de l'océan et se distinguent par un nombre de Rossby ($\mathrm{Ro} = U/f \cdot L$) et de Richardson ($\mathrm{Ri} = E_p/E_c$) de l'ordre de 1. Elles ont une contribution majeure pour les transferts verticaux et pour la variation de la densité par mélange des masses d'eau. Elles permettent aussi le transfert de l'énergie entre la mésoéchelle et l'échelle de dissipation. Si on s'intéresse au transport par advection des propriétés biogéochimiques des masses d'eau dans la couche de surface, leur étude dynamique est primordiale [*Thomas et Ferrari*, 2008]. Enfin elles vont aussi fortement contribuer au déplacement de tout objet inanimé dérivant à la surface de l'océan et contraindre le déplacement de toute la chaîne trophique aquatique (du phytoplancton jusqu'aux prédateurs supérieurs).
Les écoulements issus de ce mode de la turbulence sont fortement non-stationnaires avec des variations très irrégulières (intermittence) [*Kraichnan*, 1967b]. L'énergie contenue dans ces écoulements peut être transférée par cascade directe de l'enstrophie $\Omega = \omega^2 = (\frac{\partial v}{\partial x} - \frac{\partial u}{\partial y})^2$, w étant la vorticité) ou en sens inverse par la cascade inverse d'énergie [*Kraichnan*, 1967a; *Batchelor*, 1969]. La limite des petites structures va être étroitement liée à l'échelle de Kolmogo-

rov (échelle de dissipation où la viscosité devient prépondérante et où $\mathrm{Re} = 1$). Enfin, et nonobstant le caractère apparemment déterministe des équations de Navier-Stokes, les acquisitions de signaux de fluides en FDT constituent en quelque sorte un prototype de l'imprédictabilité auquel s'intéresse la Science de la Complexité. L'imprédictabilité peut se mesurer, entre autres, par les exposants de Lyapunov qui indiquent le caractère exponentiel de déviation des trajectoires à partir de conditions initiales infinitésimalement proches : connaître une solution à un instant t du système nécessite une précision infinie sur les conditions initiales qui implique à son tour une incertitude initiale nulle sur les petites échelles lors de leurs propagations dans les grandes échelles. Il est donc impossible en océanographie de pouvoir respecter ces deux postulats ne serait-ce que par nos moyens actuels de calcul limité et "imprécis".

Certains groupes de transformations spatiales et temporelles agissent sur l'ensemble des solutions des équations de Navier-Stokes : symétries, rotations, transformations galiléennes, et changement d'échelle [*Frisch*, 1995]. Plus le nombre de Reynolds augmente et plus on observe des "brisures de symétrie" de ces groupes d'action, jusqu'au cas extrême de la FDT où les symétries ne sont restaurées qu'en un sens statistique. C'est de là que vient l'impossibilité de "représenter" des signaux turbulents sur une base ou une trame Hilbertienne fixe et selon des techniques de projection standard, ce qui explique la difficulté de leur analyse. La théorie de Kolmogorov K41 ([*Kolmogorov*, 1991a,b]) relie ces propriétés au comportement de la fonctionnelle des incréments de vitesse (un invariant galiléen) :

$$\mathbb{T}_r \mathbf{u}(\mathbf{x}, \mathbf{r}) = \mathbf{u}(\mathbf{x} + \mathbf{r}) - \mathbf{u}(\mathbf{x}) \tag{3.3}$$

dont la fonction de structure d'ordre 3 vérifie :

$$\langle (\mathbb{T}_r \mathbf{u}(\cdot, \mathbf{r}))^3 \rangle = -\frac{4}{5}\epsilon \mathbf{r} \quad \text{(Loi de Kolmogorov du 4/5)} \tag{3.4}$$

où ϵ est le taux de dissipation de l'énergie, qui demeure fini quand $\mathrm{Re} \to +\infty$. On en déduit la forme générale des fonctions de structure dans le cadre K41 :

$$\langle (\mathbb{T}_r \mathbf{u}(\cdot, \mathbf{r}))^p \rangle = C_p \epsilon^{p/3} \mathbf{r}^{p/3} \tag{3.5}$$

d'où l'apparition d'exposants critiques universels $h_p = p/3$ et la forme standard du spectre de Kolmogorov en théorie K41 :

$$E(\mathbf{k}) = C\epsilon^{2/3}\mathbf{k}^{-5/3} \tag{3.6}$$

On sait depuis longtemps que la théorie K41 n'est qu'une approximation qui doit être corrigée. La raison essentielle provient de l'observation de *l'intermittence* qui implique une correction dans les exposants critiques universels $h_p = \zeta(p)$. Cette correction fait apparaître une décomposition du taux local de dissipation de l'énergie sous la forme d'une cascade multiplicative dont le support est un ensemble de nature fractale dont on a déterminé les caractéristiques dans le cas de modèles particuliers, par exemple le modèle noir et blanc aléatoire de Novikov et Stewart en 1964 ou encore le modèle β aléatoire de *Benzi et al.* [1991].

L'existence d'exposants critiques dans le comportement asymptotique des fonctions de structure des incréments de vitesse d'un flot turbulent est la signature de la présence d'une structure multiéchelles, de nature multifractale. L'invariance d'échelles est bien connue en physique, elle est associée à de nombreux phénomènes étudiés depuis longtemps, par exemple les transitions de phase [*Stanley*, 1987]. D'une manière générale, au voisinage d'un point critique, les variables thermodynamiques ainsi que les corrélations spatiales ont un comportement en loi de puissance qui constitue une signature de l'invariance d'échelles [*Turiel et al.*, 2008]. Il est admis que les exposants critiques, c'est-à-dire les exposants qui apparaissent dans les lois de puissance au voisinage d'un point critique, s'ils peuvent être déterminés, donnent accès à la hiérarchie multiéchelles permettant de caractériser la classe d'universalité d'un système. En particulier ils permettent de localiser les phénomènes de cascade multiplicative, par conséquence ces *variétés critiques* sont donc nécessairement de nature multifractale. Dans ce qui suit, nous allons détailler le *Formalisme Multiéchelles Microcanonique* qui permet de déterminer effectivement les variétés critiques dans un signal d'acquisition. Mais avant cela, il nous faut rappeler les approches antérieures, qui ne déterminent pas les exposants critiques localisés, mais d'autres exposants - qui leurs sont nécessairement liés - calculés, comme dans le cas des fonctions de structure de la turbulence, de manière globale au travers de l'étude

des moments. Les variétés critiques étant, comme nous l'avons dit, de nature multifractale, nous commençons par rappeler les idées de base sur la fractalité.

Il existe plusieurs définitions non-équivalentes de la notion de dimension. L'une des plus simples est la *dimension de boîte* : si X est une partie non vide d'un espace métrique, soit $N(s)$ le nombre minimal de boules de diamètre s nécessaires pour recouvrir X. La dimension de boîte de X, $\dim_B(X)$ est :

$$\dim_B(X) = \lim_{s\to 0} \frac{\log N(s)}{\log(1/s)} \tag{3.7}$$

quand cette limite existe. Cette définition ne conduit pas toujours à des "dimensions raisonnables". Par exemple si

$$X = \{1/n \ , \ n \in \mathbb{N} - \{0\}\} \cup \{0\} \subset \mathbb{R} \tag{3.8}$$

alors $\dim_B(X) = \frac{1}{2}$ alors qu'on s'attendrait à une dimension nulle. Pour remédier à ce genre de difficulté, il existe une autre définition de la dimension, qui remonte à Hausdorff et qu'on appelle pour cette raison la *dimension de Hausdorff*. Etant donné $\delta > 0$, soit un recouvrement de X par des ouverts (U_i) tels que $\text{diam}(U_i) < \delta$. On pose :

$$\dim_H^\delta(X) = \lim_{s\to 0} \inf_{U_i} \sum_i \text{diam}(U_i)^s \tag{3.9}$$

puis $\dim_H(X)$ est l'inf des δ tels que $\dim_H^\delta(X) < \infty$. La dimension de Hausdorff de l'ensemble X ci-dessus : $X = \{1/n \ , \ n \in \mathbb{N} - \{0\}\} \cup \{0\} \subset \mathbb{R}$ est nulle. Bien qu'elle soit plus satisfaisante d'un point de vue mathématique, la dimension de Hausdorff est en pratique difficile à calculer. On a toujours : $\dim_H(X) <= \dim_B(X)$. Dans les approches de la multifractalité par les fonctions de structure, que nous allons maintenant rappeler, la notion de dimension intervient pour définir le spectre de singularités.

3.3 Spectre de singularités et description canonique de la cascade multiplicative

Un signal s est multifractal s'il existe une fonctionnelle $\mathbb{T}$ telle que les moments :

$$\langle \mathbb{T}_r(s)|^p \rangle = \alpha_p r^{\tau_p} + o(r^{\tau_p})(r \to 0) \tag{3.10}$$

où $\langle \cdot \rangle$ désigne une moyenne prise sur un grand ensemble de réalisations du signal s [*Turiel et al.*, 2008]. La relation entre les τ_p et le spectre de singularité $f(\alpha)$ est alors la suivante [*Arneodo et al.*, 1995] : les variables p et τ_p s'apparentent respectivement à une température et à l'énergie libre, tandis que α et le spectre de singularités $f(\alpha)$ correspondent à des variables thermodynamiques conjuguées respectivement à p et τ_p, et on passe des unes aux autres par une transformation de Legendre :

$$f(\alpha) = \min_p(p\alpha - \tau_p) \tag{3.11}$$

En général $\mathbb{T}_r$ correspond à des incréments ou à la dissipation locale de l'énergie, définie avec l'aide du gradient du signal [*Turiel et al.*, 2008]. On notera que l'obtention pratique de grand ensembles est une limitation réelle. On fait alors habituellement une hypothèse de type ergodique, qui ramène les calculs de grands ensembles à des moments spatiaux (moyennes thermalisées).

L'écriture précédente de la multifractalité, qualifiée parfois de *canonique* [*Turiel et al.*, 2008; *Arneodo et al.*, 1995] permet de formuler un phénomène de cascade multiplicative également en mode canonique. Suivant Kolmogorov, étant données deux échelles r et L, $0 < r < L$, le processus de transfert de l'énergie se définit par un processus d'injection $\eta_{r/L}$, défini sous la forme d'une variable aléatoire par :

$$\mathbb{T}_r(s) \doteq \eta_{r/L}\mathbb{T}_L(s) \tag{3.12}$$

où '$\doteq$' signifie l'égalité *en loi*. Suivant Kolmogorov, la variable d'injection $\eta_{r/L}$ ne dépend que du rapport des échelles et s'écrit donc $\eta_{r/L} = [r/L]^{\epsilon}$. A partir de là, les fonctions de structure s'écrivent :

$$\langle \mathbb{T}_r s|^p\rangle = [r/L]^{\epsilon p}\langle|\mathbb{T}_L s|^p\rangle = A_p r^{\epsilon p} \tag{3.13}$$

avec $A_p = \langle|\mathbb{T}_L s|^p\rangle L^{-\epsilon p}$. On en déduit $\tau_p = \epsilon p$, c'est-à-dire que les exposants canoniques τ_p sont proportionnels à p, ce que démentent les expériences dans le cas de la turbulence pleinement développée. En effet la relation entre τ_p et p est telle que τ_p est une fonction convexe de p (*anomalous scaling*) [*Turiel et al.*, 2006]. Ce mode est introduit par des lois indéfiniment divisibles. On suppose que :

- $\eta_{r/L}$ est une variable aléatoire indépendante de L.
- La variable $\eta_{r/L}$ est indéfiniment divisible.

Après avoir brièvement rappelé l'approche canonique de la multifractalité, nous en arrivons à présent au formalisme microcanonique, ainsi qu'à la représentation microcanonique de la cascade multiplicative qui constitue le fondement théorique au processus d'inférence entre les échelles que nous avons utilisé dans cette thèse pour inférer la dynamique océanique turbulente à résolution submésoéchelle.

3.4 Le FMM et la formulation microcanonique de la cascade multiplicative

Dans une description microcanonique de la multifractalité, les exposants qui apparaissent au voisinage d'un point critique, et qui sont pour cette raison appelés *exposants de singularité* possèdent une définition locale, à l'origine considérée comme n'ayant qu'un intérêt que théorique en raison des difficultés inhérentes aux méthodes d'évaluation du type *counting box* [*Arneodo et al.*, 1995]. Nous dirons donc qu'un signal s est multifractal en un sens microcanonique s'il existe une fonctionnelle dépendant de l'échelle r $\mathbb{T}_r$ telle que, pour tout point x du domaine du signal s, on ait [*Turiel et al.*, 2006] :

$$\mathbb{T}_r(s)(\mathbf{x}) = \alpha(\mathbf{x})r^{h(\mathbf{x})} + o(r^{h(\mathbf{x})})(r \to 0) \tag{3.14}$$

Dans cette écriture, $h(\mathbf{x})$ est l'exposant de singularité au point $\mathbf{x}$. La connaissance de ces exposants, c'est-à-dire leur calcul à haute précision numérique permet de décomposer le domaine du signal en sous-ensembles :

$$\mathcal{F}_h = \{\mathbf{x} : h(\mathbf{x}) = h\} \tag{3.15}$$

qui correspondent à la hiérarchie multifractale définie par le spectre de singularité associé aux exposants en mode canonique ce qui conduit à la formule de [*Parisi et Frisch*, 1985] :

$$\tau_p = \inf_h\{hp + d - D(h)\} \tag{3.16}$$

où

$$D(h) = \dim_H \mathcal{F}_h \tag{3.17}$$

et d est la dimension du domaine du signal ($d = 2$ pour des images) donc le spectre de singularité, évalué de diverses manières en mode canonique [*Turiel et al.*, 2006] est simplement la transformation $h \to D(h)$. Si nous désignons par $\rho(h)$ la fonction de répartition des exposants de singularités (donc leur histogramme quand on traite des signaux numériques) il existe une relation simple avec le spectre de singularités $D(h)$; on a en effet [*Turiel et al.*, 2008] :

$$\rho(h) \propto r_0^{d-D(h)} \tag{3.18}$$

avec : d dimension du domaine du signal et r_0 : échelle de référence à laquelle les exposants de singularité sont calculés, correspondant à la résolution maximale définie par la taille du signal dans le cas digital. Ainsi : $r_0 = \sqrt{\frac{1}{n \times m}}$ pour un signal s de taille $n \times m$ (une image en ce qui nous concerne). On a alors :

$$d - D(h) = \lim_{r \to 0} \frac{\log(\rho(h))}{\log r_0} \tag{3.19}$$

Puisqu'une transformation de Legendre s'inverse facilement, on définit le spectre de Legendre $D_l(h)$ par la transformation de Legendre de $p \to \tau_p$ [*Turiel et al.*, 2006] :

$$D_l(h) = \inf_h\{hp + d - \tau_p\} \tag{3.20}$$

avec d dimension du signal s comme ci-dessus. Pour la majorité des signaux complexes, $D_l(h)$ est convexe [*Turiel et al.*, 2006].

Le calcul à haute précision des exposants de singularité est un problème difficile. Dans cette thèse nous nous occuperons uniquement de signaux qui sont des images, en conséquence nous abandonnons le terme générique d'un signal s pour nous intéresser au cas d'une image que nous noterons I, et qui désigne une image scalaire définie sur son domaine Ω, une partie compacte de $\mathbb{R}^2$; soit $\|\nabla I\|$ la norme du gradient de l'image I. Nous travaillons avec un signal numérique composé d'une acquisition d'intensités lumineuses normalisées $I(\vec{x}) - \langle I \rangle$, avec $\langle I \rangle$: moyenne des luminances sur le domaine de l'image. Il est plus utile dans les calculs de remplacer la fonctionnelle $\mathbb{T}_r$ par une mesure μ dont la densité $\mathrm{d}\mu(\mathbf{x})$ par rapport à la mesure de Lebesgue est la norme du gradient de l'image, de telle manière que l'on ait, en désignant par $\mathcal{B}_r(\mathbf{x})$ la boule ouverte de centre x et de rayon r :

$$\mu(\mathcal{B}_r(\mathbf{x})) = \int_{\mathcal{B}_r(\mathbf{x})} \mathrm{d}(\mathbf{y}) \|\nabla I\|(\mathbf{y}) \tag{3.21}$$

Ainsi la mesure μ définie ci-dessus est dite multifractale en un sens microcanonique, si pour tout point $\mathbf{x} \in \Omega$ on a [*Turiel et al.*, 2008] :

$$\mu(\mathcal{B}_r(\mathbf{x})) = \alpha(\mathbf{x}) r^{h(\mathbf{x})} + o(r^{h(\mathbf{x})}) \ (r \to 0) \tag{3.22}$$

avec $\alpha(\mathbf{x})$: préfacteur d'amplitude dépendant du signal ; $h(\mathbf{x})$: exposant de singularité au point x. Les exposants de singularité pour des données d'acquisition discrètes peuvent être calculés de plusieurs manières [*Turiel et al.*, 2006; *Pont et al.*, 2011a]. Dans ce travail, nous utilisons la projection en ondelettes de la mesure μ à l'échelle r et au point x alors définie comme :

$$\mathcal{T}_\psi \mu(\mathbf{x}, r) = \int d\mu(\mathbf{y}) \frac{1}{r^2} \psi(\frac{\mathbf{x}-\mathbf{y}}{r}) \tag{3.23}$$

avec ψ : ondelette mère (par exemple gaussienne ou lorentzienne). Dans le cas d'une mesure multifractale au sens microcanonique on a :

$$\mathcal{T}_\psi \mu(\mathbf{x}, r) = \alpha_\psi(\mathbf{x}) r^{h(\mathbf{x})} + o(r^{h(\vec{x})}) \tag{3.24}$$

et une bonne approximation des exposants de singularité est obtenue par application de la formule suivante [*Pont et al.*, 2011a] :

$$h(\mathbf{x}) = \frac{\log \mathcal{T}_\Psi \mu(\mathbf{x}, r_0) / \langle \mathcal{T}_\Psi \mu(\cdot, r_0) \rangle}{\log r_0} + o\left(\frac{1}{\log r_0}\right) \tag{3.25}$$

avec : $\langle \mathcal{T}_\Psi \mu(\cdot, r_0) \rangle$ moyenne de la projection en ondelettes sur le signal, et r_0 est choisi de manière à diminuer l'amplitude relative du terme correctif $o\left(\frac{1}{\log r_0}\right)$. Les ondelettes mères sont choisies dans la famille $\Psi^\beta(\mathbf{x}) = 1/(1+|\mathbf{x}|^2)^\beta$, avec $\beta = 1, 2, 3, 4$.

3.5 Formulation microcanonique de la cascade multiplicative et ondelettes optimales

Il est théoriquement possible d'introduire des variables d'injections localisées entre des échelles r et L ($r < L$) :

$$\theta_{r/L}(\mathbf{x}) = \frac{\mathbb{T}_r(\mathbf{x})}{\mathbb{T}_L(\mathbf{x})} \tag{3.26}$$

mais en général, le processus $\theta_{r/L}(\mathbf{x})$ ainsi défini, n'est pas indépendant des processus $\theta_{r/L}(\mathbf{x})$ et $\mathbb{T}_L(\mathbf{x})$. Ce n'est donc pas de cette manière que l'on peut définir une formulation microcanonique de la cascade multiplicative. La solution à ce problème consiste à déterminer une analyse multirésolutions permettant de "contrôler" l'inférence le long des échelles. Etant donnée une ondelette mère Ψ, et un signal s, on définit un opérateur multiéchelles :

$$\mathbb{T}_\Psi\mu(\mathbf{x},r) = \int \|\nabla s\|(\mathbf{y})\Psi(\frac{\mathbf{x}-\mathbf{y}}{r})d\mathbf{y} \tag{3.27}$$

On définit un processus aléatoire $\zeta_{r/L}(\mathbf{x})$ par :

$$\mathbb{T}_\Psi\mu(\mathbf{x},r) = \zeta_{r/L}(\mathbf{x})\mathbb{T}_\Psi\mu(\mathbf{x},L) \tag{3.28}$$

Une ondelette Ψ telle que le processus $\zeta_{r/L}(\mathbf{x})$ est indépendant de $\mathbb{T}_\Psi\mu(\mathbf{x},L)$ est appelée une *ondelette optimale* : sa détermination est délicate [*Delgado Delgado*, 2007; *Pont et al.*, 2011a]. Ainsi, l'optimalité d'une ondelette, et donc d'une analyse multirésolutions, se mesure au degré d'indépendance entre $\zeta_{r/L}(\mathbf{x})$ et $\mathbb{T}_\Psi\mu(\mathbf{x},L)$.

Dans une analyse multirésolutions définie par une ondelette proche d'une ondelette optimale, les relations entre les coefficients père-enfant prennent la forme :

$$\alpha_c = \eta_1\alpha_p + \eta_2 \tag{3.29}$$

avec α_c : coefficient d'ondelette 'child', α_p : coefficient d'ondelette 'parent', η_1,η_2 : variables aléatoires indépendantes de α_c et α_p et indépendantes entre elles. Dans le cas d'une ondelette optimale on a $\alpha_c = \eta_1\alpha_p$ avec η_1 indépendant de α_p. Donc si nous passons aux indices d'échelles j et de position k, les coefficients de l'analyse multirésolutions $\alpha_{j,k}$ s'écrivent :

$$\begin{aligned}
\alpha_{j,k} &= \eta_{j,k}\alpha_{j-1,[k/2]} \\
&= \eta_{j,k}\eta_{j-1,[k/2]}\alpha_{j-2,[k/4]} \\
&= \eta_{j,k}\eta_{j-1,[k/2]}\eta_{j-2,[k/4]}\cdots\alpha_{0,0} \\
&= \prod_{j',k}\eta_{j',[k/2^{j-j'}]}\alpha_{0,0}
\end{aligned} \tag{3.30}$$

pour toutes les orientations i.

3.6 Spectres de singularités des données d'acquisition en Océanographie

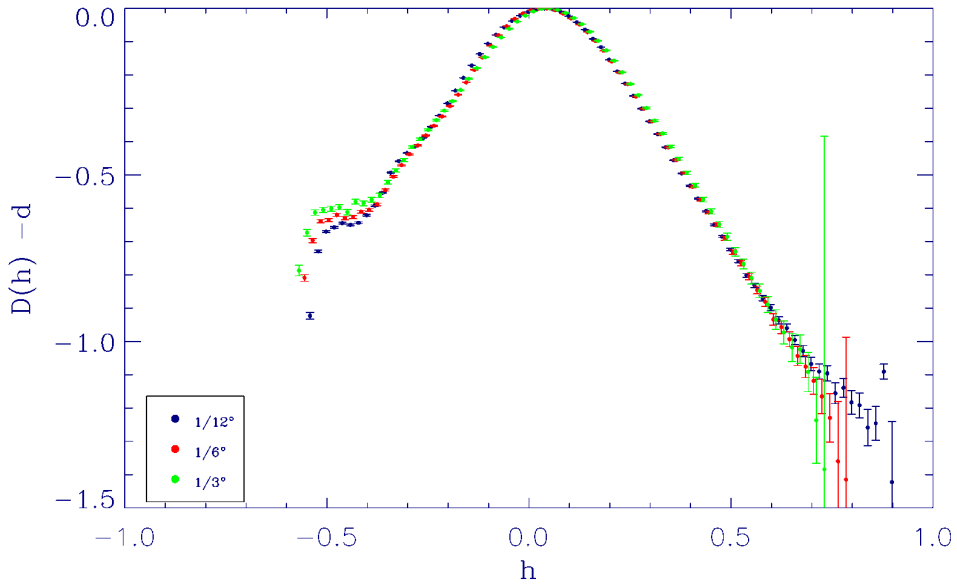

FIGURE 3.2 – *Spectre de singularité obtenu pour les données de TSM à trois différentes résolutions :* $1/12°$ *en bleue,* $1/6°$ *en rouge et* $1/3°$ *en vert. Ce spectre a été calculé à partir de 960 sous-images de* 256×256 *pixels extraites de la base globale TSM MODIS/Aqua correspondant à la période du 01 Janvier 2006 au 31 Décembre 2008 (Ces sous-images ont été sélectionnées pour avoir moins de 5% de données manquantes).*

Le spectre de singularité du produit de TSM MODIS-Aqua est représenté sur la figure 3.2. La forme convexe du spectre de singularité à toutes les échelles calculées est caractéristique de la présence d'une hiérarchie multiéchelles définie par l'équation 3.15 dans le produit de TSM. Ceci montre que le produit de TSM représente bien un écoulement en FDT, et qu'il contient une hiérarchie multifractale prévue par la théorie. Ce résultat autorise l'application de l'approche théorique au processus d'inférence entre les échelles de cette thèse sur les données de TSM.

3.7 Histogrammes conditionnels des coefficients d'ondelettes

L'équation 3.29 définissant la relation entre les coefficients père-enfant peut se réécrire dans le domaine logarithmique :

$$\log_2 |\alpha_c| = \log_2 |\eta_1| + \log_2 |\alpha_p| \tag{3.31}$$

$\eta_2 \approx 0$ pour une ondelette proche de l'optimalité. Ainsi un test d'optimalité consiste à examiner les histogrammes conditionnels $E(\log_2 |\alpha_c| \mid \log_2 |\alpha_p|)$ pour les différents types de coefficients de l'analyse multirésolutions du jeu de données. Pour ce faire, un jeu de 900 imagettes (choisies pour avoir un nombre peu important de données manquantes) du produit TSM MODIS/Aqua global a été extrait pour la période d'étude 2006 - 2008 qui représente la période d'étude.

La figure 3.3 montre que l'ondelette Battle-Lemarié d'ordre 3 calculée avec 41 coefficients centraux produit une bonne approximation de l'ondelette optimale : les dépendances fonctionnelles sont linéaires pour l'approximation et quasiment linéaires pour les coefficients orthogonaux complémentaires (horizontaux, verticaux et diagonaux). Il est à noter que cette ondelette (Battle-Lemarié d'ordre 3) avait déjà produit le même type de résultat sur des données du produit couleur de l'eau MODIS/Aqua (voir [*Pottier*, 2006; *Pottier et al.*, 2008]).

3.8 Article : Motion analysis in oceanographic satellite images using multiscale methods and the energy cascade, H. Yahia *et al.*, 2010

3.8.1 Résumé de l'article (version française)

L'analyse du mouvement dans des signaux complexes est un sujet de première importance. Cependant les approches en traitement d'image classiques, basées sur les hypothèses de conservation ou de conditions de régularité, ont montré leurs limitations inhérentes. Les signaux provenant de la télédétection spatiale en océanographie montrent la complexité du phénomène

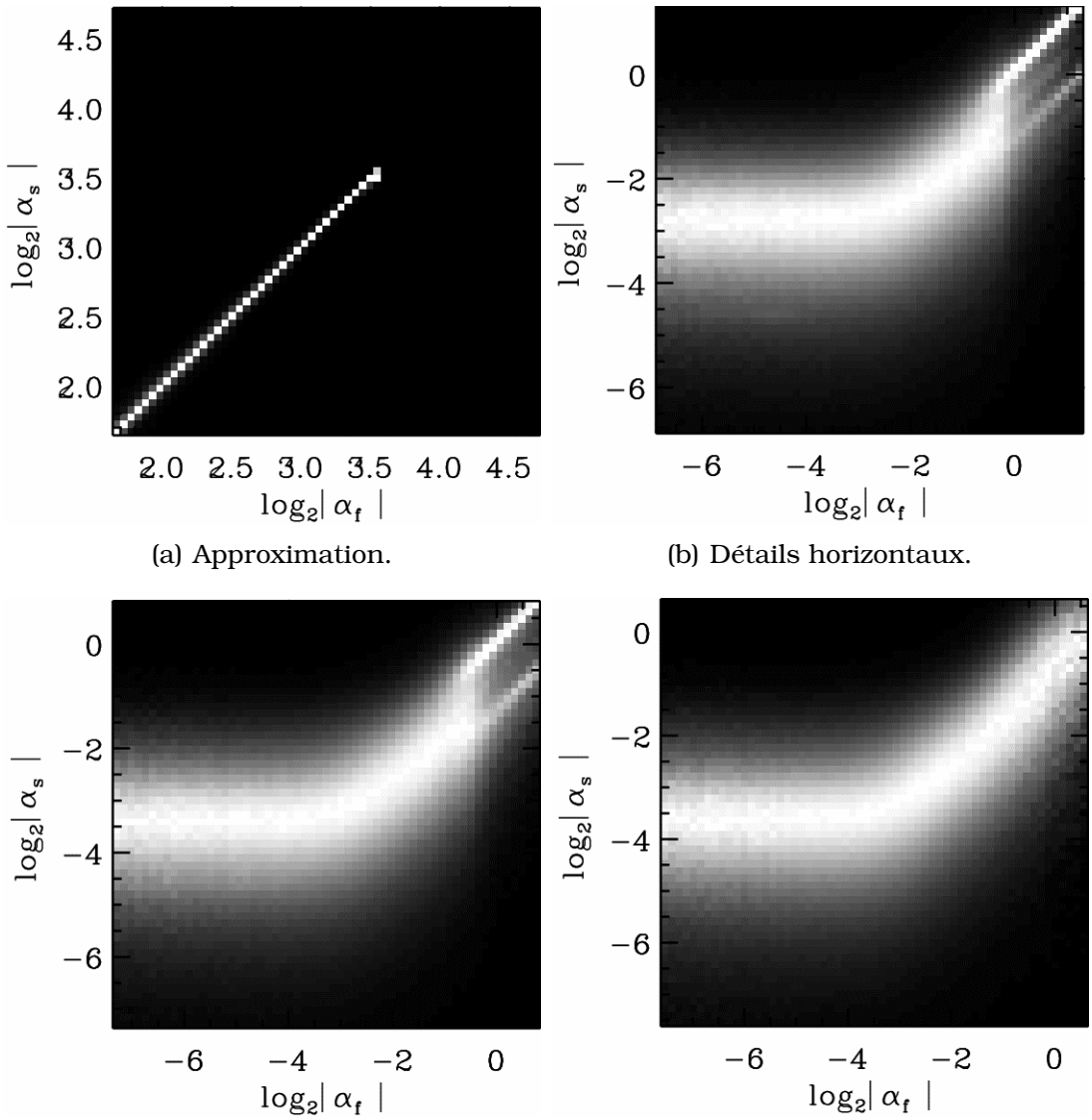

(a) Approximation.

(b) Détails horizontaux.

(c) Détails verticaux.

(d) Détails diagonaux.

FIGURE 3.3 – Histogrammes conditionnels $E(\log_2|\alpha_c| \mid \log_2|\alpha_p|)$ des coefficients d'ondelettes correspondant à l'ondelette Battle-Lemarié d'ordre 3 calculée avec 41 coefficients centraux et utilisée pour le calcul numérique de l'analyse multirésolution. L'axe horizontal correspond aux coefficients d'ondelette père et l'axe vertical aux coefficients d'ondelette enfant.

acquis (un écoulement dans un régime de *turbulence pleinement développée* - FDT) qui est conjugué aux limitations du processus d'acquisition (réflexions solaires, brume, données manquantes etc.). Il y a nécessité pour l'analyse de la dynamique et pour les algorithmes d'obtention associés de refléter les caractéristiques physiques des signaux acquis. Dans cet article, nous montrons que le problème de l'évaluation du mouvement dans des signaux complexes et turbulents peut bénéficier de l'utilisation d'une caractérisation multi-échelle et microcanonique des fronts de transitions. Ainsi l'utilisation de paradigmes appropriés provenant de la physique statistique peut-être associée à une évaluation de la cascade microcanonique de la turbulence par des méthodes de traitement non-linéaire du signal. On obtient ainsi des méthodes radicalement nouvelles pour calculer des champs de mouvement dans ces signaux. Ces approches sont dans un premier temps évaluées sur des données synthétiques d'un modèle de circulation océanique tridimensionnelle et ensuite appliqués sur des données réelles.

3.8.2 Article publié dans *Pattern Recognition*

Référence : Yahia H., J. Sudre, C. Pottier and V. Garçon, 2010 : Motion analysis in oceanographic satellite images using multiscale methods and the energy cascade, *Pattern Recognition*, **43**, 3591-3604, DOI 10.1016/j.patcog.2010.04.011.

Pattern Recognition 43 (2010) 3591–3604

Contents lists available at ScienceDirect

Pattern Recognition

journal homepage: www.elsevier.com/locate/pr

Motion analysis in oceanographic satellite images using multiscale methods and the energy cascade

H. Yahia [a,*], J. Sudre [b], C. Pottier [c], V. Garçon [b]

[a] GeoStat team, INRIA Bordeaux Sud-Ouest, 351 Cours de La Libération, 33405 Talence Cedex, France
[b] LEGOS/CNRS, UMR 5566, 18 Avenue E. Belin, F-31401 Toulouse Cedex 4, France
[c] CNES, DCT/PS/TVI, 18 Avenue E. Belin, 31401 Toulouse Cedex 9, France

ARTICLE INFO

Article history:
Received 3 July 2009
Received in revised form
24 February 2010
Accepted 14 April 2010

Keywords:
Image processing
Computer vision
Statistical models
Motion analysis
Complex signals
Statistical physics
Turbulence
Wavelets
Multiscale models

ABSTRACT

Motion analysis of complex signals is a particularly important and difficult topic, as classical Computer Vision and Image Processing methodologies, either based on some extended conservation hypothesis or regularity conditions, may show their inherent limitations. An important example of such signals are those coming from the remote sensing of the oceans. In those signals, the inherent complexities of the acquired phenomenon (a fluid in the regime of *fully developed turbulence*—FDT) are made even more fraught through the alterations coming from the acquisition process (sun glint, haze, missing data etc.). The importance of understanding and computing vector fields associated to motion in the oceans or in the atmosphere (e.g.: cloud motion) raises some fundamental questions and the need for derivating motion analysis and understanding algorithms that match the physical characteristics of the acquired signals. Among these questions, one of the most fundamental is to understand *what* classical methodologies (e.g.: such as the various implementations of the optical flow) are missing, and how their drawbacks can be mitigated. In this paper, we show that the fundamental problem of motion evaluation in complex and turbulent acquisitions can be tackled using new multiscale characterizations of *transition fronts*. The use of appropriate paradigms coming from Statistical Physics can be combined with some specific Signal Processing evaluation of the *microcanonical cascade* associated to turbulence. This leads to radically new methods for computing motion fields in these signals. These methods are first assessed on the results of a 3D oceanic circulation model, and then applied on real data.

© 2010 Elsevier Ltd. All rights reserved.

1. Introduction and state of the art

The analysis of motion information in temporal sequences of remotely sensed data constitutes an important theoretical and applicative domain in Computer Vision. In Oceanography (and Earth Observation) for example, the wealth and availability of temporal sequences of remotely sensed images at various spatial, temporal and spectral resolutions have deeply renewed the field [1]. These temporal image sequences convey key information about ocean dynamics (motion of passive tracers, vertical mixing etc.) [2–6]. Unfortunately, most existing methods in analyzing motion in Computer Vision do not take into account key features of ocean dynamics: turbulence and intermittence, which contribute importantly to the shape and motion of observed and acquired coherent structures. Besides, the specificities of these remotely sensed acquisitions (sun glint, haze, missing data etc.) lead to question the pertinence of existing Computer Vision approaches to analyze motion in these types of image sequences. Fig. 1 illustrates some of the difficulties inherently bound to these images.

Among the existing algorithms proposed for the motion analysis of fluid flow in temporal sequences, one finds methodologies based on *correlation methods* that try to estimate a vector field assumed to be locally constant in small windows $\mathcal{W}(\mathbf{x})$ centered at various pixels $\mathbf{x}$ in the image. The correlation is expressed by defining a similarity criterion, which can be implemented in Fourier space, leading to simple computational algorithms. These techniques are sometimes known under the name PIV (particle image velocity) for the visualization of motion flow [7]. We also mention particularly in our context the correlation-relaxation-labeling method [8] that was developed for SST motion. However, the locality assumption they use does not match the physical reality of turbulent fluid flows in remotely sensed images of the oceans, making them inappropriate in an operational context, and it is difficult to incorporate an *a priori* knowledge about the motion.

Another vast class of algorithms that has led to considerable extent these past few years, notably for the analysis of flow motion, hinges on *luminance conservation* hypothesis coupled with various types of *regularity constraints*. Basically, these

* Corresponding author. Tel.: +33 (0) 5 24574138.
E-mail addresses: hussein.yahia@inria.fr (H. Yahia), joel.sudre@legos.obs-mip.fr (J. Sudre), claire.pottier@cnes.fr (C. Pottier), veronique.garcon@legos.obs-mip.fr (V. Garçon).

0031-3203/$ - see front matter © 2010 Elsevier Ltd. All rights reserved.
doi:10.1016/j.patcog.2010.04.011

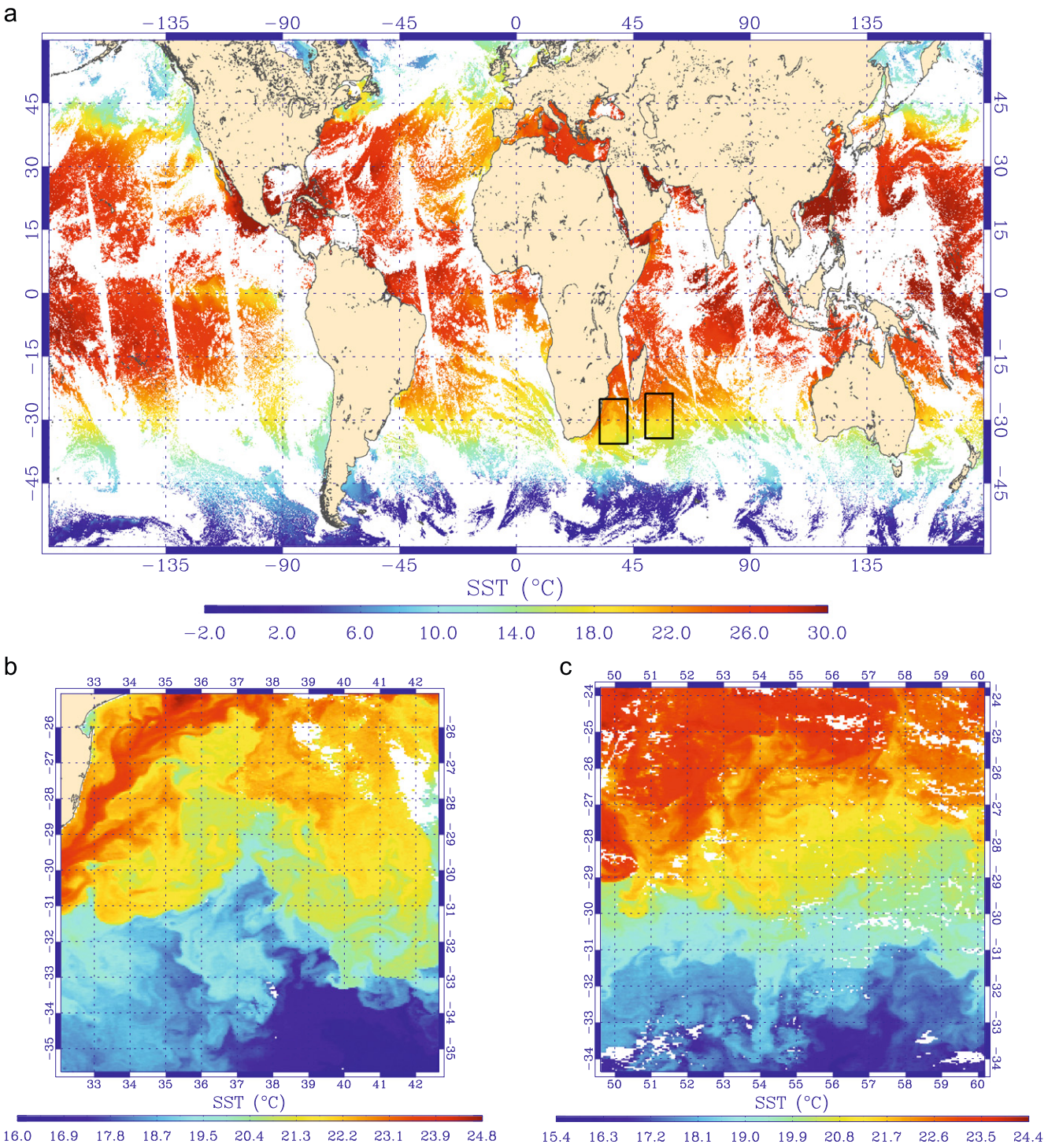

Fig. 1. Top: global mapping of Sea Surface Temperature (SST) acquired by MODIS satellite on August 2, 2007. Pixel values denote the temperature, in celsius degrees, of the upper skin layer of the oceans. Image also displays longitudes (x-axis) and latitude (y-axis). Note the missing data due to both acquisition process (scanning of the Earth's surface with large periodical discrepancies) and cloud cover. Spatial resolution: 4 kms. We selected two subimages, east of the southeast part of Africa (black rectangles) which are zoomed and displayed below (subimages (b) and (c)). **Bottom:** zooming on the subimages shows the complex mixture and coherent structures associated to the dynamics of the upper layer of the ocean (colormap of the two subimages is renormalized).

methods consist in minimizing an *energy functional* defined in the image domain Ω and made of two terms:

1. an energy functional expressing *luminance conservation* during motion, which leads, when written in differential form, to an *apparent motion constraint*,
2. a *regularization term* expressing spatial constraints on the set of possible solutions.

A typical example for the apparent motion constraint is the classical

$$E_1(I,\mathbf{v}) = \int_\Omega \varphi_1\left(\nabla I(\mathbf{x})\cdot\mathbf{v}(\mathbf{x}) + \frac{\partial I}{\partial \mathbf{t}}(\mathbf{x})\right) d\mathbf{x} \quad (1)$$

($\mathbf{x}$: pixel location, Ω: domain in the image plane, I: grey-level intensity, $\mathbf{v}(\mathbf{x})$: vector field (function of spatial position $\mathbf{x}$), φ_1: attenuation function (often the L^2 norm) [9,10]), while

regularizing terms are often written in the form of integrals of spatial derivatives of the vector field $\mathbf{v}(\mathbf{x})$. Generically, the regularization term has the form

$$E_2(\mathbf{v}) = \alpha \int_{\Omega} \varphi_2 \left(\mathbf{v}(\mathbf{x}), \ldots, \frac{\partial^k \mathbf{v}}{\partial \mathbf{x}^k}(\mathbf{x}), \ldots \right) \mathrm{d}\mathbf{x} \quad (2)$$

($\alpha \in [0,1]$: weighting parameter, φ_2: attenuation function). It is not possible to review here the immense literature about optical flow, but we notice that, in relation with the case of turbulent and irregular motion we are interested in, and since the seminal work of Horn and Schunk [11], considerable work has been done to overcome some of the limitations inherent to the approach, notably in extending the formalism to the framework of multiresolution representation of data (to try to lessen the small displacement hypothesis) [12–16], and in modifying the regularizing energy functional to allow more irregular vector field solutions [17–20]. See also [60–65]. Notable extensions of that approach, intended to better approximate fluid flow motion, consisted in deriving new conservation laws starting from continuity equations in the motion of fluids [21]. Algorithms that exploit those ideas can be implemented in an operational context [22] but they need, however, precise preprocessing calibration. In some particular types, an exact conservation law can be derived for the apparent motion of the fluid [23]. Another important extension to luminance conservation models has also been geared towards the development of *div-curl* regularization, which basically consists in modifying the regularization term to incorporate higher order derivatives of $\mathbf{v}(\mathbf{x})$ related to divergence and rotational phenomena associated to fluid motion [24,25]. However, fundamentally, in the case of turbulent fluid flow motion and the complex phenomena associated to remote sensing acquisition processes (atmospheric correction, missing data, solar glint, haze etc.), any luminance conservation hypothesis can legitimately be strongly questioned, most notably if a large number of temporal acquisitions are to be used to evaluate the vector field: the variations in luminance from one frame to another are highly *unpredictable*, and regularizing conditions do not reflect physical properties specially in the case of large Reynolds numbers [26].

Parameter estimation methods have also been proposed for dense motion estimation, like those based on vorticity discretization [27,28]. They have been extended to generate fields that try to better satisfy the Navier–Stokes equations, by estimating a vector field satisfying an *a priori* evolution law [29]. The determination of characteristic points or features used by these various methodologies often makes assumptions on regularity of the flow, like in [30]. Similarly, when contour evolution of deformable models is sought, like in [31], the level-set formulations used in the evolution model are only non-multiscale approximations of coherent structures characteristics and motions, written with level-set evolution models that do not take into account the turbulent nature of the flow. Paris and Frisch [32], in a very important paper, have put into evidence, in the case of FDT (fully developed turbulence, i.e. turbulent fluid motion with very high Reynolds Number [33]), a key observation of particular interest in the analysis of the motion in oceanographic image sequences acquired by satellites. Indeed they showed a fundamental relationship between a complex arrangement of hierarchical geometric structures associated to flow motion and the spectrum of singularity exponents related to structure functions. Consequently, it makes sense to obtain information about flow motion from the knowledge of the singularity spectrum. This has motivated the development of WTMM (Wavelet Transform Modulus Maxima) methodology by Arneodo and collaborators [34–36] which is fundamentally statistically based, (i.e. *singularity exponents* are not computed at each pixel location $\mathbf{x}$, but are related to global expectations of intensive physical variables).

To extend the analysis of turbulent flows towards an evaluation of singularity exponents at each point $\mathbf{x}$ in the signal domain, it has been shown recently [37–39] that the notion of *transition* in acquisition signals of complex and turbulent phenomena is related to the notion of *information content* in a way that necessitates a finer microlocal analysis of the natural multiscale functionals associated to these signals, such as the multiscale measures

$$\mu(\mathcal{B}_{\mathbf{r}}(\mathbf{x})) = \int_{\mathcal{B}_{\mathbf{r}}(\mathbf{x})} \|\nabla \mathbf{s}\|(\mathbf{y})\, \mathrm{d}\mathbf{y} \quad (3)$$

with: $\mathbf{s}(\mathbf{x})$: complex signal, defined over a compact domain Ω in $\mathbb{R}^d$, $\mathcal{B}_{\mathbf{r}}(\mathbf{x})$: open ball of radius $\mathbf{r}$ (the scale of observation) centered at pixel location $\mathbf{x}$ in the signal domain Ω. The limiting behaviour of $\mu(\mathcal{B}_{\mathbf{r}}(\mathbf{x}))$, as $\mathbf{r} \to 0$, if it can be accurately computed at each pixel location $\mathbf{x}$, provides information that generalizes appropriately, in the case of complex multiscale and turbulent signals, the classical notions of *edge* or *border* that forms the basic building block of many Image Processing and Pattern Recognition approaches [40]. Moreover, as it will become apparent in this work, the pointwise evaluation of singular exponents unlocks the localization of the geometric hierarchy associated to the dynamics of the flow (in the case of FDT). One important aspect of signals associated to acquisition of turbulent and complex phenomena is that the notion of transition, if properly formulated from paradigms in Statistical Physics, allows the determination of specific *geometric manifolds* in the signal domain, such as the *Most Singular Manifold*, that conveys key critical information about motion. This article develops on this idea, by showing that the determination of the motion field in oceanographic image sequences acquired by satellites can be done using only one *frame* in the temporal sequence plus extra spatial information at lower resolution, hence eliminating the problems related to temporal luminance conservation and lowering considerably all computation difficulties coming from the presence of noise and acquisition artefacts. This achievement can be done by showing that the framework of *reconstructible systems*, which comes from reconstruction formula and the notion of *Most Singular Manifold*, can be combined with the idea of *microcanonical energy cascade*. Reconstructible systems refer to signals that can be generated at any arbitrary precision using the most informative subset in the turbulent flow. Recent work about the *Microcanonical Multiscale Formalism* [41] has shown that these ideas can be used to evaluate a first order approximation of the *geostrophic stream function*. The present article provides substantial improvements on the subject, by using the microcanonical energy cascade to solve the *orientation problem* of the vector field, and by generalizing the method to non-geostrophic motion.

The Microcanonical Multiscale Formalism, or MMF, is reviewed in Section 2, along with the framework of reconstructible systems. In Section 3 the notion of optimal wavelet is discussed in the natural context of the energy cascade. Section 4 develops on the main idea presented in this work: the use of the optimal wavelet in conjunction with recontructible systems to solve the *orientation problem*. Results, discussion and conclusion end the paper. In particular, the novel method is first applied on the output of a 3D oceanic circulation model to evaluate the quality of the results on synthetic data, then on real datasets coming from remote sensing.

2. The microcanonical multiscale formalism

In the microcanonical approach to multiscale properties of complex signals [37], it is assumed that, at every point $\mathbf{x}$ in the signal domain, or equivalently in our case, at each pixel location $\mathbf{x}$

in Ω, the measure μ defined by equation (3) shows the limiting behaviour:

$$\mu(\mathcal{B}_{\mathbf{r}}(\mathbf{x})) = \int_{\mathcal{B}_{\mathbf{r}}(\mathbf{x})} \|\nabla \mathbf{s}\|(\mathbf{y})\, d\mathbf{y} = \alpha(\mathbf{x})\mathbf{r}^{h(\mathbf{x})} + o(\mathbf{r}^{h(\mathbf{x})})(\mathbf{r}\to 0) \quad (4)$$

As shown in [42–44], this limiting behaviour is characteristic of natural images and complex signal acquisitions. The coefficient $h(\mathbf{x})$ is a *singular exponent* at point $\mathbf{x}$, and can be computed for instance using log–log estimation on wavelets projections [45,37]. To understand the fundamental concept of *singular exponent* and its significance in the processing of complex signals, we note that the power-law behaviour of the measure μ in Eq. (4) is a classical observation in Statistical Mechanics for intensive variables (temperature, energy dissipation etc.) around critical points. That power-law behaviour is an indication of scale invariance, such as the one observed in higher-order phase transitions [46–48]. Systems characterized by the same value of singular exponents form a particular universality class: the macroscopic properties of the system are completely determined by the values of the exponents, independently of the particular system considered. Thus, in this approach to Signal Processing, every point is considered as critical, with a continuum of possible values for measuring criticality. The classical notion of *edge* or *border* in Computer Vision would correspond, in this analogy, only to first-order phase transitions. Instead of this, the consideration of a full continuum of potential values for critical points allows the definition of a generalized notion of edge much better suited to the case of turbulent and complex signals. This is illustrated in Fig. 2, where we display the computation of singular exponents for the subimages of Fig. 1. The image illustrates how the singular exponents quantify the transition values of pixels belonging to coherent structures.

A proper and accurate evaluation of the singularity exponents $h(\mathbf{x})$ leads to the consideration of the geometric arrangement of the sets

$$\mathcal{F}_h = \{\mathbf{x}\in\Omega | h(\mathbf{x}) = h\}, \quad (5)$$

arrangement which is naturally associated to the notion of *information content* in the signal [38,39]. Thus, in the framework of *reconstructible systems*, it should be possible to recover the signal from the set of its highest transition fronts. The points in the image domain which contribute to the highest transitions, i.e. those which maximize, in a statistical sense, the information contained in the signal, are precisely those points having the lowest (and negative) singular exponents, that is to say the points belonging to the *Most Singular Manifold* $\mathcal{F}_\infty = \{\mathbf{x}\in\Omega | h(\mathbf{x}) = h_\infty\}$ with $h_\infty = \mathrm{Min}(h(\mathbf{x}))$. The hierarchy of sets $\mathcal{F}_h$ describes the geometric arrangement of information content in the signal, with a most informative content located inside the set $\mathcal{F}_\infty$. For signals that are acquisitions of fluids under turbulent motion, like the oceans, this hierarchy is the one associated to the spectrum of exponents in the canonical formalism. Consequently, as shown in [49], there must be a reconstruction operator which enables the reconstruction of the whole signal given the restriction of its gradient vector field to the set $\mathcal{F}_\infty$. The reconstruction $\mathcal{G}(s)$ can be explicitly determined in Fourier space [49]:

$$\mathcal{G}(\widehat{\nabla s|_{\mathcal{F}_\infty}})(\mathbf{f}) = \frac{\langle \sqrt{-1}\mathbf{f} | \widehat{\nabla s|_{\mathcal{F}_\infty}} \rangle}{\|\mathbf{f}\|^2}. \quad (6)$$

($\mathbf{f}$: frequency vector, $\langle\cdot|\cdot\rangle$: scalar product in $\mathbb{C}^2$, $\widehat{\ }$: Fourier transform). This reconstruction formula shows that the whole signal can be reconstructed given the gradient restricted to the set $\mathcal{F}_\infty$ of *most informative points*. This is the framework of *reconstructible systems*.

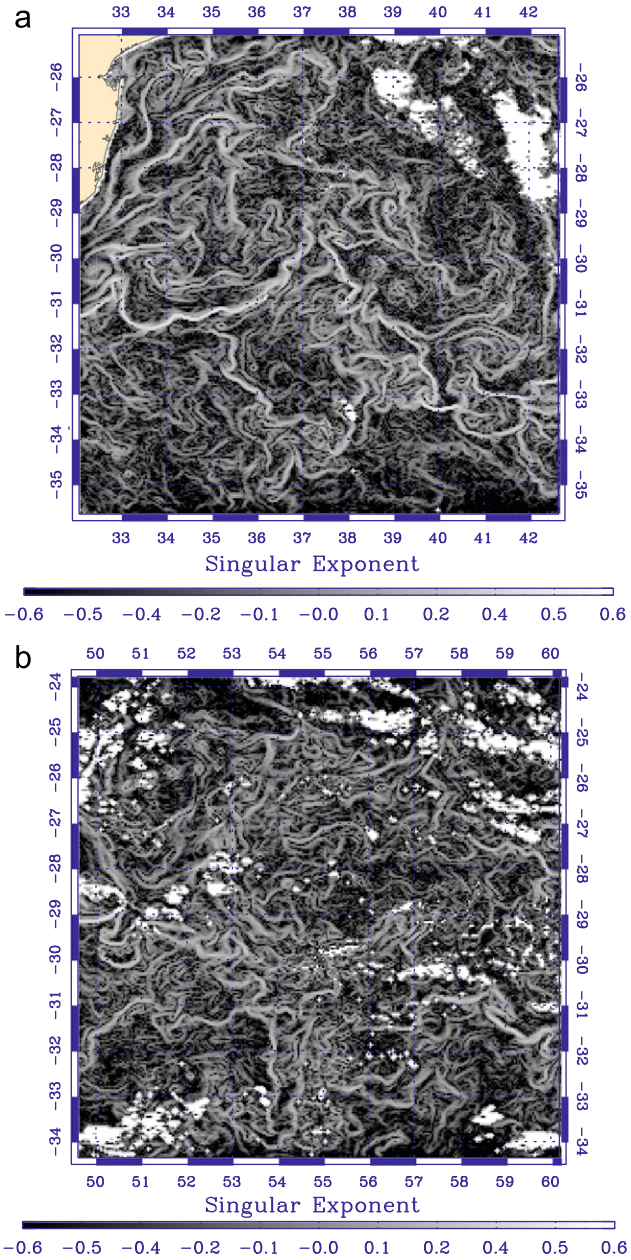

Fig. 2. Computation of singular exponents on both subimages shown in Fig. 1. The singular exponents quantify precisely the amount of transition around a point, and have been shown to be deeply connected to the turbulent motion. Negative singular exponents convey the most informative part of the signal, and they are clearly related to the borders and delimitations of structures.

3. Scale invariance and the energy cascade

In the motion of a fluid flow, the ratio between the largest scale L and the viscous dissipation scale η (corresponding to the smallest scale, where the energy is dissipated) is

$$\frac{L}{\eta} \sim \mathrm{Re}^{3/4} \quad (7)$$

(Re: Reynolds Number) which prevents the numerical simulation of all phenomena at all intermediary scales in a regular cube of size L ([50] and references herein). The energy is injected in the system at the largest scale L, entirely dissipated at viscous scale η, and, in-between, it crosses all the intermediary scales, and is responsible for the creation of a self-similar random distribution of vortices and other complex coherent structures, which

ultimately appear as a complex arrangement of fronts and oceanographic structures in acquired images of the oceans. The intermediary structures let the energy pass through the scales, where it is terminally dissipated at scale η. The dynamics of the flow is governed by the cascading process, which must be, in return, properly evaluated to assess any information about the motion. It turns out that a proper modelling of the cascading aspects in turbulence can be achieved through *multiplicative cascades* [50].

The cascading process can be retrieved easily by considering the random variables

$$\varepsilon_r(\mathbf{x}) = \mu(\mathcal{B}_{\mathbf{r}}(\mathbf{x})) = \int_{\mathcal{B}_{\mathbf{r}}(\mathbf{x})} \|\nabla \mathbf{s}\|(\mathbf{y})\, d\mathbf{y} \tag{8}$$

so that, for two different scales $\mathbf{r}_1$ and $\mathbf{r}_2$, one has, for the distributions of the variables (denoting dP_X the probability law of a random variable X):

$$dP_{\varepsilon_{r_1}} = dP_{\eta_{r_1/r_2}\varepsilon_{r_2}}. \tag{9}$$

This equation relating the distributions of random variables ε_r defines the random variables η_{r_1/r_2} which are such that ε_{r_2} and η_{r_1/r_2} are independent random variables. The variables η_{r_1/r_2} do not depend on the scales $\mathbf{r}_1$ or $\mathbf{r}_2$ but they only connect their ratio [51]. Eq. (9) shows that the statistics of variables ε_r split into two parts: one, governed by η_{r_1/r_2} describes the properties under change of scale, and the other ε_{r_2} takes into account the properties at a given scale of reference $\mathbf{r}_2$. The multiplicative cascade property becomes mathematically apparent when considering three scales $\mathbf{r}_1 < \mathbf{r}_2 < \mathbf{r}_3$ for one has

$$dP_{\eta_{r_1/r_3}} = dP_{\eta_{r_1/r_2}\eta_{r_2/r_3}} \tag{10}$$

hence for the generation of indefinitely divisible laws.

Eqs. (9) and (10) relate only the laws of the distributions, and would not imply any corresponding relation *pointwise*. However, one can formally define random variables

$$\theta_{r_1/r_2}(\mathbf{x}) = \frac{\varepsilon_{r_1}(\mathbf{x})}{\varepsilon_{r_2}(\mathbf{x})} \tag{11}$$

But in general, the variables $\theta_{r_1/r_2}(\mathbf{x})$ defined by that equation are such that there is no independence between $\theta_{r_1/r_2}(\mathbf{x})$ and $\varepsilon_{r_2}(\mathbf{x})$. To access the cascading properties of the signal pointwise (also called *the microcanonical cascade*), the concept of *optimal wavelet* can be introduced [51]. The random variables $\varepsilon_r(\mathbf{x})$ carry the multiscale properties of the signal, but their definition does not allow to extract from them the cascading properties pointwise, i.e., the microcanonical cascade. Another way of tackling this problem is to consider, for an admissible wavelet ψ, and the original signal $\mathbf{s}$, the multiscale operator

$$\mathcal{T}_\psi[\mathbf{s}](\mathbf{x},\mathbf{r}) = \int \mathbf{s}(\mathbf{y})\psi\left(\frac{\mathbf{x}-\mathbf{y}}{\mathbf{r}}\right) d\mathbf{y} \tag{12}$$

Exactly like in Eq. (11) we define the random variables $\zeta_{r_1/r_2}(\mathbf{x})$ by

$$\mathcal{T}_\psi[\mathbf{s}](\mathbf{x},\mathbf{r}_1) = \zeta_{r_1/r_2}(\mathbf{x})\mathcal{T}_\psi[\mathbf{s}](\mathbf{x},\mathbf{r}_2) \tag{13}$$

but, then, considering the wavelet ψ, as a parameter, we can ask for wavelets ψ for which the variables $\zeta_{r_1/r_2}(\mathbf{x})$ are independent of $\mathcal{T}_\psi[\mathbf{s}](\mathbf{x},\mathbf{r}_2)$. If such wavelet can be determined, it is called an *optimal wavelet*. If an optimal wavelet can be found, it has the fascinating potential of unlocking the signal's microcanonical cascading properties through simple wavelet decomposition. In other words, the turbulent properties of the signal become apparent from the optimal wavelet decomposition. In particular, all the complex aspects of motion should be derived from the optimal wavelet decomposition. This is the primary idea of this work. Unfortunately, the systematic determination of an optimal wavelet, for a given signal, is an extremely difficult and unsolved problem. In this work, we will show by simply considering *approximations* of the optimal wavelet decomposition that we are able to enhance considerably the determination of the motion field in turbulent fluid flow acquisitions of the oceans. This is described in the next sections.

4. Descending motion information through an optimal wavelet

In [41,52], authors presented a new method for the evaluation of the (geostrophic) oceanic motion field from a temporal sequence of Sea Surface Temperature satellite images. The method consists in using the framework of reconstructible systems (recalled in Section 2) to generate a first approximation of the stream function associated to oceanic flow in complex signals of Sea Surface Temperature (SST) satellite acquisitions. Once the stream function is computed, a vector field associated to oceanic motion is automatically generated by computing the gradient of the approximated stream function and turning it by a $\pi/2$ angle. The method is remarkable from the following points of views:

1. it makes use of a single temporal acquisition in an SST image sequence acquired by satellite, as opposed to all other types of algorithms based on luminance conservation described in Section 1,
2. it is robust and consistent w.r.t. acquisition artefacts and missing data.

However, the algorithm suffers from a main limitation: the orientation of the resulting vector field is not determined properly. This is the *orientation problem*. The drawback comes from the fact that the gradient is rotated by a fixed right angle. In other words, only the straight line that supports the motion is determined, but the direction on that line remains unknown. We show that using an approximation of the microcanonical cascade does help fix the orientation problem.

The idea is to propagate a correct orientation through the microcanonical cascade, in the form of scalar products with vector data acquired at the same time but with lower spatial resolution. The method is described in the following subsections.

4.1. Approximation of the microcanonical cascade

The exact determination of the optimal wavelet for a given dataset is difficult in general, and there is no systematic algorithm up to this date [53]. Consequently, we will approximate the optimal wavelet. In our experiments, we took sub-images of MODIS SST images (see Fig. 1) and made experiments with Haar, compact-supported Daubechies and order 3 Battle-Lemarié wavelets [53].

In the wavelet analysis of 2D signals, the multiresolution analysis can be seen in the form of a "genealogy tree": wavelets coefficients in one of the three orientations (horizontal, vertical and diagonal details) and at a given scale resolution are members of a same "family": a "son" coefficient has two cousins, corresponding to the other two orientations (at the same scale and spatial localization). A "son" coefficient has a "father" at lower scale and two "uncles" (two other orientations) and a "father" has four "sons" (see [45,53]). The three orientations correspond to: the signal's approximations, the horizontal and vertical details associated to the multiresolution analysis (approximation subspaces and their orthogonal complements). We

subscript the wavelet coefficients by their "genealogy" in the tree: α_f for the father α_s for the son etc.

Persistence along the scales implies a relation of the form

$$\alpha_s = \eta_1 \alpha_f + \eta_2 \tag{14}$$

with η_1 and η_2 being random variables independent of α_s and α_f and also independent of each other. For the optimal wavelet, one would have $\alpha_s = \eta \alpha_f$ [53], which implies $\log|\alpha_s| = \log_2|\eta| + \log_2|\alpha_f|$. So, a test for optimality consists in examining the conditional histograms $E(\log_2|\alpha_s||\log_2|\alpha_f|)$ for the different types of coefficients in the wavelet-based multiresolution analysis of our dataset. In this experiment, we took a set of 900 subimages (chosen for having few missing data) in the Modis dataset of all the years 2006–2008 (Fig. 1 shows the acquisition of August 2, 2007, however the 900 subimages are taken in the whole years of 2006–2008 of Modis data).

Fig. 3 shows that order 3 Battle-Lemarié wavelets with 41 central coefficients provide a good approximation of the optimal wavelet: the functional dependencies are almost linear both for the approximation and orthogonal complements, with a reasonable loss of linearity in the orthogonal complements. Consequently, we take the order 3 Battle-Lemarié wavelets with 41 central coefficients as our approximation of the optimal wavelet. Note that the exact optimal wavelet is fully dependent on a given signal.

4.2. The algorithm

Our goal is to compute the motion field $\mathcal{U}(\mathbf{x})$ of ocean dynamics at the high resolution of MODIS SST (Sea Surface Temperature) data (spatial resolution: 4 kms) using one single image (as opposed to the various optical flow and estimation techniques described in Section 1, which make use of several temporal occurrences around the frame at time t), and which resolves the orientation problem by using auxiliary data at larger resolution.

The key idea of the method lies in Eq. (13) which can be used by replacing the signal $\mathbf{s}$ by any signal representing a scalar quantity subject to the microcanonical cascade. In particular, we use the microcanonical cascading of scalar products to resolve the orientation problem.

We make use of the motion field available at much larger resolution (1/4 longitudinal degrees), and acquired at a near temporal occurrence, given from altimetric data [54]. Let $\mathbf{w}(\mathbf{x},\mathbf{r}_2)$ be this vector field, available at scale $\mathbf{r}_2 \gg \mathbf{r}_1$, where $\mathbf{r}_1$ is the high resolution of MODIS SST data at which we want to compute the motion field. Let $\mathbf{s}(\mathbf{x}, \mathbf{r}_1)$ be a signal acquired at high resolution $\mathbf{r}_1$; in our experiments, $\mathbf{s}(\mathbf{x}, \mathbf{r}_1)$ can be the SST (Sea Surface Temperature) itself or another signal computed from it: for instance the values of singularity exponents or the gradient's norms of the singularity exponents. We perform multiresolution analysis on this signal to compute the wavelet projections $\mathcal{T}_\psi[\mathbf{s}](\mathbf{x},\mathbf{r}_j)$ with order 3 Battle Lemarié approximated optimal wavelet ψ. We obtain then a projected signal:

$$\mathcal{T}_\psi[\mathbf{s}](\mathbf{x},\mathbf{r}_j) = \sum_{n \in \mathbb{Z}} \langle \mathbf{s}|\psi_{j,n}\rangle \psi_{j,n} \tag{15}$$

($\psi_{j,n}$: scaled and translated wavelet ψ at resolution $\mathbf{r}_j$). When resolution $\mathbf{r}_2$ is reached, we compute the singular exponents $h_{r_2}(\mathbf{x})$ at resolution $\mathbf{r}_2$, from which we determine the Most Singular Manifold at resolution $\mathbf{r}_2$: $\mathcal{F}_\infty^{\mathbf{r}_2}$. Using the reconstruction formula (6), an approximated stream function at resolution $\mathbf{r}_2$ can be generated using the vector field $\mathbf{v}^\perp(\mathbf{x},\mathbf{r}_2)$ which is just the *normal field* of the submanifold $\mathcal{F}_\infty^{\mathbf{r}_2}$. In other words, $\mathbf{v}^\perp(\mathbf{x},\mathbf{r}_2)$ is the unitary vector field perpendicular to $\mathcal{F}_\infty^{\mathbf{r}_2}$. The approximated stream function at resolution $\mathbf{r}_2$ is given in Fourier space by the formula:

$$\widehat{\mathcal{N}_{\mathbf{r}_2}}(\mathbf{f}) = \frac{\langle \sqrt{-1}\mathbf{f}|\mathbf{v}^\perp(\mathbf{x},\widehat{\mathbf{r}_2})|_{\mathcal{F}_\infty^{\mathbf{r}_2}}\rangle}{\|\mathbf{f}\|^2}. \tag{16}$$

The vector field $\mathcal{N}_{\mathbf{r}_2}$ is defined at altimetry resolution $\mathbf{r}_2$ and is a first order approximation of the stream function at that scale. Then, we can compute scalar products

$$\langle \mathbf{w}(\mathbf{x},\mathbf{r}_2)|\mathcal{N}_{\mathbf{r}_2}(\mathbf{x})\rangle \tag{17}$$

with the given altimetry vector field $\mathbf{w}(\mathbf{x},\mathbf{r}_2)$ and test for the negativity of these scalar products: whenever such a scalar product is negative at a point $\mathbf{x}$, the vector is changed in its opposite $-\mathcal{N}_{\mathbf{r}_2}$. Let $\mathcal{M}(\mathbf{x},\mathbf{r}_2)$ the new vector field obtained this way. Then, a new *oriented stream function* is generated in Fourier space using the reconstruction formula:

$$\widehat{\mathcal{O}_{\mathbf{r}_2}}(\mathbf{f}) = \frac{\langle \sqrt{-1}\mathbf{f}|\mathcal{M}(\mathbf{x},\widehat{\mathbf{r}_2})|_{\mathcal{F}_\infty^{\mathbf{r}_2}}\rangle}{\|\mathbf{f}\|^2}. \tag{18}$$

That low-resolution stream-function is then back-projected through the approximated optimal wavelet to obtain an *oriented stream function* at the higher SST resolution $\mathbf{r}_1$ (Eq. (15)): $\mathcal{O}_{\mathbf{r}_1}(\mathbf{x})$. As a result, we take as *unitary oriented motion field* at SST resolution $\mathbf{r}_1$ the vector field

$$\mathcal{U}(\mathbf{x}) = \left(\frac{\nabla \mathcal{O}_{\mathbf{r}_1}(\mathbf{x})}{\|\nabla \mathcal{O}_{\mathbf{r}_1}(\mathbf{x})\|}\right)^\perp \tag{19}$$

perpendicular to $\nabla \mathcal{O}_{\mathbf{r}_1}(\mathbf{x})$.

The basic idea behinds this algorithm ("*use optimal cascading to decrease spatial resolution, use motion information available at lower resolution, then go and carry that information back to higher spatial resolution using the cascade to perform corrections*") can be declined in several ways. First, the choice of the cascade itself may be subject to experimentation (on can use an optimal wavelet associated to the signal itself or an optimal wavelet associated to the singularity exponents' gradient norms for instance). Second, one can perform back-cascading on the stream function as presented above, or on a new signal generated at lower spatial resolution, and defined by the scalar product of the altimetry vectors $\mathbf{w}(\mathbf{x},\mathbf{r}_2)$ and the gradient to the stream function; once that scalar product is back-projected at higher resolution, use its sign to change the orientation of a stream function computed directly at high resolution (or re-orient directly the singularity exponents's gradients – a very good solution whenever the spatial resolution makes the geostrophic approximation no longer valid -). We found that latter variant more accurate in our experiments.

In the following two sections, we apply the methods on two types of data: first, on the output of a 3D oceanic circulation model to evaluate the performance of the method, then on real remotely sensed data.

5. Results on synthetic ROMS data

5.1. Model description

The hydrodynamic model is the Regional Ocean Modelling System (ROMS). The reader is referred to [55,56] for a more complete description of the model. It simulates the salient features of the large-scale circulation patterns as well as the coastal upwelling features of the marine ecosystem. It is a split-explicit and free-surface model which considers the Boussinesq and hydrostatic assumptions when solving the primitive equations. This model has been adapted to the Benguela upwelling subregion [57,58]. We are using here the most recent configuration covering the northern and southern Benguela system of Veitch et al. [59]. The model is discretized in the vertical on a sigma or topography—following stretched coordinate system. The

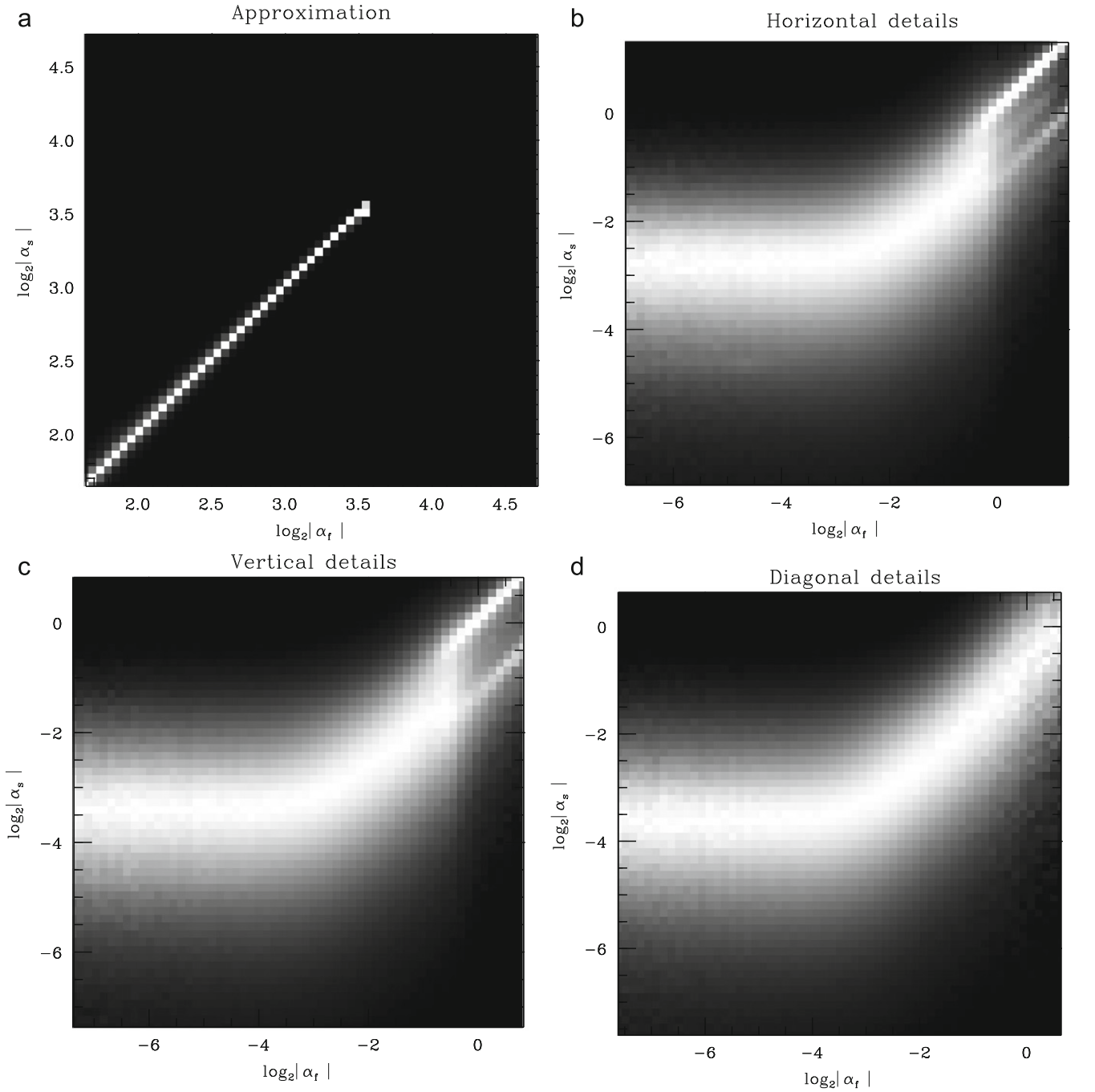

Fig. 3. Conditional histograms $E(\log_2|\alpha_s||\log_2|\alpha_f|)$ made with 900 subimages extracted from a 2006–2008 MODIS SST dataset. The horizontal axis corresponds to the father and the vertical to the sons. The wavelet used for this experiment is the order 3 Battle-Lemarié wavelet with 41 central coefficients. **Top:** approximation coefficients are depicted on the left image, horizontal details (orthogonal complements) are depicted on the right image. **Bottom:** vertical coefficients are depicted on the left image, diagonal details are depicted on the right image (both correspond to orthogonal complements in the multiresolution analysis).

simulation employs the 2-way embedding capability of ROMS, which is designed such that the output from a lower resolution "parent" domain provides boundary conditions for the higher resolution "child" domain nested within it and the "child" domain in turn feeds the parent domain. Both the parent and child grids have 32 sigma-levels stretched so that near-surface resolution increases. We use a set of 10 outputs both at high (pixel size: 4 kms) and low (pixel size: 28 kms) resolution. See Fig. 4 for a sample output of simulated passive scalar, associated motion computed with ROMS and singularity exponents. Of course, the output of the model features a computed velocity field that we use to assess the method presented in the previous sections.

5.2. Experiments

Our experiments with ROMS consisted in evaluating the results on a set of 10 samples. For each of the 10 samples, we have the following data:

- a high spatial resolution (pixel size $\mathbf{r}_1$ corresponding to 4 kms on Earth) computed SST simulation,
- the motion field $\mathbf{w}(\mathbf{x},\mathbf{r}_1)$ computed by ROMS at resolution $\mathbf{r}_1$,
- a lower spatial resolution (pixel size $\mathbf{r}_2$ corresponding to 28 kms on Earth) computed SST simulation,
- the motion field $\mathbf{w}(\mathbf{x},\mathbf{r}_2)$ computed by ROMS at resolution $\mathbf{r}_2$.

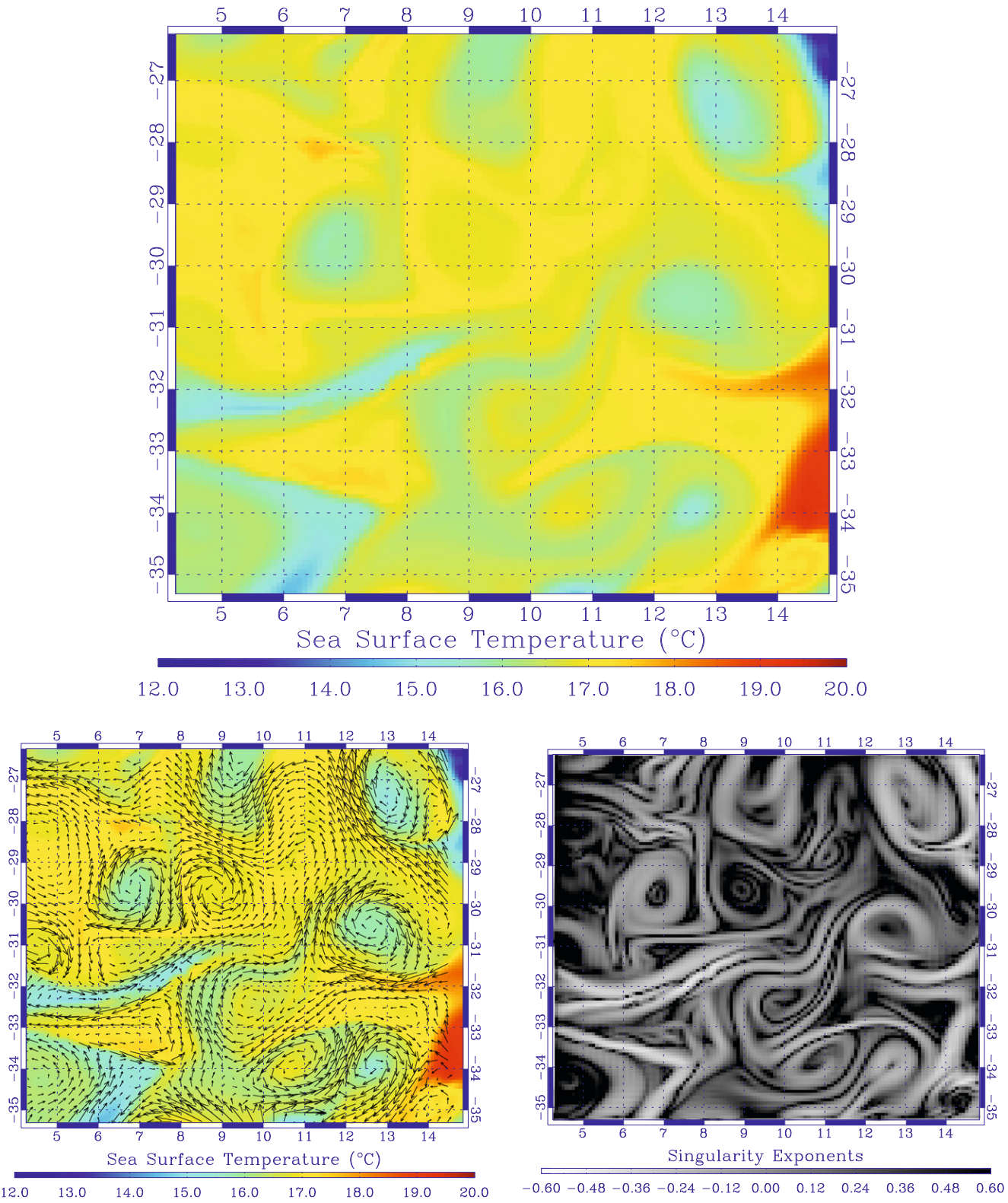

Fig. 4. Top: output of passive scalar SST (Sea Surface Temperature) generated by ROMS at high spatial resolution (pixel size corresponds to 4 kms on Earth). **Bottom:** left: computation of ocean dynamic in the form of a vector field for the top image using ROMS model. Right: singularity exponents computed on the top image above.

The experiment consisted in computing an optimal wavelet approximation of the cascade associated to the norm of the singularity exponents' gradients, starting at resolution $\mathbf{r}_1$ and reaching resolution $\mathbf{r}_2$. At resolution $\mathbf{r}_2$ a new signal is generated, defined as the scalar product between available data $\mathbf{w}(\mathbf{x},\mathbf{r}_2)/\|\mathbf{w}(\mathbf{x},\mathbf{r}_2)\|$ from ROMS simulation and the singularity exponents' gradients computed at resolution $\mathbf{r}_2$ from the approximated optimal cascading process. The scalar product is then projected back to resolution $\mathbf{r}_1$ using the same approximated optimal wavelet decomposition and the sign of this reconstructed

	Average	Best	Std. dev. (scalar product)
OW Algorithm	62.66%	64.75%	1.24
SF Algorithm	49%	50.40%	5.46

Fig. 5. Quantitative results for the evaluation of the algorithm presented in this paper on a 10-sample ROMS simulation output. **OW Algorithm** stands for the orientation determination using the "optimal wavelet" method discussed in section 5.2. **SF Algorithm** stands for the "stream function" algorithm presented in [41,52], and which consists in assigning an arbitrary orientation for the stream function, without any cascade decomposition. "Average" and "Best" refer to the percentage of vectors correctly oriented (i.e. having a positive scalar product with vectors obtained from ROMS at resolution $\mathbf{r}_1$), both in the average for the set of 10 samples, and for the best result in that set. "Standard deviation" refers to the standard deviation of the scalar product in the subset of correctly oriented vectors. Besides an overall augmentation of correctly oriented vectors obtained with the **OW Algorithm**, both in the average and in the best case, a noticeable result is the lower standard deviation obtained with the **OW Algorithm**, which indicates a more stable vector field, at least on synthetic ROMS data.

scalar product is used to invert the orientation of a stream function computed at resolution $\mathbf{r}_1$. The results are summarized in the table shown in Fig. 5.

5.3. Discussion

As the table shows, the optimal wavelet method produces much better results than the stream function method, at least with synthetic data. On the average, more than 30% points still are badly oriented. In Fig. 6 we show the resulting unitary field obtained by our optimal wavelet method, called here **OW Algorithm**, on one image in the ROMS set, its comparison with the field produced by ROMS, and a map of the scalar product between the two normalized fields.

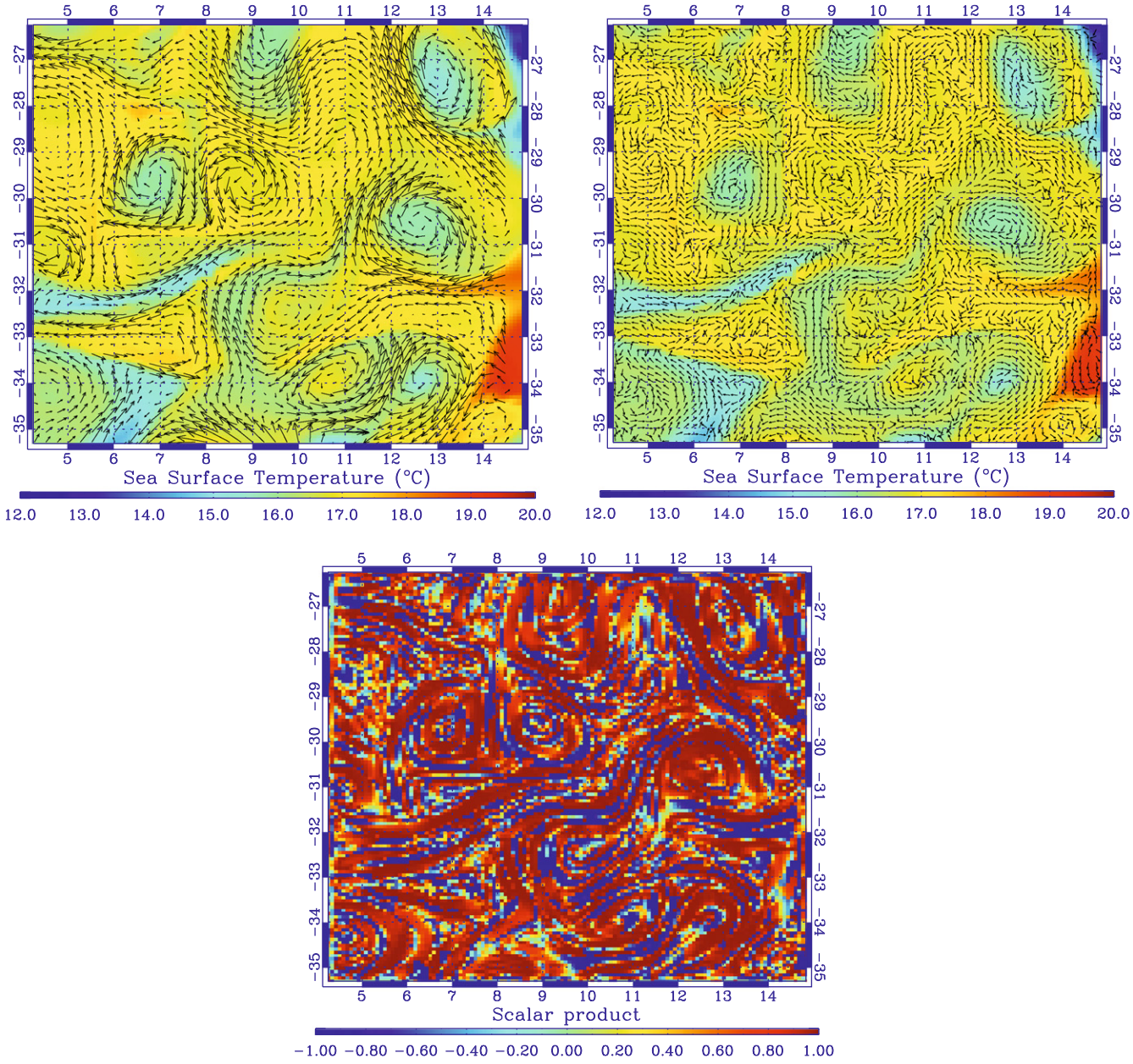

Fig. 6. Visual inspection of the vector field produced by the **OW Algorithm**. **Top:** on the left, we show the field produced by the ROMS modelling software, and on the right the unitary field computed by the **OW algorithm**. **Bottom:** map of the scalar product between the two (unitary) fields. The blue points, which denote a reversed orientation, are following coherent structures.

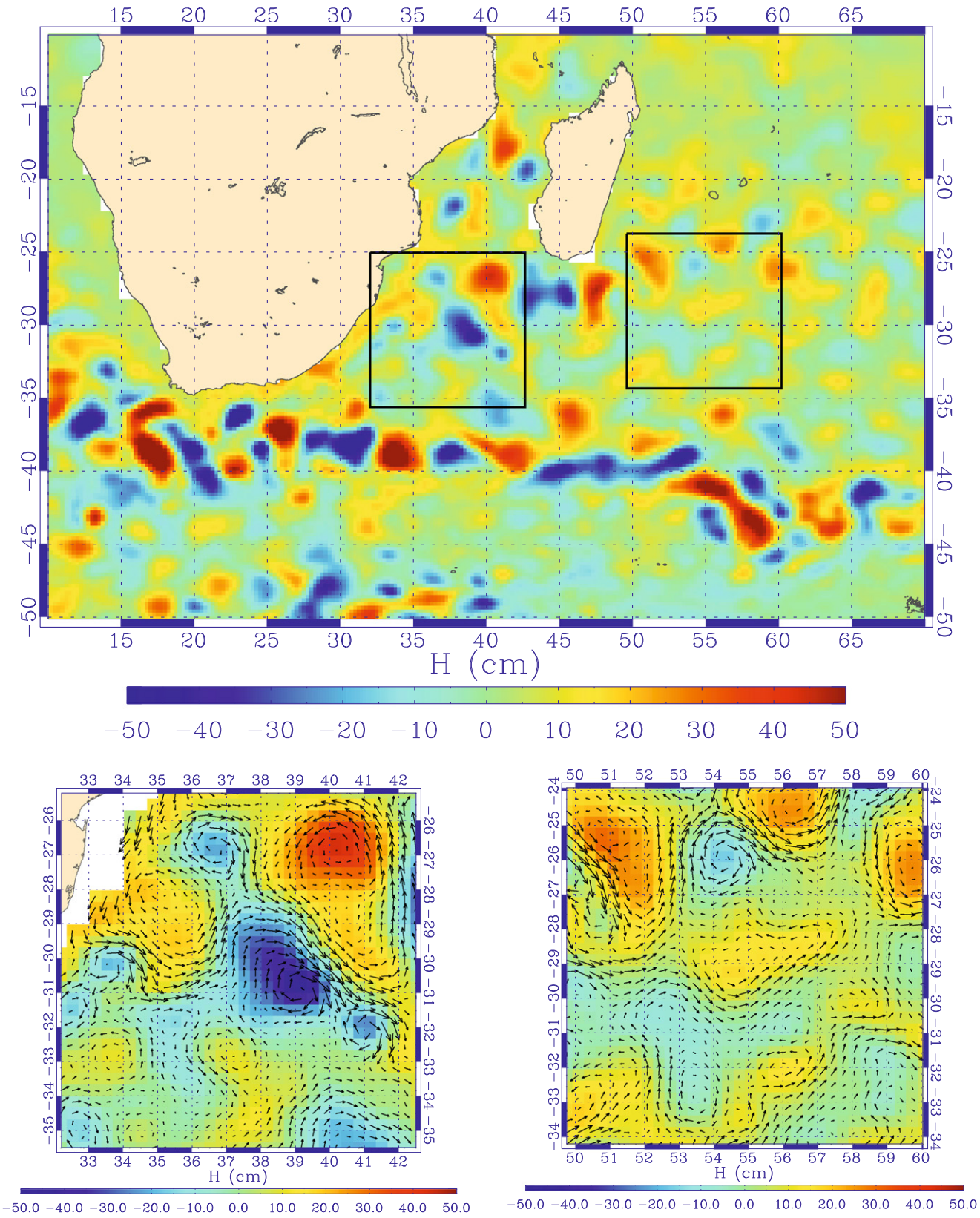

Fig. 7. Top: sample of a MSLA (*mean sea level anomaly*) dataset used in the algorithm as an input for the velocity field at lower spatial resolution. Spatial resolution is about 28 kms. Pixel values denote the deviation of the sea level surface from a standard medium value. From the MSLA, a geostrophic vector field can be generated directly. **Bottom:** geostrophic vector fields computed from MSLA in the black squares of top picture, magnified.

We think that the existence of remaining points with a reversed orientation comes, in some respect, from the fact that we use an *approximation* of the optimal wavelet, and not the optimal wavelet itself. Since the determination of an *exact optimal wavelet* is an extremely difficult problem, our research will now focus on such a determination.

6. Results on real data

We now show the results obtained by applying the previous algorithm on images extracted from the MODIS Level 3b dataset acquired in 2007. In this dataset, there is one image per day (an example is shown in Fig. 1). Pixel size is approximately 4 kms. The surface velocity field [54] used, at the much lower spatial resolution of 1/4°, comes from a combination of wind-driven Ekman currents, at 15 m depth, derived from QuikSCAT daily wind estimates, and weekly geostrophic currents calculated from Sea Surface Heights (SSH) which are obtained by weekly Mapped Sea Level Anomalies (MSLA) associated with a Mean Dynamics Topography (MDT). These velocity fields (Fig. 7) data correspond to a pixel size of $\sim$28 kms and daily periodicity which are computed by adding a temporal linear interpolation of weekly geostrophic currents with a daily Ekman currents.

In Fig. 8 we display the resulting unitary velocity field for the left subimage of Fig. 1. In the background the values of the singularity exponents are shown in grey-level values, hence evidencing the proper delimitation of complex coherent structures achieved by the values of the exponents. Along the

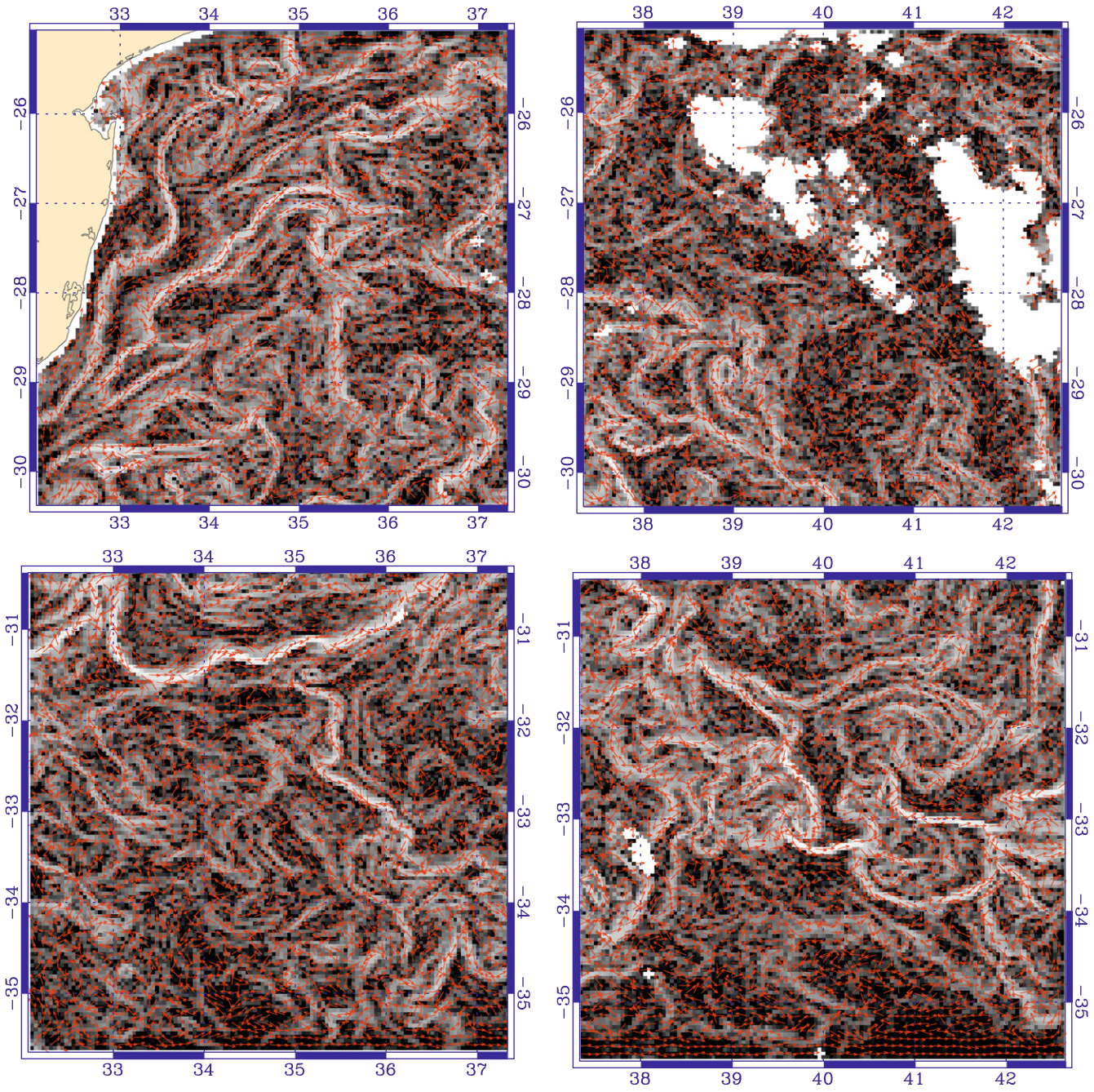

Fig. 8. The resulting unitary motion vector field for the left subimage of Fig. 1. Vectors are depicted in red, and they are drawn over the background image of the singular exponents, shown in grey-level values. For better visualization, the original subimage has been divided into four equal parts shown in this picture. The original subimage of Fig. 1 was specifically chosen for its abundance of complex currents, fronts, vortices and other oceanic structures, and also for its highly turbulent character, evidenced by a simple computation of Lyapunov exponents. The resulting vector field follows particularly well all the complex fronts and structures, with a remarkably well matching of the orientations even for the smallest vortices.

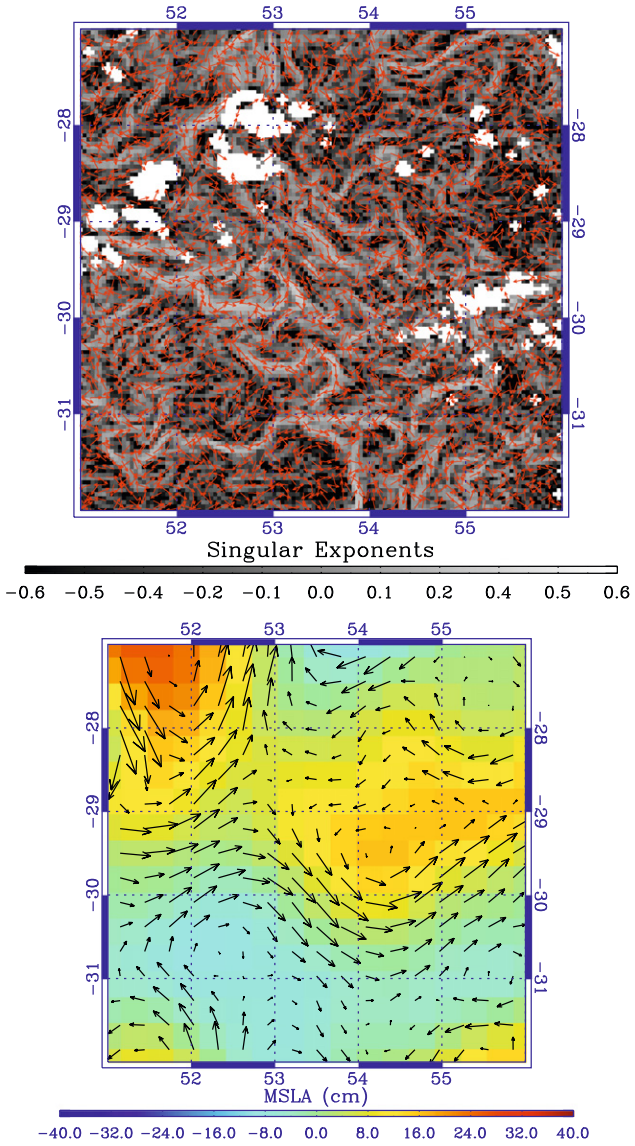

Fig. 9. Top: the resulting unitary motion vector field for another region in Fig. 1. This image was taken from a smaller subimage and zoomed in, first for better visualization, and also to show the resulting vector field at smaller spatial scales. Vectors are depicted in red, and they are drawn over the background image of the singular exponents, shown in grey-level values. The resulting vector field follows particularly well all the complex fronts and structures, with a remarkably well matching of the orientations even for the smallest vortices. **Bottom:** geostrophic vector field computed from MSLA, used for the generation of the top image according to the algorithm presented in Section 4.2. The spatial resolution of the altimetry data is much grosser, and scalar products with the vectors shown in this bottom image are used in the cascading process to produce the much finer map displayed in the top image.

fronts and coherent structures, the resulting velocity field follows the streamlines of the approximated stream function, hence showing, at least experimentally, the advection of the singularity exponents by the oceanic flow. Notice also the proper delimitation of vortices achieved by the resulting field.

The resulting vector field is also shown in Fig. 9 for the other subimage of Fig. 1, of even smaller size. We increased the magnification in this picture to show the resulting vector field at higher spatial scales. We also display the input data consisting of the vector field derived from altimetry at spatial resolution of 28 kms.

7. Conclusion

In this paper, we propose an original and better determination of an unitary oriented vector field describing ocean dynamics on high resolution satellite data using one single temporal frame and initial data given in the form of altimetry velocity field obtained at lower spatial resolution. Because it only uses one temporal frame, the method eliminates the multiple drawbacks inherent to methods that make use of several temporal frames, and does not hinge on conservation laws that can be subject to criticism (both from a physical point of view and also from all difficulties bound to the acquisition process) when dealing with complex signals displaying strong turbulent properties.

The determination of the unitary motion field makes uses of recent advances in the multiscale analysis of complexity in turbulent signals, in which the precise numerical computation of a singularity exponent around any point allows the determination of the geometric subsets both associated to transition fronts and statistical content. The significance of such geometric subsets, like the Most Singular Manifold, is asserted in the framework of reconstructible systems, which develops reconstruction formulae based on the statistical content located in these sets.

The main idea presented in this paper is in the use of an optimal wavelet, which provides a wavelet decomposition closely related to the multiscale energy cascade observed in fully developed turbulence. Since the computation of the optimal wavelet remains a difficult and open problem, we show that the consideration of an approximated optimal wavelet enhances to a large extent previous results. The optimal wavelet decomposition is used in conjunction with specific reconstruction formula in the framework of reconstructible systems to generate a motion field at lower resolution. That generated motion field is re-oriented by taking scalar products with an available motion field derived from an altimetric dataset acquired over the same temporal period, but at much lower spatial resolution. The re-oriented vector field is then back-projected through the wavelet decomposition to compute an oriented stream function at much higher spatial resolution. The systematic use of the Microcanonical Multiscale Formalism shows its ability to make use of information acquired at different spatial resolutions, a very interesting and promising approach in the field of remote sensing.

The methodology introduced in this work opens the way to a vast domain of research: the determination of the exact optimal wavelet from the signal data, the propagation of norm information through the cascade to obtain a valid normed and oriented field, the determination of a dense motion field even in the presence of large missing data. Moreover, there is a well defined generalization to the case of non-geostrophic motion, like the Ekman component of the oceanic motion field. These research topics are currently being investigated by the authors.

Acknowledgments

This work is funded by the NASA-EUMETSAT-CNES *Hiresubcolor* contract (title: *Hiresubcolor: Multiscale methods for the evaluation of high resolution ocean surface velocities and subsurface dynamics from ocean color, SST and altimetry*). *Hiresubcolor* is a participation to the Ocean Surface Topography Science Team (OST-ST). The authors also thank the anonymous reviewers for their suggestions.

References

[1] W. Munk, Oceanography before, and after, the advent of satellites, in: D. Halpern (Ed.), Satellites, Oceanography, and Society, 2000, pp. 1–4.

[2] J. Wilkin, M. Bowen, W. Emery, Mapping mesoscale currents by optimal interpolation of satellite radiometer and altimeter data, Ocean Dynamics 52 (2002) 95–103, doi:10.1007/s10236–001–0011–2.

[3] W.P.M. de Ruijter, H. Ridderinkhof, J.R.E. Lutjeharms, M.W. Schouten, C. Veth, Observations of the flow in the mozambique channel, Geophysical Research Letters 29 (10) (2002) 1502 http://dx.doi.org/10.1029/2001GL013714, doi:10.1029/2001GL013714.

[4] A. Biastoch, C.W. Boning, J.R.E. Lutjeharms, Agulhas leakage dynamics affects decadal variability in atlantic overturning circulation, Nature 456 (7221) (2008) 489–492 http://dx.doi.org/10.1038/nature07426.

[5] J.K. Willis, L. Fu, Combining altimeter and subsurface float data to estimate the time-averaged circulation in the upper ocean, Journal of Geophysical Research. http://www.agu.org/pubs/crossref/2008/2007JC004690.shtml.

[6] C.R. McClain, A decade of satellite ocean color observations*, Annual Review of Marine Science 1 (2009) 19–42, doi:10.1146/annurev.marine.010908.163650.

[7] R.J. Adrian, Twenty years of particle image velocimetry, Experiments in Fluids 39 (2) (2005) 159–169, doi:10.1007/s00348-005-0991-7.

[8] Q.X. Wu, A correlation-relaxation-labeling framework for computing optical flow—template matching from a new perspective, IEEE Transactions on Pattern Analysis and Machine Intelligence 17 (9) (1995) 843–853 ISSN: 0162-8828.

[9] M. Black, P. Anandan, Robust dynamic motion estimation over time, in: CVPR91, 1991, pp. 296-302. citeseer.ist.psu.edu/black91robust.html.

[10] M.J. Black, P. Anandan, The robust estimation of multiple motions: parametric and piecewise-smooth flow fields, Computer Vision and Image Understanding 63 (1) (1996) 75–104, URL http://dx.doi.org/10.1006/cviu.1996.0006.

[11] B.K.P. Horn, B.G. Schunck, Determining optical flow, Artificial Intelligence 17 (1981) 185–203 URL http://portal.acm.org/citation.cfm?id=136790.

[12] F. Heitz, P. Bouthemy, Multimodal estimation of discontinuous optical flow using Markov random fields, IEEE Transactions on Pattern Analysis and Machine Intelligence 15 (12) (1993) 1217–1232, doi: http://doi.ieeecomputersociety.org/10.1109/34.250841.

[13] P. Kornprobst, R. Deriche, G. Aubert, Image sequence analysis via partial differential equations, Journal of Mathematical Imaging and Vision 11 (1) (1999) 5–26 http://dx.doi.org/10.1023/A:1008318126505.

[14] S.-H. Lai, B.C. Vemuri, Reliable and efficient computation of optical flow, International Journal of Computer Vision 29 (2) (1998) 87–105, doi: http://dx.doi.org/10.1023/A:1008005509994.

[15] C. Chefd'Hotel, G. Hermosillo, O. Faugeras, A variational approach to multi-modal image matching, in: VLSM '01: Proceedings of the IEEE Workshop on Variational and Level Set Methods (VLSM'01), IEEE Computer Society, Washington, DC, USA, 2001, p. 21.

[16] I. Cohen, I. Herlin, Non uniform multiresolution method for optical flow and phase portrait models: environmental applications, International Journal of Computer Vision 33 (1) (1999) 1–22.

[17] L. Alvarez, J. Weickert, J. Sánchez, Reliable estimation of dense optical flow fields with large displacements, International Journal of Computer Vision 39 (1) (2000) 41–56, doi: 10.1023/A:1008170101536 URL http://dx.doi.org/10.1023/A:1008170101536.

[18] E. Mémin, P. Pérez, Hierarchical estimation and segmentation of dense motion fields, International Journal of Computer Vision 46 (2) (2002) 129–155 doi: http://dx.doi.org/10.1023/A:1013539930159.

[19] J. Weickert, C. Schnörr, Variational optic flow computation with a spatio-temporal smoothness constraint, Journal of Mathematical Imaging and Vision 14 (3) (2001) 245–255.

[20] D. Béréziat, I.I. Herlin, L. Younes, A generalized optical flow constraint and its physical interpretation, in: Proceedings of Computer Vision and Pattern Recognition, CVPR'00, IEEE, 2000.

[21] L. Zhou, C. Kambhamettu, D.B. Goldgof, Fluid structure and motion analysis from multi-spectrum 2d cloud image sequences, in: IEEE Computer Society Conference on Computer Vision and Pattern Recognition, vol. 2, 2000, p. 2744, doi:http://doi.ieeecomputersociety.org/10.1109/CVPR.2000.854949.

[22] X. Vigan, C. Provost, R. Bleck, P. Courtier, Sea surface velocities from sea surface temperature image sequences 1. method and validation using primitive equation model output, Journal of Geophysical Research 105 (C8) (2000) 19.

[23] E. Arnaud, E. Mémin, R. Sosa, G. Artana, A fluid motion estimator for schlieren image velocimetry, in: ECCV, vol. 1, 2006, pp. 198–210.

[24] D. Suter, Motion estimation and vector splines, in: Proceedings of the Conference on Computer Vision and Pattern Recognition, IEEE, 1994, pp. 939–942.

[25] J. Yuan, C. Schnörr, E. Mémin, Discrete orthogonal decomposition and variational fluid flow estimation, Journal of Mathematical Imaging and Vision 28 (2007) 67–80.

[26] U. Frisch, Turbulence, Cambridge University Press, Cambridge, MA, 1995.

[27] G.-H. Cottet, P. Koumoutsakos, Vortex Methods: Theory and Practice, Cambridge University Press, UK, 2000, pp. 514. ISBN: 0 521 621860.

[28] A. Cuzol, E. Mémin, Vortex and source particles for fluid motion estimation, in: 5th International Conference on Scale-Space and PDE methods in Computer Vision (Scale-Space'05), Hofgeismar, Germany, vol. 3459, Hofgeismar, Germany, 2005, pp. 254–266.

[29] A. Cuzol, E. Mémin, A stochastic filtering technique for fluid flow velocity fields tracking, IEEE Transactions on Pattern Analysis and Machine Intelligence 31 (7) (2009) 1278–1293, doi: http://doi.ieeecomputersociety.org/10.1109/TPAMI.2008.152.

[30] H. Nogawa, Y. Nakajima, Y. Sato, S. Tamura, Acquisition of symbolic description from flow fields: a new approach based on a fluid model, IEEE Transactions on Pattern Analysis and Machine Intelligence 19 (1) (1997) 58–63 doi: http://doi.ieeecomputersociety.org/10.1109/34.566811.

[31] C. Papin, P. Bouthemy, E. Mémin, G. Rochard, Tracking and characterization of highly deformable cloud structures, in: European Conference on Computer Vision, ECCV 2000, Lecture Notes in Computer Science 1843, vol. 2, Dublin, Irlande, 2000, pp. 428–442.

[32] G. Parisi, U. Frisch, On the singularity structure of fully developed turbulence, in: M. Ghil, R. Benzi, G. Parisi (Eds.), Turbulence and Predictability in Geophysical Fluid Dynamics. Proceedings of the International School of Physics E. Fermi, North Holland, Amsterdam, 1985, pp. 84–87.

[33] A.J. Chorin, J.E. Marsden, A Mathematical Introduction to Fluid Mechanics, Cambridge University Press, Cambridge, 2000.

[34] A. Arneodo, F. Argoul, E. Bacry, J. Elezgaray, J.F. Muzy, Ondelettes, Multifractales Et Turbulence, Diderot Editeur, Paris, France, 1995.

[35] J.F. Muzy, E. Bacry, A. Arneodo, Wavelets and multifractal formalism for singular signals: application to turbulence data, Physical Review Letters 67 (1991) 3515–3518.

[36] S.G. Roux, A. Arneodo, N. Decoster, A wavelet-based method for multifractal image analysis. III. Applications to high-resolution satellite images of cloud structure, European Physical Journal B 15 (2000) 765–786.

[37] A. Turiel, H. Yahia, C. Pérez Vicente, Microcanonical multifractal formalism: a geometrical approach to multifractal systems. Part I: singularity analysis, Journal of Physics A: Mathematical and Theoretical, vol. 41, doi: 10.1088/1751-8113/41/1/015501.

[38] T.A., J. Grazzini, H. Yahia, Edge-preserving smoothing of high-resolution images with a partial multifractal reconstruction scheme, in: XX ISPRS Congress, vol. XXXV(B3), 2004, pp. 1125–1129.

[39] J. Grazzini, A. Turiel, H. Yahia, Entropy estimation and multiscale processing in meteorological satellite images, in: Proceedings of ICPR 2002, vol. 3, IEEE Computer Society, Los Alamitos, CA, 2002, pp. 764–768.

[40] O. Faugeras, Three-Dimensional Computer Vision: A Geometric Viewpoint, The MIT Press, Cambridge, MA, 1993, ISBN-10:0-262-06158-9, ISBN-13: 978-0-262-06158-2.

[41] A. Turiel, J. Isern-Fontanet, E. García-Ladona, J. Font, Multifractal method for the instantaneous evaluation of the stream-function in geophysical flows, Physical Review Letters 95 (10) (2005) 104502, doi:10.1103/PhysRevLett.95.104502.

[42] A. Turiel, J.-P. Nadal, N. Parga, Orientational minimal redundancy wavelets: from edge detection to perception, Vision Research 43 (9) (2003) 1061–1079.

[43] A. Turiel, G. Mato, N. Parga, J.P. Nadal, The self-similarity properties of natural images resemble those of turbulent flows, Physical Review Letters 80 (1998) 1098–1101.

[44] A. Turiel, N. Parga, The multi-fractal structure of contrast changes in natural images: from sharp edges to textures, Neural Computation 12 (2000) 763–793.

[45] S. Mallat, A Wavelet Tour of Signal Processing, second ed., Academic Press, 1999.

[46] H. Stanley, Introduction to Phase Transitions and Critical Phenomena Oxford University Press, 1971. ISBN: 0-19.505316-8 (pbk.).

[47] D. Uzunov, Introduction to the Theory of Critical Phenomena, World Scientific, New York, 1992.

[48] A.F.J.J. Binney, N.J. Dowrick, M. Newman, The Theory of Critical Phenomena. An Introduction to Renormalization Group, Clarendon Press, Oxford, 1992.

[49] A. Turiel, A. del Pozo, Reconstructing images from their most singular fractal manifold, IEEE Transactions on Image Processing 11 (2002) 345–350.

[50] P. Chainais, Infinitely divisible cascades to model the statistics of natural images, IEEE Transactions on Pattern Analysis and Machine Intelligence 29 (12) (2007) 2105–2119, doi:http://doi.ieeecomputersociety.org/10.1109/TPAMI.2007.1113.

[51] O. Pont, A. Turiel, C. Perez-Vicente, Description, modelling and forecasting of data with optimal wavelets, Journal of Economic Interaction and Coordination 4 (1) (2009) 39–54 URL http://ideas.repec.org/a/spr/jeicoo/v4y2009i1p39-54.html.

[52] J. Isern-Fontanet, A. Turiel, E. Garcia-Ladona, J. Font, Microcanonical multifractal formalism: application to the estimation of ocean surface velocities, Journal of Geophysical Research 112 (C05024), doi:10.1029/2006JC003878.

[53] C. Pottier, A. Turiel, V. Garçon, Inferring missing data in satellite cholorophyll maps using turbulent cascading, Remote Sensing of Environment 112 (2008) 4242–4260, doi: 10.1016/j.rse.2008.07.010.

[54] J. Sudre, R. Morrow, Global surface currents: a high-resolution product for investigating ocean dynamics, Ocean Dynamics 58 (2) (2008) 101–118 doi: 10.1007/s10236-008-0134-9 URL http://dx.doi.org/10.1007/s10236-008-0134-9.

[55] A.F. Shchepetkin, J.C. McWilliams, A method for computing horizontal pressure-gradient force in an ocean model with a non-aligned vertical coordinate, Journal of Geophysical Research 108 (C3), 3090, doi: 10.1029/2001JC00110478.

[56] A.F. Shchepetkin, J.C. McWilliams, The Region Ocean Model System (ROMS): A split-explicit, free-surface, topography-following-coordinate oceanic model, Ocean Modelling, vol. 9, pp. 347–404.
[57] P. Penven, A numerical study of the southern Benguela circulation with an application to fish recruitment, Ph.D. Thesis, University de Bretagne Occidentale, Brest, France, 2000, p. 160.
[58] P. Penven, J.R.E. Lutjeharms, P. Marchesiello, C. Roy, S.J. Week, Generation of cyclonic eddies by the Agulhas Current in the lee of the Agulhas Bank, Geophysical Research Letter (28), pp. 1055–1058.
[59] J. Veitch, P. Penven, F. Shillington, The Benguela: a laboratory for comparative modelling studies, Progress in Oceanography, in press.
[60] T. Gautama, M.M. Van Hulle, A phase-based approach to the estimation of the optical flow using spatial filtering, IEEE Trans. Neural Networks 13 (5) (2002) 1127–1136.
[61] C. Liu, Beyond Pixels: Exploring New Representations and Applications for Motion Analysis, Doctoral Thesis, Masschussets Institute of Technology, May 2009.
[62] S. Baker, D. Scharstein, J. Lewis, S. Roth, M.J. Black, R. Szeliski, A database and evaluation methodology for optical flow, in: Proc. IEEE International Conference on Computer Vision (ICCV), 2007.
[63] T. Brox, A. Bruhn, N. Papenberg, J. Weickert, High accuracy optical flow estimation based on a theory for warping, in: European Conference on Computer Vision (ECCV), 2004, pp. 25–36.
[64] A. Bruhn, J. Weickert, C. Schnorr, Lucas/Kanade meets Horn/Schunk: combining local and global optical flow methods, International Journal of Computer Vision (IJCV) 61 (3) (2005) 211–231.
[65] D.J. Fleet, Y. Weiss, Optical flow estimation, in: N. Paragios, Y. Chen, O. Faugeras (Eds.), Mathematical Models for Computer Vision: The Handbook, Springer, 2005.

About this Author—H. YAHIA is a Senior Researcher at INRIA (French National Institute in Computer Science and Applied Mathematics) and head of the GeoStat team (Geometry and Statistics in acquisition data). His research interests focus on the multiscale analysis of complex signals, image processing and graphics. He is involved in international academic and contractual partnerships in the GeoStat project, and has supervised 7 Ph.D students and 5 post-doctoral fellows. He is the author or co-author of many papers in peer reviewed journals and conference proceedings.

About this Author—J. SUDRE received the Masters degree from the University of Méditerranée, Aix-Marseille II, France. He is currently a CNRS Engineer with the LEGOS Laboratory, Toulouse, France, working on satellite data analysis and Image Processing for oceanographic studies.

About this Author—C. POTTIER received an Engineering degree from the Ecole Sup'erieure d'Electronique de l'Ouest, Angers, France, in 2003, and a Master Degree in Signal and Image Processing from the University of Rennes, France. She got her Ph.D. degree at the University of Toulouse, France, in 2006. Since then, she has been working as a research engineer at CNES (France Space Agency) on software systems allowing web consultation of scientific data catalogs and access to these data.

About this Author—V. GARÇON is a Centre National de la Recherche Scientifique (CNRS) Senior Scientist and head of the Group Physical Dynamics/Marine Biogeochemistry with the LEGOS Laboratory in Toulouse, France. Her research interests lie in the areas of marine biogeochemical cycles and dynamics of ecosystems in response to climate changes. This implies activities in remote sensing, coupled physical/biogeochemical modelling, analysis of in situ data, data assimilation, and experimental work at sea. She has been and is a member of many national (IFREMER, French Oceanography Navy,...) and international (JGOFS, SOLAS,...) Scientific Steering Committes. She supervised more than 15 Ph.D candidates and 8 post-doctoral fellows. She is author or co-author of more than 65 publications in peer reviewed journals.

3.9 Article : Inferring Information across Scales in Acquired Complex Signals, S. K. Maji *et al.*, 2012

3.9.1 Résumé de l'article (version française)

La transmission d'information le long des échelles d'un signal complexe est un problème dont la solution ouvre des voies nouvelles notamment en obtention d'informations subpixelliques, en fusion de données et en super-résolution. Ce genre d'inférence nécessite la connaissance de la structuration fine des signaux, en général non-atteignable par des méthodes linéaires et peut être abordée selon le point de vue où l'on considère les signaux complexes comme des acquisitions de systèmes dynamiques dont l'espace des phases est inconnu. Dans cet article nous considérons le problème de la transmission de l'information à travers les échelles en relation avec la détermination de la structuration multifractale des signaux complexes. Nous montrons que l'optimalité d'une inférence entre les échelles peut bénéficier de la connaissance des exposants de singularité calculés en mode microcanonique. Nous présentons une méthode d'inférence et l'appliquons aux cas de données en astronomie (optique adaptative) et en observation des océans.

3.9.2 Article publié dans *European Conference on Complex Systems 2012*

Référence : Maji S. K., O. Pont, H. Yahia and J. Sudre, 2013 : Inferring Information across Scales in Acquired Complex Signals, *Proceedings of the European Conference on Complex Systems 2012*, 209-226.

Inferring Information across Scales in Acquired Complex Signals

Suman Kumar Maji[1], Oriol Pont[1], Hussein Yahia[1] and Joel Sudre[2]

[1] INRIA Bordeaux Sud-Ouest, Geostat team
suman-kumar.maji, oriol.pont, hussein.yahia@inria.fr
[2] LEGOS, UMR CNRS 5556, Dynbio Team
joel.sudre@legos.obs-mip.fr

Abstract. Transmission of information across the scales of a complex signal has some interesting potential, notably in the derivation of sub-pixel information, cross-scale inference and data fusion. It follows the structure of complex signals themselves, when they are considered as acquisitions of complex systems. In this work we contemplate the problem of cross-scale information inference through the determination of appropriate multiscale decomposition. Our goal is to derive a generic methodology that can be applied to propagate information across the scales in a wide variety of complex signals. Consequently, we first focus on the determination of appropriate multiscale characteristics, and we show that singularity exponents computed in microcanonical formulations are much better candidates for the characterization of transitions in complex signals : they outperform the classical «linear filtering» approach of the state-of-the-art edge detectors (for the case of 2D signals). This is a fundamental topic as edges are usually considered as important multiscale features in an image. The comparison is done within the formalism of reconstructible systems. Critical exponents, naturally associated to phase transitions and used in complex systems methods in the framework of criticality are key notions in Statistical Physics that can lead to the complete determination of the geometrical cascade properties in complex signals. We study optimal multiresolution analysis associated to critical exponents through the concept of «optimal wavelet». We demonstrate the usefulness of multiresolution analysis associated to critical exponents in two decisive examples : the reconstruction of perturbated optical phase in Adaptive Optics (AO) and the generation of high resolution ocean dynamics from low resolution altimetry data.

1 Introduction

Most real-world signals are complex signals, usually difficult to describe but possessing a high degree of redundancy [6]. In particular, in the case of Fully Developed Turbulence (FDT), there is a relation between the spectrum of singularity exponents associated to structure functions and the existence of a multiscale hierarchy [11]. Turbulent flows, although chaotic in nature, possess a

complex arrangement of geometrical structures related to the cascading properties of physical variables [5]. The same type of conclusion can be inferred from multiscale analysis of most natural complex signals [12]. As a consequence, the paradigm of understanding natural signals as acquisitions of complex systems with unknown phase space is a useful one [14]. The properties of physical cascading variables reflect the transfer of energy, or more generally information, taking place from larger scales to smaller ones. Recent developments in microcanonical framework for the computation of **singularity exponents** and the derivation of singularity spectra have lead to a sensible improvement in the numerical techniques for the determination of multiscale characteristics of real signals [1, 2]. Experimental analysis on different real world signals, ranging from stock market time series to atmospheric perturbated optical path shows that these systems are not only found to be multiscale, but their singularity spectra are also coincident. Consequently, the precise numerical computation of geometrically localized singularity exponents in single acquisitions of complex systems, without the averages taken on grand ensembles, unveils the determination of their universality class [1]. The statistical characteristics of information in these signals can be described from the localisation and precise value of singularity exponents. As a consequence, it should be possible to transfer across the scales extra physical information from lower scale to higher resolution, a procedure which unveils considerable enhancements of high resolution mapping of natural phenomena.

In this paper, we demonstrate that microcanonical formulations for understanding and evaluating the mechanisms that govern the evolution of dynamical systems lead to accurate inference schemes across the scales in complex signals. We show that the singularity exponents can be used in multiresolution analysis for accurate inference of information across the scales. The profound reason for this fact comes from the observation that geometrically localized singularity exponents encode transitions in complex signals in a much more accurate manner than done with linear filtering processing techniques [23, 25], as will be demonstrated in this work, in particular in the case of 2D images and the accurate determination of edges (which are typically multiscale characteristics on an image). Consequently, we study the notion of optimal wavelet for inferring information across the scales. Our fundamental contribution in this work is to show that multiresolution analysis associated to geometrically localized singularity exponents is a very good candidate for inferring information across the scales in complex signals. We take two specific examples: the reconstruction of the optical phase shift perturbated by atmospheric turbulence (Adaptive Optics) and the high resolution mapping of ocean dynamics using sea surface temperature maps. In the first example, we derive a radically new and nonlinear approach for reconstructing the perturbated optical phase; while in the second, we show that oceanic dynamical information acquired at low resolution (pixel size : 22 kms) from altimetry can be transferred across the scales at high resolution sea surface temperature data (pixel size : 4 kms) to produce high resolution mapping of oceanic currents. In both the cases we use a proper wavelet decomposition tech-

nique on the signal of the singularity exponents to help us inferring information along the scales of the signal.

The paper is organised as follows: in section 2 we present a brief discussion on the evolution of the theory of singularity exponents, in section 3 we present the numerical analysis for the singularity exponents and the idea of the most informative set within a signal. Theory behind the reconstruction of the whole signal from the most informative set is explained in section 4. Notion of optimal wavelet, for inferring information pointwise in a cascade, is introduced in 5. The experimental data used is discussed in section 6 and the results are shown in section 7. Finally, we conclude in section 8.

2 Universality class and multiscale organisation

A power-law behaviour in the thermodynamical variables, and also time and spatial correlation functions, is commonly observed in systems with high order transitions. The underlying dynamics of such systems can be observed, at the macroscopic scale, in the form of a power-law [4]. It was soon realized that the exponents of the power laws define different classes: systems characterized by same values of singularity exponents belong to the same universality class, which implies the presence of a common macroscopic behaviour independent of the microscopic dynamics of each system [10]. Different singularity spectra of very different physical systems can match a same curve. Such a correspondance can be explained by the existence of a common underlying dynamical system, the universality class, responsible for similar statistical properties of information at macroscopic scale [10].

Previous works attempt to relate the general organisation of a multiscale structure with the existence of cascade process [4]. In these works, a multiscale signal s is characterized by the power-law scaling in the order p moments of some related variable $\mathbb{T}_r$, in the way:

$$\langle |\mathbb{T}_r s|^p \rangle = A_p r^{\tau_p} + o(r^{\tau_p}) \quad (r \to 0) \tag{1}$$

The existence of multplicative cascade process was first justified by Kolmogorov in his theory on turbulence [5]. Kolmogorov proposed the following: given two scales r and L, $0 < r < L$, we can characterize the distribution of the velocity field by an injection parameter $\eta_{r/L}$ as:

$$|\mathbb{T}_r s| \doteq \eta_{r/L} |\mathbb{T}_L s| \tag{2}$$

where the symbol '$\doteq$'means that both sides are equally distributed and $\eta_{r/L} = [r/L]^{\alpha}$. From this relation, the order p moments have the following relation:

$$\langle |\mathbb{T}_r s|^p \rangle = [r/L]^{\alpha p} \langle |\mathbb{T}_L s|^p \rangle \tag{3}$$

Comparing equations (1) and (3) we get, $\tau_p = \alpha p$. However, experiments show that in the case of FDT, the relationship between τ_p and p is not linear rather it

is a convex bell-shaped curve, a condition konwn as 'anomalous scaling' [2]. To apply Kolmogorov's decomposition in anomalous scaling, certain assumptions have to be made:

- $\eta_{r/L}$ has to be interpreted as a random variable, independent of L.
- The variables $\eta_{r/L}$ has to be infinitely divisible to ensure downward process from scale L to r is verified directly or in several stages giving rise to the famous cascade process.

It has been verified [5] that an injection mechanism as the one proposed by Kolmogorov leads to the understanding of a underlying geometrical structure in a multiplicative cascade process, together with the knowledge of the exponents τ_p for infering information along the scales of the signal. This experimental outcome of self-similarity led researchers to propose a different model for the generation of exponents.

3 Singularity Analysis in the Microcanonical Framework

Criticality, and the associated *critical exponents* are key notions in Statistical Physics to understand phase transitions, which are prototypes of scale invariant phenomena [4]. The spectrum of singularity exponents in a system determine its multiscale properties which are accessible statistically. We will say that a signal s is multiscale in a microcanonical sense, if for at least one multiscale functional dependant on scale r, it is assumed that for any point $\boldsymbol{x}$ the following equation holds:

$$\mathbb{T}_r s(\boldsymbol{x}) = \alpha(\boldsymbol{x}) r^{h(\boldsymbol{x})} + o(r^{h(\boldsymbol{x})})(r \to 0) \tag{4}$$

for some functions $\alpha(\boldsymbol{x})$ and $h(\boldsymbol{x})$. The exponent $h(\boldsymbol{x})$, which is a function of the point $\boldsymbol{x}$, is called a *singularity exponent* or *Local predictability exponent (LPE)* of the point [2]. The central problem is to compute at high numerical precision the value of $h(\boldsymbol{x})$ at point $\boldsymbol{x}$: bad approximations of singularity exponents lead to poor reconstructions.

3.1 Local Predictability Exponents

According to microcanonical formulations [4], a multiscale signal is supposed to satisfy equation (4) for a family of functionals $\mathbb{T}_r$, at any point $\boldsymbol{x}$ in the signal domain, and have a singularity spectrum computed from singularity exponents as a convex curve function of h [4]. Equation (4) is a pointwise and localized version of the definition used in introducing singularity spectrum [1, 3]: we do not make use of statistical averages and grand ensembles as in practice such an ensemble average is not accessible. Rather, we seek to evaluate $h(\boldsymbol{x})$ at point $\boldsymbol{x}$. We denote $\mathcal{F}_h$ the component in the signal's domain associated to singularity exponent value h as:

$$\mathcal{F}_h = \{\boldsymbol{x} : h(\boldsymbol{x}) = h\} \tag{5}$$

In other words, we can say that each point $\boldsymbol{x}$ in the signal is characterized by a singularity exponent $h(\boldsymbol{x})$ which is typical to one component $\mathcal{F}_h$, i.e., the components are level sets of the function $h(\boldsymbol{x})$. This family of sets is naturally associated to the multiscale hierarchy in a signal and in the case of natural images, it is expected that there exists a particular set which comprises the point where sharp transitions within the signal are well recorded. We will call this set as the *Most Singular Manifold* or MSM. Geometrically speaking, it is the singularity component associated with the smallest possible value h_∞ , finite for signals corresponding to physical variables that cannot diverge. We will denote this set by $\mathcal{F}_\infty$ and can be expressesd as:

$$\mathcal{F}_\infty = \{\boldsymbol{x} : h(\boldsymbol{x}) = h_\infty = \min(h(\boldsymbol{x}))\} \tag{6}$$

The MSM plays a fundamental role in the multiscale geometrical hierarchy of natural images. Visual inspection of this set reveals a structure which is characterized by the presence of 'edges' or contours in natural images [6]. It will be understood hereafter that the MSM contains the most informative set in an image so that the whole signal can be reconstructed from the restriction of its gradient to the MSM. Moreover we will see that singularity exponents lead to a notion of edge that matches much better across the scales than the edges computed from classical filtering methods. Before we go deeper into the subject of MSM and its application to reconstructible systems, we give a brief overview for the determination of the singualrity exponents.

3.2 Singularity Analysis

The singularity exponents for experimental, discretized data can be calculated using different methods [2], but for our case we will use the *Unpredictable Points Manifold* (herein referred to as UPM) [16]. According to this method, we make point estimates of the singularity exponent, namely:

$$h(\boldsymbol{x}) = \frac{log(\tau_\Psi s(\boldsymbol{x}, r_0))/\langle \tau_\Psi s(., r_0)\rangle)}{logr_0} + o(\frac{1}{logr_0}) \tag{7}$$

where $\langle \tau_\Psi s(., r_0\rangle$ is the average value of the wavelet projection over the whole signal and $o(\frac{1}{logr_0})$ is a diminishing quantity and r_0 is the minimum scale. If the signal s is an image of size $M \times N$, then we choose $r_0 = 1/\sqrt{M \times N}$. The singularity exponents computed on our experimental dataset are shown in Fig 1.

The values $h(\boldsymbol{x})$ are computed for all points $\boldsymbol{x}$ within the signal domain. Now, coming back to MSM, sorting of these singularity exponent values based on a typical threshold value 0 defines the standard reconstruction set in the MSM method. Such a set often provides a robust and accurate reconstruction and is defined by:

$$\mathcal{E}_{\text{MSM}} = \bigcup_{h_\infty \leq h \leq 0} \mathcal{F}_h \tag{8}$$

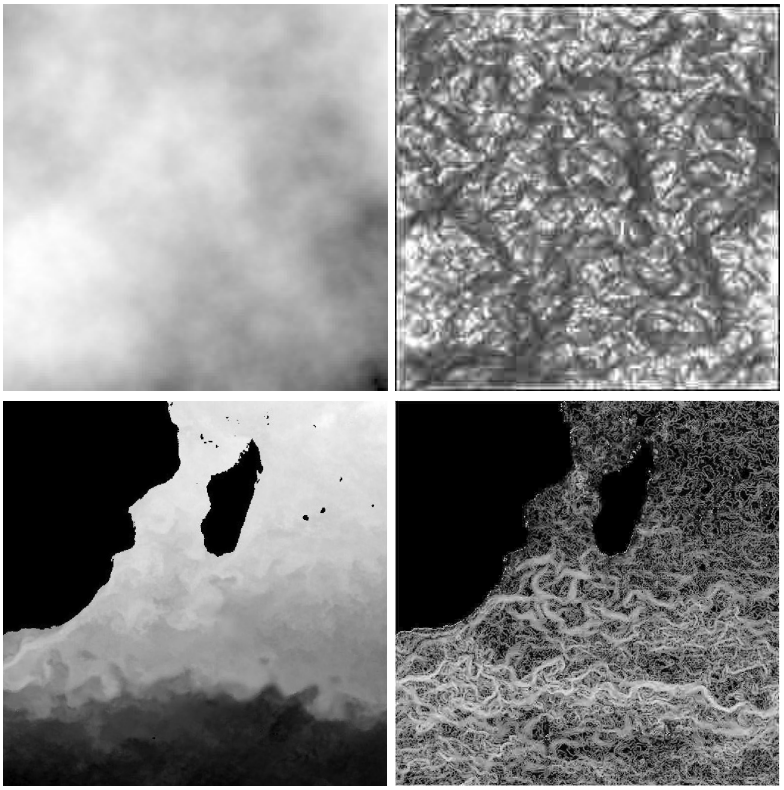

Fig. 1: **Top left:** Image of a simulated optical phase perturbated by atmospheric turbulence. The image corresponds to a 128 $\times$ 128 pixels sub-image extracted from an original 256 $\times$ 256 pixels image to avoid the pupil boundary. **Top right:** Image of the singularity exponents computed from the phase data. **Bottom left:** Excerpt of the Agulhas current below the coast of South Africa (sea surface temperature image: each pixel record the temperature of the upper layer of the sea). **Bottom right:** Singularity exponents of the Agulhas current.

4 Reconstructible Systems

In this section, we are led to find mathematically a functional $\mathcal{G}$ which permits the reconstruction of the signal's gradient from its restriction to the MSM. The functional must satisfy the properties of being deterministic, linear, translationally-invariant, isotropic and yield correct power spectrum of natural images. We consider the gradient measure of the signal $s = \nabla s(\boldsymbol{x})$ and integrate it over the multifractal set of most unpredictable points $\mathcal{F}_\infty$. A deterministic representation of the gradient measure for the signal can be:

$$\nabla s(\boldsymbol{x}) = \mathcal{G}(\nabla s|_{\mathcal{F}_\infty})(\boldsymbol{x}) \tag{9}$$

Considering the fact of $\mathcal{G}$ being linear, an integral representation can be given by:

$$\nabla s(\boldsymbol{x}) = \int_{\mathcal{F}_\infty} \nabla s(\boldsymbol{y}) G(\boldsymbol{x}, \boldsymbol{y}) \mathrm{d}\boldsymbol{y} \tag{10}$$

where $G(\boldsymbol{x}, \boldsymbol{y})$ is a density measure of the function $\mathcal{G}$ and is a 2×2 matrix. Using isotropy, standard power spectrum (in the form $1/||\boldsymbol{f}||^2$) for the associated spectral measures of natural images, one obtains the following formula [4, 6] expressed in Fourier space:

$$\hat{s}(\boldsymbol{f}) = \frac{\boldsymbol{f}.\widehat{\nabla s|_{\mathcal{F}_\infty}}(\boldsymbol{f})}{i||\boldsymbol{f}||^2} \tag{11}$$

where i is the imaginary unit, $i \equiv \sqrt{-1}$ and $\hat{}$ denotes the Fourier transform. We normalize the result by taking the vector field $\boldsymbol{v_0}$ unitary and normal to the MSM instead of $\nabla s|_{\mathcal{F}_\infty}$; where $\boldsymbol{v_0}(\boldsymbol{x}) = \nabla s(\boldsymbol{x}) \delta_{\mathcal{F}_\infty}$, $\delta_{\mathcal{F}_\infty}$ being the density of the proper Hausdorff measure restricted to the set $\mathcal{F}_\infty$ [6]. We therefore perform integration over all the space (the restriction is still present, but now introduced by $\boldsymbol{v_0}$):

$$\hat{s}(\boldsymbol{f}) = \frac{\boldsymbol{f}.\widehat{\boldsymbol{v_0}|_{\mathcal{E}}}(\boldsymbol{f})}{i||\boldsymbol{f}||^2} \tag{12}$$

Fourier inversion of this formula gives the reconstruction of the image from the restriction of the gradient field to the MSM. Results of reconstruction on the MSM of experimental datasets, and their performance over classical edge detection algorithms, are shown in tables 2 and 1. It is seen that in the case of acquisitions of turbulent signals, the reconstruction based on the MSM (we call it MSM in tables 2 and 1) performs significantly better among the algorithms tested. In fact, when it comes to the case of turbulent signals, the classical edge detectors like Sobel [20], Prewitt [18], Roberts [17], Laplacian of Gaussian (LoG) [19, 21], Zerocross [22, 24], Canny [23] to a more recent non-linear approach called NLFS [7], dedicated to the computation of edges in digital images, are systematically outperformed by MSM in terms of reconstruction from a compact representation of its edge pixels. As a consequence, the fundamental notion of edge, which is a basic multiscale feature, is much more well encoded by the set $\mathcal{E}_{\mathrm{MSM}}$ defined in equation (8). This tends to show that singularity exponents are good candidates for an accurate multiresolution analysis. In the next section, we develop the notion of optimal wavelet.

5 Inferring Information across the scales using microcanonical analysis

To infer the cascading properties pointwise (called microcanonical cascade) we introduce the concept of optimal wavelet. Let $s(\boldsymbol{x})$ be a multiscale signal and let $\Psi(\boldsymbol{x})$ be a wavelet. We define the wavelet projection of s on Ψ at position $\boldsymbol{x}$ and resolution r as:

$$T_\Psi |\nabla s|(\boldsymbol{x}, r) = \int |\nabla s|(\boldsymbol{y}) \Psi(\frac{\boldsymbol{x} - \boldsymbol{y}}{r}) d\boldsymbol{y} \tag{13}$$

We can now define a random variable $\zeta_{r/L}(\boldsymbol{x})$ as

$$T_\Psi|\nabla s|(\boldsymbol{x},r) = \zeta_{r/L}(\boldsymbol{x}) T_\Psi|\nabla s|(\boldsymbol{x},L) \tag{14}$$

Now, we can talk about a wavelet Ψ which, if determined, will make $\zeta_{r/L}(\boldsymbol{x})$ independent of $T_\Psi|\nabla s|(\boldsymbol{x},L)$. Such a wavelet is called an *optimal wavelet*. In subsection *Optimal Wavelet Analysis*, we propose a new algorithm for a very robust detection of the optimal wavelet in 2D signals. The new methodology helps us to detect the presence of an optimal wavelet, in a totally unconstrained way, from the signal itself. Once determined, the optimal wavelet has the potential of unlocking the signal's microcanonical cascading properties through simple wavelet multiresolution analysis [8].

5.1 Multiresolution Analysis & fast wavelet transform

Multiresolution analysis is a mathematical formalism that deals with the phenomenon of detail-structured viewing of objects [8]. Data redundancy is minimized by use of dyadic wavelet sequences which are hilbertian frames associated to dyadic partition of the space/frequency domain.

Any signal $|s\rangle$ can be represented in a dyadic wavelet basis of mother wavelet $|\Psi\rangle$ [13] as follows (from now on we use the notation $|s\rangle$ for the signal):

$$|s\rangle = \sum_{j=-\infty}^{\infty} \sum_{k} \alpha_{j,k} |\Psi_{j,k}\rangle \tag{15}$$

where

$$|\Psi_{j,k}\rangle(\boldsymbol{x}) = 2^{j/2}\Psi(2^j\boldsymbol{x} - k) \tag{16}$$

and $\alpha_{j,k}$, are called *wavelet coefficients*. The wavelet coefficients $\alpha_{j,k}$ can be obtained by a simple projection of the signal $|s\rangle$ onto the basis function $\Psi_{j,k}$, namely:

$$\alpha_{j,k} = \langle s|\Psi_{j,k}\rangle \tag{17}$$

The decomposition process using multiresolution analysis gives rise to an image fourth smaller than the previous one. Therefore, each *parent coefficient* $\alpha_p \equiv \alpha_{j-1,[k/2]}$, at the coarser scale $j-1$, covers the same spatial extent of four *children coefficients* $\alpha_c \equiv \alpha_{j,k}$ at the finer scale j.

5.2 Approximation of microcanonical cascade

In the wavelet analysis of 2D signals, persistence along the scales implies a realtion of the form between the wavelet coefficients:

$$\alpha_c = \eta_1 \alpha_p + \eta_2 \tag{18}$$

with η_1,η_2: random variables independant of α_c and α_p and also independant of each other. For an optimal wavelet the above equation takes the form $\alpha_c = \eta_1 \alpha_p$.

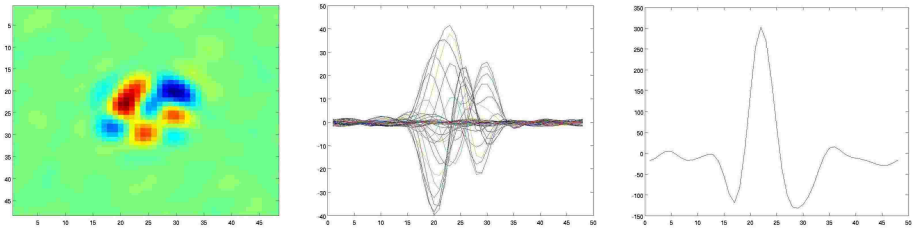

(a) (b) (c)

Fig. 2: (a) Sub-image at 48 × 48 pixels resolution obtained after orientation with the sign with the MCE (b) 2-D plot of the sub-image (c) 2-D plot for the sum over the columns.

5.3 Optimal Wavelet Analysis

Any given signal $|s\rangle$ can be represented in terms of their cascade variables η and wavelet coefficients α as:

$$|s\rangle = \sum_{j\neq 0,k} \prod_{j',k} \eta_{j',[k/2^{j-j'}]} \alpha_{0,0} |\Phi_{j,k}\rangle + \alpha_{0,0}|\Phi_{0,0}\rangle \tag{19}$$

where $\Phi_{j,k}$ is the wavelet basis for the optimal wavelet. Experimental observations show that the expectation of the signal $\langle|s\rangle\rangle = 0$ as $\langle\alpha_{0,0}\rangle = 0$ due to symmetry.

We multiply the sign of $\alpha_{0,0}$ i,e, $\sigma_{0,0}$ with the signal s and then compute the average. Since, in our case we have an ensemble of dynamically equivalent signals, we compute the average over $|s^i\rangle$ to get the expected value for all these signals; where i is the index of an ordering of the signals. Equation (19) can be generalized to:

$$\langle\sigma^i_{0,0}|s^i\rangle\rangle = \langle|\alpha_{0,0}|\rangle|\Phi_{0,0}\rangle \tag{20}$$

We try to estimate the sign of $\alpha_{0,0}$. Let $\epsilon_{0,0}$ be the estimation, we then have

$$\langle\epsilon^i_{0,0}|s^i\rangle\rangle = \langle\epsilon_{0,0}\sigma_{0,0}|\alpha_{0,0}|\rangle|\Phi_{0,0}\rangle \propto \Phi_{0,0} \tag{21}$$

Principle application of finding the optimal wavelet on a given set of images is quite simple. The procedure is as follows:

- We subdivide a given image $|s^i\rangle$ over small areas of equal sizes and normalize individually every sub-image.
- We find the correlation between the sub-images of $|s^i\rangle$: $C_i = \langle s^i|s^k\rangle$.
- For every i we find the average of the correlation.
- We then find for which l, the average correlation is maximum. Let it be i^*.
- We call $|s^{i^*}\rangle$ as the *most central element* (MCE).

Since we don't know $\Phi_{0,0}$, we make the wavelet projection of the signal on the element which has the most dependancy with all the other elements (dominant presence of the term $\langle|\alpha_{0,0}|\rangle|\Phi_{0,0}\rangle$); i,e, the MCE. So, we have

$$\begin{aligned}\epsilon^i_{0,0} &= \sigma(C_{i,i*}) = \sigma(\langle s^i|s^{i*}\rangle) \\ &= |\alpha^*_{0,0}|\sigma_{0,0}\sigma^*_{0,0}\langle s|\Phi_{0,0}\rangle \end{aligned} \tag{22}$$

If we have a correct estimate of the sign, we can say $\langle\epsilon^i_{0,0}|s^i\rangle\rangle \propto \langle\sigma^i_{0,0}|s^i\rangle\rangle$. And we estimate the wavelet from equation (21). Since wavelets are normalized by definition, we can cancel the proportionality factor in equation (21):

$$\langle\epsilon^i_{0,0}|s^i\rangle\rangle = \langle\sigma(C_{i,i*})|s^i\rangle\rangle = \langle\sigma(\langle s^i|s^{i*}\rangle)|s^i\rangle\rangle \tag{23}$$

We have tested this algorithm on Benzi model [9] to construct multiaffine fields based on an order 2 gaussian wavelet decomposition. The preliminary results are shown in Fig 2. Since, the process of finding an optimal wavelet is still under review and subjected to constant experimentation, we approximate the optimal wavelet by a Battle-Lemarié wavelet which is found to give an acceptable approximation of the optimal wavelet.

6 DATA

6.1 Atmospheric Phase

The data is shown in Fig 1 (top). The datasets consists in simulated optical phase perturbated by the Earth's upper layer turbulent atmosphere. The optical phase corresponds to the acquisition of a point source (representing a star far away enough in outer space so that the optical phase reaching the telescope is in the form of planar wavefronts). These data are provided by the French Aerospace Lab-ONERA, and they have the following imaging characteristics:

- diameter of the telescope: 8 m,
- seeing at 5 microns: 0.85 arcseconds,
- wind's speed: 12.5 m/s,
- acquisition frequency: 250 Hz,
- pupil size: 256 $\times$ 256 pixels, but for our experimental purpose we take 128 $\times$ 128 pixels from the centre to eliminate boundary effects.

We have the Hartmann-Shack (HS) acquisition of the x and y slopes for the phase data provided by onera given by 208 effective HS sub-pupils (size 16 $\times$ 16) which samples the pupil of the telescope. The distribution of the sub-pupils within the telescope is shown in Fig 4(a). Fig 4(b) and Fig 4(c) shows the x and y low resolution acquisition of the phase data, which gives us an approximation of low resolution x and y components of the gradients for the phase, by the HS sensor.

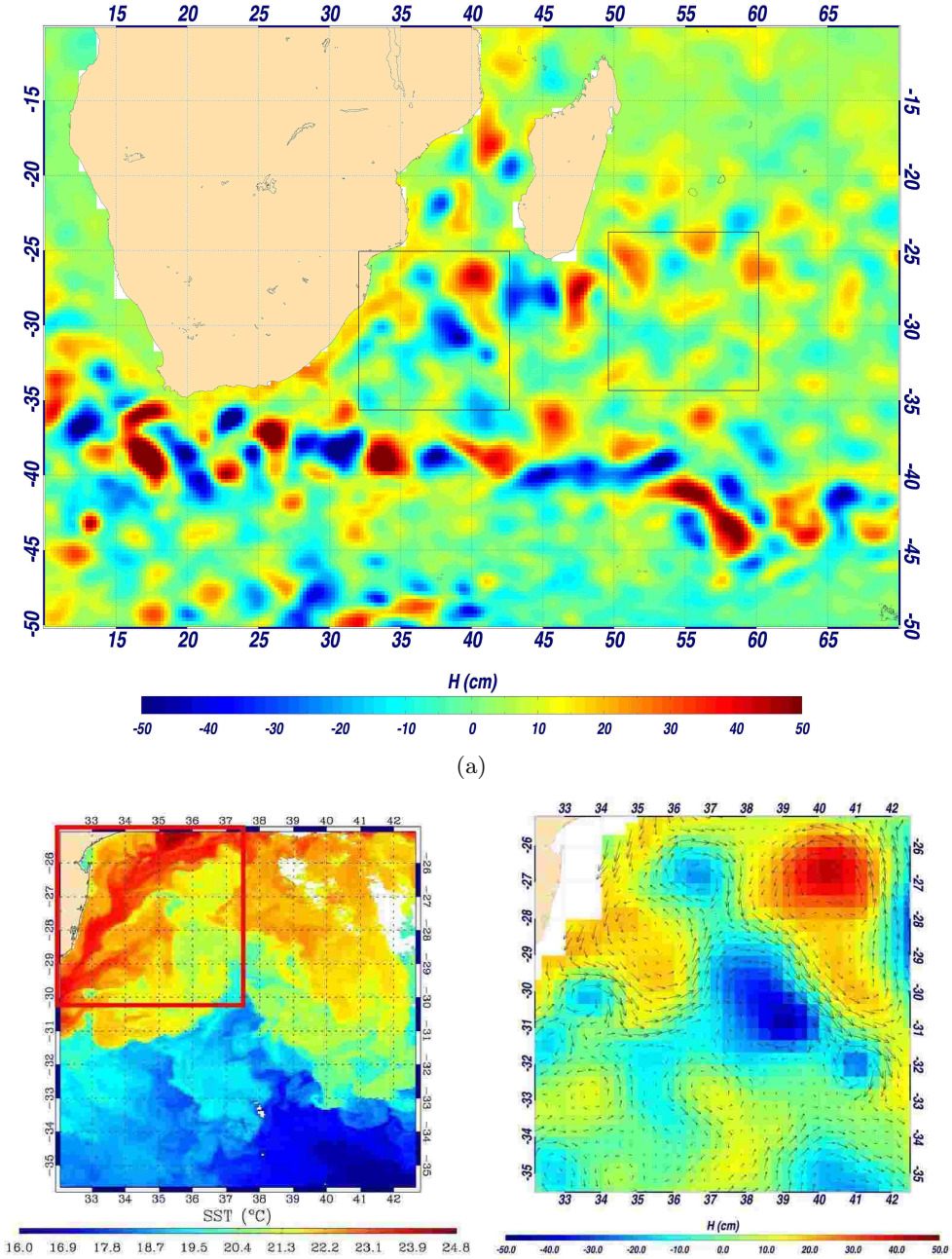

(a)

(b)

(c)

Fig. 3: (a) Altimetry data (b) Sea Surface Temperature (SST) acquired by MODIS satellite on August 2, 2007 (c) low-resolution motion field derived from altimetry.

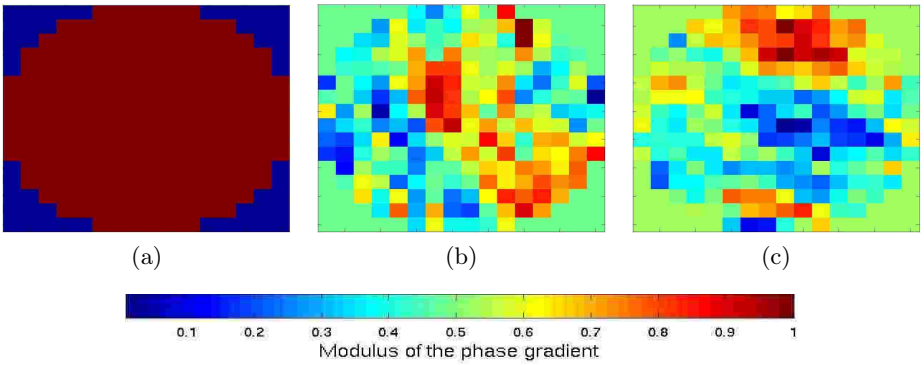

Fig. 4: (a) Distribution of the sub-pupils within the telescope (b) HS acquisition of the x slope for the phase data (c) HS acquisition of the y slope for the phase data.

6.2 Sea Surface Temperature

Sea surface temperature data (SST) are global acquisitions of the temperature of the ocean's upper layer. Data is radiometrically corrected so that pixels values represent celsius degrees. Data is acquired by the MODIS instrument orbiting around earth, pixel resolution is 4 kms, data is acquired on 02 August 2007. In our experiment, we also use low resolution products representing geostrophy and Ekman currents deduced from altimetry data according to method exposed in [26]. Pixel size of altimetry products is 22 kms. Figure 3(a) shows the altimetry, figure 3(b) the MODIS data and figure 3(c) shows the low-resolution motion field derived from altimetry according to [26].

7 Results

7.1 Edge detection and singularity exponents

First we detail the comparison results on edge detection using classical linear filtering and the set provided by equation (8). Reconstruction has been performed on the edge files computed on the phase and sea surface temperature images. Performance of the reconstruction on classical edge detectors to a more recent nonlinear derivative approach (called NLFS) [7] and MSM has been presented in table 1. Also, we evaluate the quality of the reconstruction using the *peak signal to noise ratio* (psnr, expressed in decibels dB) defined by:

$$\text{psnr} = -20.0 \times \log_{10}\left(\frac{1}{\lambda(\Omega)}\frac{\left(\int_{\Omega}(s(\boldsymbol{x})-s_r(\boldsymbol{x}))^2 \mathrm{d}\boldsymbol{x}\right)^{1/2}}{\Delta_s}\right) \tag{24}$$

where Ω is the image domain, $\lambda(\Omega)$ its Lebesgue measure (image size), s the original image, s_r the reconstructed image, and Δ_s is the dynamical range of s ,

i.e. the difference between the maximal and minimal values. Better reconstructions tend to have a higher psnr. A quantitative evaluation of the results are presented in table 2.

7.2 Reconstruction of optical phase

Also, we show that the application of wavelet multiresolution analysis technique on the signal (optical phase perturbated by atmospheric turbulence) of the singularity exponents provided by a simple approximation of an optimal wavelet (here a third order Battle-Lemarié wavelet) help us to infer information along the scales of the signal which in turn can be used to properly reconstruct the signal from low resolution to high resolution. The process is summarized below:

- We first compute the third order Battle-Lemarié wavelet coefficients associated to the signal of the singularity exponents computed on the perturbated phase signal,
- for each component (x and y) of the phase gradient at low reslution (16×16 sub-image, see section 6.1), back project the component from low to high resolution to get a phase's gradient at higher spatial resolution of 128×128.

Consequently, we reconstruct the phase by performing inverse gradient operation on the norms of the gradients. We also check the robustness of our reconstruction algorithm by adding different proportions of gaussian white noise to the data. Results obtained, as shown in Fig 6, show visual resemblance of the reconstructed signal with the original one.

7.3 High resolution ocean dynamics

In this experiment, the low resolution vector field shown in figure 3(c) and derived from altimetry data is used to generate a high resolution vector field corresponding to SST data. First, the singularity exponents are computed on SST data. Then a multiresolution analysis is performed on the resulting singularity exponents from SST spatial resolution (4 kms) down to altimetry resolution (22 kms). The low resolution vector field shown in figure 3(c) is propagated, componentwise, up to SST resolution and the resulting vector field is prefiltered using an $1/||f||$ filter. The results are shown in figure 5: a high resolution vector field representing the ocean dynamics at resolution 4 kms is obtained from the multiresolution analysis of the singularity exponents. Validation has been performed on the outputs of a 3D simulation model, and shows proper reconstruction of the high resolution vector field both in norm and direction: 80% of vectors are correctly computed. This method provides a very interesting alternative to classical motion computation techniques that use conservation hypothesis (optical flow) or Maximum Correlation methods.

Table 1: Performance of different edge detection algorithms. **row 1:** Atmospheric phase data. **row 2:** SST data of the Agulhas current below the coast of South Africa.

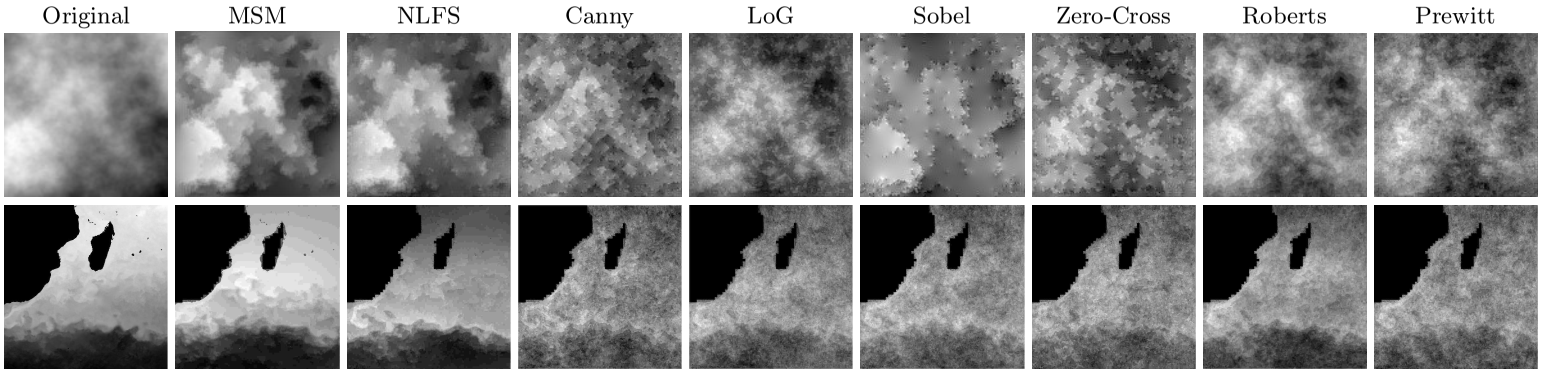

Table 2: Evaluation of edge detection algorithms

Image	Algorithm	Parameter(s)	Density	Reconstruction (psnr)
sea temp.	NLFS [7]	$\sigma = 0.2$	22.24 %	10.15 dB
sea temp.	Canny	$\sigma = 0.001$, $\alpha = 01$	13.094 %	9.65 dB
sea temp.	Laplacian	$\sigma = 0.001$, $\alpha = 01$	24.47 %	10.16 dB
sea temp.	Sobel	$\sigma = 0.001$	24.58 %	9.58 dB
sea temp.	Zero-crossing	$\sigma = 0.001$	13.95 %	9.60 dB
sea temp.	Roberts	$\sigma = 0.001$	27.97 %	10.22 dB
sea temp.	Prewitt	$\sigma = 0.001$	24.83 %	9.83 dB
sea temp.	MSM	parameter free	17.24 %	11.30 dB
phase	NLFS [7]	$\sigma = 0.25$	24.92 %	8.30 dB
phase	Canny	$\sigma = 0.001$, $\alpha = 01$	14.11 %	7.25 dB
phase	Laplacian	$\sigma = 0.001$, $\alpha = 01$	28.48 %	7.24 dB
phase	Sobel	$\sigma = 0.3$	5.83 %	6.48 dB
phase	Zero-crossing	$\sigma = 0.001$	15.88 %	6.61 dB
phase	Roberts	$\sigma = 0.001$	34.74 %	7.77 dB
phase	Prewitt	$\sigma = 0.001$	26.72 %	6.96 dB
phase	MSM	parameter free	15.75 %	13.18 dB

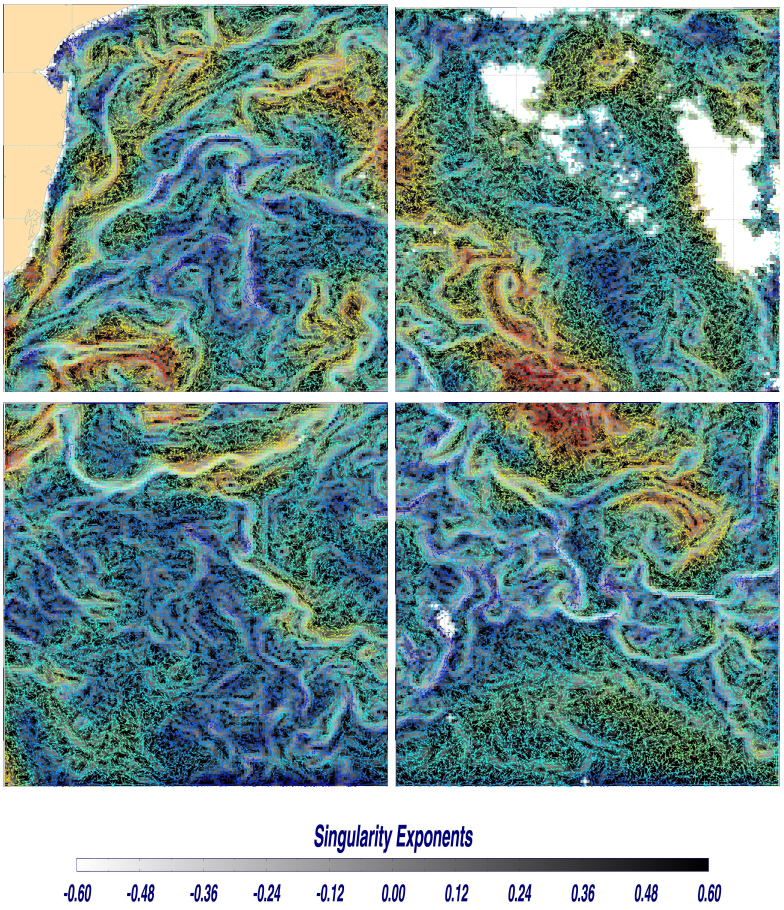

Fig. 5: Vector field computed at high resolution SST MODIS data using the low resolution altimetry of Fig 3(c) and the multiresolution analysis of the SST singularity exponents as explained in section 7. The color of the vectors indicate their norm from 0.0 $\mathrm{cm} \cdot \mathrm{s}^{-1}$ (blue) to 83.9 $\mathrm{cm} \cdot \mathrm{s}^{-1}$ (red). In the background we also display the singularity exponents.

8 Conclusion

In this work we set up and study a multiresolution analysis scheme general enough to suit the case of acquisitions of general complex systems. We first study geometrically localized singularity exponents in natural signals, computed in a microcanonical framework, from which singularity spectra can be derived. We study their relations with high order transitions in associated phase spaces, and conclude that they unlock a notion of transition that outperforms all classical «linear filtering» approaches for edge detection in the case of 2D images. Edges

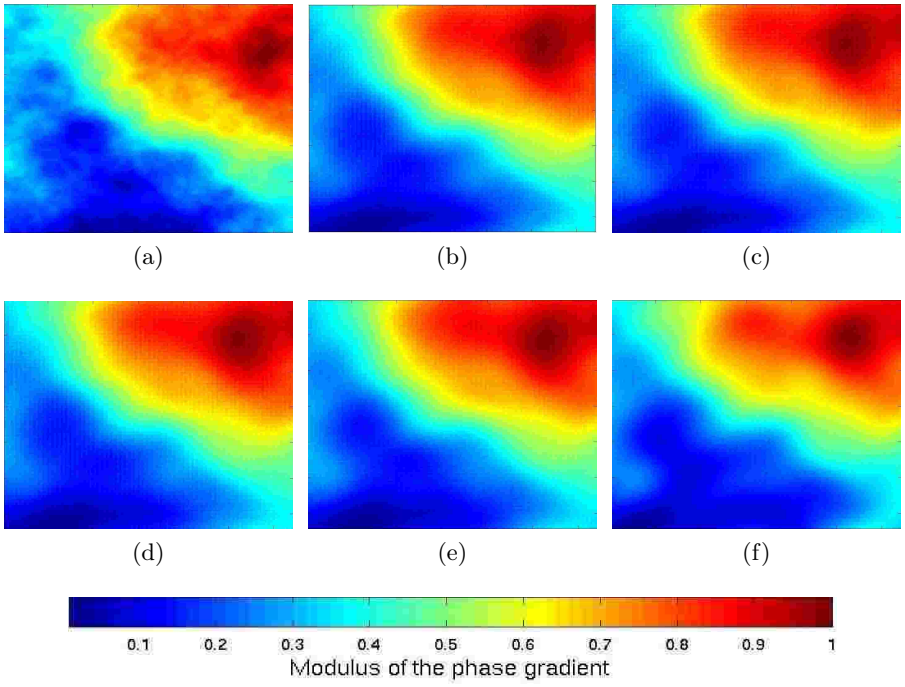

Fig. 6: (a) The original phase. Reconstructed phase (b) without noise. (c) with an input SNR of 40 dB. (d) with an input SNR of 26 dB. (e) with an input SNR of 14 dB. (f) with an input SNR of 6 dB.

are typical multiscale features, which should maximize information content in natural signals. We study the performance of reconstructible systems both with transitions associated to singularity exponents and the edge pixels provided by standard edge detection techniques. Examples are chosen among the most difficult natural signals: acquisition of turbulent phenomena (perturbated optical phase and ocean dynamics acquired from space). We study a multiresolution analysis scheme associated to the signal of singularity exponents, and in doing so we provide an effective determination of optimal wavelets, which are wavelets whose associated multiresolution analysis is optimal w.r.t inference across the scales. We show the power of the approach by studying two specific examples: the reconstruction of the phase perturbated by atmospheric turbulence applied to adaptive optics and the generation of high resolution ocean dynamics from low resolution acquired altimetry signals. The method is general enough to provide an effective approach to infer sub-pixel information in most natural complex signals.

Acknowledgment

Suman Kumar Maji's PhD is funded by a CORDIS grant and Région Aquitaine OPTAD research project grant.

References

1. O. Pont, A. Turiel, C. Perez-Vicente: Empirical evidences of a common multifractal signature in economic, biological and physical systems. *Physica A*, Elsevier, 388, 2009, 2025-2035.
2. A. Turiel, C. Perez-Vicente, J. Grazzini: Numerical methods for the estimation of multifractal singularity spectra on sampled data: A comparative study. *Journal of Computational Physics*, Elsevier, 216, 2006, 362-390.
3. A. Arneodo, E. Bacry, J. Muzy: The thermodynamics of fractals revisited with wavelets. *Physica A* 213, 232-275, 1995.
4. A. Turiel, H. Yahia and C. Perez-Vicente: Microcanonical Multifractal Formalism: a geometrical approach to multifractal systems. Part I: singularity analysis. *Journal of Physics A: Mathematical and Theoretical, vol 41*, doi: 10.1088/1751-8113/41/1/015501.
5. U. Frisch: 1995 Turbulence (Cambridge: Cambridge University Press).
6. A. Turiel and A. del. Pozo Reconstructing images from their most singular fractal manifold. *IEEE Transactions Image Processing*, 2002, 11, 345-50.
7. O. Laligant, F. Truchetet: A nonlinear derivative scheme applied to edge detection. *IEEE PAMI*, 2010, 32, 242–257.
8. C. Pottier, A. Turiel, V. Garçon: Inferring missing data in satellite chlorophyll maps using turbulent cascading. *Remote Sensing of Environment*, Elsevier, 112, 2008, 4242-4260.
9. R. Benzi, L. Biferale, A. Crisanti, G. Paladin, M. Vergassola, A. Vulpiani: A random process for the construction of multiaffine fields. *Physica D: Nonlinear Phenomena*, Volume 65 Issue 4, June 15, 1993.
10. S. Lovejoy, D. Schertzer: Multifractals, universality classes, satellite and radar measurements of clouds and rain. *Journal of Geophysical Research* 95, 2021-2034, 1990.
11. G. Parisi, U. Frisch: On the singularity structure of fully developed turbulence Turbulence and Predictability in Geophysical Fluid Dynamics. *Proc. Intl School of Physics E. Fermi ed* M Ghil, R Benzi and G Parisi (Amsterdam: North-Holland) pp 84-7, 1985.
12. A. Turiel and N. Parga: The multi-fractal structure of contrast changes in natural images: from sharp edges to textures. *Neural Computation* 12, 763-93, 2000.
13. Stéphane Mallat, *A Wavelet Tour of Signal Processing*, Academic Press, 2nd Edition, 1999.
14. G. Boffetta, M. Cencini, M. Falcioni, et al: Predictability: a way to characterize complexity. *Physics Reports* 356 (6): 367-474 JAN 2002.
15. O. Pont, A. Turiel, C. Perez-Vicente, Description, modelling and forecasting of data with optimal wavelets, *J.Econ Interact Coord*, 2009, 4: 39-54, doi 10.1007/s11403-009-0046-x.
16. O. Pont, A. Turiel, H. Yahia: An Optimized Algorithm for the Evaluation of Local Singularity Exponents in Digital Signals. *IWCIA*, 6636, 2011, 346-357.

17. L. G. Roberts: Machine perception of three dimensional solids. in *Optical and Electro-Optical Information Processing*, J. T. Tippett et al., Eds. Cambridge, MA: MIT Press, 1965.
18. J. Prewitt: Object Enhancement and Extraction. Picture Process Psychopict, 1970, pp. 75-149.
19. A. Rosenfeld: Picture Processing by Computer. New York: Academic Press, 1969.
20. I. Sobel: Neighbourhood coding of binary images fast contour following and general array binary processing. *Computer Graphics and Image Processing* 8, pp. 127-135, 1978.
21. D. Marr, E. Hildreth: Theory of edge detection. *Proc. Royal Soc. London B* 207, 187-217, 1980.
22. R. M. Haralick: Digital step edges from zero crossing of second directional derivatives. *IEEE PAMI* 6, 58-68, 1984.
23. J. Canny: A computational approach to edge detection. *IEEE PAMI* 8, 679–698, 1986.
24. V. Torre, T. A. Poggio: On edge detection. *IEEE PAMI* 8, 147-163, 1986.
25. O. Faugeras: Three-dimensional computer vision:a geometric viewpoint. *MIT Press* 1993, ISBN: 0-262-06158-9.
26. J. Sudre and R. Morrow: Global surface currents, a high resolution product for investigating ocean dynamics, 58, 101-118, doi:10.1007/s10236-008-0134-9, 2008.

3.10 Détermination de la norme

Dans l'article [*Yahia H. et al.*, 2010], la détermination de l'orientation du champ de vitesses normalisé a été obtenue par l'utilisation combinée de données de TSM au $1/24°$ et du produit GEKCO au $1/4°$ via l'utilisation de la cascade multiplicative en formulation microcanonique. Nous allons donc dans cette section présenter la détermination de la norme de ce même champ de vitesse avec une méthode similaire permettant ainsi de quantifier complètement l'écoulement turbulent océanique.

La détermination de la norme est effectuée avec le même jeu de données que pour l'orientation, à savoir :

- Le signal TSM au $1/24°$ du produit MODIS/Aqua, permettant d'avoir une représentation de la turbulence pleinement développée océanique prenant en compte toute la dynamique submésoéchelle,
- le produit de courants océaniques GEKCO au $1/4°$ développé au cours de cette thèse à partir de l'altimétrie et du stress de vent, qui permet d'avoir une estimation qualitative et quantitative à une résolution plus faible de la norme des vitesses de la dynamique océanique.

Le principe de l'algorithme énoncé ci-dessous est d'utiliser l'analyse multirésolutions pour inférer la norme de la vitesse à basse résolution sur un signal provenant à plus haute résolution et d'obtenir la norme à cette même superrésolution :

- étape 1 : une fonction de courant est calculée à la plus haute résolution disponible (ici $1/24°$) au moyen de la TSM et en utilisant la variété la plus singulière des exposants de singularité [*Isern-Fontanet et al.*, 2007],
- étape 2 : l'analyse multirésolution (voir équation 3.27) est générée sur la fonction de courant obtenue à l'étape 1 avec l'ondelette Battle-Lemarié d'ordre 3,
- étape 3 : en utilisant l'analyse multirésolution associée à la fonction de courant provenant des données de TSM, la norme du produit GEKCO est inférée pour obtenir une norme à la même résolution que les données de TSM.

Cet algorithme permet d'obtenir une estimation de la norme du champ de vecteurs à la même résolution et pour les mêmes points du signal (i.e. la TSM) que ceux pour lesquels on a obtenu la direction au moyen de la méthode décrite dans l'article [*Yahia H. et al.*, 2010]. L'écoulement océanique bidimensionnel est donc parfaitement déterminé dans le domaine de l'espace euclidien $\mathbb{R}^2$ par la connaissance de sa norme et de sa direction.

Les figures 3.4 et 3.5 montrent les données de TSM et du produit GEKCO utilisé pour la détermination de l'écoulement pour la date du 02 août 2007. La figure 3.6 montre le champ de vecteurs turbulent obtenu par l'utilisation de l'analyse multirésolutions à cette même date. On constate sur cette image que le champ de vecteurs obtenu pour la dynamique océanique est bien turbulent. La direction des vecteurs est collinéaire aux fronts de transition représentés par les zones claires des exposants de singularité. La norme du champ de vecteurs correspond à la norme à plus basse résolution du produit GEKCO. Par cet exemple nous voyons que l'analyse multirésolutions permet une inférence d'un champ de vecteurs collocalisé à basse résolution sur une représentation de la dynamique turbulente issue des données de TSM à plus haute résolution.
Afin de confirmer ce résultat, le calcul de la dynamique turbulente a été effectué sur une série temporelle de quatre ans correspondant à la période du 01 janvier 2006 au 31 décembre 2009. La section suivante va donc être consacrée à la nécessaire étape de validation au moyen de données de bouées Lagrangiennes de surface droguées à $15\ m$ sur toute la période calculée.

3.11 Validation de la dynamique turbulente à haute résolution

3.11.1 Méthodes de validation

Afin de valider les résultats de la dynamique océanique turbulente, 373 bouées Lagrangiennes droguées à $15\ m$ sur la période du 01 janvier 2006 au 31 décembre 2009), provenant du "Global Drifter Program", ont été utilisées. Ces données représentent le déplacement de bouées dérivantes interpolées sur

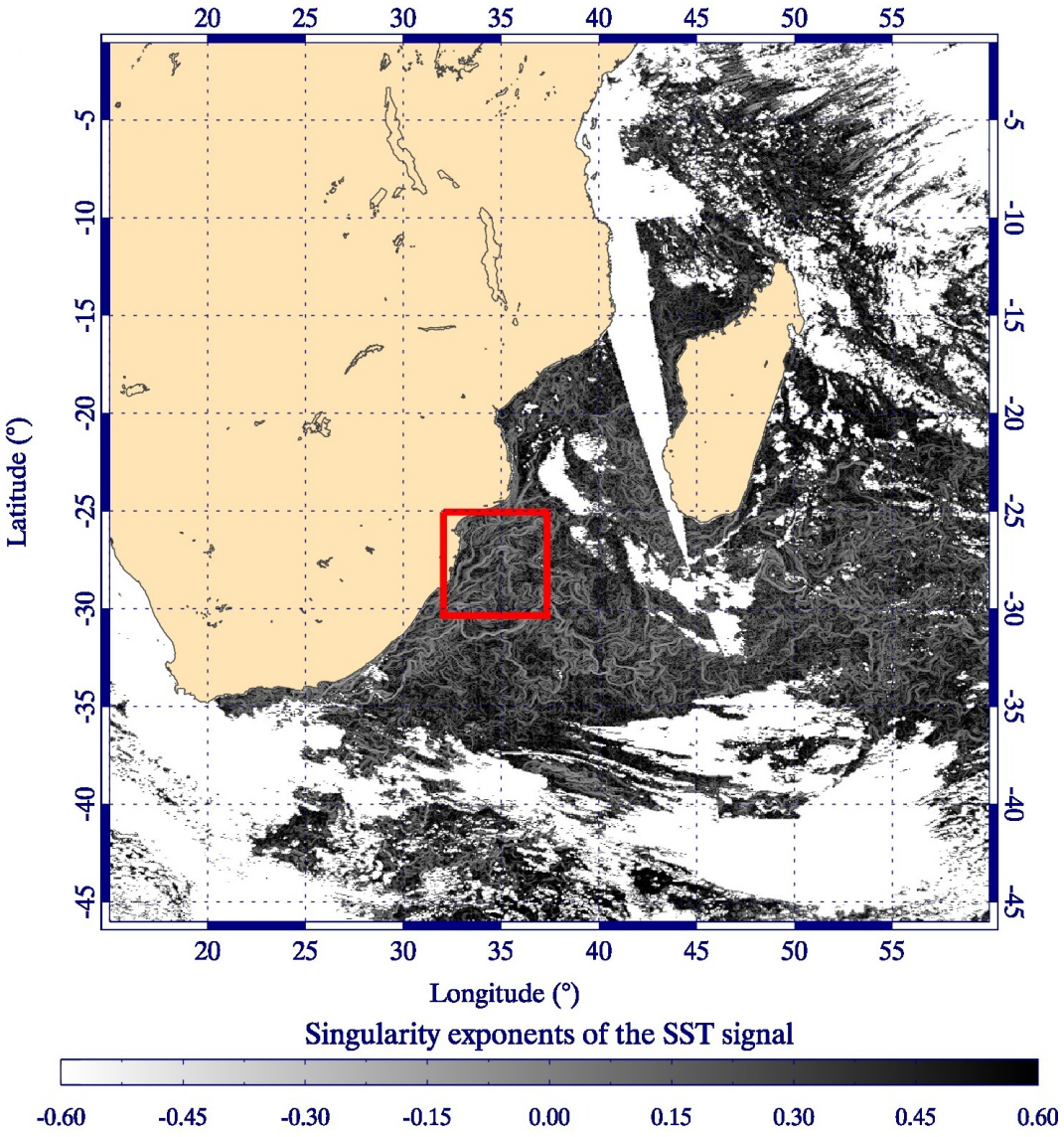

FIGURE 3.4 – *Exposants de singularité, pour la date du 02 août 2007, dérivés à partir des données de TSM MODIS/Aqua. Les fronts de transition représentés par les courbes claires sur cette image représentent les zones où les gradients de température sont importants dans l'océan en délimitant les structures océaniques cohérentes à différentes échelles. Le carré noir représente la sous-zone de la figure 3.6.*

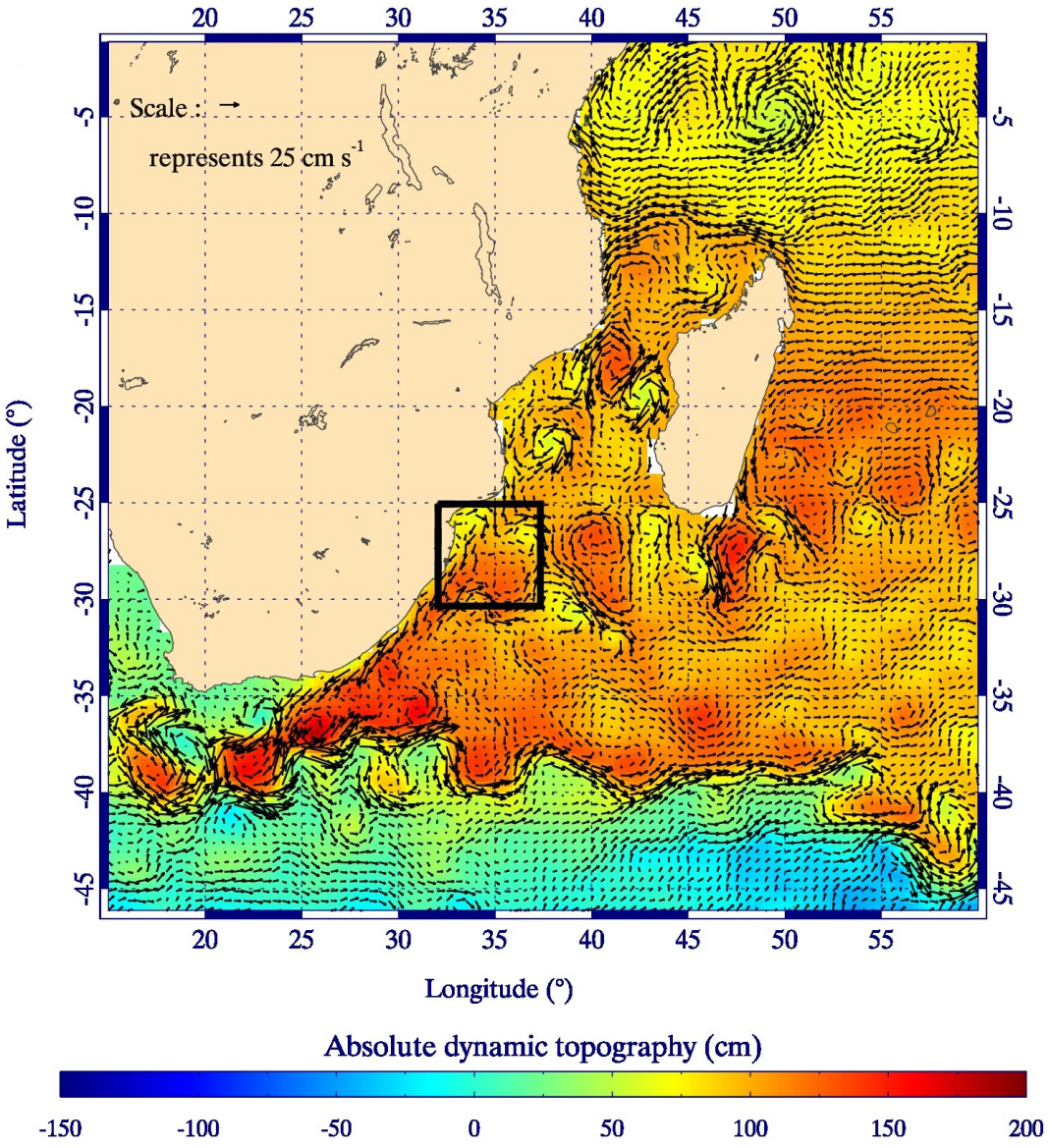

FIGURE 3.5 – *Dynamique océanique du produit GEKCO, pour la date du 02 août 2007, superposée à la topographie dynamique absolue. Le carré noir représente la sous-zone de la figure 3.6.*

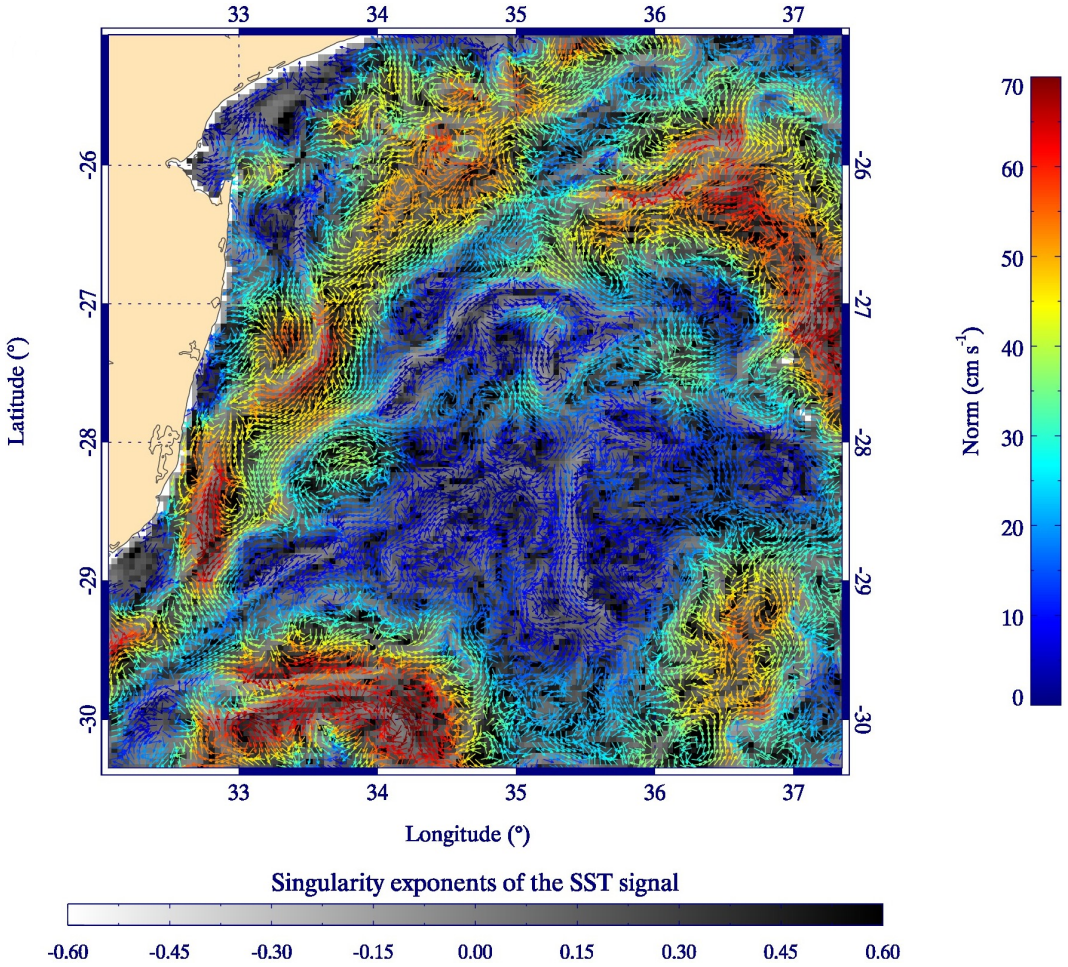

FIGURE 3.6 – *Dynamique océanique turbulente obtenue par l'analyse multirésolutions au moyen des données GEKCO à basse résolution et des exposants de singularité à haute résolution pour propager la dynamique turbulente à travers les échelles. Du fait de la très haute densité du champ de vecteurs résultant, l'image montre uniquement les valeurs à l'intérieur du sous-domaine carré des figures 3.4 et 3.5.*

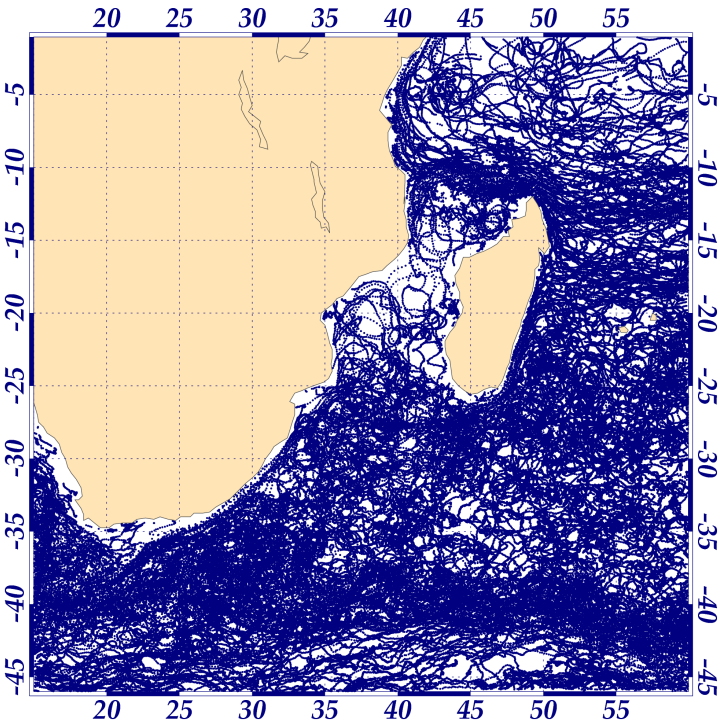

FIGURE 3.7 – *Déplacement des 373 bouées Lagrangiennes droguées à* $15\ m$ *sur la période du 01 janvier 2006 au 31 décembre 2009.*

un pas de temps de six heures, il est donc difficile de séparer la variabilité mésoéchelle de la variabilité submésoéchelle dans ce jeu de données. De ce fait, la validation a été conduite de la manière suivante ; la surface océanique correspondant à la zone d'étude a été divisée en sous-domaines carrés de taille $2.25° \times 2.25°$. Soit M un de ces sous-domaines pour lequel deux jeux de données sont présents : le jeu de données provenant des bouées dérivantes et les courants collocalisés avec la position de ces bouées :

$$M_b = \{\mathbf{u}_1, \mathbf{u}_2, \cdots, \mathbf{u}_n\} \tag{3.32}$$

$$M_c = \{\mathbf{w}_1, \mathbf{w}_2, \cdots, \mathbf{w}_n\} \tag{3.33}$$

Pour chaque jeu de données, un vecteur moyen est calculé :

$$a = \frac{1}{n} \sum_{i=1}^{n} \frac{\mathbf{u}_i}{||\mathbf{u}_i||} \tag{3.34}$$

$$b = \frac{1}{n} \sum_{i=1}^{n} \frac{\mathbf{w}_i}{||\mathbf{w}_i||} \tag{3.35}$$

Dans chaque sous-domaine M la valeur $||a|| - ||b||$ est représentée pour avoir une estimation de la différence de la norme moyenne entre les bouées Lagrangiennes et les courants estimés. La direction a aussi été validée en calculant le produit scalaire ($< \frac{a}{||a||} | \frac{b}{||b||} >$).

3.11.2 Validation de la dynamique à haute résolution obtenue à partir de la TSM MODIS/AQUA

Afin de valider les courants à super-résolution, le jeu de données de bouées Lagrangiennes a été utilisé pour représenter des données *in situ*. Cependant ce jeu de données étant délivré avec une interpolation temporelle à six heures, il est nécessaire d'évaluer sa variabilité submésoéchelle. En d'autre termes, est-ce que le déplacement des bouées Lagrangiennes suit le mouvement des structures cohérentes à fine échelle ?
Pour évaluer la présence de cette variabilité submésoéchelle dans les données

de bouées Lagrangiennes, ce jeu de données a été utilisé soit sans aucun filtrage (en gardant les courants inertiels et la variabilité submésoéchelle), soit en effectuant un lissage sur les positions des bouées. Ce lissage est le même que celui utilisé pour la validation du produit GEKCO dans le chapitre 2. Les tests de validation (norme et direction) expliqués dans la sous-partie précédente ont ensuite été exécutés sur le produit de dynamique océanique à super-résolution avec le jeu de données des positions des bouées Lagrangiennes (lissés ou pas).

La TSM MODIS/Aqua comportant des données manquantes dues à la nature du capteur utilisé (bande spectrale dans l'infra-rouge), il a aussi été nécessaire au préalable de calculer, pour les deux jeux de bouées Lagrangiennes, le nombre de positions de bouées ayant permis le calcul des tests pour chaque boîte (voir figure 3.8). Le nombre de positions étant quasiment identique par boîte entre les deux tests, les résultats obtenus pour ces deux jeux de données seront donc comparables.
La figure 3.9 présente la validation de la norme des courants pour ces deux premiers tests. La figure 3.10 présente la validation de la direction des courants pour ces deux premiers tests.

Les résultats obtenus pour la norme ainsi que pour la direction indiquent que le lissage effectué sur les déplacements des bouées Lagrangiennes (pour le même nombre de positions) dégrade les résultats de la validation.
Ceci peut facilement s'expliquer : le lissage qui a été effectué sur les déplacements des bouées Lagrangiennes avait pour but d'éliminer la variabilité submésoéchelle pour ne laisser uniquement que la variabilité mésoéchelle. Le produit de courant développé par l'analyse multirésolutions a justement comme objectif de faire apparaître toute la turbulence pleinement développée à ces deux échelles de résolution. On constate, par exemple, pour la validation de la norme une dégradation des résultats surtout dans les zones de la branche Nord du SEC et du NEMC (entre $5°$S - $20°$S), du AC, et dans toute sa rétroflexion. Ce résultat n'est pas surprenant car ces zones sont connues pour avoir une forte activité submésoéchelle. Le résultat sur la direction corrobore cette constatation ; en effet, dans ce cas : le lissage a l'effet contraire puisque le champ de courant est turbulent bien qu' il ne représente pas les courants inertiels. En conséquence les bouées non lissées (dont la direction de déplacement est dominée par les courants inertiels), ne vont pas avoir la même

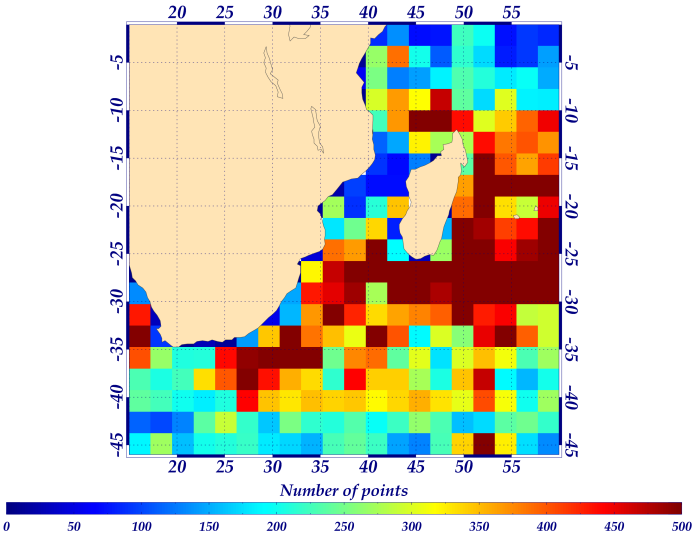

(a) Nombre de positions non lissées de bouées Lagrangiennes collocalisées avec les données de courant.

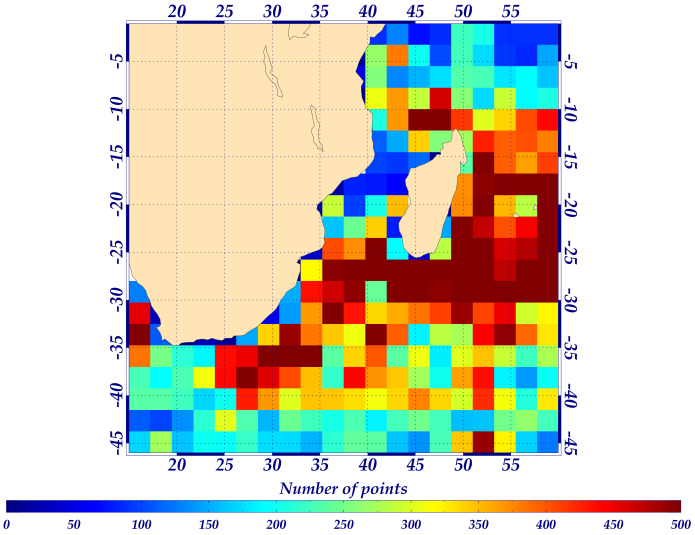

(b) Nombre de positions lissées de bouées Lagrangiennes collocalisées avec les données de courant.

FIGURE 3.8 – Nombre de positions de bouées Lagrangiennes collocalisées avec les données de courant pour la période de validation du 01 Janvier 2006 au 31 Décembre 2009.

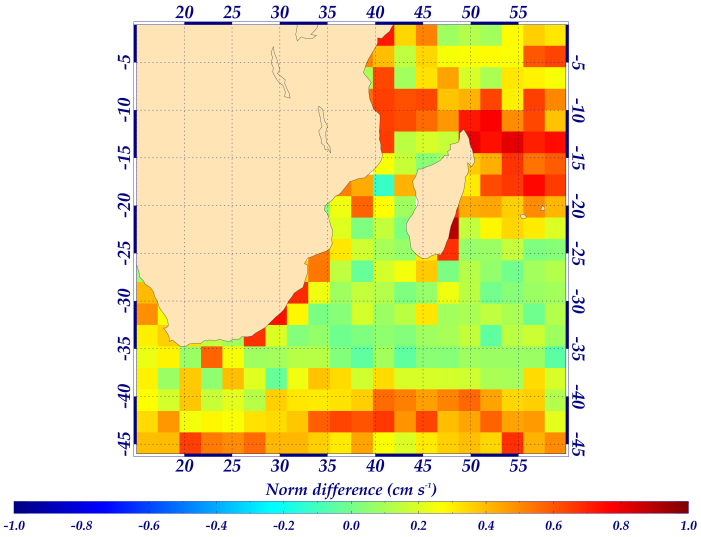

(a) Validation de la norme par les positions non lissées des bouées Lagrangiennes.

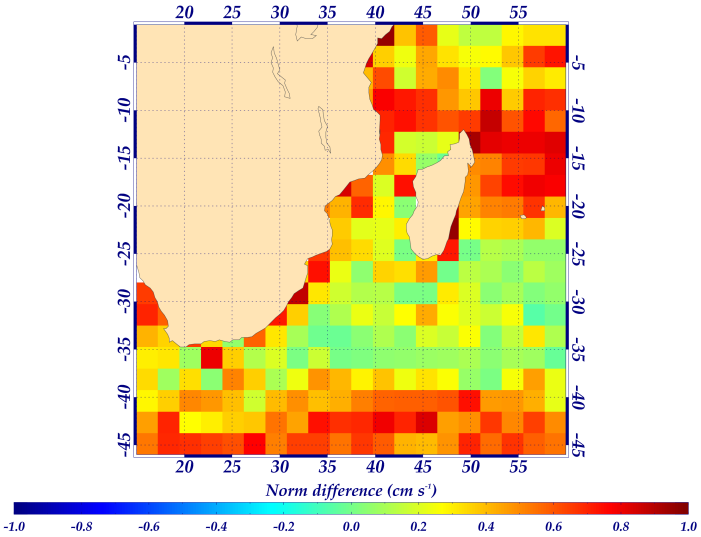

(b) Validation de la norme par les positions lissées des bouées Lagrangiennes.

FIGURE 3.9 – Différence de la norme calculée entre les positions des bouées Lagrangiennes collocalisées avec les données des courants pour la période de validation du 01 Janvier 2006 au 31 Décembre 2009.

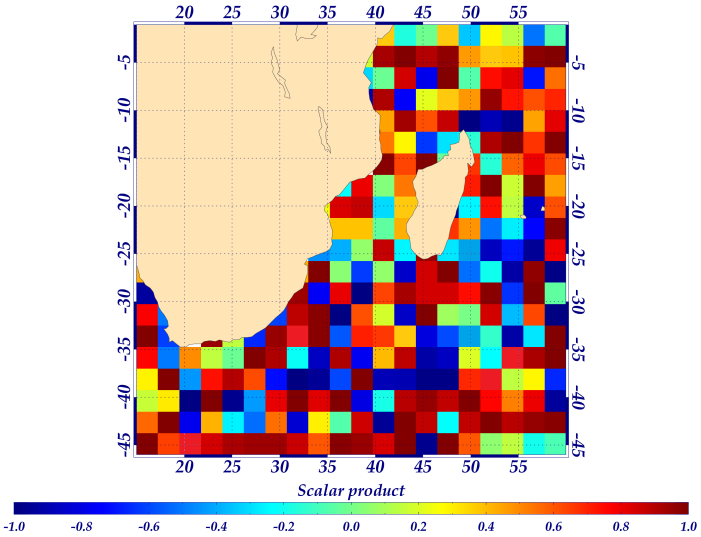

(a) Validation de la direction des courants par les positions non lissées des bouées Lagrangiennes.

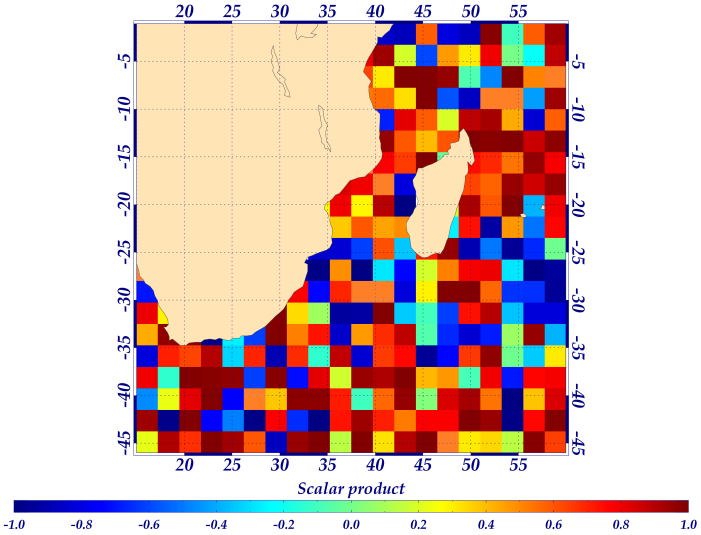

(b) Validation de la direction par les positions lissées des bouées Lagrangiennes.

FIGURE 3.10 – Produit scalaire calculé entre les positions des bouées Lagrangiennes collocalisées avec les données des courants pour la période de validation du 01 Janvier 2006 au 31 Décembre 2009.

direction que les courants estimés y compris dans le cas où le déplacement général de la bouée peut coïncider en direction avec les courants estimés. Ceci entraîne une validation beaucoup plus délicate avec des bouées Lagrangiennes.

Pour se convaincre de ces premiers résultats, un lissage sur les courants avec un noyau de convolution de 5×5 pixels sans pondération a été effectué. Ce lissage a pour conséquence de supprimer une partie de la variabilité submésoéchelle des courants à super-résolution. La comparaison a ensuite été faite avec les données de bouées Lagrangiennes lissées (non montré dans ce document) et non lissées. Le lissage sur des images avec des données manquantes ayant pour effet de rejeter un plus grand nombre de pixels, la figure 3.11 montre le nombre de points de validation dans chaque boîte.

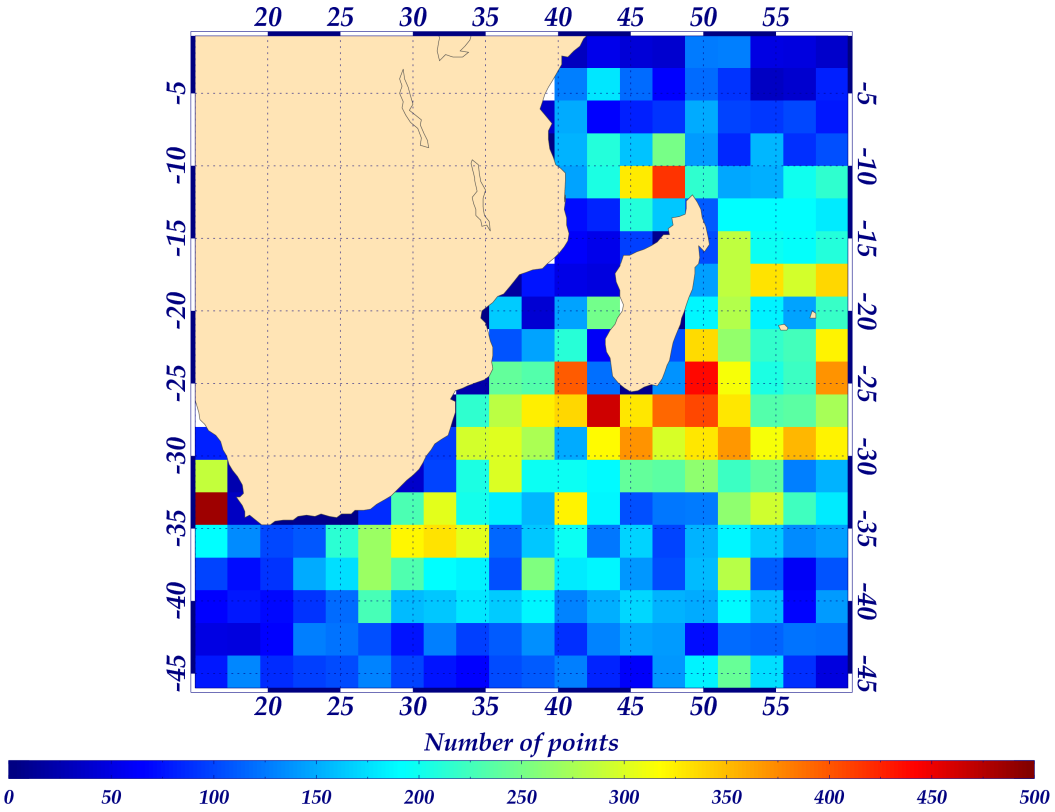

FIGURE 3.11 – *Nombre de positions de bouées Lagrangiennes collocalisées avec les données de courant pour la période de validation du 01 Janvier 2006 au 31 décembre 2009.*

La figure 3.12 montre que si l'on filtre la variabilité submésoéchelle sur le produit de courants, les résultats sur la validation de la norme et la direction sont meilleurs sur l'ensemble du domaine. Ces résultats pourraient conforter

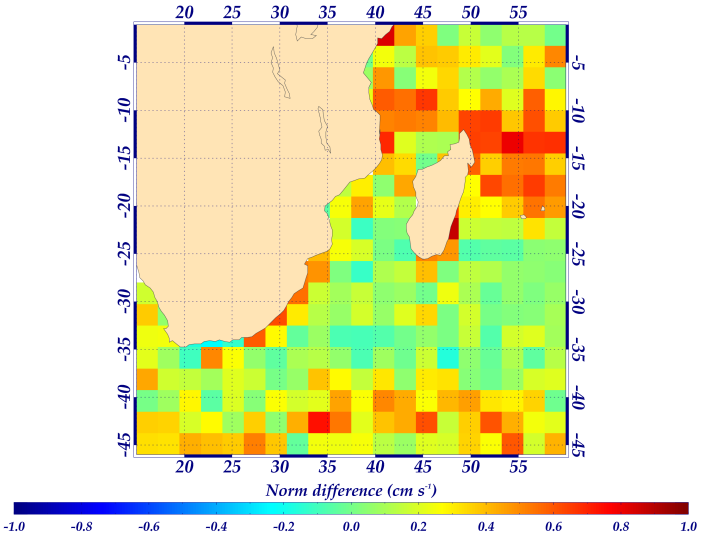

(a) Validation de la norme par les positions non lissées des bouées Lagrangiennes.

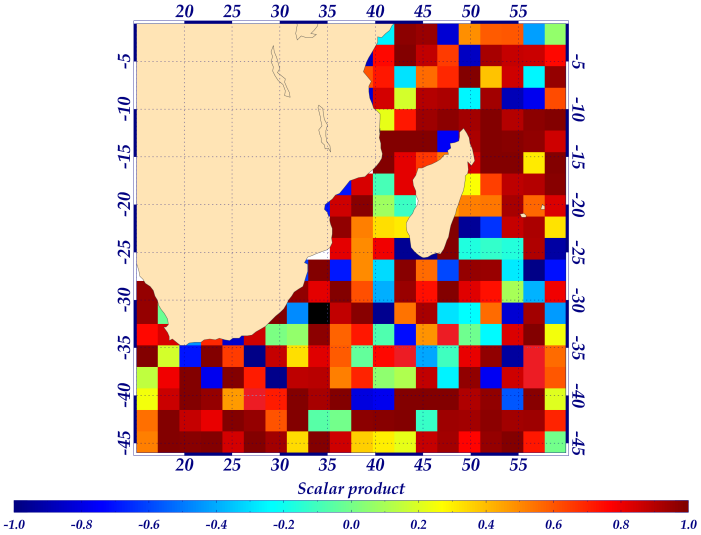

(b) Validation de la direction par les positions non lissées des bouées Lagrangiennes.

FIGURE 3.12 – Validation de la norme et du produit scalaire entre les positions des bouées Lagrangiennes collocalisées avec les données des courants lissées pour la période de validation du 01 Janvier 2006 au 31 Décembre 2009.

ceux du précédent test. Cependant le nombre de points de validation étant extrêmement différent, il n'est pas vraiment possible de conclure car :

- soit l'amélioration des résultats provient du sous-échantillonnage,
- soit elle provient du filtrage des courants qui a pour effet d'éliminer la variabilité submésoéchelle,
- soit les bouées Lagrangiennes dont les positions sont interpolées à six heures ne permettent pas d'avoir une représentation *in situ* et réaliste de la variabilité submésoéchelle.

Pour pouvoir conclure sur ce sujet, les courants à super-résolution ont été recalculés avec les données de TSM du produit OSTIA. Ce produit étant généré par fusion de différentes TSM par une variante de l'interpolation optimale (voir chapitre 1), a la particularité de ne pas avoir de données manquantes et l'interpolation optimale a pour conséquence de détruire une grande partie de la variabilité submésoéchelle.
Ces particularités vont permettre d'éliminer le sous-échantillonnage, et de tester la méthode d'analyse multirésolutions sur un produit dont la variabilité submésoéchelle est tronquée.

Une publication a été soumise afin de diffuser la méthode pour la détermination de la norme et la validation du champ de vecteurs à haute résolution. Cette publication se trouve en annexe (A, section A.1).

3.11.3 Validation de la dynamique turbulente obtenue à partir de la TSM OSTIA

La figure 3.13 représente le nombre de points par boîte pour les quatre expériences de validation effectuées sur les données de courant turbulent issues des données TSM OSTIA.

La validation de la norme et de la direction des courants pour ces tests est présentées respectivement sur les figures 3.14 et 3.15.

Le nombre de points de validation dans chaque boîte étant le même, ces résultats ne proviennent pas du sous-échantillonnage dû aux données manquantes dans ce produit.
Ces tests montrent :

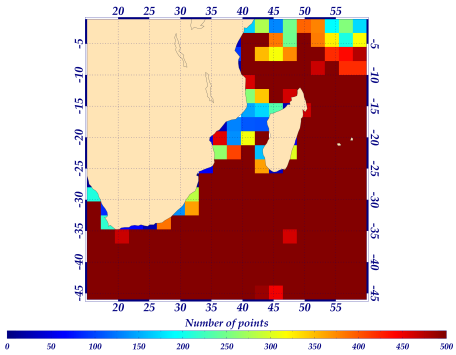

FIGURE 3.13 – *Nombre de positions de bouées Lagrangiennes collocalisées avec les données de courant pour la période de validation du 01 Janvier 2006 au 31 Décembre 2009.*

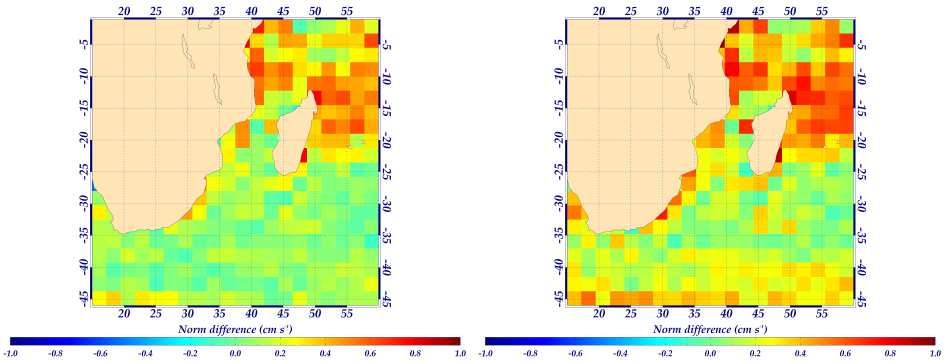

(a) Validation de la norme par les positions non lissées des bouées Lagrangiennes et des courants non lissés.

(b) Validation de la norme par les positions lissées des bouées Lagrangiennes et des courants non lissés.

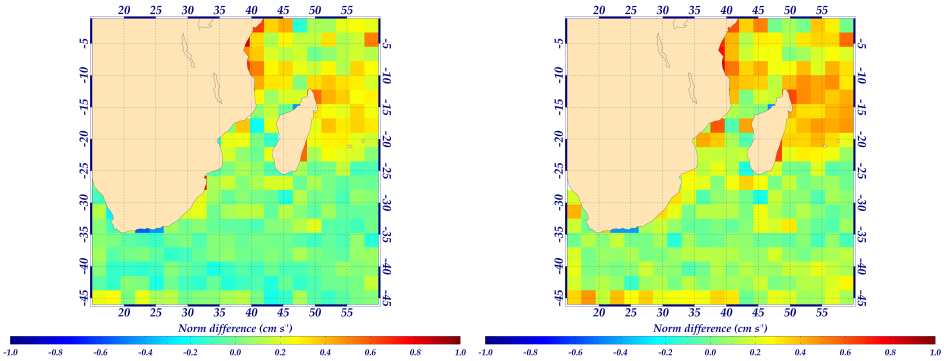

(c) Validation de la norme par les positions non lissées des bouées Lagrangiennes et des courants lissés.

(d) Validation de la norme par les positions lissées des bouées Lagrangiennes et des courants lissés.

FIGURE 3.14 – Différence de la norme calculée entre les positions des bouées Lagrangiennes collocalisées avec les données des courants pour la période de validation du 01 Janvier 2006 au 31 Décembre 2009.

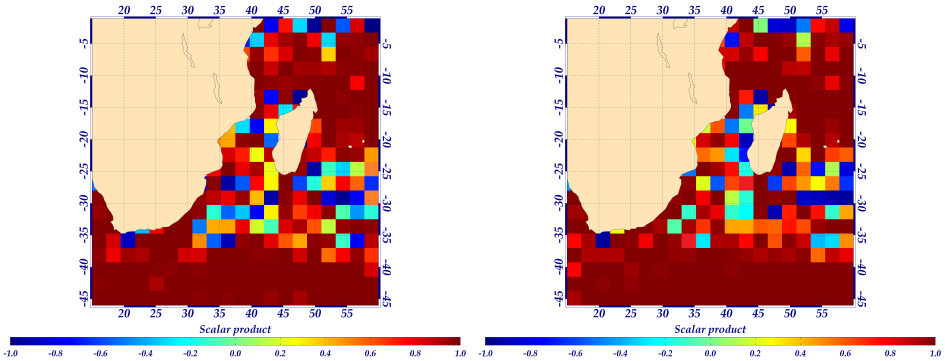

(a) Validation de la direction des courants par les positions non lissées des bouées Lagrangiennes et des courants non lissés.

(b) Validation de la direction par les positions lissées des bouées Lagrangiennes et des courants non lissés.

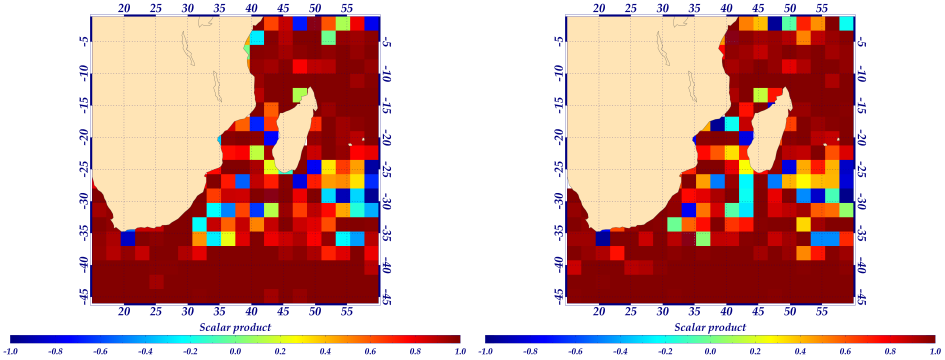

(c) Validation de la direction des courants par les positions non lissées des bouées Lagrangiennes et des courants lissés.

(d) Validation de la direction par les positions lissées des bouées Lagrangiennes et des courants lissés.

FIGURE 3.15 – Produit scalaire calculé entre les positions des bouées Lagrangiennes collocalisées avec les données des courants pour la période de validation du 01 Janvier 2006 au 31 Décembre 2009.

- plus on lisse les courants issus du produit OSTIA, plus les normes sont proches,
- plus on lisse les courants issus du produit OSTIA, plus les directions sont colinéaires,
- plus on lisse les positions des déplacements des bouées, moins les normes sont proches,
- plus on lisse les positions des déplacements des bouées, plus les directions sont colinéaires.

Ces tests indiquent donc que plus la variabilité sumésoéchelle est éliminée dans les courants, plus les courants (en norme et direction) se rapprochent des données de bouées Lagrangiennes. Donc les déplacements des bouées Lagrangiennes sont plus représentatifs de la variabilité mésoéchelle que submésoéchelle. Plus les zones océaniques vont être turbulentes (traduisant une forte présence d'activité submésoéchelle) moins le résultat entre bouées et courant va être bon. Ceci explique les résultats obtenus précédemment avec le produit de TSM MODIS/Aqua. De plus en comparant visuellement les résultats entre la dynamique océanique obtenue par la TSM du produit MODIS/Aqua (voir figure) et celle du produit OSTIA (voir figure) on peut en déduire que le produit issu de MODIS/Aqua est représentatif de la FDT à submésoéchelle.

Mais ces tests indiquent aussi que plus la variabilité submésoéchelle est éliminée des positions des bouées Lagrangiennes, plus les bouées Lagrangiennes s'écartent en norme et se rapprochent en direction de la variabilité submésoéchelle des courants. Cela corrobore aussi les résultats obtenus avec la dynamique océanique dérivée du produit de TSM MODIS/Aqua.

En conclusion de cette partie de validation, la dynamique océanique dérivée du produit de TSM MODIS/Aqua est bien représentative d'une dynamique provenant de la turbulence pleinement développée issue de l'activité submésoéchelle que ce soit en norme et en direction. Les résultats sont tout à fait cohérents avec l'hypothèse qui était avancée, selon laquelle les bouées Lagrangiennes ne sont pas capables de valider correctement une zone océanique où la turbulence pleinement développée est dominée par une forte activité à submésoéchelle mais seulement les zones où l'activité est à mésoéchelle.

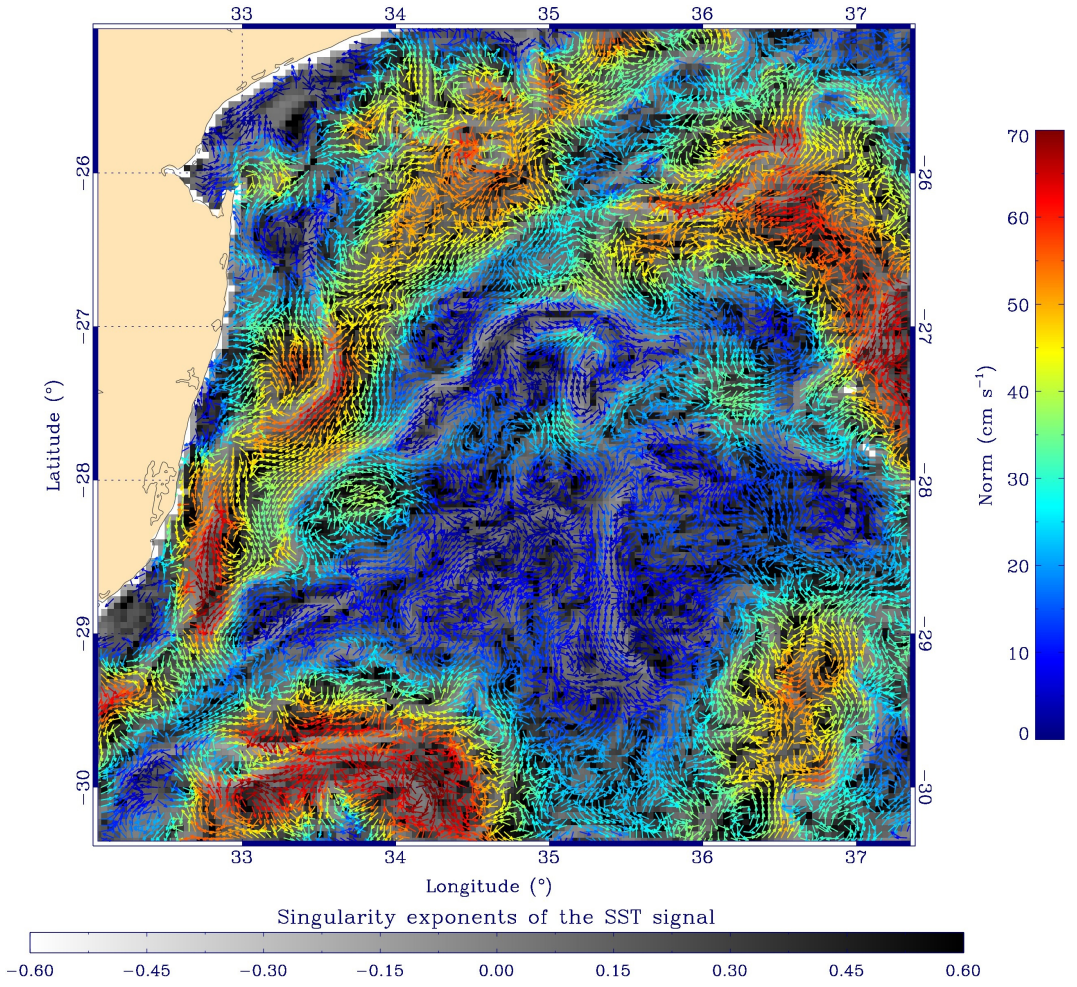

FIGURE 3.16 – *Dynamique océanique turbulente obtenue par l'analyse multirésolutions au moyen des données GEKCO à basse résolution et des exposants de singularité à haute résolution du produit MODIS/Aqua pour propager la dynamique turbulente à travers les échelles (dynamique obtenue pour le 02 Août 2007).*

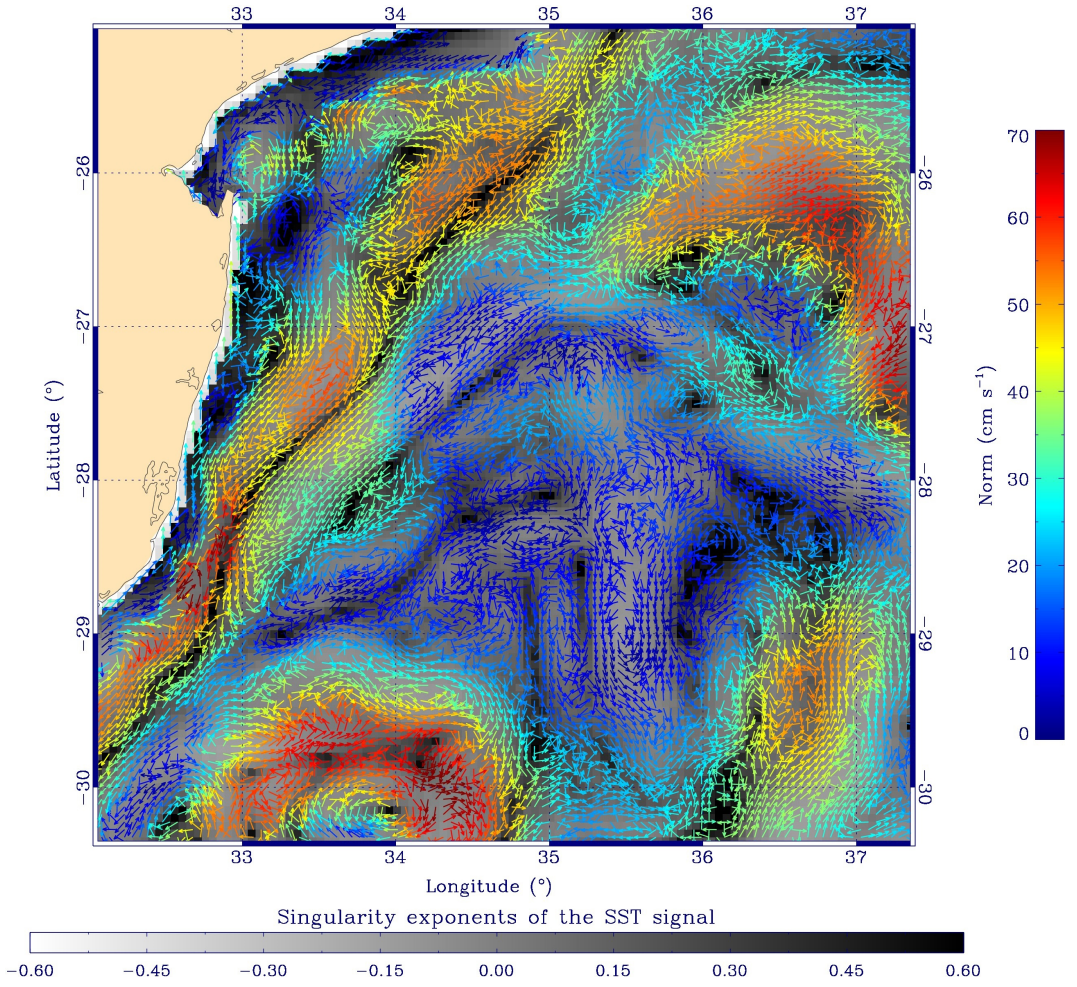

FIGURE 3.17 – *Dynamique océanique turbulente obtenue par l'analyse multirésolutions au moyen des données GEKCO à basse résolution et des exposants de singularité à haute résolution du produit OSTIA pour propager la dynamique turbulente à travers les échelles (dynamique obtenue pour le 02 Août 2007).*

3.12 Conclusions

Dans ce chapitre une méthode interdisciplinaire entre l'océanographie physique et la "Science de la Complexité" a permis de construire un outil de traitement non-linéaire du signal permettant la génération de la dynamique océanique à super-résolution traduisant l'activité submésoéchelle contenue dans les images super-résolution de TSM. Cet outil permet d'inférer un signal océanique connu à basse résolution (ici la dynamique océanique provenant du produit GEKCO - chapitre 2 -), à une résolution supérieure par l'utilisation de l'information sur la FDT contenue dans un produit de TSM à super-résolution. Cette méthode de traitement non-linéaire du signal a été utilisée pour générer quatre ans de données de dynamique océanique à super-résolution dans la zone Sud-Ouest de l'Océan Indien. Afin de valider ce nouveau produit, des données de positions de bouées Lagrangiennes de surface ont été utilisées. Ce jeu de données permettant de déduire une estimation des courants océaniques *in situ* de surface, ceux-ci ont été utilisés pour valider les courants océaniques à super-résolution sur la période allant du 01 Janvier 2006 au 31 Décembre 2009. La validation a permis de conclure que ces courants sont bien représentatifs de l'activité submésoéchelle issue de la FDT détectable via les données de TSM à super-résolution [1].
De plus cette validation a permis de mettre en évidence que l'échantillonnage temporel des positions des bouées Lagrangiennes de surface (6 heures entre chaque position) ne reflète pas l'activité océanique à submésoéchelle et que cette activité est masquée par les courants inertiels présents dans les déplacements de ces bouées.

La dynamique océanique de surface est la conséquence de la mise en mouvement des masses d'eau à la surface de l'océan par différents forçages extérieurs. Par le biais des courants, l'océan redistribue la chaleur, la salinité ainsi que les traceurs biogéochimiques. Ces courants influencent donc très fortement l'activité biologique. Si l'impact de l'activité mésoéchelle de surface sur le monde du vivant a été beaucoup étudiée au cours des dernières décennies, il n'en est pas de même de l'interaction entre les processus physiques et biologiques à submésoéchelle que nous allons étudier dans le chapitre 4.

1. Nous avons produit avec INRIA un film montrant la dynamique océanique submésoéchelle calculée selon la méthode décrite dans ce chapitre et pour l'année 2006, dans la zone de l'Océan Indien détaillée plus haut. Ce film est disponible à l'adresse http://geostat.bordeaux.inria.fr/exj1309/annee2006_SHORTER_2ipj.mov.Thesizeofthemovie

Chapitre 4
De l'inanimé au vivant

Chapitre 4

Impact de dynamique océanique sur le monde marin du vivant

Sommaire

4.1 Introduction 222

4.2 Les exposants de Lyapunov 224

4.2.1 Définition mathématique des exposants de Lyapunov . . . 224

4.2.2 Exemple sur exposants de Lyapunov : les campagnes BATS Val / Submesoscale Biogeochemistry Cruise Logistics 225

4.3 Les systèmes d'upwellings de bord est 231

4.4 Impact de la dynamique océanique sur les prédateurs marins supérieurs 232

4.4.1 La dynamique océanique du Canal du Mozambique 233

4.4.2 Zone d'alimentation des Frégates du Pacifique (Fregata minor) 236

4.4.3 Capacités d'orientation des tortues vertes (Chelonia mydas) et impact des courants marins sur leurs déplacements 239

4.5 Article : The Role of Geomagnetic Cues in Green Turtle Open Sea Navigation, S. Benhamou *et al.*, 2011 245

4.5.1 Résumé de l'article 245

4.5.2 Article publié dans *PLoS ONE* 246

4.6 Conclusions 258

4.1 Introduction

Le milieu marin, et en particulier la couche océanique de surface, est un fluide en perpétuel mouvement et en régime de turbulence pleinement développée se traduisant par une dynamique océanique s'exprimant à toutes les échelles spatio-temporelles, de manière imprédictible et intermittente. Du simple organisme phytoplanctonique jusqu'aux grands écosystèmes marins, toute la chaîne trophique marine est fortement influencée par la dynamique océanique. Elle en est son reflet vivant.
Les structures océaniques entraînent de fortes variations dans la couche de surface où l'activité biologique prédomine. Le mélange, l'étirement, la filamentation, les fronts et les structures tourbillonnaires sont des processus physiques issus de la turbulence pleinement développée qui vont favoriser les trois processus fondamentaux de la triade de Bakun *Bakun* [1996] qui sont :

- l'enrichissement de zones par des sels nutritifs remontant dans la couche euphotique. Différentes études ont permis de montrer l'interaction entre les processus biogéochimiques présents dans la couche euphotique et les processus physiques permettant leurs remontées [*Garçon et al.*, 2001]. On peut citer plus particulièrement : les travaux de *Williams et Follows* [1998] s'intéressant à l'impact de l'advection horizontale, *Haine et Marshall* [1998]; *Thomas et Lee* [2005]; *Giordani et al.* [2006] sur l'instabilité de fronts permettant le transport vertical et *McGillicuddy et al.* [1998]; *Lima et al.* [2002] sur l'effet du pompage vertical effectué par l'activité tourbillonnaire,
- la concentration des proies zooplanctoniques (favorable à la croissance des petits poissons pélagiques [*Muhling et al.*, 2007]) se nourrissant de proies phytoplanctoniques dont les sels nutritifs et l'insolation permettent la croissance [*Llido et al.*, 2004; *Llido*, 2004; *Llido et al.*, 2005],
- la rétention de poissons, en particulier de larves et de juvéniles, dans ces zones riches [*Huntley et al.*, 2000; *Mackas et al.*, 2005; *Waite et al.*, 2007].

Ces trois processus favorisent la productivité biologique et le succès de reproduction de nombreuses espèces marines [*Bakun*, 2006]. Ces différents aspects ont été étudiés dans le Canal du Mozambique, [*Tew Kai*, 2009] montre le rôle des tourbillons à mésoéchelle dans la structuration spatiale de l'écosystème pélagique et l'utilisation de la dynamique océanique comme descripteur physique pour caractériser l'importance des structures à mésoéchelle sur la dynamique des communautés et populations marines. La connaissance de

l'écoulement à une résolution spatio-temporelle adéquate permet d'analyser le comportement d'une population animale ou le déplacement d'un (ou de plusieurs) individu(s) particulier(s).
Pour faciliter l'interprétation et l'analyse de l'impact des processus physiques sur la biologie marine certains descripteurs sont déduits de l'écoulement ; citons par exemple :

- l'énergie cinétique tourbillonnaire $EKE = \frac{u'^2 + v'^2}{2}$ ($m^2 s^{-2}$) (u' et v' étant les anomalies du courant par rapport à sa moyenne),
- la vorticité relative $\omega = \frac{\partial v}{\partial x} - \frac{\partial u}{\partial y}$ (s^{-1}),
- le cisaillement $\sigma_n = \frac{\partial u}{\partial x} - \frac{\partial v}{\partial y}$ (s^{-1}),
- l'étirement $\sigma_s = \frac{\partial v}{\partial x} + \frac{\partial u}{\partial y}$ (s^{-1}),
- le taux de déformation $\sigma = \sqrt{\sigma_s^2 + \sigma_n^2}$ (s^{-1}),
- le critère d'Okubo-Weiss qui caractérise la dynamique du gradient $Q = \sigma^2 - \omega^2$ (s^{-2}) [*Okubo*, 1970; *Weiss*, 1991]. Ce critère détermine si le taux de déformation (la filamentation - $Q > 0$ -) ou la vorticité relative (les tourbillons - $Q < 0$ -) domine l'écoulement du fluide.

Ce dernier critère ne permet pas de discriminer les structures cohérentes de l'écoulement. Si on cherche à caractériser l'impact biogéochimique ou biologique des structures océaniques, le calcul des exposants de Lyapunov sur l'écoulement à mésoéchelle permet la localisation spatio-temporelle de barrières de transport (les fronts) et la représentation d'une partie de la dynamique à submésoéchelle.

Nos travaux sur la dynamique océanique ont permis différentes études caractérisant : les relations entre processus physiques et processus biogéochimiques, le comportement de certaines populations animales et le déplacement de certains individus. Ce dernier chapitre est consacré à ces études.
Les exposants de Lyapunov (descripteurs de la dynamique océanique) sont utilisés dans certaines études. La section suivante décrit cette méthode d'intégration temporelle et son utilisation permettant de mieux caractériser l'impact de la dynamique océanique sur le monde du vivant.

4.2 Les exposants de Lyapunov

Les exposants de Lyapunov sont des observables dynamiques caractérisant la divergence exponentielle de trajectoires initialement proches. Ils donnent une information quantitative sur la sensibilité aux conditions initiales d'un système dynamique complexe. Une valeur d'exposant de Lyapunov quantifie l'imprédictabilité de l'écoulement turbulent considéré.

4.2.1 Définition mathématique des exposants de Lyapunov

Si on considère un système dynamique (indépendant du temps) quelconque représenté par une relation de récurrence telle que $x_n = f(x_{n-1})$ et dont la condition initiale x_0 est affectée d'une erreur infinitésimale ε_0, au bout de n itérations cette erreur est amplifiée d'un facteur :

$$\left|\frac{\varepsilon_n}{\varepsilon_0}\right| = \prod_{i=1}^{n} \left|\frac{\varepsilon_i}{\varepsilon_{i-1}}\right| \tag{4.1}$$

Si on applique le logarithme à cette équation on obtient :

$$ln\left|\frac{\varepsilon_n}{\varepsilon_0}\right| = \sum_{i=1}^{n} ln\left|\frac{\varepsilon_i}{\varepsilon_{i-1}}\right| \tag{4.2}$$

Si on fait tendre la moyenne de cette somme vers l'infini, on obtient l'exposant de Lyapunov (λ) tel que :

$$\lambda = \lim_{n\to\infty} \frac{1}{n} \sum_{i=1}^{n} ln\left|\frac{\varepsilon_i}{\varepsilon_{i-1}}\right| \tag{4.3}$$

Si les valeurs des ε_i et ε_{i-1} sont infinitésimales, leur rapport correspond à la dérivée de la fonction associée. Dans le cas d'une fonction dérivable on obtient :

$$\lim_{\delta x\to 0} \frac{f(x+\delta x) - f(x)}{\delta x} = f'(x) \tag{4.4}$$

Par conséquent la formulation classique de l'exposant de Lyapunov est :

$$\lambda = \lim_{n\to\infty} \frac{1}{n} \sum_{i=1}^{n} ln \left| f^{'}(x_{i-1}) \right| \tag{4.5}$$

La dynamique océanique étant un système dépendant du temps, il est nécessaire d'introduire dans l'équation 4.3 une relation de récurrence dépendante du temps. Cette relation est définie comme la distance de séparation en fonction du temps de deux particules virtuelles lâchées dans l'écoulement turbulent et dont la distance de séparation initiale est égale à $\delta x(t_0)$. La localisation de chaque particule est définie à l'instant t_0 par $x_1(t_0)$ et $x_2(t_0) = x_1(t_0) + \delta x(t_0)$. On considère le $\delta x(t_0)$ comme une erreur infinitésimale de position évoluant dans le temps. Pour un temps infini, la formulation globale de l'exposant de Lyapunov est :

$$\lambda = \lim_{t\to\infty} \lim_{\delta x(t_0)\to 0} \frac{1}{t} ln \left| \frac{\delta x(t)}{\delta x(t_0)} \right| \tag{4.6}$$

L'exposant de Lyapunov possède deux caractères asymptotiques (en temps et en espace) qui rendent son calcul impossible puisqu'il nécessite d'avoir un écoulement du fluide connu en tout point de l'espace et pour tous les temps. On peut définir cet exposant en éliminant un de ses deux caractères asymptotiques ; soit en temps fini (Finite Time Lyapunov Exponent - FTLE -), soit en taille finie (Finite size Lyapunov Exponent - FSLE -).

4.2.2 Exemple sur exposants de Lyapunov : les campagnes BATS Val / Submesoscale Biogeochemistry Cruise Logistics

Dès 1954, H. M. Stommel a initié la création du programme Hydrostation "S" au large de l'île des Bermudes (voir figure 4.1 pour sa localisation précise), dédié à l'obtention de longues séries temporelles de divers paramètres physiques, biogéochimiques et biologiques en océan profond. Les données obtenues par la revisite systématique et fréquente de cette station fixe a permis de très nombreuses études sur la variabilité temporelle de différents paramètres océaniques. En accord avec le programme international Joint

Global Ocean Flux Study (JGOFS), le "Bermuda Institute of Ocean Science" (BIOS) a décidé de mettre en place une seconde station fixe plus au large : "the Bermuda Atlantic Time-series Study (BATS)". Cette station fixe est spécialement dédiée à l'obtention de longues séries temporelles pour observer et interpréter la variabilité annuelle et inter-annuelle de la biogéochimie, de la couche de mélange, de la zone euphotique, des taux des flux de particules et de reminéralisation sur toute la colonne d'eau, afin de comprendre les relations entre la biologie, les processus chimiques et les caractéristiques physiques de la colonne d'eau. L'échantillonnage à cette station fixe a commencé en Octobre 1988 et à ce jour elle fournit des séries temporelles décadaires. Les campagnes BATS, d'une durée de 4 à 5 jours, consistent à échantillonner mensuellement cette station. De nombreux laboratoires participent à ces campagnes à la mer. Certaines campagnes sont valorisées pour effectuer des études le long du transit. En collaboration avec le Dr David Siegel de l'Université de Californie, Santa Barbara, nous avons fourni en temps quasi-réel au cours de transits, les données de courants et de FSLEs associés, pour localiser et échantillonner les structures à méso et submésoéchelle.
Ce projet a pour but de quantifier l'exportation de carbone de la surface océanique vers les couches profondes par l'évaluation du transport vertical du carbone organique et de comprendre les processus mis en jeu pour cet exportation.
Au cours des transits, des échantillons d'eau de mer permettent d'évaluer les concentrations de thorium-234 et uranium-238. La différence de ces deux concentrations est un excellent indicateur de l'exportation des particules de carbone organique de la couche euphotique. De récentes avancées technologiques permettent d'échantillonner ces deux radio-isotopes le long des transits, alors que le navire est en mouvement, à une résolution de 10 km (échantillonnages de surface). Des prélèvements sont aussi effectués par une rosette pour échantillonner la colonne d'eau à différentes profondeurs.
Les structures cohérentes Lagrangiennes, issues du calcul des FSLEs ou FTLEs, permettent de déterminer les fronts où les particules s'accumulent. L'envoi à bord de cartes représentant les LCSs (anti-chronologique) permet de privilégier l'échantillonnage de ces fronts où le transport vertical doit être plus important et l'exportation accrue.

Au cours des campagnes de valorisation de 2011 et 2012, les données de courants fournies ont été utilisées pour calculer les FSLEs et les FTLEs

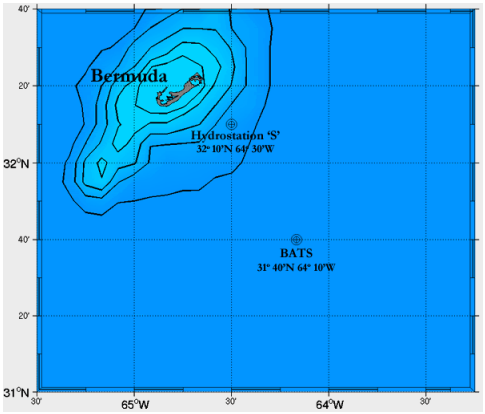

FIGURE 4.1 – Position du mouillage BATS. ©BIOS.

permettant une comparaison de ces deux descripteurs (voir figures 4.2). Les FSLEs permettent une meilleure hiérarchisation des fronts qui sont des zones de transitions imprédictibles.

Les figures 4.2(b), 4.3 et 4.4 illustrent les différences obtenues par le calcul des structures cohérentes Lagrangiennes (LCSs) lorsque la composante d'Ekman est associée, ou n'est pas associée, à la composante géostrophique. Ces figures mettent en évidence l'impact de la tension du vent sur le déplacement des particules au sein de structures cohérentes. Elles permettent d'identifier ce processus physique. Si la composante d'Ekman (images en haut de la figure 4.4) n'est pas prise en compte, les fronts (barrières de transport) du tourbillon sont quasiment circulaires et d'intensité (indiquée par le code couleur des fronts) pratiquement identique. Ces fronts se situent au pourtour du tourbillon. Par contre, si la composante d'Ekman est prise en compte (images en bas de la figure 4.4), les fronts du tourbillon sont en forme de spirale. Ceci indique que la friction du vent sur la surface océanique déplace les fronts au sein même du tourbillon. Les particules du centre du tourbillon ont des déplacements circulaires (dus aux courants géostrophiques) et latéraux (dus à la friction du vent). L'association de ces deux déplacements horizontaux induit de la convection verticale non seulement sur les bords du tourbillon mais aussi dans sa zone interne. Ces zones sont sujettes à des remontées de masses d'eau entraînant des apports d'eau dans la zone euphotique (cas de fronts obtenus par les méthodes FSLE ou FTLE calculées chronologiquement). Ces masses d'eau peuvent contenir une concentration en sels nutritifs importante. Dans ce cas, elles enrichissent et rendent fertiles le pourtour et la zone centrale du tourbillon.

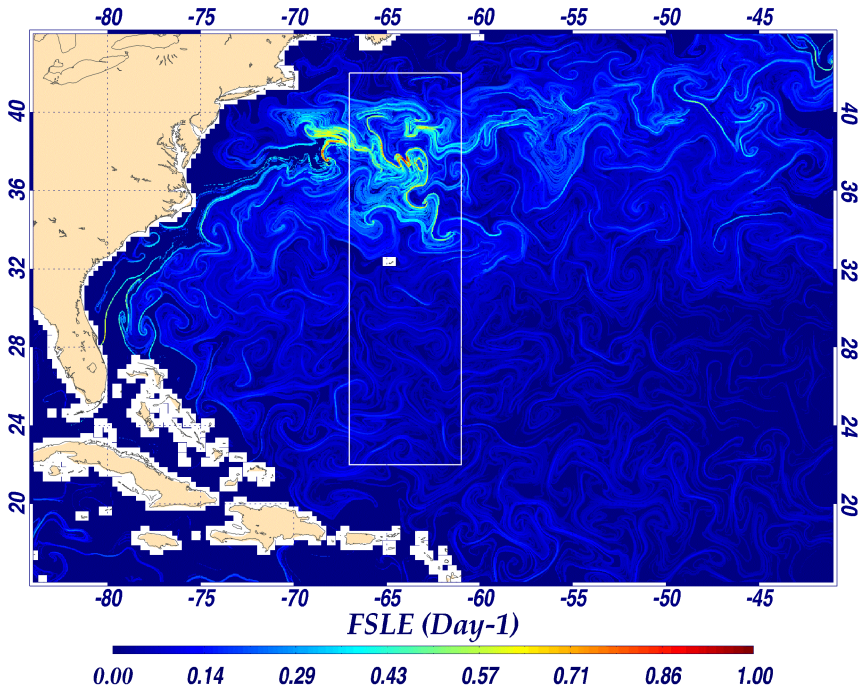

(a) FSLEs calculés en sens anti-chronologique.

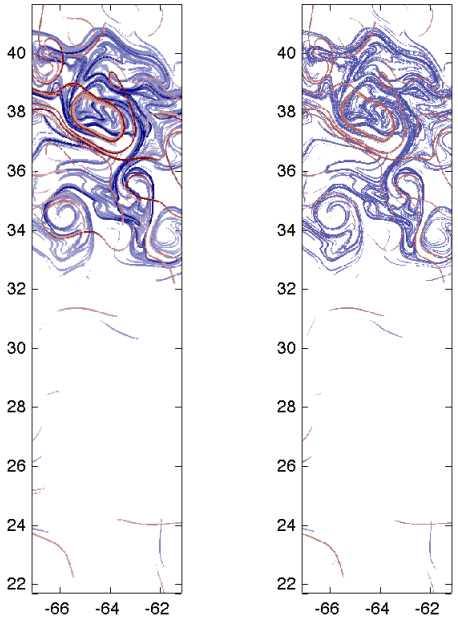

(b) Comparaison entre les structures cohérentes Lagrangiennes (LCSs) obtenues par la méthode FSLE (Gauche) et la méthode FTLE (Droite) dans le Nord de la zone d'étude. En rouge LCS FSLE / LCS FTLE calculées chronologiquement, en bleu anti-chronologiquement. ©Erik Fields.

FIGURE 4.2 – LCSs obtenues par la méthode FSLE et par la méthode FTLE à partir des courants GEKCOs, au cours de la campagne BATS Val / Submesoscale Biogeochemistry Cruise Logistics en 2011.

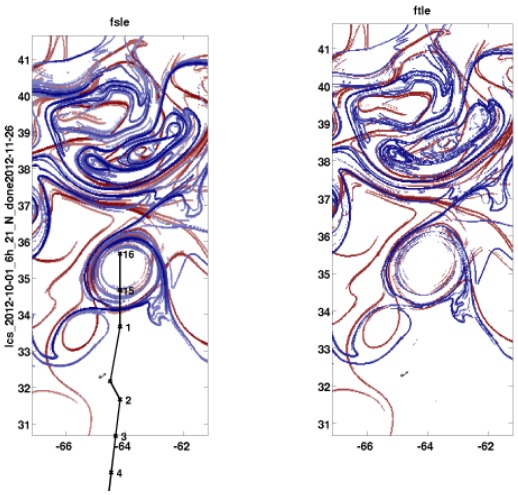

(a) Comparaison entre les LCSs obtenues par la méthode FSLE (Gauche) et par la méthode FTLE (Droite) dans le Nord de la zone d'étude en utilisant uniquement la composante géostrophique des courants GEKCOs. En rouge LCSs FSLE / LCSs FTLE calculées chronologiquement, en bleu anti-chronologiquement.

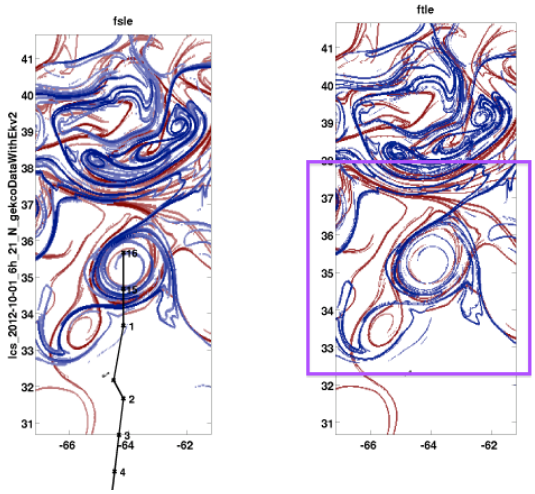

(b) Comparaison entre les LCSs obtenues par la méthode FSLE (Gauche) et par la méthode FTLE (Droite) dans le Nord de la zone d'étude en utilisant la composante géostrophique et la composante d'Ekman des courants GEKCOs. En rouge LCSs FSLE / LCSs FTLE calculées chronologiquement, en bleu anti-chronologiquement.

FIGURE 4.3 – LCSs obtenues par la méthode FSLE et par la méthode FTLE à partir des courants GEKCOs en utilisant la composante géostrophique avec ou sans la composante d'Ekman au cours de la campagne BATS Val / Submesoscale Biogeochemistry Cruise Logistics en 2012. La ligne noire (sur les images à gauche) représente le transit du navire et les points noires la position des stations. Le cadre violet sur la figure (b) indique la position du zoom de la figure 4.4. Le fond de carte représente la topographie dynamique absolue. ©Erik Fields.

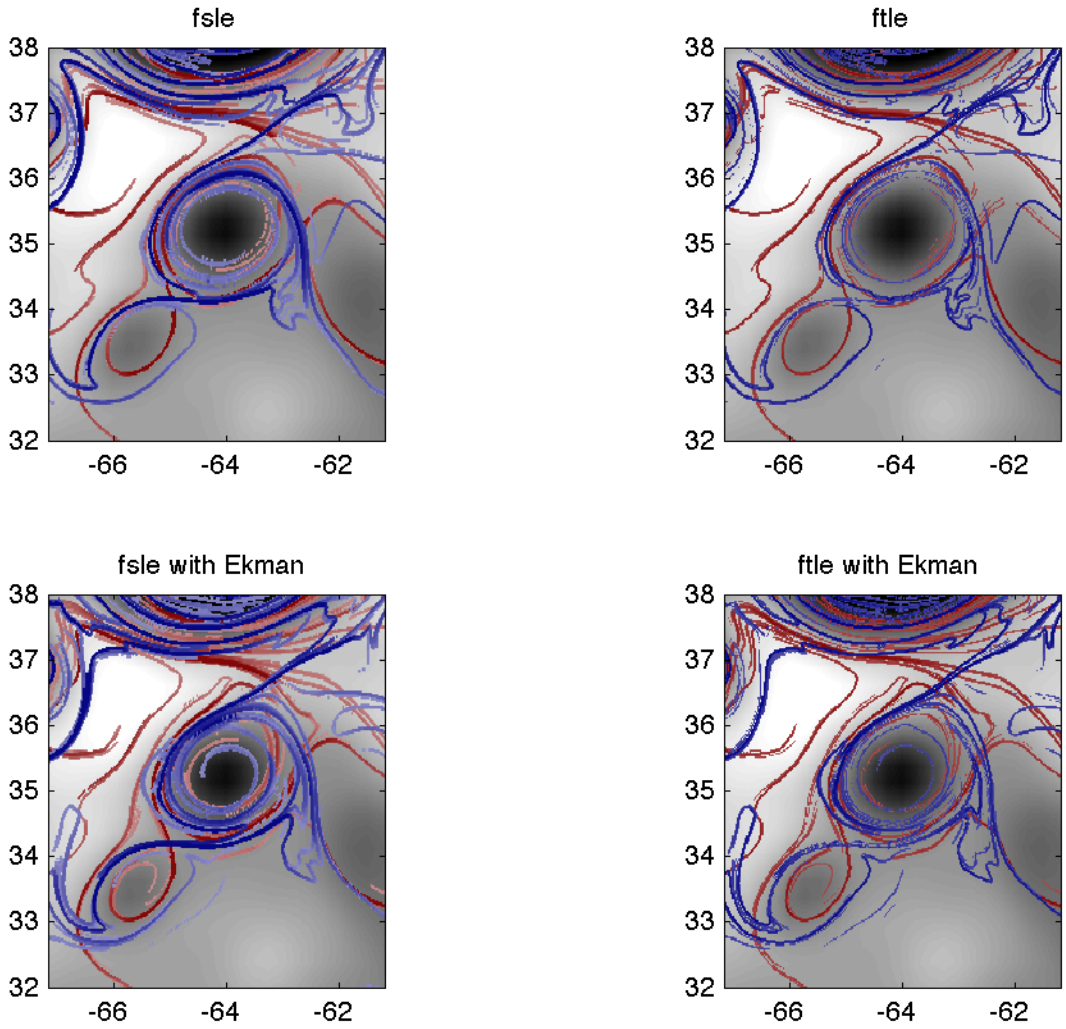

FIGURE 4.4 – LCSs obtenues par la méthode FSLE (Gauche) et la méthode FTLE (Droite) en utilisant la composante géostrophique uniquement (en haut) et en association avec la composante d'Ekman des courants GEKCOs (en bas). En rouge LCSs FSLE / LCSs FTLE calculées chronologiquement, en bleu anti-chronologiquement.

La figure 4.4 montre une différence d'intensité des fronts sur le pourtour du tourbillon lorsque les courants géostrophiques sont associés aux courants d'Ekman. Ces fronts de divergence ou de convergence sont plus intenses dans les parties Nord et Sud du tourbillon. Cette différence d'intensité est due à la prise en compte du vent et à son impact, via la friction induite, sur la masse d'eau en rotation. Ceci indique l'association d'une advection tourbillonnaire et d'un pompage d'Ekman tourbillonnaire, ce qui corrobore les hypothèses émises par *Siegel et al.* [2011].

Cet exemple montre le potentiel des courants GEKCOs en association avec des diagnostics Lagrangiens (FSLE ou FTLE) pour comprendre et analyser les processus physiques.

4.3 Les systèmes d'upwellings de bord est

Certaines zones océaniques sont plus fortement impactées par la friction du vent à la surface de l'océan. Les zones d'upwelling de bord Est sont particulièrement sujettes à ce type de forçage physique. Les quatre grandes zones d'upwelling mondiales sont : la zone des Canaries et la zone du Benguela en Atlantique, la zone du Pérou/Chili (Humboldt) et la zone de Californie dans le Pacifique. Ces zones représentent à elles seules plus de 20% de la production mondiale de pêche [*Pauly et Christensen*, 1995]. Cette productivité exceptionnelle est due à l'interaction des processus physiques et des processus biologiques particulière de ces zones. Les cellules de hautes pressions subtropicales génèrent dans ces zones des vents parallèles à la côte provoquant dans la zone de talus, une remontée de masses d'eau profondes, froides, riches en sels nutritifs par pompage d'Ekman, dans la couche euphotique. Ces zones sont caractérisées par une très forte productivité planctonique associée à une richesse exceptionnelle de la chaîne trophique. Cependant il existe une très forte hétérogénéité au sein même de ces upwellings tant sur le plan physique que sur le plan biologique. *Rossi* [2010] a caractérisé cette hétérogénéité, en utilisant des données satellites, la dynamique océanique issue des courants GEKCOs présentée dans le chapitre 2 et des diagnostics Lagrangiens (FSLE). Les principaux résultats mettent en évidence [*Rossi et al.*, 2008, 2009] que :

- les propriétés du mélange horizontal au sein des zones d'upwelling permettent de subdiviser les zones d'upwelling en deux sous-systèmes nettement différents en terme d'activité de mélange turbulent,
- ces sous-systèmes coïncident avec des signatures biologiques différentes, (les signatures biologiques étant identifiées avec des données de couleur de l'eau),
- la concentration en chlorophylle a est inversement proportionnelle à l'intensité de l'étirement et du mélange dans ces zones d'upwelling. Cet effet inhibiteur du mélange sur la biomasse phytoplanctonique est en opposition avec l'effet observé dans les gyres oligotrophiques de l'océan mondial,
- le transport d'Ekman, induit par les vents, est positivement corrélé avec la concentration chlorophyllienne,
- les sous-systèmes d'upwelling caractérisés par de fortes valeurs de FSLE (forte activité turbulente) sont associés à des dynamiques verticales (ascendante et descendante) intenses. Les sous-systèmes caractérisés par de faibles valeurs de FSLE (faible activité turbulente) sont dominés par une dynamique verticale ascendante. En conséquence, l'augmentation de l'activité tourbillonnaire turbulente dans ces zones d'upwelling contrecarre la dynamique propre du pompage d'Ekman issue de la friction du vent sur la couche océanique de surface.

4.4 Impact de la dynamique océanique sur les prédateurs marins supérieurs

La turbulence pleinement développée, observable par les capteurs satellitaires, joue un rôle clef sur la mise en place de toute la chaîne trophique marine. Son activité définit et contrôle de façon spatio-temporelle les zones d'accroissement de la productivité biologique via les transports horizontaux et verticaux. Cette dynamique océanique contrôle le comportement d'alimentation et le déplacement des populations marines y compris les prédateurs marins supérieurs dont les différentes espèces de thons, les oiseaux marins, et les tortues marines font partie. La connaissance simultanée de la position de certains individus de ces espèces (au moyen de balises de localisation ou de journaux de bords des navires de pêches) et des données de capteurs satellitaires permet d'étudier l'impact de la dynamique océanique sur leurs

déplacements, de comprendre leurs stratégies d'alimentation, ou d'identifier par quels moyens (sens olfactif, visuel, etc.) ces animaux arrivent à détecter leurs zones d'alimentation ou de ponte. Différentes études utilisant cette connaissance simultanée sont menées dans l'Ouest de l'Océan Indien en particulier dans le Canal du Mozambique zone océanique riche en terme de prédateurs marins supérieurs.

4.4.1 La dynamique océanique du Canal du Mozambique

Le Canal du Mozambique a une dynamique océanique très particulière et complexe faisant de cette zone un "laboratoire" parfait pour l'étude des processus physiques et de leurs impacts sur différentes espèces marines. La figure 4.5 montre une climatologie de LCSs calculés par la méthode FSLE anti-chronologique permettant de mettre en évidence la complexité de la dynamique mésoéchelle et submésoéchelle contenue dans le produit GEKCOs présenté dans le chapitre 2.

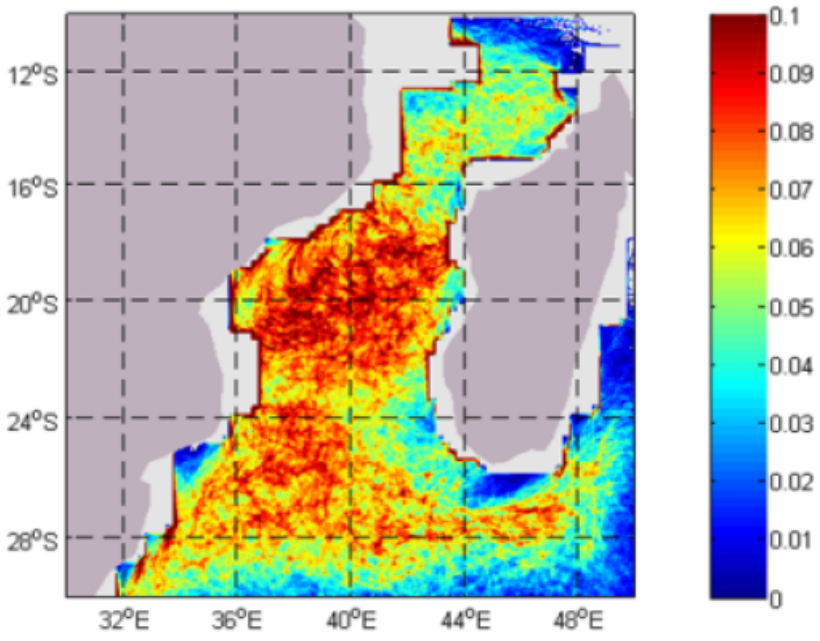

FIGURE 4.5 – Climatologie moyenne des LCSs calculées par la méthode FSLE anti-chronologique dans le Canal du Mozambique de Janvier 2001 à Décembre 2006. ©[*Tew Kai*, 2009].

A l'Est de Madagascar, le courant dominant est le Courant Sud-Equatorial (SEC) se déplaçant vers l'Ouest. Sa branche la plus au Sud ($\sim 20°S$) au contact de Madagascar va se scinder en deux branches formant le Courant Sud et Nord de Madagascar (SEMC et NEMC).
Au cap d'Ambre (qui se situe à la pointe Nord de Madagascar), le NEMC rejoint le SEC. Cette nouvelle branche en allant toujours vers l'Ouest se divise à l'approche des côtes Africaines vers $10 - 12°S$. Sa partie Nord forme le Courant Côtier Est Africain (EACC) qui remonte vers la Somalie pour ensuite alimenter le Contre Courant Equatorial (ECC) qui s'écoule vers l'Est. Sa partie Sud entre dans le Canal du Mozambique de manière inhomogène en générant une circulation complexe de tourbillons [*Ridderinkhof et al.*, 2001], et sporadiquement et de façon discontinue le Courant du Mozambique [*Lutjeharms et al.*, 2012]. Il n'y a pas *per se* un Courant du Mozambique mais plutôt un train de tourbillons se déplaçant du Nord au Sud dans ce canal.

Dans la partie Nord du Canal du Mozambique, entre les îles Comores, Mayotte et Glorieuses et les sites d'Angoche et du Cap Saint André (zone la plus étroite du canal), une circulation anticyclonique est présente dans le Bassin des Comores. Proche de la côte Malgache, cette circulation en interaction avec une partie du flux de NEMC génère une dynamique océanique complexe peuplé de tourbillons à submésoéchelle qui ne sont pas détectés par l'altimétrie. La partie centrale du canal possède à l'Ouest une dynamique océanique très variable où résident des structures anticycloniques tourbillonnaires [*Schouten et al.*, 2003], à la différence de sa partie Est qui connaît une faible variabilité.
La branche Sud du Courant Est de Madagascar se détache de la côte Malgache vers $47°E - 26°$S en prenant une direction Est-Sud-Est. Ce courant peut se comporter comme un "canon à dipôle" en générant des structures dipolaires entre la côte Malgache et le plateau de Madagascar. Ces dipôles s'acheminent dans la direction du Courant des Aiguilles en traversant le Bassin du Mozambique pour la plupart du temps se disloquer au contact de la dorsale du Mozambique [*Lutjeharms*, 2006] (voir figure 4.6). Le SEMC en s'éloignant de la côte malgache peut aussi rétrofléchir vers l'Est [*Lutjeharms et Machu*, 2000] de la même façon que le Courant des Aiguilles plus au Sud-Ouest.

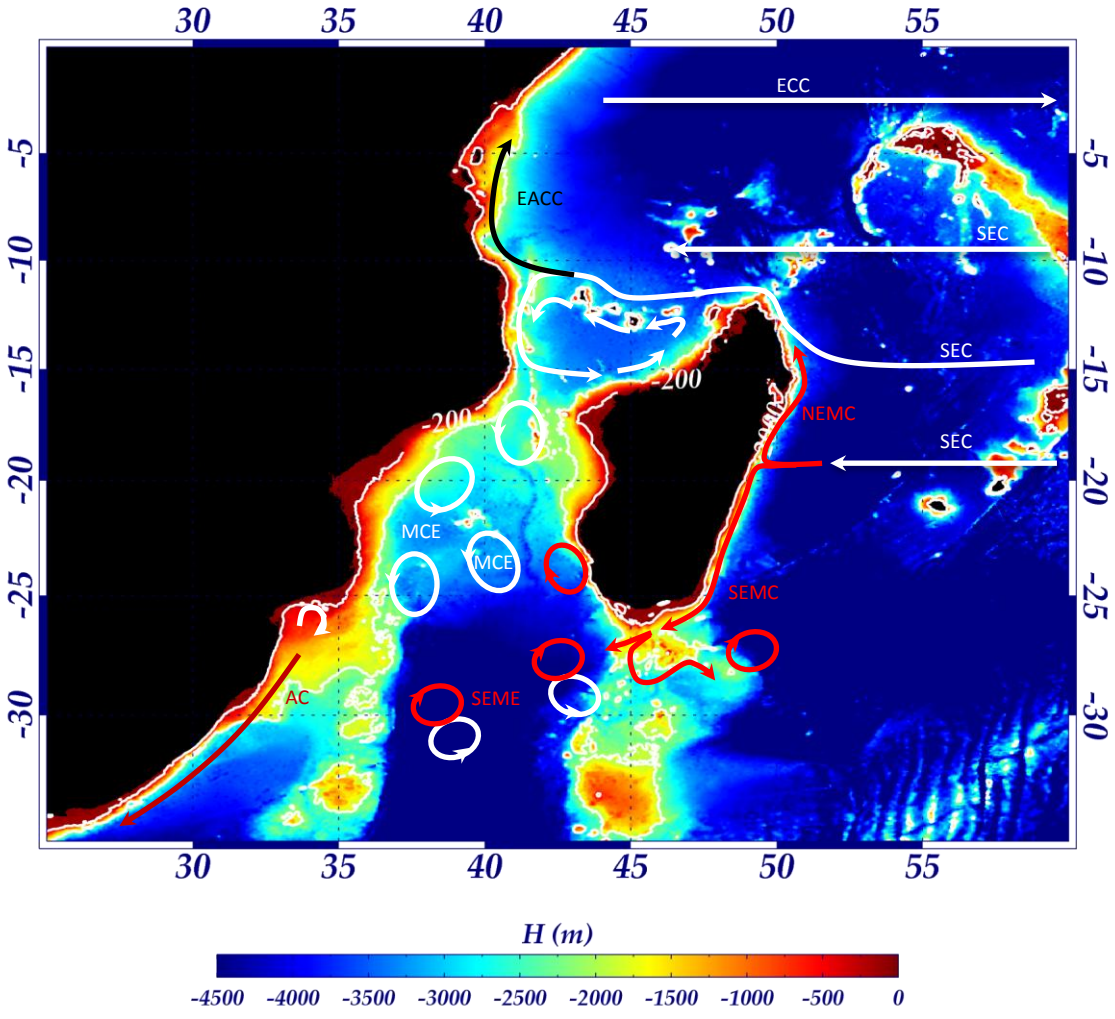

FIGURE 4.6 – Bathymétrie dans le Canal du Mozambique avec le schéma de circulation générale superposé. SEC : Courant Sud-Equatorial, SEMC : Courant Sud-Est Malgache, NEMC : Courant Nord-Est Malgache, EACC : Courant Côtier Est Africain, AC : Courant des Aiguilles, MCE : Tourbillons du Canal du Mozambique, SEME : dipôle formé par la branche Sud-Est du Courant Malgache.

4.4.2 Zone d'alimentation des Frégates du Pacifique (Fregata minor)

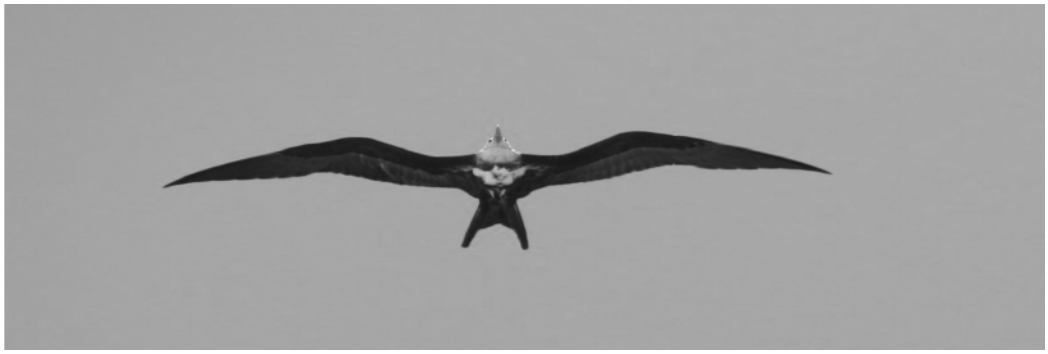

FIGURE 4.7 – Photo de la Frégate du Pacifique (Fregata minor), ©Christer Sundstrom.

La Frégate du Pacifique (Fregata minor - voir figure 4.7) est un oiseau marin présent dans la zone tropicale des 3 océans, pouvant parcourir des milliers de kilomètres à partir de sa colonie de reproduction pour s'alimenter. Ses mensurations typiques (d'une taille de 80 à 105 cm, son envergure de 205 à 230 cm et son poids de 1 à 1.6 kg) en font un excellent planeur et même l'oiseau marin qui a la plus grande portance (ratio entre surface des ailes et poids du corps). Dans le Canal du Mozambique, les deux plus grandes colonies se trouvent sur l'île d'Aldabra ($9.45°$S - $46.45°$E) et sur l'île d'Europa ($22.3°$S - $40.3°$E).
Lors de la période de ponte, elles restreignent leurs déplacements pour la phase de reproduction et de nourrissage car ces oiseaux sont organisés en couple et se relayent pour couver leurs oeufs. Bien qu'ils soient restreints à cette période, leurs déplacements peuvent tout de même se faire sur des centaines de kilomètres [*Weimerskirch et al.*, 2004].
Son plumage étant perméable, cet oiseau est incapable de se poser sur l'eau ou de plonger pour s'alimenter, bien que son alimentation provienne du milieu marin. Sa stratégie d'alimentation est de repérer les remous qui se forment lorsque les grands prédateurs comme les thons, les dauphins etc. remontent leurs proies vers la surface. Les proies, cherchant à échapper à leurs captures, n'ayant que le choix de sauter au dessus de la surface, deviennent dès lors des proies pour la Frégate qui va les capturer à cet instant. Une autre stratégie d'alimentation est le kleptoparasitisme mais ce comportement reste marginal pour cette espèce [*Vickery et Brooke*, 1994]. Son comportement d'alimentation permet de localiser avec une bonne précision les bancs de thons, les observations en mer des bancs de thons ayant un taux d'association élevés avec la

position des frégates (70%).

La population étudiée dans le cadre de cette étude peuple l'île d'Europa, s'élevant entre 700 et 1100 couples scindée en sous colonies de 2 à 50 nids [*Weimerskirch et al.*, 2004]. Neuf balises Argos miniaturisées ont été positionnées sur certains individus adultes en période de reproduction (2 sur des mâles, 7 sur des femelles). Ces dispositifs estiment la localisation géographique ainsi que la vitesse de vol des Frégates. Les déplacements de chaque individu sont enregistrés. Les positions (de 3 à 4 par jour) sont ensuite interpolées spatio-temporellement pour être cohérentes avec les données satellites.

La vitesse de déplacement permet d'identifier si l'animal se déplace pour rejoindre sa zone d'alimentation ($16.4 \pm 4\ km.h^{-1}$) ou s'il est en recherche de proie (vitesse de $10\ km.h^{-1}$ calculée avec 3 positions consécutives) [*Hyrenbach et al.*, 2002; *Weimerskirch et al.*, 2004]. Les voyages sont subdivisés en deux catégories [*Weimerskirch et al.*, 2004] :

- les voyages "longs" : voyage d'une durée supérieure à $72\ h$ correspondant à la période d'incubation et post-reproduction,
- les voyages "courts" : voyage d'une durée inférieure à $72\ h$ correspondant à la phase d'élevage et de nourrissage des poussins et post-reproduction.

La position des frégates obtenue par télémétrie, l'analyse de leurs déplacements, et les différentes données satellites, nous informent sur les liens entre la répartition de ces animaux et leur habitat. Des études précédentes [*Weimerskirch et al.*, 2004; *Tew-Kai et Marsac*, 2009] montrent que les frégates dans le Canal du Mozambique concentrent leurs efforts d'alimentation le long des bordures de tourbillons en évitant le centre peu productif. Cependant ces études en utilisant des données satellites au tiers de degré ne déterminent pas avec précision les zones de fronts. La dynamique océanique à submésoéchelle est nécessaire pour détecter avec précision les zones d'alimentation dans le Canal du Mozambique, pour identifier les zones de fortes productions et pour comprendre la stratégie de déplacement liée au comportement d'alimentation. *Tew Kai et al.* [2009] utilisent les données de dynamique océanique issues du produit GEKCO en association avec la méthode FSLE (chronologique et anti-chronologique) pour déterminer l'activité de mélange et les structures cohérentes Lagrangiennes contrôlant le transport aux différentes échelles afin

de révéler les structures à submésoéchelle dont la distribution est proche de celle des traceurs passifs comme la TSM ou la couleur de l'eau [*d'Ovidio et al.*, 2009].
L'analyse montre une distribution spatiale des oiseaux pour les deux types de voyage en relation étroite avec la position des structures cohérentes et une répartition non aléatoire des frégates. Suivant les types de voyage, les stratégies d'exploration sont différentes. Pour les voyages "longs", les oiseaux suivent aussi bien les structures cohérentes divergentes (LCSs provenant de la méthode FSLE chronologique) que les structures cohérentes convergentes (LCSs provenant de la méthode FSLE anti-chronologique). Pour les voyages "courts", les oiseaux suivent principalement les structures convergentes. Ces structures advectent les traceurs passifs le long de leurs lignes de convergence. Ces lignes sont des attracteurs pour le zooplancton qui est un attracteur pour les proies des frégates. La relation unissant le déplacement des frégates lors de leurs voyages "longs" et les lignes de divergence est plus complexe et n'est pas encore déterminée.
L'analyse montre aussi une distribution sur les LCSs de la position des frégates identique de jour comme de nuit. Les frégates ne s'alimentant que le jour [*Weimerskirch et al.*, 2004], elles utilisent les structures cohérentes non seulement pour s'alimenter mais aussi pour se déplacer [*Tew Kai*, 2009].

Ces différents résultats montrent que la turbulence pleinement développée joue un rôle crucial et impacte le déplacement des frégates. Cette turbulence contrôle les zones d'alimentation, amène les oiseaux marins à développer des stratégies complexes de déplacement et d'alimentation adaptées à la détection et au suivi des structures océaniques qui en sont issues. Ces animaux arrivent à suivre ces structures. Il existe plusieurs hypothèses pour la détection de ces structures par ces animaux ; la détection visuelle, la détection olfactive du dimethylsulphide (DMS) produit par la dégradation du phytoplancton brouté par le zooplancton, la détection des changements de direction du vent au dessus des structures océaniques tourbillonnaires [*Chelton et al.*, 2007; *Frenger et al.*, 2013]. *Monte et al.* [2012] qui a repris notre étude sur un plus grand jeu de données de déplacements de frégates confirment nos hypothèses. Cependant ces hypothèses ne sont pas exhaustives et nécessitent de plus amples investigations !

4.4.3 Capacités d'orientation des tortues vertes (Chelonia mydas) et impact des courants marins sur leurs déplacements

Classée comme espèce menacée par l'union internationale pour la conservation de la nature (UICN), la tortue verte (Chelonia mydas) est une des sept espèces de tortues marines dont la survie est fortement compromise par les méthodes de pêche actuelles, l'exploitation de ses oeufs et la destruction de son habitat. La disparition de ces espèces causera un déséquilibre dans le réseau trophique océanique aux conséquences dramatiques assez mal connues.
L'Océan Indien et en particulier le Canal du Mozambique sont des zones importantes de reproduction de ces espèces. Ces tortues sont connues pour être fidèles à leurs sites d'alimentation et de ponte. Elles possèdent une capacité d'orientation étonnante dans le milieu marin permettant de retourner sur leur site de naissance pour pondre alors qu'elles se trouvent sur leurs sites d'alimentation se situant à plusieurs centaines voire milliers de kilomètres [*Hughes et al.*, 1998; *Luschi et al.*, 1998]. Cette surprenante capacité soulève de nombreuses questions, notamment :

- quel est l'effet des courants océaniques sur leurs déplacements ?
- après un déplacement à partir de la plage de ponte, sont-elles capables d'y retourner ?
- quelles sont les capacités sensorielles mises à contribution pour l'orientation de la tortue ?

Pour répondre à ces questions plusieurs approches peuvent être envisagées pour étudier le comportement d'orientation à grande distance des tortues marines.
Des expériences en bassin sur des individus capturés sont effectuées pour tester leurs capacités sensorielles en les soumettant à divers *stimuli* [*Papi et al.*, 1995; *Luschi et al.*, 1998] et/ou à diverses perturbations [*Papin et al.*, 2000].
Des expériences en milieu naturel sont réalisées (expérimentations de retour au gîte) [*Luschi et al.*, 1996; *Papi et al.*, 1997; *Hays et al.*, 2003; *Avens et al.*, 2003]. Jusqu'à récemment, bien que ces tortues évoluent dans un milieu océanique complexe et turbulent, l'impact mécanique des courants sur leurs déplacements n'a jamais été quantifié mais seulement discuté [*Luschi et al.*, 1998, 2003b]. Dans le but de mettre un aspect quantitatif à cet impact,

différentes études sont menées pour estimer si les courants sont susceptibles de faciliter la progression des tortues marines ou s'ils sont une contrainte mécanique en perturbant la direction de nage ou en les écartant de leur route de migration optimale.

Quelques notions sur le cycle de vie, le comportement d'orientation et la capacité sensorielle des tortues vertes

Dans le Canal du Mozambique cinq espèces de tortues sont présentes. La tortue verte est l'espèce la plus abondante et la plus étudiée. Les sites de ponte dans cette région se situent sur les côtes africaine, malgache et sur des îles comme Europa, Juan de Nova, l'archipel des Comores et les Glorieuses. Les sites d'alimentation se situent le long des côtes du canal ainsi que sur celles des Comores. Ces sites d'alimentation sont proches des sites de ponte, cependant les tortues semblent préférer des zones d'alimentation et de ponte éloignées les unes des autres. Les femelles venant pondre ne s'alimentent pas à proximité du site de ponte. Ces femelles gravides sont les seules représentantes de leur espèce à retourner sur la terre ferme (pour pondre), les mâles passant l'essentiel de leur vie en mer proche de leurs zones d'alimentation côtières et les juvéniles ayant une phase de vie pélagique assez mal connue avec des migrations qui peuvent être transocéaniques. Les tortues vertes immatures âgées d'une dizaine d'années restent fidèles à des zones d'alimentation assez restreintes bien qu'elles puissent, si les ressources viennent à s'amenuiser, exploiter des domaines côtiers plus vastes.
Suite à leur maturité sexuelle, les tortues vertes sont fortement fidèles à une aire d'alimentation [*Godley et al.*, 2002] et à un site de reproduction qui semble être le même que leur lieu de naissance [*Bowen et Karl*, 1997]. Lors de la phase de reproduction (périodicité de 1 à 9 ans), les adultes sont capables de parcourir plusieurs centaines voire milliers de kilomètres ce qui représente la distance qui sépare les zones d'alimentation des zones de reproduction [*Carr*, 1987]. Les femelles passent plusieurs mois à proximité de la plage de ponte où elles vont déposer leurs oeufs (20 à 250 par ponte) à plusieurs reprises (4 à 6 fois par saison de ponte) avec une fréquence moyenne de $\sim$12 jours [*Le Gall et al.*, 1988].

Les capacités d'orientation des tortues sont remarquables. Plusieurs études ont permis de suivre certains individus au moyen de balises de positionnement.

Des expériences de retour au gîte sont réalisées sur des femelles déplacées de leur site de ponte et relâchées à quelques kilomètres de celle-ci. Ces expériences montrent que si elles sont relâchées à proximité de leur site de ponte, elles sont capables de le rejoindre rapidement et que si elles sont relâchées au large, elles vont avoir plus ou moins de réussite au terme de trajets plus ou moins bien orientés. Ces expériences impliquent que les tortues sont capables de s'orienter vers leur site de ponte. Ceci peut-être expliqué par différentes hypothèses d'orientation [*Luschi et al.*, 2003a] :

- le suivi d'un cap codé génétiquement ou appris d'un précédent déplacement : cette hypothèse de navigation vectorielle suppose qu'elles possèdent une boussole biologique (magnétique ou solaire), ce qui est vraisemblablement le cas [*Lohmann*, 1991; *Light et al.*, 1993]. Le champ magnétique peut fournir des informations directionnelles, cependant ce type d'orientation ne peut en aucun cas expliquer la capacité d'orientation des femelles relâchées sur un lieu *a priori* inconnu, car il nécessite la connaissance du point d'origine,
- le suivi de repères terrestres ou bathymétriques : ce second type de navigation vectorielle [*Luschi et al.*, 1996] peut être uniquement utilisée lorsque les côtes sont proches ou lorsque la bathymétrie est faible et donc il n'explique pas les migrations transocéaniques,
- l'intégration de trajet : ce processus consiste à mettre à jour de façon régulière l'emplacement de son point de départ en fonction de sa propre position en ayant au préalable acquis des informations au cours du trajet aller pour effectuer le trajet retour [*Luschi et al.*, 2001; *Hays et al.*, 2003]. Cependant un animal déplacé de façon passive au cours d'une expérience et privé d'information extérieure lors de son déplacement n'est pas en mesure d'utiliser ce processus,
- la navigation basée sur un ou plusieurs champs de gradients : Les tortues sont capables de percevoir la variation d'inclinaison et d'intensité du champ géomagnétique. Elles peuvent utiliser ces cartes géomagnétiques pour obtenir à partir de leur emplacement la direction du but à atteindre [*Lohmann et al.*, 2004].
- la navigation basée sur des champs de gradients chimiques : la tortue marine a un odorat très développé. Il est possible que les tortues utilisent des plumes olfactives sous-marines [*Koch et al.*, 1969] ou aériennes [*Luschi et al.*, 2001; *Hays et al.*, 2003] pour détecter la direction du point d'origine lorsque celui-ci se trouve suffisamment proche. Ce type de

navigation est restreint du fait de la caractéristique turbulente des fluides (dispersion rapide d'un composé chimique) .

Trois expériences de retour au gîte ont été réalisées entre novembre 2003 et mai 2009, en début de cycle de ponte où la probabilité de capture de femelles est élevée, ce qui permet de supposer que les tortues femelles sont motivées pour retrouver leur plage de ponte afin de continuer leur saison de reproduction. Le protocole expérimental mis en place consiste à capturer des femelles sur la plage de ponte, de les équiper d'un émetteur fixé sur la carapace, de les maintenir séparées dans des caisses en bois lors de leur déplacement jusqu'au point de largage déterminé au préalable. Lors du déplacement ces tortues sont arrosées (pour éviter la déshydratation) et maintenues à l'ombre pour éviter qu'elles aient une vue du ciel.

Pour faire ces expériences de retour au gîte, trois sites ont été privilégiés :

- le site de l'île d'Europa où trois tortues ont été capturées et équipées d'émetteurs puis relâchées à $115\ km$ de la plage pour deux d'entre elles et à $245\ km$ pour la troisième,
- le site de l'île de Mayotte où 20 tortues ont été capturées (8 en juin 2004, et 12 en mai 2005). Treize tortues ont été équipées d'aimant mobile de très forte puissance afin de brouiller la perception du champ magnétique (soit pendant le déplacement passif à bord du navire afin d'éliminer la possibilité à la tortue de connaître le trajet aller, soit au moment du lâcher pour perturber la capacité sensorielle géomagnétique lors du trajet de retour au gîte). Sept tortues ont été appareillées de faux aimants pour simuler la gêne occasionnée par la pose sur la tête du dispositif et ainsi avoir des contrôles. Les tortues ont été relâchées sur 4 sites distincts éloignés de 100 à $120\ km$ de la plage de ponte,
- le site de l'île de Grande Glorieuse où 24 tortues ont été capturées (12 en mai 2008 et 12 en mai 2009) et équipées soit de faux aimants pour servir de contrôle, soit comme l'expérience précédente d'aimant avec une forte intensité lors du trajet aller (pour confirmer l'hypothèse de l'expérience ci-dessus), soit d'aimant ayant une intensité du même ordre de grandeur que le champ magnétique terrestre lors du trajet retour au gîte.

Les courants océaniques (géostrophique et d'Ekman) ont été estimés aux moyens des champs de dynamique océanique obtenus par les données océanographiques satellitales [*Sudre et Morrow*, 2008] pour les deux premières experiences (pour les sites des îles d'Europa et Mayotte) et au moyen de ceux estimés par [*Sudre et al.*, 2013] pour les expériences du site de Grande Glorieuse.

Girard et al. [2006] ont développé une méthode novatrice permettant de prendre en compte les courants océaniques dans l'estimation du déplacement des tortues et de quantifier l'impact de ces courants sur ces déplacements.
La vitesse de déplacement d'une tortue a le même ordre de grandeur que les courants océaniques $O(25\ cm.s^{-1})$. Pour étudier le comportement d'orientation et la capacité sensorielles des tortues, il est nécessaire de prendre en compte les courants océaniques. Autour du site de l'île d'Europa, la dynamique océanique présente est caractérisée par une forte activité mésoéchelle (voir figure 4.5), permettant d'obtenir une bonne estimation des courants marins avec un produit au quart de degré.
Les positions (latitudes et longitudes) de la tortue donnent un trajet qui est relatif aux positions terrestres et qui ne tient pas compte des courants. La méthode consiste à prendre à chaque position de la tortue, le vecteur vitesse des courants collocalisés, et de soustraire ce vecteur au vecteur vitesse de la tortue. On obtient le *trajet moteur* qui est relatif à la masse d'eau.

L'analyse des trajets moteurs montre que l'action mécanique des courants océaniques sur la tortue est une contrainte pour son déplacement et que les tortues ne peuvent pas compenser la dérive des courants (à la manière d'un navire anticipant sa dérive). Les tortues ont une capacité de navigation assez rudimentaire qui leur permet de corriger la dérive due aux courants uniquement *a posteriori*. Cet capacité peut s'expliquer par une navigation basée sur des champs de gradients où le but à atteindre a été mémorisé au préalable. Celles-ci estimeraient alors la direction locale du but en se basant sur une différence entre la valeur du champ au point d'évaluation et celle qui a été mémorisée. Il semble que les tortues utilisent au cours de leurs déplacements une combinaison d'indices sensoriels de natures différentes (différents types de gradients) en fonction de l'information disponibles dans l'environnement.

Cette étude définit un nouveau protocole pour obtenir le trajet que la tortue a tenté de faire (et non le trajet effectué), nécessitant de prendre en compte la dynamique océanique avant de tenter d'interpréter le comportement animal, pour avoir comme base de départ la véritable efficacité d'orientation de la tortue [*Girard*, 2005]. Ce résultat majeur permet actuellement de mieux quantifier l'impact des courants sur le déplacement des animaux marins et doit-être généralisé à l'ensemble des espèces marines étudiées.

Pour faciliter la mise en place de ce protocole, un logiciel est mis à la disposition de la communauté scientifique (nommé *mesoscale oceanic current extraction program* téléchargeable sur la page http ://www.legos.obs-mip.fr/sudre) permettant de calculer directement à partir d'une extraction de la base de données GEKCO les trajets moteurs (extraction effectuée sur demande).

En suivant le même protocole établi par [*Girard et al.*, 2006], *Luschi et al.* [2007] confirment l'incapacité d'anticipation des tortues vertes à prendre en compte l'action mécanique des courants à mésoéchelle. Ils montrent que les trajets des tortues magnétiquement traitées (pour les deux types de traitement magnétique) sont significativement plus longs que les contrôles. Ceci met en évidence pour la première fois, par une expérience *in situ*, que les tortues vertes utilisent des informations provenant du géomagnétisme terrestre pour leur navigation. Les tests statistiques effectués sur les trajets moteurs révèlent qu'il n'y a pas de différence significative entre les tortues ayant un aimant positionné sur la tête lors du transport pour rejoindre le point de lâcher et les tortues équipées d'un aimant lors du lâcher. Ces expériences ne déterminent pas le rôle joué par le géomagnétisme comme source d'information pour la navigation de la tortue verte. Elles ne permettent pas de savoir si la tortue utilise l'information géomagnétique lors de son déplacement pour rejoindre le retour au gîte via des "cartes géomagnétiques" ou si, de façon plus surprenante, elles collectent des informations géomagnétiques lors du trajet (passif) jusqu'au point de lâcher pour ensuite les utiliser pour le retour au gîte. Les aimants utilisés lors de cette expérience sont de forte puissance (délivrant $200\ \mu T$ autour de toute la tête de l'animal) par rapport à l'intensité du champ magnétique terrestre qui est $\sim 33\ \mu T$ autour de Mayotte. Ces aimants peuvent altérer durablement la capacité sensorielle des tortues avec une persistance de

la perturbation après le lâcher pour les tortues perturbées uniquement lors du trajet aller. Le trajet des tortues équipées d'aimant est significativement plus long. Ces tortues (sauf une), sont arrivées sur la plage de ponte. Ceci prouve que l'information géomagnétique est utilisée par les tortues mais qu'elle n'est pas essentielle et l'unique moyen d'orientation pour retrouver la plage de ponte.

4.5 Article : The Role of Geomagnetic Cues in Green Turtle Open Sea Navigation, S. Benhamou *et al.*, 2011

4.5.1 Résumé de l'article

Contexte de l'étude : Des expériences en laboratoire et *in situ* ont mis en évidence que les tortues marines utilisent des informations géomagnétiques pour la navigation en plein océan. Par exemple, des tortues vertes (Chelonia mydas) déplacées de $100\ km$ de leur site de ponte ont vu leur performance pour retourner au gîte se dégrader lorsqu'elles portaient un aimant de forte intensité collé sur leur tête. Cependant, le rôle de l'information géomagnétique reste peu clair actuellement, car des tortues vertes ayant subi un traitement magnétique peuvent exécuter des migrations post-reproductions à grande échelles (> 2000 km) de la même manière que des contrôles.

Méthodologie / Principaux résultats : Au cours de cette expérience, 24 tortues vertes ont été déplacées de $200\ km$ de leur site de ponte se situant sur une île océanique, et suivies, pour la première fois pour ce type d'expérience, avec le système global de positionnement (GPS) qui est capable de fournir des données plus fréquentes et plus précises que les méthodes télémétriques antérieures. Huit tortues ont été traitées magnétiquement sur une durée de $24\text{-}48\ h$ sur la plage de ponte avant leur déplacement, et huit autres ont été équipées d'un aimant collé sur la tête au point de lâcher. Les huit dernières ont été utilisées comme contrôles. L'analyse détaillée des trajets relatifs à la masse d'eau (i.e., trajets corrigés des courants océaniques) a montré que les tortues traitées magnétiquement étaient capables de naviguer jusqu'à leur site

de ponte avec la même efficacité que les contrôles, mais que leur performance se dégradait significativement quant elles arrivaient à $50\ km$ du gîte.

Conclusions / Signification : Alors que les tortues vertes ne semblent pas avoir besoin d'informations géomagnétiques loin du but à atteindre, ces informations deviennent nécessaires à l'approche du gîte. Comme la toute dernière partie du retour au gîte (quelques kilomètres du gîte) dépend probablement d'informations non-magnétiques, nos résultats suggèrent que des informations magnétiques jouent un rôle clef dans la navigation des tortues marines à une échelle intermédiaire, comblant le fossé entre la grande et petite échelle des processus de navigation qui semblent dépendre d'informations non-magnétiques.
A grande distance du but, le nombre d'anomalies magnétiques, ayant approximativement la même intensité que le but a atteindre (ici l'île de ponte), est trop élevé pour que la tortue puisse déterminer la position du but avec suffisamment de précision pour le rejoindre. Il semble que pour ce type de distance, elle utilise une combinaison de deux types de processus de navigation : le "*getting-there*" [1] et le "*knowing-where*" [2]. Divers gradients olfactifs sur la route pourraient jouer ce rôle. Ce type de navigation est imprécis mais il est suffisant pour se rapprocher du but.
A distance intermédiaire, elles utiliseraient ces mêmes types de processus mais avec le géomagnétisme.
A courte distance, elles utiliseraient probablement des informations visuelles ou olfactives (éoliennes).

4.5.2 Article publié dans *PLoS ONE*

Référence : Benhamou S., J. Sudre, J. Bourjea, S. Ciccione, A. De Santis and P. Luschi, 2011 : The Role of Geomagnetic Cues in Green Turtle Open Sea Navigation , *PLoS ONE*, **6**, 10, e26672, DOI 10.1371/journal.pone.0026672.

1. Ce processus de navigation consiste à suivre différents gradients connus sur la route de navigation pour rejoindre le but.
2. Ce processus de navigation consiste à savoir où aller.

OPEN ACCESS Freely available online

PLoS one

The Role of Geomagnetic Cues in Green Turtle Open Sea Navigation

Simon Benhamou[1]*, Joël Sudre[2], Jérome Bourjea[3], Stéphane Ciccione[4], Angelo De Santis[5], Paolo Luschi[6]

1 CEFE, CNRS, Montpellier, France, **2** LEGOS, CNRS, Toulouse, France, **3** IFREMER, La Réunion, France, **4** Kélonia, La Réunion, France, **5** Istituto Nazionale di Geofisica e Vulcanologia, Roma, Italy, **6** Dipartimento di Biologia, Università di Pisa, Italy

Abstract

Background: Laboratory and field experiments have provided evidence that sea turtles use geomagnetic cues to navigate in the open sea. For instance, green turtles (*Chelonia mydas*) displaced 100 km away from their nesting site were impaired in returning home when carrying a strong magnet glued on the head. However, the actual role of geomagnetic cues remains unclear, since magnetically treated green turtles can perform large scale (>2000 km) post-nesting migrations no differently from controls.

Methodology/Principal Findings: In the present homing experiment, 24 green turtles were displaced 200 km away from their nesting site on an oceanic island, and tracked, for the first time in this type of experiment, with Global Positioning System (GPS), which is able to provide much more frequent and accurate locations than previously used tracking methods. Eight turtles were magnetically treated for 24–48 h on the nesting beach prior to displacement, and another eight turtles had a magnet glued on the head at the release site. The last eight turtles were used as controls. Detailed analyses of water masses-related (i.e., current-corrected) homing paths showed that magnetically treated turtles were able to navigate toward their nesting site as efficiently as controls, but those carrying magnets were significantly impaired once they arrived within 50 km of home.

Conclusions/Significance: While green turtles do not seem to need geomagnetic cues to navigate far from the goal, these cues become necessary when turtles get closer to home. As the very last part of the homing trip (within a few kilometers of home) likely depends on non-magnetic cues, our results suggest that magnetic cues play a key role in sea turtle navigation at an intermediate scale by bridging the gap between large and small scale navigational processes, which both appear to depend on non-magnetic cues.

Citation: Benhamou S, Sudre J, Bourjea J, Ciccione S, De Santis A, et al. (2011) The Role of Geomagnetic Cues in Green Turtle Open Sea Navigation. PLoS ONE 6(10): e26672. doi:10.1371/journal.pone.0026672

Editor: Wayne M. Getz, University of California, Berkeley, United States of America

Received July 23, 2011; **Accepted** September 30, 2011; **Published** October 26, 2011

Copyright: © 2011 Benhamou et al. This is an open-access article distributed under the terms of the Creative Commons Attribution License, which permits unrestricted use, distribution, and reproduction in any medium, provided the original author and source are credited.

Funding: The work was funded by Agence nationale de la Recherche http://www.agence-nationale-recherche.fr/, Programme ESTVOI (ANR-07-BLAN-0220-01). The funder had no role in study design, data collection and analysis, decision to publish, or preparation of the manuscript.

Competing Interests: The authors have declared that no competing interests exist.

* E-mail: simon.benhamou@cefe.cnrs.fr

Introduction

As the geomagnetic field is present everywhere at the Earth surface, it has been considered a major candidate for providing large scale locational cues, beyond its well-documented role in providing directional cues (geomagnetic compass; e.g. see [1]). Large scale oceanic travelers such as pelagic birds and sea turtles are likely to rely on geomagnetic locational cues because they have to navigate through vast stretches of featureless open sea where other cues may be unavailable. However, experiments involving pelagic birds [2,3] showed that their navigational skills were not impaired when these birds were prevented from perceiving the geomagnetic field by carrying strong magnets on the head. In contrast, a number of experiments with hatchling and juvenile sea turtles in arenas showed that these animals are able to obtain locational information from the geomagnetic field [4].

In a previous homing experiment, we showed that geomagnetic information may help adult female green turtles (*Chelonia mydas*) to return to their egg-laying sites on an island after having been experimentally displaced in the open sea [5]. Some individuals were prevented from perceiving the geomagnetic field by carrying an extremely strong magnet glued on the head, either during the homing phase or during the displacement from the nesting beach to the release site. The turtles of both groups were nevertheless able to home, albeit less efficiently than controls. The impairment of the turtles of the former group provided evidence that sea turtles use geomagnetic cues to improve their pelagic navigation efficiency. The effect on the turtles of the latter group, whose magnet was removed just before release, could be explained in two ways: (i) the strong magnet produced some long lasting after-effect, which may cause a kind of ''memory reset'' of the geomagnetic location of the nesting site or (ii) the treatment prevented turtles from acquiring some critical route-based navigational information during the (passive) outward journey. More generally, it cannot be excluded that the application of a strong magnetic field to the turtles' head might result in poor navigation abilities because of some unspecific effects of the artificial magnetic field on brain functioning.

In the present study, we further investigate the role of geomagnetic information in green turtle open sea navigation in

two ways. We studied the homing performances of nesting green turtles released in the open sea (1) when carrying a weak magnet on the head during the return path or (2) when wearing a very strong magnet (the same type as the one used in our previous experiment [5]) while still on the nesting beach. The field generated by the weak magnet had an intensity of the same order of magnitude as that of the Earth's magnetic field and so should make turtles experience an altered magnetic field providing biologically plausible but misleading magnetic cues. The treatment with the strong magnet applied before the displacement to the release point, aimed to test a possible long-lasting effect of strong magnets on the turtle navigational skills.

Thanks to the high spatial and temporal resolution provided by GPS tracking, we were able to analyze the turtles' navigational performances in detail, distinguishing different – initial, central and final – phases of the pelagic trips. These three phases are expected to involve a different balance between movement persistence and goal attractiveness, with the consequence that, from a practical point of view, the navigational efficiency during each phase has to be evaluated in a specific way (see Material and Methods). The central and final phases are also expected to involve different, scale-dependent navigation processes with different spatial resolutions, because of a trade-off between working scale and accuracy. Indeed, the navigational processes working at a large scale usually only enable an animal to reach a general area surrounding the goal location, whereas those allowing the animal to pinpoint the goal can work only at a small scale, when the animal is in the close vicinity of its target [4,6–7]. The hierarchy of the navigational process required to reach a goal from a very distant starting point should therefore involve a series of concentric ''circles of confusion'', each corresponding to a scale-specific navigational process. Each of these circles is centered at the goal and encompasses the set of locations that are indiscernible from the goal in terms of the cues used by the navigational process in question [8,9]. Thus, when a homing turtle is within a few kilometers of its nesting site, it is likely to be within the circles of confusion of the navigation processes it used at larger scales. To reach its nesting site, it then should rely on a very small scale (pinpointing) process, for which an involvement of wind-borne (presumably olfactory) cues and/or visual cues of the goal, has been proposed [10,11].

The homing tracks we recorded in previous studies [5,12] showed that homing turtles, and particularly those that were magnetically treated, were usually able to navigate quite efficiency towards their nesting site but may miss it by a few dozen of kilometers (a result also confirmed in the present study). This suggested the existence of a medium scale, magnetic-based navigational process, enabling turtles to bridge the large scale (true pelagic) and the small scale (pinpointing) navigational processes. The distinction between the different phases of homing paths thus enabled us to examine at which specific spatial scale magnetic cues may play a major role during the sea turtle oceanic navigation.

Results

Eight out of the 24 GPS-tracked female turtles were magnetically treated for 24–48 h on the nesting beach prior to displacement (MB group) using a strong magnet, and other eight turtles had a weak magnet glued on the head at the release site (MH group). The last eight turtles were used as controls (CO group). Four turtles were removed from analysis because they did not show a high motivation to home (Fig. 1). Three of them (CO7, MB7 and MH7) moved more or less directly towards their feeding grounds along the African coast. A fourth one (CO8) initially orientated towards home, but she was only able to come only within 84 km of home before eventually giving up and moving towards her feeding grounds. The computation of the motor (water masses related; see Material and Methods) paths of these four females confirmed that their current-corrected headings were not consistently directed towards their nesting beach.

Three of the remaining 20 turtles (MB4, MB6, and MH5) were also unable to home. They covered long distances often along convoluted routes while apparently searching for home (Fig. 2), and eventually abandoned homing by stopping at another place (Aldabra Island for MB6, Madagascar for MB4 and MH5). They nevertheless showed a strong motivation to home and were able to arrive a few (14–27) kilometers of home during their quests. Indeed, their motor paths were globally oriented homewards until they were close to home (Fig. 3). This also applied to a fourth turtle (MH2) whose Argos/GPS device stopped working after 54 days (probably due to exhausted batteries), while the turtle was still searching for home (so we do not know if this turtle eventually did or did not home). The movements of these four turtles were therefore analyzed exactly in the same way as those of the 16 successful ones.

Track durations and lengths (calculated from release point to home or, for non-homers, to the point they abandoned homing) suggest that CO and MB turtles behaved similarly, and that MH turtles were partially impaired (Table 1, columns 2 and 3). However, from a detailed examination of the whole set of tracks (Fig. 2), it is quite clear that MH turtles may have initially navigated similarly to CO and MB turtles but started to become impaired when arriving relatively close to home. The simple computation of the mean path lengths required to halve the distance to home confirmed this impression. These mean ($\pm$SE) lengths were 203 ± 42 km in the CO group, 243 ± 41 km in the MB group, and 269 ± 65 km in the MH group, while the mean ($\pm$SE) lengths of the paths required to complete homing (or abandon) were 518 ± 116 km in the CO group, 726 ± 273 km in the MB group, and 1090 ± 418 km in the MH group.

However, variables such as homing duration or track length are too coarse to provide reliable figures of homing efficiency because they are quite sensitive to the drift of oceanic currents (see Material and Methods). The current speed (with respect to ground) and the turtles' swimming speed (with respect to water masses) can indeed be very similar (a few kilometers per hour), so that the resultant track durations and lengths could be dramatically affected by the direction of the currents encountered. The turtles' motor (water masses-related) movements better represent the turtles' orientation behavior than their recorded, ground-related, movements [5,12]. The global analysis of motor paths, as well as the analyses of initial and central phases of these paths (Table 1, columns 4–6), did not show any significant difference in homing efficiency between CO and MB or MH turtles. Both magnetically-treated groups performed worse than CO turtles, although not significantly, either globally or during the initial phase (Table 1, columns 4 and 5), but their mean efficiency was similar to that of CO turtles during the central phase (Table 1, column 6). It is worth noting that about half of the turtles of each group were able to move in the correct hemicycle (home direction $\pm90^\circ$) at the release site (0 values in column 5 of Table 1), suggesting that turtles chose their initial moving direction (first 5-km step) at random, independently of the treatment they had been subjected to. During the final phase (Table 1, last column), MH turtles significantly performed less efficiently than CO turtles (exact permutation test: $p<0.03$). MB turtles also seemed to perform less efficiently than CO turtles, but the difference was not statistically significant ($p>0.10$).

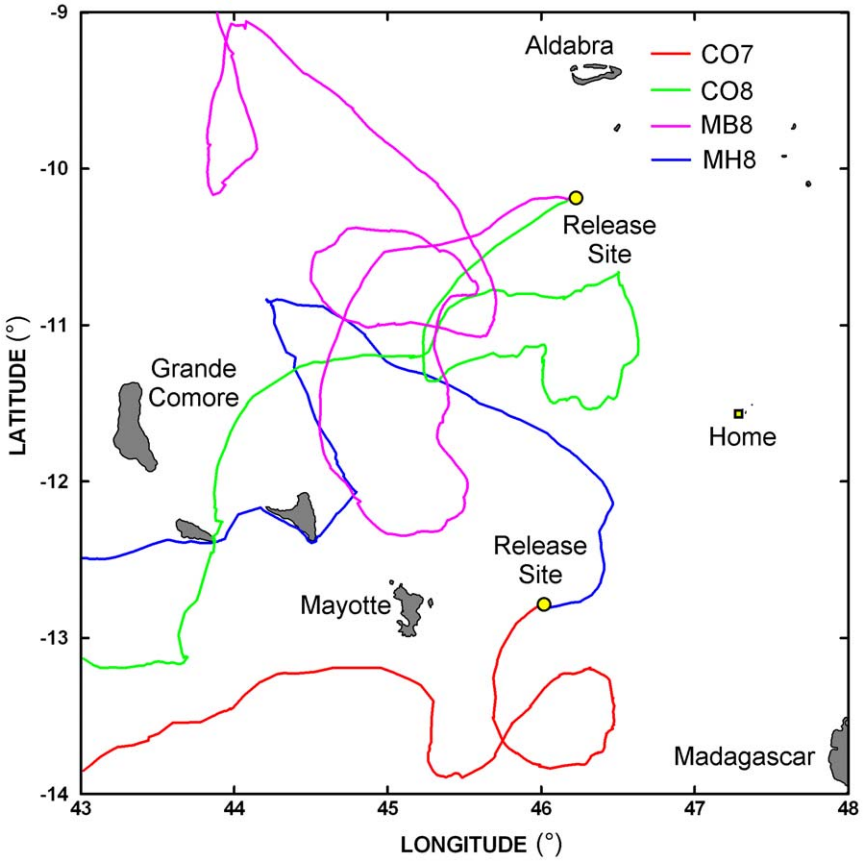

Figure 1. Paths of four turtles (two belonging to the CO group, one to the MB group and one to the MH group) that did not attempt to home but migrated towards their feeding sites along the African coast.
doi:10.1371/journal.pone.0026672.g001

It is also worth noting that many turtles, irrespective of the group to which they belonged and the release site, showed a tendency to initially move in a common direction that was different from the home direction. They thus made a sort of mistake in their orientation over the first few days. This was especially clear in both 2008 releases (north-western site), when all turtles initially moved roughly south-westwards, and in the first 2009 release (south-western site), when 5 out of the 6 released turtles (2 CO, 2 MB and 1 MH) moved first eastwards before shifting north-eastwards (Fig. 2). This initial bias was only partly due to the action of currents, as such a tendency to display a common biased orientation is evident in the current-corrected motor paths as well.

Discussion

Our results show that turtles exposed to a strong magnetic field for one or two days at the nesting site prior to displacement (MB group) or carrying a weak magnet on the head during the homing trip (MH group) were not particularly impaired with respect to controls before they arrived within 50 km of home. The mean homing performance of the turtles belonging to the MB or MH groups appeared to be lower than that of the control group once they arrived within 50 km of home, but the difference was statistically significant only for the MH group. The hypothesis of a long-lasting after-effect exerted by strong magnets [5], which might have cause a kind of "memory reset" of the geomagnetic location of the nesting site, is therefore not supported. However, it cannot be excluded that the absence of statistical significance for the MB group may have been due to a lack of statistical power caused by the small samples of the present study. Further investigations thus would be necessary before reaching a definitive conclusion. More importantly, it clearly appears that a homing green turtle does not need access to geomagnetic information when navigating far from its goal. This result is in general agreement with previous findings by Papi et al. [13], who showed that magnetically-treated green turtles were not impaired during their oceanic (trans-Atlantic) migration from their nesting site at Ascension Island to their Brazilian feeding grounds (more than 2000 km westwards). In contrast, MH turtles appeared to be dramatically impaired once they arrived relatively close to their goal. This suggests that geomagnetic cues would be really useful to navigating turtles only at this late stage.

The picture emerging from our results is that green turtles would rely on non-magnetic cues (whose actual nature remains to be determined) to navigate at large scale through the open sea, shift to magnetic ones when closer to their target, and shift again to non-magnetic cues for the very final, pinpointing stage [4]. A possible reason why sea turtles would not rely on geomagnetic cues to estimate the goal direction at large distances is that there exist numerous magnetic anomalies in the open sea [14,15]. A number of magnetic anomalies with intensities above 50 nT could be identified in our study area (Fig. 4). These anomalies appear to be strong enough to prevent the use of geomagnetic cues in a large scale (hundreds of kilometers) navigational system. Indeed, most green turtles nesting on islands in the Northern Mozambique

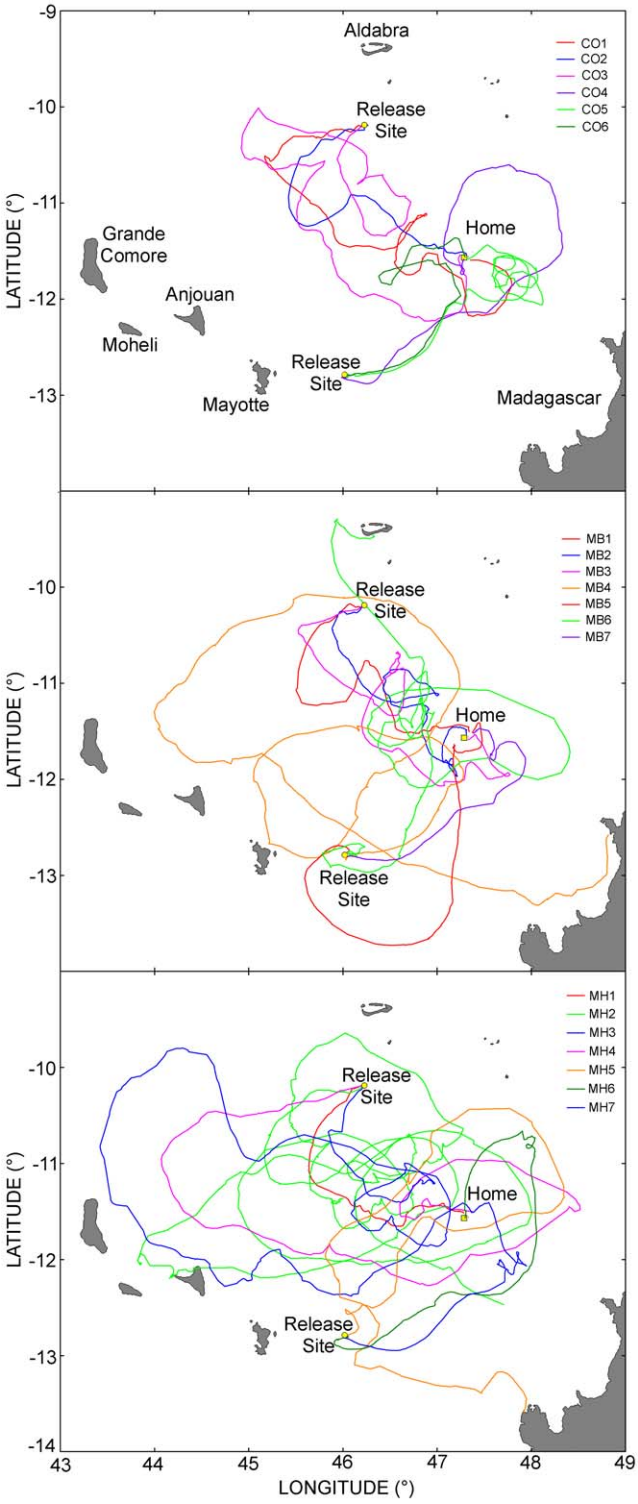

Figure 2. Paths of the 20 turtles which attempted to home, 16 of them being successful. The paths turtles belonging to the CO, MB and MH groups are represented in the top, middle, and bottom panel respectively.
doi:10.1371/journal.pone.0026672.g002

channel have their feeding grounds along the African coast, about 1000 km westwards (unpublished data). In this part of the world, the geomagnetic intensity globally changes by about 1.1 nT/km along the migration route. Such a situation is not limited to our study area but seems to be quite widespread. For instance, the change is about 1.5 nT/km along the migration route of green turtles nesting on Ascension Island. Under such circumstances, if green turtles would rely on geomagnetic cues to perform their large scale navigation, even the weakest anomalies they cross would involve large localization errors (several dozen of kilometers), and turtles could also be easily "trapped" in wrong places characterized by a magnetic intensity close to the one experienced at destination. Consequently, it would be a much safer option for sea turtles migrating from their foraging grounds to their nesting sites or *vice versa* to rely on a non-magnetic navigational process until they arrive relatively close to their goal.

As the oceanic environment is apparently featureless, the pelagic navigation process should be based on large scale environmental gradients, possibly of olfactory nature as proposed for homing pigeons [16]. The initial directional bias affecting most turtles, which was also observed in our previous experiment [5], suggests that this large scale navigation process rests on a mixed "getting-there" – "knowing-where" solution. The fact that sea turtles are not able to compensate for the current drift, although they are able to correct it, leads to the same conclusion [12]. A pure "getting-there" solution involves a mechanical procedure enabling an animal to reach its goal without any locational knowledge (e.g. gradient following), whereas a pure "knowing where" solution involves some kind of cognitive map. Numerous navigational processes appear to mix elements from these two types of solutions, involving the joint use of mechanical procedures and partial spatial memory [7]. In the present case, the biased initial orientation may be due to the reliance of the turtles on non-orthogonal gradient fields considered independently from each other [17]. Furthermore, the fact that this bias was shown by turtles from all three groups in a similar way provides additional indications that this large scale pelagic process rests on non-magnetic information.

This non-magnetic process operating at large scale is likely to be imprecise, i.e. characterized by a large circle of confusion, within which turtles may then shift to another navigational process based on local geomagnetic cues to approach further their nesting site. Geomagnetic cues may indeed be used by green turtles a few dozen of kilometers around home, as indicated by the present findings because, even in the presence of anomalies, the geomagnetic field should remain sufficiently monotonical (i.e. predictable) at this smaller scale to allow navigation based on its local characteristics. To use such a navigational process, turtles would need to memorize the local characteristics of the geomagnetic field around the home location (which may be quite different of the global characteristics expected at larger scale because of the presence of an anomaly). This may be achieved through some kind of learning taking place during their previous visits to the home area. As sea turtles tend to be faithful to their place of birth and use it later as nesting site [18–20], this learning may at first rest on some form of geomagnetic imprinting [21], and would be regularly reinforced and updated later in life at each every new breeding season (every 3–4 years for female green turtles in our study area [22], and possibly more often for males [23], which hence might have improved island finding abilities than females). Like for the large scale non-magnetic process, this medium scale magnetic process may rely on a mixed "getting-there" – "knowing-where" procedure, possibly involving local gradients of total intensity and inclination [4].

Under this scenario, the sea turtle long-distance navigation in oceanic environments would be based on three successive navigational processes: 1. A large scale, non-magnetic process to reach the relative vicinity of the target; 2. A medium scale magnetic process, to be used when approaching the circle of

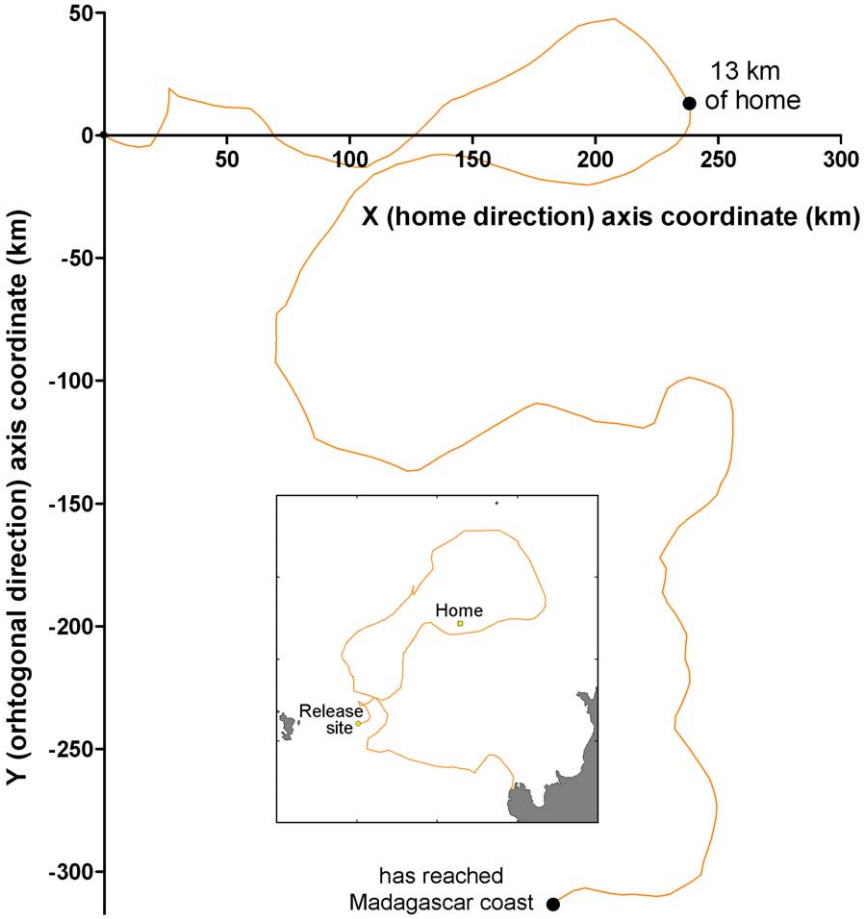

Figure 3. Example of motor (i.e. current corrected) path of a MH turtle (MH5), which was able to come close to home (13 km) in four days but missed it and was eventually unable to reach it. In the special frame of reference used here, the X axis corresponds to the home direction, and the Y axis to the orthogonal direction ($X_k = X_{k-1} + l.\cos(\theta_k - \gamma_{k-1})$; $Y_k = Y_{k-1} + l.\sin(\theta_k - \gamma_{k-1})$, where $l = 5$ km is the step length, θ_k is the orientation of the k^{th} step, and γ_{k-1} is the goal direction at the $k-1^{th}$ location). The inset shows the ground-related path in the geographic frame of reference. It can be clearly seen that this magnetically treated turtle was quite efficient in moving in the home direction during the first part of its homing path: to come within 13 km of home, she swan only 305 km (61 5-km steps) for a move of 239 km in the goal direction (navigational efficiency: 0.78).
doi:10.1371/journal.pone.0026672.g003

confusion of the large scale non-magnetic process, based upon predictable magnetic gradient fields around the nesting area, whose characteristics are learnt (and updated) during successive visits; 3. A third, small scale, pinpointing process based on non-magnetic cues (presumably wind borne and/or visual cues; [4]), to be used when approaching the circle of confusion of the magnetic process. By acting at the intermediate scale, the magnetic process would play a key role in green turtles by bridging the gap between large scale and small scale, both non-magnetic, navigational processes. This scenario is based on results obtained on relatively small samples (for logistical reasons, it is always hard to work with large samples in this kind of experiment). Further experiments will therefore be necessary to confirm our results. In particular, it is quite possible that the absence of significant difference during the final homing phase between turtles exposed to a strong magnetic field before displacement and controls derived from the low statistical power inherent to small samples. We could not exclude that the significant difference during the final homing phase between controls and turtles equipped with a weak magnet during the whole homing phase was due to the behavior of some particularly unlucky individual belonging to the magnetic group. This seems however unlikely because most turtles in this magnetic group did appear to be disturbed during the final homing phase, only a few ones appearing lucky enough to quickly reach their home. Furthermore, despite the smallness of the samples, the navigational efficiencies of the three groups during the central (i.e. pelagic) phase are sufficiently consistent within and across groups to enable us to claim with confidence that a magnetic perturbation has no significant effect on the turtles' navigation behavior during this phase.

Materials and Methods

Subjects and experimental treatments

The experiment was performed in accordance with institutional and national (French) guidelines and regulations (Permit number 34-100, covering any behavioral experiment conducted on vertebrates in the wild, including the present one, attributed to the senior author and approved by Veterinary Services of the French Ministry of Agriculture).

A total of 24 female green turtles served as subjects. They were caught during the night at their nesting site on Grande Glorieuse (11.57°S, 47.29°E), a small, isolated island in the northern part of the Mozambique Channel. They were then kept on the beach in

Table 1. Turtles' homing performances.

Turtle	Homing duration	Homing length	Global efficiency	Initial phase	Central phase	Final phase
CO1	13 days	806 km	0.75	18	0.84	2032 km^2
CO2	6 days	447 km	0.72	12	0.80	810 km^2
CO3	16 days	1132 km	0.58	0	0.56	648 km^2
CO4	10 days	682 km	0.27	0	0.24	769 km^2
CO5	9 days	786 km	0.71	0	0.72	865 km^2
CO6	6 days	472 km	0.50	0	0.41	3335 km^2
mean±SE	**10±2**	**721±103**	**0.59±0.07**	**5.0±3.3**	**0.60±0.10**	**1410±438**
MB1	6 days	484 km	0.63	11	0.68	710 km^2
MB2	6 days	641 km	0.69	4	0.83	1289 km^2
MB3	15 days	806 km	0.67	6	0.76	2264 km^2
MB4[a]	*29 days*	*2122 km*	0.28	0	0.69	43241 km^2
MB5	6 days	593 km	0.29	52	0.97	598 km^2
MB6[b]	*29 days*	*1746 km*	0.36	21	0.76	14688 km^2
MB7	5 days	395 km	0.30	0	0.33	1033 km^2
mean±SE	**14±4**	**970±257**	**0.46±0.07**	**13.4±7.0**	**0.72±0.07**	**9118±6001**
MH1	6 days	368 km	0.80	3	0.78	841 km^2
MH2[c]	*54 days*	*3646 km*	0.47	15	0.58	37399 km^2
MH3	31 days	1870 km	0.55	0	0.80	77896 km^2
MH4	23 days	1255 km	0.31	40	0.71	4563 km^2
MH5[d]	*18 days*	*1265 km*	0.17	0	0.80	18783 km^2
MH6	9 days	643 km	0.29	7	0.23	867 km^2
MH7	6 days	463 km	0.42	0	0.44	911 km^2
mean±SE	**21±7**	**1359±431**	**0.43±0.08**	**9.3±5.5**	**0.62±0.08**	**20180±10902**

[a]came only within 23 km of home in 60 hours; path stopped at 203 km of home (Madagascar).
[b]came only within 27 km of home in 14 days; path stopped at 256 km of home (Aldabra).
[c]came within 21 km of home in 44 days; path stopped at 112 km of home (battery exhausted).
[d]came only within 13 km of home in 4 days; path stopped at 227 km of home (Madagascar).
The global path and central phase efficiencies were estimated as the mean cosine of directional errors. The initial phase efficiency was estimated as the number of 5-km steps travelled (with respect to water masses) before the turtle considered definitely took the correct $\pm 90^\circ$ direction. The final phase efficiency was estimated as the mean of the squared distances between successive locations and home when the turtle came within 50 km of home. CO: control group; MB: magnetic treatment on the nesting beach, prior to displacement; MH: magnetic treatment during homing.
doi:10.1371/journal.pone.0026672.t001

wooden crates for 24 to 48 h. Crates were placed in the shade and turtles were regularly wetted with seawater during the day to minimize their stress. Six turtles, two of each group (see below), were displaced at the same time using an aluminum (amagnetic) boat. They were released in the open sea 190–200 km from their nesting site. Two north-western displacements were performed in May 2008 (release site coordinates: 10.19°S, 46.23°E) and two south-western displacements in June 2009 (release site coordinates: 12.79°S, 46.02°E). During the boat travel, which lasted around 24 h, the turtles were kept in covered wooden crates to prevent them from seeing the sky and to protect them from the sun. They were also regularly wetted with seawater.

In our study area, the total intensity of the geomagnetic field is about 34 μT, and it changes by about 1.8 nT/km along a WSW-ENE axis. The expected (i.e. without taking anomalies into account) difference between home and NW and SW release sites were 200 and 350 nT, respectively (www.ngdc.noaa.gov/geomagmodels/struts/calcIGRFWMM). Turtles were assigned to three groups of eight: two experimental groups – Magnetic Beach (MB) and Magnetic Homing (MH) – and a control group (CO, no treatment except displacement). Turtles belonging to the MH group were magnetically treated during the homing trip by putting a weak magnet above their heads just before release. We used a 5 mm long cylindrical magnet, with a very small magnetic moment ($m = 0.015$ A.m^2) that we placed horizontally 6.5 cm above the head using an aluminum inverse-T-shaped support. Given that the exact location of the biological magnetoreceptor is not known in turtles (as well as in any animal; [24]), increasing the distance between the magnet and the head enabled us to minimize the variations of the total intensity of the artificial magnetic field induced across the brain (Fig. 5). The total intensity of the resultant magnetic field (vectorial sum of the geomagnetic field and the magnetic field induced by the weak magnet) experienced by MH turtles in any part of their brain thus remained within the range of the geomagnetic field, but corresponded to intensities experienced at locations several hundreds of kilometers away from the actual location. Turtles belonging to the MB group were magnetically treated by gluing a very strong magnet ($m = 1.2$ A.m^2) to the top of the head, but only while they stayed in wooden crates on the beach. These strong magnets, identical to those used in previous experiments [5,13], generated a magnetic field larger than 500 μT across the whole brain. They were removed as soon as the boat left Grande Glorieuse (treatment time: 24–48 h).

Because the possible impairment due to wearing a very strong magnet at the nesting site before displacement and to wearing a

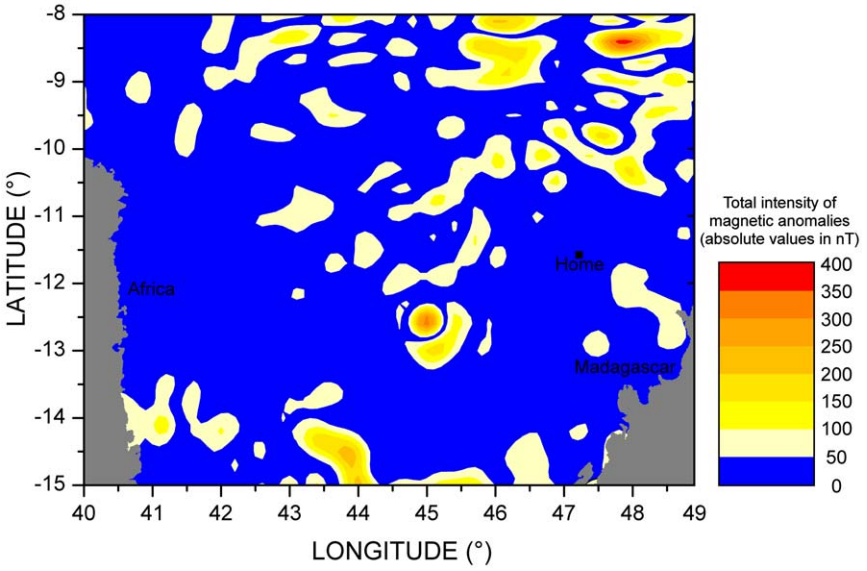

Figure 4. Map of geomagnetic anomalies around Glorieuses Islands (Home). This map has been constructed as the absolute value of the difference in the total intensity between Enhanced Magnetic Model 2010 and World Magnetic Model 2010 (see www.ngdc.noaa.gov/geomag/). The former is a complete representation of the real magnetic field up to a spherical harmonic degree n = 720 (minimum wavelength L = 40000/n = 56 km, corresponding to a spatial accuracy of 28 km). The latter corresponds to the main (outer core) field model. The difference between the two models is a good representation of the crustal magnetic field.
doi:10.1371/journal.pone.0026672.g004

weak magnet during the homing trip are likely to be qualitatively different, we thought that the quantitative comparison of the homing performances of MB and MH groups was not meaningful. We therefore considered that we performed a two-in-one experiment, with a common control group, rather than a single three- group experiment. Statistical comparisons of the turtles' navigation performances were therefore performed between CO and MB turtles on one hand, and between CO and MH turtles on

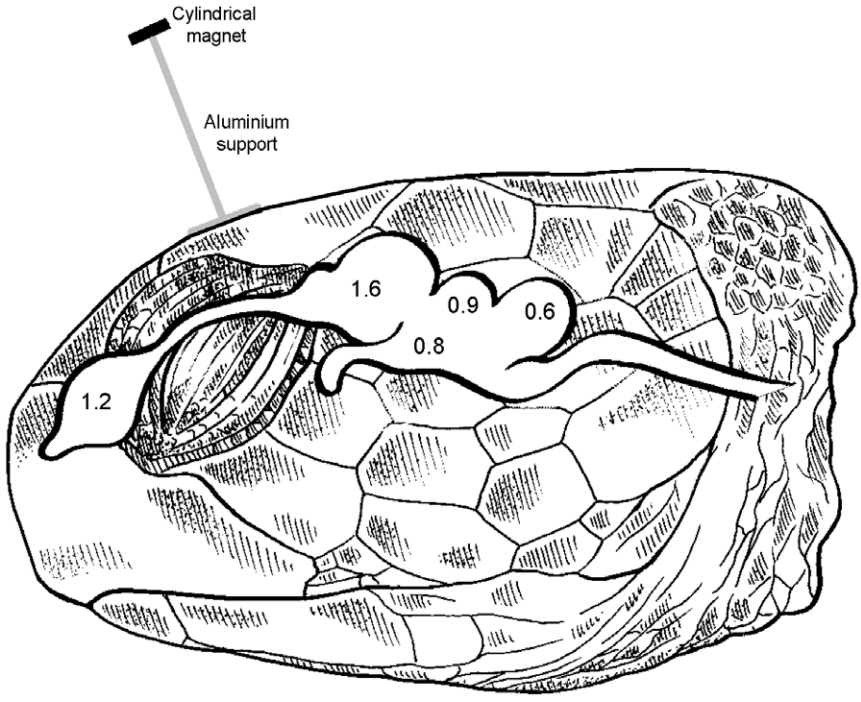

Figure 5. Intensity *B* of the magnetic field, expressed in μT, induced in various parts of a green turtle's brain by a cylindrical magnet placed horizontally 6.5 cm above the head. The values were computed as $B = 0.1\ m\ (3\cos^2(\delta)+1)^{0.5}/d^3$ where $m = 0.015$ A.m^2 is the magnetic moment of the cylindrical magnet, d is the distance from the magnet expressed in meters, and δ is the angular deviation from the cylinder axis (colatitude). The drawing of the turtle's head and brain was adapted from Fig. 172 in [25].
doi:10.1371/journal.pone.0026672.g005

the other hand, using exact permutation tests, which are the most powerful tests that can be performed when sample sizes are small.

Movement recordings and oceanic current corrections

The turtles' movements were recorded with MK10 Argos-linked GPS loggers (Wildlife Computers, Seattle WA). These devices can acquire GPS locations through 'Fastloc^{TM,} technology during turtle surfacings, store them in an onboard memory and transmit them to the Argos system satellites. The GPS locations were programmed to be acquired every 20 min, but only a fraction of the programmed locations was eventually acquired and stored, and only a fraction of the stored locations could be transmitted (probably because of the low bandwidth and intermittent satellite coverage of the Argos system). We eventually obtained about one GPS location per hour, which allowed us to reconstruct the homing journeys with fair accuracy.

Green turtles' oceanic movements take place in the upper layers of the water column (10–20 m depth; [26]) and so are affected by surface currents. The recorded homing movements therefore corresponded to the vectorial sum of the turtles' own 'motor' movements within the water masses and the action of surface currents. In the Mozambique Channel, oceanic currents are far from being negligible: their speed can be of the same order of magnitude as of a turtle's speed within the water masses. Thus, a turtle may even actually move away from home while it is swimming homewards. As we showed in two previous studies [5,12], green turtles are not able to compensate for the current drift, although they are able to correct it: they are indeed able to continuously update the home direction after displacement due to current drift (as well as after the passive displacement by boat), but are unable to adopt a voluntary biased heading to anticipate the current drift. To reliably estimate the turtles' navigational efficiency, we therefore estimated their motor (current-corrected) movements, which better represent the turtles' orientation behavior than the recorded, ground-related movements.

Surface current velocity fields were computed as the vectorial sum of geostrophic and Ekman components [27]. The geostrophic component results from the balance between the horizontal pressure gradient force and the Coriolis force. It was computed as the vectorial sum of the mean geostrophic surface currents, calculated from the mean dynamic topography, and the currents due to geostrophic anomalies, derived from the Ssalto/Duacs gridded altimetric Sea Level Anomaly data available weekly on a $1/3^\circ$ grid (www.jason.oceanobs.com). Note that the geostrophic component was computed using an updated model, based on a new assessment of the mean dynamic topography [28]. The Ekman component results from the balance between friction by wind and the Coriolis force. It was estimated from daily wind stress data provided by Quikscat scatterometry on a $1/2^\circ$ grid (www.ifremer.fr/cersat). Both components underwent a bi-linear spatial interpolation so as to get $1/4^\circ$ velocity fields, and then the geostrophic component underwent a temporal third-order Lagrange polynomials interpolation [29] to obtain both geostrophic and Ekman fields on a daily basis. The two fields were then vectorially summed up to obtain the global surface velocity field at $1/4^\circ$ on a daily basis. The oceanic current velocity occurring at each turtle location was then estimated through spatial and temporal interpolation from the daily global maps. By applying it to Argos-tracked drifting buoys (whose movements were only due to currents), this method was shown to provide reliable estimates of mesoscale current velocities [27], except for coastal locations. Daily surface current velocity maps at $1/4^\circ$ resolution, as well as a user-friendly program making it possible to easily compute the oceanic current velocities at specified locations worldwide, can be downloaded from www.legos.obs-mip.fr/contacts/page-perso-equipe-dynbio/joel-sudre. The oceanic current velocity occurring at any turtle's location was then subtracted from the turtle ground velocity at this location to obtain the turtle motor velocity (see [12] for details).

As the spatial resolution of the current velocity field estimations are limited to 0.25° in both latitude and longitude (about 28 km), only mesoscale oceanic currents can be estimated, thus leaving out submesoscale currents. These smaller scale structures usually occur in the form of filaments or eddies with radii of a few kilometers lasting a few days. They may be very dynamic, involving locally strong currents, but are unpredictably distributed in both space and time [30]. Even if these submesoscale currents cannot yet be properly estimated, it is nevertheless possible to identify them by using Sea Surface Temperature (SST, obtained in the infra-red light spectrum) and Chlorophyll A (ChA, obtained in the visible light spectrum) daily data from MODIS-Aqua aboard EOS-PM satellite (http://modis.gsfc.nasa.gov/). To this aim, we built up ChA- and SST-based singular exponents maps, which provide a clear view of local turbulent motion [31,32], using Yahia and Turiel's "FluidExponents"® software [33]. Because parts of the homing paths possibly disturbed by these submesoscale currents could not be properly corrected, they were removed from analysis (see an example in Fig. 6).

Homing path analyses

Motor paths were rediscrestized with a 5-km step length and represented in a home-based frame of reference, with the X axis corresponding to the home direction (see [12] for details). Changes in abscissa ($\Delta X = 5*\cos(\theta-\gamma)$, where θ and γ stand for the local movement and the home directions, respectively), thus directly correspond to the homeward component, i.e. the extent to which a turtle moves towards (positive value) or away from (negative value) home at each step. For convenience, the release point coordinates were set to $X_0 = 0$ and $Y_0 = 0$. The homing paths of the 20 turtles that showed a strong motivation to home were first analyzed globally. For this purpose, we computed the homing efficiency of each turtle as the mean cosine of directional errors ($\theta-\gamma$), which is equivalent to the straightness index (the ratio beeline distance/path length travelled; [34]).

Afterwards, we split the homing paths in three phases – initial, central and final – to perform separate analyses for each of them. The initial phase was defined as the phase starting at the release site and ending when the X coordinate of the motor path (i.e. the motor homeward component) became definitively positive. For turtles that initially and consistently swam in a correct direction (home direction $\pm 90^\circ$) the X coordinate was always positive, and the initial phase was therefore reduced to zero. For turtles that initially swam in a wrong direction (opposite home direction $\pm 90^\circ$) for a while before taking the correct one, the X coordinate of the motor was first more and more negative, but started to become less and less negative as soon as the turtle took a correct direction and finally became definitively positive. Some other turtles, however, tended to perform loops around the release point, as other displaced animals often do (e.g. [35]). In this case, the X coordinate of the motor path was alternatively positive and negative until the turtle stopped its looping behavior and started to home. Because of this potential looping behavior, the first occurrence of a positive X value does not necessarily indicate the end of the initial phase, which can be estimated to end when the X value became definitively positive. The final phase was defined as the phase starting when a turtle came for the first time within 50 km of home and ending when it entered the lagoon surrounding the home island (to filter out the very final,

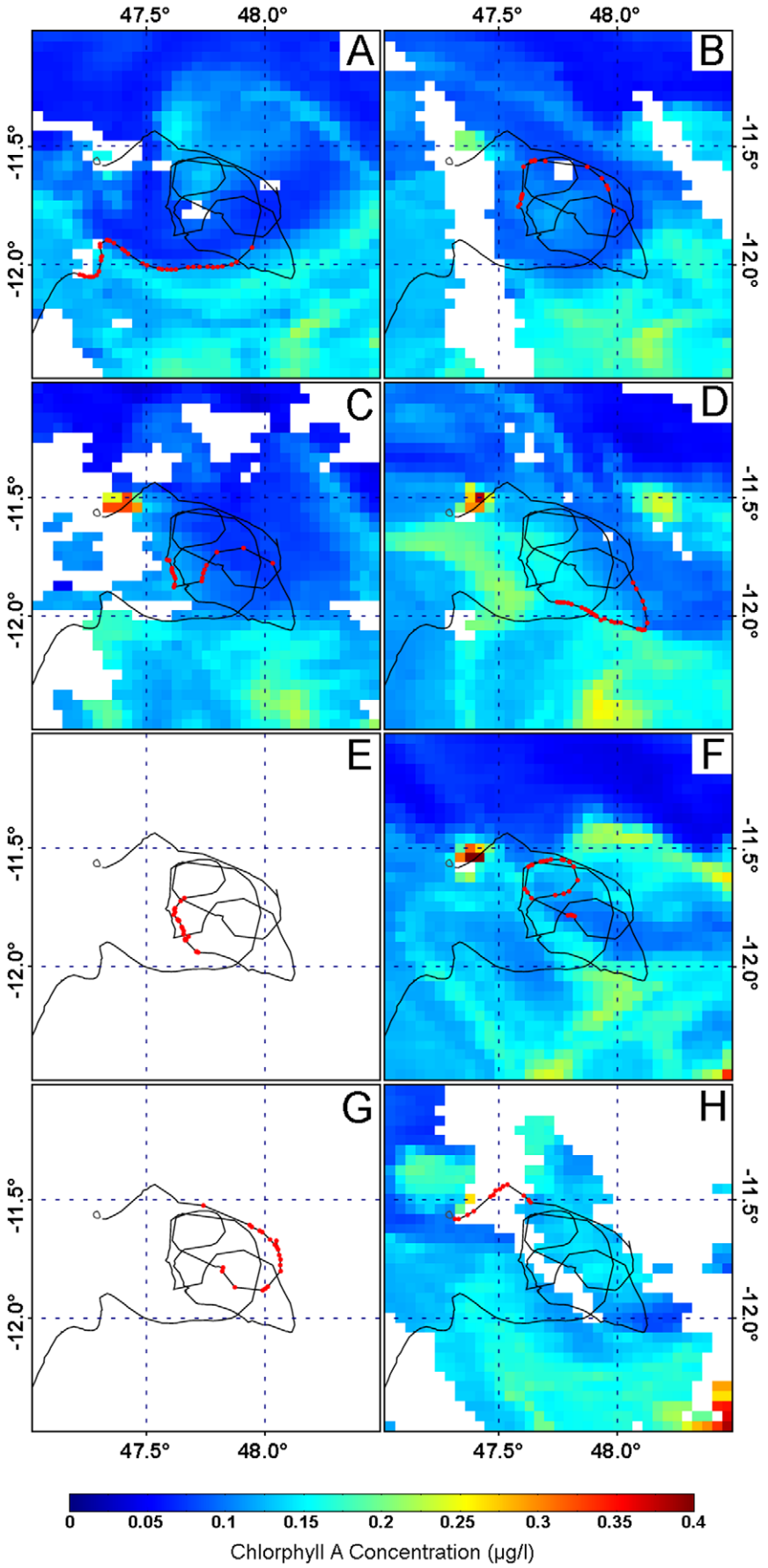
47.5°
48.0°
A
B
C
D
E
F
G
H
-11.5°
-12.0°
0
0.05
0.1
0.15
0.2
0.25
0.3
0.35
0.4
Chlorphyll A Concentration (µg/l)

Figure 6. Daily maps of Chlorophyll A (ChA) concentration provided by MODIS-Aqua along with the last part of the homing path of turtle CO5, from 04 to 11 June 2009. The red dots represent the turtle' GPS locations recorded the same day as the map, and therefore illustrate the homing movements possibly impacted by submesoscale activity. ChA concentration is considered as a passive tracer advected by the ocean dynamics. Coherent meso- and submeso-scale structures are clearly observed in this temporal image sequence and the high ChA concentration represents the borders of these oceanographic structures. In these areas the norm of the current motion field is higher. White pixels represent areas where ChA concentration cannot be measured due to the cloud cover. Panel A: the path was following the external active border of a dipole mesoscale structure, composed of two eddies (not detectable as sea level anomalies because of theirs small sizes): the anticyclonic part is centered at 11.5°S–47.8°E and the cyclonic one at 11.7°S–47.4°E. Panel B: the dipole structure moved to south-east. The turtle was advected by the cyclonic eddy of the dipole. The displacement of the turtle followed the internal border of the cyclonic eddy. Panel C: the turtle reached the cyclonic structure to enter in a complex ocean dynamics configuration created by ejection of numerous energetic filaments by the principal dipole structure described in panel A. Panel D: ChA concentration increased and the different ejection filaments can be clearly represented. Panel E: no data available because of cloud cover. Panel F: the turtle turned around a submesoscale structure but the mixing of ChA is too high and gradient too low to have a clear detection of this submesoscale structure. Panels G & H: no ChA data available for the turtle's locations because of cloud cover.
doi:10.1371/journal.pone.0026672.g006

pinpointing stage of the homing journey, assumed to involve a fully different navigation process that operates only at small spatial scale) or abandoned homing. We acknowledge that this 50 km threshold is somewhat arbitrary. Given the results of our previous studies [5,10–13], a radius of a few dozens of kilometers seems to be a suitable choice for looking at a navigation process working at medium scale. Globally similar results were obtained with other radii within the same order of magnitude, suggesting that this order of magnitude corresponds to the circle of confusion of the pelagic navigation mechanism. The central phase, which corresponds to the main pelagic phase, was defined simply as the intermediate phase occurring between the initial and final phases.

Each of these three phases required to be analyzed in a specific way. Animal movements are indeed best considered as biased correlated random walks, whose shape is determined by three main factors: goal attractiveness (directional bias), movement persistence (directional correlation, i.e. the tendency to keep the current moving direction for a while) and randomness degree [36,37]. A strong movement persistence is extremely useful in enabling an animal to navigate quite efficiently even when it has to rely on noisy gradient fields [38], but can in turn be somewhat costly during the initial or final phase of a homing path. During the initial phase (at the release site and soon afterwards), an animal may start to move in a direction that does not lead towards home. As movement persistence and goal attractiveness will work against each other in this case, their interplay will generate a loop which can be quite large, depending on the relative weights of the two factors. A similar situation may occur during the final homing phase: the interplay between the two factors will lead the animal to perform a loop each time it misses the goal [39]. In contrast, during the central phase, goal attractiveness and movement persistence tend to work in synergy as the animal tends to head towards the goal at this stage. The mean cosine of directional errors is the best means to measure the navigational efficiency in this case [34]. In contrast, this parameter is an inappropriate estimator of navigational efficiency when movement persistence and goal attractiveness work in opposite ways because, in this case, they are likely to generate movement loops and the mean cosine of directional errors tends to be close to zero regardless the number and the sizes of the loops. Consequently, the mean cosine of directional errors was used to estimate the navigational efficiency of the turtles during the central phase, but other estimators had to be used to assess the performances of turtles during the initial and final phases of their trips.

The performances during the initial phase were simply estimated as the number of 5-km steps involved. The larger the step number (i.e. the path length) was, the greater difficulties a turtle experienced to quickly take the correct home direction after release. To estimate the difficulty of turtles to localize their nesting site during the final phase of their homing movement, we computed the mean square distance between turtles' successive locations and the goal location once they came within 50 km of home. This method provides reliable results in standard cases (e.g. [40]) but applying it directly to an animal that may have been drifted by currents may introduce some biases, as changes in distance can be due to the currents as well as to the turtle's own moving behavior. Potentially, this may have led to a lowering of statistical power through an increase of variance of the distribution of squared distances. To overcome this problem, we computed the mean squared distance based on serially equidistant (5 km) turtle locations along the motor paths instead of the ground-related paths. This approach is not perfect, but we could not identify a more sensible means to assess turtle performances in this particular case.

Acknowledgments

We warmly thank M. Baret, R. Bochard, M. Dalleau, G. Janeau, H. Sauvignet and V. Séguinot, as well as the FAZOI and the Gendarmerie Nationale, for their invaluable help in the field. Authorization to work on Grande Glorieuse was kindly provided by the TAAF administration. We also thank S. Benvenuti and S. Galli for useful discussions and help. A. Nesterova kindly improved the English. G. Hays and an anonymous referee provided useful comments on a previous version of the paper.

Author Contributions

Conceived and designed the experiments: SB PL. Performed the experiments: SB PL JB SC. Analyzed the data: SB JS. Contributed reagents/materials/analysis tools: SB JS ADS. Wrote the paper: SB PL.

References

1. Wiltschko R, Wiltschko W (2006) Magnetoreception. Bioessay 28: 157–168.
2. Benhamou S, Bonadonna F, Jouventin P (2003) Successful homing of magnet-carrying white-chinned petrels released in the open sea. Animal Behaviour 65: 729–734.
3. Bonadonna F, Bajzak C, Benhamou S, Igloi K, Jouventin P, et al. (2005) Orientation in the wandering albatross: interfering with magnetic perception does not affect orientation performance. Proceedings of the Royal Society B: Biological Sciences 272: 489–495.
4. Lohmann KJ, Luschi P, Hays GC (2008) Goal navigation and island-finding in sea turtles. Journal of Experimental Marine Biology and Ecology 356: 83–95.
5. Luschi P, Benhamou S, Girard C, Ciccione S, Roos D, et al. (2007) Marine turtles use geomagnetic cues during open-sea homing. Current Biology 17: 126–133.
6. Bingman VP, Chen K (2005) Mechanisms of animal global navigation: comparative perspectives and enduring challenges. Ethology Ecology & Evolution 17: 295–318.
7. Benhamou S (2010) Orientation and Navigation. In: Koob GF, LeMoal M, Thomson RF, eds. Encyclopedia of behavioral neurociences vol. 2. Oxford: Academic Press. pp 497–503.
8. Kendall DG (1974) Pole-seeking brownian motion and bird navigation. Journal of the Royal Statistical Society B 36: 365–417.

9. Mills Flemming J, Field CA, James MC, Jonsen ID, Myers RA (2006) How well can animals navigate? Estimating the circle of confusion from tracking data. Environmetrics 17: 351–362.
10. Luschi P, Åkesson S, Broderick AC, Glen F, Godley BJ, et al. (2001) Testing the navigational abilities of oceanic migrants: displacement experiments on green sea turtles (Chelonia mydas). Behavioural Ecology and Sociobiology 50: 528–534.
11. Hays GC, Åkesson S, Broderick AC, Glen F, Godley BJ, et al. (2003) Island finding ability of marine turtles. Proceedigs of the Royal Society of London. Biological Science 270(Suppl. 1): 5–7.
12. Girard C, Sudre J, Benhamou S, Roos D, Luschi P (2006) Homing in green turtles (*Chelonia mydas*): oceanic currents act as a constraint rather than as an information source. Marine Ecology Progress Series 322: 281–289.
13. Papi F, Luschi P, Åkesson S, Capogrossi S, Hays GC (2000) Open-sea migration of magnetically disturbed sea turtles. Journal of Experimental Biology 203: 3435–3443.
14. Maus S, Sazonova T, Hemant K, Fairhead JD, Ravat D (2007) National Geophysical Data Center candidate for the World Digital Magnetic Anomaly Map. Geochemistry Geophysisc Geosystems 8(6) Q06017: 1–10.
15. Thébault E, Purucker M, Whaler KA, Langlais B, Sabaka TJ (2010) The Magnetic Field of the Earth's Lithosphere. Space Science Review 155: 95–127.
16. Wallraff HG (2004) Avian olfactory navigation: its empirical foundation and conceptual state. Animal Behaviour 67: 189–204.
17. Benhamou S (2003) Bicoordinate navigation based on non-orthogonal gradient fields. Journal of Theoretical Biology 225: 235–239.
18. Meylan A, Bowen B, Avise JC (1990) A genetic test of the natal homing versus social facilitation models for green turtle migration. Science 248: 724–727.
19. Norman JA, Moritz C, Limpus C (1994) Mitochondrial DNA control region polymorphisms: genetic markers for ecological studies of marine turtles. Molecular Ecology 3: 363–373.
20. Bowen BW, Avise JC (1996) Conservation genetics of marine turtles. In Avise JC, Hamrick JL, eds. Conservation genetics – case histories from nature. New York: Chapman & Hall. pp 190–237.
21. Lohmann KJ, Putman NF, Lohmann CM (2008) Geomagnetic imprinting: A unifying hypothesis of long-distance natal homing in salmon and sea turtles. Proceedings of the National Academy of Sciences 105: 19096–19101.
22. Bourjea J, Frappier J, Quillard M, Ciccione S, Roos D, et al. (2007) Mayotte Island: another important green turtle nesting site in the southwest Indian Ocean. Endangered Species Research 3: 273–282.
23. Hays GC, Fossette S, Katselidis KA, Schofield G, Gravenor MB (2010) Breeding periodicity for male sea turtles, operational sex ratios, and implications in the face of climate change. Conservation Biology 24: 1636–1643.
24. Johnsen S, Lohmann K (2008) Magnetorecption in animals. Physics Today 61(3): 29–35.
25. Wyneken J, Witherington D (2001) The anatomy of sea turtles. U.S. Department of Commerce, NOAA Technical Memorandum NMFS-SEFSC-470. 172 p.
26. Hays GC, Åkesson S, Broderick AC, Glen F, Godley BJ, et al. (2001) The diving behaviour of green turtles undertaking oceanic migration to and from Ascension Island: dive durations, dive profiles and depth distribution. Journal of Experimental Biology 204: 4093–4098.
27. Sudre J, Morrow R (2008) Global surface currents: a high-resolution product for investigating ocean dynamics. Ocean Dynamics 58: 101–118.
28. Rio M-H, Guinehut S, Larnicol G (2011) New CNES-CLS09 global mean dynamic topography computed from the combination of data, altimetry, and in situ measurements. Journal of Geophysical Research 116: C07018.
29. Mancho AM, Small D, Wiggins S (2006) A comparison of methods for interpolating chaotic flows from discrete velocity data. Computers & Fluids 35: 416–428.
30. Thomas LN, Tandon A, Mahadevan A (2008) Submesoscale processes and dynamics. In Hecht MW, Hasumi H, eds. Ocean modeling in an eddying regime. Geophysical Monograph Series 177. Washington DC: American Geophysical Union. pp 17–38.
31. Turiel A, Mato G, Parga N, Nadal J-P (1998) The self-similarity properties of natural images resemble those of turbulent flows. Physical Review Letters 80: 1098–1101.
32. Yahia H, Sudre J, Pottier C, Garçon V (2010) Motion analysis in oceanographic satellite images using multiscale methods and the energy cascade. Pattern Recognition 43: 3591–3604.
33. Turiel A, Yahia H, Pérez-Vicente C (2008) Microcanonical multifractal formalism: a geometrical approach to multifractal systems. Part I: singularity analysis. Journal of Physics A 41: 015501.
34. Benhamou S (2004) How to reliably estimate the tortuosity of an animal's path: straightness, sinuosity, or fractal dimension? Journal of Theoretical Biology 229: 209–220.
35. Benhamou S, Bried J, Bonadonna F, Jouventin P (2003) Homing in pelagic birds: a pilot experiment with white-chinned petrels released in the open sea. Behavioural Processes 61: 95–100.
36. Benhamou S (2006) Detecting an orientation component in animal paths when the preferred direction is individual-dependent. Ecology 87: 518–528.
37. Codling EA, Plank MJ, Benhamou S (2008) Random walk models in biology. Journal of the Royal Society Interface 5: 813–834.
38. Benhamou S, Bovet P (1992) Distinguishing between elementary orientation mechanisms by means of path analysis. Animal Behaviour 43: 371–377.
39. Benhamou S (1994) Spatial memory and searching efficiency. Animal Behaviour 47: 1423–1433.
40. Benhamou S (1996) No evidence for cognitive mapping in rats. Animal Behaviour 52: 201–11.

4.6 Conclusions

Au cours de ce chapitre, nous nous sommes intéressés à l'apport de la dynamique océanique à l'étude de différents maillons de la chaîne trophique. Pour cela, nous avons rappelé les principes fondamentaux de la triade de Bakun qui relie les processus physiques issus de la dynamique océanique aux processus biogéochimiques qui définissent les zones d'enrichissement en sels nutritifs, la rétention par les structures cohérentes de ces zones privilégiées où la vie marine se concentre.
L'utilisation combinée de la dynamique océanique obtenue par le traitement de données multi-capteurs et des méthodes de diagnostics Lagrangiens, nous a permis de mettre en évidence la complexité inhérente de l'écoulement océanique turbulent. Par l'analyse de diagnostics Lagrangiens, nous avons montré que les vents jouent un rôle important dans la convection verticale au sein même des structures cohérentes. La prise en compte des courants d'Ekman va entrainer des enrichissements en sels nutritifs possibles du centre des tourbillons en océan ouvert.
Ensuite nous nous sommes interessés aux zones d'upwelling qui sont des zones où les vents jouent un rôle clef, via la friction à la surface de l'océan. Nous avons montré que l'activité turbulente n'a pas le même comportement dans ces zones. L'augmentation de son activité va avoir tendance à inhiber le développement phytoplanctonique par une dynamique verticale trop intense et va contrecarrer la dynamique propre du pompage d'Ekman.

Dans les parties consacrées au Canal du Mozambique, nous nous sommes intéressés aux prédateurs marins supérieurs. L'analyse des déplacements des frégates montre une étroite relation entre la position des structures à submésoéchelle et la répartition des frégates en recherche alimentaire. Les frégates sont capables de trouver et d'exploiter les structures éphémères que sont les filaments et les structures à submésoéchelle en bordure de tourbillons à mésoéchelle. Cet exemple montre que la dynamique océanique à toutes les échelles de résolution gouverne la stratégie d'alimentation des prédateurs marins supérieurs.
Les tortues marines sont des espèces en péril, il est primordial actuellement de comprendre leur comportement de navigation, ne serait-ce que pour éviter leurs pêches accidentelles. Le Canal du Mozambique fournit un terrain d'étude idéal pour analyser leurs comportements. Plusieurs expériences de retour au

gîte ont été utilisées au cours de nos travaux. La mise en place d'une nouvelle méthode d'analyse permettant de prendre en compte la dynamique océanique, a permis de prouver que les tortues marines n'ont pas connaissance du déplacement de la masse d'eau qui les environne, qu'elles sont advectées par les courants océaniques à toutes les échelles et qu'elles corrigent leurs positions *a posteriori*. Enfin, nous avons confirmé que les tortues marines utilisent le géomagnétisme pour s'orienter mais que cette méthode d'orientation n'est pas essentielle pour elles et qu'elles vont la privilégier uniquement à l'approche des côtes.
Il est important de noter que *Benhamou et al.* [2011] n'ont pas pu analyser certains tronçons de trajets de tortues évoluant dans des structures à submésoéchelle. Les courants GEKCO utilisés dans cette étude n'ont pas permis de calculer le trajet moteur provenant de ces tronçons car les structures à submésoéchelle ne sont pas présentes dans ce produit. Cependant les structures à submésoéchelle ont pu être détectés au moyen de données de TSM et de chlorophylle *a*. Ceci montre la nécessité d'avoir des courants à submésoéchelle permettant d'analyser ce type de tronçon.

Ces différentes études ont permis de montrer que la dynamique océanique turbulente à méso et submésoéchelle joue un rôle crucial pour l'activité phytoplanctonique présente dans la couche de surface et pour la mise en place de la chaîne trophique jusqu'aux déplacements des prédateurs marins supérieurs.

Conclusions et perspectives

Conclusions et perspectives générales

Conclusions générales

Comme nous l'avons vu en filigrane au cours de cette thèse, la découverte et la compréhension de certains processus qui régissent l'océan, l'une des enveloppes fluides qui gouvernent notre système terre, n'a pu se faire que grâce à la pluridisciplinarité scientifique.
La dynamique de cet océan en régime de turbulence pleinement développée a pu être représentée au moyen de différentes méthodes d'obtention permettant sa description à méso et submésoéchelle via l'utilisation de données satellitaires. L'objectif de cette thèse, centrée en océanographie physique et qui utilise des techniques avancées en systèmes complexes et traitement non-linéaire du signal, a été de résoudre l'épineux problème de la génération de nouveaux produits de dynamique océanique à différentes échelles de résolution et d'utiliser cette dynamique afin d'évaluer son impact sur le monde marin du vivant.

Dans un premier temps, nous avons étudié l'équilibre géostrophique et hydrostatique pour déterminer les courants géostrophiques au moyen de l'altimétrie. Les équations classiques de la géostrophie ne permettant pas de déterminer ces courants au niveau de la singularité équatoriale (force de Coriolis nulle à l'équateur), nous avons développé deux méthodes pour obtenir la dynamique océanique dans la zone équatoriale. Une part non négligeable au premier ordre de la variabilité de la dynamique océanique de surface provient des processus agéostrophiques, en particulier ceux provenant de la friction du vent à la surface de l'océan. Pour tenir compte de ce processus,

nous avons introduit un second type de courant : les courants d'Ekman. Ces courants ont été calculés à partir de la tension du vent provenant de capteurs diffusiométriques. La principale difficulté de cette approche réside dans la détermination de la profondeur de la couche d'Ekman et celle du coefficient de traînée associé. Ces paramètres ont pu être déterminés spatio-temporellement par l'utilisation conjointe des vitesses géostrophiques, de la tension du vent et de bouées Lagrangiennes de surface. Le produit final, nommé GEKCO, combine les courants géostrophiques et les courants d'Ekman et a été validé par différentes données *in situ*. Ce produit est global, journalier, au quart de degré et permet l'étude de la dynamique océanique à mésoéchelle sur la période allant de 1992 à aujourd'hui. Il est actuellement distribué à l'ensemble de la communauté scientifique.

Cependant la dynamique océanique étant un écoulement en régime de turbulence pleinement développée implique que la dynamique mésoéchelle étudiée précédemment ne permet pas de décrire de nombreux processus à submésoéchelle. Cette activité submésoéchelle peut-être observée au moyen de capteurs délivrant des informations sur la couche de surface océanique à super-résolution comme la TSM ou la couleur de l'eau. Cependant, ces données permettent uniquement d'avoir une image qui représente la dynamique océanique. Pour avoir accès au champ complet de l'écoulement, il est nécessaire de faire appel à des méthodes de traitement non-linéaire du signal. Notre méthode fait appel à la "Science de la Complexité" qui consiste à déterminer quantitativement les paramètres permettant de rendre compte de l'organisation complexe issue de la turbulence pleinement développée. Notre méthode permet à partir du champ de vitesse à basse résolution et de l'information sur la position des fronts de transition d'une image de TSM collocalisée, d'obtenir un champ de vecteurs dense à super résolution. Ce produit de dynamique océanique à super-résolution a été généré sur quatre années de données dans la zone Sud-Ouest de l'Océan Indien et a été validé au moyen de bouées Lagrangiennes. La dynamique obtenue est représentative de la turbulence pleinement développée.

Dans une dernière partie, nos travaux se sont focalisés sur les relations entre les processus physiques, les processus biogéochimiques et les processus biologiques. Nous avons montré que les processus non-linéaires associés à la

dynamique océanique impactent fortement les premiers maillons de la chaîne trophique. L'activité turbulente associée à ces processus peut permettre, dans le cas de l'océan ouvert, la mise en place de ces premiers maillons dans la couche euphotique. Cette activité turbulente peut aussi, dans le cas des upwellings de bord Est, être un facteur inhibant de la production chlorophyllienne si elle est trop intense. Ces deux exemples montrent la complexité avec laquelle la circulation à submésoéchelle s'exprime et impacte les premiers maillons de la chaîne trophique. Nos travaux se sont ensuite intéressés à l'autre extrémité de cette chaîne en analysant le comportement de certains prédateurs marins supérieurs : la frégate et la tortue verte. Pour la frégate nous avons montré que sa stratégie de recherche alimentaire est basée sur la détection et le suivi de structures océaniques - en particulier les filaments et les structures à submésoéchelle en bordure de tourbillons à mésoéchelle -. Pour les tortues marines, des expériences de retour au gîte ont permis de mesurer quantitativement l'impact des courants océaniques de surface sur le trajet de tortues marines. Une méthode d'estimation du trajet moteur a été développée et a permis de montrer qu'il était inapproprié d'interpréter un trajet relatif au fond pour analyser le comportement d'orientation de ces animaux. Cette méthode a prouvé que l'action mécanique des courants était une contrainte aux déplacements des tortues et que les tortues ne compensent pas la dérive des courants. Enfin plusieurs expériences ont été effectuées avec des aimants positionnés sur la tête de certaines tortues afin de tester la capacité sensorielle géomagnétique de cette espèce. L'analyse des résultats nous a montré que le géomagnétisme n'est pas absolument nécessaire pour la navigation des tortues, et que celles-ci l'utilisent plus spécifiquement à l'approche des côtes du site à atteindre.

L'ensemble de ces études a révélé l'importance de prendre en compte la dynamique océanique et ses processus associés pour la compréhension du monde marin du vivant.

Perspectives

Comme nous l'avons vu dans le chapitre 2, la composante méridienne des courants GEKCO a une faible corrélation avec les données de courants *in situ*. Cette estimation imparfaite provient des ondes d'instabilité barotrope qui ne sont pas détectées par l'altimétrie. Les méthodes mises en place dans le chapitre 3 sont capables de capturer la dynamique océanique issue de ces

structures. Une perspective de nos travaux à court terme est d'intégrer au produit GEKCO dans la bande équatoriale la dynamique océanique provenant du produit à super-résolution en dégradant sa résolution par des méthodes linéaires simples. Ceci devrait permettre d'obtenir une composante méridienne plus réaliste.
Une autre perspective a court terme sur l'obtention des courants à mésoéchelle est d'améliorer la détermination des courants d'Ekman. L'estimation de ces courants nécessite d'avoir un calcul préalable des paramètres suivants : profondeur de la couche d'Ekman et coefficient de traînée. Dans la version actuelle des courants GEKCO, nous avons effectué une régression linéaire pour faire évoluer ces paramètres en fonction de la norme de la tension du vent. Cette régression linéaire est uniquement en fonction de la latitude et par bassin océanique. La dynamique atmosphérique n'étant pas identique pour l'ensemble d'un bassin, cette méthode n'est pas complètement satisfaisante. Il semble donc naturel d'envisager une nouvelle version du produit GEKCO prenant en compte la dynamique atmosphérique de manière locale.

Toujours à court terme et concernant cette fois-ci la dynamique océanique à submésoéchelle, nous allons générer des champs de vecteurs à super-résolution globaux sur toute la période disponible des données de TSM MODIS/Aqua afin d'analyser la dynamique océanique turbulente à super-résolution de manière globale pour mieux caractériser l'écoulement océanique. Des essais concluants ayant été obtenus en générant la dynamique océanique à partir des données de couleur de l'eau du capteur MODIS/Aqua, nous souhaitons aussi faire dans un proche avenir une comparaison de ces deux dynamiques océaniques pour en analyser les similitudes et les différences. Par cette analyse nous espérons obtenir des informations sur la dynamique propre de la biomasse phytoplanctonique.

Actuellement, l'altimétrie nadir qui fournit une donnée ponctuelle le long de traces au sol espacées de plusieurs dizaines ou centaines de km, restreint fortement l'étude des structures à submésoéchelle ainsi que leurs dynamiques propres. Il devient nécessaire de développer de nouveaux instruments capables de surmonter ces limitations. C'est le défi que propose de relever la mission Surface Water and Ocean Topography (SWOT) avec à son bord l'instrument Ka-band Radar INterferometer (KaRIN - radar interféromètre en bande Ka -).

L'objectif de la mission SWOT est de mesurer la hauteur d'eau des fleuves, lacs et zones inondées mais aussi celles des océans. L'interférométrie altimétrique va fournir une image bidimensionnelle avec une résolution horizontale de l'ordre de 50-100 m sur les eaux continentales et de l'ordre du kilomètre pour les surfaces océaniques avec une trace au sol de 120 km de large. Ce satellite, en phase de réalisation avec un lancement prévu en 2019, va permettre entre autres de caractériser la dynamique à submésoéchelle océanique. Nos travaux sont donc précurseurs dans ce domaine et permettent d'ores et déjà d'évaluer la complexité de cette dynamique océanique turbulente à super-résolution afin de se préparer à l'analyse de ce que fournira SWOT dans l'avenir. Ils permettront aussi de déterminer la dynamique océanique dans les zones spatio-temporelles non couvertes par ce satellite (zones inter-traces et entre les revisites du satellite), car cette dynamique nécessite de prendre en compte sa caractéristique turbulente. Ce sujet a fait l'objet d'un projet au CNES pour notre participation à "l'Ocean Surface Topography Science Team" qui a été accepté cette année : ICARODE.
Ce projet vise à poursuivre nos études sur la dynamique océanique à super résolution avec la formulation microcanonique de la cascade multiplicative. Un deuxième volet de ce projet est d'estimer la salinité à super-résolution. Par l'utilisation conjointe de cette salinité avec la TSM, il sera possible d'obtenir des cartes de surface de densité et d'alcalinité totale [*Lee et al.*, 2006]. L'augmentation de la concentration de CO_2 dans l'atmosphère et de son absorption par l'océan entraîne l'acidification de l'océan. La connaissance de son pH de surface est de ce fait cruciale. L'alcalinité totale permet de quantifier la capacité de l'eau de mer à neutraliser les acides et si on la combine avec une information de DIC ou de pCO_2, on peut alors en déduire une estimation du pH. Il sera donc possible par la connaissance du pH globale d'avoir une meilleure estimation de ce paramètre qui depuis l'ére industrielle est passé de 8.2 à 8.1 (ce qui représente une augmentation significative de l'acidité de l'océan de 30%).

La formulation microcanonique de la cascade multiplicative a ouvert un vaste champ d'applications en océanographie. Au cours du projet OCEANFLUX financé par le STSE (Support to Science Element) de l'ESA (European Space Agency), qui est mené depuis quelques mois, nous avons appliqué cette méthode pour obtenir les flux à l'interface océan-atmosphère des gaz à effet de serre à super-résolution au moyen de données satellitaires. Ces données sont

en cours de validation et pourraient permettre une estimation plus fine des zones de puits et de sources de CO_2 (par exemple) de l'océan. Cette étude est actuellement effectuée sur la zone de l'upwelling du Benguela et sur celle du Pérou/Chili.

L'intérêt de prendre en compte les courants à toutes les échelles pour analyser les trajets et comprendre le comportement des animaux marins a été démontré dans ce manuscrit. Il est nécessaire pour toutes études futures sur le comportement des prédateurs marins supérieurs d'avoir au préalable caractérisé son environnement pour comprendre son comportement (navigation, recherche alimentaire, etc.). L'océan étant turbulent, il nous semble obligatoire d'avoir une bonne estimation de la dynamique océanique pour répondre à ces questions. Nos recherches sur l'impact de la dynamique océanique sur le monde du vivant sont majoritairement issues de collaborations avec des écologues (travaux sur les frégates et les tortues). Actuellement, nos travaux sur le comportement de navigation des tortues marines se poursuit, et nous avons récemment eu l'opportunité de commencer une collaboration sur des trajets d'éléphants de mer. Ces derniers sont actuellement utilisés comme des "expérimentateurs océanographes" qui constituent des observatoires Lagrangiens en enregistrant au moyen de divers capteurs, installés sur des colliers placés sur ces animaux, des paramètres comme la température, la salinité, la fluorescence etc. Ce type d'expérimentation a un double rôle : le premier est d'utiliser ces animaux comme de véritables plateformes Lagrangiennes fournissant des données dans les milles premiers mètres et le second est de comprendre le comportement de navigation de cette espèce. Fort de ces premières expérimentations, dans un avenir plus lointain, il va être donc possible d'équiper d'autres espèces pour avoir une véritable flotte de "living argos" enregistrant des paramètres physiques et biologiques des masses d'eau.

Comme il a été constaté au cours de cette thèse, l'essor technologique toujours croissant de ces dernières décennies, combiné à la pluridisciplinarité scientifique, ont permis, permettent et permettront de nouveaux moyens d'observer et d'analyser l'océan. La robotique est actuellement une discipline en plein développement [*Grémillet*, 2012]. Ces robots initialement créés à des fins militaires commencent à être conçus pour des applications plus pacifiques. Ils permettent entre autres d'explorer des milieux hostiles (zones contaminées,

avec de fortes radiations nucléaires, à haut risque, etc.), lointains (planètes). Ils remplacent petit à petit les êtres humains pour des tâches industrielles fastidieuses et répétitives. Par leurs miniaturisations et la nano-technologie on commence même à les utiliser à des fins d'exploration et de traitement du corps humain.
La robotique touche donc de plus en plus de disciplines scientifiques et l'océanographie va connaître, par l'application de ce récent domaine de la science, une nouvelle ère de découvertes et de connaissances. Demain, il est évident que l'exploration de l'océan sera effectuée par des drones et des robots. Il sera possible d'accéder à des informations dans des zones où il est dangereux de s'aventurer comme par exemple les fronts orageux en mer, les zones sous la glace, etc. On peut déjà imaginer des campagnes à la mer où une plateforme opérationnelle à bord effectuera des lancements de drones et de robots (aériens et sous-marins) permettant d'échantillonner sur plusieurs kilomètres carrés tout l'environnement autour du navire. Actuellement il existe déjà des "gliders" utilisés en flottille qui effectuent des transits pour collecter plusieurs paramètres de la masse d'eau. On peut alors imaginer une flotte de drones, pilotés depuis la terre ferme, sillonnant nos côtes pour obtenir de façon permanente une surveillance de celles-ci, afin d'avoir une observation systématique de la dynamique particulière de ces zones, de suivre une nappe d'hydrocarbure due à un dégazage, ou pour secourir des naufragés en perdition. D'autres applications peuvent aussi être imaginées, comme de créer des robots ou des cyborgs se fondant dans un banc de poissons pour en étudier les déplacements et les comportements. Tous ces nouveaux défis sont dès aujourd'hui à notre portée, alors pour finir cette conclusion je ne dirai plus que quelques mots :

"Soyons pluridiscinaires, multidisciplinaires et inventons nos outils de demain".

Bibliographie

Adrian, R. J., Twenty years of particle image velocimetry, *Experiments in Fluids*, *39*(2), 159–169, doi :10.1007/s00348-005-0991-7, 2005. 149

Alvarez, L., J. Weickert, et J. Sánchez, Reliable estimation of dense optical flow fields with large displacements, *International Journal of Computer Vision*, *39*(1), 41–56, doi :10.1023/A:1008170101536, 2000. 150

Amara, R., Impact de l'anthropisation sur la biodiversité et le fonctionnement des écosystèmes marins. exemple de la manche-mer du nord., *VertigO - la revue électronique en sciences de l'environnement*, (Hors-série 8), doi : 10.4000/vertigo.10129, 2010. 11

Anding, D., et R. Kauth, Estimation of sea surface temperature from space, *Remote Sensing of Environment*, *1*(4), 217–220, doi :10.1016/S0034-4257(70) 80002-5, 1970. 53

Antoine, D., Apports de la télédétection spatiale de la "couleur de l'océan" à l'océanographie, *Océanis*, *24*(2), 81–150, 1998. 61

Arneodo, A., E. Bacry, et J. Muzy, The thermodynamics of fractals revisited with wavelets, *Physica A : Statistical Mechanics and its Applications*, *213*(1–2), 232–275, doi :10.1016/0378-4371(94)00163-N, 1995. 151, 156, 157

Arnéodo, A., F. Argoul, E. Bacry, J. Elezgaray, et J. F. Muzy, *Ondelettes, multifractales et turbulences : de l'ADN aux croissances cristallines*, Science en actes, Diderot Editeur Arts Sciences, Amsterdam, North Holland, 1995. 151

Attema, E. P., The active microwave instrument on-board the ERS-1 satellite, *Proceedings of the IEEE*, *79*(6), 791–799, doi :10.1109/5.90158, 1991. 42

Avens, L., J. Braun-McNeill, S. Epperly, et K. J. Lohmann, Site fidelity and homing behavior in juvenile loggerhead sea turtles (caretta caretta), *Marine Biology*, *143*(2), 211–220, doi :10.1007/s00227-003-1085-9, 2003. 239

Bakun, A., *Patterns in the ocean : ocean processes and marine population dynamics*, California Sea Grant College System, California Sea Grant College System, National Oceanic and Atmospheric Administration, in cooperation with Centro de Investigaciones Biologicas del Noroeste, 1996. 222

Bakun, A., Fronts and eddies as key structures in the habitat of marine fish larvae : opportunity, adaptive response and competitive advantage, *Scientia Marina*, *70*(2), 105–122, 2006. 222

Batchelor, G. K., Computation of the energy spectrum in homogeneous two-dimensional turbulence, *Physics of Fluids*, *12*(12), II–233, doi :10.1063/1.1692443, 1969. 152

Becker, M., B. Meyssignac, C. Letetrel, W. Llovel, A. Cazenave, et T. Delcroix, Sea level variations at tropical pacific islands since 1950, *Global and Planetary Change*, *80–81*, 85–98, doi :10.1016/j.gloplacha.2011.09.004, 2012. 11

Benhamou, S., J. Sudre, J. Bourjea, S. Ciccione, A. De Santis, et P. Luschi, The role of geomagnetic cues in green turtle open sea navigation, *PLoS ONE*, *6*(10), e26,672, doi :10.1371/journal.pone.0026672, 2011. 259

Bentamy, A., et D. C. Fillon, Gridded surface wind fields from Metop/ASCAT measurements, *International Journal of Remote Sensing*, *33*(6), 1729–1754, doi :10.1080/01431161.2011.600348, 2012. 45

Bentamy, A., P. Queffeulou, Y. Quilfen, et K. Katsaros, Ocean surface wind fields estimated from satellite active and passive microwave instruments, *Geoscience and Remote Sensing, IEEE Transactions on*, *37*(5), 2469–2486, doi :10.1109/36.789643, 1999. 44

Benzi, R., L. Biferale, G. Paladin, A. Vulpiani, et M. Vergassola, Multifractality in the statistics of the velocity gradients in turbulence, *Physical Review Letters*, *67*(17), 2299–2302, doi :10.1103/PhysRevLett.67.2299, 1991. 154

Bowen, B., et S. Karl, Population genetics, phylogeography, and molecular evolution, dans *The Biology of Sea Turtles*, CRC press ed., pp. 29 – 50, Lutz P.L. et Musick J.A., New York, 1997. 240

Boyen, C., C. Heip, P. M. Cury, P.-F. Baisnée, C. Brownlee, K. Tessmar-Raible, et al., EuroMarine research strategy report, *Rep. Tech. FP7-ENV-2010.2.2.1-3*, 2012. 12

Bradley, G. A., Remote sensing of ocean wind using a radar scatterometer, 1971. 39

Carr, A., New perspectives on the pelagic stage of sea turtle development, *Conservation Biology*, *1*(2), 103–121, doi :10.1111/j.1523-1739.1987.tb00020.x, 1987. 240

Chefd'Hotel, C., G. Hermosillo, et O. Faugeras, A variational approach to multimodal image matching, p. 21, IEEE Computer Society, 2001. 150

Chelton, D. B., M. G. Schlax, et R. M. Samelson, Summertime coupling between sea surface temperature and wind stress in the california current system, *Journal of Physical Oceanography*, *37*(3), 495–517, doi :10.1175/JPO3025.1, 2007. 238

Chelton, D. B., M. G. Schlax, et R. M. Samelson, Global observations of nonlinear mesoscale eddies, *Progress In Oceanography*, *91*(2), 167–216, doi :16/j.pocean.2011.01.002, 2011. 80

Cheney, R., L. Miller, R. Agreen, N. Doyle, et J. Lillibridge, TOPEX/POSEIDON : The 2-cm solution, *Journal of Geophysical Research*, *99*(C12), PP. 24,555–24,563, doi :199410.1029/94JC02050, 1994. 30

Chereskin, T. K., et D. Roemmich, A comparison of measured and wind-derived ekman transport at 11°n in the atlantic ocean, *Journal of Physical Oceanography*, *21*(6), 869–878, doi :10.1175/1520-0485(1991)021<0869:ACOMAW>2.0.CO;2, 1991. 86

Chereskin, T. K., W. D. Wilson, H. L. Bryden, A. Ffield, et J. Morrison, Observations of the ekman balance at 8°30' n in the arabian sea during the 1995 southwest monsoon, *Geophysical Research Letters*, *24*(21), PP. 2541–2544, doi :199710.1029/97GL01057, 1997. 86

Cheung, W. W. L., R. Watson, et D. Pauly, Signature of ocean warming in global fisheries catch, *Nature*, *497*(7449), 365–368, doi :10.1038/nature12156, 2013. 11

Cohen, I., et I. Herlin, Non uniform multiresolution method for optical flow and phase portrait models : Environmental applications, *Int. J. Comput. Vision*, *33*(1), 29–49, doi :10.1023/A:1008161130332, 1999. 150

Cottet, G.-H., et P. D. Koumoutsakos, *Vortex Methods : theory and practice*, Cambridge University Press, 2000. 150

Crocker, R., D. Matthews, W. Emery, et D. Baldwin, Computing coastal ocean surface currents from infrared and ocean color satellite imagery, *IEEE Transactions on Geoscience and Remote Sensing*, *45*(2), 435–447, doi :10.1109/TGRS.2006.883461, 2007. 149

Cuzol, A., et E. Mémin, Vortex and source particles for fluid motion estimation, dans *Computer Vision (Scale-Space'05)*, vol. 3459, pp. 254–266, Hofgeismar, Germany, 2005. 150

Cuzol, A., et E. Mémin, A stochastic filtering technique for fluid flow velocity fields tracking, *IEEE Transactions on Pattern Analysis and Machine Intelligence*, *31*(7), 1278–1293, doi :10.1109/TPAMI.2008.152, 2009. 150

Davis, R. E., L. A. Regier, J. Dufour, et D. C. Webb, The autonomous lagrangian circulation explorer (ALACE), *Journal of Atmospheric and Oceanic Technology*, *9*(3), 264–285, doi :10.1175/1520-0426(1992)009<0264:TALCE>2.0.CO;2, 1992. 74

Davis, R. E., J. T. Sherman, et J. Dufour, Profiling ALACEs and other advances in autonomous subsurface floats, *Journal of Atmospheric and Oceanic Technology*, *18*(6), 982–993, doi :10.1175/1520-0426(2001)018<0982:PAAOAI>2.0.CO;2, 2001. 74

Delgado Delgado, J. M., Filtro óptimo para imágenes naturales, aplicación al sistema visual, doctoral thesis, Universidad Autonoma de Madrid, Madrid, 2007. 161

Dickey, T., M. Lewis, et G. Chang, Optical oceanography : Recent advances and future directions using global remote sensing and in situ observations, *Reviews of Geophysics*, *44*(1), n/a–n/a, doi :10.1029/2003RG000148, 2006. xi, 147

Donlon, C. J., T. J. Nightingale, T. Sheasby, J. Turner, I. S. Robinson, et W. J. Emergy, Implications of the oceanic thermal skin temperature deviation at high wind speed, *Geophysical Research Letters*, *26*(16), PP. 2505–2508, doi : 199910.1029/1999GL900547, 1999. 50

Donlon, C. J., P. J. Minnett, C. Gentemann, T. J. Nightingale, I. J. Barton, B. Ward, et M. J. Murray, Toward improved validation of satellite sea surface skin temperature measurements for climate research, *Journal of Climate*, *15*(4), 353–369, doi :10.1175/1520-0442(2002)015<0353:TIVOSS>2.0.CO;2, 2002. 51

Donlon, C. J., M. Martin, J. Stark, J. Roberts-Jones, E. Fiedler, et W. Wimmer, The operational sea surface temperature and sea ice analysis (OSTIA) system, *Remote Sensing of Environment*, *116*, 140–158, doi :10.1016/j.rse.2010.10.017, 2012. 57

d'Ovidio, F., J. Isern-Fontanet, C. López, E. Hernández-García, et E. García-Ladona, Comparison between eulerian diagnostics and finite-size lyapunov exponents computed from altimetry in the algerian basin, *Deep Sea Research Part I : Oceanographic Research Papers*, *56*(1), 15–31, doi :10.1016/j.dsr.2008.07.014, 2009. 238

Ducet, N., P. Y. L. Traon, et G. Reverdin, Global high-resolution mapping of ocean circulation from TOPEX/Poseidon and ERS-1 and -2, *Journal of Geophysical Research*, *105*(C8), PP. 19,477–19,498, doi :200010.1029/2000JC900063, 2000. 34

Emery, W., D. Baldwin, et D. Matthews, Maximum cross correlation automatic satellite image navigation and attitude corrections for open-ocean image navigation, *IEEE Transactions on Geoscience and Remote Sensing*, *41*(1), 33–42, doi :10.1109/TGRS.2002.808061, 2003. 149

Fairall, C. W., E. F. Bradley, J. S. Godfrey, G. A. Wick, J. B. Edson, et G. S. Young, Cool-skin and warm-layer effects on sea surface temperature, *Journal of Geophysical Research*, *101*(C1), PP. 1295–1308, doi :199610.1029/95JC03190, 1996. 50

Figa-Saldaña, J., J. J. Wilson, E. Attema, R. Gelsthorpe, M. R. Drinkwater, et A. Stoffelen, The advanced scatterometer (ASCAT) on the meteorological operational (MetOp) platform : A follow on for european wind scatterometers, *Canadian Journal of Remote Sensing*, *28*(3), 404–412, doi :10.5589/m02-035, 2002. 43

Franz, B. A., S. W. Bailey, P. J. Werdell, et C. R. McClain, Sensor-independent approach to the vicarious calibration of satellite ocean color radiometry, *Applied Optics*, *46*(22), 5068, doi :10.1364/AO.46.005068, 2007. 63

Frenger, I., N. Gruber, R. Knutti, et M. Münnich, Imprint of southern ocean eddies on winds, clouds and rainfall, *Nature Geoscience*, *6*(8), 608–612, doi :10.1038/ngeo1863, 2013. 238

Frisch, U., *Turbulence : The Legacy of A. N. Kolmogorov*, cambridge university press ed., Cambridge University Press, 1995. 150, 151, 153

Fu, L.-L., E. J. Christensen, C. A. Y. Jr, M. Lefebvre, Y. Ménard, M. Dorrer, et P. Escudier, TOPEX/POSEIDON mission overview, *Journal of Geophysical Research*, *99*(C12), PP. 24,369–24,381, doi :199410.1029/94JC01761, 1994. 30

Fu, L.-L., D. Chelton, P.-Y. Le Traon, et R. Morrow, Eddy dynamics from satellite altimetry, *Oceanography*, *23*(4), 14–25, doi :10.5670/oceanog.2010.02, 2010. 80

Fuglister, F. C., Annual variations in current speeds in the gulf stream system, *Journal of Marine Research*, *10*, 119–127, 1951a. 8

Fuglister, F. C., Multiple currents in the gulf stream system, *Tellus*, *3*(4), 230–233, doi :10.1111/j.2153-3490.1951.tb00804.x, 1951b. 8

Fuglister, F. C., et L. V. Worthington, Some results of a multiple ship survey of the gulf stream, *Tellus*, *3*(1), 1–14, doi :10.1111/j.2153-3490.1951.tb00771.x, 1951. 8

Garçon, V. C., A. Oschlies, S. C. Doney, D. McGillicuddy, et J. Waniek, The role of mesoscale variability on plankton dynamics in the north atlantic, *Deep Sea Research Part II : Topical Studies in Oceanography*, *48*(10), 2199–2226, doi :10.1016/S0967-0645(00)00183-1, 2001. 222

Gentemann, C. L., C. J. Donlon, A. Stuart-Menteth, et F. J. Wentz, Diurnal signals in satellite sea surface temperature measurements, *Geophysical Research Letters*, *30*, 4 PP., doi :200310.1029/2002GL016291, 2003. 50

Giordani, H., L. Prieur, et G. Caniaux, Advanced insights into sources of vertical velocity in the ocean, *Ocean Dynamics*, *56*(5-6), 513–524, doi : 10.1007/s10236-005-0050-1, 2006. 222

Girard, C., Etude du comportement d'orientation d'espèces pélagiques tropicales vis-à-vis d'attracteurs, Thèse, Université de la Réunion, 2005. 244

Girard, C., J. Sudre, S. Benhamou, D. Roos, et P. Luschi, Homing in green turtles chelonia mydas : oceanic currents act as a constraint rather than as an information source, *Marine Ecology Progress Series*, *322*, 281–289, doi : 10.3354/meps322281, 2006. 243, 244

Godley, B. J., S. Richardson, A. C. Broderick, M. S. Coyne, F. Glen, et G. C. Hays, Long-term satellite telemetry of the movements and habitat utilisation

by green turtles in the mediterranean, *Ecography*, *25*(3), 352–362, doi :10.1034/j.1600-0587.2002.250312.x, 2002. 240

Grantham, W., E. Bracalente, W. Jones, et J. Johnson, The SeaSat-A satellite scatterometer, *IEEE Journal of Oceanic Engineering*, *2*(2), 200–206, doi :10.1109/JOE.1977.1145338, 1977. 42

Grémillet, D., Robots in ecology : Welcome to the machine, *Open Journal of Ecology*, *02*(02), 49–57, doi :10.4236/oje.2012.22006, 2012. 268

Grodsky, S. A., R. Lumpkin, et J. A. Carton, Spurious trends in global surface drifter currents, *Geophysical Research Letters*, *38*(6 PP.), L10,606, doi :201110.1029/2011GL047393, 2011. 138

Guinotte, J. M., et V. J. Fabry, Ocean acidification and its potential effects on marine ecosystems, *Annals of the New York Academy of Sciences*, *1134*(1), 320–342, doi :10.1196/annals.1439.013, 2008. 11

Haine, T. W. N., et J. Marshall, Gravitational, symmetric, and baroclinic instability of the ocean mixed layer, *Journal of Physical Oceanography*, *28*(4), 634–658, doi :10.1175/1520-0485(1998)028<0634:GSABIO>2.0.CO;2, 1998. 222

Hayes, S. P., L. J. Mangum, J. Picaut, A. Sumi, et K. Takeuchi, TOGA-TAO : A moored array for real-time measurements in the tropical pacific ocean, *Bulletin of the American Meteorological Society*, *72*(3), 339–347, doi :10.1175/1520-0477(1991)072<0339:TTAMAF>2.0.CO;2, 1991. 70

Hays, G. C., S. Åkesson, A. C. Broderick, F. Glen, B. J. Godley, F. Papi, et P. Luschi, Island-finding ability of marine turtles, *Proceedings of the Royal Society of London. Series B : Biological Sciences*, *270*(Suppl 1), S5–S7, doi :10.1098/rsbl.2003.0022, PMID : 12952621, 2003. 239, 241

Heitz, F., et P. Bouthemy, Multimodal estimation of discontinuous optical flow using markov random fields, *Pattern Analysis and Machine Intelligence, IEEE Transactions on*, *15*(12), 1217–1232, doi :10.1109/34.250841, 1993. 150

Helm, K. P., N. L. Bindoff, et J. A. Church, Observed decreases in oxygen content of the global ocean, *Geophysical Research Letters*, *38*(23), n/a–n/a, doi :10.1029/2011GL049513, 2011. 11

Horn, B. K., et B. G. Schunck, Determining optical flow, *Artificial Intelligence*, *17*(1-3), 185–203, doi :10.1016/0004-3702(81)90024-2, 1981. 149

Hughes, G., P. Luschi, R. Mencacci, et F. Papi, The 7000-km oceanic journey of a leatherback turtle tracked by satellite, *Journal of Experimental Marine Biology and Ecology*, *229*(2), 209–217, doi :10.1016/S0022-0981(98)00052-5, 1998. 239

Hummon, J. M., et E. Firing, A direct comparison of two RDI shipboard ADCPs : a 75-kHz ocean surveyor and a 150-kHz narrow band, *Journal of Atmospheric and Oceanic Technology*, *20*(6), 872–888, doi :10.1175/1520-0426(2003)020<0872:ADCOTR>2.0.CO;2, 2003. 68

Hunkins, K., The oceanic boundary layer and stress beneath a drifting ice floe, *Journal of Geophysical Research*, *80*(24), PP. 3425–3433, doi :197510.1029/JC080i024p03425, 1975. 84

Huntley, M. E., A. Gonzales, Y. Zhu, M. Zhou, et X. Irigoien, Zooplankton dynamics in a mesoscale eddy-jet system off california, *Marine Ecology Progress Series*, (201), 165–178, doi :10.3354/meps201165, 2000. 222

Hyrenbach, K. D., P. Fernndez, et D. J. Anderson, Oceanographic habitats of two sympatric north pacific albatrosses during the breeding season, *Marine Ecology Progress Series*, *233*, 283–301, doi :10.3354/meps233283, 2002. 237

Isern-Fontanet, J., A. Turiel, E. García-Ladona, et J. Font, Microcanonical multifractal formalism : Application to the estimation of ocean surface velocities, *Journal of Geophysical Research : Oceans*, *112*(C5), n/a–n/a, doi :10.1029/2006JC003878, 2007. 199

Jayles, C., B. Nhun-Fat, et C. Tourain, DORIS : System description and control of the signal integrity, *Journal of Geodesy*, *80*(8), 457–472, doi :10.1007/s00190-006-0046-8, 2006. 28

Jerlov, N. G., *Marine Optics*, vol. 14, elsevier oceanography series ed., Elsevier, Amsterdam, 1976. 61

Jońca, J., V. León Fernández, D. Thouron, A. Paulmier, M. Graco, et V. Garçon, Phosphate determination in seawater : Toward an autonomous electrochemical method, *Talanta*, *87*, 161–167, doi :10.1016/j.talanta.2011.09.056, 2011. 11

Joseph, G., *Fundamentals of Remote Sensing*, Universities Press, 2005. 26

Katsaros, K. B., The aqueous thermal boundary layer, *Boundary-Layer Meteorology*, *18*(1), 107–127, doi :10.1007/BF00117914, 1980. 50

Kaula, W. M., *Theory of satellite geodesy ; applications of satellites to geodesy*, Blaisdell Pub. Co., Waltham, Mass., 1966. 27

Koch, A., A. Carr, et D. Ehrenfeld, The problem of open-sea navigation : The migration of the green turtle to ascension island, *Journal of Theoretical Biology*, *22*(1), 163–179, doi :10.1016/0022-5193(69)90085-X, 1969. 241

Kolmogorov, A. N., Dissipation of energy in the locally isotropic turbulence, *Proceedings : Mathematical and Physical Sciences*, *434*(1890), 15–17, doi : 10.2307/51981, ArticleType : research-article / Issue Title : Turbulence and Stochastic Process : Kolmogorov's Ideas 50 Years On / Full publication date : Jul. 8, 1991 / Copyright © 1991 The Royal Society, 1991a. 153

Kolmogorov, A. N., The local structure of turbulence in incompressible viscous fluid for very large reynolds numbers, *Proceedings : Mathematical and Physical Sciences*, *434*(1890), 9–13, doi :10.2307/51980, ArticleType : research-article / Issue Title : Turbulence and Stochastic Process : Kolmogorov's Ideas 50 Years On / Full publication date : Jul. 8, 1991 / Copyright © 1991 The Royal Society, 1991b. 153

Kornprobst, P., R. Deriche, et G. Aubert, Image sequence analysis via partial differential equations, *Journal of Mathematical Imaging and Vision*, *11*(1), 5–26, doi :10.1023/A:1008318126505, 1999. 150

Kraichnan, R. H., Inertial ranges in two-dimensional turbulence, *Physics of Fluids*, *10*(7), 1417–1423, doi :doi:10.1063/1.1762301, 1967a. 152

Kraichnan, R. H., Intermittency in the very small scales of turbulence, *Physics of Fluids*, *10*(9), 2080–2082, doi :doi:10.1063/1.1762412, 1967b. 152

Kwiatkowska, E. J., B. A. Franz, G. Meister, C. R. McClain, et X. Xiong, Cross calibration of ocean-color bands from moderate resolution imaging spectroradiometer on terra platform, *Applied Optics*, *47*(36), 6796, doi : 10.1364/AO.47.006796, 2008. 63

Lacombe, M., V. Garçon, D. Thouron, N. Le Bris, et M. Comtat, Silicate electrochemical measurements in seawater : Chemical and analytical aspects towards a reagentless sensor, *Talanta*, *77*(2), 744–750, doi :10.1016/j.talanta.2008.07.023, 2008. 11

Lagerloef, G. S. E., G. T. Mitchum, R. B. Lukas, et P. P. Niiler, Tropical pacific near-surface currents estimated from altimeter, wind, and drifter data, *Journal of Geophysical Research*, *104*(C10), 23,313 – 23,326, doi : 199910.1029/1999JC900197, 1999. 86, 87

Lai, S.-H., et B. C. Vemuri, Reliable and efficient computation of optical flow, *International Journal of Computer Vision*, *29*(2), 87–105, doi :10.1023/A: 1008005509994, 1998. 150

Le Gall, J.-Y., M. Taquet, D. Cluet, et G. Biais, Caractéristiques topographiques et thermiques d'un site de ponte majeur de la tortue verte chelonia mydas dans l'Océan indien sud-ouest : Europa, *Mésogée*, (48), 43–49, 1988. 240

Le Traon, P. Y., F. Nadal, et N. Ducet, An improved mapping method of multisatellite altimeter data, *Journal of Atmospheric and Oceanic Technology*, *15*(2), 522–534, 1998. 34

Lee, K., L. T. Tong, F. J. Millero, C. L. Sabine, A. G. Dickson, C. Goyet, G.-H. Park, R. Wanninkhof, R. A. Feely, et R. M. Key, Global relationships of total alkalinity with salinity and temperature in surface waters of the world's oceans, *Geophysical Research Letters*, *33*(19), n/a–n/a, doi : 10.1029/2006GL027207, 2006. 267

Light, P., M. Salmon, et K. J. Lohmann, Geomagnetic orientation of loggerhead sea turtles : Evidence for an inclination compass, *Journal of Experimental Biology*, *182*(1), 1–10, 1993. 241

Lima, I. D., D. B. Olson, et S. C. Doney, Biological response to frontal dynamics and mesoscale variability in oligotrophic environments : Biological production and community structure, *Journal of Geophysical Research : Oceans*, *107*(C8), 25–1–25–21, doi :10.1029/2000JC000393, 2002. 222

Llido, J., Variabilité spatiale et temporelle du système biologique dans la convergence subtropicale au sud de l'Afrique, Thèse, Université Paul Sabatier, Toulouse, 2004. 222

Llido, J., E. Machu, J. Sudre, I. Dadou, et V. Garçon, Variability of the biological front south of africa from SeaWiFS and a coupled physical-biological model, *Journal of Marine Research*, *62*(4), 595–609, doi :10.1357/ 0022240041850020, 2004. 222

Llido, J., V. Garçon, J. R. E. Lutjeharms, et J. Sudre, Event-scale blooms drive enhanced primary productivity at the subtropical convergence, *Geophysical Research Letters*, *32*, L15,611, doi :10.1029/2005GL022880, 2005. 222

Lohmann, K. J., Magnetic orientation by hatchling loggerhead sea turtles (caretta caretta), *Journal of Experimental Biology*, *155*(1), 37–49, PMID : 2016575, 1991. 241

Lohmann, K. J., C. M. F. Lohmann, L. M. Ehrhart, D. A. Bagley, et T. Swing, Animal behaviour : Geomagnetic map used in sea-turtle navigation, *Nature*, *428*(6986), 909–910, doi :10.1038/428909a, 2004. 241

Lumpkin, R., et S. L. Garzoli, Near-surface circulation in the tropical atlantic ocean, *Deep Sea Research Part I : Oceanographic Research Papers*, *52*(3), 495–518, doi :10.1016/j.dsr.2004.09.001, 2005. 73

Lurton, X., *An Introduction to Underwater Acoustics*, Principles and Applications Series, 2nd ed., Springer Verlag, 2010. 68

Luschi, P., F. Papi, H. C. Liew, E. H. Chan, et F. Bonadonna, Long-distance migration and homing after displacement in the green turtle (chelonia mydas) : a satellite tracking study, *Journal of Comparative Physiology A*, *178*(4), 447–452, doi :10.1007/BF00190175, 1996. 239, 241

Luschi, P., G. C. Hays, C. Del Seppia, R. Marsh, et F. Papi, The navigational feats of green sea turtles migrating from ascension island investigated by satellite telemetry, *Proceedings of the Royal Society of London. Series B : Biological Sciences*, *265*(1412), 2279 –2284, doi :10.1098/rspb.1998.0571, 1998. 239

Luschi, P., S. Akesson, A. Broderick, F. Glen, B. Godley, F. Papi, et G. Hays, Testing the navigational abilities of ocean migrants : displacement experiments on green sea turtles (chelonia mydas), *Behavioral Ecology and Sociobiology*, *50*(6), 528–534, doi :10.1007/s002650100396, 2001. 241

Luschi, P., G. C. Hays, et F. Papi, A review of long-distance movements by marine turtles, and the possible role of ocean currents, *Oikos*, *103*(2), 293–302, doi :10.1034/j.1600-0706.2003.12123.x, 2003a. 241

Luschi, P., A. Sale, R. Mencacci, G. R. Hughes, J. R. E. Lutjeharms, et F. Papi, Current transport of leatherback sea turtles (dermochelys coriacea) in the ocean, *Proceedings of the Royal Society of London. Series B : Biological*

Sciences, *270*(Suppl 2), S129–S132, doi :10.1098/rsbl.2003.0036, PMID : 14667360, 2003b. 239

Luschi, P., S. Benhamou, C. Girard, S. Ciccione, D. Roos, J. Sudre, et S. Benvenuti, Marine turtles use geomagnetic cues during open-sea homing, *Current Biology*, *17*(2), 126–133, doi :10.1016/j.cub.2006.11.062, 2007. 244

Lutjeharms, J. R., A. Biastoch, P. M. Van der Werf, H. Ridderinkhof, et W. P. De Ruijter, On the discontinuous nature of the mozambique current, *South African Journal of Science*, *108*(1/2), doi :10.4102/sajs.v108i1/2.428, 2012. 234

Lutjeharms, J. R. E., *The Agulhas Current*, Springer-Verlag, Berlin, 2006. 234

Lutjeharms, J. R. E., et E. Machu, An upwelling cell inshore of the east madagascar current, *Deep Sea Research Part I : Oceanographic Research Papers*, *47*(12), 2405–2411, doi :10.1016/S0967-0637(00)00026-1, 2000. 234

Mackas, D., M. Tsurumi, M. Galbraith, et D. Yelland, Zooplankton distribution and dynamics in a north pacific eddy of coastal origin : II. mechanisms of eddy colonization by and retention of offshore species, *Deep Sea Research Part II : Topical Studies in Oceanography*, *52*(7–8), 1011–1035, doi :10.1016/j.dsr2.2005.02.008, 2005. 222

Martin, M. J., A. Hines, et M. J. Bell, Data assimilation in the FOAM operational short-range ocean forecasting system : a description of the scheme and its impact, *Quarterly Journal of the Royal Meteorological Society*, *133*(625), 981–995, doi :10.1002/qj.74, 2007. 57

Maximenko, N., P. Niiler, L. Centurioni, M.-H. Rio, O. Melnichenko, D. Chambers, V. Zlotnicki, et B. Galperin, Mean dynamic topography of the ocean derived from satellite and drifting buoy data using three different techniques, *Journal of Atmospheric and Oceanic Technology*, *26*(9), 1910–1919, doi :10.1175/2009JTECHO672.1, 2009. 80

McGillicuddy, D. J., A. R. Robinson, D. A. Siegel, H. W. Jannasch, R. Johnson, T. D. Dickey, J. McNeil, A. F. Michaels, et A. H. Knap, Influence of mesoscale eddies on new production in the sargasso sea, *Nature*, *394*(6690), 263–266, doi :10.1038/28367, 1998. 222

McPhaden, M., A. Busalacchi, et D. Anderson, A TOGA retrospective, *Oceanography*, *23*(3), 86–103, doi :10.5670/oceanog.2010.26, 2010. 70

McPhaden, M. J., G. Meyers, K. Ando, Y. Masumoto, V. S. N. Murty, M. Ravichandran, F. Syamsudin, J. Vialard, L. Yu, et W. Yu, RAMA : The research moored array for African–Asian–Australian monsoon analysis and prediction, *Bulletin of the American Meteorological Society*, *90*(4), 459–480, doi : 10.1175/2008BAMS2608.1, 2009. 71

Mcwilliams, J. C., The emergence of isolated coherent vortices in turbulent flow, *Journal of Fluid Mechanics*, *146*, 21–43, doi :10.1017/S0022112084001750, 1984. 81

Meister, G., E. J. Kwiatkowska, B. A. Franz, F. S. Patt, G. C. Feldman, et C. R. McClain, Moderate-resolution imaging spectroradiometer ocean color polarization correction, *Applied Optics*, *44*(26), 5524, doi :10.1364/AO.44.005524, 2005. 63

Mémin, E., et P. Pérez, Hierarchical estimation and segmentation of dense motion fields, *International Journal of Computer Vision*, *46*(2), 129–155, doi : 10.1023/A:1013539930159, 2002. 150

Monte, S. D., C. Cotté, F. d'Ovidio, M. Lévy, M. L. Corre, et H. Weimerskirch, Frigatebird behaviour at the ocean–atmosphere interface : integrating animal behaviour with multi-satellite data, *Journal of The Royal Society Interface*, *9*(77), 3351–3358, doi :10.1098/rsif.2012.0509, PMID : 22951344, 2012. 238

Moore, R. K., A. K. Fung, J. D. Young, J. P. Claassen, H. L. Chan, M. Afarani, W. J. Pierson, V. J. Cardone, J. Hayes, W. Spring, et C. Greenwood, Skylab s-193 radscat microwave measurements of sea surface winds, 1975. 39

Morel, A., et L. Prieur, Analysis of variations in ocean color, *Lymnology and Oceanography*, *22*(4), 709–722, 1977. 61

Muhling, B., L. Beckley, et M. Olivar, Ichthyoplankton assemblage structure in two meso-scale leeuwin current eddies, eastern indian ocean, *Deep Sea Research Part II : Topical Studies in Oceanography*, *54*(8–10), 1113–1128, doi : 10.1016/j.dsr2.2006.05.045, 2007. 222

Munk, W., Achievement in physical oceanography, dans *50 Years of Ocean Discovery*, vol. 90, national academic press ed., pp. 44–50, National Academic Press, 2000a. 9

Munk, W., Oceanography before, and after, the advent of satellites, dans *Satellites, Oceanography and Society*, no. 63 dans Elsevier Oceanography series, elsevier ed., pp. 1–4, D. Halpern, 2000b. 148

Naderi, F. M., M. H. Freilich, et D. G. Long, Spaceborne radar measurement of wind velocity over the ocean-an overview of the NSCAT scatterometer system, *Proceedings of the IEEE*, *79*(6), 850–866, doi :10.1109/5.90163, 1991. 40

Nerem, R. S., r. Leuliette, et A. Cazenave, Present-day sea-level change : A review, *Comptes Rendus Geoscience*, *338*(14–15), 1077–1083, doi :10.1016/j.crte.2006.09.001, 2006. 11

Niiler, P., Chapter 4.1 the world ocean surface circulation, dans *Ocean Circulation and Climate Observing and Modelling the Global Ocean*, vol. Volume 77, pp. 193–204, Academic Press, 2001. 73

Niiler, P. P., et J. D. Paduan, Wind-driven motions in the northeast pacific as measured by lagrangian drifters, *Journal of Physical Oceanography*, *25*(11), 2819–2830, 1995. 85

Niiler, P. P., N. A. Maximenko, et J. C. McWilliams, Dynamically balanced absolute sea level of the global ocean derived from near-surface velocity observations, *Geophysical Research Letters*, *30*, 2164 – 2168, doi : 200310.1029/2003GL018628, 2003. 86

Nogawa, H., Y. Nakajima, Y. Sato, et S. Tamura, Acquisition of symbolic description from flow fields : A new approach based on a fluid model, *IEEE Transactions on Pattern Analysis and Machine Intelligence*, *19*(1), 58–63, doi : 10.1109/34.566811, 1997. 150

Okubo, A., Horizontal dispersion of floatable particles in the vicinity of velocity singularities such as convergences, *Deep Sea Research and Oceanographic Abstracts*, *17*(3), 445–454, doi :10.1016/0011-7471(70)90059-8, 1970. 223

Orr, J. C., V. J. Fabry, O. Aumont, L. Bopp, S. C. Doney, R. A. Feely, A. Gnanadesikan, N. Gruber, A. Ishida, F. Joos, R. M. Key, K. Lindsay, E. Maier-Reimer, R. Matear, P. Monfray, A. Mouchet, R. G. Najjar, G.-K. Plattner, K. B. Rodgers, C. L. Sabine, J. L. Sarmiento, R. Schlitzer, R. D. Slater, I. J. Totterdell, M.-F. Weirig, Y. Yamanaka, et A. Yool, Anthropogenic ocean acidification over the twenty-first century and its impact on calcifying organisms, *Nature*, *437*(7059), 681–686, doi :10.1038/nature04095, 2005. 11

Papi, F., H. C. Liew, P. Luschi, et E. H. Chan, Long-range migratory travel of a green turtle tracked by satellite : evidence for navigational ability in the open sea, *Marine Biology*, *122*(2), 171–175, doi :10.1007/BF00348929, 1995. 239

Papi, F., P. Luschi, E. Crosio, et G. R. Hughes, Satellite tracking experiments on the navigational ability and migratory behaviour of the loggerhead turtle caretta caretta, *Marine Biology*, *129*(2), 215–220, doi :10.1007/s002270050162, 1997. 239

Papin, C., P. Bouthemy, E. Mémin, et G. Rochard, Tracking and characterization of highly deformable cloud structures, dans *Computer Vision — ECCV 2000*, pp. 428–442, 2000. 150, 239

Parisi, G., et U. Frisch, On the singularity structure of fully developed turbulence, dans *Turbulence and Predictability in Geophysical Fluid Dynamics*, Proc. Intl. School of Physics E. Fermi, pp. 84–87, M. Ghil, R. Benzi, G. Parisi, Amsterdam, North Holland, 1985. 151, 158

Pascual, A., Y. Faugère, G. Larnicol, et P.-Y. L. Traon, Improved description of the ocean mesoscale variability by combining four satellite altimeters, *Geophysical Research Letters*, *33*, 4 PP., doi :200610.1029/2005GL024633, 2006. 34

Paul, S., *Introduction à l'étude de la télédétection aérospatiale et de son vocabulaire*, La Documentation française, 1991. 26

Pauly, D., et V. Christensen, Primary production required to sustain global fisheries, *Nature*, *374*(6519), 255–257, doi :10.1038/374255a0, 1995. 231

Pearlman, M., J. Degnan, et J. Bosworth, The international laser ranging service, *Advances in Space Research*, *30*(2), 135–143, doi :10.1016/S0273-1177(02)00277-6, 2002. 28

Picaut, J., et R. Tournier, Monitoring the 1979-1985 equatorial pacific current transports with expendable bathythermograh data, *Journal of Geophysical Research*, *96, suppl.*, 3263–3277, 1991. 140

Plimpton, P. E., H. P. Freitag, et M. J. McPhaden, Processing of subsurface ADCP data in the equatorial pacific, *Tech. Memo OAR PMEL-125*, NOAA/Pacific Marine Environmental Laboratory, Seattle, 2004. 70

Pont, O., A. Turiel, et C. J. Pérez-Vicente, Empirical evidences of a common multifractal signature in economic, biological and physical systems, *Physica A : Statistical Mechanics and its Applications*, *388*(10), 2025–2035, doi :10.1016/j.physa.2009.01.041, 2009. 151

Pont, O., A. Turiel, et C. J. Perez-Vicente, On optimal wavelet bases for the realization of microcanonical cascade processes, *International Journal of Wavelets Multiresolution and Information Processing*, *9*, 35 – 61, 2011a. 159, 160, 161

Pont, O., A. Turiel, et H. Yahia, An optimized algorithm for the evaluation of local singularity exponents in digital signals, dans *Combinatorial Image Analysis*, édité par J. K. Aggarwal, R. P. Barneva, V. E. Brimkov, K. N. Koroutchev, et E. R. Korutcheva, no. 6636 dans Lecture Notes in Computer Science, pp. 346–357, Springer Berlin Heidelberg, 2011b. 151

Pottier, C., Combinaison multi-capteurs de données de couleur de l'eau : Application en océanographie opérationnelle, Thèse, Université Paul Sabatier, Toulouse, 2006. x, 61, 163

Pottier, C., A. Turiel, et V. Garçon, Inferring missing data in satellite chlorophyll maps using turbulent cascading, *Remote Sensing of Environment*, *112*(12), 4242–4260, doi :10.1016/j.rse.2008.07.010, 2008. 163

Prabhakara, C., G. Dalu, et V. G. Kunde, Estimation of sea surface temperature from remote sensing in the 11- to 13- {μ}m window region, *Journal of Geophysical Research*, *79*(33), PP. 5039–5044, doi :197410.1029/JC079i033p05039, 1974. 53

Provost, C., et M. Du Chaffaut, Yoyo profiler : an autonomous multisensor, *Sea Technology*, *37*(10), 39–45, 1996. 10

Provost, C., et M. Du Chaffaut, Moored yoyo profiler : an autonomous multisensor, *Proceeding of he Brighton meeting*, *1*, 243–249, 1998. 10

Pörtner, H., Contribution to the theme section 'Effects of ocean acidification on marine ecosystems' ecosystem effects of ocean acidification in times of ocean warming : a physiologist's view, *Marine Ecology Progress Series*, *373*, 203–217, doi :10.3354/meps07768, 2008. 11

Ralph, E. A., et P. P. Niiler, Wind-driven currents in the tropical pacific, *Journal of Physical Oceanography*, *29*(9), 2121–2129, 1999. 86

Reeves, R. G., A. Anson, D. Landen, et A. S. o. Photogrammetry, *Manual of remote sensing : Theory, instruments and techniques*, American Society of Photogrammetry, 1975. 26

Remondi, B. W., Global positioning system carrier phase : Description and use, *Bulletin Géodésique*, *59*, 361 – 377, 1985. 28

Reverdin, G., P. P. Niiler, et H. Valdimarsson, North atlantic ocean surface currents, *Journal of Geophysical Research*, *108*, 21 PP., doi :200310.1029/2001JC001020, 2003. 86

Reynolds, R. W., N. A. Rayner, T. M. Smith, D. C. Stokes, et W. Wang, An improved in situ and satellite SST analysis for climate, *Journal of Climate*, *15*(13), 1609–1625, doi :10.1175/1520-0442(2002)015<1609:AIISAS>2.0.CO;2, 2002. 56

Ridderinkhof, H., J. R. E. Lutjeharms, et W. P. M. De Ruijter, A research cruise to investigate the mozambique current, *South African journal of science*, *97*(11-12), 461–464, 2001. 234

Rio, M.-H., et F. Hernandez, A mean dynamic topography computed over the world ocean from altimetry, in situ measurements, and a geoid model, *Journal of Geophysical Research*, *109*, C12,032, doi :10.1029/2003JC002226, 2004. 36, 37

Robinson, I. S., N. C. Wells, et H. Charnock, Review article. the sea surface thermal boundary layer and its relevance to the measurement of sea surface temperature by airborne and spaceborne radiometers, *International Journal of Remote Sensing*, *5*(1), 19–45, doi :10.1080/01431168408948787, 1984. 50

Rossi, V., Influence des processus physiques à mésoéchelle sur l'écosystème planctonique : application aux zones d'Upwelling de bord est., Thèse, Paul Sabatier, Toulouse, 2010. 231

Rossi, V., C. López, J. Sudre, E. Hernández-García, et V. Garçon, Comparative study of mixing and biological activity of the benguela and canary upwelling systems, *Geophysical Research Letters*, *35*, L11,602, doi : 10.1029/2008GL033610, 2008. 231

Rossi, V., C. López, E. Hernández-García, J. Sudre, V. Garçon, et Y. Morel, Surface mixing and biological activity in the four eastern boundary upwelling systems, *Nonlin. Processes Geophys.*, *16*(4), 557–568, 2009. 148, 231

Schluessel, P., W. J. Emery, H. Grassl, et T. Mammen, On the bulk-skin temperature difference and its impact on satellite remote sensing of sea surface temperature, *Journal of Geophysical Research*, *95*(C8), PP. 13,341–13,356, doi :199010.1029/JC095iC08p13341, 1990. 50

Schouten, M. W., W. P. M. de Ruijter, P. J. van Leeuwen, et H. Ridderinkhof, Eddies and variability in the mozambique channel, *Deep Sea Research Part II : Topical Studies in Oceanography*, *50*(12-13), 1987–2003, doi :10.1016/S0967-0645(03)00042-0, 2003. 234

Servain, J., A. J. Busalacchi, M. J. McPhaden, A. D. Moura, G. Reverdin, M. Vianna, et S. E. Zebiak, A pilot research moored array in the tropical atlantic (PIRATA), *Bulletin of the American Meteorological Society*, *79*(10), 2019–2031, doi :10.1175/1520-0477(1998)079<2019:APRMAI>2.0.CO;2, 1998. 71

Siegel, D. A., P. Peterson, D. J. M. Jr, S. Maritorena, et N. B. Nelson, Bio-optical footprints created by mesoscale eddies in the sargasso sea, *Geophysical Research Letters*, *38*, 6 PP., doi :201110.1029/2011GL047660, 2011. 231

Smith, S. D., Coefficients for sea surface wind stress, heat flux, and wind profiles as a function of wind speed and temperature, *Journal of Geophysical Research*, *93*(C12), PP. 15,467–15,472, doi :198810.1029/JC093iC12p15467, 1988. 45

Smith, W. L., P. K. Rao, R. Koffler, et W. R. Curtis, The determination of sea-surface temperature from satellite high resolution infrared window radiation measurements, *Monthly Weather Review*, *98*(8), 604–611, doi :10.1175/1520-0493(1970)098<0604:TDOSST>2.3.CO;2, 1970. 53

Soloviev, A. V., et P. Schluessel, Evolution of cool skin and direct air-sea gas transfer coefficient during daytime, *Boundary-Layer Meteorology*, *77*(1), 45–68, doi :10.1007/BF00121858, 1996. 50

Spencer, M. W., C. Wu, et D. G. Long, Improved resolution backscatter measurements with the SeaWinds pencil-beam scatterometer, *IEEE Transactions on Geoscience and Remote Sensing*, *38*(1), 89–104, doi :10.1109/36.823904, 2000. x, 42

Stanley, H. E., *Introduction to Phase Transitions and Critical Phenomena*, no. 46 dans International series of monographs on physiscs, oxford university press ed., 1987. 154

Stommel, H., The westward intensification of wind-driven ocean currents, *Transactions, American Geophysical Union*, *29*(2), 202 – 206, 1948. 80

Stommel, H., Direct measurements of sub-surface currents, *Deep Sea Research (1953)*, *2*(4), 284–285, doi :10.1016/0146-6313(55)90006-X, 1955. 74

Stommel, H., The abyssal circulation, *Deep Sea Research (1953)*, *5*(1), 80–82, doi :10.1016/S0146-6291(58)80014-4, 1958. 8

Stommel, H., et A. Arons, On the abyssal circulation of the world ocean—I. stationary planetary flow patterns on a sphere, *Deep Sea Research (1953)*, *6*, 140–154, doi :10.1016/0146-6313(59)90065-6, 1959a. 8

Stommel, H., et A. Arons, On the abyssal circulation of the world ocean — II. an idealized model of the circulation pattern and amplitude in oceanic basins, *Deep Sea Research (1953)*, *6*, 217–233, doi :10.1016/0146-6313(59)90075-9, 1959b. 8

Sudre, J., et R. Morrow, Global surface currents : a high-resolution product for investigating ocean dynamics, *Ocean Dynamics*, *58*(2), 101–118, doi :10.1007/s10236-008-0134-9, 2008. iv, ix, x, 36, 37, 47, 79, 138, 139, 243

Sudre, J., C. Maes, et V. Garçon, On the global estimates of geostrophic and ekman surface currents, *Limnology & Oceanography : Fluids & Environments*, *3*, 1–20, doi :10.1215/21573689-2071927, 2013. iv, ix, x, 38, 47, 79, 129, 138, 139, 243

Suter, D., Computer vision and pattern recognition, 1994. proceedings CVPR '94., 1994 IEEE computer society conference on, pp. 939–942, doi :10.1109/CVPR.1994.323929, 1994. 150

Sverdrup, H. U., Wind-driven currents in a baroclinic ocean ; with application to the equatorial currents of the eastern pacific, *Proceedings of the National Academy of Sciences*, *33*(11), 318–326, 1947. 80

Swallow, J., A neutral-buoyancy float for measuring deep currents, *Deep Sea Research (1953)*, *3*(1), 74–81, doi :10.1016/0146-6313(55)90037-X, 1955. 74

Sybranly, A. L., et P. P. Niiler, WOCE/TOGA lagrangian drifter construction manual, *Rep. Tech. WOCE 63, SOI Ref. 91/6*, Scripps Institution of Oceanography, La Jolla, Calif., 1992. 72

Tew Kai, E., Rôle des tourbillons méso-échelle dans la structuration spatiale de l'écosystème pélagique : le cas du canal de mozambique, Thèse, Université Pierre et Marie Curie, Paris, 2009. xiii, 222, 233, 238

Tew-Kai, E., et F. Marsac, Patterns of variability of sea surface chlorophyll in the mozambique channel : A quantitative approach, *Journal of Marine Systems*, *77*(1-2), 77–88, doi :10.1016/j.jmarsys.2008.11.007, 2009. 237

Tew Kai, E., V. Rossi, J. Sudre, H. Weimerskirch, C. Lopez, E. Hernandez-Garcia, F. Marsac, et V. Garçon, Top marine predators track lagrangian coherent structures, *Proceedings of the National Academy of Sciences*, *106*(20), 8245 – 8250, doi :10.1073/pnas.0811034106, 2009. 237

Thomas, L., et R. Ferrari, Friction, frontogenesis, and the stratification of the surface mixed layer, *Journal of Physical Oceanography*, *38*(11), 2501–2518, 2008. 152

Thomas, L. N., et C. M. Lee, Intensification of ocean fronts by down-front winds, *Journal of Physical Oceanography*, *35*(6), 1086–1102, doi :10.1175/JPO2737.1, 2005. 222

Thouron, D., R. Vuillemin, X. Philippon, A. Lourenço, C. Provost, A. Cruzado, et V. Garçon, An autonomous nutrient analyzer for oceanic long-term in situ biogeochemical monitoring, *Anal. Chem.*, *75*(11), 2601–2609, doi :10.1021/ac020696+, 2003. 10

Turiel, A., G. Mato, N. Parga, et J.-P. Nadal, Self-similarity properties of natural images resemble those of turbulent flows, *Physical Review Letters*, *80*(5), 1098, doi :10.1103/PhysRevLett.80.1098, copyright (C) 2009 The American Physical Society ; Please report any problems to prola@aps.org, 1998. 151

Turiel, A., C. J. Pérez-Vicente, et J. Grazzini, Numerical methods for the estimation of multifractal singularity spectra on sampled data : A comparative study, *Journal of Computational Physics*, *216*(1), 362–390, doi :10.1016/j.jcp.2005.12.004, 2006. 151, 157, 158, 159

Turiel, A., H. Yahia, et C. J. Pérez-Vicente, Microcanonical multifractal formalism—a geometrical approach to multifractal systems : Part i. singularity analysis, *Journal of Physics A : Mathematical and Theoretical*, *41*(1), 015,501, doi :10.1088/1751-8113/41/1/015501, 2008. 151, 154, 156, 158, 159

Ulaby, F. T., R. K. Moore, et A. K. Fung, *Radar remote sensing and surface scattering and emission theory*, *Microwave Remote Sensing : Active and Passive*, vol. 2, new edition ed., Artech House, 1982. 40, 41

Van Meurs, P., et P. P. Niiler, Temporal variability of the large-scale geostrophic surface velocity in the northeast pacific, *Journal of Physical Oceanography*, *27*(10), 2288–2297, doi :10.1175/1520-0485(1997)027<2288:TVOTLS>2.0.CO;2, 1997. 86

Vickery, J. A., et M. Brooke, The kleptoparasitic interactions between great frigatebirds and masked boobies on henderson island, south pacific, *The Condor*, *96*(2), 331–340, doi :10.2307/1369318, 1994. 236

Vigan, X., C. Provost, R. Bleck, et P. Courtier, Sea surface velocities from sea surface temperature image sequences 1. method and validation using primitive equation model output, 2009a. 150

Vigan, X., C. Provost, et G. Podesta, Sea surface velocities from sea surface temperature image sequences 2. application to the brazil-malvinas confluence area, 2009b. 150

Vuillemin, R., D. Thouron, G. Gallou, L. Pares, B. Brient, A. Dubreule, et V. Garçon, ANAIS : Autonomous nutrient analyser in situ, *Sea Technology*, (40), 75–78, 1999. 10

Waite, A., B. Muhling, C. Holl, L. Beckley, J. Montoya, J. Strzelecki, P. Thompson, et S. Pesant, Food web structure in two counter-rotating eddies based on δ15N and δ13C isotopic analyses, *Deep Sea Research Part II : Topical Studies in Oceanography*, *54*(8–10), 1055–1075, doi :10.1016/j.dsr2.2006.12.010, 2007. 222

Walton, C. C., Nonlinear multichannel algorithms for estimating sea surface temperature with AVHRR satellite data, *Journal of Applied Meteorology*, *27*(2), 115–124, doi :10.1175/1520-0450(1988)027<0115:NMAFES>2.0.CO;2, 1988. 56

Weickert, J., et C. Schnörr, Variational optic flow computation with a spatio-temporal smoothness constraint, *Journal of Mathematical Imaging and Vision*, *14*(3), 245–255, doi :10.1023/A:1011286029287, 2001. 150

Weimerskirch, H., M. L. Corre, S. Jaquemet, M. Potier, et F. Marsac, Foraging strategy of a top predator in tropical waters : great frigatebirds in the

mozambique channel, *Marine Ecology Progress Series*, *275*, 297–308, doi : 10.3354/meps275297, 2004. 236, 237, 238

Weiss, J., The dynamics of enstrophy transfer in two-dimensional hydrodynamics, *Physica D : Nonlinear Phenomena*, *48*(2–3), 273–294, doi :10.1016/0167-2789(91)90088-Q, 1991. 223

Wick, G. A., J. J. Bates, et D. J. Scott, Satellite and skin-layer effects on the accuracy of sea surface temperature measurements from the GOES satellites, *Journal of Atmospheric and Oceanic Technology*, *19*(11), 1834–1848, doi :10.1175/1520-0426(2002)019<1834:SASLEO>2.0.CO;2, 2002. 54

Williams, R. G., et M. J. Follows, Oceanography : Eddies make ocean deserts bloom, *Nature*, *394*(6690), 228–229, doi :10.1038/28285, 1998. 222

Wu, C., J. Graf, M. Freilich, D. Long, M. Spencer, W. Tsai, D. Lisman, et C. Winn, The SeaWinds scatterometer instrument, dans *Geoscience and Remote Sensing Symposium, 1994. IGARSS '94. Surface and Atmospheric Remote Sensing : Technologies, Data Analysis and Interpretation., International*, vol. 3, pp. 1511–1515 vol.3, IEEE, doi :10.1109/IGARSS.1994.399483, 1994. 40, 43

Wu, Q., A correlation-relaxation-labeling framework for computing optical flow-template matching from a new perspective, *Pattern Analysis and Machine Intelligence, IEEE Transactions on*, *17*(9), 843–853, doi :10.1109/34.406650, 1995. 149

Xie, J., et J. Zhu, Estimation of the surface and mid-depth currents from argo floats in the pacific and error analysis, *Journal of Marine Systems*, *73*(1–2), 61–75, doi :10.1016/j.jmarsys.2007.09.001, 2008. 74

Xie, J., et J. Zhu, A dataset of global ocean surface currents for 1999-2007 derived from argo float trajectories : Comparison with surface drifter and TAO measurements, *Atmospheric and Oceanic Science Letters*, *2*(2), 97 – 102, 2009. 74

Yahia H., Sudre J., Pottier C., et Garçon V., Motion analysis in oceanographic satellite images using multiscale methods and the energy cascade, *Pattern Recognition*, *43*(10), 35913,604, doi :doi:10.1016/j.patcog.2010.04.011, 2010. 199, 200

Yuan, J., C. Schnörr, et E. Mémin, Discrete orthogonal decomposition and variational fluid flow estimation, *Journal of Mathematical Imaging and Vision*, *28*(1), 67–80, doi :10.1007/s10851-007-0014-9, 2007. 150

Zhang, H.-M., J. J. Bates, et R. W. Reynolds, Assessment of composite global sampling : Sea surface wind speed, *Geophysical Research Letters*, *33*, 5 PP., doi :200610.1029/2006GL027086, 2006. 44

Zhou, L., C. Kambhamettu, et D. B. Goldgof, Fluid structure and motion analysis from multi-spectrum 2D cloud image sequences, CVPR, pp. 2744–2751, IEEE Computer Society, doi :http://doi.ieeecomputersociety.org/10.1109/CVPR.2000.854949, 2000. 150

Les Annexes

Annexe A : Article soumis

Annexe A

Annexe A : Article soumis

A.1 Article soumis : Ocean Turbulent Dynamics at Super Resolution : A True Picture, Sudre et al.

A.1.1 Abstract

Synoptic determination of ocean circulation with a coherent depiction of its turbulent characteristics remains a fundamental challenge in oceanography. This determination has the potential of revealing all aspects of the ocean dynamic variability on a wide range of spatio-temporal scales and will enhance our understanding of ocean-atmosphere exchanges at super resolution, as required in the present context of climate change (1). Here we show a 4-year time series of spatial super resolution (4 kms) turbulent ocean dynamics generated from satellite data using criticality in nonlinear physics, low resolution dynamics and super resolution oceanic sea surface temperature data acquired from optical sensors. The method at its core consists in propagating across the scales the low resolution dynamics in a multiresolution analysis computed on adimensional critical transition information. Nonlinear analysis of complex remotely-sensed signals has the potential of computing super resolution ocean circulation maps while revealing the complexity of turbulent dynamics.

A.1.2 Article soumis dans *Nature Geoscience*

Référence Sudre J., H. Yahia, O. Pont and V. Garçon : Ocean Turbulent Dynamics at Super Resolution : A True Picture, *Article soumis*.

nature geoscience

Title: Ocean Turbulent Dynamics at Super Resolution: A True Picture

Authors: J. Sudre[1,*]; H. Yahia[2]; O. Pont[2]; V. Garçon[1]

Affiliations:

[1] CNRS/LEGOS, UMR 55 66 (CNRS, CNES, IRD, UPS), Observatoire Midi-Pyrénées, 14 Avenue Edouard Belin, 31400 Toulouse, France.

[2] INRIA, 200 rue de la Vieille Tour, 33405 Talence Cedex, France.

*Correspondence to: joel.sudre@legos.obs-mip.fr

Main Text:

Synoptic determination of ocean circulation with a coherent depiction of its turbulent characteristics remains a fundamental challenge in oceanography. This determination has the potential of revealing all aspects of the ocean dynamic variability on a wide range of spatio-temporal scales and will enhance our understanding of ocean-atmosphere exchanges at super resolution, as required in the present context of climate change (*1*). Here we show a 4-year time series of spatial super resolution (4 kms) turbulent ocean dynamics generated from satellite data using criticality in nonlinear physics, low resolution dynamics and super resolution oceanic sea surface temperature data acquired from optical sensors. The method at its core consists in propagating across the scales the low resolution dynamics in a multiresolution analysis computed on adimensional critical transition information. Nonlinear analysis of complex remotely-sensed signals has the potential of computing super resolution ocean circulation maps while revealing the complexity of turbulent dynamics.

During the second half of the 20th century, more than 80% of the energy in the Earth's climate system coming from anthropogenic forcing has accumulated in the subsurface ocean (*2*). Consequently, the precise evaluation of ocean mixing at meso- and submeso-scale is essential in better understanding the ocean's role in climate regulation. Such an evaluation is fundamentally absent in existing global ocean circulation models, although turbulence is specifically taken into account in 1D vertical models along a water column such as for instance in General Ocean Turbulence Model (GOTM - http://www.gotm.net). While on time scales longer than a few days and space scales above 50 kms, and sufficiently outside of the equator, altimetry techniques provide an adequate synoptic picture of ocean circulation (*3*), a global and accurate depiction of turbulent ocean dynamics at submesoscale and below (where most of the ocean's kinetic energy and its dissipation take place) remains an immense challenge (*4*).

Before the advent in 2019 of future observations of higher resolution altimetry coming from the Surface Water Ocean Topography (SWOT) mission, it is fundamental to make use of optical sensors which acquire super resolution[1] datasets of physical variables (e.g. Sea Surface

[1] Super resolution: of the order of the kilometer; low resolution: of the order of 25 kms.

nature geoscience

Temperature -SST-), whose knowledge is important for the evaluation of heat exchange at the air-sea interface. In particular, existing ocean circulation models miss the interactions that mesoscale eddies infer to larger scale and for ocean-atmosphere interactions (*5*). Ocean turbulence plays a fundamental role not only in the evaluation of ocean dynamics, but in the determination of mixing properties that are so important in the exchange of energy, gases and particles at the ocean-atmosphere interface (*6–9*). The inertial range, which properly defines the range over which oceanic turbulence (and the energy cascade) takes place, goes from millimeter scales up to mesoscale eddies with sizes of a few hundred kilometers (*10*), the latter affecting the whole marine ecosystems (i.e. (*11–13*)).

Ocean dynamics belong to the domain of Fully Developed Turbulence (FDT): at high Reynolds numbers, symmetries are restored only in a statistical sense (*14*) because, when time $t \to +\infty$ the finite mean energy dissipation rate does not guarantee boundedness of the flow's high spatial derivatives (*15*), resulting in unpredictable behavior of the flow's speed appearing in finite time. Therefore, as first noticed by Kolmogorov (K41 theory) and followers, the flow possesses self-similarity properties, which translate into specific power laws for the structure functions associated to intensive variables. Cascading phenomena take place within the inertial range and are observed for intensive variables (*16*). Turbulence affects ocean-atmosphere exchange of heat moisture, momentum, gases and aerosol-borne chemicals (*9*) and these effects must be evaluated at all scales, in particular submesoscale, for a proper assessment in climate studies.

Here, we show that the determination of *singularity exponents* (or *critical exponents* as they are called in nonlinear physics) in a microcanonical setting (*17*), provides an adimensional quantitative representation of critical transitions which can, in turn, serve as an optimal multiresolution analysis capable of maximizing the inference of physical variables across the scales. As a result, we derive a powerful novel method for computing super resolution ocean dynamics validated by Lagrangian buoy data.

It is known that an energy cascade, associated to energy injection across the scales, is taking place in FDT (*18*); the cascade is geometrically localized (*19*) and associated to a multifractal geometrical hierarchy F_h where h is a **scaling exponent.** One of the principal advantages of having adimensional transition information is the ability to use it for performing data fusion of different physical variables acquired at different spatio-temporal resolutions. For determining a synoptical representation of ocean dynamics at super spatial resolution, we use two separate satellite datasets described in supplementary material SM1 (see also Suppl. Fig. S1).

Figure 1A shows the results of the combination of geostrophy and Ekman currents that can be determined at low resolution as described in Sudre et al. (*20*). The signal carried by the SST data at super resolution conveys information about the value of an intensive physical variable, the temperature, which behaves as a passive tracer. Following (*17*), power-law correlations of a physical variable (here, SST) are better evaluated through the study of a measure which sums the variations of the signal around a point. These power-law correlations give access to the singularity exponents (see below). They must be distinguished from long-range correlations,

nature geoscience

which account, in oceanography, to variations at basin scale, while power-law correlations are better evidenced at across the boundaries of coherent structures which exist at all scales within the inertial range. Consequently, given a mother wavelet Ψ, a *d*-dimensional turbulent signal s[2] with associated gradient measure μ such that $d\mu(x) = \|\nabla s\|(x)dx$, the wavelet projection of measure μ:

$$\Im_\Psi \mu(\mathbf{x}, r) = \int_{\mathbb{R}^d} d\mu(\mathbf{x}') \frac{1}{r^d} \Psi\left(\frac{x-x'}{r}\right), \qquad (1)$$

satisfies:

$$\Im_\Psi \mu(\boldsymbol{x}, r) = \alpha_\Psi(x) r^{h(x)} + \mathrm{o}\left(\mathrm{r}^{\mathrm{h(x)}}\right), \quad (\mathrm{r} \to 0) \qquad (2)$$

The collection of adimensionals scalars $h(x)$ define the set of *singularity exponents* discussed above. As opposed to Finite Size Lyapunov Exponents (*21*), they are computed at instantaneous times, and do not need time series. Equation (2) is also a fingerprint for universality: as noticed in the description of phase transitions, around a singular point, the macroscopic properties are determined by the value of the singularity exponent (*22*) $h(x)$.

In the formulation of equation (2) we assume that most points are critical, i.e. whenever $h(x) < 0$, the "strength" of the transition at point x being properly characterized by the value of the singularity exponent $h(x)$. For the practical computation of $h(x)$, see (*23*). The relationships between the singularity exponents $h(x)$, the multifractal hierarchy F_h, the scaling exponents h, and the singularity spectrum (*18*) come from the fact that:

$$F_h = \left\{x \middle| h(x) = h\right\} \qquad (3)$$

for each h belonging in the bounded interval of available exponents: $[h_\infty, \max h(x)]$ $(h_\infty = \min h(x))$. The collection F_h is related to the cascading properties of random variables associated to macroscopic description of the flow. In particular, they must maximize the statistical information content; however their precise determination is difficult. She and Leveque (*19*) related energy injection quantities linked to the cascade and computed in terms of thermalized averages over microcanonical ensembles $\left\langle e_r^{(p)} \right\rangle = \left\langle e_r^{p+1} \right\rangle / \left\langle e_r^p \right\rangle$, to filament structures observed in fully developed turbulence, for $p \to +\infty$. In other terms, the cascade relates geometrically to the energy injection mechanisms, it is localized, and thus must play a great role in the fluid dynamics.

Also, the set F_{h_∞} associated to the strongest transition is equal to the set of most "unpredictable" points in the turbulent flow. In the Kolmogorov description of the cascade, the power laws associated to structure functions provide only its "canonical" representation, i.e. the moments of energy dissipation "split" in function of the scale according to:

[2] Throughout this study, we consider signal images, which correspond to *d=2*.

nature geoscience

$$\left\langle \varepsilon_{r_1}^p \right\rangle = \eta_{r_1/r_2} \left\langle \varepsilon_{r_2}^p \right\rangle , \qquad (4)$$

where the laws of random variables η_r are indefinitely divisible. But since the multifractal hierarchy associated to the energy transfer between the scales can be determined by the precise computation of the singularity exponents $h(x)$, and since the values taken by $h(x)$ are a continuum, the signal $h(x)$ itself can undergo a *multiresolution analysis* (*24*):

$$L^2(\mathbb{R}^2) \supset \cdots \supset V_0 \supset V_1 \supset \cdots \supset V_n \supset V_{n+1} \supset \cdots \supset \{0\} \qquad (5)$$

The definition of a multiresolution analysis computed on the $h(x)$ is the cornerstone of the methodology which permits the propagation of physical variables across the scales for enhancing resolution: the singularity exponents defined by equation (2) are adimensional, and correspond to critical transitions in a signal. As a consequence, a multiresolution analysis computed on them approximates a microcanonical cascade for inference across the scales of the signal. Note that optimizing the inferences along the scales in complex signal analysis has been tried in somewhat different contexts of inference in pyramidal models (*25*). The algorithm for determining a super resolution ocean dynamics from low resolution data is made of two parts: the first one (**Supplementary Algorithm S1**) determines the orientation of a normalized super resolution velocity field, while the second part (**Supplementary Algorithm S2**) determines the norm. These two parts are described in the supplementary materials.

We illustrate the whole process described in supplementary algorithms S1 and S2 in Supplementary Figure S1, Figures 1, and 2A. The algorithms permit the generation of a super resolution vector field by propagating the low resolution ocean dynamics computed from altimetry and wind stress data down to the super resolution of SST data. The fundamental idea of the algorithms is to use the microcanonical cascade described by the singularity exponents (in the form of a multiresolution analysis) of the SST signal to propagate dynamic information across the scales of a turbulent physical variable. Indeed, the true multiscale information in a signal is conveyed by the transitions, i.e. the singularity exponents, not the signal itself. In our experiments, similar results are obtained by using, instead of SST, ocean color data associated to phytoplankton chlorophyll *a* concentration (acquired at the same super resolution than SST). Ocean color data records in a similar way a passive tracer chlorophyll *a*, although the remotely sensed signals are acquired over the optical depth and SST over the skin of the ocean. The resulting super resolution vector field is very similar, because the energy cascade associated to it represents equivalent transfers of energy between the scales. Please refer to the movie in the supplementary material movie S1.Validation of the results is presented in supplementary material SV. The validation experiment is conducted on four years of data from 01/01/2006 to 31/12/2009 (See Fig. 2B).

Critical exponents in nonlinear physics give access to geometric realization of the multifractal hierarchy in FDT (*19*). This multifractal hierarchy, which is related to the multiplicative

processes associated to cascading phenomena observed in turbulence, is not attainable through linear operators in signal processing, due to the lack in localization inherent to the Fourier Transform. When a multiresolution analysis (*24*) is operated on the singularity exponents, inference of physical variables is optimized along the scales of a turbulent acquisition. In this work, we show a fundamental application of this novel idea in presenting a new method for inferring a true (validated) picture of super resolution turbulent ocean dynamics at submesoscale from low resolution altimetry data and simultaneously acquired super resolution SST data: the low resolution dynamics is optimally propagated along the scales of SST transitions, down to super resolution, resulting in a true picture of ocean dynamics at super resolution. The resulting dynamics reveals the submesocale turbulence, a characteristic that is not reached in present ocean dynamics computational methods from acquired data. The method presented has phenomenal potential, as it does not make use of successive temporal acquisitions, but only of two distinct acquisitions of a physical phenomenon at different scales.

Acknowledgments:

We are sincerely grateful to the different data providers, mainly including the CERSAT, the CNES/AVISO teams, and the NASA Oceancolor team. This work is supported by CNES funding through the OST-ST proposals Hiresubcolor and Icarode.

References and Notes:

1. P. Niiler, in *Ocean Circulation and Climate Observing and Modelling the Global Ocean*, (Academic Press, 2001), vol. Volume 77, pp. 193–204.

2. S. Levitus, J. Antonov, T. Boyer, Warming of the world ocean, 1955–2003, *Geophysical Research Letters* **32**, L02604 (2005).

3. D. Chelton, J. Ries C., B. Haines J., L.-L. Fu, P. Callahan S., in *Satellite Altimetry and Earth Sciences: A Handbook of Techniques and Applications*, International geophysics series. (Lee-Lueng Fu, Anny Cazenave, 2001), vol. 69, pp. 1–122.

4. L. N. Thomas, A. Tandon, A. Mahadevan, in *Ocean Modeling in an Eddying Regime*, Geophysical Monograph Series. M. W. Hecht, H. Hasumi, Eds. (American Geophysical Union, Washington, D. C., 2008), vol. 177, pp. 17–38.

5. T. Lee *et al.*, in (Hall, J., Harrison, D.E. & Stammer, D., Eds., ESA Publication WPP-306., 2009).

6. A. E. Gargett, Ocean Turbulence, *Annual Review of Fluid Mechanics* **21**, 419–451 (1989).

7. D. B. Chelton, M. G. Schlax, M. H. Freilich, R. F. Milliff, Satellite Measurements Reveal Persistent Small-Scale Features in Ocean Winds, *Science February 13, 2004* **303**, 978–983 (2004).

8. R. J. Small *et al.*, Air-sea interaction over ocean fronts and eddies, *Dynamics of Atmospheres and Oceans* **45**, 274–319 (2008).

9. P. S. Liss, M. T. Johnson, *Ocean-Atmosphere Interactions of Gases and Particles* (Springer Open, Spinger Earth Systems Sciences., 2014).

10. J. Jimenez, Oceanic turbulence at millimeter scales, *Scientia Marina* **61 (Suppl.1)**, 1–6 (1997).

11. V. C. Garçon, A. Oschlies, S. C. Doney, D. McGillicuddy, J. Waniek, The role of mesoscale variability on plankton dynamics in the North Atlantic, *Deep-Sea Res., Part II* **48**, 2199–2226 (2001).

12. E. Tew Kai *et al.*, Top marine predators track Lagrangian coherent structures, *Proc. Natl. Acad. Sci. U. S. A.* **106**, 8245 – 8250 (2009).

13. P. S. Sabarros, F. Ménard, J.-J. Lévénez, E. TewKai, J. Ternon, Mesoscale eddies influence distribution and aggregation patterns of micronekton in the Mozambique Channel, *Mar Ecol Prog Ser* **395**, 101–107 (2009).

14. U. Frisch, *Turbulence : The Legacy of A. N. Kolmogorov* (Cambridge University Press, Cambridge University Press., 1995).

15. J. Leray, Sur le mouvement d'un liquide visqueux emplissant l'espace, *Acta Math.* **63**, 193–248 (1934).

16. B. K. Arbic, K. L. Polzin, R. B. Scott, J. G. Richman, J. F. Shriver, On Eddy Viscosity, Energy Cascades, and the Horizontal Resolution of Gridded Satellite Altimeter Products*, *Journal of Physical Oceanography* **43**, 283–300 (2013).

17. A. Turiel, H. Yahia, C. J. Pérez-Vicente, Microcanonical multifractal formalism—a geometrical approach to multifractal systems: Part I. Singularity analysis, *J. Phys. A: Math. Theor.* **41**, 015501 (2008).

18. G. Parisi, U. Frisch, in *Turbulence and Predictability in Geophysical Fluid Dynamics*, Proc. Intl. School of Physics E. Fermi. (M. Ghil, R. Benzi, G. Parisi, Amsterdam, North Holland, 1985), pp. 84–87.

19. Z.-S. She, E. Leveque, Universal scaling laws in fully developed turbulence, *Phys. Rev. Lett.* **72**, 336 (1994).

20. J. Sudre, C. Maes, V. Garçon, On the global estimates of geostrophic and Ekman surface currents, *Limnology & Oceanography: Fluids & Environments* **3**, 1–20 (2013).

21. F. d' Ovidio, V. Fernández, E. Hernández-García, C. López, Mixing structures in the Mediterranean Sea from finite-size Lyapunov exponents, *Geophys. Res. Lett.* **31**, L17203 (2004).

22. H. E. Stanley, *Introduction to Phase Transitions and Critical Phenomena* (Oxford University Press., 1987).

23. O. Pont, A. Turiel, H. Yahia, in *Combinatorial Image Analysis*, Lecture Notes in Computer Science. J. K. Aggarwal, R. P. Barneva, V. E. Brimkov, K. N. Koroutchev, E. R. Korutcheva, Eds. (Springer Berlin Heidelberg, 2011), pp. 346–357.

24. S. Mallat, *A Wavelet Tour of Signal Processing : The sparse way* (Academic Press, ed. 3rd, 2008).

25. M. J. Choi, V. Chandrasekaran, D. M. Malioutov, J. K. Johnson, A. S. Willsky, Multiscale stochastic modeling for tractable inference and data assimilation, *Computer Methods in Applied Mechanics and Engineering* **197**, 3492–3515 (2008).

nature geoscience

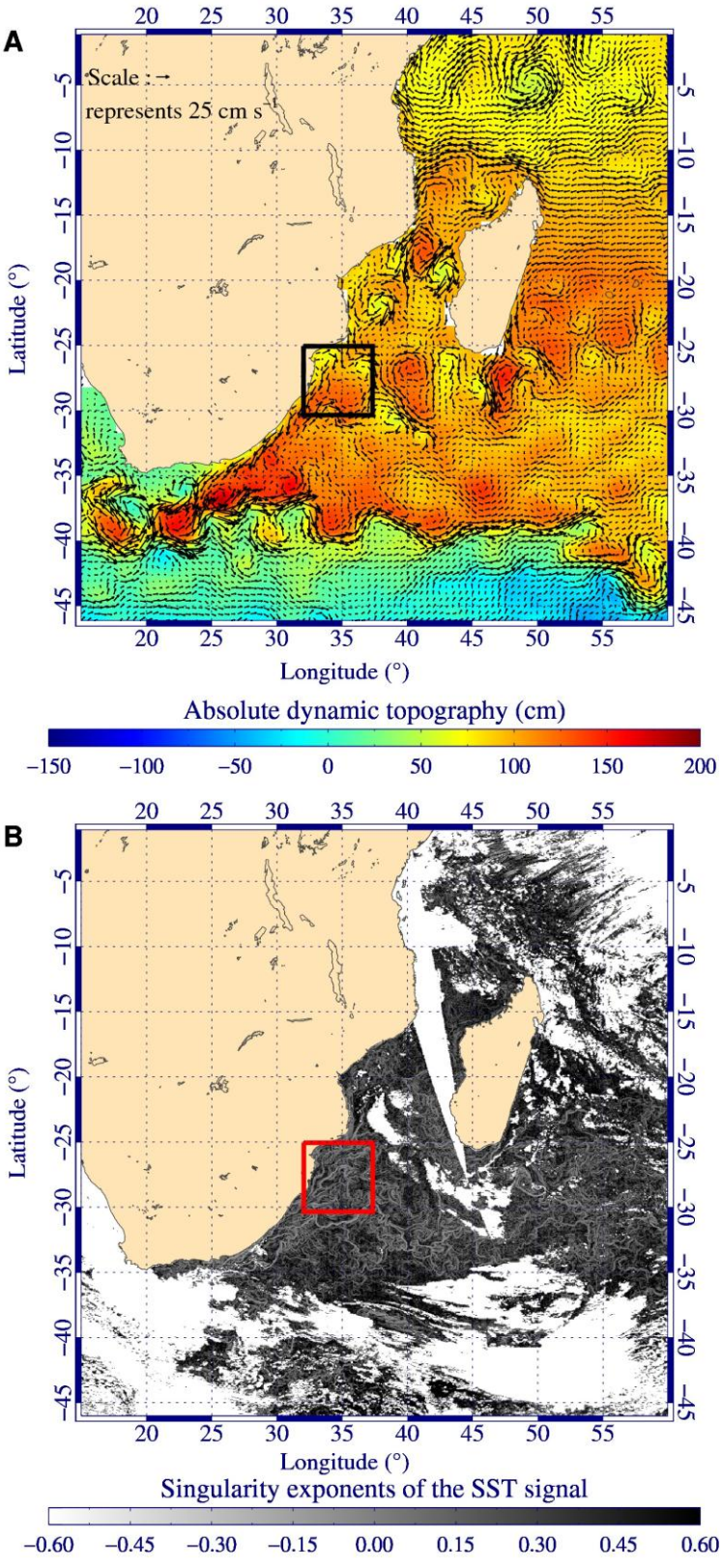

nature geoscience

Fig. 1. Oceanic satellite data in the southwestern part of the Indian Ocean represented by the dotted square in Suppl. Fig S1 where we compute oceanic circulation at super resolution on 4-year data. (**A**) Representation of the GEKCO quarter degree currents (vector field) with an overlaid of ADT for the 02/08/2007, in the southwestern part of the Indian Ocean. (**B**) This map represents the singularity exponents derived from SST signal (see Suppl. Fig. S1B). The transition fronts (light curves) represent areas where the temperature gradients are important in the ocean delimiting the oceanic coherent structures at different scales.

nature geoscience

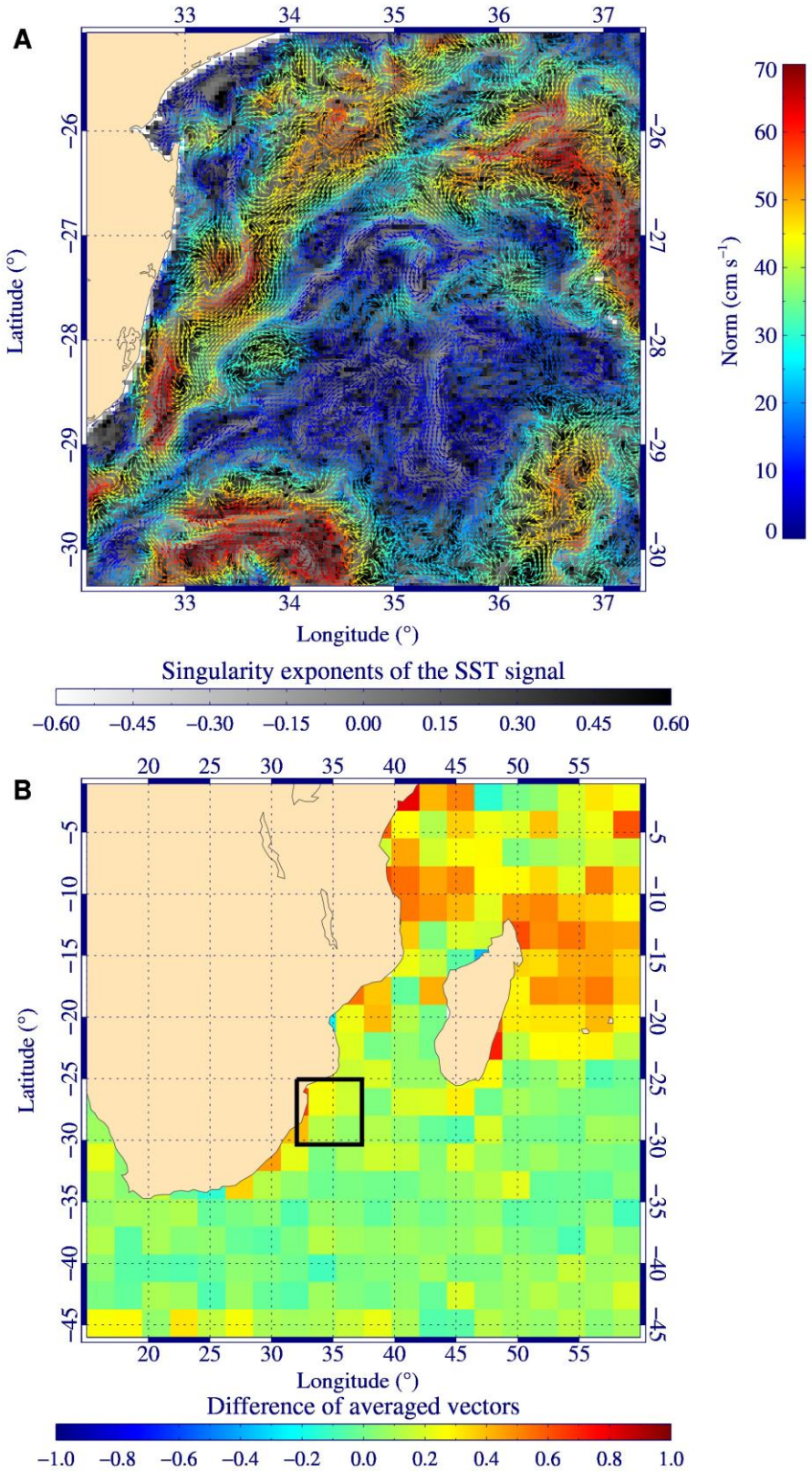

nature geoscience

Fig. 2. (**A**) Turbulent vector field obtained by multiresolution analysis using the GEKCO currents at low resolution and the singularity exponents of the SST signal at super resolution to propagate the turbulent dynamics across the scales. Due to the high density of the resulting vector field, it is shown only inside the black solid line square drawn on Figure 1A. (**B**) Difference of the averaged vectors corresponding to the validation experiment conducted on four years of data from 01/01/2006 to 31/12/2009.

nature geoscience

Supplementary Materials for

Title: Ocean Turbulent Dynamics at Super Resolution: A True Picture

Authors: J. Sudre[1,*]; H. Yahia[2]; O. Pont[2]; V. Garçon[1]

Affiliations:

[1] CNRS/LEGOS, UMR 55 66 (CNRS, CNES, IRD, UPS), Observatoire Midi-Pyrénées, 14 Avenue Edouard Belin, 31400 Toulouse, France.

[2] INRIA, 200 rue de la Vieille Tour, 33405 Talence Cedex, France.

*Correspondence to: joel.sudre@legos.obs-mip.fr

nature geoscience

Materials and Methods

Description of input data Supplementary Material SM1

i. The so-called GEKCO product at low resolution 1/4° (*20*) is used to access to the ocean dynamics. It is the sum of geostrophic and Ekman components and is derived from altimetry (see Supplementary Fig. S1A, map of absolute dynamic topography – ADT – available on the AVISO website - http://www.aviso.oceanobs.com) and from wind stress product (not shown) provided by the KU-band microwave scatterometer onboard the QuickSCAT satellite, distributed by the Centre ERS d'Archivage et de Traitement (CERSAT).

ii. The super resolution of MODIS-AQUA Level 3b Sea Surface Temperature (daily SST, acquired at 1/24° corresponding to pixel size of 4kms), delivered by NASA (http://oceancolor.gsfc.nasa.gov); see Supplementary Figure S1B.

Supplementary Algorithm 1

Input data:

- Singularity exponents $h(x)$ of super-resolution SST signal (resolution: r_1).
- Unitary vector field $g(x,r_2)$ at low resolution $r_2 < r_1$ given by the GEKCO product (see above).

Step 1. Compute a multiresolution analysis associated to signal $h(x)$:

$$h(x,r_j) = \sum_{n\in\mathbb{Z}} \langle h|\psi_{j,n}\rangle\, \psi_{j,n} \qquad \text{(Supplementary Equation S1)}$$

Step 2. At low resolution r_2, compute a low resolution version of the singularity exponents $h(x,r_2)$, then their gradients $\nabla h(x,r_2)$ rotated according to a fixed convention: $-\pi/2$. This procedure gives a vector field $z(x,r_2)$ at resolution r_2.

Step 3. Compute the scalar products $\langle g|z\rangle$, which defines a signal $s(x,r_2)$ at low resolution r_2.

Step 4. Using the multiresolution analysis (Supplementary Equation S1), generate a super resolution version of signal $s(x,r_1)$.

Step 5. At super resolution r_1, compute the vector field $\nabla h(x,r_1)$ rotated by the same convention as in Step2, and post-filter it with kernel $k(f) = 1/\|f\|$ in Fourier space, to obtain a vector field $w(x,r_1)$. This post-filtering reduces the contribution of spurious data.

Output data:

- Normalized vector field $w(x,r_1)/\|w(x,r_1)\|$ at super resolution r_1.

The output of this Supplementary Algorithm 1 is a unitary vector field at super resolution. Supplementary Algorithm 2 restores the values of the norms at super resolution.

nature geoscience

Supplementary Algorithm 2

Input data:

- SST signal at super resolution: r_1.
- At low resolution r_2, norm of the GEKCO product.

Step 1. Compute an approximated stream function $\Xi(x, r_1)$ at super resolution using SST data and its Most Singular Manifold (*17*, *26*, *27*).

Step 2. Generate a multiresolution analysis (Supplementary Equation S1) associated to signal Ξ

Step 3. Using the multiresolution analysis (Suppplementary Equation S1) associated to signal Ξ, generate at super resolution the norm of the GEKCO product: $\|v(x, r_1)\|$.

Output data:

- Normed vector field $\|v(x, r_1)\| \times w(x, r_1) / \|w(x, r_1)\|$ at super resolution r_1.

Supplementary Validation SV

To validate the results, we use a set of 373 drifters (corresponding to 222334 drifter positions) drogued at 15-m depth during the period from 01 January 2006 to 31 December 2009 from the Global Drifter Program at the Atlantic Oceanographic and Meteorological Laboratory (AOML). Since the buoys display an integrated trajectory computed other a time interval of six hours, it is difficult to separate the submesoscale variability from the mesoscale variability in the buoy data. Consequently, we perform validation in the following manner; the ocean surface is divided into square areas of size 2.25° x 2.25°. Let M be a given square area. In M we have two datasets, namely the buoy data and the computed currents at the location of the buoys:

$$M_b = \{u_1, u_2, ..., u_n\} \qquad \text{(Supplementary Equation S2)}$$

$$M_c = \{w_1, w_2, ..., w_n\} \qquad \text{(Supplementary Equation S3)}$$

In each set an averaged vector is computed:

$$a = \frac{1}{n} \sum_{i=1}^{n} \frac{u_i}{\|u_i\|} \qquad \text{(Supplementary Equation S4)}$$

$$b = \frac{1}{n} \sum_{i=1}^{n} \frac{w_i}{\|w_i\|} \qquad \text{(Supplementary Equation S5)}$$

nature geoscience

Then in each box M we display the value $\|a\| - \|b\|$. The validation experiment is conducted on four years of data ranging from 01/01/2006 to 31/12/2009 (See Fig. 2B).

nature geoscience

Supplementary Figure S1.

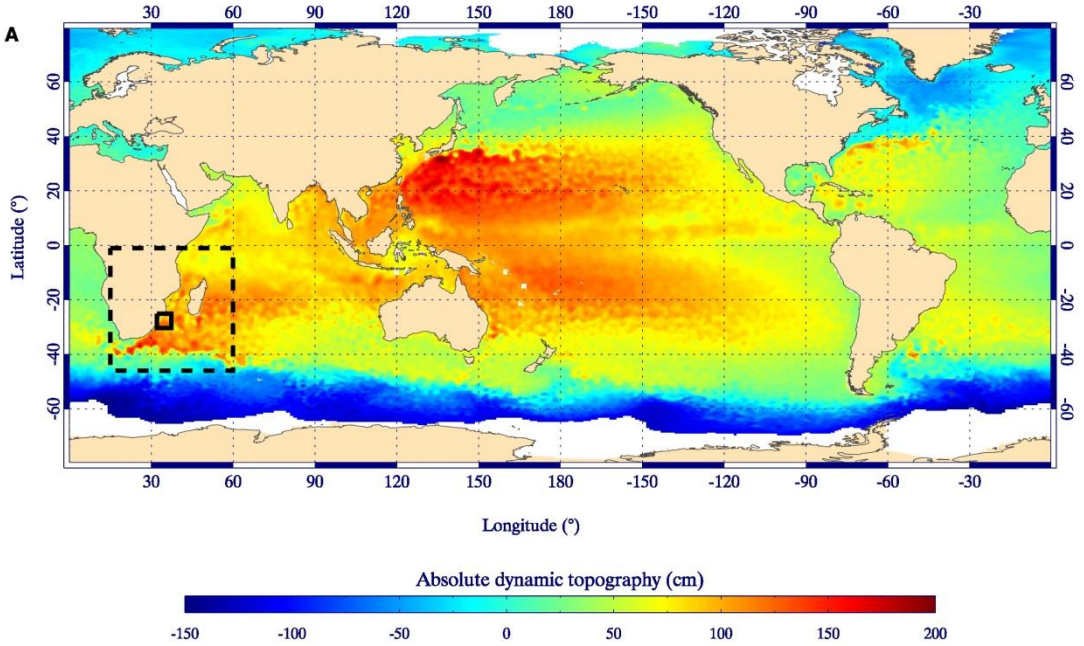

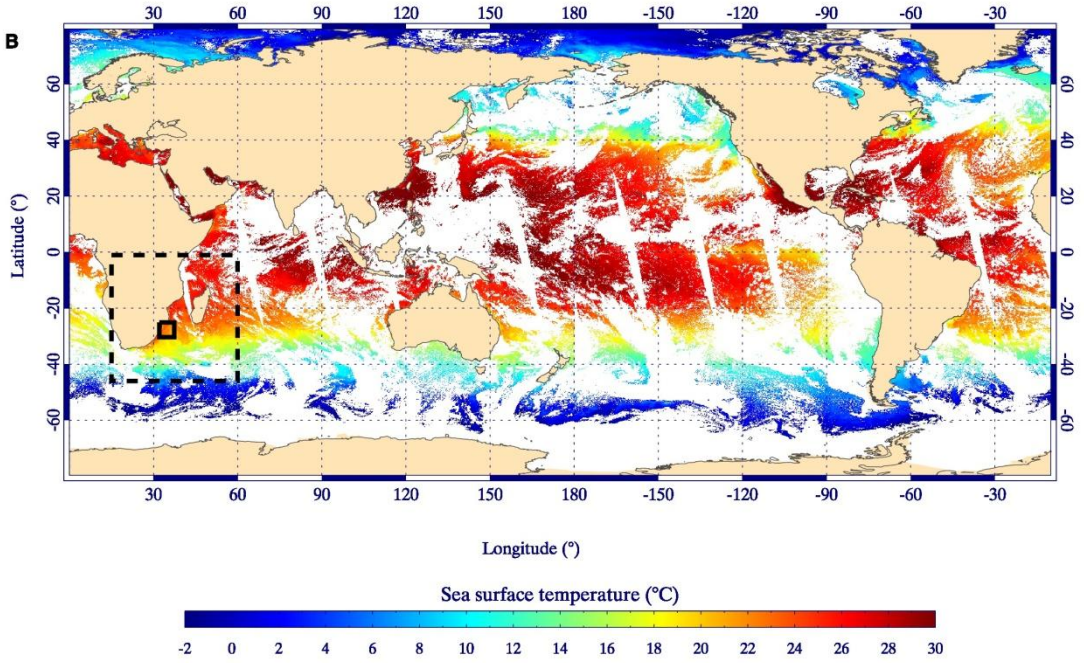

nature geoscience

Suppl. Fig. S1. Oceanic satellite data: in the lower left part of the figure are depicted two subareas; the dotted square shows the region where we compute oceanic circulation at super resolution on 4-year data and the solid line square delimits the region shown in Supplementary Fig S2A.) Oceanic currents result from movements of fluid particles in response to internal forces (pressure gradient and Coriolis forces), external forces (gravity force) and frictional forces (dominated in the surface ocean by wind stress). Steady ocean currents derive from balances between these different forces. A primary balance is between the horizontal pressure gradient and the Coriolis force, resulting in "geostrophic flow". This map represents the Absolute Dynamic Topography (ADT - cm) on 02/08/2007, giving access to that pressure gradient. From this ADT we derive the geostrophic component of the current at low resolution (see Fig. 1A) which will serve as one of the input data for the energy cascade. (**B**) This map represents the Sea Surface Temperature (SST – Celcius degree) at 1/24° (super resolution, pixel size ~4kms) on 02/08/2007 provided by Modis Aqua sensor on Near Infra-Red band (11 µm daytime). The associated wavelengths cannot penetrate through the clouds, resulting in large areas of missing data, adding to other missing data resulting from the limited swath of the sensor. This super resolution SST data is used in the work presented herein to compute the turbulent energy cascade associated to the dynamics of the flow and, consequently, to infer the propagation of the dynamics from the low resolution (~ 25kms) of altimetry data down to super resolution (~ 4kms).

nature geoscience

Supplementary Movie S1

We have realized a demonstration movie entitled "Ocean turbulent dynamics at super resolution: A true picture". This movie shows the turbulent ocean dynamics at SST resolution of 4 kms computed from SST microcanonical cascade and low resolution GEKCO product for year 2006 over the southwestern part of the Indian Ocean. We replace the missing data in SST MODIS product (clouds, satellite swath) by corresponding data available from Operational Sea Surface Temperature and Sea Ice Analysis (OSTIA) provided by the Group for High Resolution Sea Surface Temperature (GHRSST) project (*28*) which is however of lower quality. Two images per day are generated for the whole year 2006. The resulting images show the norm of the vector field in the background rendered using the LIC (Line Integrated Convolution) algorithm. In the foreground we show the resulting vector field in a linear greyscale colormap. The supplementary movie is downloadable by following the link: http://geostat.bordeaux.inria.fr/exj1309/annee2006_SHORTER_2ipj.mov. The size of the supplementary movie is ~800 Mo of high resolution data.

References

1. P. Niiler, in *Ocean Circulation and Climate Observing and Modelling the Global Ocean*, (Academic Press, 2001), vol. Volume 77, pp. 193–204.

2. S. Levitus, J. Antonov, T. Boyer, Warming of the world ocean, 1955–2003, *Geophysical Research Letters* **32**, L02604 (2005).

3. D. Chelton, J. Ries C., B. Haines J., L.-L. Fu, P. Callahan S., in *Satellite Altimetry and Earth Sciences: A Handbook of Techniques and Applications*, International geophysics series. (Lee-Lueng Fu, Anny Cazenave, 2001), vol. 69, pp. 1–122.

4. L. N. Thomas, A. Tandon, A. Mahadevan, in *Ocean Modeling in an Eddying Regime*, Geophysical Monograph Series. M. W. Hecht, H. Hasumi, Eds. (American Geophysical Union, Washington, D. C., 2008), vol. 177, pp. 17–38.

5. T. Lee *et al.*, in (Hall, J., Harrison, D.E. & Stammer, D., Eds., ESA Publication WPP-306., 2009).

6. A. E. Gargett, Ocean Turbulence, *Annual Review of Fluid Mechanics* **21**, 419–451 (1989).

7. D. B. Chelton, M. G. Schlax, M. H. Freilich, R. F. Milliff, Satellite Measurements Reveal Persistent Small-Scale Features in Ocean Winds, *Science February 13, 2004* **303**, 978–983 (2004).

8. R. J. Small *et al.*, Air-sea interaction over ocean fronts and eddies, *Dynamics of Atmospheres and Oceans* **45**, 274–319 (2008).

9. P. S. Liss, M. T. Johnson, *Ocean-Atmosphere Interactions of Gases and Particles* (Springer Open, Spinger Earth Systems Sciences., 2014).

10. J. Jimenez, Oceanic turbulence at millimeter scales, *Scientia Marina* **61 (Suppl.1)**, 1–6 (1997).

11. V. C. Garçon, A. Oschlies, S. C. Doney, D. McGillicuddy, J. Waniek, The role of mesoscale variability on plankton dynamics in the North Atlantic, *Deep-Sea Res., Part II* **48**, 2199–2226 (2001).

12. E. Tew Kai *et al.*, Top marine predators track Lagrangian coherent structures, *Proc. Natl. Acad. Sci. U. S. A.* **106**, 8245 – 8250 (2009).

nature geoscience

13. P. S. Sabarros, F. Ménard, J.-J. Lévénez, E. TewKai, J. Ternon, Mesoscale eddies influence distribution and aggregation patterns of micronekton in the Mozambique Channel, *Mar Ecol Prog Ser* **395**, 101–107 (2009).

14. U. Frisch, *Turbulence : The Legacy of A. N. Kolmogorov* (Cambridge University Press, Cambridge University Press., 1995).

15. J. Leray, Sur le mouvement d'un liquide visqueux emplissant l'espace, *Acta Math.* **63**, 193–248 (1934).

16. B. K. Arbic, K. L. Polzin, R. B. Scott, J. G. Richman, J. F. Shriver, On Eddy Viscosity, Energy Cascades, and the Horizontal Resolution of Gridded Satellite Altimeter Products*, *Journal of Physical Oceanography* **43**, 283–300 (2013).

17. A. Turiel, H. Yahia, C. J. Pérez-Vicente, Microcanonical multifractal formalism—a geometrical approach to multifractal systems: Part I. Singularity analysis, *J. Phys. A: Math. Theor.* **41**, 015501 (2008).

18. G. Parisi, U. Frisch, in *Turbulence and Predictability in Geophysical Fluid Dynamics*, Proc. Intl. School of Physics E. Fermi. (M. Ghil, R. Benzi, G. Parisi, Amsterdam, North Holland, 1985), pp. 84–87.

19. Z.-S. She, E. Leveque, Universal scaling laws in fully developed turbulence, *Phys. Rev. Lett.* **72**, 336 (1994).

20. J. Sudre, C. Maes, V. Garçon, On the global estimates of geostrophic and Ekman surface currents, *Limnology & Oceanography: Fluids & Environments* **3**, 1–20 (2013).

21. F. d' Ovidio, V. Fernández, E. Hernández-García, C. López, Mixing structures in the Mediterranean Sea from finite-size Lyapunov exponents, *Geophys. Res. Lett.* **31**, L17203 (2004).

22. H. E. Stanley, *Introduction to Phase Transitions and Critical Phenomena* (Oxford University Press., 1987).

23. O. Pont, A. Turiel, H. Yahia, in *Combinatorial Image Analysis*, Lecture Notes in Computer Science. J. K. Aggarwal, R. P. Barneva, V. E. Brimkov, K. N. Koroutchev, E. R. Korutcheva, Eds. (Springer Berlin Heidelberg, 2011), pp. 346–357.

24. S. Mallat, *A Wavelet Tour of Signal Processing : The sparse way* (Academic Press, ed. 3rd, 2008).

25. M. J. Choi, V. Chandrasekaran, D. M. Malioutov, J. K. Johnson, A. S. Willsky, Multiscale stochastic modeling for tractable inference and data assimilation, *Computer Methods in Applied Mechanics and Engineering* **197**, 3492–3515 (2008).

26. Yahia H., Sudre J., Pottier C., Garçon V., Motion analysis in oceanographic satellite images using multiscale methods and the energy cascade, *Pattern Recognition* **43**, 35913604 (2010).

27. S. K. Maji, O. Pont, H. Yahia, J. Sudre, Inferring Information across Scales in Acquired Complex Signals, *European Conference on Complex Systems,ECCS'12* (2012).

28. C. J. Donlon *et al.*, The Operational Sea Surface Temperature and Sea Ice Analysis (OSTIA) system, *Remote Sensing of Environment* **116**, 140–158 (2012).

Annexe B : Articles cités dans ce manuscrit

Annexe B

Annexe B : Articles cités dans ce manuscrit dont je suis co-auteurs

Sommaire

B.1 Article : Homing in green turtles Chelonia mydas : oceanic currents act as a constraint rather than as an information source, C. Girard *et al.*, 2006 323

B.1.1 Abstract 323

B.1.2 Article publié dans *Marine Ecology Progress Series* 323

B.2 Article : Marine Turtles Use Geomagnetic Cues during Open-Sea Homing, P. Luschi *et al.*, 2007 333

B.2.1 Abstract 333

B.2.2 Article publié dans *Current Biology* 333

B.3 Article : Comparative study of mixing and biological activity of the Benguela and Canary upwelling systems, V. Rossi *et al.*, 2008 342

B.3.1 Abstract 342

B.3.2 Article publié dans *Geophysical Research Letters* 342

B.4 Article : Top marine predators track Lagrangian coherent structures, E. Tew Kai *et al.*, 2009 348

B.4.1 Abstract 348

B.4.2 Article publié dans *Proceedings of the National Academy of Sciences* 348

B.5 Article : Surface mixing and biological activity in the four Eastern Boundary Upwelling Systems, V. Rossi *et al.*, 2009 . . 355

B.5.1 Abstract 355

B.5.2 Article publié dans *Nonlinear Processes in Geophysics* . . . 355

B.1 Article : Homing in green turtles Chelonia mydas : oceanic currents act as a constraint rather than as an information source, C. Girard *et al.*, 2006

B.1.1 Abstract

As open sea navigators, green turtles Chelonia mydas have to deal with oceanic currents. These currents may have a mechanical influence, forcing turtles away from their desired course, but they may also provide information to navigating turtles by bringing chemical cues downcurrent from their target area. In the present paper, we have introduced new path analysis methods, coupling remote-sensing oceanographic data and satellite-tracking data in order to test these hypotheses. These methods were exemplified on the homing routes of 3 green turtles nesting on Europa, an isolated island in the southern part of Mozambique Channel. The turtles, displaced by ship east-southeast from Europa, returned to their nesting island in 13 to 59 d, following long, circuitous routes, and hence apparently displaying poor navigational abilities. Path analysis showed that turtles were unable to compensate for the deflecting action of currents, which moved them away from their intended course and lowered their orientation performance. At large distances from Europa, green turtles did not appear to find navigational information in water masses that had previously been in contact with their target area.

B.1.2 Article publié dans *Marine Ecology Progress Series*

Référence : Girard C., Sudre J., Benhamou S., Roos D. and Luschi P, 2006 : Homing in green turtles Chelonia mydas : oceanic currents act as a constraint rather than as an information source, *Marine Ecology Progress Series*, **322**, 281-289, DOI 10.3354/meps322281.

Vol. 322: 281–289, 2006 | MARINE ECOLOGY PROGRESS SERIES
Mar Ecol Prog Ser | Published September 20

Homing in green turtles *Chelonia mydas*: oceanic currents act as a constraint rather than as an information source

Charlotte Girard[1], Joël Sudre[2], Simon Benhamou[3,*], David Roos[4], Paolo Luschi[5]

[1]Institut de Recherche pour le Développement, Centre de la Réunion, BP 172, 97492 Sainte Clotilde, La Réunion, France
[2]Laboratoire d'Études en Geophysique et Océanographie Spatiales, CNRS, 18 av. Edouard Belin, 31401 Toulouse Cedex 9, France
[3]Centre d'Écologie Fonctionelle et Évolutive, CNRS, 1919 route de Mende, 34293 Montpellier Cedex 5, France
[4]Ressources Halieutiques, IFREMER, BP 60, 97822 Le Port, La Réunion, France
[5]Dipartimento di Biologia, University of Pisa, 6 via Volta, 56126 Pisa, Italy

ABSTRACT: As open sea navigators, green turtles *Chelonia mydas* have to deal with oceanic currents. These currents may have a mechanical influence, forcing turtles away from their desired course, but they may also provide information to navigating turtles by bringing chemical cues downcurrent from their target area. In the present paper, we have introduced new path analysis methods, coupling remote-sensing oceanographic data and satellite-tracking data in order to test these hypotheses. These methods were exemplified on the homing routes of 3 green turtles nesting on Europa, an isolated island in the southern part of Mozambique Channel. The turtles, displaced by ship east-southeast from Europa, returned to their nesting island in 13 to 59 d, following long, circuitous routes, and hence apparently displaying poor navigational abilities. Path analysis showed that turtles were unable to compensate for the deflecting action of currents, which moved them away from their intended course and lowered their orientation performance. At large distances from Europa, green turtles did not appear to find navigational information in water masses that had previously been in contact with their target area.

KEY WORDS: Current drift · Homing · Navigation · Oceanography · Satellite telemetry · Sea turtle

Resale or republication not permitted without written consent of the publisher

INTRODUCTION

Sea turtles migrate for hundreds or thousands of kilometres between their foraging grounds and their nesting sites (Papi & Luschi 1996, Lohmann et al. 1999). During these migrations in the open sea, oceanic currents are likely to influence turtles' movements (Luschi et al. 2003), but the way they affect turtle navigational efficiency is very poorly understood. First, oceanic currents play an obvious mechanical role. The force that currents exert on a turtle resolves into a forward–backward (body-axis aligned) component, which speeds up or slows down the turtle, and a lateral component, which tends to make it drift away from the intended route. This deflecting action may be particularly harmful by leading turtles away from the optimal route. Oceanic currents may also act as an information source providing navigational clues. Green turtles migrating from Brazil to Ascension Island, for instance, have been hypothesised to find their way thanks to a water-borne chemical plume downstream of the goal island (Koch et al. 1969), although homing experiments specifically conducted on Ascension turtles (Luschi et al. 2001) did not confirm this hypothesis.

To fully understand the mechanical action of the currents, it is worth distinguishing between 2 different, independent but complementary ways of dealing with the passive displacement they induce. The first way, which applies to any passive displacement (including

*Corresponding author. Email: simon.benhamou@cefe.cnrs.fr
© Inter-Research 2006 · www.int-res.com

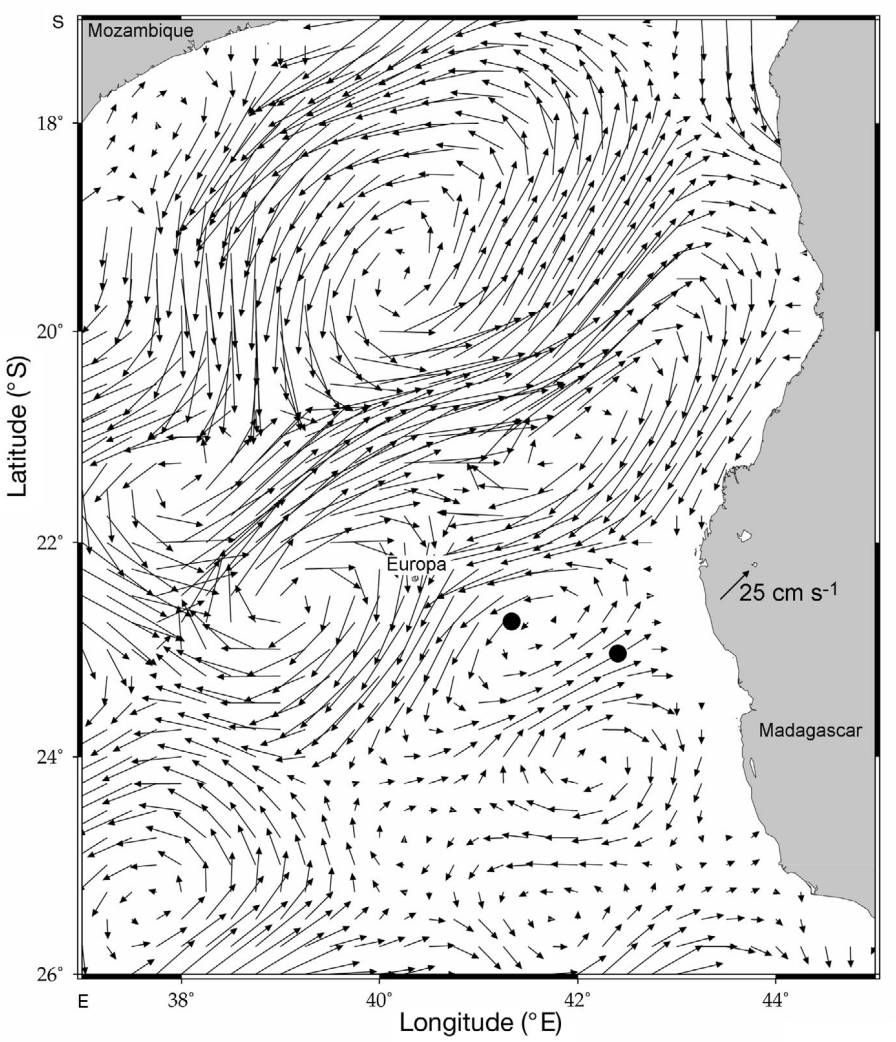

Fig. 1. Surface oceanic currents in the southern part of the Mozambique Channel, 4 d after release of turtles (*Chelonia mydas*). At this time, surface currents around Europa were mainly generated by 2 cyclonic eddies (low sea level anomalies, which turn clockwise in the southern hemisphere) to the northeast and the southwest of the island, and by an anticyclonic eddy to the southeast (●: release sites)

man-made passive displacement as occurring in homing experiments), rests on the ability of an animal to correct for the displacement. It implies that the animal relies on a location-based navigation process that enables it to orientate toward the goal whatever its own location, rather than on a fixed compass-based direction (e.g. genetically encoded; see Berthold 2003). The second way, which can apply only to passive displacements due to movements of the surrounding medium (air or water), rests on the ability of the animal to compensate for the unwanted drift by adopting a biased heading such that the resultant movement points to the goal (Green & Alerstam 2002). For example, an animal migrating northward that is aware that it is being exposed to an eastward wind drift with a 0.7 speed ratio should head northwestward to maintain its track northward. In other words, displacement correction involves the ability to correctly estimate the goal direction from any location, whereas drift compensation involves the ability to head in a shifted direction, in order to get a resultant direction corresponding to the estimated goal direction. If an animal is able to both correct and compensate, it should adopt headings that are less homeward oriented than the resultant track. Conversely, a homeward tendency that is more accurate for headings than for the track would indicate correction without compensation. In the absence of ground features, which are thought to play a key role in wind drift compensation for birds migrating over land, testing the ability of a homing pelagic animal to compensate for an oceanic current drift may provide valuable insights about the navigation process used (see 'Discussion').

To investigate how sea turtles moving toward a specific target deal with oceanic currents, we developed new methods of path analysis and exemplified them on the homing paths of 3 female green turtles *Chelonia mydas* nesting on Europa, a small isolated atoll (7 to 8 km in diameter) located in the middle of the southern Mozambique Channel. This oceanographic area is highly dynamic, being swept by an intermittent train of large anticyclonic eddies (each roughly 200 km in diameter), leading to a predominant southward water transport along the African coast (Schouten et al. 2003, Quartly & Srokosz 2004). In late November 2003, the turtles were displaced away from their nesting island to distant open sea sites, and were tracked by satellite. As this date is early in the nesting season on Europa, the turtles were assumed to be highly motivated to get back to the island to complete their nesting cycle (Luschi et al. 2001). Since the goal of these turtles was a specific isolated island, this homing experiment provided a well-defined reference for the turtles' intended direction and was therefore particularly well suited to test the influence of oceanic currents on sea turtle navigation. In this way, we were able to explore both whether green turtles are able to correct for passive displacement and whether they can,

in some way, compensate for current drift while moving in the oceanic environment. In addition, we tested whether they obtain useful navigational information from the water masses that have previously been in contact with the target area.

MATERIALS AND METHODS

Turtles and satellite tracking. Three adult green turtles *Chelonia mydas* (curved carapace length between 107 and 115 cm) were caught by night on a beach on Europa (22°20′S, 40°21′E), kept in individual wooden crates, and then loaded on a ship to be displaced. During transportation, they were kept shaded and wet. Two turtles were individually released at 115 km east-southeast of Europa in the afternoon, and the third one was released at 245 km in the same direction by night. They were equipped with Argos satellite transmitters (Telonics ST-20), attached to the carapace with fibre glass cloth and epoxy resin. Location data were filtered out as follows. First, Argos locations of poorest quality (Class B) were discarded. The speed between successive remaining locations was computed, and locations leading to values >10 km h^{-1} were discarded. Afterwards, filtered locations were 'standardised' as a fix every 4 h by linear time interpolation. In this way, for each turtle, we obtained a ground-related 'track path' in the form of a sequence of purely spatial track vectors that join any given location and the location occurring 4 h later.

Oceanic currents. As upper-layer dives predominate during oceanic movements of green turtles (Hays et al. 2001), currents experienced by turtles in the open ocean could be estimated based on satellite-derived oceanographic data (Fig. 1). To this end, we computed the surface current velocity as the sum of geostrophic and Ekman components, which are assumed to account for the lowest-order dynamics. They were obtained independently from remote sensing data on sea surface height and wind stress. The geostrophic component, resulting from the balance between the horizontal pressure gradient force and the Coriolis force, was calculated as the sum of the mean surface geostrophic current, estimated from climatological data (Rio & Hernandez 2004), and the surface geostrophic current anomalies. These current anomalies were calculated from surface topographic slope anomalies, which were derived from altimetric sea level anomalies issued from the combined processing of Topex-Poseidon and ERS-1/2 data (Ducet et al. 2000), available weekly on a ⅓° Mercator projection grid. The Ekman component, resulting from the balance between friction by wind and the Coriolis force, was estimated for the surface layer (15 m depth) by applying a regression model (Van Meurs & Niiler 1997, Lagerloef et al. 1999) on weekly wind stress data provided by Quikscat on a ½° regular projection grid. Both geostrophic and wind stress data underwent a bi-linear spatial interpolation, leading to ¼° velocity fields, and then a time linear interpolation to obtain such fields on a daily basis.

Turtle movement analysis with respect to currents. For each turtle's interpolated location, we computed 3 velocities: (1) the track velocity, obtained by dividing the purely spatial track vector by 0.144 (to convert km to cm s^{-1}); (2) the current velocity, calculated by spatial bi-linear interpolation at the turtle's location of the daily surface current fields derived from the computations previously described; and (3) the heading velocity, computed as the difference between the track and current velocities (Fig. 2), which thus expresses the turtles' actual forward movement. By removing the current movement component in this way, we obtained a water-related 'motor path' in the form of the sequence of purely spatial heading vectors (obtained by multiplying the heading velocities by 0.144) from each turtle's ground-related track path.

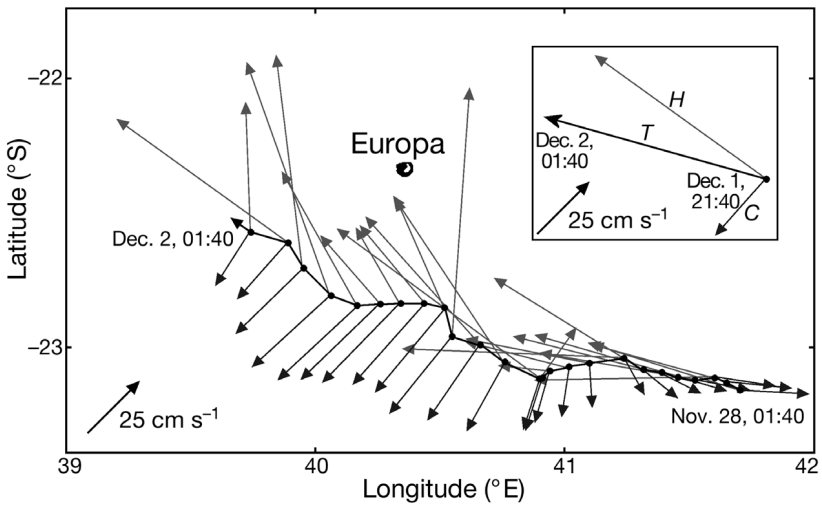

Fig. 2. *Chelonia mydas.* Section of track path recorded over 4 d for Turtle T2. (●): turtle's location every 4 h; dark and light grey vectors are current (*C*) and heading (*H*) velocities, respectively, scale given by 25 cm s^{-1} vector length; spatial track path scale given by latitudes (1° ≈ 111.12 km). Inset illustrates principle of heading vector determination, exemplified by final 4 h step of this track path section. Heading velocity (cm s^{-1}) is computed by subtracting current velocity (cm s^{-1}) from track velocity *T* (black vector; cm s^{-1}), obtained by dividing track vector (km) by 0.144

To measure the orientation efficiency and to test whether the turtles compensated for the current drift, we measured the heading and track 'homeward components' as the cosines of the angular differences between the home direction and the directions of the heading and track vectors, respectively. This was done in 2 different ways. (1) The orientation efficiency of a homing path (O) can be reliably estimated as the average of the homeward components measured along the path at a very high spatial frequency (see Benhamou 2004). This applies to 'track paths' (O_t) as well as to 'motor paths' (O_m). The value obtained for a track path is also equal to the ratio of the beeline distance from the release site to the home over the total path length (straightness index), but this practical proxy is not suitable for motor paths, because the goal location is fixed in the ground-related system of reference but not in the water-related system of reference. In practice, the motor and track paths were rediscretised with a small constant step length l (l = 1 km in the present study) and, hence, appear as sequences of s steps with orientation θ_i, for i = 1, 2… s, starting at location (x_0, y_0) and ending at location (x_s, y_s). The orientation efficiency was then computed as $O = \sum_{i=1}^{s}\cos(\theta_i - \gamma_{i-1})/s$, where γ_i is the goal direction at location (x_i, y_i). (2) To test for possible drift compensation, we computed the track and heading homeward components at locations in 4 h intervals when the current speed was >25 cm s^{-1}. Measuring successive movement vectors of an oriented path, however, may result in autocorrelated angular values because of some forward persistence propensity (Benhamou 2006). Although this autocorrelation does not tend to bias the mean value obtained in the long term, it artificially increases the apparent sample size and hence may lead to erroneous rejections of the null hypothesis. Since autocorrelation obviously decreases when the locations involved become more spaced out, we sub-sampled the data by taking only one measurement every n locations into account, where n is the minimum integer value allowing for statistically independent directions for both heading and track vectors expressed relative to Europa direction (using an angular rank correlation test set at p = 0.10; see Batschelet 1981). We then compared the heading and track homeward components obtained for each turtle using Wilcoxon signed ranks test. If a turtle were compensating for the current drift, she should have adopted biased headings such that the resultant movement (track) pointed to Europa: in such a case the mean homeward component should be significantly higher for track vectors than for heading vectors. Conversely, a mean homeward component significantly lower for track vectors than for heading vectors would indicate no drift compensation.

Turtle heading analysis with respect to water mass origin. Finally, to determine whether oceanic currents may have been an information source, we examined whether our turtles headed preferentially upcurrent at locations where the water masses had previously been in close contact with Europa. To estimate the origin of the surface water mass surrounding the turtles' locations, 100 evenly spaced virtual drifters were released in a 1/8° side 'square' (13.9 × 12.9 km) centred on each turtle's location. Their backward movements for the 30 previous days were simulated on an hourly basis from the 2-dimensional surface velocity field of the area. As surface water masses did not converge or diverge in the area during the tracking period, the vertical velocity component (upwelling or downwelling) was negligible. Consequently, the drifters were likely to be moved by a unique surface water mass and therefore to indicate its origin reliably. Turtles' locations were sorted into 2 groups based on the number of virtual drifters that had been within 20 km of Europa at any time during the previous 30 days: locations not connected to Europa, with 0 drifters (L_0) and locations strongly connected to Europa, with >50 drifters (L_{50}). The remaining group, which contained only a few locations with intermediate scores, was discarded to compare turtles' locations with a maximum contrast.

For each L_0 or L_{50} location, we computed the 'currentward component' as the cosine of the angular difference between the heading and current vectors at this location. We sub-sampled these locations in a similar way as explained above to obtain statistically independent angular values (at p = 0.10), and compared the mean currentward components obtained at the 2 types of locations by a Mann-Whitney test (see Batschelet 1981 for the rationale of this test). If the island generated any water-borne cues useful for navigation, the turtles would have headed upcurrent (negative mean currentward component) at L_{50} locations, and headed at random (null mean currentward component) at L_0 locations. We can therefore expect a significant difference at these 2 types of locations in the turtles' orientation behaviour with respect to the current direction.

RESULTS

Homing and orientation efficiency

The 3 displaced turtles (*Chelonia mydas*) were not able to relocate Europa quickly, and homed only after having performed circuitous movements, over short (T1), medium (T2), or long (T3) ranges (Fig. 3). Turtles T1 and T2, released 115 km from Europa, homed in 13 and 21 d, travelling 590 and 1435 km, respectively. Turtle T3, released 245 km from Europa, homed in

59 d, travelling 3515 km. After moving to the west, she performed 2 clockwise followed by 2 anticlockwise loops in the southwest of Europa, and finally reached the island after a 60 km final leg. All turtles were clearly motivated to return to their nesting island: indeed, none of them showed any tendency to move toward their feeding grounds located along the Madagascar or Mozambique coast (Le Gall & Hughes 1987). Being herbivorous, adult green turtles do not find suitable food in the open ocean (Bjorndal 1997), so that the circuitous homing routes observed are unlikely to correspond to foraging activity. For each turtle, the track (ground-related) orientation efficiency was quite low, but the heading (water-related) orientation efficiency was somewhat higher (Table 1). From all locations, turtles tended to move toward Europa rather than in a fixed direction, so they appeared to be able to correct for the various passive displacements (initial displacement by boat and subsequent displacements due to currents) to which they were subjected. The low track orientation efficiencies with respect to the heading orientation efficiencies, however, suggest that turtles did not compensate for current drift (see below).

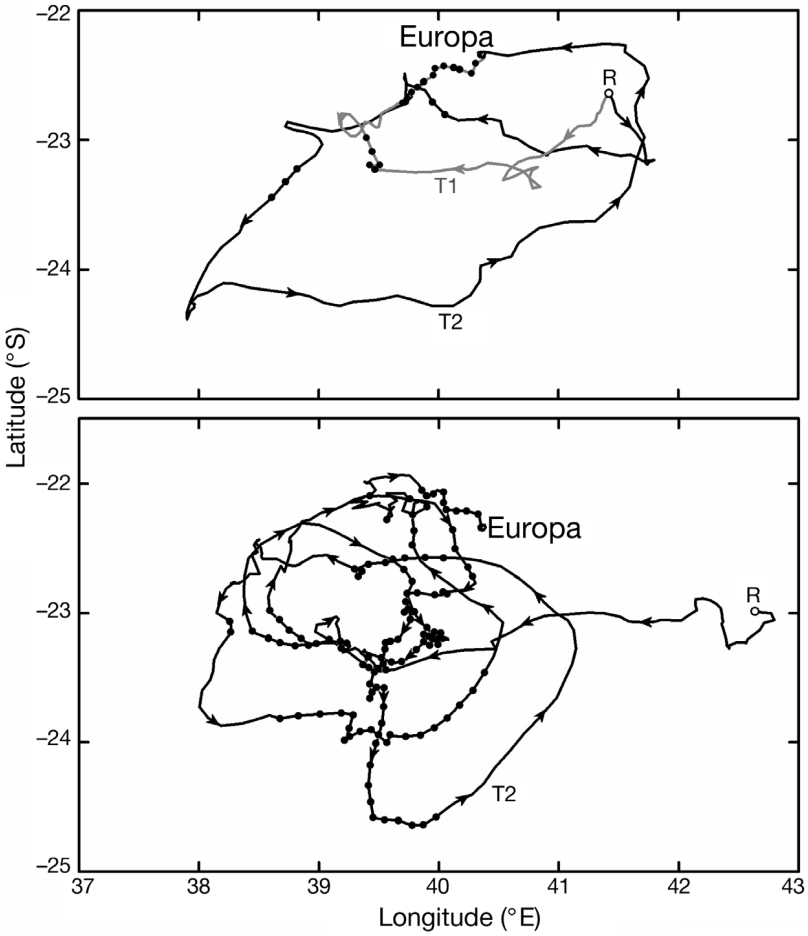

Fig. 3. *Chelonia mydas.* Tracks of the 3 turtles (T1, T2 and T3) from release sites R to Europa. Dots along the paths correspond to L_{50} locations, arrows indicate motion direction

Mechanical action of oceanic currents

In the southern part of the Mozambique Channel, surface velocity currents were mainly due to the geostrophic component, with little contribution due to the Ekman (wind-driven) component. At the beginning of the experiment, the north of Europa was characterised by a large cyclonic eddy, which divided into 2 structures: one to the northeast and the other to the southwest of Europa. They generated a southwest flow of about 30 cm s^{-1} around the island. Turtles were released in a small anticyclonic eddy west-southwest of the island generating weaker currents of about 15 cm s^{-1}, which intensified and slowly moved southwest (Fig. 1). During the remaining part of the turtles' journeys, the overall current field around Europa was very variable both in space and time, with cyclonic and anticyclonic eddies appearing and moving through the whole area. On average, however, all 3 turtles experienced oceanic currents that tended to make them drift away from Europa. The mean current speed components on the Europa axis were −29 cm s^{-1} (T1), −19 cm s^{-1} (T2) and −22 cm s^{-1} (T3). As turtles moved with a water-related mean speed of 70 cm s^{-1}, such a globally upcurrent pattern was likely to reduce their ground-related mean speed by about ⅓ when they headed toward Europa.

The mean difference (ΔH in Table 1) between the homeward components of heading vectors and track vectors is significantly higher than zero in Turtle T1 (Wilcoxon T+ = 257, $p < 0.001$), T2 (T+ = 283, $p < 0.01$) and T3 (T+ = 1274, $p < 0.001$). In other words, for each turtle, the mean heading direction was significantly closer to the home direction than the mean track direction, in agreement with the previous result about orientation efficiencies. Hence, the turtles did not attempt to compensate for current drift by biasing their heading so as to adjust their track in the home direction. Rather, they appeared to head more or less accurately toward Europa, but the currents made them take other, less efficient paths.

Table 1. *Chelonia mydas.* Homing path characteristics. O_t and O_m are orientation efficiencies for track (ground-related) and motor (water-related) paths, ΔH (mean ± SEM) is difference between heading and track homeward components measured at locations where current speed was >25 cm s^{-1}, C_{50} and C_0 (mean ± SEM) are currentward components for L_{50} and L_0 locations, N is resulting sample size after sub-sampling and n is sub-sampling integer value used for obtaining statistically independent angular data (i.e. only locations spaced out by minimum 4n h were considered in analysis)

Turtle	O_t	O_m	ΔH (N, n)	C_{50} (N, n)	C_0 (N, n)
T1	0.20	0.64	0.33 ± 0.06 (23, 3)	−0.83 ± 0.05 (19, 1)	−0.08 ± 0.14 (23, 2)
T2	0.08	0.32	0.24 ± 0.08 (26, 4)	0.02 ± 0.22 (3, 2)	−0.33 ± 0.15 (22, 5)
T3	0.07	0.41	0.39 ± 0.08 (53, 5)	−0.09 ± 0.09 (71, 2)	0.01 ± 0.15 (24, 5)

Analysis of turtles' orientation behaviour

As the turtles did not compensate for current drift, the heading vectors are better estimates of what they intended to do than the track vectors. The distributions of heading directions expressed relative to the direction of Europa were first sub-sampled (as previously, by taking only 1 measurement every n locations into account, in order to obtain statistically independent angular values at p = 0.10), and then analysed using circular statistics (Batschelet 1981). They differed significantly (V-test at $p < 0.05$) from a uniform distribution for T1 (r = 0.75, ϕ = 18°, N = 20, n = 4), T2 (r = 0.37, ϕ = −32°, N = 25, n = 5) and T3 (r = 0.38, ϕ = 16°, N = 71, n = 5). The low values of the mean vector length r (which measures the concentration of the distribution around the mean direction ϕ) obtained in particular for Turtles T2 and T3 indicate, however, that a large amount of random noise was involved. The value of ϕ differed significantly from 0° (Europa direction) only for T1 ($0.01 < p < 0.05$; tests based on charts, in Batschelet 1981 p. 86). This suggests some systematic directional bias for this turtle, but there was no global systematic bias. Drawing motor paths (sequences of heading vectors) with respect to Europa direction (Fig. 4) provides a useful representation that clearly shows the tendency of turtles to head toward Europa. Hence, a comparison of the motor and track paths drawn with respect to Europa direction highlights the mechanical impact of currents on the homing journeys of turtles unable to compensate for current drift.

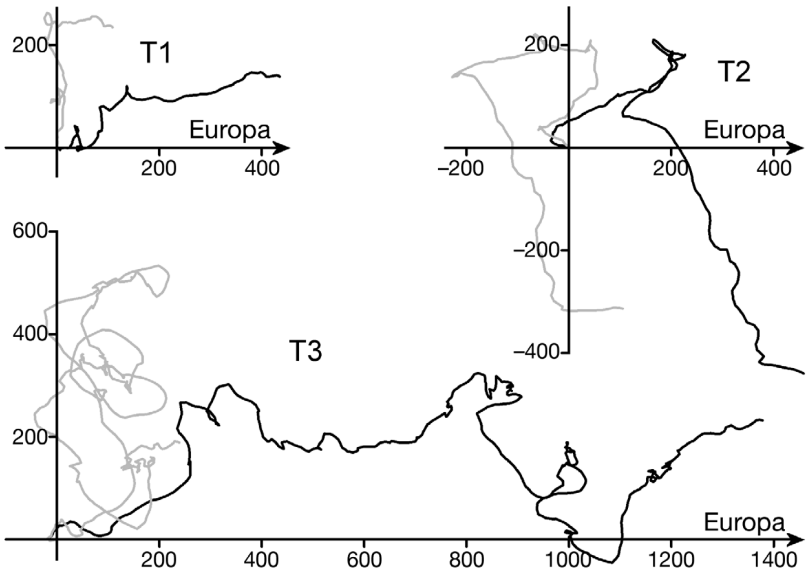

Fig. 4. *Chelonia mydas.* Motor (water-related; black) and track (ground-related; grey) paths expressed with respect to Europa direction. Axes X (Europa direction) and Y (orthogonal direction) report distance values (km): $X_k = \Sigma_{i=1}^{k} l\cos(\theta_i - \gamma_{i-1})$ and $Y_k = \Sigma_{i=1}^{k} l\sin(\theta_i - \gamma_{i-1})$, for k = 1, 2…, s, computed from paths rediscretized as sequences of s steps with orientations θ and a small constant length l. Orientation efficiency (O) corresponds to ratio of the whole home-directed movement component (X_s) over path length ($L = sl$); $O = \Sigma_{i=1}^{s}\cos(\theta_i - \gamma_{i-1})/s = X_s/L$

Oceanic currents as a possible information source

For Turtles T2 and T3, there was no significant difference in mean currentward components between L_{50} and L_0 locations (Table 1; T2: U = 21, ns; T3: U = 789, ns). Turtle T2 homed along a final straight segment longer than 100 km, during which she never experienced water that had been in contact with Europa during the previous 30 d. In contrast, T3 homed along a 60 km long upcurrent final stage. Previously, she had often experienced water masses that had been in contact with Europa, even when she was relatively close to it, but such experience did not lead her to head toward the target. For T1, the headings were significantly more oriented upcurrent at L_{50} locations (U = 72, $p < 0.001$), but most of the L_{50} locations occurred in the last stage (80 km long) of the homing path, when the turtle was moving upcurrent while

approaching the island. It is worth noting that the mean current directions with respect to Europa direction were similar between L_0 and L_{50} locations for T2 (156° versus 150°) and T3 (–166° versus –170°), but not for T1 (133° versus –165°): currents were on average more or less opposite to the home direction at any location for T2 and T3, while for T1 the home direction was clearly more upcurrent at L_{50} than at L_0 locations. The apparent tendency of T1 to head significantly more upcurrent at L_{50} than at L_0 locations might, therefore, simply reflect her tendency to head preferentially toward Europa at any location, irrespective of the local current direction.

DISCUSSION

We aimed to initiate a new approach to the study of sea turtle navigation by looking at the possible effects of oceanic currents in a homing context. To date, the analyses of adult movements with respect to oceanic currents have focused on postnesting migrations (e.g. Luschi et al. 1998, Horrocks et al. 2001). A homing experiment is, however, more liable to provide a clear picture, thanks to a very well-defined goal direction, especially when the goal is a small isolated island like Europa. With a sample size of only 3 turtles, no firm conclusions on the navigational mechanisms at work can conclusively be drawn, although some preliminary inferences can be made.

Oceanic currents certainly act as a mechanical factor, forcing turtles to drift away from the most suitable route. Birds face a similar problem with winds, and appear to compensate for wind drift only over land, in the presence of ground features (e.g. Bäckam & Alerstam 2001, Green & Alerstam 2002, Thorup et al. 2003). For example, a bird migrating northward over land may be aware that it is being subjected to an eastward wind drift because of the diverging line between the right and left visual flow hemifields generated by ground features, which should lay north, but is shifted somewhat to the right. In the pelagic environment, where ground features are not available, monitoring drift is much more arduous, because it requires an estimation of the discrepancy between the actual and expected locations. Hence, drift compensation cannot be accomplished by a pelagic animal that relies on a simple navigation process enabling it only to infer the goal direction without being able to determine its own location. However, it might still be possible, if the animal relies on a more sophisticated navigation process enabling it to assess its own location within the environment.

The difference between these 2 types of processes is illustrated in the history of human navigation. Ancient navigators relied on 'dead-reckoning' (known in animals as path integration; review in Benhamou 1997), by which they conjointly estimated the (water-related) speed of the ship using a knotted rope and the course steered with respect to a magnetic compass to infer the distance and direction from the starting harbour. In the absence of ground features, they had no means to compensate for possible leeway (off-course lateral movement induced by currents and winds), and had no means to simply correct for this displacement, because dead-reckoning is a route-based navigation process: it does not allow a seafarer to estimate the actual (ground-related) locations of the ship and the harbour, but only their locations relative to each other (this latter estimation being correct only in the absence of drift). Later, human navigators used a sextant, and very recently the Global Positioning System, to determine their actual location in the open sea. Thus, thanks to a sophisticated location-based navigation process, they became able both to correct for possible displacement due to leeway (i.e. to re-estimate the goal direction at regular intervals) and to compensate for it by adopting a biased heading aimed to reduce the discrepancy between their actual and expected locations. The comparative analysis of location-based navigation in rats and bees (review in Benhamou 1997) also provides an illustration of the different kinds of processes that may be involved in this type of navigation. A rat is known to rely on a kind of map-like system to determine both its own location and its goal location with respect to proximal landmarks. Thus, it can navigate using a landmark-based system of reference, which is functionally similar to a seafarer equipped with a sextant who is navigating according to a celestial-based system of reference. In contrast, a bee is thought to infer the direction of its goal in a much more rigid way, from the discrepancy between the actual retinotopic coordinates of the landmarks and those memorised at the goal location as a snapshot, so without determining its own location. Both rats and bees re-estimate the goal direction at regular intervals, and thus are fully able to correct for possible displacement (in this context, however, even a bee may compensate for wind drift by relying on the visual flow generated by ground features).

It can be hypothesised that sea turtles rely on a 'map and compass' process based on intersecting gradient fields (see Benhamou 2003, Wiltschko & Nehmzow 2005 for recent accounts on this concept). Contrary to what its name suggests, this process does not necessarily refer to sophisticated map-based navigation, but can take 2 forms. In the simplest form, analogous to the bee's location-based navigation system, the animal is assumed to establish the local home direction based on the differences in gradient field values perceived at its present location and memorised at the home location, without determining its own location. The other, more

sophisticated form is analogous to the rat's location-based navigation system. It involves a kind of map-like representation of the environment on which any location can be specified with respect to the environment based on its respective gradient field coordinates. Both solutions enable an animal to correct for any passive displacement (man-made or due to oceanic currents), but only the latter enables it to compensate for current drift, because, in the absence of ground features, a continuous appraisal of drift rests upon the comparison of actual and expected locations, which cannot be achieved by relying on the simplest method. The fact that our homing turtles did not compensate for current drift, although this would have led to better navigational efficiency, suggests that they relied on a simple navigational solution enabling them to move more or less efficiently in the home direction, but not being able to fully assess their own location in the environment.

While displaced turtles eventually managed to get back to their nesting island, they did so with long, winding routes, which may be indicative of poor navigational abilities (see also Luschi et al. 2001). The fact that they headed roughly homeward shows, however, that they actually had some indication of the home direction after passive displacement. Their poor navigational performance suggests that the navigation process at work is noisy and biased, besides not allowing current drift compensation. The tendency of our turtles to bias their initial search toward a location south of Europa is intriguing, being only partly explained through the action of current drift. It may also be caused by a bicoordinate navigational process involving non-orthogonal gradient fields (Benhamou 2003).

Finally, we looked at whether turtles were able to sense some type of additional navigational information brought by water masses that had previously been in contact with their nesting island. This type of information, if at all relevant, should be secondary, as it is available only at particular locations and times, but may enable a turtle to home faster when the circumstances are favourable. Because of diffusion processes, the concentrations of chemical cues in water masses that have previously been in contact with a source decrease progressively along the current mainstream. Hence, turtles could use some elementary orientation mechanism (see Benhamou & Bovet 1992) to head toward the areas of higher concentration, and therefore indirectly upcurrent, without determining the current's direction, provided the flow turbulence is not too high (Balkovsky & Shraiman 2002). Although the disparate results obtained prevent definitive conclusions, no such information seems to be available or detected by turtles at large distances from their nesting island, possibly because the cues involved are ephemeral and disappear in a few days. This view is in general accordance with the conclusions drawn for Ascension Island green turtles, which were displaced downcurrent and failed to return quickly to their home (Luschi et al. 2001). Nevertheless, as 2 of our 3 turtles moved upcurrent during the final leg of their homing journey, information borne by oceanic currents may have been used when turtles were closer to the island.

The conclusions drawn above should be considered preliminary, because they are based on 3 turtles only. Our data did not allow us to determine which kind of information is used by navigating turtles, but we can at least assume that such information is not likely to be provided by water-borne chemical cues issuing from the nesting island. In this paper the methodological implications are clearly our most important contribution to the study of sea turtles, as we showed how a new path analysis approach can be developed by coupling satellite remote-sensing oceanographic data and satellite-tracking data. This approach enables us to distinguish between what the turtles actually did (track paths) and what they intended to do (motor paths), and to determine the origin of the water masses encountered. The representation of both water- and ground-related paths with respect to the goal direction highlights the mechanical impact of oceanic currents on turtles' journeys and makes it possible to estimate the turtles' true orientation efficiency. In the future, special care should be taken to compute motor paths before drawing any conclusions on the orientation behaviour of sea turtles in the open ocean.

Acknowledgements. We are grateful to the Préfet de La Réunion for authorisation to experiment on Europa's green turtles (under S.B.'s French Living Animals Experiment licence No. 34-100), to the French Navy, FAZSOI and DAF (Mayotte) for transport and logistical support, and to M.-H. Rio and F. Hernandez for their estimations of currents in the Mozambique Channel. Altimeter and wind data were obtained from CLS Space Oceanography Division, as part of the Environment and Climate EU Enact project, with support from CNES, and from CERSAT (IFREMER Plouzané), respectively. C.G. acknowledges La Région Réunion for providing her a PhD grant. Special thanks to L. Dagorn, M. Taquet and F. Papi for their invaluable help.

LITERATURE CITED

Bäckam J, Alerstam A (2001) Confronting the winds: orientation and flight behaviour of roosting swifts, *Apus apus*. Proc R Soc Lond Ser B 268:1081–1087

Balkovsky E, Shraiman BI (2002) Olfactory search at high Reynolds number. Proc Natl Acad Sci USA 99: 12589–12593

Batschelet E (1981) Circular statistics in biology. Academic Press, London

Benhamou S (1997) On systems of reference involved in spatial memory. Behav Proc 40:149–163

Benhamou S (2003) Bicoordinate navigation based on non-orthogonal gradient fields. J Theor Biol 225:235–239

Benhamou S (2004) How to reliably estimate the tortuosity of an animal's path: Straightness, sinuosity, or fractal dimension? J Theor Biol 229:209–220

Benhamou S (2006) Detecting an orientation component in animal paths when the preferred direction is individual-dependent. Ecology 87:518–528

Benhamou S, Bovet P (1992) Distinguishing between elementary orientation mechanisms by means of path analysis. Anim Behav 43:371–377

Berthold P (2003) Genetic basis and evolutionary aspects of bird migration. Adv Study Behav 33:175–229

Bjorndal KA (1997) Foraging ecology and nutrition of sea turtles. In: Lutz PL, Musick JA (eds) The biology of sea turtles. CRC Press, NewYork, p 199–231

Ducet N, Le Traon PY, Reverdin G (2000) Global high resolution mapping of ocean circulation from TOPEX/Poseidon and ERS-1 and -2. J Geophys Res Oceans 105: 19477–19498

Green M, Alerstam T (2002) The problem of estimating wind drift in migrating birds. J Theor Biol 218:485–496

Hays GC, Åkesson S, Broderick AC, Glen F and 5 others (2001) The diving behaviour of green turtles undertaking oceanic migration to and from Ascension Island: dive durations, dive profiles and depth distribution. J Exp Biol 204:4093–4098

Horrocks JA, Vermeer LA, Krueger B, Coyne M, Schroeder BA, Balazs GH (2001) Migration routes and destination characteristics of post-nesting hawksbill turtles satellite-tracked from Barbados, West Indies. Chelonian Conserv Biol 4:107–114

Koch AL, Carr A, Ehrenfeld DW (1969) The problem of open sea navigation: the migration of the green turtle to Ascension Island. J Theor Biol 22:163–179

Lagerloef GS, Mitchum GT, Lukas RB, Niiler PP (1999) Tropical Pacific near-surface currents estimated from altimeter, wind, and drifter data. J Geophys Res Oceans 104: 23313–23326

Le Gall JY, Hughes GR (1987) Migrations de la tortue verte *Chelonia mydas* dans l'Océan Indien Sud-Ouest observées à partir des marquages sur les sites de ponte Europa et Tromelin (1970–1985). Amphib-Reptilia 8: 277–282

Lohmann KJ, Hester JT, Lohmann CM (1999) Long-distance navigation in sea turtles. Ethol Ecol Evol 11:1–23

Luschi P, Hays GC, Del Seppia C, Marsh R, Papi F (1998) The navigational feats of green sea turtles migrating from Ascension Island investigated by satellite telemetry. Proc R Soc Lond Ser B 265:2279–2284

Luschi P, Åkesson S, Broderick AC, Glen F, Godley BJ, Papi F, Hays GC (2001) Testing the navigational abilities of oceanic migrants: displacement experiments on green sea turtles (*Chelonia mydas*). Behav Ecol Sociobiol 50:528–534

Luschi P, Hays GC, Papi F (2003) A review of long-distance movements by marine turtles, and the possible role of ocean currents. Oikos 103:293–302

Papi F, Luschi P (1996) Pinpointing 'Isla Meta': the case of sea turtles and albatrosses. J Exp Biol 199:65–71

Quartly GD, Srokosz MA (2004) Eddies in the southern Mozambique Channel. Deep-Sea Res II 51:69–83

Rio MH, Hernandez F (2004) A mean dynamic topography computed over the world ocean from altimetry, *in situ* measurement, and a geoid model. J Geophys Res Oceans 109:C12032

Schouten MW, de Ruijter WP, Jan van Leeuwen P, Ridderinkhof H (2003) Eddies and variability in the Mozambique Channel. Deep-Sea Res II 50:1987–2003

Thorup K, Alerstam T, Hake M, Kjellén N (2003) Bird orientation: compensation for wind drift in migrating raptors is age dependent. Proc R Soc Lond Ser B (Suppl) 270:8–11

Van Meurs P, Niiler PP (1997) Temporal variability of the large-scale geostrophic surface velocity in the northeast Pacific. J Phys Oceanogr 27:2288–2297

Wiltschko R, Nehmzow U (2005) Simulating pigeon navigation. Anim Behav 69:813–826

Editorial responsibility: Howard I. Browman (Associate Editor-in-Chief), Storebø, Norway

Submitted: December 5, 2005; Accepted: February 27, 2006
Proofs received from author(s): August 30, 2006

B.2 Article : Marine Turtles Use Geomagnetic Cues during Open-Sea Homing, P. Luschi *et al.*, 2007

B.2.1 Abstract

Marine turtles are renowned long-distance navigators, able to reach remote targets in the oceanic environment ; yet the sensory cues and navigational mechanisms they employ remain unclear [1–3]. Recent arena experiments indicated an involvement of magnetic cues in juvenile turtles' homing ability after simulated displacements [4, 5], but the actual role of geomagnetic information in guiding turtles navigating in their natural environment has remained beyond the reach of experimental investigations. In the present experiment, twenty satellite-tracked green turtles (Chelonia mydas) were transported to four open-sea release sites 100-120 km from their nesting beach on Mayotte island in the Mozambique Channel ; 13 of them had magnets attached to their head [6] either during the outward journey or during the homing trip. All but one turtle safely returned to Mayotte to complete their egg-laying cycle, albeit with indirect routes, and showed a general inability to take into account the deflecting action of ocean currents as estimated through remote sensing oceanographic measurements [7]. Magnetically treated turtles displayed a significant lengthening of their homing paths with respect to controls, either when treated during transportation or when treated during homing. These findings represent the first field evidence for the involvement of geomagnetic cues in sea-turtle navigation.

B.2.2 Article publié dans *Current Biology*

Référence : Luschi P., Benhamou S., Girard C., Ciccione S., Roos D., Sudre J. and Benvenuti S., 2007 : Marine Turtles Use Geomagnetic Cues during Open-Sea Homing, *Current Biology*, **17**, 126-133, DOI 10.1016/j.cub.2006.11.062.

Current Biology 17, 126–133, January 23, 2007 ©2007 Elsevier Ltd All rights reserved DOI 10.1016/j.cub.2006.11.062

Report

Marine Turtles Use Geomagnetic Cues during Open-Sea Homing

Paolo Luschi,[1,*] Simon Benhamou,[2] Charlotte Girard,[3,7] Stephane Ciccione,[4] David Roos,[5] Joël Sudre,[6] and Silvano Benvenuti[1]
[1] Dipartimento di Biologia
University of Pisa
Via A. Volta 6
I-56126 Pisa
Italy
[2] Centre d'Ecologie Fonctionnelle et Evolutive
Centre National de la Recherche Scientifique
1919 route de Mende
F-34293 Montpellier Cedex 5
France
[3] Institut de Recherche pour le Développement
PO Box 570
Victoria
Seychelles
[4] Kelonia
l'Observatoire des Tortues Marines
Pointe des Chateaux
Route Nationale
F-97898 Saint Leu Cedex
La Réunion
France
[5] Institut Français de Recherche pour l'Exploitation de la Mer
Laboratoire Ressources Halieutiques
Rue Jean Bertho
F-97822 Le Port Cedex
La Réunion
France
[6] Laboratoire d'Etudes en Géophysique et Océanographie Spatiales
Centre National de la Recherche Scientifique
18, avenue Edouard Belin
F-31401 Toulouse, Cedex 9
France

Summary

Marine turtles are renowned long-distance navigators, able to reach remote targets in the oceanic environment; yet the sensory cues and navigational mechanisms they employ remain unclear [1–3]. Recent arena experiments indicated an involvement of magnetic cues in juvenile turtles' homing ability after simulated displacements [4, 5], but the actual role of geomagnetic information in guiding turtles navigating in their natural environment has remained beyond the reach of experimental investigations. In the present experiment, twenty satellite-tracked green turtles (*Chelonia mydas*) were transported to four open-sea release sites 100-120 km from their nesting beach on Mayotte island in the Mozambique Channel; 13 of them had magnets attached to their head [6] either during the outward journey or during the homing trip. All but one turtle safely returned to Mayotte to complete their egg-laying cycle, albeit with indirect routes, and showed a general inability to take into account the deflecting action of ocean currents as estimated through remote-sensing oceanographic measurements [7]. Magnetically treated turtles displayed a significant lengthening of their homing paths with respect to controls, either when treated during transportation or when treated during homing. These findings represent the first field evidence for the involvement of geomagnetic cues in sea-turtle navigation.

*Correspondence: pluschi@biologia.unipi.it
[7] Present address: Centre National de la Recherche Scientifique (CNRS), Institut Pluridisciplinaire Hubert Curien, Département d'Ecologie, Physiologie et Ethologie, unité mixte de recherche 7178, CNRS-Université Louis Pasteur, 23 rue Becquerel, 67087 Strasbourg, France.

Results and Discussion

Experimental displacements constitute one useful approach to investigating animal navigation systems [2, 8]. An animal translocated away from a site to which it is faithful (e.g., a breeding site) will most likely attempt to return to it, thus allowing the study of its navigational abilities in the field. In marine turtles, females typically display a strong fidelity to their nesting beach, where they faithfully return every few years from their residential feeding grounds, often located hundreds of kilometres away [9, 10]. Within a reproductive season, each turtle lays multiple clutches of eggs and remains in the waters close to the nesting beach between successive egg-laying events [9]. Previous homing experiments showed that, when experimentally translocated early during their reproductive period, turtles tend to return to their nesting beach to complete their seasonal egg-laying cycle [7, 11–16]. We employed this type of experiment to investigate the role of magnetic information in the homing abilities of green turtles nesting at Mayotte, the easternmost island of the Comoros archipelago in the Northern Mozambique Channel.

Turtles were captured while ashore to nest at Saziley beach (12.98°S; 45.19°E), in the southeastern part of Mayotte, and were then translocated to four release sites northeast, southwest, and southeast of Saziley (see Table S1 in the Supplemental Data available online). Five releases of four turtles each were performed (Table 1), with three different treatments: turtles magnetically disturbed only during transportation to the release site (MT group, n = 6), turtles magnetically treated during the homing trip (MH group, n = 7), and controls (C group, n = 7). Magnetically disturbed turtles had powerful, mobile magnets attached to their head (Figure 1A) to induce a randomly varying magnetic field around it [17]. Magnets were attached at the nesting beach (MT turtles) or on board just before release (MH turtles). MH turtles were therefore prevented from detecting geomagnetic cues during the homing process, whereas MT turtles

Table 1. Homing Performances of the Three Turtle Groups

Turtle (CCL, cm)	Release (Direction)	Length of Homing Trip (km)	Speed of Homing Trip (km/d)	Straightness Index of Track Path	Straightness Index of Motor Path
C GROUP					
C1 (104)	1 (SW)	310	29.9	0.34	0.35
C2 (117)	1 (SW)	214	41.4	0.39	0.59
C3 (115)	2 (NE)	90	50.0	0.69	0.72
C4 (103)	2 (NE)	116	43.7	0.58	0.85
C5 (110)	3 (SE)	385	10.6	0.19	0.44
C6 (107)	4 (SE)	348	26.5	0.28	0.42
C7 (102)	5 (SE)	334	14.1	0.26	0.71
Mean ± SEM		257 ± 44	30.9 ± 5.7	0.39 ± 0.07	0.58 ± 0.07
MH GROUP					
MH1 (103)	1 (SW)	397	17.2	0.19	0.08
MH2 (109)	1 (SW)	—	—	−0.26	−0.18
MH3 (111)	2 (NE)	285	17.0	0.24	0.54
MH4 (107)	2 (NE)	97	67.4	0.65	0.72
MH5 (95)	4 (SE)	1435	6.8	0.05	0.03
MH6 (107)	4 (SE)	400	29.4	0.24	0.34
MH7 (108)	4 (SE)	492	27.1	0.19	0.25
Mean ± SEM		518 ± 192	27.5 ± 8.1	0.19 ± 0.10	0.25 ± 0.12
MT GROUP					
MT1 (110)	3 (SE)	763	7.2	0.08	0.25
MT2 (106)	3 (SE)	914	8.2	0.07	0.00
MT3 (105)	3 (SE)	371	19.5	0.19	0.35
MT4 (102)	5 (SE)	2214	4.4	0.04	0.05
MT5 (108)	5 (SE)	691	15.3	0.12	0.05
MT6 (112)	5 (SE)	861	18.5	0.11	0.09
Mean ± SEM		969 ± 261	12.2 ± 2.6	0.10 ± 0.02	0.13 ± 0.06

CCL = Curved Carapace Length. For turtle MH2, which stopped at Mohéli Island, homing-trip length and speed could not be calculated. See text for further explanations.

were made unable to collect these cues during transportation. In this way, we investigated the relative importance of geomagnetic cues detected during transportation and during homing and aimed to assess the role of alternative navigational strategies potentially exploitable by homing turtles. If turtles were relying on a "magnetic map" to fix their position with respect to home (by comparing magnetic parameters detected at the release site with those memorized at the nesting beach [3, 8]), we expected that MH turtles only would have been affected by the treatment. If turtles paid attention to magnetic cues picked up en route (e.g., to monitor the direction of passive displacement), or if magnets produce some long-lasting after-effect on magnetic receptors, then MT turtles would have exhibited an impairment in homing.

All displaced turtles but one returned to Mayotte in 2–29 days, with 18 of them later returning to Saziley beach. The only turtle that did not home (MH2) reached the coastal waters of Mohéli (another Comoros island 140 km westward of Mayotte) by following a straight path (Figure 1C) and remained there for the rest of the tracking period (83 days). Green turtles are known to frequent Mohéli, either to feed in its coastal waters or to breed in its beaches [18], but it is unknown whether turtle MH2 nested there. Most homing routes were not immediately directed toward Mayotte, with turtles often exhibiting curved or looping paths before reaching their target (Figures 1B–1D). The majority of turtles approached the island from the northern quadrants, as is especially evident for the releases from the southeast.

We first compared the homing performances of the three treatments by relying on track straightness index, which best represents the orientation efficiency of tracked paths [19]. A one-way ANOVA revealed a significant ($F = 3.82$, $p = 0.04$) difference among the indexes of the three groups, and a post-hoc Tukey test showed that controls had a significantly ($p < 0.05$) higher mean index than the MT group but not the MH group, with no significant difference between magnetically treated groups. However, these straightness indexes, being directly derived from recorded tracks, do not take into account the possible deflecting action of ocean currents. They may consequently be unreliable if turtles do not compensate for current drift (i.e., if they are unable to anticipate the drift effects by adopting a heading that, albeit not immediately directed toward home, results in a movement leading to home with a shorter route when combined with drift action [20]). Such an inability has actually been suggested by a pilot study conducted on three green turtles displaced from their breeding sites at Europa Island (southern Mozambique Channel [7]). It is worth noting that, in any case, homing turtles are assumed to have been able to correct for passive displacements (including current drift and the initial displacement by boat) by estimating the home direction along their homing journey. Their possible ability to compensate for the current drift is another, independent question (see [7] for a detailed discussion of this complex matter).

To properly evaluate the turtles' homing abilities, we therefore estimated the ocean surface currents in the

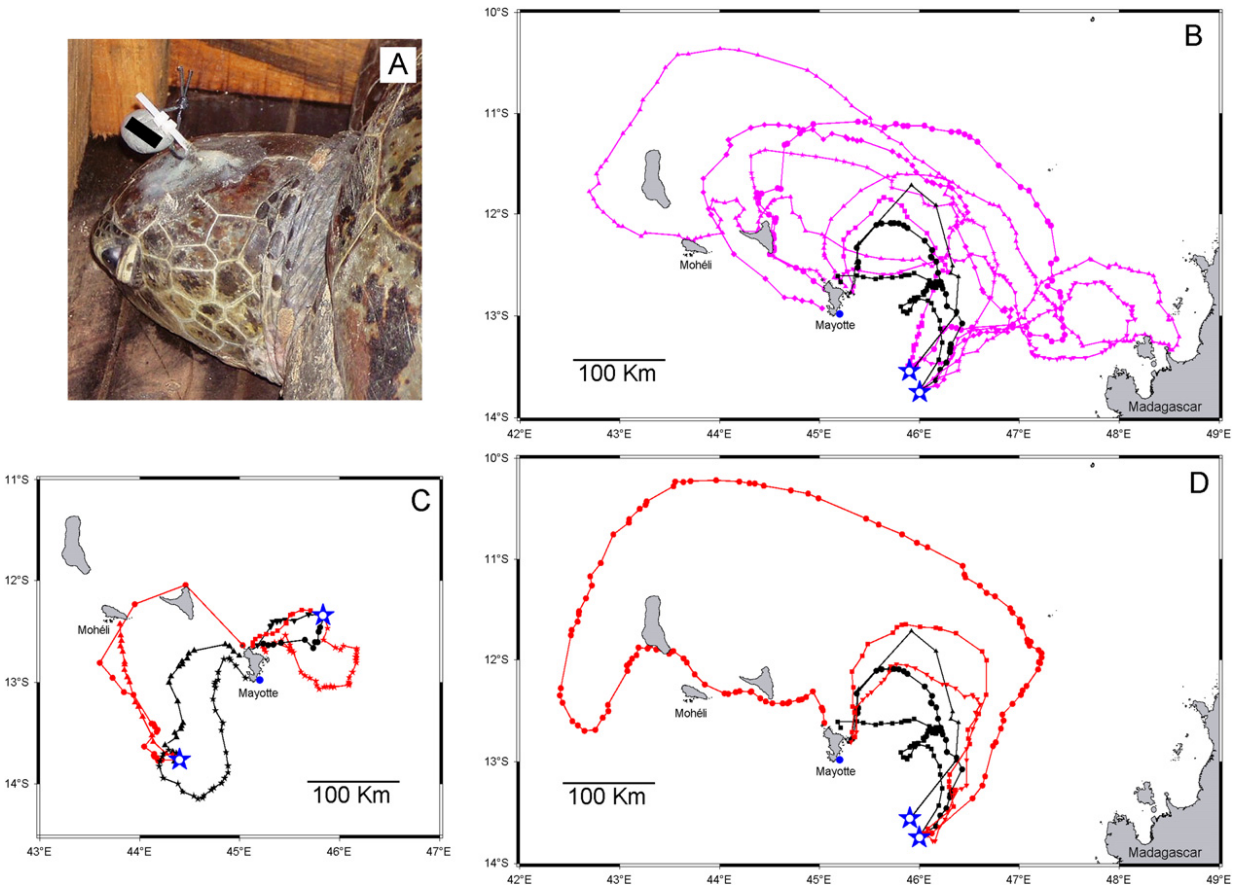

Figure 1. Routes of Turtles Displaced from Their Nesting Beach as Reconstructed by Satellite Telemetry

(A) Magnet attachment on a turtle's head. Disk-shaped magnets (18 mm diameter; 5 mm height) were incorporated with a cable tie in an oval-shaped body (gray colored) made of a fast-setting epoxy resin. This cable tie was connected to a second one linked to a third cable tie glued to the turtle's skin with a two-component epoxy glue and a few fiberglass strips. In this way, the magnet was suspended at about 3 cm from the top of the turtle's head and was free to make small random oscillations. These random movements ensured that unpredictable variations in the applied magnetic field were produced and thus prevented turtles from recalibrating their magnetic sense (see also [17]). Magnets used were of the same model as in a previous study [6], i.e., they were neodymium cylinders (type Neo 35, Calamit Trading, Milan) able to mask the geomagnetic field all around the turtle head (see [6] for a complete description of the magnetic fields produced). The black rectangle represents the magnet inside the epoxy resin.

(B) Homing routes of MT turtles (magenta) and of controls (black, releases 3–5). Different symbols refer to different turtles. The blue stars stand for the release sites, and the blue dot stands for the location of Saziley beach on Mayotte Island.

(C and D) Homing routes of MH turtles (red) and of controls (black) in releases 1 and 2 (C) and 3–5 (D). The routes of controls are shown in both panels (B) and (D) to facilitate comparisons with experimental turtles. Other explanations are as above.

northern part of the Mozambique Channel (see Experimental Procedures for details) and assessed their mechanical impact on the turtles' homing journeys. During the tracking periods, currents were quite variable in time and space and were mainly linked to the occurrence of local sea-level anomalies and associated eddies. The turtles' behavior in relation to these currents was variable too: in some cases, the turtles' movement was directed against the current flow, whereas in other instances the turtles tended to follow the currents (Figure 2 and Movie S1 in the Supplemental Data available online). This latter behavior was especially evident in the 2005 releases when some turtles moved in fair accordance with the substantial currents associated with a large anticyclonic eddy (Figure 2B) during long parts of their homing trips.

The quantitative estimation of surface current velocities allowed us to remove the current contribution to the recorded (ground-related) movement of each turtle and thus to compute the water-related heading vectors, which represent the swimming movements actually made by the turtles in the various phases of their homing trip ([7], see inset in Figure 2B]. The sequence of heading vectors obtained in this way for each turtle's ground-related path constitutes a corresponding water-related "motor path" (Figure S1). Mean current speeds along the tracks ranged between 12.6 and 32.2 cm/s, whereas turtles were found to swim 1.7–5.4 times faster than this (current contribution excluded). The movements recorded were therefore largely determined by the turtles' active swimming. Computer simulations of the movements of virtual turtles passively drifting within the same current field as the experimental individuals indicate that no drifting turtle could have reached Mayotte within one month after release [21].

We then evaluated turtles' ability to compensate for current drift by comparing the homeward components of the calculated track and heading vectors for single

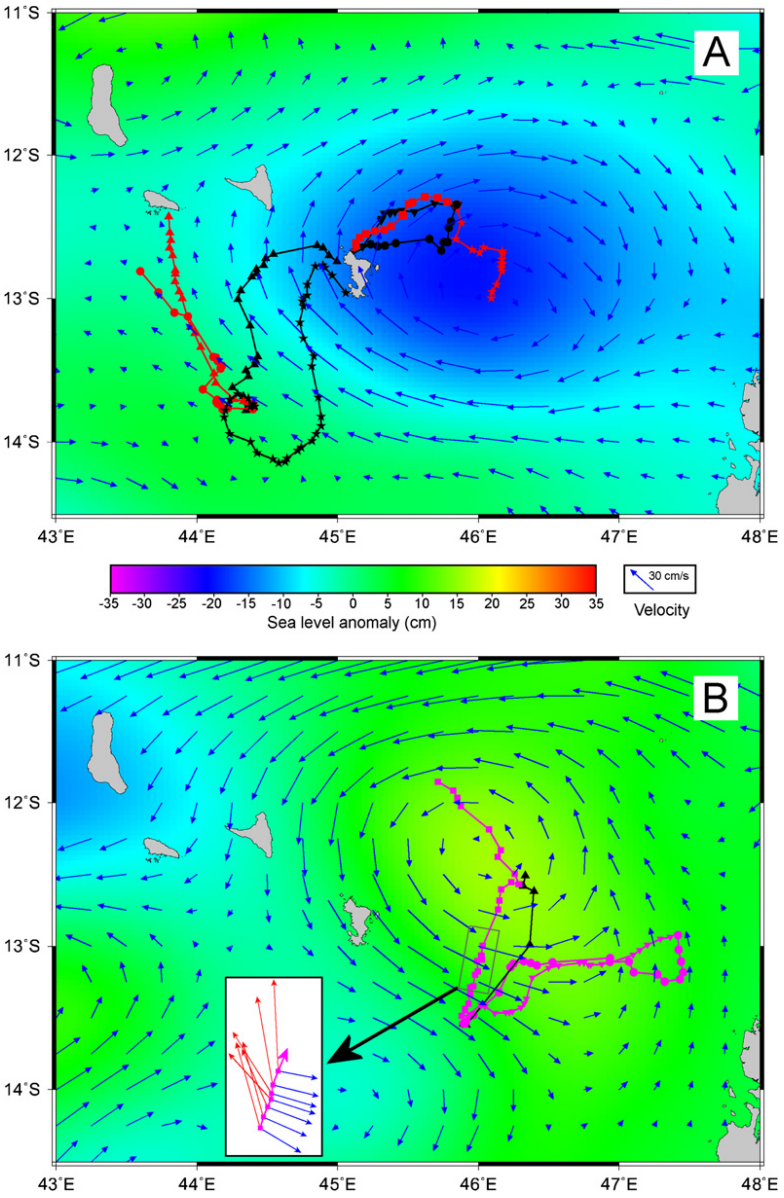

Figure 2. Examples of Turtle Movements in Relation to Ocean Currents

The initial parts (4 days) of the turtles' routes are plotted together with the surface current field estimated for the northern Mozambique Channel for the second day after release: (A) June 16, 2004 and (B) May 26, 2005. The current vectors (blue arrows) and the routes are superimposed on an image of sea-level anomalies for the corresponding day; these anomalies are representative of the eddies that were mainly responsible for the currents in the area at these times. The inset in (B) shows a 24 hr track segment of an MT turtle (on 26 May 2005) showing, for each interpolated location (every 4 hr), the estimated current vector (blue) and the deduced, water-related heading vector (red) representing the actual swimming movement made by the turtle at each 4 hr step. The scale of the inset is the same as that in the main panel. Other explanations are as in Figure 1. See also Movie S1.

turtles; if a turtle indeed compensated for drift, its motor path would have been less homeward oriented than its track path, with the opposite occurring in the absence of drift compensation. Such within-subject comparisons of homeward components (in subsampled datasets to allow for statistical independence; see Experimental Procedures) were performed on six of the seven control turtles (there was not enough data for the remaining one; this procedure was not applied to MT and MH turtles because magnet application may have prevented them from determining the home direction). They revealed that the mean homeward component of the track path was significantly lower than that of the corresponding motor path in all cases (Wilcoxon signed rank tests: $p < 0.05$ or less). This result confirms the conclusion of our previous study on three green turtles [7]: Considered individually, none of them was able to compensate for the current drift. To further investigate this issue, we performed a supplemental interindividual analysis by comparing the straightness indexes of each turtle's track and motor paths in the seven control turtles. These indexes turned out to be significantly higher for motor, water-related paths than for track, ground-related paths (Wilcoxon signed rank test, $T^+ = 28$, $p < 0.02$), confirming at the population level that the orientation efficiency of motor paths is higher than that of track paths.

Because motor paths better represent the turtles' intended movements than track paths, the three experimental groups were then compared on the basis of the straightness indexes of the single motor paths instead of those of the track paths previously used (Table 1). A one-way ANOVA revealed a highly significant ($F = 7.02$; $p = 0.006$) difference among the three groups, with control turtles performing significantly better ($p < 0.05$; Tukey test) than both magnetically treated groups, whose performances did not differ significantly from each other. Furthermore, we considered that a statistical bias may have been introduced in our global analysis by

the fact that, for logistical reasons, MT turtles were all released at the same site. We therefore performed additional two-sample tests on motor-path indexes by considering MT and MH turtles separately. Mann-Whitney tests revealed a significant difference between C and MH turtles (when all releases were considered; $U = 8.5$, $p < 0.04$) and between MT turtles and the three controls released at the southeast site ($U = 0$; $p < 0.025$). Thus, these tests independently confirmed the outcome of the global analysis and showed that the effects previously highlighted were not due to a release-site bias.

Despite the small sample size, the experiment yielded statistically significant evidence for both track and motor straightness indexes and showed a worsening in the homing abilities of both experimental groups after the experimental displacement from their nesting beach. Magnetic treatment en route was as effective as magnet application prior to release; the homing performances of the MT turtles were not significantly different from those of the MH turtles.

According to these findings, magnetic cues play a role in sea-turtle homing. It is difficult to determine the actual magnetic-field alteration produced by the attached magnets (given that they were randomly oscillating), but it can be safely estimated that they produced a disturbance of at least 200 μT around the whole turtle head [6], where all the putative magnetoreception sites (e.g., trigeminal nerve, eye, and pineal gland) are located [22, 23]. The treatment therefore prevented the turtles from correctly detecting the Earth's magnetic field (whose total intensity is about 33 μT in the Mayotte area; Table S1), making reliance on both a magnetic compass and location sense impossible (see [24] for a detailed presentation of the navigational impairments produced by magnet application). Attachment of (less powerful) magnets was indeed effective in disturbing the orientation of hatchling loggerhead turtles in arena tests, a response that could have derived either from an effect on a compass or from an effect on a position-finding mechanism, or both ([25]; see also [26] for preliminary experiments on magnet-equipped adult turtles). At present, it is difficult to understand how geomagnetic information is implemented in the turtles' navigational system or to assess which magnetic parameters (especially intensity and/or inclination [3, 27]) are involved in these processes. Magnet attachment does not make it possible to produce specific magnetic-field alterations detected by the treated animal. Because the location and the functioning of the putative magnetoreceptor are still debated, the artificial field actually produced at that site cannot be predicted.

The most immediate way by which displaced turtles may exploit magnetic cues would be to rely on some kind of "magnetic map" [2, 3, 8, 28, 29]. For instance, newborn loggerhead turtles and juvenile green turtles have been shown to detect differences in magnetic-field intensity and inclination and to display appropriate orientation responses in arenas when they are presented with these two parameters in specific combinations that simulate long-distance translocations [4, 30]. At least for juvenile green turtles, these results have been interpreted as indications of reliance on navigational magnetic maps, possibly at a coarse resolution [3, 4]. In the Mozambique Channel area, magnetic-field conditions are indeed quite favorable for reliance on such a magnetic map because inclination and intensity gradients are quite uniform and intersect each other at wide angles so that they form a grid potentially suitable for navigation (data from IGRF model, see also [29]). The behavior of the MH turtles is in accordance with such a mechanism; displaced turtles that use magnetic information would be greatly affected by magnet attachment at the release site in that they would be unable to properly evaluate the geomagnetic parameters after release and hence would be unable to establish their present location in relation to home. Our results, however, do not allow us to determine whether the effect recorded in the MH turtles is only due to a disturbance of their location-fixing mechanism because a similar impairment would have also been recorded if the MH turtles were relying on nonmagnetic positional information and on a magnetic compass to determine the home direction.

Conversely, the impairment shown by the MT turtles, which were treated only during transportation to the release site, is not directly explainable by an effect on a navigational mechanism based on geomagnetic cues detected during homing. These turtles were not wearing magnets during their homing trip, and so they should have been able to collect positional information while homing (at the latest after recovering from the treatment), whereas they were as disturbed as the MH turtles. This rather surprising finding indicates a possible navigational role of geomagnetic information collected during (passive) transportation; this information may have provided untreated turtles with some indications on the displacement direction [28]. For instance, displaced turtles might have sensed swell-induced accelerations of the boat and have consequently assessed, at least crudely, the general direction of travelling with respect to their magnetic compass. Such a reliance on navigational information collected during passive transportation is actually known for pigeons; in these birds the ability is based on olfactory cues [31], but a complementary role of compass magnetic information has also been proposed ([32], but see [33]). An alternative possibility is that magnetic disturbance during transportation may have persisted for some time after the removal of magnets, and this may have rendered the MT and MH turtles functionally equivalent during their homing journey. For instance, the magnets' field may have physically altered magnetite particles possibly involved in magnetoreception, with an effect lasting longer than magnet application. In this view, the application of strong magnets might have had an effect similar to that of pulse magnetization treatments, altering for some days orientation responses mediated by magnetite-based magnetoreceptors [22]. To our knowledge, long-lasting after-effects of magnet application have not been described, nor can they be immediately inferred from the proposed models of animal magnetoreception [23]. However, such a possibility cannot be dismissed.

A number of characteristics of the homing routes of the tracked turtles (controls included) remain unclear; these include the initial northward movements common to all the 2005 turtles and the tendency to follow indirect, curved routes to home (as already recorded in previous displacement experiments [15, 16]). These

characteristics are not readily explainable by current action alone (see above) and may indicate bicoordinate navigation based on nonorthogonal gradient fields [34]. A careful analysis of the relationship of the turtle water-related movements with the other environmental (and possibly navigational) factors present in the area would be helpful in this respect. Most likely, the homing turtles relied on additional, nonmagnetic navigational cues that may have contributed to shaping the turtles' routes, besides allowing the magnetically disturbed turtles to home (even if less efficiently than controls). It is currently hard to figure out how magnetically treated turtles managed to home. Following previous suggestions [15], one may hypothesize that Mayotte turtles homed thanks to a beaconing process [28] based on locally available navigational cues. For instance, homing in Ascension Island green turtles is known to be easier from the downwind side of the island, with wind-borne cues having been proposed to play a major role in the final homing steps [15, 16]. During our experiments, winds around Mayotte were mostly blowing from southern quadrants (information provided by local measurements and Quickscat satellite wind observations), which might have favored the prevalence of island approaches from northern directions (Figure 1). Ocean currents, conversely, do not seem to bear useful navigational information for displaced turtles [7, 15].

In conclusion, the present experiment provides the first field-collected evidence of the involvement of geomagnetic cues in the navigation of freely moving sea turtles and suggests a so-far-unsuspected navigational role of magnetic information collected during passive transportation to the release site. It is currently difficult to provide a full and detailed interpretation of the present findings. However, because the magnetically disturbed turtles did home, our findings show that the geomagnetic field provides important, although not essential, cues for sea-turtle navigation after displacement. These conclusions are in accordance with similar indications obtained through arena experiments in juvenile turtles [4] but are somewhat at variance with those deriving from a previous field experiment showing that magnet attachment did not affect the navigational performances of Ascension Island green turtles during their oceanic migration toward foraging sites along the Brazilian coast [6]. However, because nonmagnetic cues are likely to be involved in sea turtles' homing processes (as also indicated by the present experiment), it may be hypothesized that although nonmagnetic cues alone may be sufficient to allow efficient open-sea navigation directed to large goals (like the Brazilian coast), geomagnetic information has a major, albeit still not exclusive, role in pinpointing isolated targets.

Experimental Procedures

Displacements and Releases

The experiments were carried out in May-June 2004 (releases 1 and 2) and 2005 (releases 3–5), i.e., just before the peak of the green turtle nesting season in Mayotte. Environmental conditions with regard to water temperature, wind patterns, and meteorology were broadly similar in the two experimental periods (this information was provided by the local meteorological station and by satellite-derived data on sea-surface temperatures and wind stress). Thirteen of the 20 turtles were captured before they layed their eggs; the remaining ones were captured after nesting was completed. Individuals of these two categories were equally distributed in the various treatments. After capture at night, turtles were kept confined singly in wooden crates on Saziley beach. On the following day, Argos-linked satellite transmitters were glued to the turtles' carapace by means of fiberglass stripes or epoxy resin, and the cable ties used for magnet attachments were glued to the central scute of the turtles' head (Figure 1A). Control turtles had brass disks identical in size and shape to the magnets, and these were attached to the head in the same way without, however, producing any magnetic disturbance. The transmitter models used—Telonics A-210, A-410, and A-1010—have all been previously applied to adult turtles with success [6, 7, 15, 16]. Models A-210 and A-410 only slightly differ for their size and weight (maximum dimension 10.2 to 13.0 cm; weight 190 to 215 g; see www.telonics.com), whereas the somewhat bigger A-1010 has been applied only to control turtle C1. The different models employed are therefore unlikely to have differentially affected the behavior of large (>120 cm long) adult turtles. Having been attached on the first central scute of the carapace, i.e., around 40 cm from the head, the transmitters produced negligible magnetic disturbances at the brain level (see [6, 24] for more information on this aspect).

The turtles were then loaded onto a 12 m wooden sailboat powered by an outboard motor. They mainly stayed aligned with the head facing the prow. During transportation, turtles were mostly prevented from accessing visual navigational cues; the sea view was screened by the crate's and the ship's sides, and sky cues were screened from above by moist cloths and screens that were placed on the turtles' head and/or above the crates to keep them cool. Moreover, in releases 1, 3, and 4, the journeys were performed at night and/or under overcast conditions. Once at the release site (trip durations around 12 hr), the turtles were set free by removing the wooden crates and lifted overboard or induced to move toward the bulwark-free back side of the boat from where they could freely slide into the sea. Each turtle was released singly, a few minutes after the preceding one.

The release sites were chosen as to be symmetrically distributed around Mayotte and far from the other Comoros islands. They were located outside the usual migratory pathway of the Mayotte-nesting green turtles, which migrate westward to feeding grounds along the Mozambique/Tanzanian coast (D.R., unpublished data). All releases were planned at 120 km from Saziley beach, but releases 2 and 3 had to be made at 100 km because of the presence of a sand mount at 120 km or bad weather conditions, respectively. Magnetic parameters at the release sites differed by 0.14–0.22 μT in intensity and by 0.6°–1.3° in inclination with respect to Saziley beach (see Table S1). Of the 18 turtles that returned to Saziley, nine were observed on the beach again. Two of these were MT turtles. Among the remaining ones, one MH turtle, and two controls still had the magnet or the brass disk attached on the head, whereas two controls and two MH turtles were found with only the glue but without the cable ties and the disks. It is likely that these turtles lost their magnet or disk while staying in the coral reef around Mayotte (e.g., in cavities where they are known to rest before emerging for egg laying). In any case, even if the loss of the magnet in MH turtles had occurred during the homing journey, this would have minimized the difference between MH and C turtles, making the detection of a significant difference less likely.

Route Reconstructions

Tracked turtles were localized by the Argos System, which classifies the locations into six classes of different accuracy levels (see www.argosinc.com). We reconstructed the routes by using sea locations (i.e., discarding land locations) and filtering out low-accuracy locations as follows. For each individual, we first determined a speed threshold from high-accuracy locations and then discarded all the locations resulting in speeds above that threshold. In addition, we removed locations involving changes of direction larger than 120°. The turtles were considered to have successfully homed as soon as they were located inside or close to (<5 km) the lagoon surrounding Mayotte, where the homing mechanism used may be different from that employed in the open sea.

Estimation of Ocean Currents

Because green turtles' oceanic movements take place in the upper layers of the water column (10–20 m depth [35]), the currents

experienced by turtles were estimated with satellite-derived oceanographic data according to the procedure described in [7]. In short, surface velocity fields were computed on a daily basis as the combination of (1) geostrophic current anomalies, derived from the DUACS gridded altimetric sea level anomaly product (Topex/Poseidon and ERS satellite data; see www.jason.oceanobs.com); (2) mean geostrophic surface currents, calculated from the mean dynamic topography [36]; and (3) Ekman (i.e., wind-induced) currents, derived from Quikscat scatterometry (see www.ifremer.fr/cersat).

Path Analysis

The filtered turtle locations were first standardized as a fix every 4 hr by linear time interpolation. The current data similarly underwent a bilinear spatial interpolation and a time linear interpolation so that the current vectors corresponding to the turtles' locations every 4 hr could be estimated. At each of these locations, we then computed the water-related heading vector of the turtle by subtracting the current vector from the ground-related track vector (see [7] for details). In this way, for each of the twenty turtles, data were summarized in the form of a (ground-related) track and a (water-related) motor homing path.

The orientation efficiency of track and motor paths was estimated with the generalized straightness index $(D_i\text{-}D_f)/L$, where D_i is the initial homing distance (between the release site and Saziley), D_f is the final homing distance (between the last path location and Saziley), and L is the distance travelled. This index (which obviously reduces to the classical straightness index D_f/L when the animal reaches its home at the end of its path) has been shown to constitute the most reliable measure of the efficiency of an oriented path because it corresponds to the mean cosine of directional errors computed at a high spatial frequency [19]. The computation of this index for track paths is straightforward. For motor paths, a more complex approach is required because these paths cannot be suitably represented in a geographical (earth-bound) system of reference. The motor straightness index thus has to be computed either on an ad-hoc path representation where the home is virtually located at infinity (Figure S1; see also [7]) or as the mean cosine of the motor directional errors, i.e., of the discrepancies between the turtle headings and the home direction measured at a high spatial frequency (every 1 km in the present case). Both methods are strictly equivalent and obviously provide fully consistent results if applied to track paths. Parts of the motor paths within 20 km of a coast or a reef barrier were not taken into account in this computation because the ocean current estimates are known to be unreliable in this context.

We performed within-subject analyses to assess the turtles' ability to compensate for current drift by computing the homeward components of heading and track vectors as the cosines of the angular differences between the home and vector directions. This was done for every interpolated open-sea location (>20 km from coast or reef) where the current speed was above 25 cm/s. To avoid serial autocorrelation, we subsampled these location data by taking only one every *n* locations, where *n* is the minimum integer value specific to each path, allowing for statistical independence (at $p > 0.1$ based on an angular rank correlation test) for both heading and track vectors (see [7]). The mean track and motor homeward components were then compared with Wilcoxon signed rank tests.

Supplemental Data

Supplemental Data include two movies, one table, and one figure and are available online at http://www.current-biology.com/cgi/content/full/17/2/126/DC1/.

Acknowledgments

These experiments have only been possible thanks to the support provided by the Direction de l'Agriculture et de la Forêt (DAF) of Mayotte (in particular by R. Rolland) and its Brigade Tortue, the Collectivité Départementale of Mayotte (CDM), and the Conservatoire du Littoral. We gratefully acknowledge the most valuable field help of M. Quillard (formerly DAF and presently CDM), of J. Bourjea (Institut Français de Recherche pour l'Exploitation de la Mer, La Réunion), of Nicolas and the Passengers of the Wind (owners of the boat "Nomade"), and of all the volunteers. All the experiments have been authorized by the DAF of Mayotte. Altimeter and wind data were obtained from Collecte Localisation Satellites, Space Oceanography Division, as part of the Environment and Climate European Union Enact project with support from the Centre National d'Etudes Spatiales and from the Centre ERS d'Archivage et de Traitement (Institut Français de Recherche pour l'Exploitation de la Mer, Plouzané), respectively. Funding was provided by the Italian Space Agency and the Ministero dell'Università e della Ricerca. C.G. acknowledges La Région Réunion for providing her with a PhD grant. L. Dagorn and M. Taquet provided helpful advices and kind logistic support; F. Papi made useful comments on earlier versions of the manuscript. The manuscript substantially benefited from the constructive comments of four anonymous referees. Chris Powell (International House of Pisa) corrected the English wording.

Received: June 28, 2006
Revised: October 23, 2006
Accepted: November 3, 2006
Published: January 22, 2007

References

1. Alerstam, T. (2006). Conflicting evidence about long-distance animal navigation. Science *313*, 791–794.
2. Bingman, V.P., and Cheng, K. (2006). Mechanisms of animal global navigation: Comparative perspectives and enduring challenges. Ethology, Ecology, and Evolution *17*, 295–318.
3. Lohmann, K.J., and Lohmann, C.M.F. (2006). Sea turtles, lobsters, and oceanic magnetic maps. Marine and Freshwater Behavior and Physiology *39*, 49–64.
4. Lohmann, K.J., Lohmann, C.M.F., Ehrhart, L.M., Bagley, D.A., and Swing, T. (2004). Geomagnetic map used in sea-turtle navigation. Nature *428*, 909–910.
5. Avens, L., and Lohmann, K.J. (2004). Navigation and seasonal migratory orientation in juvenile sea turtles. J. Exp. Biol. *207*, 1771–1778.
6. Papi, F., Luschi, P., Åkesson, S., Capogrossi, S., and Hays, G.C. (2000). Open-sea migration of magnetically disturbed sea turtles. J. Exp. Biol. *203*, 3435–3443.
7. Girard, C., Sudre, J., Benhamou, S., Roos, D., and Luschi, P. (2006). Homing in green turtles *Chelonia mydas*: Oceanic currents act as a constraint rather than as an information source. Mar. Ecol. Prog. Ser. *322*, 281–289.
8. Papi, F. (1992). General aspects. In Animal Homing, F. Papi, ed. (London: Chapman and Hall), pp. 1–18.
9. Miller, J.D. (1997). Reproduction in sea turtles. In The Biology of Sea Turtles, P.L. Lutz and J.A. Musick, eds. (Boca Raton, FL: CRC Press), pp. 51–82.
10. Luschi, P., Hays, G.C., and Papi, F. (2003). A review of long-distance movements by marine turtles, and the possible role of ocean currents. Oikos *103*, 293–302.
11. Carr, A. (1972). The case for long-range chemoreceptive piloting in Chelonia. In Animal Orientation and Navigation, S.R. Galler, K. Schmidt-Koenig, G.J. Jacobs, and R.E. Belleville, eds. (Washington, D.C: NASA SP-262), pp. 469–483.
12. Murphy, T.M., and Hopkins-Murphy, S.R. (1990). Homing of translocated gravid loggerhead turtles. In Proceedings 10th Annual Symposium on Sea Turtle Biology and Conservation. NOAA Technical Memorandum NMFS-SEFC-278, T.H. Richardson, J.I. Richardson, and M. Donnelly, eds. (Miami, FL: National Oceanographic Atmospheric Administration), pp. 123–124.
13. Luschi, P., Papi, F., Liew, H.C., Chan, E.H., and Bonadonna, F. (1996). Long-distance migration and homing after displacement in the green turtle (*Chelonia mydas*): A satellite tracking study. J. Comp. Physiol. *178A*, 447–452.
14. Papi, F., Luschi, P., Crosio, E., and Hughes, G.R. (1997). Satellite tracking experiments on the navigational ability and migratory behaviour of the loggerhead turtle *Caretta caretta*. Mar. Biol. *129*, 215–220.
15. Luschi, P., Åkesson, S., Broderick, A.C., Glen, F., Godley, B.J., Papi, F., and Hays, G.C. (2001). Testing the navigational abilities of ocean migrants: Displacement experiments on green sea turtles (*Chelonia mydas*). Behav. Ecol. Sociobiol. *50*, 528–534.

16. Hays, G.C., Åkesson, S., Broderick, A.C., Glen, F., Godley, B.J., Papi, F., and Luschi, P. (2003). Island-finding ability of marine turtles. Proc. R. Soc. Lond. B. Biol. Sci. *270* (*Suppl. 1*), 5–7.
17. Bonadonna, F., Bajzak, C., Benhamou, S., Igloi, K., Jouventin, P., Lipp, H.-K., and Dell'Omo, G. (2005). Orientation in the wandering albatross: Interfering with magnetic perception does not affect orientation performance. Proc. R. Soc. Lond. B. Biol. Sci. *272*, 489–495.
18. Frazier, J. (1984). Marine turtles in the Seychelles and adjacent territories. In Biogeography and Ecology of the Seychelles Islands, D.R. Stoddart, ed. (The Hague, The Netherlands: Junk W. Publishers), pp. 417–468.
19. Benhamou, S. (2004). How to reliably estimate the tortuosity of an animal's path: straightness, sinuosity, or fractal dimension? J. Theor. Biol. *229*, 209–220.
20. Green, M., and Alerstam, T. (2002). The problem of estimating wind drift in migrating birds. J. Theor. Biol. *218*, 485–496.
21. Girard, C. 2005. Etude du comportement d'orientation d'espèces pélagiques tropicales vis-à-vis d'attracteurs. PhD thesis, University of La Réunion.
22. Wiltschko, W., and Wiltschko, R. (2005). Magnetic orientation and magnetoreception in birds and other animals. J. Comp. Physiol. *191A*, 675–693.
23. Johnsen, S., and Lohmann, K.J. (2005). The physics and neurobiology of magnetoreception. Nat. Rev. Neurosci. *6*, 703–712.
24. Mouritsen, H., Huyvaert, K.P., Frost, B.J., and Anderson, D.J. (2003). Waved albatrosses can navigate with strong magnets attached to their head. J. Exp. Biol. *206*, 4155–4166.
25. Irwin, W.P., and Lohmann, K.J. (2003). Magnet-induced disorientation in hatchling loggerhead sea turtles. J. Exp. Biol. *206*, 497–501.
26. Baldwin, H.A. (1972). Long-range radio tracking of sea turtles and polar bear—Instrumentation and preliminary results. In Animal Orientation and Navigation, S.R. Galler, K. Schmidt-Koenig, G.J. Jacobs, and R.E. Belleville, eds. (Washington, D.C: NASA SP-262), pp. 19–35.
27. Lohmann, K.J., and Lohmann, C.M.F. (1996). Detection of magnetic field intensity by sea turtles. Nature *380*, 59–61.
28. Able, K.P. (2001). The concepts and terminology of bird navigation. J. Avian Biol. *32*, 174–183.
29. Lohmann, K.J., Hester, J.T., and Lohmann, C.M.F. (1999). Long-distance navigation in sea turtles. Ethology, Ecology, and Evolution *11*, 1–23.
30. Lohmann, K.J., Cain, S.D., Dodge, S.A., and Lohmann, C.M.F. (2001). Regional magnetic fields as navigational markers for sea turtles. Science *294*, 364–366.
31. Wallraff, H.G. (2005). Avian Navigation: Pigeon Homing as a Paradigm (Berlin: Springer Verlag).
32. Wiltschko, R., and Wiltschko, W. (1985). Pigeon homing: Change in navigational strategy during ontogeny. Anim. Behav. *33*, 583–590.
33. Luschi, P., Del Seppia, C., Crosio, E., and Papi, F. (1996). Pigeon homing: Evidence against reliance on magnetic information picked up en route to release sites. Proc. R. Soc. Lond. B. Biol. Sci. *263*, 1219–1224.
34. Benhamou, S. (2003). Bicoordinate navigation based on non-orthogonal gradient fields. J. Theor. Biol. *225*, 235–239.
35. Hays, G.C., Åkesson, S., Broderick, A.C., Glen, F., Godley, B.J., Luschi, P., Martin, C., Metcalfe, J.D., and Papi, F. (2001). The diving behaviour of green turtles undertaking oceanic migration to and from Ascension Island: Dive durations, dive profiles and depth distribution. J. Exp. Biol. *204*, 4093–4098.
36. Rio, M.-H., and Hernandez, F. (2004). A mean dynamic topography computed over the world ocean from altimetry, in situ measurement, and a geoid model. J. Geophys. Res. *109*, C12032.

B.3 Article : Comparative study of mixing and biological activity of the Benguela and Canary upwelling systems, V. Rossi *et al.*, 2008

B.3.1 Abstract

We present a comparative study of the horizontal mixing properties, from satellite derived data of the surface velocity field, of the two eastern boundary Canary and Benguela upwelling systems, based on a Finite Size Lyapunov Exponents analysis. Each area can be subdivided into two subsystems attending to their mixing activity values. These coincide nicely with distinct biological signatures. When investigating links with chlorophyll as a proxy for biological activity in these two upwelling systems, results show that surface horizontal stirring and mixing vary inversely with chlorophyll standing stocks. Ekman-transport induced upwelling exhibits a positive correlation with chlorophyll. These two findings are complementary since spatial structure in plankton distributions results from both dynamics of the 3D turbulent medium and of the marine ecosystem.

B.3.2 Article publié dans *Geophysical Research Letters*

Référence : Rossi V., López C., Sudre J., Hernández-Garcia E. and Garçon V., 2008 : Comparative study of mixing and biological activity of the Benguela and Canary upwelling systems, *Gerophycal Research Letters*, **35**, L11602, DOI 10.1029/2008GL033610.

Click Here for Full Article

Comparative study of mixing and biological activity of the Benguela and Canary upwelling systems

V. Rossi,[1] C. López,[2] J. Sudre,[1] E. Hernández-García,[2] and V. Garçon[1]

Received 13 February 2008; accepted 8 April 2008; published 7 June 2008.

[1] We present a comparative study of the horizontal mixing properties, from satellite derived data of the surface velocity field, of the two eastern boundary Canary and Benguela upwelling systems, based on a Finite Size Lyapunov Exponents analysis. Each area can be subdivided into two subsystems attending to their mixing activity values. These coincide nicely with distinct biological signatures. When investigating links with chlorophyll as a proxy for biological activity in these two upwelling systems, results show that surface horizontal stirring and mixing vary inversely with chlorophyll standing stocks. Ekman-transport induced upwelling exhibits a positive correlation with chlorophyll. These two findings are complementary since spatial structure in plankton distributions results from both dynamics of the 3*D* turbulent medium and of the marine ecosystem.
Citation: Rossi, V., C. López, J. Sudre, E. Hernández-García, and V. Garçon (2008), Comparative study of mixing and biological activity of the Benguela and Canary upwelling systems, *Geophys. Res. Lett.*, *35*, L11602, doi:10.1029/2008GL033610.

1. Introduction

[2] Eastern boundary upwelling zones constitute a major contribution to the world ocean productivity. They include the Canary and Benguela upwelling systems (hereafter CUS and BUS, respectively), located along the African coast symmetrically with respect to the Equator. Both areas are characterized, among other features, by a significant equatorward alongshore advection, physical forcings by local and large scale winds, a high sub- and mesoscale activity, seaward extension beyond the continental shelf of the boundary current and an intense biological activity via filament formation.

[3] The aim of this work is to make a comparative study of these two upwelling systems, focussing on their mesoscale activity and the interaction between marine surface hydrodynamics and biological processes (similar studies in other upwelling systems can be consulted [e.g., see *Chase et al.*, 2007].

[4] The basic inputs to our analysis are satellite data of the marine surface, including velocity field and chlorophyll concentration. We quantify horizontal transport processes by the well-known technique of the Finite Size Lyapunov Exponents (FSLE) [*Aurell et al.*, 1997], which is specially suited to study the stretching and contraction properties of transport in geophysical data [*d'Ovidio et al.*, 2004]. The calculation of the FSLE goes through computing the time, τ, at which two fluid parcels initially separated at a distance δ_0, reach a final separation δ_f. At position $\mathbf{x}$ and time t the FSLE is given by $\lambda(\mathbf{x}, t, \delta_0, \delta_f) = \frac{1}{\tau}\log\frac{\delta_f}{\delta_0}$. In a typical snapshot of the FSLE [see e.g. *d'Ovidio et al.*, 2004, Figure 1] the maximum values organize in lines which are a good approximation for the areas of maximal convergence, if they are calculated for the backwards-in-time dynamics, which is the one performed all along this work. In work by *d'Ovidio et al.* [2004, also, Comparison between Eulerian diagnostics and finite-size Lyapunov exponents computed from altimetry in the Algerian basin, submitted to Deep Sea Research, 2008] and *Lehahn et al.* [2007] the adequacy of the FSLE to characterize horizontal mixing and transport structures in the upper ocean has been demonstrated, as well as its usefulness, when correlating with distributions of tracers such as temperature or chlorophyll, despite the strong intrinsic dynamics of these tracers. In particular, it is discussed that FSLEs, because of the averaging effect produced by computing them by integrating over trajectories which extend in time and space, are rather robust against noise and uncertainties in the velocity data. Here we have checked this explicitly by considering a random perturbation of the velocity field at every spatial point at any time. The error obtained in our computations of averages of FSLEs ranges between 0.3% and 2.8% for multiplicative perturbations of the velocity field of 5% and 10%, respectively. In addition, spatial averages of FSLEs can define a measure of mixing in a given spatial area, the larger this average the larger the mixing activity. Inverses of FSLEs values give estimations of mixing times. We will use the FSLEs as an analyzer tool to highlight differences and similarities between the CUS and BUS. Finally, we quantify the amount of Ekman-transport induced upwelling and find a positive correlation with chlorophyll standing stocks. We discuss how vertical and horizontal processes may lead to the observed chlorophyll distributions.

2. Data

2.1. Computation and Analysis Areas

[5] Our study focuses on the transitional area of exchange processes between the shelf and offshore in the open ocean. Among these processes, sub- and mesoscale structures such as filaments contribute to the offshore export of organic matter produced in the very coastal upwelling [*Mackas et al.*, 2006]. These filaments in the fluctuating boundary between the upwelling and the edge of the oligotrophic subtropical gyres play a key role in the modulation of the carbon balance by seeding the inner ocean. The role of this

[1] LEGOS/CNRS, Toulouse, France.
[2] Instituto de Física Interdisciplinar y Sistemas Complejos, Universitat de les Illes Balears, Palma de Mallorca, Spain.

Copyright 2008 by the American Geophysical Union.
0094-8276/08/2008GL033610$05.00

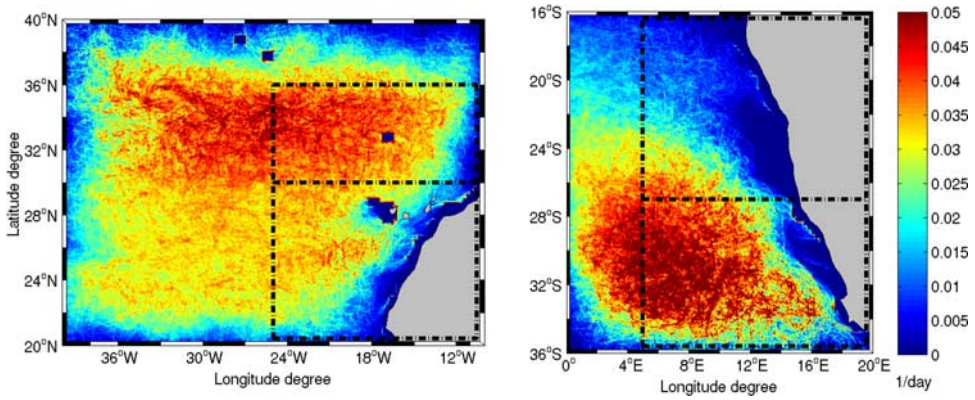

Figure 1. Time average over the period June 2000–June 2005 of the FSLEs (left) for the CUS and (right) for the BUS. The boxes denote the analysis areas of our study. The central horizontal line in each plot divides the two subregions.

moving transitional area, at the border of the gyre, westward of the maximum extension of the chlorophyll filaments, must be considered. To investigate the island effect from the Canary Archipelago and to have, at the same time, a similar analysis area for CUS and BUS, we have adapted the areas from *Mackas et al.* [2006], by approximating them to the best fitting rectangle whose lateral sides are meridionally oriented. In Figure 1, the analysis areas are shown delimited by the dashed lines (25–10°W, 20–36°N for CUS and 5–20°E, 16–36°S for BUS). We used the full geographical areas shown in Figure 1 to make our numerical computations. Note that the computation areas are larger than the analysis ones, considering the fact that particles may leave the area before reaching the fixed final distance δ_f. In addition, several tests with different shapes and area selections (not shown) lead to similar results.

2.2. Velocity and Wind Stress Data

[6] The weekly global 1/4° resolution product of surface currents developed by *Sudre and Morrow* [2008] has been used. The surface currents are calculated from a combination of wind-driven Ekman currents, at 15 m depth, derived from Quickscat wind estimates, and geostrophic currents computed from time variable Sea Surface Heights. These SSH were calculated from mapped altimetric sea level anomalies combined with a mean dynamic topography from *Rio et al.* [2005]. These weekly velocity data, which are then interpolated linearly to obtain a daily resolution, depend on the quality of their sources as the SSH fields and the scatterometer precision. However, they were validated by *Sudre and Morrow* [2008] with different types of in situ data such as Lagrangian buoys, ADCP, and current-meter float data. In both areas, zonal and meridional components show an average correlation with for e.g. Lagrangian buoy data, between 0.52 and 0.76. The Ekman transport U_E along the East-West direction was computed using the formula $U_E = T_y/(f\rho)$ where T_y is the meridional wind stress (obtained from the scatterometer Quickscat weekly wind estimates), ρ is the density of seawater and f is the Coriolis parameter.

2.3. Chlorophyll Data

[7] A 5 year long time series from June 2000 to June 2005 of ocean color data is used. Phytoplankton pigment concentrations are obtained from monthly SeaWiFS (Sea-viewing Wide Field-of-view Sensor) products of level 3 binned data, generated by the NASA Goddard Earth Science (GES)/Distributed Active Archive Center (DAAC) with reprocessing 5.1. The bins correspond to grid cells on a global grid, with each cell approximately 9 by 9 km.

3. Results

3.1. Horizontal Mixing Properties

[8] In Figure 1 we draw the time average (covering the period June 2000 – June 2005) of the FSLE computed for the CUS and BUS. Following *d'Ovidio et al.* [2004] the prescribed length-scales in our analysis are $\delta_0 = 0.025°$ and $\delta_f = 1°$ so that we focus on the mesoscale horizontal features. Choosing a slightly different value of δ_f does not alter qualitatively our results (see caption of Figure 2). For both the CUS and BUS, two different subsystems, according to their mixing activity, can be defined: north and south of 30°N for the CUS, and north and south of 27°S (latitude of the intense Lüderitz upwelling cell) for the BUS. Comparing both zones, the most clear distinction is that while in the BUS the subdivision in two areas of activity is rather evident, in the CUS this is not so sharp. Note also that the imaginary division line passes north of the Canary Archipelago.

[9] A further detailed comparison between the different subsystems follows by considering the averages of the FSLEs over the analysis areas. Results indicate similar values for the horizontal mixing times in the most active subsystems of both regions, ranging from 26 to 40 days. On the contrary, the least active subsystem in the Canary has much larger values for the FSLEs than the least active one in the BUS. While in the CUS the mixing times are in the range 37–56 days, in the BUS this is 53–90 days.

[10] *Waugh et al.* [2006] found a close relationship between the mean FSLE and the mean eddy kinetic energy (EKE) in the Tasman Sea. We have confirmed that a geographical subdivision similar to the one in Figure 1 is obtained from EKE. However, a clear relationship between these two quantities does not appear. Indeed, the Eulerian diagnostic EKE calculated for a given day only considers the corresponding snapshot of the velocity field and can not catch any temporal variability whereas the FSLE Lagrangian method does. Thus a robust relationship between EKE and FSLE is not expected when velocity fields are highly

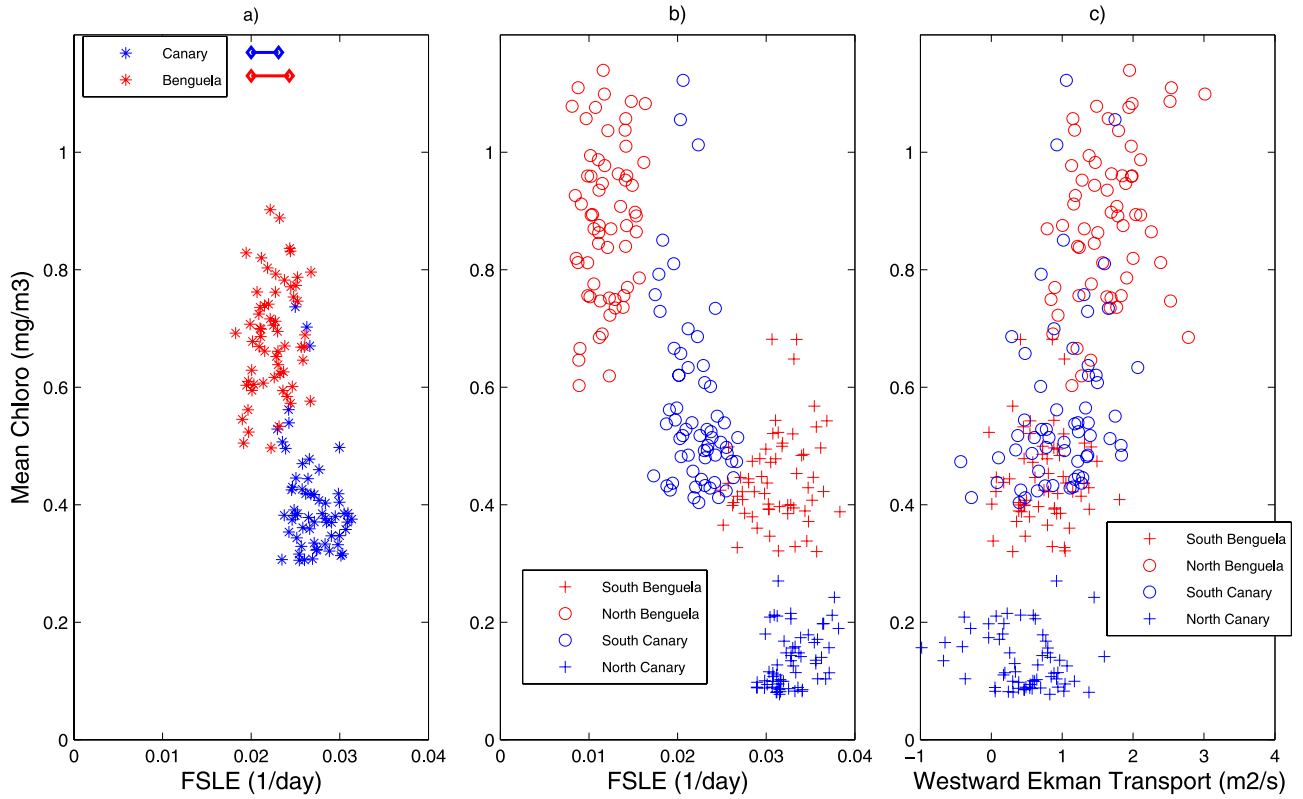

Figure 2. (a) Monthly-mean chlorophyll concentrations versus FSLE for the whole area: blue asterisks for CUS and red for BUS. Each horizontal bar represents the spatial averaged standard error of a FSLE mean for each domain, BUS (red) and CUS (blue). These errors were calculated at each grid point from temporal FSLE means over the 5 years time series. (b) Same for the different subregions as denoted in the legend. (c) Same as Figure 2b but for monthly-mean chlorophyll concentrations vs Ekman transport. The correlation coefficient for all the data in a) is $R^2 = -0.62$. This coefficient changes to -0.53, and -0.66, when changing δ_f to $\delta_f = 0.8°$ and $\delta_f = 1.2°$, respectively. If we consider the different subregions in b), the correlation coefficient is $R^2 = -0.83$. For $\delta_f = 0.8°$ and $\delta_f = 1.2°$, it becomes -0.80 and -0.85, respectively.

variable. A detailed study of the relation between FSLE and Eulerian measurements is given by d'Ovidio et al. (submitted manuscript, 2008).

3.2. Biological Activity

[11] We study here the correlation of the FSLEs (horizontal mixing) with chlorophyll concentration data. Hovmöller plots of the surface chlorophyll distribution in both the BUS and CUS (not shown here) reveal the existence of two spatial zones with very distinct degree of chlorophyll in each upwelling system. The lines separating them (around 30°N for CUS and 27°S for BUS) coincide with those obtained from the FSLE analysis.

[12] If one plots spatial averages of chlorophyll concentration versus spatial averages of FSLE, over the entire analysis area (Figure 2a) and over each subsystem (Figure 2b), for each month from June 2000 to June 2005, a negative correlation between FSLEs and chlorophyll concentration emerges. For both areas, the subsystems with more mixing activity are the ones poorer in chlorophyll. This is in the line of *Gruber et al.* [2007] findings of meso and sub-mesoscale processes associated to reduced biological activity in coastal upwelling systems. We note that theoretical studies in idealized settings, in which nutrients reach plankton only by lateral stirring, display also negative correlation between mixing and biomass (although mixing and productivity may be positively correlated) [*Tél et al.*, 2005; *Birch et al.*, 2007].

[13] Upwelling areas are definitely affected by water vertical movements and velocities which are not captured by the surface analysis provided by FSLEs. Thus, the vertical part of the physical forcing will be taken in consideration in the following. Moreover, we examine the influence of Ekman transport which brings nutrients from the coast and can also play a very relevant role in the chlorophyll signature.

[14] First we evaluate the horizontal divergence of the surface velocity field: $\Delta(x, y, t) \equiv \partial_z v_z = -(\partial_x v_x + \partial_y v_y)$. Negative (positive) values of Δ indicate upwelling (downwelling) areas because it signals surface spatial points where fluid parcels diverge (converge). Figure 3 shows the average value of Δ over the period June 2000–June 2005 for the CUS and BUS. The blue color of the Δ field in the coastal areas indicates the presence of upwelling processes there. Note that in the coastal zones of the Benguela, the well known upwelling cells Cape Frio, Walvis Bay and Lüderitz in the northern subsystem appear clearly, being more intense than the southern cells, in agreement with *Monteiro*'s [2008] estimates of the northern system accounting for 80%, on average, of the total upwelled flux over the whole BUS.

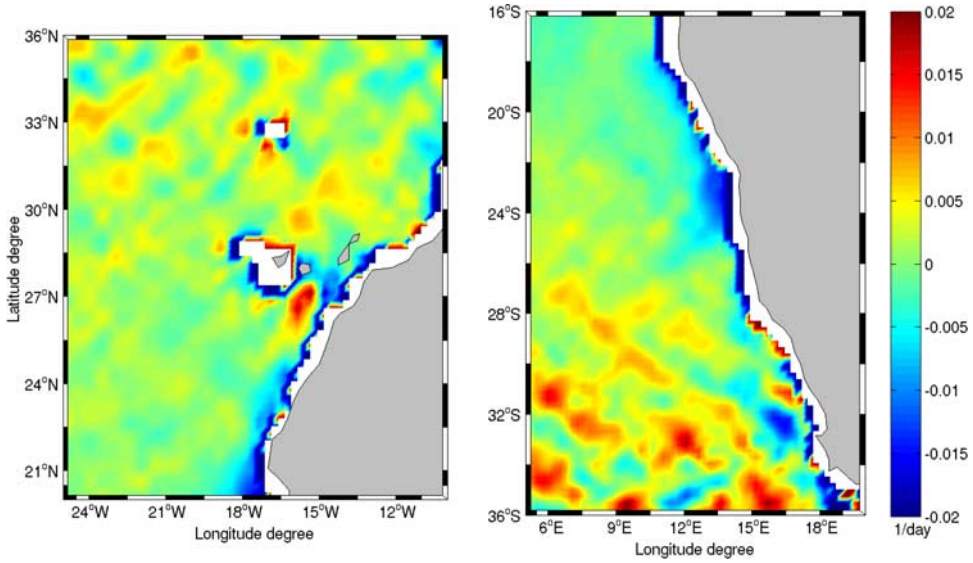

Figure 3. Temporal average value of the field $\Delta\,(x, y, t) \equiv \partial_z\, v_z = -(\partial_x\, v_x + \partial_y\, v_y)$ over the period June 2000–June 2005 for (left) CUS and (right) BUS. The blue color indicates upwelling areas whereas red signals downwelling ones.

Concerning the CUS (Figure 3, left) one can see a slight blue-color predominancy (enhanced upwelling) in the southern subregion.

[15] When we compute the Ekman transport we observe that the northern region of the BUS, richer in chlorophyll, is characterized by a higher offshore transport. In the CUS, both sub-areas have high values for the offshore transport very close to the coast, with similar values in the southern and northern subregions. Further from the coast, the highest westward transport in the southern CUS area coincides again with the highest chlorophyll content. Figure 2c shows spatial averages of chlorophyll concentration vs averages of Ekman transport over each subsystem. Negative values of the average from June 2000 to June 2005 indicate an offshore transport to the east, whereas positive ones indicate a transport to the west. A positive correlation appears confirming the effect of Ekman-transport induced upwelling on biological productivity. This finding is not incompatible with the distinct clustering (Figures 2a and 2b) since horizontal currents are strongly related to the vertical circulation. Creation of sub- and mesoscale surface chlorophyll structures results from the full 3*D* turbulent motion of the ocean.

4. Summary and Conclusions

[16] The distribution of FSLEs computed over a 5 year period with state of the art velocity fields derived from multiple sensors (altimeter, scatterometer) allowed us to compute horizontal stirring rates in the surface ocean of two major eastern boundary upwelling systems of the Atlantic ocean: the Canary and Benguela systems. A clear subdivision within each system appeared according to the mixing activity, coinciding with distinct levels of chlorophyll richness.

[17] Previous studies have suggested that eddies tend to enhance biological productivity in the open ocean, particularly in low nutrient environments. Finding a negative correlation between horizontal mixing and chlorophyll standing stocks suggests that this may not apply to upwelling regions. Comparing Figures 1 and 3 shows that areas characterized by high FSLE are correlated with intense vertical movements (downwellings as well as upwellings), whereas the areas with low FSLE are mainly dominated by upwards vertical velocities (upwellings). *Lehahn et al.* [2007] recently showed that vertical motions associated with eddies are more precisely located close to the lines of high FSLE. Regions of high FSLE averages indicate a high occurrence of intense eddies which modify the three dimensional mean flow. The nutrient Ekman pumping, dominant process in upwelling areas, weakened and the fueling of nutrients toward the surface decreased.

[18] Another possible explanation may rest upon the fact that upwelling from deeper waters and offshore Ekman transport of nutrients are important mechanisms for surface-waters enrichment. In the areas where the Ekman drift dominates over mesoscale activity, like in the northern BUS and southern CUS, a large dispersion of fluid particles, i.e., large values of FSLEs, does not occur. This would also indicate that the horizontal turbulent mixing of nutrients in surface waters is a second-order effect for biomass enhancement as compared to the vertical mechanisms.

[19] Other factors may of course influence the phytoplanktonic biomass. *Chase et al.* [2007] for instance showed in the upwelling system of the U. S. West Coast that there is a link between chlorophyll concentration and iron availability through river inputs and shelf deposition/re-suspension processes. In our two systems BUS and CUS exhibiting a larger shelf than that of the U.S. West coast, the very low river runoff can not deliver any major iron input to the inner shelf. Moreover, high dust deposition occurs leading to non-limiting iron concentration in both systems [*Jickells et al.*, 2005; *Mackas et al.*, 2006]. Consequently we did not consider these controls as primary factors in our analysis. Further work should investigate the robustness of the relationship found in our two systems when examining FSLEs versus production. Still much needs to be done to fully understand how plankton distributions are controlled

by the interplay between their turbulent medium and the non-linear processes of their ecology. However FSLEs lead to a clear clustering of subsystems suggesting that one may use these simple Lagrangian diagnostics as integrated and comparative indices for characterizing horizontal dynamical features in all eastern boundary upwellings.

[20] **Acknowledgments.** V.R. and C.L. were awarded a EUR-OCEANS Network of Excellence grant. V.R. is supported by a Ph.D. grant from DGA. V.G. acknowledges funding support from CNES, and C.L. and E.H-G. acknowledge funding support from PIF project OCEANTECH of the Spanish CSIC and FISICOS of MEC and FEDER. Ocean color data are produced by the SeaWiFS project at GES and obtained from the DAAC. We thank anonymous reviewers for their constructive comments.

References

Aurell, E., G. Boffetta, A. Crisanti, G. Paladin, and A. Vulpiani (1997), Predictability in the large: An extension of the concept of Lyapunov exponent, *J. Phys. A Math Gen.*, *30*, 1–26.

Birch, D. A., Y.-K. Tsand, and W. R. Young (2007), Bounding biomass in the Fisher equation, *Phys. Rev. E*, *75*, 066304, doi:10.1103/PhysRevE.75.066304.

Chase, Z., P. G. Strutton, and B. Hales (2007), Iron links river runoff and shelf width to phytoplankton biomass along the U. S. West Coast, *Geophys. Res. Lett.*, *34*, L04607, doi:10.1029/2006GL028069.

d'Ovidio, F., V. Fernández, E. Hernández-García, and C. López (2004), Mixing structures in the Mediterranean Sea from finite-size Lyapunov exponents, *Geophys. Res. Lett.*, *31*, L17203, doi:10.1029/2004GL020328.

Gruber, N., H. Frenzel, P. Marchesiello, J. C. McWilliams, T. Nagai, and G.-K. Plattner (2007), On the role of eddies for coastal productivity and carbon export to the open ocean, *Geophys. Res. Abstr.*, *9*, 07743.

Jickells, T. D., et al. (2005), Global iron connections between desert dust, ocean biogeochemistry, and climate, *Science*, *308*, 67–71.

Lehahn, Y., F. d'Ovidio, M. Lévy, and E. Heyfetz (2007), Stirring of the northeast Atlantic spring bloom: A Lagrangian analysis based on multi-satellite data, *J. Geophys. Res.*, *112*, C08005, doi:10.1029/2006JC003927.

Mackas, D., P. T. Strub, A. C. Thomas, and V. Montecino (2006), Eastern ocean boundaries pan-regional view, in *The Sea*, vol. 14a, *The Global Coastal Ocean: Interdisciplinary Regional Studies and Syntheses: Pan-Regional Syntheses and the Coasts of North and South America and Asia*, edited by A. R. Robinson and K. H. Brink, chap. 2, pp. 21–60, Harvard Univ. Press, Cambridge, Mass.

Monteiro, P. M. S. (2008), Carbon fluxes in the Benguela Upwelling system, in *Carbon and Nutrient Fluxes in Continental Margins: A Global Synthesis*, edited by K. K. Liu et al., chap. 2.4, Springer, New York, in press.

Rio, M.-H., P. Schaeffer, F. Hernández, and J.-M. Lemoine, (2005), The estimation of the ocean Mean Dynamic Topography through the combination of altimetric data, in-situ measurements and GRACE geoid: From global to regional studies. paper presented at GOCINA Workshop, Cent. Eur. de Geodyn. et de Seismol., Kirchberg, Luxembourg.

Sudre, J., and R. Morrow (2008), Global surface currents: A high resolution product for investigating ocean dynamics, *Ocean Dyn*, in press.

Tél, T., A. de Moura, C. Grebogi, and G. Karolyi (2005), Chemical and biological activity in open flows: A dynamical system approach, *Phys. Rep.*, *413*, 91–196.

Waugh, D., E. Abraham, and M. Bowen (2006), Spatial variations of stirring in the surface ocean: A case study of the Tasman Sea, *J. Phys. Oceanogr.*, *36*(3), 526–542.

V. Garçon, V. Rossi, and J. Sudre, LEGOS/CNRS, Toulouse, F-31401 CEDEX 9, France. (veronique.garcon@legos.obs-mip.fr)

E. Hernández-García and C. López, Instituto de Física Interdisciplinar y Sistemas Complejos IFISC, Campus Universitat de les Illes Balears, E-07122 Palma de Mallorca, Spain.

B.4 Article : Top marine predators track Lagrangian coherent structures, E. Tew Kai *et al.*, 2009

B.4.1 Abstract

Meso- and submesoscales (fronts, eddies, filaments) in surface ocean flow have a crucial influence on marine ecosystems. Their dynamics partly control the foraging behavior and the displacement of marine top predators (tuna, birds, turtles, and cetaceans). In this work we focus on the role of submesoscale structures in the Mozambique Channel in the distribution of a marine predator, the Great Frigatebird. Using a newly developed dynamic concept, the finite-size Lyapunov exponent (FSLE), we identified Lagrangian coherent structures (LCSs) present in the surface flow in the channel over a 2-month observation period (August and September 2003). By comparing seabird satellite positions with LCS locations, we demonstrate that frigatebirds track precisely these structures in the Mozambique Channel, providing the first evidence that a top predator is able to track these FSLE ridges to locate food patches. After comparing bird positions during long and short trips and different parts of these trips, we propose several hypotheses to understand how frigatebirds can follow these LCSs. The birds might use visual and/or olfactory cues and/or atmospheric current changes over the structures to move along these biologic corridors. The birds being often associated with tuna schools around foraging areas, a thorough comprehension of their foraging behavior and movement during the breeding season is crucial not only to seabird ecology but also to an appropriate ecosystemic approach to fisheries in the channel.

B.4.2 Article publié dans *Proceedings of the National Academy of Sciences*

Référence : Tew Kai E., Rossi V., Sudre J., Weimerskirch H., Lopez C., Hernandez-Garcia E., Marsac F. and Garçon V., 2009 : Top marine predators track Lagrangian coherent structures, *Proceedings of the National Academy of Sciences*, **106**, 20, 8245-8250, DOI 10.1073/pnas.0811034106.

Top marine predators track Lagrangian coherent structures

Emilie Tew Kai[a,1], Vincent Rossi[b], Joel Sudre[b], Henri Weimerskirch[c], Cristobal Lopez[d], Emilio Hernandez-Garcia[d], Francis Marsac[a], and Veronique Garçon[b]

[a]Institut de Recherche pour le Développement, UR 109, Centre de Recherche Halieutique Méditerranéenne et Tropicale, 34203 Sète Cedex, France; [b]Laboratoire d'Etudes en Géophysique et Océanographie Spatiale, Centre National de la Recherche Scientifique, 31401 Toulouse Cedex 9, France; [c]Centre d'Etudes Biologiques de Chizé, Centre National de la Recherche Scientifique, 79360 Villiers en Bois, France; and [d]Instituto de Física Interdisciplinar y Sistemas Complejos, Consejo Superior de Investigaciones Cientificas–Universitat de les Illes Balears, E-07122 Palma de Mallorca, Spain

Edited by David M. Karl, University of Hawaii, Honolulu, HI, and approved March 30, 2009 (received for review October 31, 2008)

Meso- and submesoscales (fronts, eddies, filaments) in surface ocean flow have a crucial influence on marine ecosystems. Their dynamics partly control the foraging behavior and the displacement of marine top predators (tuna, birds, turtles, and cetaceans). In this work we focus on the role of submesoscale structures in the Mozambique Channel in the distribution of a marine predator, the Great Frigatebird. Using a newly developed dynamic concept, the finite-size Lyapunov exponent (FSLE), we identified Lagrangian coherent structures (LCSs) present in the surface flow in the channel over a 2-month observation period (August and September 2003). By comparing seabird satellite positions with LCS locations, we demonstrate that frigatebirds track precisely these structures in the Mozambique Channel, providing the first evidence that a top predator is able to track these FSLE ridges to locate food patches. After comparing bird positions during long and short trips and different parts of these trips, we propose several hypotheses to understand how frigatebirds can follow these LCSs. The birds might use visual and/or olfactory cues and/or atmospheric current changes over the structures to move along these biologic corridors. The birds being often associated with tuna schools around foraging areas, a thorough comprehension of their foraging behavior and movement during the breeding season is crucial not only to seabird ecology but also to an appropriate ecosystemic approach to fisheries in the channel.

frigatebird | finite-size Lyapunov exponent | Mozambique Channel | submesoscale

In the oligotrophic open ocean mesoscale and submesoscale oceanic turbulence, which spans spatiotemporal scales from one to hundreds of kilometers and from hours to weeks, strongly modulates the structure, biomass, and rates of marine pelagic ecosystems. Eddies can stimulate the primary productivity (1, 2), affect plankton community composition (3–5), or play a significant role in exchange processes in the transitional area between the coast and offshore by transporting organic matter and marine organisms from the coast to the open ocean and vice versa (6). In view of the strong influence of eddies on physical and biogeochemical properties, it is not surprising that higher-level predators concentrate around them, where prey can be found. In fact, all investigations on the relationship between eddies and top-predator communities, using satellite imagery observations, have shown strong ties between them (7, 8). Upper predators particularly used the boundary between 2 eddies (9–12). The key point is that interactions between eddies generate strong dynamic interfaces (13) and make them a complex and energetic physical environment. In these interfaces the energy of the physical system is available to biologic processes, increasing the trophic energy of the biologic system (8). Eddies and associated structures therefore have a crucial ecologic significance, especially in tropical and subtropical regions, characterized by low mixing during winter, inferring weak supply of nutrients to the photic zone (11).

Most previous work dealing with the influence of eddies on top-predator distribution show the necessity of concentrating on submesoscale (<10 km) to fully appreciate the role of eddy–eddy interfaces on biologic production (11). Many different studies confirm that submesoscale tracer patches and filaments are strongly related to interactions between mesoscale surface eddies (1, 14). Despite this, studies on top predators using remote sensing have only used sea surface height as an indicator of eddy activity, which does not resolve submesoscale structures such as filaments, where production should be concentrated. In addition, a fundamental question remains: how do top predators find these zones of higher productivity? This is particularly difficult to understand for central-place foragers, such as seabirds, that breed on land but have to make continuous return trips between feeding zones and the colony where they care for their chick or egg. The additional difficulty in the case of eddies is that the location of production zones moves continuously.

In the West Indian Ocean, the Mozambique Channel (MC) can be considered a natural laboratory to study interactions between biologic and physical processes at mesoscale in oligotrophic areas (subtropical region) because of the transient activity of eddies. Indeed, mesoscale dynamics of the MC have been well described by previous works using remote sensing data, modeling, and in situ observations (15–17). Mesoscale activity is dominant in 2 areas, the central part of the MC and south of Madagascar (17, 18). Weimerskirch et al. (10) have shown the main role of mesoscale eddies on the foraging strategy of Great Frigatebirds. These birds fly hundreds or thousands of kilometers from the colony in a few days and spend their entire foraging trips in flight, being unable to sit on the water or enter the water column. Bird pathways are preferentially associated with eddies in the MC during their long trips and especially with the edge of eddies, avoiding their core (10). However, it is not clear where exactly they forage in the eddy system and whether and how they locate the zones of high production. The aim of the present study is to describe the fine-scale activity occurring at the edge of eddies and other submesoscale structures and to quantify the role of these on a top predator's foraging movements. We also try to understand how and why these predators might locate these structures.

For the physical environment, we have used horizontal velocity fields computed from satellite altimetry products (19). We have applied to them a recently developed Lagrangian technique, the finite-size Lyapunov exponent (FSLE), which allows computing from marine surface velocity field data, mixing activity and coherent structures that control transport at specified scales (20). FSLEs

Author contributions: E.T.K. and V.G. designed research; E.T.K., V.R., and V.G. performed research; E.T.K., V.R., J.S., C.L., E.H.-G., and F.M. contributed new reagents/analytic tools; E.T.K. and V.R. analyzed data; and E.T.K., V.R., H.W., C.L., E.H.-G., and V.G. wrote the paper.

The authors declare no conflict of interest.

This article is a PNAS Direct Submission.

Freely available online through the PNAS open access option.

[1]To whom correspondence should be addressed. E-mail: emilie.tewkai@ird.fr.

This article contains supporting information online at www.pnas.org/cgi/content/full/0811034106/DCSupplemental.

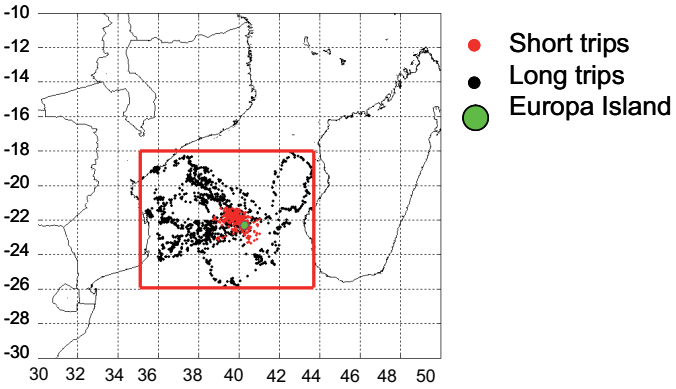

Fig. 1. Argos locations of Great Frigatebirds during long trips (black points) and short trips (red points) in the MC, between August 18 and September 30, 2003. The green point denotes Europa Island.

measure how fast fluid particles separate to a specified distance. Lagrangian coherent structures (LCSs) (e.g., transport barriers, filamental structures, or vortex boundaries) are identified as ridges (locations containing the maximum values) of Lyapunov exponent fields (21–24). Dispersion rates of tracer particles can be calculated by integrating trajectories toward the future (forward) or toward the past (backward), giving rise to 2 different quantifiers, $FSLE_f$ and $FSLE_b$, respectively, containing complementary information (see *Materials and Methods*). Ridges of $FSLE_b$ attract neighboring trajectories, whereas $FSLE_f$ repel them. This is why we call them *attracting* and *repelling* LCSs, respectively. Sometimes, especially for plotting, it is convenient to write $FSLE_b$ and $FSLE_f$ as having negative and positive values, respectively, and expressions such as |FSLE| refer simultaneously to both types of exponents. For the marine top predators, we have used Argos positions of Great Frigatebirds from the colony on Europa Island in the MC during August and September 2003. Additional details are given in *Materials and Methods*.

In this study we test whether seabird positions during their foraging trips are related to dynamic structures. This is performed in different contexts: during short and long trips, day and night, and during the outward part of their foraging trips and the return back to the colony. We finally discuss which foraging strategy these top predators might use to locate prey patches.

Results

Seabird Locations During Trips and FSLE Fields. We compare here the locations of the LCSs identified as ridges in FSLE maps and measured bird positions during August and September 2003. We will see that the latter are not random but correlated with the former.

First, Fig. 1 shows Argos positions of Great Frigatebirds during long trips (black points) and short trips (red points) between August 18 and September 30, 2003. Locations of seabirds during long trips superimposed on FSLEs fields (September 24 to October 6, 2003) are shown in Fig. 2. During the week of September 24, bird 11377 (green circles) is located on high $FSLE_b$ values (the attracting LCSs), as is bird 16255 (blue circles). The positions of bird 8023 (red circles) seem to be linked to fluid repelling structures (the ridges of $FSLE_f$) instead. For bird 8023, at the beginning of travel, the trajectory is rectilinear in the northeast direction and then follows the repelling mushroom-like structures. Foraging patches (triangles), where birds reduce flying speed, seem to exhibit the same distribution as the birds' moving positions. During the week of October 6 the movements of bird 8023 are mostly on repelling structures (Fig. 2*D*), as during the week of September 24, and perhaps also on some attracting structures. The important point is that any of both types of LCSs is more visited than locations outside. The positions of bird 19827 (magenta circles) are well superimposed on fluid attracting structures (ridges of $FSLE_b$) but not on repelling ones. These 2 examples of the overlay of seabird movement and foraging positions on FSLE fields during long trips show that the locations of birds tend to overlay on LCSs, either on attracting (Fig. 2 *A* and *C*) or repelling ones (Fig. 2 *B* and *D*).

To put the above observations in quantitative form, we specified a threshold defining a significant presence of LCSs: $|FSLE| > 0.1$ d^{-1}. It corresponds to mixing times smaller than 1 month. This value is chosen because it is a typical value for Lyapunov exponents in different areas of the globe (14, 20) and because regions where the Lyapunov exponents are larger already have the shape of 1-dimensional lines (see Fig. 2). The distributions of FSLEs in the whole MC and the central part and in areas crossed by seabirds were tested for conformity to the normal distribution using the Kolmogorov-Smirnov (KS) sample test, and they all are clearly non-normal. Histograms of relative frequency of FSLE in the whole MC, the central part, and in areas visited by seabirds are shown in Fig. 3. In the whole MC and the central part, Lagrangian structures detected by $|FSLE| > 0.1$ day^{-1} represent a minority of locations, occupying ≤30% of the total area. However, in areas crossed by frigatebirds

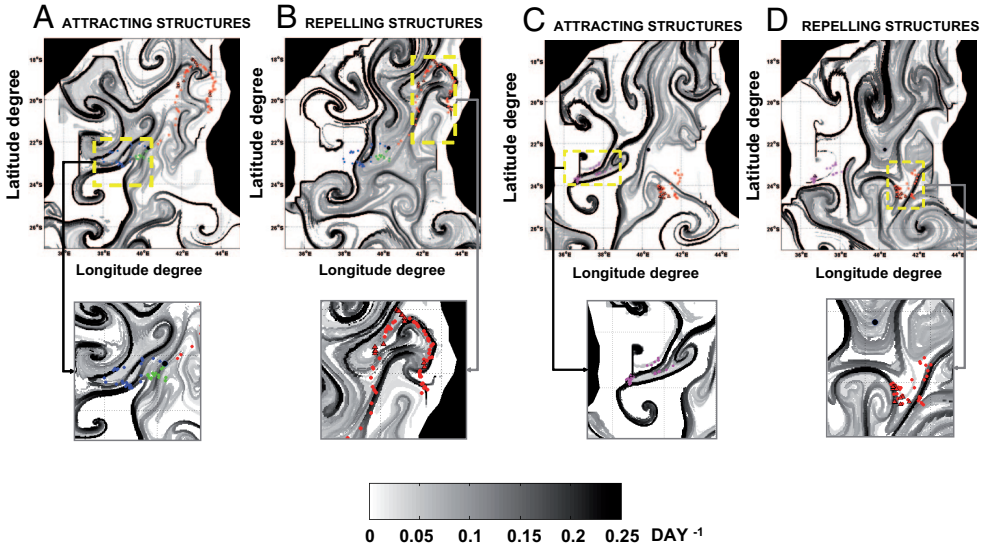

Fig. 2. Overlays of seabird positions on FSLE maps. (*A* and *C*) Backward integration in time for FLSE computation (d^{-1}). (*B* and *D*) Forward integration in time (d^{-1}). *A* and *B*, week of September, 24, 2003. *C* and *D*, week of October, 6, 2003. Circles represent seabird trajectories and triangles foraging patches. Each color represents the tag of a different bird (red, tag 8023; blue, tag 16255; green, tag 11377; magenta, tag 19827).

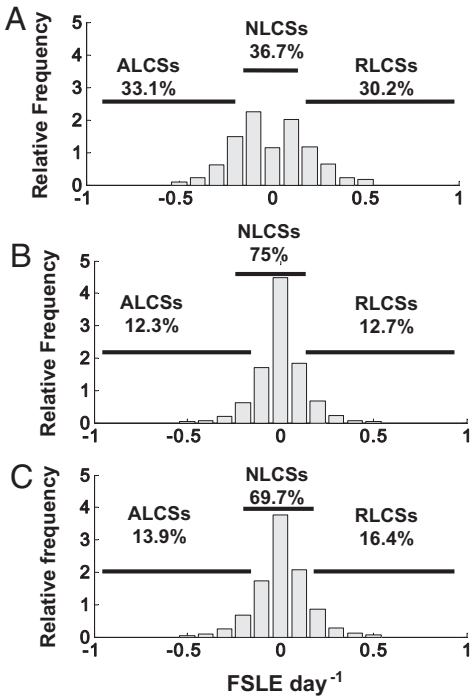

Fig. 3. Histograms of relative frequency of FSLEs with percentage of attracting (ALCSs) and repelling LCSs (RLCSs). Positive values refer to $FSLE_f$ and negative to $FSLE_b$. (*A*) Areas crossed by seabirds (long and short trips); (*B*) in the whole MC; and (*C*) in the central part (16°–24°S/30°–45°E).

>60% of the birds are on LCSs. Five KS 2-sample (KS-2) tests comparing the distributions of FSLEs in the whole MC and in the central part with the distribution of FSLEs on areas visited by seabirds during long and short trips were performed. The tests confirmed that distributions of FSLEs in areas crossed by seabirds are highly different from those found over the whole area and the central part ($P < 0.0001$ for both long and short trips). Distribution patterns provide clear evidence that Great Frigatebirds are not randomly distributed throughout the FSLE range (both backward and forward) and that seabirds move over specific areas rich in LCSs, despite the area occupied by LCSs being small. Nearly two-thirds of the birds' positions are on LCSs, even though only ≤30% of the whole area or the central part (Fig. 3) contain high |FSLE| and are then occupied by LCSs. These numbers were further checked by χ^2 analyses using the 1-tailed G-test for goodness of fit (log-likelihood ratio), which clearly show that there are significant differences between positions of birds on LCSs and on other structures (Table 1) (G-test, $P < 0.001$); this confirms again that seabird positions are located more on LCSs ($|FSLE| > 0.1$ day $^{-1}$) than outside during long and short trips, despite the small area occupied by LCSs (Fig. 3). An additional test checking the relationship between bird positions at a given week t and the LCSs computed for that week and for the following weeks, t + 1, t + 2, . . . t + 9, is described in the supporting information (SI) *Methods*. The association of bird tracks and LCSs, measured by the significance of a G-test, is highest for the LCSs of week t and decreases with the time lag to the other weeks ($p_{t+1} = 0.81 > p_{t+3} = 0.19 > p_{t+5} = 0.12$) (Table S1).

FSLE Distributions over Different Types of Flights. We performed several statistical tests to determine whether there are statistically significant differences among travel/foraging locations, outgoing/return trips, and day/night flights.

Boxplots of FSLEs on seabird positions during long and short trips are presented in Fig. 4. The range of variation of FSLE is clearly more dispersed during long trips than short trips, and the median between both kinds of trips is similar. Furthermore, distributions are clearly different between long and short trips, as confirmed by a KS-2 test ($P \ll 0.001$). Indeed, 65.9% of seabird positions during long trips and 56% during short trips are on LCSs (Table 1). During long trips, Great Frigatebirds forage during a longer time and so cover a larger range of variation of FSLE values than during short trips. One-tailed G-test for goodness of fit confirms that there is a difference between the number of seabird locations on FSLE ridges and outside the ridges (Table 1) ($G = 30.613, P = 0.001$, df = 10 for long trips; and $G = 32.057, P \ll 0.001$, df = 6 for short trips).

KS-2 tests show that the distribution of the birds between attracting and repelling LCSs displays no statistically significant difference during long trips ($P > 0.05$) but differs during short trips ($P < 0.01$). During short trips birds follow the attracting LCSs more than the repelling ones. The analyses clearly demonstrate that

Table 1. Absolute frequency of seabird positions on LCSs and on no Lagrangian structures for long and short trips per week and result of the G-test for goodness of fit

	All trips		Long trips		Short trips	
Week	LCSs: $\|FSLE\| > 0.1$ day^{-1}	$\|FSLE\| < 0.1$ day^{-1}	LCSs: $\|FSLE\| > 0.1$ day^{-1}	$\|FSLE\| < 0.1$ day^{-1}	LCSs: $\|FSLE\| > 0.1$ day^{-1}	$\|FSLE\| < 0.1$ day^{-1}
1	38	9	19	7	19	2
2	78	40	55	12	23	28
4	208	85	147	54	61	31
5	167	109	137	84	30	25
6	120	77	89	51	31	26
7	79	55	72	32	7	23
8	53	34	53	34	—	—
9	61	59	61	59	—	—
10	55	31	45	24	10	7
14	35	12	35	12	—	—
15	10	5	10	5	—	—
%	63.7	36.3	65.9	34.1	56.0	44.0
G-test (log-likelihood ratio)						
n	1420		1097		323	
k	11		11		7	
df	10		10		6	
G	28.119		30.613		32.057	
P	0.00173		0.001		0.000	

One-tailed tests. Null hypothesis Ho: Seabird positions share equally LCSs ($|FSLE| > 0.1$ day^{-1} and on no LCSs. $\alpha = 5\%$.

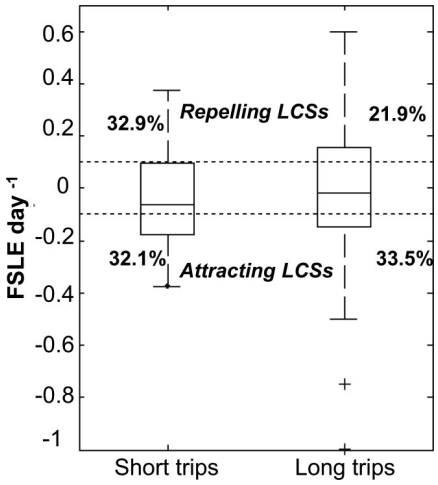

Fig. 4. Box plots of the distribution of FSLEs during short and long trips. The upper and lower ends of the center box indicate the 75th and 25th percentiles of the data; the center of the box indicates the median. Suspected outliers appear in a box plot as individual points (+) outside the box. Dotted lines represent the threshold for detection of LCSs.

seabirds follow the FSLE ridges during their foraging trips, but more during long trips than during short trips. This result emphasizes the probable difference in Great Frigatebird behavior during long vs. short trips.

Boxplots of FSLE show that patterns of distribution of FSLE are not very different between flying and foraging positions (Fig. S1). Distributions of FSLEs are statistically similar for foraging and crossed areas (KS-2 test, $P = 0.29$ for long trips and $P = 0.51$ for short trips) but differ from FSLE distribution in the whole area (KS test, $P < 0.0001$). During long trips 69.6% of seabird positions during flying and 62% during foraging are on LCSs (Fig. S1); these figures are 61.8% and 66.7%, respectively, during short trips. During flying and foraging seabirds split almost equally between repelling and attracting structures (G-test, $P > 0.05$) (Table S2). All of this indicates that seabirds seem to prefer being on ridges of FSLE both for travel and foraging.

We have also investigated differences in seabird distributions in relation to FSLEs between the outward and return parts of the trip (Fig. S2 *A* and *C*). KS-2 test shows that there is no significant difference of seabird distribution during long trips (KS-2, $P > 0.01$) and during short trips ($P > 0.05$), between the outward and return parts of the trip. For all types of trips (short and long) there is no significant difference of seabird positions, either on repelling or attracting flow structures, during the outward and return parts of the trip (G-test, $P > 0.05$) (Table S3).

Great Frigatebirds feed mainly during daytime (10). We therefore examined whether we could identify differences between day- and nighttime distribution of seabirds. Boxplots of seabird distribution on FSLE between day and night show that patterns of distribution of FSLEs are similar during day and night during short (Fig. S2*B*) and long trips (Fig. S2*D*). The range of variation of FSLE during long trips is, however, more dispersed at night than during short trips. KS-2 test shows that there is no significant difference between FSLE distributions visited by birds during day and night ($P > 0.05$ during long or short trips). The probability for the frigatebirds to fly over attracting or repelling structures during day and night is statistically similar (G-test, $P > 0.05$) for long trips but may be different for short trips (G-test, $P = 0.025$) (Table S3). During daytime short trips, seabirds may follow the attracting structures more than the repelling ones.

Discussion

Because eddies affect all stages of the marine ecosystem, they are determinant for the triad "enhancement–concentration–retention" identified by Bakun (8, 25). From upwelling-driven processes at the center of cyclonic eddies (1, 2), or from other processes at the boundaries between eddies (13), local enrichment and new production have been observed. The cyclic circulation in vortices also produces retention of larvae and other planktonic organisms in their core, whereas concentration occurs in the convergence zones located at the boundary between them, which are detected by FSLEs.

Transport barriers and filament generation by interaction between eddies induce horizontal and vertical biogeochemical and biologic enhancement (13). FSLEs seem very well suited to detect such transport barriers, vortex boundaries, and filaments at meso- and submesoscale (20, 26) and to study the link with the ecologic behavior of marine top predators. However, a word of caution is required about the spatial resolution we used. Indeed, the FSLEs are computed from satellite altimetry products (19), with a spatial resolution of 1/4° interpolated here onto a 1/40° grid. This interpolation might induce some bias in the data. However, FSLEs, because of the averaging effect produced by computing them by integrating over trajectories that extend in time and space, are rather robust against noise and uncertainties in velocity data (26, 27) (see also *SI Methods*). The velocity field used here has been validated, and the correlation with velocities from Lagrangian drifting buoy data in the MC was satisfactory (*SI Methods* and Fig. S3). Furthermore, Argos positioning of birds is not of equivalent quality. Some positions have a margin of error of a few hundred meters, whereas others have an error margin of more than 1 km. Definite improvements would be to reduce interpolation by using an original higher-resolution velocity field and to obtain more precise bird locations.

In the central part of the MC, it is known that the boundary of eddies is very energetic and allows the aggregation of top-predator foraging, especially Great Frigatebirds (10), which preferentially stay in this part of the channel. To date it was believed that Great Frigatebirds used edges of eddies mainly for food because these areas are rich in forage species and associated top predators [especially tuna and dolphins (28)]. Superimposing Great Frigatebird positions on FSLE fields shows that their spatial distribution is linked to eddies and more generally to the different types of LCSs, and not only for foraging but also for traveling. Observations are in agreement with the histograms and KS tests, which demonstrate that seabirds are not randomly distributed in relation to attracting and repelling LCSs.

However, analysis of location of seabirds during long and short trips shows that the percentage of positions on LCSs is different between both kinds of trips (Table 1). During long trips, birds seem to take full measure of the LCSs, whereas on short trips they do not take full advantage of them. This difference between long and short trips is probably due to the behavior of seabirds. During short trips birds have to bring food frequently to their chick, so they feed in areas where prey are easily accessible, close to Europa Island. They used preferentially attracting structures during daytime, probably because these structures are conducive to the aggregation of prey. During long trips birds avoid areas near Europa Island, probably because the foraging yield is less rich than that of more distant waters and/or because of strong interspecific competition near the island (10). However, birds preferentially follow the LCSs in both cases.

In addition, seabirds follow LCSs not only for their foraging but also for their traveling movements. The distributions of FSLEs during the outward and inbound journeys to the colony indicate that they exhibit the same flying behavior before and after their foraging activity. Furthermore, the fact that the distribution of visited FSLEs is identical during day and night indicate that they are able to use these LCSs to move during periods of darkness. Frigatebirds move continuously during day and night at an average altitude of 200 m and never completely stop moving when they forage, but they come to the sea surface to eat only during daytime (10). If they used these structures only for food availability, then the distribution of FSLEs

for areas crossed by birds should be different between day and night. This is not the case. This means that frigatebirds do not go to FSLEs ridges only to forage but that they follow them most of the time as cues to eventually find prey patches there.

It is relatively easy to understand why the attracting LCSs could be places for prey accumulation, given that horizontal flow will make passively advected organisms close to these lines approach them. More puzzling is the role of the repelling LCSs, which are also preferred locations for the frigatebirds. First we should mention that at the vortex edges, lines of the attracting and repelling types are very close and nearly tangent. Thus, it may be the case that birds' positions located at repelling lines are simultaneously also located on attracting ones; in *SI Methods* we explain that a position is said to be on an LCS if it is closer to it than 0.025°. Thus, if the attracting and repelling LCSs are close enough, the same bird position may be attributed to both structures. We have determined that, among the 30.2% of bird positions that were found on repelling coherent structures, 53.7% of these were in fact visiting both structures, and thus the interpretation is that they are associated to vortex edges (or to other structures in which both types of lines are tangent). For the remaining fraction that does not seem to be associated to these edges, we believe that the 3-dimensional dynamics of the flow close to these structures gives the clue for their association to bird positions. Note that FSLE values have been calculated on the basis of the 2-dimensional surface flow, and the FSLE methodology identifies these regions as places of filament and submesoscale structure formation by horizontal advection. But there is growing evidence (29, 30) of strong links between submesoscale structures from different origins and vertical motions. Thus, in an indirect manner, the calculated LCSs may be indicating the places in the ocean where vertical upwelling and/or downwelling of nutrients and organisms could occur. This is obviously important for the birds and may explain why they prefer to fly and to forage on top of them. The role of these LCSs in biologic activity is rather complex and may vary depending on the area and scale of study. For instance, Rossi et al. (31) found an inverse relationship between mixing activity (high FSLEs) and phytoplankton stocks in very productive areas, such as coastal eastern boundary upwelling.

The above arguments linking LCSs and vertical motion can be more easily justified for the attracting LCS case, because the vorticity involved in the interaction between vertical and horizontal motion will also tend to be aligned with these structures (30). But we note that in flows consisting of slowly moving eddies, we are close to the so-called integrable situation in which a large proportion of tangencies between attracting and repelling structures is expected (as indeed observed). As a consequence, it may happen that a bird starts a trip by following an attracting LCS, loses its surface signal, and finds itself on top of a repelling one simply by continuing its previous path in a more-or-less straight way. We stress, however, that all explanations we give to the observed relationship between LCSs and bird paths contain a number of hypotheses that need additional research.

One may ask how frigatebirds "follow" the LCSs during day and night. Several hypotheses can be put forward.

First, because frigatebirds use atmospheric currents, especially to gain altitude by soaring and then glide over long distances (32), we can suppose that the coupling between the ocean and the atmosphere at meso- and submesoscale generates atmospheric currents followed by seabirds. Indeed some investigators (33–36) emphasize the role of local air–sea feedbacks arising from ocean mesoscale features. For example, Chelton et al. (36) showed that an ocean–atmosphere coupling is observed in the California Current System during summer. They conclude that sea surface temperature fronts generated by mesoscale activity (eddies and upwelling) have a clear influence on the perturbation of summertime wind stress curl and divergence. In the MC, mesoscale eddies and their interaction would force the atmosphere and generate air currents favorable to Great Frigatebirds, which might take advantage of the wind to spend the least possible energy in flight.

Second, we cannot exclude that birds may follow visual or, more likely, olfactory cues. Foraging behavior of seabirds is complex and results from a number of behavioral parameters, such as sight, smell (37, 38), memory effect (39), and environmental parameters [chlorophyll concentration (10) or wind speed and direction]. Nevitt et al. (40) suggest that seabirds use olfaction to track high concentrations of odor compounds, such as dimethyl sulfide (DMS), and sight when they locate prey patches. The use of models of odor transport suggests that olfaction plays a role in foraging behavior (40). Structures detected using FSLEs are dynamic and, as mentioned above, may induce vertical mixing favorable to phytoplankton enhancement (41, 42) and their patchy distribution. The grazing of phytoplankton by zooplankton induces the production of DMS (43), which is very attractive for different species of seabirds (44). Even if there is no study on the role of olfaction in Great Frigatebird foraging behavior, we can hypothesize that they use olfaction to detect DMS and productive areas and find food patches. The interaction between the ocean and the atmosphere at submesoscale and wind may allow the dispersion of the DMS or other odors and favor their detection by seabirds that follow LCSs until they see a patch of prey. These LCSs could be viewed as moving habitat facilitating movement of seabirds. Indeed, frigatebirds might use these odorous corridors to move between food patches with efficacy.

Whatever the cue used by frigatebirds to locate and follow these LCSs, our results provide the first evidence that a top predator tracks these FSLE ridges to locate food patches. It allows us to better understand how top predators search prey and why they are able to concentrate precisely at LCSs. Because these structures are mobile, a simple memory is not sufficient for a central-place forager to return to a productive prey area. Predators could thus take a general bearing where eddies are likely to be found (e.g., to the northwest in the MC for a colony located in the central MC) and then move until they cross an FSLE ridge, which they will follow until they encounter a prey patch. Because they are unable to sit on the water, frigates are often in association with subsurface top predators to forage. We can suppose that if frigatebirds track LCSs to locate prey, it is possible that they are associated with tuna schools around foraging areas (10). Thus, understanding the rationale behind their localization is crucial not only in seabird ecology but also in the detection of the presence of tuna schools. This kind of multidisciplinary approach opens up interesting prospects in the management of ecosystems and fisheries and can be useful in the ecosystemic approach to fisheries, especially to better characterize temporary tuna habitats in the MC. Future work is to identify the responsible mechanism by which an aerial predator may spot and follow LCSs.

Materials and Methods

In this part we provide a brief overview of the methodology; further details for each section are given in *SI Methods*.

Great Frigatebirds. Europa (22.3° S, 40.3° E) is 1 of the 2 colonies (with Aldabra) of Great Frigatebirds in the West Indian Ocean. The island is located in the central part of the MC. Great Frigatebirds have the ability to undertake long-range movements out of the breeding season (10), but they behave as central-place foragers when breeding. Their diet is composed essentially of flying fish and Ommastrephid squids (10), but Great Frigatebirds are also kleptoparasites, meaning they can steal prey from others. One of their particularities is that they cannot wet their feathers or dive into the water to feed. They forage mainly through association with tuna and dolphin schools, which bring prey to the surface.

To track movements of frigatebirds, 8 birds were tracked with satellite transmitters and altimeters between August 18 and September 30, 2003, resulting in 1864 Argos positions. The mean time between each position is 0.07 days, with a minimum of 0.001 days and a maximum of 1.1 days. All seabird positions from a given week were collocated on the time and space grid on which the FSLEs were calculated (with 0.025° resolution).

LCSs by FSLEs: FSLE Method. Oceanic variability in surface velocities is not probably sensed directly by Great Frigatebirds but rather indirectly via transported substances. This calls for a Lagrangian perspective on the problem. Thus, we quantify horizontal transport processes and LCSs by the Lagrangian technique of FSLE (45), which is specially suited to study the stretching and contraction properties of transport in geophysical data (20). Because of their Lagrangian character, FSLEs describe submesoscale details that cannot be detected by other means, like the inspection of the sea level anomaly maps of the marine surface.

The calculation of the FSLE goes through computing the time, τ, at which 2 tracer particles initially separated at a distance δ_0, reach a final separation distance δ_f, following their trajectories in the marine surface velocity field. At position x and time t the FSLE is given by:

$$\lambda(x,\, t,\, \delta_0,\, \delta_f) = \frac{1}{\tau} \log\left(\frac{\delta_f}{\delta_0}\right).$$

We follow the trajectories for 200 days, so that if τ is larger than this, we define $\lambda = 0$. It is clear that the FSLEs depend critically on the choice of 2 length scales: the initial separation, δ_0, and the final one, δ_f. δ_0 has to be close to the intergrid spacing among the points x on which the FSLEs will be computed (20). In our case we calculate FSLE on all of the points of a latitude–longitude grid with a spacing of $\delta_0 = 1/40° = 0.025°$. On the other hand, because we are interested in mesoscale structures, δ_f is chosen as $\delta_f = 1°$ (i.e., separation of approximately 110 km). In this respect, the FSLE represents the inverse time scale for mixing up fluid parcels between the grid and the characteristic scales of the MC eddies. Maps of FSLE are calculated weekly. An alternative to FSLE is the finite-time Lyapunov exponents (22, 46). At the scales and parameters we are working no significant differences are expected for the locations of LCS by any of the 2 methods.

The time integration of the particle trajectories can be performed in 2 ways: forward and backward in time. For the backward computation, maximum values of FSLE organize in lines that are good approximations of the so-called *unstable manifolds of hyperbolic points*, which for our purposes are lines toward which neighboring fluid trajectories, while escaping from hyperbolic points, approach at long times (20, 23, 24). In consequence they are called attracting LCSs. FSLEs computed integrating trajectories toward the future (i.e., forward) take large values on lines (stable manifolds) from which neighboring trajectories appear to be repelled (repelling LCSs). These lines of maximum separation or convergence rates, or ''ridges,'' delineate fluid domains with quite distinct origin and characteristics. Such lines strongly modulate the fluid motion when reaching maximum values, and they act as transport barriers for particle trajectories, thus constituting a powerful tool for predicting fronts generated by, for example, passive advection, eddy boundaries, and material filaments. Other studies (20, 26, 27, 31, 42) have demonstrated the adequacy of the FSLE to characterize horizontal mixing and transport structures in the marine surface, as well as its usefulness when correlating with tracer fields like temperature or chlorophyll.

ACKNOWLEDGMENTS. We thank the 2 anonymous reviewers for their helpful comments on the manuscript. A Ph.D. fellowship for E.T.K was provided by the Institut de Recherche pour le Développement and the University Pierre and Marie Curie. Ph.D. financial support for V.R was provided by the Direction Générale de l'Armement. The Laboratoire d'Etudes en Géophysique et Océanographie Spatiale contribution is supported by Centre National d'Etudes Spatiales funding. The Instituto de Física Interdisciplinar y Sistemas Complejos contribution is supported by Ministerio de Ciencia e Innovación and le Fonds Européen de Développement Régional through project FISICOS (FIS2007–60327), and by Consejo Superior de Investigaciones Cientificas through the Intramural Frontier Projects OCEANTECH. H.W.'s contribution was supported by the REMIGE project funded by Agence Nationale de la Recherche (ANR 2005 Biodiv-011).

1. McGillicuddy J, et al. (1998) Influence of mesoscale eddies on new production in the Sargasso Sea. *Nature* 394:263–266.
2. Oschlies A, Garcon V (1998) Eddy-induced enhancement of primary production in a model of the North Atlantic Ocean. *Nature* 394:266–268.
3. Owen RW (1981) Fronts and eddies in the sea: Mechanisms, interactions and biological Effects. *Fronts and Eddies in the Sea*, ed Owen RW (Academic, London).
4. Kang J, Kim W, Chang K, Noh J (2004) Distribution of plankton related to the mesoscale physical structure within the surface mixed layer in the southwestern East Sea, *Korea J Plankton Res* 26:1515–1528.
5. Mackas D, Tsurumi M, Galbraith M, Yelland D (2005) Zooplankton distribution and dynamics in a North Pacific Eddy of coastal origin: II. Mechanisms of eddy colonization by and retention of offshore species. *Deep-Sea Res II* 52:1011–1035.
6. Moore T, Matear R, Marra J, Clementson L (2007) Phytoplankton variability off the Western Australian Coast: Mesoscale eddies and their role in cross-shelf exchange, *Deep-Sea Res II* 54:943–960.
7. Polovinia J, Howell E, Kobayashi D, Seki M (2001) The transition zone chlorophyll front, a dynamic global feature defining migration and forage habitat for marine resources. *Prog Oceanogr* 49:469–483.
8. Bakun A (2006) Fronts and eddies as key structures in the habitat of marine fish larvae: Opportunity, adaptive response and competitive advantage. *Scientia Marina* 70:105–122.
9. Nel D, et al. (2001) Exploitation of mesoscale oceanographic features by grey-headed albatross *Thalassarche chrysostoma* in the southern Indian Ocean. *Mar Ecol Prog Ser* 217:15–26.
10. Weimerskirch H, Le Corre M, Jaquemet S, Potier M, Marsac F (2004) Foraging strategy of a top predator in tropical waters: Great Frigatebirds in the Mozambique Channel. *Mar Ecol Prog Ser* 275:297–308.
11. Hyrenbach K, Veit R, Weimerskirch H, Hunt G, Jr (2006) Seabird associations with mesoscale eddies: The subtropical Indian Ocean. *Mar Ecol Prog Ser* 324:271–279.
12. Domokos R, Seki MP, Polovinia JJ, Hawn DR (2007) Oceanographic investigation of the American Samoa albacore (*Thunnus alalunga*) habitat and longline fishing grounds. *Fish Oceanogr* 16:555–572.
13. Lima I, Olson D, Doney S (2002) Biological response to frontal dynamics and mesoscale variability in oligotrophic environments: Biological production and community structure. *J Geophys Res* 107:3111.
14. Abraham ER, Bowen MM (2002) Chaotic stirring by a mesoscale surface ocean flow. *Chaos* 12:373–381.
15. De Ruijter WPM, Ridderinkhof H, Lutjeharms R, Schouten M, Veth C (2002) Observations of the flow in the Mozambique Channel. *Geophys Res Lett* 29:1502.
16. Ridderinkhof H, de Ruijter WPM (2003) Moored current observations in the Mozambique Channel. *Deep-Sea Res II* 5:1933–1955.
17. Schouten MW, de Ruijter WPM, van Leeuwen PJ, Ridderinkhof H (2003) Eddies and variability in the Mozambique Channel. *Deep-Sea Res II* 50:1987–2003.
18. Tew Kai E, Marsac F (2009) Patterns of variability of sea surface chlorophyll in the Mozambique Channel: A quantitative approach. *J Mar Syst* 77:77–88.
19. Sudre J, Morrow R (2008) Global surface currents: A high resolution product for investigating ocean dynamics. *Ocean Dyn* 58:101–118.
20. d'Ovidio F, Fernandez V, Hernández-García E, López C (2004) Mixing structures in the Mediterranean Sea from Finite-Size Lyapunov Exponents. *Geophys Res Lett* 31:L17203.
21. Haller G, Yuan G (2000) Lagrangian coherent structures and mixing in two-dimensional turbulence. *Physica D* 147:352–370.
22. Haller G (2001) Lagrangian structures and the rate of strain in a partition of two-dimensional turbulence. *Phys Fluids* 13:3365–3385.
23. Joseph B, Legras B (2002) Relation between kinematic boundaries, stirring and barriers for the Antarctic polar vortex. *J Atmosph Sci* 59:1198–1212.
24. Koh T-Y, Legras B (2002) Hyperbolic lines and the stratospheric polar vortex. *Chaos* 12:382–394.
25. Bakun A (1996) *Patterns in the Ocean: Oceanic Processes and Marine Population Dynamics* (University of California Sea Grant, San Diego, CA, in cooperation with Centro de Investigaciones Biologicas de Noroeste, La Paz, Baja California Sur, Mexico).
26. D'Ovidio F, Isern-Fontanet J, López C, Hernández-García E, García-Ladona E (2009) Comparison between Eulerian diagnostics and Finite-Size Lyapunov Exponents computed from altimetry in the Algerian basin. *Deep-Sea Res I* 56:15–31.
27. Haza A, Poje AC, Özgökmen TM, Martin P (2008) Relative dispersion from a high-resolution coastal model of the Adriatic Sea. *Ocean Modelling* 22:48–65.
28. Jaquemet S, Le Corre M, Weimerskirch H (2004) Seabird community structure in a coastal tropical environment: Importance of natural factors and fish aggregating devices (FADs). *Mar Ecol Prog Ser* 268:281–292.
29. Mahadevan A, Tandon A (2006) An analysis of mechanisms for submesoscale vertical motion at ocean fronts. *Ocean Modelling* 14:241–256.
30. Klein P, Lapeyre G (2009) The oceanic vertical pump induced by mesoscale eddies. *Ann Rev Mar Sci* 1:351–375.
31. Rossi V, Lopez C, Sudre J, Hernandez-Garcia E, Garçon V (2008) Comparative study of mixing and biological activity of the Benguela and Canary upwelling systems. *Geophys Res Lett* 35: L11602.
32. Weimerskirch H, Chastel O, Barbraud C, Tostain O (2003) Frigatebirds ride high on thermals. *Nature* 421:333–334.
33. Xie S (2004) Satellite observations of cool ocean–atmosphere interaction. *Bull Am Meteor Soc* 85:195–209.
34. Chelton D, Schlax MG, Freilich MH, Milliff RF (2004) Satellite measurements reveal persistent small-scale features in ocean winds. *Science* 303:978–983.
35. Seo H, Miller A, Roads J (2007) The Scripps Coupled Ocean–Atmosphere Regional (SCOAR) model, with applications in the eastern Pacific sector. *J Clim* 27:381–401.
36. Chelton D, Schlax MG, Samelson RM (2007) Summertime coupling between sea surface temperature and wind stress in the California Current System. *J Phys Oceanogr* 37:495–517.
37. Nevitt GA (2000) Olfactory foraging by Antarctic procellariiform seabirds: Life at high Reynolds numbers. *Biol Bull* 198:245–253.
38. Nevitt GA, Bonadonna F (2005) Seeing the world through the nose of a bird: New developments in the sensory ecology of procellariiform seabirds. *Mar Ecol Prog Ser* 287:292–295.
39. Davoren GK, Montevecchi WA, Anderson JT (2003) Distributional patterns of a marine bird and its prey: Habitat selection based on prey and conspecific behaviour. *Mar Ecol Prog Ser* 256:229–242.
40. Nevitt GA, Losekoot M, Weimerskirch H (2008) Evidence for olfactory search by wandering albatross, *Diomedea exulans. Proc Natl Acad Sci USA* 105:4576–4581.
41. Martin A (2003) Phytoplankton patchiness: The role of lateral stirring and mixing. *Prog Oceanogr* 57:125–174.
42. Lehahn Y, d'Ovidio F, Lévy M, Heyfetz E (2007) Stirring of the northeast Atlantic spring bloom: A Lagrangian analysis based on multisatellite data. *J Geophys Res* 112:C08005.
43. Dacey JWH, Wakeham SG (1986) Oceanic dimethylsulfide: Production during zooplankton grazing on phytoplankton. *Science* 233:1314–1316.
44. Nevitt GA, Veit RR, Kareiva P (1995) Dimethyl sulphide as a foraging cue for Antarctic procellariiform seabirds. *Nature* 376:680–682.
45. Aurell E, Boffetta G, Crisanti A, Paladin G, Vulpiani A (1997) Predictability in the large: An extension of the concept of Lyapunov exponent. *J Phys A* 30:1–26.
46. Beron-Vera FJ, Olascoaga MJ, Goni GJ (2008) Oceanic mesoscale eddies as revealed by Lagrangian coherent structures. *Geophys Res Lett* 35: L12603.

B.5 Article : Surface mixing and biological activity in the four Eastern Boundary Upwelling Systems, V. Rossi *et al.*, 2009

B.5.1 Abstract

Eastern Boundary Upwelling Systems (EBUS) are characterized by a high productivity of plankton associated with large commercial fisheries, thus playing key biological and socio-economical roles. Since they are populated by several physical oceanic structures such as filaments and eddies, which interact with the biological processes, it is a major challenge to study this sub- and mesoscale activity in connection with the chlorophyll distribution. The aim of this work is to make a comparative study of these four upwelling systems focussing on their surface stirring, using the Finite Size Lyapunov Exponents (FSLEs), and their biological activity, based on satellite data. First, the spatial distribution of horizontal mixing is analysed from time averages and from probability density functions of FSLEs, which allow us to divide each areas in two different subsystems. Then we studied the temporal variability of surface stirring focussing on the annual and seasonal cycle. We also proposed a ranking of the four EBUS based on the averaged mixing intensity. When investigating the links with chlorophyll concentration, the previous subsystems reveal distinc biological signatures. There is a global negative correlation between surface horizontal mixing and chlorophyll standing stocks over the four areas. To try to better understand this inverse relationship, we consider the vertical dimension by looking at the Ekman-transport and vertical velocities. We suggest the possibility of a changing response of the phytoplankton to sub/mesoscale turbulence, from a negative effect in the very productive coastal areas to a positive one in the open ocean. This study provides new insights for the understanding of the variable biological productivity in the ocean, which results from both dynamics of the marine ecosystem and of the 3-D turbulent medium.

B.5.2 Article publié dans *Nonlinear Processes in Geophysics*

Référence : Rossi V., López C., Hernández-Garcia E., Sudre J., Garçon V. and Morel Y., 2009 : Surface mixing and biological activity in the four Eastern

Boundary Upwelling Systems, *Nonlinear Processes in Geophysics*, **16**, 557-568, DOI 10.5194/npg-16-557-2009.

Nonlin. Processes Geophys., 16, 557–568, 2009
www.nonlin-processes-geophys.net/16/557/2009/
© Author(s) 2009. This work is distributed under
the Creative Commons Attribution 3.0 License.

Nonlinear Processes in Geophysics

Surface mixing and biological activity in the four Eastern Boundary Upwelling Systems

V. Rossi[1,2], C. López[2], E. Hernández-García[2], J. Sudre[1], V. Garçon[1], and Y. Morel[3]

[1]Laboratoire d'Études en Géophysique et Océanographie Spatiale, CNRS, Observatoire Midi-Pyrénées, 14 avenue Edouard Belin, Toulouse, 31401 Cedex 9, France
[2]Instituto de Física Interdisciplinar y Sistemas Complejos IFISC (CSIC-UIB), Campus Universitat de les Illes Balears, 07122 Palma de Mallorca, Spain
[3]Service Hydrographique et Océanographique de la Marine, (SHOM), 42 avenue Gaspard Coriolis, 31057 Toulouse, France

Received: 3 June 2009 – Revised: 11 August 2009 – Accepted: 14 August 2009 – Published: 27 August 2009

Abstract. Eastern Boundary Upwelling Systems (EBUS) are characterized by a high productivity of plankton associated with large commercial fisheries, thus playing key biological and socio-economical roles. Since they are populated by several physical oceanic structures such as filaments and eddies, which interact with the biological processes, it is a major challenge to study this sub- and mesoscale activity in connection with the chlorophyll distribution. The aim of this work is to make a comparative study of these four upwelling systems focussing on their surface stirring, using the Finite Size Lyapunov Exponents (FSLEs), and their biological activity, based on satellite data. First, the spatial distribution of horizontal mixing is analysed from time averages and from probability density functions of FSLEs, which allow us to divide each areas in two different subsystems. Then we studied the temporal variability of surface stirring focussing on the annual and seasonal cycle. We also proposed a ranking of the four EBUS based on the averaged mixing intensity. When investigating the links with chlorophyll concentration, the previous subsystems reveal distinct biological signatures. There is a global negative correlation between surface horizontal mixing and chlorophyll standing stocks over the four areas. To try to better understand this inverse relationship, we consider the vertical dimension by looking at the Ekman-transport and vertical velocities. We suggest the possibility of a changing response of the phytoplankton to sub/mesoscale turbulence, from a negative effect in the very productive coastal areas to a positive one in the open ocean. This study provides new insights for the understanding of the variable biological productivity in the ocean, which results from both dynamics of the marine ecosystem and of the 3-D turbulent medium.

Correspondence to: V. Rossi
(vincent.rossi@legos.obs-mip.fr)

1 Introduction

Although they represent only a very small fraction of the total surface of the world's ocean, the Eastern Boundary Upwelling Systems (EBUS) are the most productive regions of the world due to their important coastal biological productivities which support large commercial fisheries, up to 20% of the global fish catch (Pauly and Christensen, 1995). They include the Canary (CUS) and the Benguela upwelling systems (BUS) in the Atlantic Ocean and the Peru/Chile (or Humboldt HUS) and California upwelling systems (CalUS) in the Pacific Ocean. Under the action of wind from quasi-stationary high pressure cells over the subtropical ocean basins, a surface uprising of deep cold water rich in nutrients occurs over continental shelves almost all year long. This process explains the high primary production in these regions which constitutes the base of a highly dynamical and rich food chain. Roughly, the intensity of coastal upwelling is modulated by the force and direction of the wind, by the local topography and by the ambient oceanic characteristics.

These EBUS are spatially and temporally heterogeneous from both a physical and biological point of view. The development of diverse structures such as intense fronts, coastal plumes in retention areas, offshore filaments and eddies interplays with the complex spatial distribution of phytoplankton. This mesoscale and sub-mesoscale oceanic turbulence is known to strongly modulate the structure, biomasses and rates of marine ecosystems, since it can stimulate the primary productivity (McGillicuddy et al., 1998; Oschlies and Garçon, 1998), affect plankton community composition (Owen, 1981; Kang et al., 2004; Mackas et al., 2005) and play a significant role in exchange processes in the transitional area between the productive coastal zone and the oligotrophic open ocean by transporting organic matter and marine organisms from the coast to the open ocean (Moore et al., 2007). This latter mechanism, i.e. the large coastal

productivity and its export to the inner ocean via filament formation, identifies them as key regions in the global marine element cycles, such as carbon and nitrogen (Mackas et al., 2006).

While sharing common bio-physical characteristics, their biological productivity is highly variable and governed by diverse factors and their interaction, which are still poorly understood. Several previous comparative studies investigated these major environmental factors and leading physical processes that may control it. When considering all EBUS together, Carr and Kearns (2003) showed that phytoplankton productivity results from a combined effect of large-scale circulation and local factors. Patti et al. (2008) suggested that several driving factors, as nutrients concentration, light availability, shelf extension and among others a surface turbulence proxy from a wind-mixing index, must be taken into account when investigating the phytoplankton biomass distribution. Globally, their statistical study pointed out that all these factors are playing a role whereas they are acting at different levels on the productivity. It is then highly relevant to consider an original Lagrangian measure of mixing for comparative approach among EBUS.

The aim of this study is first to quantify and compare the mixing activity in the EBUS using the technique of the Finite-Size Lyapunov Exponents. The spatial distribution and the temporal evolution of the mixing and stirring activity is analysed. The link between turbulence and chlorophyll concentration (as a proxy for biological activity) is then investigated, leading to propose some underlying mechanisms behind the relationship revealed. Finally, we discuss previous comparative approaches performed among these EBUS with new insights from the present mixing analysis.

2 Methods

The basic ingredients of our comparative analysis are satellite data of the marine surface including a two dimensional velocity field and chlorophyll concentration data as a proxy for biological activity and a specific numerical tool employed to analyze these data. We quantify horizontal transport processes by the Lagrangian technique of the Finite Size Lyapunov Exponents (FSLEs) (Aurell et al., 1997), which is specially suited to study the stretching and contraction properties of transport in geophysical data (d'Ovidio et al., 2004). The calculation of the FSLE goes through computing the time, τ, at which two fluid particles initially separated by a distance δ_0 reach a final separation distance δ_f, following their trajectories in a 2 D velocity field. At position x and time t the FSLE is given by: $\lambda\ (x,t,\delta_0,\delta_f)=\frac{1}{\tau}\log\frac{\delta_f}{\delta_0}$. We are in fact considering the four neighbors of each gridpoint and we selected the orientation of maximum separation rate (fastest neighbor to reach the final separation distance). The equations of motion that describe the horizontal evolution of particle trajectories are computed in longitudinal and latitudinal spherical coordinates (ϕ,θ, measured in degrees; δ_0 and δ_f are also measured in degrees): $\frac{d\phi}{dt}=\frac{u(\phi,\theta,t)}{R\cos\theta}$, $\frac{d\theta}{dt}=\frac{v(\phi,\theta,t)}{R}$. u and v represent the eastward and northward components of the surface velocity field, and R is the radius of the Earth. Numerical integration is performed by using a standard fourth-order Runge-Kutta scheme with an integration time step of dt=1 day. Spatiotemporal interpolation of the velocity data is achieved by bilinear interpolation. We follow the trajectories for 300 days, so that if τ gets larger than 300 days, we define λ=0. FSLEs depend critically on the choice of two length scales: the initial separation δ_0 and the final one δ_f. d'Ovidio et al. (2004) argued that δ_0 has to be close to the intergrid spacing among the points x on which FSLEs will be computed, which is δ_0=0.025°. On the other hand, since we are interested in mesoscale structures, δ_f is chosen equal to 1°, implying a separation distance of about 110 km close to the equator. In this respect, the FSLEs represent the inverse time scale for mixing up fluid parcels between the small-scale grid and the characteristic scales of eddies in these upwelling areas. Choosing slightly different values for δ_f does not alter qualitatively our results, the main pattern and averages remain the same. To sum up, maps of FSLE are computed monthly for the period June 2000 to June 2005 on all points of a latitude-longitude grid with a spacing of δ_0=0.025°. An alternative tool to FSLE is the Finite-Time Lyapunov exponents (Haller, 2001; Beron-Vera et al., 2008) but we expect that similar results would be obtained by this last technique for the present spatial and temporal scales. This is so because we use a value of δ_0 smaller than the typical structures in the velocity field, so that FSLE is close to the value of the local Lyapunov exponent and thus of the FTLE at large times (Aurell et al., 1997; Artale et al., 1997). The time integration of the particle trajectories can be performed in two different ways: forward or backward in time. In a typical snapshot of the backwards-in-time dynamics, the maximum values of FSLE organize in lines which are a good approximation for the areas of maximal convergence. On the other hand, FSLE calculated with the forward-in-time integration exhibit large values in the regions of maximal divergence. The line-shaped regions of maximal convergence (divergence) approximate the so-called unstable (stable) manifolds of the hyperbolic trajectories in the flow (Boffeta et al., 2001; Koh and Legras, 2002; d'Ovidio et al., 2004). As a consequence, these ridges, i.e. lines of maximum separation or convergence rates, move with the flow as if they were material lines and thus delineate fluid domains with quite distinct origin and characteristics. Although it would be good to have for ridges in FSLEs some rigorous analysis, of the type of Shadden et al. (2005) for ridges in FTLEs, putting it in a firmer mathematical basis and identifying its limits of validity, there is ample numerical and theoretical evidence confirming this behavior (Koh and Legras, 2002; Lehahn et al., 2007; d'Ovidio et al., 2009). We focus in this work on the backward-in-time dynamics since FSLEs' lines have a

clear interpretation as fronts of passive scalars driven by the flow (d'Ovidio et al., 2009). These lines strongly modulate the fluid motion since when reaching maximum values, they act as transport barriers for particle trajectories thus constituting a powerful tool for predicting fronts generated by passive advection, eddy boundaries, material filaments, etc. In a different set of papers (d'Ovidio et al., 2004, 2009; Lehahn et al., 2007; Rossi et al., 2008), the adequacy of FSLE to characterize horizontal mixing and transport structures in the marine surface has been demonstrated as well as its usefulness when correlating with tracer fields like temperature or chlorophyll. Related Lagrangian diagnostics (FTLEs) have even been used to understand harmful algae development (Olascoaga et al., 2008). In addition, spatial averages of FSLEs can define a measure of horizontal mixing in a given spatial area, the larger this spatial average the larger the mixing activity. Following these studies, we will use in this work the FSLE as an analysis tool of the horizontal mixing activity of the surface ocean and will highlight similarities and differences both at a hydrodynamic and biological level.

We study the transitional area of exchange processes between the shelf and offshore in the open ocean. The filaments in the fluctuating boundary between the upwelling and the edge of the oligotrophic subtropical gyres play a key role in the modulation of the carbon balance by seeding the inner ocean. To consider the role of this moving transitional area, we chose as analysis areas coastal strips of 8 degrees (in the meridional direction) in each system. However we used the full geographical areas to make our numerical computations. Note that the computation areas are larger than the analysis ones, considering the fact that particles may leave the area before reaching the fixed final distance δ_f. In addition, several tests with different shapes and area selections (not shown) exhibit similar results.

3 Satellite data

A five year long time series from June 2000 to June 2005 of ocean colour data is used. Phytoplankton pigment concentrations (chlorophyll-*a*) are obtained from monthly SeaWiFS (Sea viewing Wide Field-of-view Sensor) products[1], generated by the NASA Goddard Earth Science (GES)/Distributed Active Archive Center (DAAC). The bins correspond to grid cells on a global grid, with approximately 9 by 9 km.

The weekly global 1/4° resolution product of surface currents developed by Sudre and Morrow (2008) has been used. The surface currents are calculated from a combination of wind-driven Ekman currents, at 15 m depth, derived from Quikscat wind estimates, and geostrophic currents computed from time variable Sea Surface Heights. These SSH were calculated from mapped altimetric sea level anomalies combined with a mean dynamic topography from Rio et al. (2004). These weekly velocity data, which are then interpolated linearly to obtain a daily resolution with a 0.025° intergrid spacing, depend on the quality of their sources as the SSH fields and the scatterometer precision. However, they were validated with different types of *insitu* data such as Lagrangian buoys, ADCP and current meter float data. In our four areas, zonal and meridional components show respectively an average correlation coefficient (R^2) with for e.g. Lagrangian buoy data of 0.64 and 0.57.

We analyse satellite data which are two-dimensional fields. We are also interested in the third dimension and the influence of vertical movements in upwelling, which are known to be relatively intense. To perform this, we propose to compute the Ekman transport and the divergence of the velocity field from the available data. The Ekman transport was calculated using $U_E = \frac{T_y}{f\rho}$, where T_y is the meridional wind stress (obtained from the Quikscat scatterometer weekly wind estimates), ρ is the density of seawater and f is the Coriolis parameter. We also look at the vertical dimension by quantifying the horizontal divergence of the surface velocity field, using the incompressibility assumption: $\Delta(x, y, t) \equiv \partial_z V_z = -(\partial_x V_x + \partial_y V_y)$. This calculation gives an estimate of the mean vertical velocities over the whole period. Negative (positive) values of Δ indicate upwelling (downwelling) areas because they signal surface spatial points where fluid parcels diverge (converge).

4 Results

4.1 Comparative study of the mixing activity

4.1.1 Spatial distribution of the mixing properties from FSLEs

In Fig. 1 we draw the time average (covering the period June 2000–June 2005) of the FSLEs computed for the four EBUS. For all areas, two different subsystems, according to their mean mixing activity, can be defined. The zonal limits are as follows: 30° N for the Canary (CUS) and the California upwelling system (CalUS), 27° S for the Benguela (BUS) and 25°S for the Humboldt (HUS). Comparing these four upwelling zones, a distinction appears in both upwellings of the Southern Hemisphere where the limit between subsystems is clearly marked while in areas of the Northern Hemisphere it is not so sharp. Note also that the imaginary division lines are usually associated with particular topographic or hydrographic features: for the CUS, the line passes north of the Canary archipelago, the offshore HUS limit coincides with the Nazca Ridge and the BUS limit matches the latitude of the intense Lüderitz upwelling cell. The dark blue areas (FSLE value below 0.005 day^{-1}) located close to the coast indicate some retention zone since the mixing time is very large or infinite (the computation of FSLE gives zero when particles move toward the coast).

[1]We used the level 3 binned data with reprocessing 5.1. See http://oceancolor.gsfc.nasa.gov for further details.

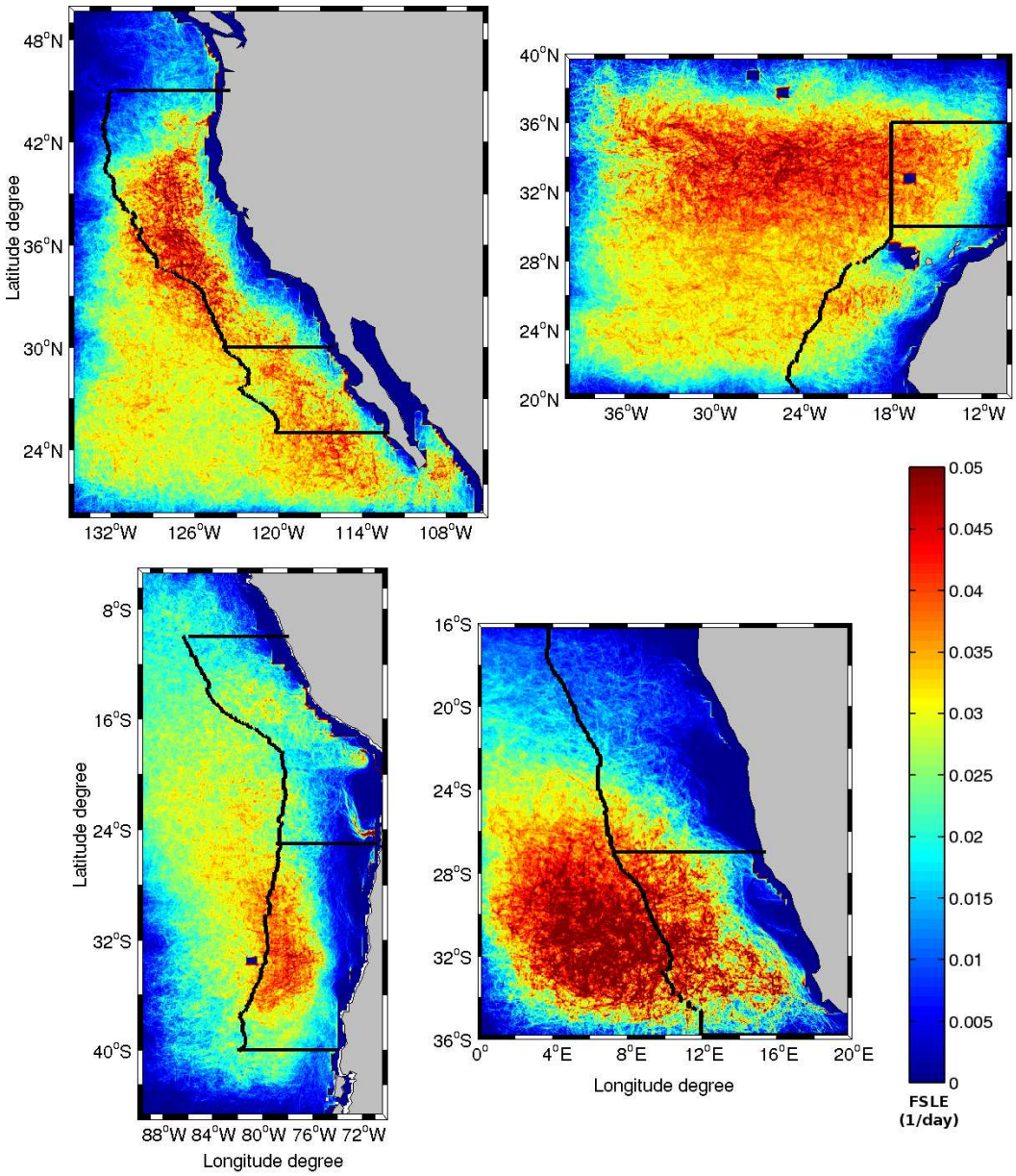

Fig. 1. Time average over the period June 2000–June 2005 of the FSLEs for the CalUS (upper left), the CUS (upper right), the HUS (lower left), and the BUS (lower right). Black lines indicate the analysis area as 8 degrees coastally oriented strips and the corresponding subdivisions.

To further quantify the variations in the stirring we examine the probability density functions (PDF) of FSLEs. These distributions are calculated for the FSLEs' time average normalized by the mean values from all grid points within each area (Fig. 2a). For all regions except the BUS (red line), the PDFs have a similar shape: their distributions are broad and slightly asymmetric, with a peak at low mixing activity and a quite long tail of high mixing. However the width and peak values vary depending on the considered system. The PDF of the BUS exhibits a particular asymmetric shape: we can observe one high peak in the low FSLEs values (around half of the spatial mean value, corresponding to $\sim$0.008 day^{-1}) and a bump standing in moderate values of FSLEs (between 2 to 3 times the mean value, corresponding to 0.03–0.04 day^{-1}). Considering the very distinct PDFs of FSLEs between both BUS subsystems (as compared to the HUS) we can associate the high peak of low FSLEs to the northern subsystem, whereas the moderate FSLEs' bump constitutes a signature of the intense mixing in the southern subsystem constantly fed by numerous and powerful Agulhas rings. Note also that

the CalUS exhibits a thinner and higher peak as compared to the others, indicating that the mean mixing is moderate and quite homogeneous over the entire analysis area (high occurrence of values close to 1, meaning many values are found around the spatial mean). Waugh and Abraham (2008) showed that the PDFs of FTLEs (for Finite-Time Lyapunov Exponents) have a near-universal distribution in the global open surface ocean since they are reasonably well fit by Weibull distributions following: $P(\lambda)=\frac{b}{a}\left(\frac{\lambda}{a}\right)^{b-1}\exp(\frac{-\lambda^b}{a^b})$, with $a=\overline{\lambda}/0.9$ and b=1.6−2.0. We expected a similar behavior for FSLEs because of the close relation among these quantities. We confirmed that normalized PDFs computed over the upwelling areas are quite well fitted by a Weibull distribution with parameters close to those proposed by these authors, except for the BUS. In Fig. 2b, the normalized PDFs of FSLEs from the CUS and HUS are quite well modeled by a Weibull distribution with parameter b=2.2 whereas the PDFs' from CalUS (Fig. 2c) fits better a Weibull distribution with parameter b=3.4 related with the higher and thinner peak around the average. The particular shape of the PDF of normalized FSLEs over the BUS indicates again that mixing in this upwelling system is much more heterogeneous.

4.1.2 Temporal evolution of the mixing intensity along the period 2000–2005

A more detailed comparison between the different subsystems can be performed by calculating the time evolution of the spatial averages over the analysis area of each of the four upwellings (Fig. 3a) and each subsystem (Fig. 3b and c). First of all we can sort each area according to their global averaged mixing activity. The mixing in the CalUS appears to be the most vigorous one (spatial average over the whole period: 0.025 day^{-1}), followed by the CUS (0.021 day^{-1}), and finally the HUS (0.019 day^{-1}) and BUS (0.017 day^{-1}) which presents the lowest mixing activity. A strong annual signal is observed in the time evolution of the mixing in the Humboldt, Canary and California upwelling systems. The five peaks of high mixing, corresponding to the five years of data, reflect the seasonal variability of the surface wind. In each hemispheric winter, the sea surface exhibits a more turbulent behaviour due to stronger winds. The last year of these time series reveals a somewhat different pattern of mixing, with a double peak for both upwellings of the Northern Hemisphere, suggesting that 2005 might be a particular year. In fact, this event has been already documented by Schwing et al. (2006) who studied the large-scale atmospheric forcing that contributed to these unusual physical oceanic conditions and the associated ecosystems responses. Note that both systems of the Northern Hemisphere oscillate in phase and are out of phase with the Southern Hemisphere systems. Periods of minimum turbulence values, for instance in the HUS, occur from March through May and coincide with the upwelling relaxation period, linked with the coastal wind regimes. A similar observation may be done for the BUS: the minimum mixing values during austral summer/autumn coincide with the upwelling relaxation period. Despite the fact that a high variability of the mixing is observed in all systems, the Benguela exhibits the strongest interannual variability of the mixing among all four EBUS. Note also an increasing trend of the mixing in the CalUS over these five years, confirmed by the computation of FSLE anomalies (not shown), suggesting a long-term change linked with global climate change (Bograd et al., 2009, and references therein). In all four regions, the difference of horizontal mixing activity is clear between tropical and temperate subsystems which showed the maximum of mixing (Fig. 3b and c). This observation can be explained by the intensification of large scale atmospheric forcing at mid-latitudes. When going away from the relatively calm equator, the intensity of the trade winds is increased in the gyre, associated to the presence of jet streams and increased pressure gradient. As already mentioned, this difference is more pronounced in areas of the Southern Hemisphere than of the Northern one. In Fig. 1, one can see a weak predominance of red colour in the temperate subsystem of the CalUS (north), suggesting

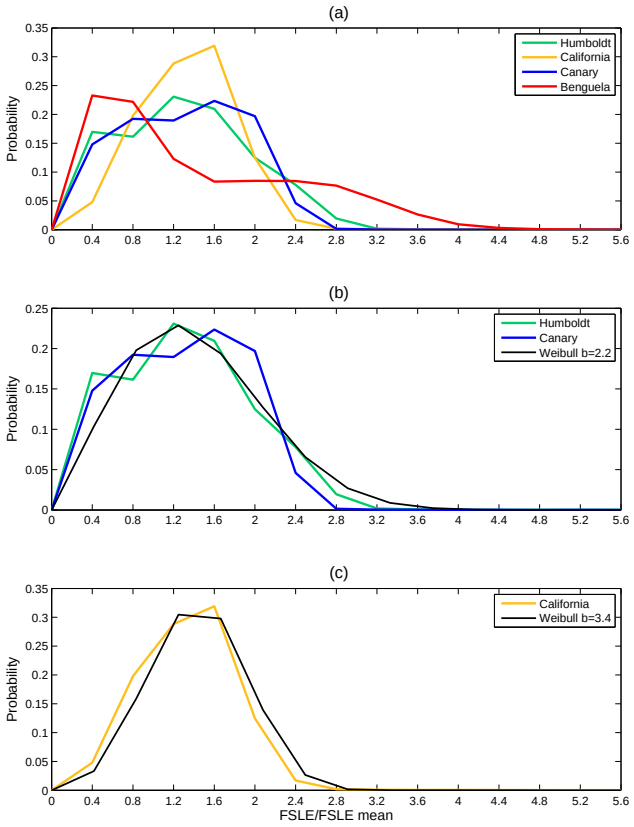

Fig. 2. (a) Normalized Probability Density Function calculated over the FLSEs time average of Fig. 1 for each EBUS (whole analysis area, i.e. 8 degrees coastal strip). Panels **(b)** and **(c)** same as in (a) for three of the PDFs fitting a Weibull distribution.

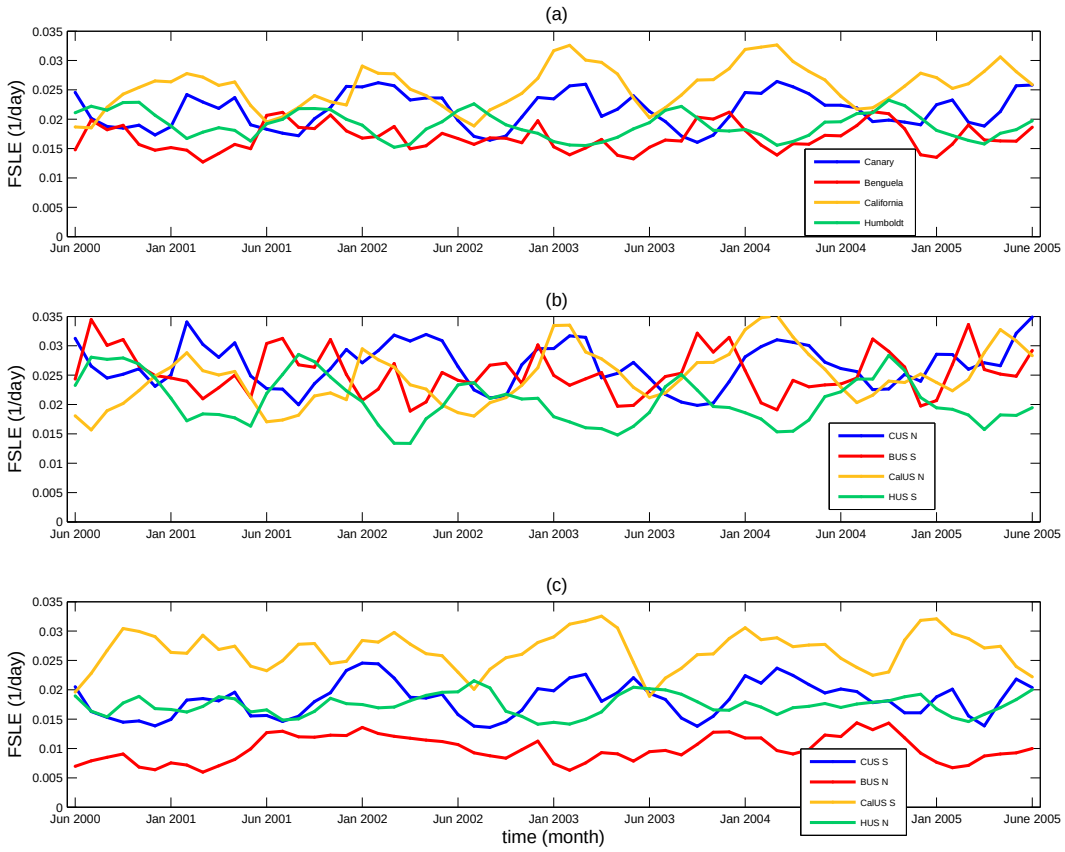

Fig. 3. (a) Spatial average versus time of the backward FSLEs. Spatial averages are computed over the analysis areas (8 degrees coastal strip): Canary (blue), Benguela (red), California (yellow) and Humboldt (green); **(b)** Same as in (a) but for the most temperate subsystems; **(c)** Same as in (a) but for the tropical subsystems.

it might be the most turbulent one. However the picture is more complex due to the particular temporal evolution of their mixing activity. Initially slightly less active than the southern one, the northern subsystem exhibits a positive tendency of increase, whereas the former is characterized by a flat long term pattern. As a consequence, the temperate subsystem becomes more turbulent than the tropical one at around year 2003. These different behaviors of the northern and southern CalUS subsystems were recently studied by Bograd et al. (2009) using newly developed upwelling index. Finally, the CalUS is quite particular as compared to the others since its horizontal mixing activity is more homogeneous: when averaging it over space and time in each subsystem, the FSLE means are very comparable, the southern one being slightly higher. Comparing these four upwelling zones, one can note that in the most turbulent temperate subsystems the values of the FSLEs are quite similar: within the range 0.018–0.04 day^{-1}, i.e., horizontal mixing times between 40 and 90 days. On the contrary, the least active tropical subsystems (excluding Southern California) are characterized by FSLE ranges from 0.003–0.025 day^{-1} equivalent to horizontal mixing times from 65 to 530 days. Again on Fig. 3b and c, the mixing activity of the four subsystems from the Northern Hemisphere seems to vary in phase and shows a minimum during the boreal summer/autumn. On the other hand, in the BUS and HUS, the most turbulent temperate systems exhibit a visible annual cycle, with a minimum occurring during the austral summer/autumn, whereas the least active tropical ones show a high non linear variability and no obvious trend. Note that the northern BUS shows the smallest mixing activity of all areas.

The high spatio-temporal variability of the surface mixing revealed from FSLEs may strongly modulate the biological components of these complex and dynamic ecosystems. Next we proceed to investigate the correlation between horizontal mixing with the biological activity in our regions of interest.

4.2 Relationship with the biological activity

Now we study the relationship between the FSLEs and surface chlorophyll concentration estimated from space. First we performed Hovmöller plots of the surface chlorophyll

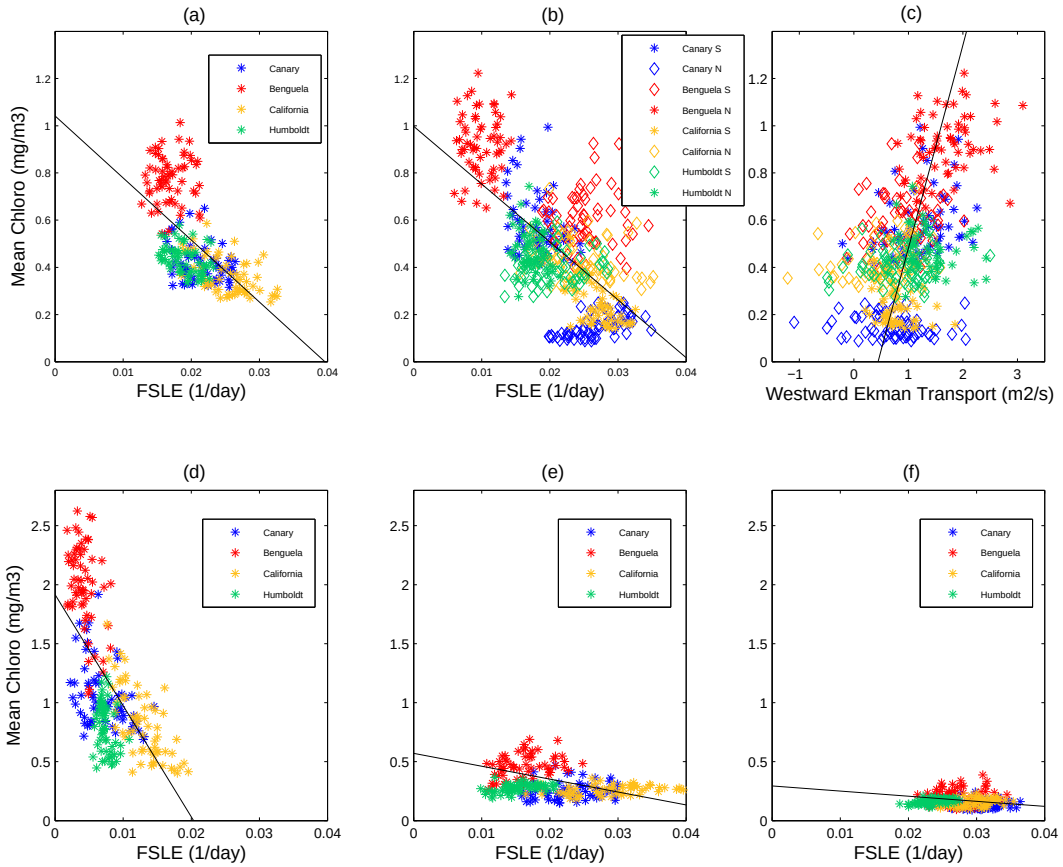

Fig. 4. Chlorophyll-*a* versus backward FSLEs, both averaged over the analysis areas (8 degrees coastal strips) for: **(a)** Whole analysis areas (R^2=0.38); **(b)** Same as in (a) but per subsystem (R^2=0.43); **(c)** Same as in (b) but for chlorophyll-*a* versus westward Ekman transport per subsystem (R^2=0.21; for visual improvement, the regression line has been obtained with the opposite order, x-axis versus y-axis); **(d, e, f)** Same as in (a) but for three successive strips oriented along the coast, **(d)** 2° from the coast, **(e)** within the 2° to 5° coastally oriented strip and **(f)** within the 5° to 9° coastally oriented strip.

distribution in the four upwellings by averaging the chlorophyll concentration along lines of constant latitude within the analysis areas for our five years of study (not shown). In each upwelling system, a clear distinction appears between two different zones, a southern one and a northern one, characterized by a very distinct degree of chlorophyll richness. In fact, the limits of the subsystems observed in the chlorophyll concentration Hovmöller plots coincide with the previous latitutinal limits deduced from FSLEs (around 30° N for CUS and CalUS, 27° S for BUS and 25° S for HUS). We also noticed that the poorest subsystem in chlorophyll matches the most turbulent one and vice-versa; this remark stands for the four EBUS. The spatial averaged chlorophyll over each analysis area (8° degrees coastal strips) reveals that the BUS admits the highest chlorophyll-*a* content (0.78 mg/m^3), followed by the HUS (0.43 mg/m^3), CUS (0.42 mg/m^3) and CalUS (0.36 mg/m^3). This ranking is just the opposite as the one based on the mixing activity of the surface ocean.

If one plots spatial averages of FSLE versus spatial averages of chlorophyll concentration, over the entire analysis area and over each subsystem (Fig. 4a and b), for each month from June 2000 to June 2005, a negative correlation between FSLEs and chlorophyll concentration emerges. For all four areas, the subsystems with the highest mixing activity are the poorest in chlorophyll. Note on Fig. 4a that each upwelling system is characterized by a clear clustering, with an exception of the CalUS which presents a more widespread distribution. The same observation is valid for each subsystem on Fig. 4b. Although these EBUS present common features, they seem also to have particular functioning revealed by these clusters. When considering only the most turbulent subsystems of each EBUS, the correlation is rather clear (R^2=0.75, not shown) suggesting that the higher the mixing activity is, the stronger the inverse relationship is between surface chlorophyll and mixing. The inhibiting effect of stirring revealed by the negative correlation seems to occur above a certain value – a turbulence threshold – and might act differently depending on the system. Following similar

calculations of spatial means over strips oriented along the coast (see Fig. 4, three lower panels d, e, and f), we observe a high negative correlation at the coast, decreasing when shifting to offshore strips, and even becoming flat when approaching the oligotrophic gyre further offshore. This finding obtained from an analysis over the four EBUS seems to indicate a variable response of the biology to physical stirring, valid in such diverse areas widespread over the world ocean.

Upwelling areas are definitely affected by water vertical movements and velocities, through uplift of rich nutrients water and 3-D turbulence, which are not captured by our previous analysis. We will also examine the influence of Ekman transport which creates pumping of nutrients and carries them from the deep layer to the coastal surface waters where light is not limiting. Vertical velocities and Ekman transport, which can both play a very relevant role in the chlorophyll signature detected from space, will be considered in the following.

We evaluated the horizontal divergence, Δ, of the surface velocity field and averaged it over the period June 2000–June 2005 at each point of the CUS, BUS, CalUS and HUS (not shown). The negative values of the Δ field in the coastal areas indicates the presence of upwelling events. We noticed that in the coastal zones of the BUS, the well known upwelling cells Cape Frio, Walvis Bay and Lüderitz in the northern subsystem appear clearly, being more intense than the southern cells, in agreement with Monteiro (2009) estimates of the northern subsystem accounting for 80%, on average, of the total upwelled flux over the whole BUS. The intense upwelling cells spread along the Peru/Chile coast are also visible, whereas the area above 15° S is mainly characterized by negative velocities which represent the equatorial upwelling. When averaging the temporal mean of the Δ field over the analysis area of each subsystem, representing a measure of the mean vertical velocities averaged over space and time, we confirm that the less (most) horizontally stirred system is associated with negative (positive) mean vertical velocities indicating predominance of upwelling phenomena (downwelling, respectively). This stands for the BUS, HUS and CUS since their less turbulent systems are respectively characterized by $\overline{\Delta}_{\mathrm{nBUS}}=-0.0036\,\mathrm{day}^{-1}$, $\overline{\Delta}_{\mathrm{nHUS}}=-0.002\,\mathrm{day}^{-1}$ and $\overline{\Delta}_{\mathrm{sCUS}}=-0.0016\,\mathrm{day}^{-1}$ whereas their most turbulent exhibit positive means ($\overline{\Delta}_{\mathrm{sBUS}}=0.0012$, $\overline{\Delta}_{\mathrm{sHUS}}=2.2\times10^{-4}\,\mathrm{day}^{-1}$ and $\overline{\Delta}_{\mathrm{nCUS}}=8.7\times10^{-4}\,\mathrm{day}^{-1}$). For the CalUS, the distinction of two different subregions is not so clear, as compared to the others, confirmed by the very close negative average $\overline{\Delta}_{\mathrm{nCalUS}}=-8\times10^{-4}\,\mathrm{day}^{-1}$ and $\overline{\Delta}_{\mathrm{sCalUS}}=-1\times10^{-3}\,\mathrm{day}^{-1}$. It seems that areas dominated with upward processes are restricted to the very coastal areas whereas the offshore waters are dominated by downward ones. The global averages of Δ over the whole domain reveal negative values (upwelling) and give the following ranking: the most intense upward velocities are found in the BUS, followed by the CalUS, then comes the HUS and finally the CUS.

To complete the analysis, we have calculated the Ekman transport U_E along the E-W direction. Not surprisingly, its spatial distribution (not shown) is particularly linked to the spatial distribution of chlorophyll: high chlorophyll contents are often associated with intense Ekman transport, indicating high upwelling intensity. Indeed the northern regions of the BUS and HUS, the richest in chlorophyll and presenting the minimum mixing activity, are characterized by the highest offshore transport. In the CUS, both sub-areas have high values for the offshore transport very close to the coast, with similar values in the southern and northern subregions. Further from the coast, the highest westward transport in the southern CUS area coincides again with the highest chlorophyll content. The same analysis may be done for the CalUS with a less marked difference in the offshore southern subsystem. Figure 4c represents the spatially averaged westward Ekman transport U_E versus spatial averages of chlorophyll concentration, over each subsystem from June 2000 to June 2005 (one point per month). Negative values indicate an Ekman transport to the east, whereas positive ones indicate an offshore Ekman transport to the west. A positive correlation appears confirming the effect of Ekman-transport induced upwelling on biological productivity. This finding is not surprising and compatible with previous results (Thomas et al., 2004) since horizontal currents are strongly related to the vertical circulation. A global average of Ekman transport over space (analysis areas) and time reveals similar ranking deduced from the chlorophyll content, except a shift between CUS and HUS. The BUS has the highest ($-1.33\,\mathrm{m}^2/\mathrm{s}$), then come the CUS ($-1.07\,\mathrm{m}^2/\mathrm{s}$) and HUS ($-1.01\,\mathrm{m}^2/\mathrm{s}$) and finally the CalUS ($-0.7\,\mathrm{m}^2/\mathrm{s}$).

5 General discussion

Divisions of each area into two subsystems, based on different levels of temporal averaged horizontal stirring rates, are quite consistent with limits deducted from different criteria in other studies (Carr and Kearns, 2003; Mackas et al., 2006; Monteiro, 2009). We also proposed a ranking of horizontal mixing that gives new insights as compared to the classification made by Patti et al. (2008) based simply on a wind-mixing index. Systems from the same hemisphere seem to exhibit a similar behaviour with a dominant annual cycle when studying the temporal evolution of their spatially averaged horizontal mixing activity. The study from PDFs confirmed the statistical structure of these Lagrangian diagnostics already documented by Waugh and Abraham (2008). They showed that PDFs of FTLEs (Finite-Time Lyapunov Exponents, comparable to FSLEs) computed over the global surface ocean may be reasonably modelled by two kinds of distributions: in weak strain regions they are well fitted by Rayleigh distributions whereas for large-strain regions PDFs are better fitted by a general Weibull distribution. Since most of the regions under study reveal a quite nice fitting to a

Weibull distribution, with slightly different parameters values as indicated in Waugh and Abraham (2008), they can be considered as large-strain regions. The PDF of normalized FSLEs over the BUS shows a particular distribution, indicating that the mixing activity over this system is quite unique. The ranking in terms of chlorophyll content is the same than the one proposed by Cushing (1969), linking chlorophyll content and higher trophic level production. Carr (2001) and Carr and Kearns (2003) compared the EBUS depending on their primary productivity estimated from remote sensing and found also the same ranking, except for a switch between the HUS and CUS. The temporal variations of the chlorophyll stocks and their coupling with Ekman transport was studied in details by Thomas et al. (2004) over the four EBUS and more precisely over the CUS by Lathuilière et al. (2008). We globally confirmed that chlorophyll stocks are positively correlated with westward Ekman transport intensity.

When investigating the link of FLSEs with biological data, the scatterplots reveal a negative correlation between horizontal mixing activity and chlorophyll concentration in upwelling areas. This negative effect is in line with Lachkar et al. (2009) who showed that strong eddy activity acts as an inhibiting factor for the biological productivity in coastal upwelling systems. They confirmed that the CUS and CalUS appear to be the most contrasting systems of the 4 EBUS, in terms of biological productivity and mixing activity as well. Patti et al. (2008) also mentioned a negative correlation between turbulence, calculated as the cube of wind speed, and logarithm of the chlorophyll-*a* concentration for the BUS; however this finding did not hold for the other areas showing a positive relationship. We note that theoretical studies in idealized settings, in which nutrients reach plankton only by lateral stirring, display also negative correlation between mixing and biomass (although mixing and productivity may be positively correlated) (Tél et al., 2005; Birch et al., 2007; McKiver and Neufeld, 2009). In the following we propose some mechanisms to explain this inverse relationship, as compared to the open ocean and other low nutrient environments, where several studies showed that eddies and turbulent mesoscale features tend to rather enhance biological productivity (McGillicuddy et al., 1998; Oschlies and Garçon, 1998).

In our case, we focussed on very productive areas where the high biological productivity is maintained by a large nutrient supply from deep waters driven by Ekman pumping. Horizontal turbulent mixing of nutrients in surface waters, which was significant in the oligotrophic areas, is now a second order effect as compared to the vertical mechanisms (nutrient Ekman pumping) in the most productive subsystems. McKiver and Neufeld (2009), lay the emphasis on a ratio between the biological ecosystem timescale (inverse of the growth rate) and the flow timescales. When increasing the ratio, corresponding to an increase of turbulence, they indicate a negative effect on the phytoplankton mean concentration as it is the case in our study. The localized pulses of nutrients are rapidly being dispersed by intense mixing before being used efficiently by the phytoplankton to grow. Similar processes were documented in a theoretical modeling study from Pasquero et al. (2005). When associating an upwelling of nutrient with coherent vortices, they find a lower primary productivity than without vortices. They explained this observation by the trapping properties of eddies and the limited water exchange between the vortex cores and the surrounding waters. Eddies are able to trap and export offshore rich coastal waters which are not being used efficiently by the phytoplankton, resulting in a lateral loss of nutrients of the coastal upwelling. We also observed that areas characterized by high FSLEs are correlated with intense vertical movements (downwellings as well as upwellings), whereas the areas with low FSLEs are mainly dominated by upward vertical velocities (upwellings). Lehahn et al. (2007) recently showed that vertical motions associated with eddy are more precisely located close to the lines of high FSLEs. Regions of high FSLE averages indicate a high occurrence of intense eddies which modify the three dimensional mean flow. The nutrient Ekman pumping, dominant process in upwelling areas, is weakened and the fuelling of nutrients toward the surface decreased. A significant stirring revealed by high FSLEs may decrease the Ekman transport induced upwelling leading to weaker surface chlorophyll stocks.

In the scope of previous works concentrating in the open ocean, and considering Fig. 4 (3 lower panels), we suggest the possibility of a variable response of the phytoplankton to the mesoscale oceanic turbulence. This changing behavior, represented by the high negative correlation at the coast decreasing when moving offshore, may be explained when considering the different dominant processes in the areas of interest. In very coastal areas, intense biological productivity is supported by the intensity of Ekman induced upwelling of nutrients. However, a high turbulence caused by eddies may induce an offshore lateral loss of nutrients and may decrease the vertical fuelling of surface waters from nutrients Ekman pumping, thus leading to a negative effect on biological production. Then, when moving offshore in the transitional area between the very coastal upwelling and the oligotrophic gyre, the moderate production regime relies on the offshore export of coastal rich waters. In this case, the turbulent mixing of nutrients may have a minor influence on moderate productivity, from the compensation of weak positive and negative effects. Then, in the open ocean where the biological productivity is weak and limited by very low nutrient concentrations, the resultant effect of horizontal mixing on phytoplankton growth becomes positive. The phytoplankton development is being promoted by eddies which induce vertical velocities and an upward flux of nutrients toward the very depleted surface waters (McGillicuddy et al., 1998; Oschlies and Garçon, 1998).

Other factors are of course influencing at different levels the biological productivity in the ocean, more particularly in these highly variable areas. Several studies tried to iden-

tify the main factors among the four EBUS. Carr and Kearns (2003) distinguished different types of factors and discussed which ones control primary productivity. Oxygen concentrations and displacement of the thermocline symbolized the large-scale upwelling intensity; the local forcings were represented by quantities such as Photosynthetically Available Radiation, offshore transport and SST gradient, but the authors omitted the turbulence. They showed that large-scale circulation patterns are responsible for the main differences between EBUS. Then, the local forcings, and their combination with large-scale factors, explain the weaker variations. If we would consider only the nutrient concentration and Ekman pumping intensity (from their study) on one hand, and the turbulence from FSLEs (from our study) on the other hand, we can easily explain differences among EBUS without taking into account all other factors. Here we argue that adding our turbulence data from FSLEs to nutrients concentration and Ekman transport intensity allow us to simply obtain similar results, suggesting the fact that the turbulence effect is important to be considered. Patti et al. (2008) studied the factors driving the chlorophyll content and they found that nutrient local concentrations, mainly governed by local upwelling intensity (Ekman pumping), explain the main differences between very productive areas (HUS and BUS) as compared to the other two (CalUS and CUS). These processes act as first order factors whereas the continental shelf width appears to be the key secondary order factor explaining the difference between HUS and BUS, also mentioned by Carr and Kearns (2003). The mixing from FSLEs can also explain the main differences observed since the CalUS and CUS admit the highest surface mixing activity. Moreover, the highest chlorophyll content observed in the northern Benguela coincides again with the minimum of mixing measured by FSLEs. The BUS appears to be the most productive system since the Ekman pumping over a large width shelf is maximum and associated with the lowest mixing. Patti et al. (2008) also discussed other factors such as light limitation, solar cycle, presence of retention areas, etc., concluding that they should act at different levels, in different areas. It is also well known that micronutrient availability and alternative biogeochemical processes such as N_2 fixation or denitrification may also play a role in nature. However, the variability among all these factors over all areas is too large to identify trivial patterns. Consequently we did not consider these controls as primary factors in our analysis.

6 Conclusions

The distribution of FLSEs computed from multi-sensor velocity fields over a 5 year period allowed us to make a comparative study of the mixing activity in the four eastern boundary upwelling systems. Each area was divided into two subsystems showing different levels of temporal averaged horizontal stirring rates. When studying the temporal evolution of their spatially averaged mixing, we proposed a ranking in terms of horizontal mixing intensity for all four EBUS. We also found that the more vigorous mixing occurs in subsystems further away the equator explained by the intensification of large scale atmospheric forcing at higher latitudes. Systems from the same hemisphere seem to exhibit a similar behavior with a dominant annual cycle. The PDF computations of FSLEs reveal the statistical structure of these Lagrangian diagnostics. When investigating the link of FSLEs with biological data, the subdivisions detected from FSLEs' maps appeared to be also visible on chlorophyll concentration Hovmöllers suggesting that these two quantities are linked. The scatterplots revealed a negative correlation between horizontal mixing activity and chlorophyll concentration in upwelling areas. We then confirmed that chlorophyll stocks are positively correlated with westward Ekman transport intensity over the four EBUS. It thus seemed that the horizontal turbulent mixing of nutrient is a second order effect as compared to the vertical mechanisms. After estimating the mean vertical velocities from incompressibility assumption, we proposed another explanation: the regions of high FSLEs are characterized by occurence of intense eddies and their verticals velocities associated. This will modify the whole 3-D flow and lead to a global decrease of the nutrient Ekman pumping (supported by low Ekman transport). We finally suggest the possibility of a variable response of the phytoplankton to the sub/mesoscale oceanic turbulence depending on the distance to the coast. This changing behavior is represented by the high negative correlation at the coast decreasing when moving offshore. It may be explained when considering the different areas and their associated dominant bio-physical processes. We then discuss the effect of others factors not considered here, and compare our approach to all previous comparative works.

Further work should investigate the robustness of the relationship found in our four systems when examining FSLEs versus biological stocks. Still much needs to be done to fully understand how plankton distributions are controlled by the interplay between their turbulent medium and the non-linear processes of their ecology. Coupled modelling approaches appear to be the only way to consider all these factors simultaneously. Besides a better understanding of the interactions between biological and physical processes, these coupled modelling studies will allow us to investigate and determine the respective effect of abiotic and biotic factors.

Although dealing with other scales of study may lead to different conclusions, chaotic stirring and turbulence in the ocean play a very important role by influencing biological processes at any scale. The negative effect of horizontal stirring on biological productivity in upwelling areas shown here needs to be considered when trying to estimate the carbon-pump efficiency on a global scale since upwelling areas shelter more than 20% of the global biological productivity (Ryther, 1969; Cushing, 1969; Chavez and Toggweiler, 1995). The global estimation of CO_2 fluxes at the ocean-atmosphere

interface will gain in accuracy when considering this effect through, for instance, a spatial parameterization of turbulence.

Acknowledgements. V. R. and C. L. were awarded a EUR-OCEANS network of Excellence short visit grants. V. R. is supported by a PhD grant from Direction Générale de l'Armement. V. G. and J. S. acknowledge funding support from CNES and C. L. and E. H.-G. from PIF project OCEANTECH of the Spanish CSIC and FISICOS (FIS2007-60327) of MEC and FEDER. We also thank A.M. Tarquis and the two anonymous referees for their constructive comments.

Edited by: A. Turiel
Reviewed by: A. M. Tarquis and two other anonymous referees

The publication of this article is financed by CNRS-INSU.

References

Artale, V., Boffetta, G., Celani, A., Cencini, M., and Vulpiani, A.: Dispersion of passive tracers in closed basins: Beyond the diffusion coefficient, Phys. Fluids, 9, 3162–3171, 1997.

Aurell, E., Boffetta, G., Crisanti, A., Paladin, G., and Vulpiani, A.: Predictability in the large: an extension of the concept of Lyapunov exponent, J. Phys. A, 30, 1–26, 1997.

Beron-Vera, F. J., Olascoaga, M. J., and Goni, G. J.: Oceanic mesoscale eddies as revealed by Lagrangian coherent structures. Geophys. Res. Lett., 35, L12603, doi:10.1029/2008GL033957, 2008.

Birch, D. A., Tsand, Y. K., and Young, W. R.: Bounding biomass in the Fisher equation, Phys. Rev. E, 75, 066304, 2007.

Boffetta, G., Lacorata, G., Redaelli, G., and Vulpiani, A.: Detecting barriers to transport: A review of different techniques, Phys. D, 159, 58–70, 2001.

Bograd, S. J., Schroeder, I., Sarkar, N., Qiu, X., Sydeman, W. J., and Schwing, F. B.: Phenology of coastal upwelling in the California Current, Geophys. Res. Lett., 36, L01602, doi:10.1029/2008GL035933, 2009.

Carr, M. E.: Estimation of potential productivity in Eastern Boundary Currents using remote sensing, Deep-Sea Res. II, 49, 59–80, 2001.

Carr, M. E. and Kearns, E. J.: Production regimes in four Eastern Boundary Current Systems, Deep-Sea Res. II, 50, 3199–3221, 2003.

Chavez, F. P. and Toggweiler, J. R.: Physical estimates of global new production: The upwelling contribution, in: Upwelling in the Ocean: Modern Processes and Ancient Records, John Wiley and Sons Ltd., 313–320, 1995.

Cushing, D. H.: Upwelling and fish production, in FAO Fisheries Technical Papers, 84, 1–40, 1969.

d'Ovidio, F., Fernández, V., Hernández-García, E., and López, C.: Mixing structures in the Mediterranean Sea from finite-size Lyapunov exponents, Geophys. Res. Lett., 31, L17203, doi:10.1029/2004GL020328, 2004.

d'Ovidio, F., Isern-Fontanet, J., López, C., Hernández-García, E. and García-Ladona, E.: Comparison between Eulerian diagnostics and Finite-Size Lyapunov Exponents computed from Altimetry in the Algerian basin, Deep-Sea Res. I, 56, 15–31, 2009.

Haller, G.: Lagrangian structures and the rate of strain in a partition of two dimensional turbulence, Phys. Fluids, 13, 3365–3385, 2001.

Kang, J., Kim, W., Chang, K., and Noh, J.: Distribution of plankton related to the mesoscale physical structure within the surface mixed layer in the southwestern East Sea, Korea, J. Plankton Res., 26(12), 1515–1528, 2004.

Koh, T. and Legras, B.: Hyperbolic lines and the stratospheric polar vortex, Chaos, 12, 382–394, 2002.

Lachkar, Z., Gruber, N., and Plattner, G. K.: A comparative study of biological productivity in Eastern Boundary Upwelling Systems using an Artificial Neural Network, Biogeosciences Discus., submitted, 2009.

Lathuilière, C., Echevin, V., and Lévy, M.: Seasonal and intraseasonal surface chlorophyll-*a* variability along the northwest African coast, J. Geophys. Res., 113, C05007, doi:10.1029/2007JC004433, 2008.

Lehahn, Y., d'Ovidio, F., Lévy, M., and Heyfetz, E.: Stirring of the Northeast Atlantic spring bloom: a Lagrangian analysis based on multisatellite data, J. Geophys. Res., 112, C08005, doi:10.1029/2006JC003927, 2007.

Mackas, D., Tsurumi, M., Galbraith, M., and Yelland, D.: Zooplankton distribution and dynamics in a North Pacific Eddy of coastal origin: II. Mechanisms of eddy colonization by and retention of offshore species, Deep-Sea Res. II, 52, 1011–1035, 2005.

Mackas, D., Strub, P. T., Thomas, A. C., and Montecino, V.: Eastern Ocean Boundaries Pan-Regional View, in: The Sea, Chapter 2, p 21–60, edited by: Robinson, A. R. and Brink, K. H., Harvard Press Ltd., 2006.

McGillicuddy J., Robinson A., Siegel D., Jannasch H., Johnson R., Dickey T., McNeil, J., Michaels, A., and Knap, A.: Influence of mesoscale eddies on new production in the Sargasso Sea, Nature, 394, 263–266, 1998.

McKiver, W. J. and Neufeld, Z.: The influence of turbulent advection on a phytoplankton ecosystem with non-uniform carrying capacity, Phys. Rev. E., 79, 061902, 2009.

Monteiro, P. M. S.: Carbon fluxes in the Benguela Upwelling system, in: Carbon and Nutrient Fluxes in Continental Margins: a Global Synthesis, chapter 2.4, edited by: Liu, K. K., Atkinson, L., Quiñones, R. and Talaue-McManus, L., to appear (October), 2009.

Moore, T., Matear, R., Marra, J., and Clementson, L.: Phytoplankton variability off the Western Australian Coast: Mesoscale eddies and their role in cross-shelf exchange, Deep-Sea Res. II, 54, 943–960, 2007.

Olascoaga, M. J., Beron-Vera, F. J., Brand, L. E., and Kocak, H.: Tracing the early development of harmful algal blooms with the aid of Lagrangian coherent structure, J. Geophys. Res., 113, C12014, doi:10.1029/2007JC004533, 2008.

Oschlies, A. and Garçon, V.: Eddy-induced enhancement of pri-

mary production in a model of the North Atlantic Ocean, Nature, 394, 266–268, 1998.

Owen, R. W.: Fronts and Eddies in the sea: mechanisms, interactions and biological Effects, in: Fronts and Eddies in the Sea, p 197–233, edited by: Owen, R.W., Academic Press, London, 1981.

Patti, B., Guisande, C., Vergara, A.R., Riveiro, I., Barreiro, A., Bonanno, A., Buscaino, A., Basilone, G., and Mazzola, S.: Factors responsible for the differences in satellite-based chlorophyll *a* concentration between the major upwelling areas, Est. Coast. Shelf Sc., 76, 775–786, 2008.

Pasquero, C., Bracco, A., and Provenzale, A.: Impact of the spatiotemporal variability of the nutrient flux on primary productivity in the ocean, J. Geophys. Res., 110, C07005, doi:10.1029/2004JC002738, 2005.

Pauly, D. and Christensen, V.: Primary production required to sustain global fisheries, Nature, 374, 255–257, 1995.

Rio, M.-H. and Hernández F.: A mean dynamic topography computed over the world ocean from altimetry, in-situ measurements, and a geoid model, J. Geophys. Res., 109, C12032, doi:10.1029/2003JC002226, 2004.

Rossi, V., López, C., Sudre, J., Hernández-García, E., and Garçon, V.: Comparative study of mixing and biological activity of the Benguela and Canary upwelling systems, Geophys. Res. Lett., 35, L11602, doi:10.1029/2008GL033610, 2008.

Ryther, J. H.: Photosynthesis and fish production in the sea, Science, 166, 72–76, 1969.

Schwing, F. B., Bond, N. A., Bograd, S. J., Mitchell, T., Alexander, M. A., and Mantua, N.: Delayed coastal upwelling along the U.S. West Coast in 2005: A historical perspective, Geophys. Res. Lett., 33, L22S01, doi:10.1029/2006GL026911, 2006.

Shadden, S. C., Lekien, F., and Marsden, J. E.: Definition and properties of Lagrangian coherent structures from finite-time Lyapunov exponents in two-dimensional aperiodic flows, Phys. D, 212, 3–4, 271–304, 2005.

Sudre, J. and Morrow, R.: Global surface currents: a high resolution product for investigating ocean dynamics, Ocean Dyn., 58(2), 101–118, 2008.

Tél, T., de Moura, A., Grebogi, C., and Karolyi, G.: Chemical and biological activity in open flows: A dynamical system approach, Phys. Rep., 413, 91–196, 2005.

Thomas, C. A., Strub, T. P., Carr, M. E., and Weatherbee, R.: Comparisons of chlorophyll variability between the four major global eastern boundary currents, Int. J. Rem. Sens., 25, 7, 1443–1447, 2004.

Waugh, D. W. and Abraham, E. R.: Stirring in the global surface ocean, Geophys. Res. Lett., 35, L20605, doi:10.1029/2008GL035526, 2008.

Annexe C : Articles dans le domaine de l'optique adaptative

Annexe C

Annexe C : Articles dans le domaine de l'optique adaptative (Science de l'univers : Astronomie)

Sommaire

C.1 Article : A multiscale approach to phase reconstruction for Adaptive Optics, Maji S. K. *et al.*, 2011 372

C.1.1 Abstract 372

C.1.2 Article publié dans *IEEE NASA/ESA Conference on Adaptive Hardware and Systems (AHS-2012)* 372

C.2 Article : Towards Multiscale Reconstruction of Perturbated Phase from Hartmann-Shack Acquisitions, Maji S. K. *et al.*, 2012 377

C.2.1 Abstract 377

C.2.2 Article publié dans *IEEE NASA/ESA Conference on Adaptive Hardware and Systems (AHS-2012)* 377

C.1 Article : A multiscale approach to phase reconstruction for Adaptive Optics, Maji S. K. *et al.*, 2011

C.1.1 Abstract

Adaptive Optics (AO) refers to (servo-control) methods used in astronomical imaging to compensate in real time for the loss of spatial resolution power of the instrument caused by the earth's upper atmosphere turbulence, which produces inhomogeneties of air refractive index and hence modifies in a chaotic manner the optical phase of incoming light from space. In this paper we present the first results of a radically new approach to phase reconstruction in AO based on non linear methods for the processing of complex signals having multiscale properties. We make use of the Microcanonical Multiscale Formalism (herein referred to as MMF) to infer properties along the scales of the complex signal made of the perturbated optical phase, and we perform the reconstruction of the phase using appropriate wavelet decomposition associated to the cascading properties of fully developped turbulence.

C.1.2 Article publié dans *IEEE NASA/ESA Conference on Adaptive Hardware and Systems (AHS-2012)*

Référence : S. K. Maji, H. Yahia, O. Pont, J. Sudre, T. Fusco, and V. Michau 2012 : Towards Multiscale Reconstruction of Perturbated Phase from Hartmann-Shack Acquisitions, *IEEE NASA/ESA Conference on Adaptive Hardware and Systems (AHS-2012)*, 77-84, DOI 10.1109/AHS.2012.6268633.

A multiscale approach to phase reconstruction for Adaptive Optics

Suman Kumar Maji, Hussein Yahia, Oriol Pont
INRIA Bordeaux Sud-Ouest
GeoStat team
http://geostat.bordeaux.inria.fr
sumankumar.maji,
hussein.yahia, oriol.pont@inria.fr

Thierry Fusco, Vincent Michau
ONERA
DOTA/E
http://www.onera.fr/
thierry.fusco,
vincent.michau@onera.fr

Joel Sudre
LEGOS
UMR CNRS 5566
DynBio team, Toulouse
http://www.legos.obs-mip.fr/
joel.sudre@legos.obs-mip.fr

***Abstract*—Adaptive Optics (AO) refers to (servo-control) methods used in astronomical imaging to compensate in real time for the loss of spatial resolution power of the instrument caused by the earth's upper atmosphere turbulence, which produces inhomogeneties of air refractive index and hence modifies in a chaotic manner the optical phase of incoming light from space. In this paper we present the first results of a radically new approach to phase reconstruction in AO based on non linear methods for the processing of complex signals having multiscale properties. We make use of the Microcanonical Multiscale Formalism (herein referred to as MMF) to infer properties along the scales of the complex signal made of the perturbated optical phase, and we perform the reconstruction of the phase using appropriate wavelet decomposition associated to the cascading properties of fully developped turbulence.**

***Index Terms*—adaptive optics, turbulence, phase reconstruction, microcanonical multiscale formalism, complex signals, nonlinear methods in signal processing, wavelets, time-frequency analysis.**

I. Introduction

Atmospheric turbulence in earth's atmosphere upper layers plays a fundamental role in limiting the resolution of ground based instruments. These turbulent layers perturbate to a great extent incoming light from outer space, resulting in an overspreaded impulse response of the diffraction-limited instrument and a shortening of the cutoff frequency. Adaptive Optics (AO) is one of the best known solution methods to overcome this hurdle [1], [2]. It provides real-time compensation by deforming a mirror through a servo-loop, according to phase measurements provided by a wavefront sensor (WFS). In most AO systems, the perturbated phase is acquired through a specific sensor and the mirror deformations are approximated in real-time through least-square inverse problems and deconvolution techniques [1]. A common version of the WFS is given by the Hartmann-Shack sensor (HS).

A Hartmann-Shack WFS is used to measure the slope of an incoming wavefront [2]. In a HS sensor, an array of lenses (called lenslets) is placed in a plane parallel to the pupil of the telescope in order to sample the incoming wavefront [1], [2]. A detector, placed at the focus of each lenslet, captures the sub-image sampled by the corresponding lenslet. The focussed sub-images are low resolution identical images of the object captured by the telescope. In an ideal case when the wavefront is plane, the sub-images are formed at the focus of each lenslet. But, in general, due to atmospheric turbulence when the wavefront gets distorted, each lenslet sees an inclined version of the wavefront and the corresponding sub-images are hence shifted from their reference position. The amount of shift in the position of the sub-images withrespect to its reference position is proportional to the mean slope of the wavefront [1] and henceforth can be measured. The reconstruction of the wavefront from the measurements is generally seen as an inverse problem and can be expressed in a matrix-algebra framework [2]. The best estimation of the phase can be calculated using two methods [2]:

- the maximum likelihood technique,
- the maximum a posteriori technique.

Both these techniques yield to the generalized *least-square solution* which is the solution traditionally used for estimating the phase under real-time constraints (AO) [1].

In the case of long time exposures, the optical transfer function of the imaging instrument is multplied by an atmospheric transfer function which is expressed using classical correlation functions and related to the Kolmogorov model of turbulence [2]. This suggests that an acquired image behaves like a complex signal having multiscale properties. Consequently, recent advances in the framework of reconstructible systems for complex signals are likely to apply to the case of an acquired perturbated optical phase, and, in particular, other reconstruction techniques of the perturbated phase, based on the cascading properties of fully developped turbulence can be taken into consideration.

In this paper we propose and experiment with a new model for phase reconstruction from an acquired sub-image of the perturbated phase: instead of recontructing the phase gradient using least-square methods or deconvolution, we propagate along the scales phase information, from the low resolution of the HS to higher resolution, using specific wavelet projections that mimic inference along the scales associated to cascading properties of fully developped turbulence [6], [7], [8]. As our first results show on simulated data, this leads to a new promising technique for phase reconstruction.

The paper is organised as follows: in section II we present the data used in the experiment. The phase reconstruction

978-1-61284-398-8/11/$26.00 ©2011 IEEE

technique is presented in section III and the results are shown in section IV. Finally, we conclude in section V.

II. Data

The data used in our work are datasets of simulated turbulent optical phase generated at ONERA. Data consists of 1000 occurences of turbulent phases defined on a pupil support and the associated psfs (point spread functions), corresponding to the following imaging characteristics:

- diameter of the telescope: 8 m,
- seeing at 5 microns: 0.85 arcseconds,
- Fried parameter r_0 at imaging wavelengths: 70 cm,
- $\frac{D}{r_0} = 11.4$,
- wind's speed: 12.5 m/s. Taylor's hypothesis is used: translation of the phase along x-axis,
- acquisition frequency: 200 Hz.

The pupil is defined on 128×128 pixels. Consequently the physical size of the pixel for the phase is 6.25 cm. Point spread function is generated for a Nyquist subsampling corresponding to 256×256 pixels. Physical size of the pixel for the psf is $\frac{\lambda}{2D} = 0.1375$ microradians corresponding to 28.35 milliarcseconds. Total field of the psf is 7.26×7.26 arcseconds. Data is generated in the FITS format [3]. For the statistical work shown in the section IV we need a set of appropriate sub-images, which must be, due to the requirements imposed by dyadic wavelet analysis, square sampled with a sampling size being a power of 2 (because we use a dyadic multiresolution algorithm). To avoid sub-reconstruction and Gibbs phenomena coming from the strong transition associated to the pupil's boundary, we take a sub-image made of 64×64 pixels centered in the middle of the pupil in the original data. From these data, we compute the gradients of the phase and produce an averaged gradient over a window of size 4×4 pixels, normalized by the size of the window (16 square pixels) thus resulting in a 16×16 restricted sub-image corresponding to a simulated HS acquisition. Each averaged phase gradient corresponds to two files (for the x and y derivatives of the averaged phase gradient). See figures 1,2 for a typical sample of the perturbated phase and the associated psf.

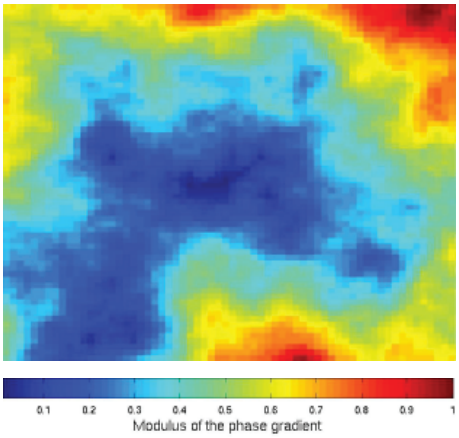

Fig. 1. Image of a simulated phase perturbated by atmospheric turbulence (see main text for the imaging characteristics). The image corresponds to a 64×64 pixels sub-image extracted from an original 128×128 pixels image to avoid the pupil's boundary.

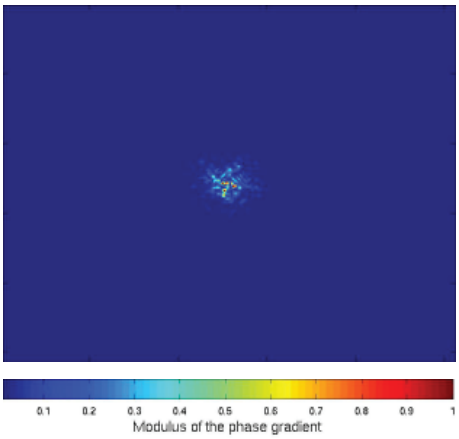

Fig. 2. Point spread function (psf) image associated to the image of the perturbated phase in figure 1.

III. Reconstruction

In the microcanonical analysis of complex signals it is assumed that, around each point $\mathbf{x}$ in the signal domain, there exists a singularity exponent $h(\mathbf{x})$ that can be effectively computed. One such example of a complex signal with multiscale properties is the perturbated optical phase. The singularity exponent $h(\mathbf{x})$ accounts to measuring the strength of the local transitions around point $\mathbf{x}$ [4] within the signal. Such singularity exponents can be effectively computed through $\log - \log$ regression on wavelet projections of the original signal's gradient. The singularity exponents are the basic ingredients in the framework of reconstructible systems: they allow the determination of specific subsets in the signal, such as the Most Singular Manifold (MSM). Knowledge of MSM permits an accurate reconstruction of the original signal, with a prior information of the signal's gradient on the MSM [5]. The effective determination of these singularity exponents lies in the hypothesis that form the so-called Microcanonical Multiscale Formalism (MMF) [4]. In the case of fully developped turbulence (which is the case of the earth's atmosphere), energy is passed down from the large scales to the smaller ones by means of an injection process until the medium attains a state of dynamic equilibrium [6]. One main assumption is that this injection process has to be infinitely divisible to give rise to complex cascade processes. It has been shown, in a different but similar context of turbulent signals [7], that the cascading properties of turbulent complex signals can be determined from the MMF through the determination of an *optimal wavelet* in the microcanonical sense: it is a wavelet that characterizes, around each point $\mathbf{x}$ in the signal domain, the injection process associated to the cascading process around $\mathbf{x}$ and between the scales. The optimal wavelet has the fascinating potential of unlocking the

signal's microcanonical cascading properties through simple wavelet multi-resolution analysis. Unfortunately, the effective determination of an optimal wavelet for a given turbulent acquisition is a very complicated and unsolved problem. This is the reason why, in this study and like in [7], we use a simple approximation of the optimal wavelet provided by a Battle Lemarié wavelet of degree 3 and with 41 coefficients. Experiments, similar to the ones described in [7] but performed on the phase signal instead, show that such an approximation of the optimal wavelet is acceptable.

In the wavelet analysis of 2D signals, persistence along the scales implies a relation of the form between the wavelet coefficients:

$$\alpha_c = \eta_1 \alpha_p + \eta_2 \tag{1}$$

(α_c: "child" wavelet coefficient, α_p: "parent" wavelet coefficient, η_1,η_2: random variables independant of α_c and α_p and also independant of each other). If the wavelet is optimal, then $\alpha_c = \eta\alpha_p$. Consequently, a method of reconstructing a signal from low resolution to higher resolution knowing an optimal wavelet is the following:

- compute the wavelet coefficients associated to the multiresolution analysis of the optimal wavelet between the two scales (low and high resolution),
- back-project the signal at low resolution to high resolution using the optimal wavelet coefficients.

The key point consists in the determination of the signal for which approximated optimal wavelet coefficients α_c and α_p are determined. For reasons similar as those described in [7], it appears that it is the signal of the *singularity exponents* that provide the best results. Experiments and results are shown in the following section.

IV. Results

From the considerations presented in section III, we perform the following experiment:

- compute Battle-Lemarié 3-41 wavelet coefficients associated to the following signal $\mathbf{s}$: *singularity exponents computed on the perturbated phase signal*,
- for each component (x and y) of the averaged phase gradient at low reslution (16×16 sub-image, see section II), back project the component from low to high resolution to get a phase's gradient at higher spatial resolution of 64×64.

Results are displayed in figure 4. They show visual resemblance of the reconstructed signal with the original one. Although there are imperfections, we clearly recognize the original phase's gradients. To better evaluate the quality of the reconstruction, we compute the absolute and relative errors of the norm of the gradients $\mathcal{G}_{abs}$ and $\mathcal{G}_{rel}$ for position $\vec{x}$ and time interval t as follows:

$$\mathcal{G}_{abs} = \langle \|\nabla\varphi^o(\vec{x},t) - \nabla\varphi^r(\vec{x},t)\| \rangle \tag{2}$$

$$\mathcal{G}_{rel} = \frac{\langle \|\nabla\varphi^o(\vec{x},t) - \nabla\varphi^r(\vec{x},t)\| \rangle}{\langle \|\nabla\varphi^o(\vec{x},t)\| \rangle} \tag{3}$$

TABLE I
Measurement of Error

Case	Relative error	Absolute error
$\mathcal{G}$	0.4 ± 0.1	0.2 ± 0.08
$\mathcal{M}$	0.3 ± 0.2	0.2 ± 0.1
$\mathcal{P}$	0.1 ± 0.08	0.4 ± 0.2

where $\langle \cdot \rangle$ denotes an average over an ensemble of pixel locations, φ^o: original phase gradient, φ^r: reconstructed phase gradient.
We also calculate the modulus of the absolute error and the modulus of the relative error of the norm of the gradients $\mathcal{M}_{abs}$ and $\mathcal{M}_{rel}$ as follows:

$$\mathcal{M}_{abs} = \langle |\|\nabla\varphi^o(\vec{x},t)\| - \|\nabla\varphi^r(\vec{x},t)\|| \rangle \tag{4}$$

$$\mathcal{M}_{rel} = \frac{\langle |\|\nabla\varphi^o(\vec{x},t)\| - \|\nabla\varphi^r(\vec{x},t)\|| \rangle}{\langle \|\nabla\varphi^o(\vec{x},t)\| \rangle} \tag{5}$$

We reconstruct the phase (shown in figure 4) from its gradient φ^r and calculate the absolute ($\mathcal{P}_{abs}$) and the relative errors ($\mathcal{P}_{rel}$) of the phase as follows:

$$\mathcal{P}_{abs} = \langle |\varphi^o(\vec{x},t) - \varphi^r(\vec{x},t)| \rangle \tag{6}$$

$$\mathcal{P}_{rel} = \frac{\langle |\varphi^o(\vec{x},t) - \varphi^r(\vec{x},t)| \rangle}{\langle |\varphi^o(\vec{x},t)| \rangle} \tag{7}$$

The results of all the calculations for the dataset are provided in table I.

V. Discussion and Conclusion

The use of MMF in signal processing is in the process of continuous evolution. Infact, the potential of MMF is now being tested on different natural systems ranging from natural images [19], [20] to stock market series [21], phytoplankton distribution in ocean [8], [9], heartbeat dynamics [22] to speech signal [23]. The main aim is to improve signal processing for self-similar multiscale systems and wavelets have a major role to play in this context [15]. The objective of this paper was to introduce a wavelet-based new method for the reconstruction of phase from a subset of its gradients. Convincing results of a new method for phase reconstruction using multiscale signal processing method and optimal wavelet approximation has been presented, which allows a reconstruction of the phase gradient by inference along the scales, using the signal of the singularity exponents of the original phase signal. Experiments have been performed on a datset of simulated perturbated phase. Of course, in real situation, one does not have access to the singularity exponents of the phase signal. We are now investigating a method to derive these singularity exponents from a priori knowledge of the atmosphere characteristics.

Acknowledgment

Suman Kumar Maji's PhD is funded by a CORDIS grant and Région Aquitaine's research project grant.

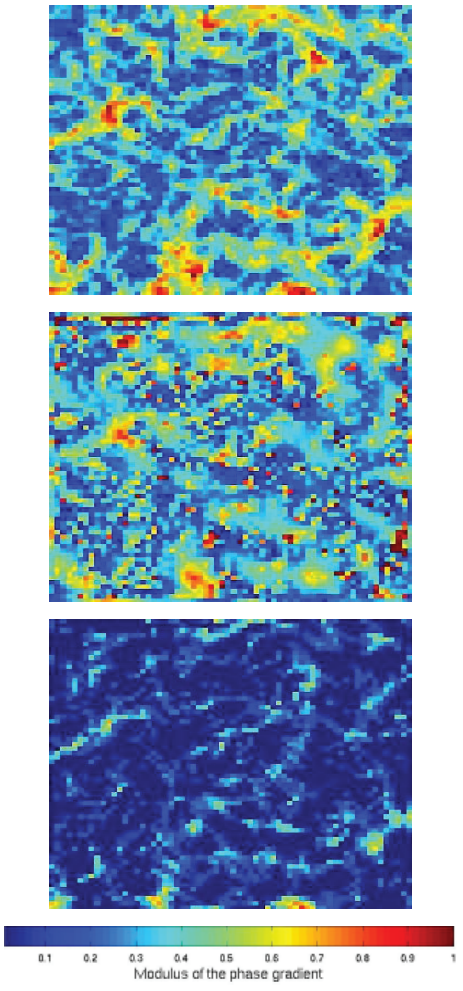

Fig. 3. Top: norm of the original phase gradient. Middle: norm of the reconstructed phase gradient. Bottom: difference between the norms of the original and the reconstructed phase gradient.

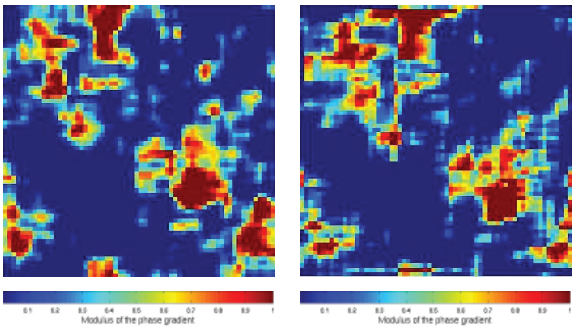

Fig. 4. Left: the original phase after its gradient has been normalized. Right: the phase corresponding to the gradients reconstructed using wavelets after normalization.

REFERENCES

[1] L. Mugnier, G. Le Besnerais, S. Meimon, Inversion in optical imaging through atmospheric turbulence in *Bayesian approach to inverse problems*, Jérôme Idier ed., ISTE, John Wiley & Sons Inc., ISBN 878-1-84821-032-5, 2008.

[2] F. Roddier, The design of an adaptive optics system in *Adaptive Optics in Astronomy*, François Roddier ed., Cambridge University Press, ISBN 0 521 55375 X, 1999.

[3] The FITS format: *http://fits.gsfc.nasa.gov/*.

[4] A. Turiel, H. Yahia and C. Perez-Vicente, Microcanonical Multifractal Formalism: a geometrical approach to multifractal systems. Part I: singularity analysis, *Journal of Physics A: Mathematical and Theoretical, vol 41*, doi: 10.1088/1751-8113/41/1/015501.

[5] A. Turiel, A. del Pozo, Reconstructing images from their most singular fractal manifold, *IEEE Transactions on Image Processing*, 11, 2002, 345-350.

[6] P. Chaisnais, Infinitely divisible cascades to model the statistics of natural images, *IEEE Transactions on Pattern Analysis and Machine Intelligence*, 29 (12), 2007, 2105-2119.

[7] H. Yahia, J. Sudre, C. Pottier, V. Garçon, Motion analysis in oceanographic satellite images using multiscale methods and the energy cascade, *Pattern Recognition*, Elsevier, 43 (10), 2010, 3591-3604.

[8] C. Pottier, A. Turiel, V. Garçon, Inferring missing data in satellite chlorophyll maps using turbulent cascading, *Remote Sensing of Environment*, Elsevier, 112, 2008, 4242-4260.

[9] S. Lovejoy, W. J. S. Curri, Y. Tessier, M. R. Claereboudt, E. Bourget, J. C. Roff, E. Schertzer, Universal multifractals and ocean patchiness: Phytoplankton, physical fields and coastal heterogeneityp, *Journal of Plankton Research*, 23 (2), 2001, 117-141.

[10] O. Pont, A. Turiel, C. Perez-Vicente, Empirical evidences of a common multifractal signature in economic, biological and physical systems, *Physica A*, Elsevier, 388, 2009, 2025-2035.

[11] A. Turiel, C. Perez-Vicente, J. Grazzini, Numerical methods for the estimation of multifractal singularity spectra on sampled data: A comparative study, *Journal of Computational Physics*, Elsevier, 216, 2006, 362-390.

[12] R. Benzi, G. Paladin, G. Parisi, A. Vulpiani, On the multifractal nature of fully developed turbulence and chaotic systems, *Journal of Physics*, A, 17, 1984, 3521-3531.

[13] O. Pont, A. Turiel, C. Perez-Vicente, Application of the microcanonical multifractal formalism to monofractal systems, *Physical Review*, Elsevier, 74, 2006, 061110-061123.

[14] A. Turiel, J. Grazzini, H. Yahia, Multiscale techniques for the detection of precipitation using thermal ir satellite images, *IEEE Geoscience and Remote Sensing Letters*, 2(4), 2005, 447-450, doi:10.1109/LGRS.2005.852712.

[15] O. Pont, A. Turiel, C. Perez-Vicente, Description, modelling and forecasting of data with optimal wavelets, *J.Econ Interact Coord*, 2009, 4: 39-54, doi 10.1007/s11403-009-0046-x.

[16] A. Arneodo, F. Argoul, E. Bacry, J. Elezgaray, and J. F. Muzy, *Ondelettes, multifractales et turbulence*, Diderot Editeur, Paris, France, 1995.

[17] R. Benzi, S. Patarnello, P. Santangelo, Self-similar coherent structures in two-dimensional decaying turbulence, *Journal of Physics A: Mathematical and General*, 21, 1998, 1221-1237.

[18] Stéphane Mallat, *A Wavelet Tour of Signal Processing*, Academic Press, 2nd Edition, 1999.

[19] A. Turiel, G. Mato, N. Parga, J. P. Nadal, The self-similarity properties of natural images resemble those of turbulent flows, *Physical Review Letters*, 80, 1998, 1098-1101.

[20] A. Turiel, N. Parga, The multi-fractal structure of contrast changes in natural images: From sharp edges to textures, *Neural Computation*, 12, 2000, 763-793.

[21] R. N. Mantegna, H. E. Stanley, Turbulence and financial markets, *Nature*, 383, 1996, 587-588.

[22] L. A. N. Amaral, A. L. Goldberger, P. Ch. Ivanov, H. E. Stanley, Scale-independent measures and pathologic cardiac dynamics, *Physical Review Letters*, 81 (11), 1998, 2388-2391.

[23] V. Khanagha, K. Daoudi, O. Pont, H. Yahia, A novel text-independent phonetic segmentation algorithm based on the microcanonical multiscale formalism, In *Interspeech*, Makuhari, Japan, 2010. Iscam.

C.2 Article : Towards Multiscale Reconstruction of Perturbated Phase from Hartmann-Shack Acquisitions, Maji S. K. *et al.*, 2012

C.2.1 Abstract

Atmospheric turbulence perturbates to a great extent the optical path of incoming light from outer space thereby limiting the resolution power of capturing devices. One of the most common techniques used in astronomical imaging to compensate for this perturbation is Adaptive Optics (AO). In this paper we explore the potential of Microcanonical Multiscale Formalism (MMF) for the reconstruction of the perturbated wavefront, from the low-resolution acquisition of the turbulent phase by a Hartmann-Shack wavefront sensor used in AO. In fact, turbulent flows, although chaotic in nature, are characterised by scale hierarchy and develop cascade like structures where transfer of energy takes place from one scale to the other. We make use of MMF to infer properties along the scales of the complex signal consisting of optical phase perturbation and perform reconstruction using an appropriate wavelet decomposition associated to the cascading properties of the turbulent flow.

C.2.2 Article publié dans *IEEE NASA/ESA Conference on Adaptive Hardware and Systems (AHS-2012)*

Référence : S. K. Maji, H. Yahia, O. Pont, J. Sudre, T. Fusco, and V. Michau 2012 : Towards Multiscale Reconstruction of Perturbated Phase from Hartmann-Shack Acquisitions, *IEEE NASA/ESA Conference on Adaptive Hardware and Systems (AHS-2012)*, 77-84, DOI 10.1109/AHS.2012.6268633.

Towards Multiscale Reconstruction of Perturbated Phase from Hartmann-Shack Acquisitions

Suman Kumar Maji[1], Hussein Yahia[1], Oriol Pont[1], Joel Sudre[2], Thierry Fusco[3], and Vincent Michau[3]

[1]INRIA Bordeaux Sud-Ouest, Geostat team
[2]LEGOS, UMR CNRS 5556, Dynbio Team
[3]ONERA, DOTA/E
[1]suman-kumar.maji, hussein.yahia, oriol.pont@inria.fr
[2]joel.sudre@legos.obs-mip.fr
[3]thierry.fusco, vincent.michau@onera.fr

Abstract—Atmospheric turbulence perturbates to a great extent the optical path of incoming light from outer space thereby limiting the resolution power of capturing devices. One of the most common techniques used in astronomical imaging to compensate for this perturbation is Adaptive Optics (AO). In this paper we explore the potential of Microcanonical Multiscale Formalism (MMF) for the reconstruction of the perturbated wavefront, from the low-resolution acquisition of the turbulent phase by a Hartmann-Shack wavefront sensor used in AO. In fact, turbulent flows, although chaotic in nature, are characterised by scale hierarchy and develop cascade like structures where transfer of energy takes place from one scale to the other. We make use of MMF to infer properties along the scales of the complex signal consisting of optical phase perturbation and perform reconstruction using an appropriate wavelet decomposition associated to the cascading properties of the turbulent flow.

Keywords—adaptive optics, inverse problem, cascade processes, microcanonical multiscale formalism, phase reconstruction, wavelets.

I. Introduction

Turbulence in the Earth atmosphere upper layers lead to the loss in spatial resolution power of ground based telescopes. The incoming light from outer space is perturbated to a great extent while passing through these turbulent layers. Adaptive Optics (AO) seeks to overcome the problem of loss in resolution power by deforming a mirror through a servo-control loop, in real-time, according to the phase measurements provided by a wavefront sensor (WFS). In most AO systems, the perturbated phase is acquired through a specific sensor and the mirror deformations are approximated in real-time through least-square inverse problems and deconvolution techniques [1], [13]. One of the most commonly used wavefront sensor is the Hartmann-Shack sensor (HS).

A Hartmann-Shack wavefront sensor is used to measure, at each point of a low resolution sub-image, the slope of an incoming wavefront. In a HS sensor, an array of lenses is placed in a conjugate pupil plane at the entrance of the telescope. These lenses sample, or in other words cut the incoming wavefront [1]. A detector is placed at the focus of each lenses which captures the sub-image sampled by the corresponding lens. The focused sub-images are low resolution identical images of the object captured by the telescope. When the wavefront is plane, each lens forms an image of the object at its focus. But, in general, due to turbulence when the wavefront gets distorted, each lens sees a tilted version of the wavefront and the corresponding sub-images are hence shifted from their reference position [1], [3], [4]. This shift in position is proportional to the mean slope of the wavefront and therefore can be measured [4]. The reconstruction of the wavefront from the measurements is generally seen as an inverse problem and can be expressed in a matrix-algebra framework [2]. The best estimation of the phase can be calculated using two methods [2]:

- the maximum likelihood technique,
- the maximum a posteriori technique.

Both these techniques yield to the generalized *least-square solution* which is the solution classically used for estimating the phase under real-time constraints [1].

In the case of long time exposures, the optical transfer function of the imaging instrument is multplied by an atmospheric transfer function which is expressed using classical correlation functions and related to the Kolmogorov model of turbulence [2]. This suggests that an acquired image behaves like a complex signal having multiscale properties [16]. Consequently, recent advances in the framework of reconstructible systems for complex signals are likely to apply to the case of an acquired perturbated optical phase, and, in particular, other reconstruction techniques of the perturbated phase, based on the cascading properties of fully developed turbulence can be taken into consideration [6], [7].

The general organization of a multiscale structure in complex signals has been related to the existence of cascade processes. The Microcanonical Multiscale Formalism (herein referred to as MMF) proves to be a suitable approach for the study of multiscale properties in real signals which generalize previous approaches [19]. A multiscale system is a scale-independent system, that is, the smaller regions exhibit the same statistical properties as that of the whole system: they are self-similar [6]. In section II we present a brief discussion on multiscale complex signals. Self-similarity is also a common property of fractal components. The behaviour of a fractal

978-1-4673-1916-4/12/$31.00 ©2012 IEEE

component under different scales is characterized only by its fractal dimension; whereas in a multiscale system, which is an association of multiple geometrical sets, the dimensions of all the components are taken into account to describe its behaviour under scale changes. Therefore, we can say that the key parameter that defines a multiscale system is the collection of its Hausdorff dimensions, commonly known as the *singularity spectrum*.

In this paper we will make use of the MMF scheme for phase reconstruction from an acquired sub-image of the perturbated phase. We will also check the performance after adding different proportions of gaussian white noise to the phase data and performing reconstruction on the noisy sub-images. Instead of using the conventional methods of least-square estimation or deconvolution [13], we will try to obtain the reconstruction from a restricted subset of the phase gradient by propagating along the scales phase information, from low resolution to high resolution, using the multiresolution analysis and specific wavelet projections [17]. This work is new in comparison to classical reconstruction techniques in AO [4]. We will propose to reconstruct all the images using only the subset of its gradient and radiate it using the Battle-Lemarié wavelet. We will also study the theoretical properties of MMF and discuss its experimental performance over real data.

The paper is organised as follows: in section II we present a brief discussion on the concept of multiscale theory (MMF), in section III we present the phase reconstruction technique. The experimental data used is discussed in section IV and the results are shown in section V. Finally, we conclude in section VI.

II. Complex signals and multiscale organization

A multiscale system is characterised by the distribution of Hausdorff dimensions to describe its behaviour under changes of scale. According to Canonical Formulations (herein referred to as CMF), a signal s is multiscale if for a given family of functions Γ_r we have:

$$\langle |\Gamma_r s|^p \rangle = \alpha_p r^{\tau_p} + o(r^{\tau_p})(r \to 0) \tag{1}$$

where $\langle \cdot \rangle$ denotes the average over an ensemble of signals s for a particular scale [6]. For a given signal $s(\vec{x})$, there exists at least one local function Γ_r which defines the function $\Gamma_r s(\vec{x})$ with desired properties [6]. However, in general, such averages are inaccessible. Instead, the average for different points $\vec{x}$ within the same signal domain s is calculated.

The first instances of multiscale theory was found in the Kolmogorov's theory on turbulence. Under conditions of intense turbulence (fully developed turbulence), energy is passed down from the large-scales to the smaller ones by an injection process until the fluid attains a state of dynamic equilibrium where we can expect a balance in the amount of energy stored in each scale [6]. Kolmogorov proposed that for two given scales r and L, $0 < r < L$, we can define the process of energy transfer by the injection parameter $\eta_{r/L}$ as:

$$|\Gamma_r s| \doteq \eta_{r/L} |\Gamma_L s| \tag{2}$$

where '$\doteq$'means that both sides are equally distributed. According to Kolmogorov, the injection process $\eta_{r/L}$ depends only on the ratio of the scales and can be written as $\eta_{r/L} = [r/L]^{\epsilon}$. From this we can say that the p-order moments have the following relationship

$$\langle |\Gamma_r s|^p \rangle = [r/L]^{\epsilon p} \langle |\Gamma_L s|^p \rangle = A_p r^{\epsilon p} \tag{3}$$

where $A_p = \langle |\Gamma_L s|^p \rangle L^{-\epsilon p}$. Comparing the equations (1) and (3) we can say that $\tau_p = \epsilon p$, that is, the canonical exponents τ_p have a linear relationship with p; a condition known as 'normal scaling' [6]. However, experiments show that in the case of fully developed turbulence (FDT), the relationship between τ_p and p is not linear rather it is a convex curve, a condition known as 'anomalous scaling' [19].

In equation (1) the exponants τ_p are not geometrically localized, because of the use of average over ensembles. The microcanonical approach (MMF) proposes to overcome this limitation by introducing localized versions of the exponents, while providing effective means to compute them without stationarity hypothesis. We will say that a signal s is multiscale in a microcanonical sense if, for at least one multiscale functional depending on scale r, it is assumed that for any point $\vec{x}$ the following equation holds [19]:

$$\Gamma_r s(\vec{x}) = \alpha(\vec{x}) r^{h(\vec{x})} + o(r^{h(\vec{x})})(r \to 0) \tag{4}$$

The exponent $h(\vec{x})$, which is a function of the point $\vec{x}$, is called a *singularity exponent* or *Local predictability exponent (LPE)* at point $\vec{x}$ [19]. This is the microcanonical approach to multiscale theory which says that a signal is multiscale if every point in the signal is characterized by a local power-law scaling behaviour. We will now discuss a bit about the two main characteristics of a multiscale signal.

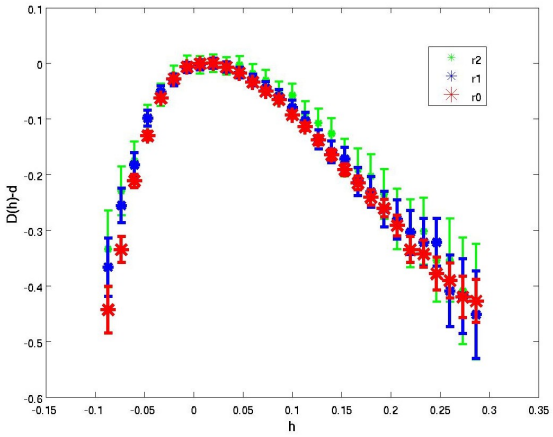

Fig. 1: Reduced singularity spectra $D(h) - d$ for the experimental phase data, calculated with errorbars at the finest possible scale r_0, twice the finest possible scale r_1 and three times the finest scale r_2.

A. Singularity analysis

At each point $\vec{x}$ in a multiscale signal, we can compute a singularity exponent $h(\vec{x})$ defined by equation (4). A multiscale hierarchy associated to the cascading property in the

signal [6] can then be defined by the level sets of the function $h(\vec{x})$ as:

$$\mathcal{F}_h = \{\vec{x} : h(\vec{x}) = h\} \tag{5}$$

The singularity exponents for experimental, discretized data can be calculated using different methods [19], but for our case we will use the *Unpredictable Points Manifold* (herein referred to as UPM). According to this method, we make point estimates of the singularity exponent [20] accordingly:

$$h(x) = \frac{log(\tau_\Psi s(x, r_0))/\langle \tau_\Psi s(., r_0)\rangle}{logr_0} + o(\frac{1}{logr_0}) \tag{6}$$

where $\langle \tau_\Psi s(., r_0)\rangle$ is the average value of the wavelet projection over the whole signal and $o(\frac{1}{logr_0})$ is a diminishing quantity and r_0 is the minimum scale.

B. Singularity spectrum

The distribution of the singularity exponents, given by $\rho(h)$, has a simple relation with the singularity spectrum $D(h)$. It verifies that [6]:

$$\rho(h) \propto r_0^{d-D(h)} \tag{7}$$

where d is the dimension of the signal domain. If the signal has total support, we can say that there is a component $\mathcal{F}_{h_1}$ of maximum dimension [19] such that $D(h_1) = d$ and this value corresponds to the most probable value of $\rho(h)$ [6], we call it as $\rho(h_1)$. We can now easily obtain the singularity spectrum as:

$$D(h) = d - \frac{log(\rho(h)/\rho(h_1))}{logr_0} \tag{8}$$

where $r_0 = \sqrt{\frac{1}{n \times m}}$ is the scale at which the singularity exponents are calculated, $n \times m$ is the size of s (image in our case). The singularity spectrum of our experimental data has been shown in Fig 1. The convex shape of the singularity spectra is characteristic of the presence of a multiscale hierarchy of the signal defined by equation (5). The result shown in Fig 1 clearly indicates that the perturbated optical phase has multiscale properties, which justifies the approach undertaken in this work. In the following sections, we will describe how to compute, through the microcanonical formula provided by MMF, the key parameters associated to the multiscale properties of the turbulent phase.

III. Reconstruction

In MMF, a commonly used function Γ_r for equation (4) is obtained through a measure μ defined by the norm of the signal's gradient in the following way

$$\Gamma_r(\vec{x}) = \mu(B_r(\vec{x})) = \int_{B_r(\vec{x})} |\nabla s|(\vec{y})d\vec{y} \tag{9}$$

where $B_r(\vec{x})$ is a ball of radius r centered at pixel location $\vec{x}$. The random variables $\Gamma_r(\vec{x})$ carry the multiscale properties of the signal. Moreover, it is possible to retrieve the cascading properties around a given point (called microcanonical cascade) by projecting the measure μ with a mother wavelet Ψ

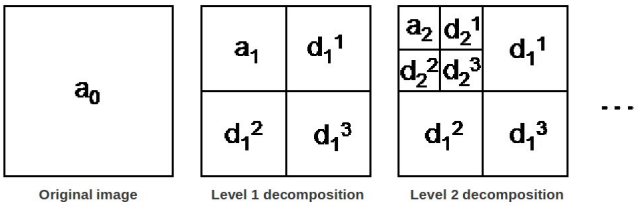

Fig. 2: Representation of the decomposition in multiresolution analysis. «a_j» is the approximation of the initial image «a_0» at the resolution j. «d_j^1», «d_j^2» and «d_j^3» are the horizontal, vertical and diagonal details respectively at the resolution j.

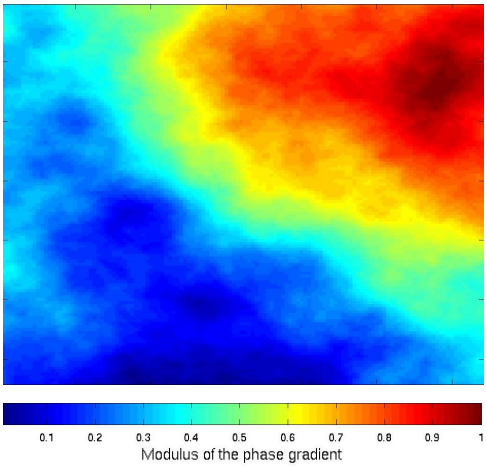

Fig. 3: Image of a simulated phase perturbated by atmospheric turbulence (see main text for the imaging characteristics). The image corresponds to a 128 $\times$ 128 pixels sub-image extracted from an original 256 $\times$ 256 pixels image to avoid the pupil's boundary.

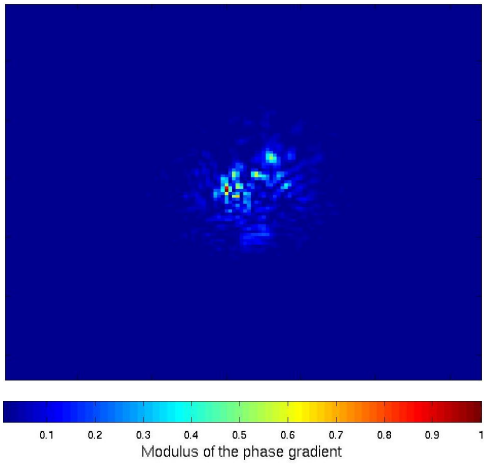

Fig. 4: Point spread function (psf) image associated to the image of the perturbated phase in figure 3.

in the following way; we first introduce the multiscale operator T_Ψ defined as

$$T_\Psi|\nabla s|(\vec{x}, r) = \int |\nabla s|(\vec{y})\Psi(\frac{\vec{x} - \vec{y}}{r})d\vec{y} \tag{10}$$

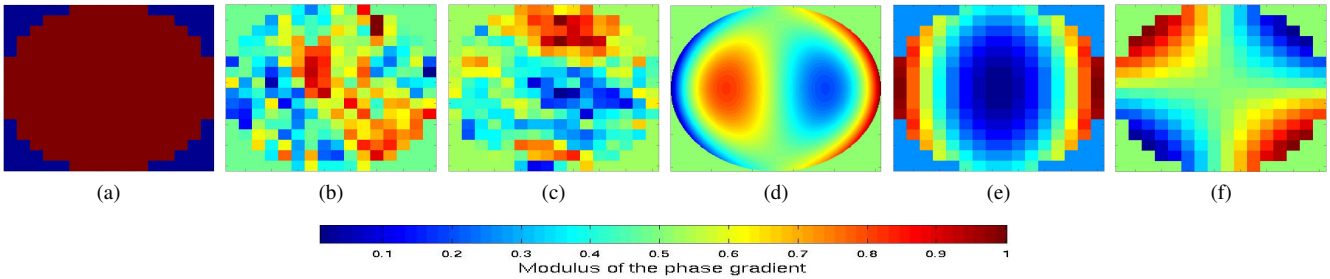

Fig. 5: (a) Distribution of the sub-pupils within the telescope (b) HS acquisition of the x slope (16×16 pixels) for the phase data (c) HS acquisition of the y slope (16×16 pixels) for the phase data. (d) Mode map, size 256×256 pixels, corresponding to a phase map associated to the Zernike coefficients. (e) low resolution x component of the mode map (16×16 pixels). (f) low resolution y component of the mode map (16×16 pixels).

Exactly like in equation (10), we can now define a random variable $\eta_{r/L}(\vec{x})$ as

$$T_\Psi|\nabla s|(\vec{x},r) = \eta_{r/L}(\vec{x})T_\Psi|\nabla s|(\vec{x},L) \tag{11}$$

Now, we can talk about a wavelet Ψ which, if determined, will make $\eta_{r/L}(\vec{x})$ independent of $T_\Psi|\nabla s|(\vec{x},L)$. Such a wavelet is called an *optimal wavelet*; it has the potential of unlocking the signal's microcanonical cascading properties through simple wavelet multiresolution analysis.

A. Multiresolution Analysis & fast wavelet transform

Multiresolution analysis is mathematically formulated by the $L2$ sub-space decomposition associated to wavelet projection. Data redundancy is minimized by the use of Hilbertian frames such as the one obtained by the use of dyadic wavelets [12].

The decomposition process using multiresolution analysis gives rise to an image fourth smaller than the previous one, as shown in Fig 2. The fast wavelet transform decomposes successively each approximation image (shown as a_0 in Fig 2) into a coarser approximation (a_1) plus the wavelet coefficients (i.e. details, shown as d_1^1, d_1^2 and d_1^3 in Fig 2). Any signal $s(\vec{x})$ can be represented in a dyadic wavelet basis of mother Ψ_r [12]. The wavelet coefficients $\alpha_{r,j,k}$ can be obtained by a simple projection of the signal onto $\Psi_{r,j,k}$ as:

$$\alpha_{r,j,k} = \int \Psi_{r,j,k}(\vec{x})s(\vec{x})dx \tag{12}$$

where the basis functions $\Psi_{r,j,k}(\vec{x}) = 2^{-j}\Psi_r(2^{-j}\vec{x} - k)$ represent the contribution to the signal $s(\vec{x})$ (image in our case) due to a basic feature of orientation r ($r = 0$ represents the approximation of the image at the resolution j, $r = 1$ represents the horizontal details d_j^1, $r = 2$ the vertical details d_j^2, and $r = 3$ the diagonal details d_j^3) at the dyadic scale 2^j and at the position $2^j k$ [17] (see Fig 2). Hence, the fast wavelet transform decomposes successively each approximation a_j into a coarser approximation a_{j+1} plus the wavelet coefficients (i.e. details) d_{j+1}^r.

Reconstruction from the wavelet coefficients finds each a_j from a_{j+1} and d_{j+1}^r and is given by:

$$s(x) = \sum_{r=0,1,2,3} \sum_j \sum_k \alpha_{r,j,k}\Psi_{r,j,k}(\vec{x}) \tag{13}$$

The decomposition of an image into coarser approximations defines two filters, $\bar{h}$ and $\bar{g}$, that can be recursively applied along the rows and columns of the image to produce a fast wavelet decomposition [12]. The filter $\bar{h}$ removes the high frequency content of a_j while $\bar{g}$, which is a high-pass filter, collects the remaining high frequency content. The reconstruction is an interpolation which puts zeros to enlarge a a_{j+1} and d_{j+1}^r and filter the signal thus obtained. Fig 2, plus equations (12) and (13) summarize a well known implementation of multiresolution analysis as described in [12]. A fundamental idea of this paper, which will be explained in the following sections, is to use this classical numerical scheme to the signal of singularity exponents $h(\vec{x})$: this is justified by the fact that these exponents carry the most essential multiscale properties in a complex signal.

Notice that when obtaining the multiresolution decomposition of an image the details at each resolution level refer to the same physical positions, but after each iteration they are defined at a coarser scale [8], [17]. Therefore, each 'parent coefficient' $\alpha_p = \alpha_{r,j+1,[k/2]}$, at the coarser scale, covers the same spatial extent of four 'children coefficients' $\alpha_c = \alpha_{r,j,k}$ at the finer scale.

B. Approximation of microcanonical cascade

The effective determination of an optimal wavelet for a given turbulent acquisition is a very complicated and unsolved problem. This is the reason why, in this study and like in [8], we use a simple approximation of the optimal wavelet provided by a Battle Lemarié wavelet of order 3 and with 41 coefficients.

The child-parent dependancy valid for most wavelets, which are not too far from the optimal case, can be described in terms of a particular model:

$$\alpha_c = \eta_1\alpha_p + \eta_2 \tag{14}$$

with α_c: "child" wavelet coefficient, α_p: "parent" wavelet coefficient, η_1,η_2: random variables independant of α_c and α_p and also independant of each other. For an optimal wavelet the above equation takes the form $\alpha_c = \eta_1\alpha_p$.

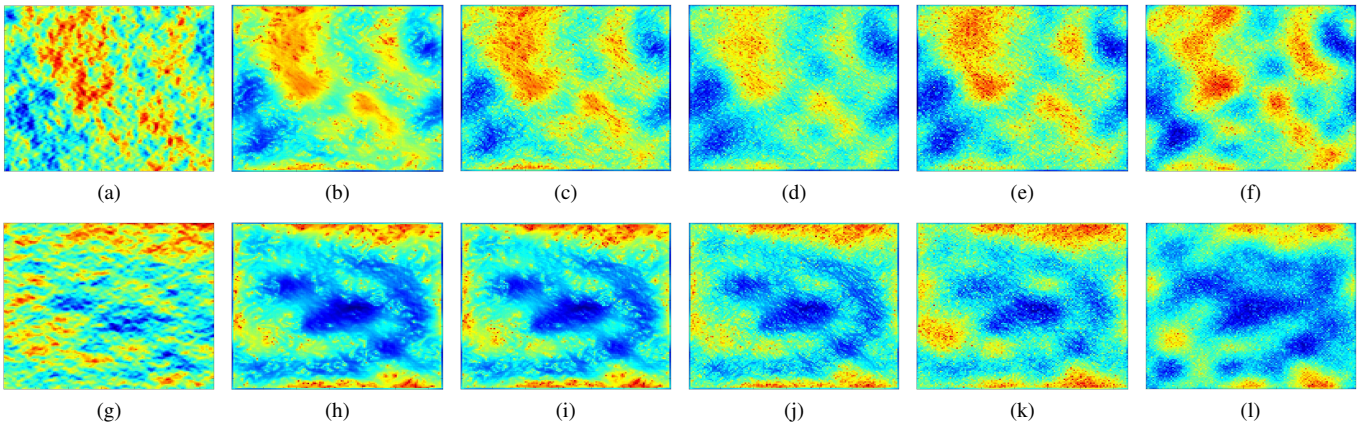

Fig. 6: Images are of size 128 $\times$ 128 pixels. x component of reconstructed phase gradient from the low resolution HS acquisitions (a) original. (b) without noise. (c) with an input SNR of 40 dB. (d) with an input SNR of 26 dB. (e) with an input SNR of 14 dB. (f) with an input SNR of 6 dB.
y component of reconstructed phase gradient (g) original. (h) without noise. (i) with an input SNR of 40 dB. (j) with an input SNR of 26 dB. (k) with an input SNR of 14 dB. (l) with an input SNR of 6 dB.

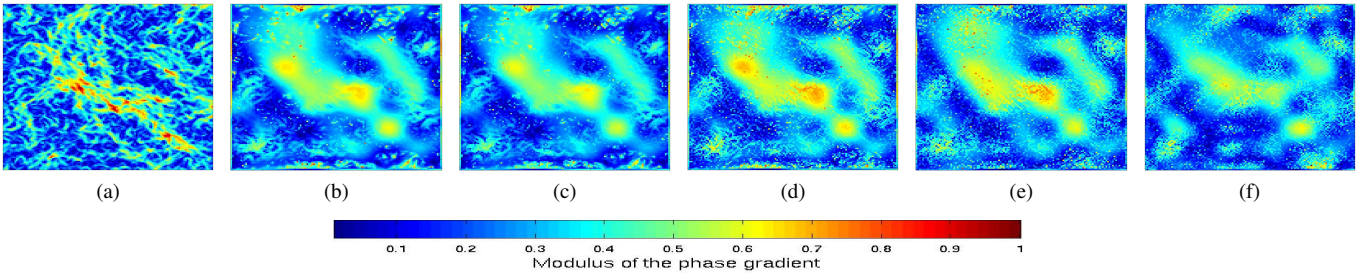

Fig. 7: Norm of the reconstructed phase gradient (a) original. (b) without noise. (c) with an input SNR of 40 dB. (d) with an input SNR of 26 dB. (e) with an input SNR of 14 dB. (f) with an input SNR of 6 dB. Images are of size 128 $\times$ 128 pixels.

C. Reconstruction technique

The method of reconstructing a signal from low resolution to high resolution with the prior knowledge of an optimal wavelet is the following:

- First, we compute the singularity exponents on the high resolution phase data (see Fig 3).
- Compute the wavelet coefficients on the signal of singularity exponents between the two scales (low and high resolution) using multiresolution analysis,
- back-project the signal at low resolution (see Fig 5(b) and Fig 5(c)) to high resolution using the optimal wavelet coefficients.

IV. Data

The datasets used in our work are of simulated turbulent optical phase provided by the French Aerospace Lab-ONERA. We have 1000 occurences (slices) of turbulent phase (high resolution data of our experiment) and the associated psf's (point spread functions) for our experimental purpose.

A. Point spread function (psf)

The point spread function (psf) describes the response of an imaging system to a point source or point object. The psf is the image that would result from an idealized point object, and it characterizes atmospheric blurring effects which are spatially invariant in the immediate field of view [11]. The psf dependence on the phase or wavefront profile $\phi(x, y)$, is given by [11], [10]:

$$s[\phi] = |\mathcal{F}^{-1}\{p.e^{i\phi}\}|^2 \tag{15}$$

where $\mathcal{F}$ denotes the $2-D$ Fourier transform, $i = \sqrt{-1}$ and $p = p(x, y)$ denotes the pupil, or aperture, function. The turbulent phase and the psf for our experiment are shown in Fig 3 and Fig 4 respectively.

B. Description of data

The phase and the psf are associated to the following imaging characteristics:

- diameter of the telescope: 8 m,
- seeing at 5 microns: 0.85 arcseconds,
- wind's speed: 12.5 m/s,
- acquisition frequency: 250 Hz.

The pupil is defined on 256 $\times$ 256 pixels. Data is generated in the FITS format [5]. For the statistical purpose of our experiment we need a set of appropriate sub-images. These sub-images must be as large as possible (for statistical confidence)

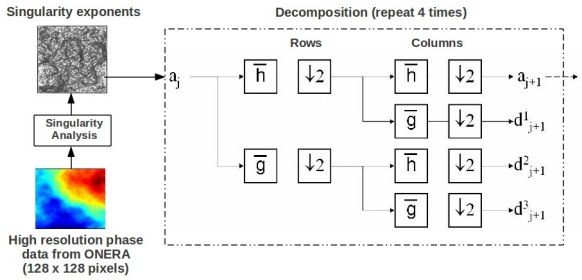

Fig. 8: Decomposition in multiresolution analysis

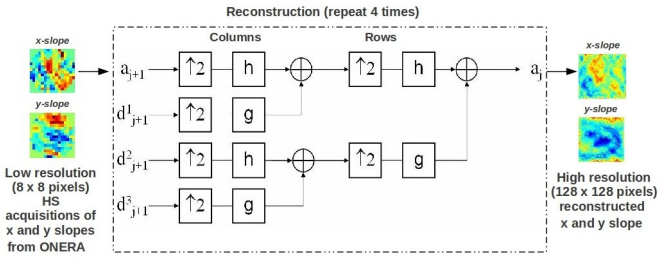

Fig. 9: Reconstruction in multiresolution analysis

TABLE I: Error Calculation - Gradients (Fig 6)

SNR	no noise	40 dB	26 dB	14 dB	6 dB
$\mathcal{G}_{x_{mse}}$	0.3161	0.3177	0.3193	0.3226	0.3546
$\mathcal{G}_{x_{rms}}$	0.5622	0.5637	0.5651	0.5680	0.5955
$\mathcal{G}_{y_{mse}}$	0.3353	0.3375	0.3452	0.3534	0.4586
$\mathcal{G}_{y_{rms}}$	0.5790	0.5810	0.5876	0.5945	0.6722

TABLE II: Error Calculation - Norm of Gradients (Fig 7)

SNR	no noise	40 dB	26 dB	14 dB	6 dB
$\mathcal{N}_{mse}$	0.5173	0.5198	0.5223	0.5290	0.6421
$\mathcal{N}_{rms}$	0.7192	0.7210	0.7227	0.7273	0.8013

and clean (without missing pixels). In addition, due to the requirements imposed by our wavelet analysis, we also require these sub-images to be square sampled and a sampling size being a power of 2. To avoid sub-reconstruction and Gibbs phenomena coming from the strong transition associated to the pupil's boundary, we take a sub-image made of 128×128 pixels (high resolution phase data for our experiment, see Fig 3) centered in the middle of the pupil in the original phase data and a sub-image of size 8×8 pixels (low resolution phase data for our experiment) for the x and y slopes (extracted from the 16×16 pixels HS acquisitions corresponding to sub-image gradients, see Fig 5(b) and Fig 5(c)). We are provided with the original phase data and the HS data by onera.

C. Generation procedure of HS data by ONERA

In our experiments, we performed the phase reconstruction technique both on simulated perturbated turbulent optical phase, as shown in Fig 3, and also on 'zernike mode' phase maps [18] as is shown in Fig 5(d). From the phase map (turbulent or zernike), a sub-sample is extracted corresponding to each HS sub-pupil. There are 208 effective HS sub-pupils (size 16×16 pixels) which sample the pupil of the telescope. The distribution of the sub-pupils within the telescope is shown in Fig 5(a). From every sub-pupil, a psf is formed and the measure of its center of gravity (with respect to a reference position provided by the same operation with the null phase) is taken. It is this value which provides the measurement of the slope, normalised in displacement in pixels. Hence, for every 208 sub-pupils (both for the x and y slopes), we have 208 values corresponding to the measure of the center of gravity. We rearrange these values to form 16×16 pixels sub-image to be used for reconstruction. Fig 5(b) and Fig 5(c) shows the sub-images corresponding to the phase map and Fig 5(e) and Fig 5(f) shows the sub-images corresponding to the mode map.

V. Results

A. Experimental procedure

From the discussions made in the subsection *Reconstruction technique*, we perform the reconstruction of the phase and the mode from a subset of its gradient. We use a simple approximation of the optimal wavelet provided by a Battle Lemarié (B-L) wavelet of degree 3 and 41 coefficients.

- We first compute the third order B-L wavelet coefficients associated to the signal of the singularity exponents computed on the perturbated phase signal (and the given mode), as shown in Fig 8. We get an approximation image (a_{j+1}) and the details i.e.,wavelet coefficients (d^1_{j+1}, d^2_{j+1} and d^3_{j+1} are the horizontal, vertical and diagonal details respectively) for the next coarser scale.
- Every level gives rise to an image fourth smaller than the previous one. We repeat the operation 4 times to an approximation of size 8×8 pixels. We store the details obtained for every resolution.
- We replace the resultant approximation image with the low resolution (8×8 pixels sub-image, see subsection *Description of data*) HS acquisition of the x and y slopes for the phase data.
- for each component (x and y) of the phase gradient (and the mode gradient) at low reslution, back project the component from low to high resolution to get a phase's gradient (and the mode's gradient) at higher spatial resolution of 128×128 pixels, as shown in Fig 9.

B. Analysis of the results

Results obtained show visual resemblance of the reconstructed signal with the original one and is comparable with the results of standard reconstruction technique in [9]. The results of reconstruction of the x component, y component and norm of the gradients are shown in Fig 6 and Fig 7 respectively.

The result of reconstruction on the zernike modes are shown in Fig 10. The results of the reconstructed phase and psf's are shown in Fig 11. Although there are imperfections, we clearly recognize the original phase gradients. Also, to check the robustness of our reconstruction algorithm we have performed reconstruction by adding different proportion of gaussian white noise, w.r.t the standard deviation of the given phase data, to the x and y low resolution HS acquisitions corresponding to sub-image gradients. The experiment has been performed over a single occurence of the phase.

C. Quantitative analysis

To better evaluate the quality of the reconstruction, we compute the mean square error (denoted by $\mathcal{G}_{x_{mse}}$, $\mathcal{G}_{y_{mse}}$) and root mean square errors (denoted by $\mathcal{G}_{x_{rms}}$, $\mathcal{G}_{y_{rms}}$) for the x and y component of the gradients, for position $\vec{x}$ and time interval t as follows:

$$\mathcal{G}_{x_{mse}} = \frac{1}{n \times m} \sum_{n,m} |\nabla \phi_x^o(\vec{x},t) - \nabla \phi_x^r(\vec{x},t)|^2 \quad (16)$$

$$\mathcal{G}_{y_{mse}} = \frac{1}{n \times m} \sum_{n,m} |\nabla \phi_y^o(\vec{x},t) - \nabla \phi_y^r(\vec{x},t)|^2 \quad (17)$$

$$\mathcal{G}_{x_{rms}} = \sqrt{\frac{\sum_{n,m} |\nabla \phi_x^o(\vec{x},t) - \nabla \phi_x^r(\vec{x},t)|^2}{n \times m}} \quad (18)$$

$$\mathcal{G}_{y_{rms}} = \sqrt{\frac{\sum_{n,m} |\nabla \phi_y^o(\vec{x},t) - \nabla \phi_y^r(\vec{x},t)|^2}{n \times m}} \quad (19)$$

where $n \times m$ is the size of our image, ϕ_x^o, ϕ_y^o : x and y component of the original phase gradient, ϕ_x^r, ϕ_y^r : x and y component of the reconstructed phase gradient. The results of the calculations are shown in table I.

We construct the norms from ϕ_x and ϕ_y, for the original and the reconstructed gradients, as $\|\phi\| = \sqrt{\phi_x^2 + \phi_y^2}$. We compute the mean square ($\mathcal{N}_{mse}$) and the root mean square ($\mathcal{N}_{rms}$) errors for the norm of the gradients respectively, as follows:

$$\mathcal{N}_{mse} = \frac{1}{n \times m} \sum_{n,m} |\|\nabla \phi^o(\vec{x},t)\| - \|\nabla \phi^r(\vec{x},t)\||^2 \quad (20)$$

$$\mathcal{N}_{rms} = \sqrt{\frac{\sum_{n,m} |\|\nabla \phi^o(\vec{x},t)\| - \|\nabla \phi^r(\vec{x},t)\||^2}{n \times m}} \quad (21)$$

The results of the calculations are shown in table II.

Consequently from the norms, we reconstruct the phase by performing an inverse gradient operation and also obtain their corresponding psf's using inverse fourier transform. If I and I_R are respectively the original and the reconstructed image, we calculate the mean square ($\mathcal{P}_{mse}$) and root mean square error ($\mathcal{P}_{rms}$) for the normalized phase accordingly:

$$\mathcal{P}_{mse} = \frac{1}{n \times m} \sum_{n,m} |I(\vec{x},t) - I_R(\vec{x},t)|^2 \quad (22)$$

$$\mathcal{P}_{rms} = \sqrt{\frac{\sum_{n,m} |I(\vec{x},t) - I_R(\vec{x},t)|^2}{n \times m}} \quad (23)$$

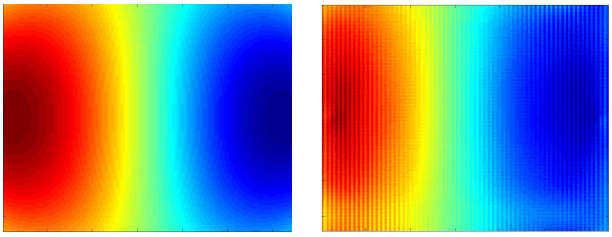

(a) (b)

Fig. 10: Mode map, of size 128×128 pixels, corresponding to the phase map associated to the Zernike coefficients (a) original (b) reconstructed.

The results are shown in table III. The numerical values obtained show a quality in reconstruction at least as good as the one obtained with classical techniques [1], [4], [13], [14], [15], but with a superior tolerance to noise. This is a very important feature as one known hurdle encountered in Adaptive Optics (AO) is to overcome the effect of noise.

Singularity exponents, which are the basic ingredients used in our reconstruction technique, can be computed in real-time; however this paper is not focused on real-time implementation, but on an exposition of the method itself. We will focus on real-time implementation in future works.

VI. Discussion and Conclusion

In this paper we have introduced a wavelet-based new method for the reconstruction of phase from a subset of its gradients, by propagating along the scales phase information, from low resolution to high resolution. We propose an alternative technique for estimating the phase instead of using the conventional methods of least-square solution [2] or deconvolution [13]. The idea is the use of an optimal wavelet, which provides a close approximation of the multiscale energy cascade through wavelet decomposition. Since the deduction of an optimal wavelet remains an unsolved problem, we determine the quality of reconstruction by approximating an optimal wavelet by Battle-Lemarié 3-41 wavelet (using an idea exposed in another context in [8]) and perform the multiresolution analysis on the signal of the singularity exponents (properly computed). We also check the robustness of our algorithm in a noisy environment, where we add different proportions of gaussian white noise to the phase data and perform reconstruction on the noisy sub-images. Results obtained show visual resemblence of the reconstruction with the original one. In fact, the potential of MMF is now being tested on different natural systems ranging from natural images to stock market series [22], phytoplankton distribution in ocean [17], heartbeat dynamics [23] to speech signal. In this method we have used the information from the high-resolution phase data. Our next approach is to perform reconstruction from the low-resolution HS acquisitions without using any information from the high-resolution data.

Acknowledgment

Suman Kumar Maji's PhD is funded by a CORDIS grant and Région Aquitaine OPTAD research project grant. The

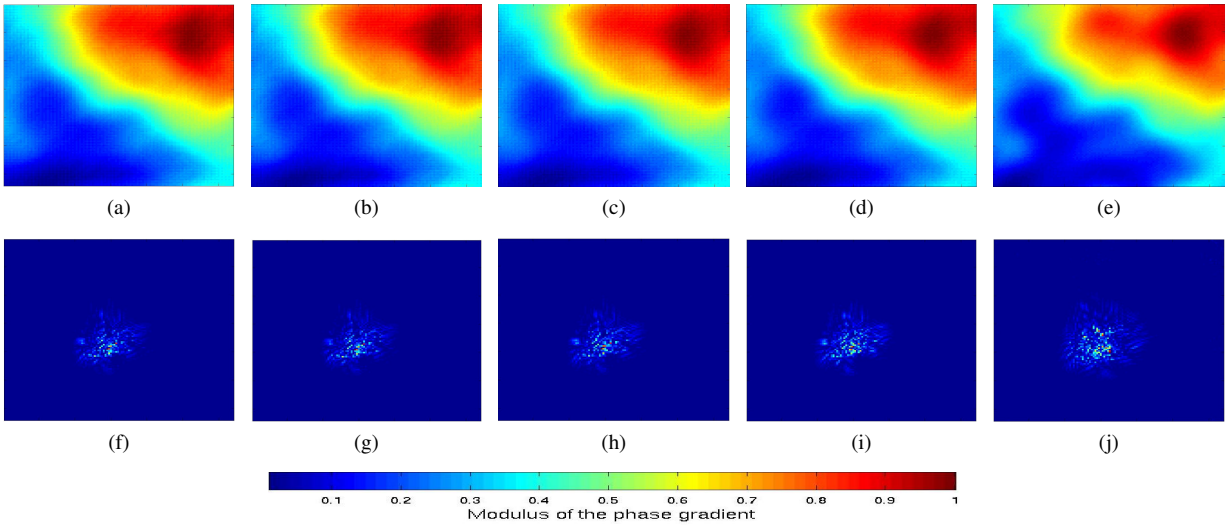

Fig. 11: Phase obtained from the reconstructed gradients (a) without noise. (b) with an input SNR of 40 dB. (c) with an input SNR of 26 dB. (d) with an input SNR of 14 dB. (e) with an input SNR of 6 dB.
Psf obtained from the reconstructed phase (g) without noise. (h) with an input SNR of 40 dB. (i) with an input SNR of 26 dB. (j) with an input SNR of 14 dB. (k) with an input SNR of 6 dB. All images are of size 128×128 pixels.

TABLE III: Error Calculation - Phase

SNR	no noise	40 dB	26 dB	14 dB	6 dB
$\mathcal{P}_{mse}$	0.0388	0.0389	0.0404	0.0427	0.0569
$\mathcal{P}_{rms}$	0.1970	0.1973	0.2010	0.2067	0.2385

authors also thank the anonymous reviewers for enhancing the paper.

REFERENCES

[1] L. Mugnier, G. Le Besnerais, S. Meimon, Inversion in optical imaging through atmospheric turbulence in *Bayesian approach to inverse problems*, Jérôme Idier ed., ISTE, John Wiley & Sons Inc., ISBN 878-1-84821-032-5, 2008.

[2] F. Roddier, The design of an adaptive optics system in *Adaptive Optics in Astronomy*, François Roddier ed., Cambridge University Press, ISBN 0 521 55375 X, 1999.

[3] G. Rousset, F. Lacombe, P. Puget, N. Hubin, E. Gendron, J.-M. Conan, P. Kern, P.-Y. Madec, D. Rabaud, D. Mouillet, A.-M. Lagrange and F. Rigaut, Design of the Nasmyth Adaptive Optics System (NAOS) of the VLT, *Astronomical Telescopes and Instrumentation*, volume 3353, Kona, Hawaii, mars 1998. Proc. Soc. Photo-Opt. Instrum. Eng.

[4] G. Rousset, Wavefront sensing, in *Adaptive Optics in Astronomy*, F. Roddier, ed. (Cambridge University, 1999).

[5] The FITS format: *http://fits.gsfc.nasa.gov/*.

[6] A. Turiel, H. Yahia and C. Perez-Vicente, Microcanonical Multifractal Formalism: a geometrical approach to multifractal systems. Part I: singularity analysis, *Journal of Physics A: Mathematical and Theoretical, vol 41*, doi: 10.1088/1751-8113/41/1/015501.

[7] A. Beghi, A. Cenedese and A. Masiero, Multiscale stochastic approach for phase screens synthesis, *Applied Optics* 50, 4124-4133 (2011).

[8] H. Yahia, J. Sudre, C. Pottier, V. Garçon, Motion analysis in oceanographic satellite images using multiscale methods and the energy cascade, *Pattern Recognition*, Elsevier, 43 (10), 2010, 3591-3604.

[9] S.K. Maji, H. Yahia, O. Pont, T. Fusco, V. Michau, J. Sudre, A multiscale approach to phase reconstruction for Adaptive Optics, *IEEE ECMS*, Liberec, Czech Republic, 2011.

[10] C. Denker, A. Tritschler, M. Lofdahl, Image Reconstruction, *Encyclopedia of Optical Engineering*, R. Barry Johnson and Ronald G. Driggers (eds.), Marcel Dekker Inc., New York, 2004.

[11] W. Cochran, R. Plemmons and T. Torgersen, Exploiting Toeplitz Structure in Atmospheric Image Restoration, *Contemporary Mathematics*, Vol. 280, 2001 pp.

[12] Stéphane Mallat, *A Wavelet Tour of Signal Processing*, Academic Press, 2nd Edition, 1999.

[13] L. M. Mugnier, C. Robert, J.-M. Conan, V. Michau and S. Salem, Myopic deconvolution from wave-front sensing, *Journal of Optical Society of America A* 18, 862-872 (2001).

[14] T. J. Schulz, Multiframe blind deconvolution of astronomical images, *J. Opt. Soc. Am. A* 1993, 10, 1064-1073.

[15] J.-M. Conan, V. Michau and G. Rousset, Signal-to-noise ratio and bias of various deconvolution from wavefront sensing estimators, *Image Propagation through the Atmosphere*, J. C. Dainty and L. R. Bissonnette, eds., Proc. SPIE 2828, 332-339 (1996).

[16] C. Schwartz, G. Baum and E. N. Ribak, Turbulence-degraded wave fronts as fractal surfaces, *J. Opt. Soc. Am. A* 11, 444-451, 1994.

[17] C. Pottier, A. Turiel, V. Garçon, Inferring missing data in satellite chlorophyll maps using turbulent cascading, *Remote Sensing of Environment*, Elsevier, 112, 2008, 4242-4260.

[18] N. A. Roddier, Atmospheric wavefront simulation using Zernike polynomials, *Optical Engineering* 29, 1174, 1990.

[19] A. Turiel, C. Perez-Vicente, J. Grazzini, Numerical methods for the estimation of multifractal singularity spectra on sampled data: A comparative study, *Journal of Computational Physics*, Elsevier, 216, 2006, 362-390.

[20] O. Pont, A. Turiel, H. Yahia, An Optimized Algorithm for the Evaluation of Local Singularity Exponents in Digital Signals, *IWCIA*, 6636, 2011, 346-357.

[21] A. Arneodo, F. Argoul, E. Bacry, J. Elezgaray, and J. F. Muzy, *Ondelettes, multifractales et turbulence*, Diderot Editeur, Paris, France, 1995.

[22] R. N. Mantegna, H. E. Stanley, Turbulence and financial markets, *Nature*, 383, 1996, 587-588.

[23] L. A. N. Amaral, A. L. Goldberger, P. Ch. Ivanov, H. E. Stanley, Scale-independent measures and pathologic cardiac dynamics, *Physical Review Letters*, 81 (11), 1998, 2388-2391.

Publications

Liste des publications, conférences internationales

Publications dans des revues à comité de lecture

Sudre J., H. Yahia, O. Pont et V. Garçon, Ocean Turbulent Dynamics at Super Resolution : A True Picture, *Nature Geoscience*, soumis.

Rossi V., A. Schaeffer, G. Galibert, J. Wood, J. Sudre, B. Morris, M. Roughan et A. M. Waite, Seasonality of sporadic physical processes driving temperature and nutrient variability in the coastal ocean : a multi-sensor approach over the southeast Australian continental shelf, *Journal of Geophysical Research - Oceans*, en révision.

Sudre J., C.Maes et V. Garçon, On the global estimates of geostrophic and Ekman surface currents, *Limnology and Oceanography : Fluids and Environments*, **03**, 1-20, DOI : 10.1215/21573689-2071927, 2013.

Maes C., B. Dewitte, J. Sudre, V. Garçon et D. Varillon, Small-scale features of temperature and salinity surface fields in the Coral Sea, *Journal of Geophysical Research - Oceans*, sous presse, DOI : 10.1002/jgrc.20344, 2013.

Sudre J., H. Yahia et V. Garçon, Analyse multirésolution opérée sur des exposants de singularité en formalisme microcanonique : détermination de la dynamique océanique et des échanges océan/atmosphère submésoéchelle, *XXIVe Colloque Gretsi - Traitement du Signal et des Images - Brest - 3 au 6 Sept 2013*, in press, 2013.

Maji S. K., O. Pont, H. Yahia et J. Sudre, Inferring Information across Scales in Acquired Complex Signals, *European Conference on Complex Systems, ECCS'12, Brussels, 2012, The Complex Systems Society, Springer Verlag LNCS*, 209-226, ISBN : 978-3-319-00394-8, 978-3-319-00395-5, 2013.

Maji S. K., H. Yahia, O. Pont, J. Sudre, T. Fusco, et V. Michau, Towards Multiscale Reconstruction of Perturbated Phase from Hartmann-Shack Acquisitions, *IEEE NASA/ESA Conference on Adaptive Hardware and Systems (AHS-2012)*, 2012.

Garbe C., V. Garçon, A. Butz, H. Yahia, J. Sudre, B. Dewitte, A. Paulmier et I. Dadou, Climatically-active gases in the Eastern Boundary Upwelling and Oxygen Minimum Zone (OMZ) systems, *Geoscience and Remote Sensing Symposium (IGARSS), 2012 IEEE International*, 6150-6153, DOI : 10.1109/IGARSS.2012.6352740, 2012.

Sudre J., V. Garçon, C. Provost, N. Sennéchael, O. Huhn, et M. Lacombe, Short-term variations of deep water masses in Drake Passage revealed by a multiparametric analysis of the ANT-XXIII/3 bottle data, *Deep Sea Research Part II : Topical Studies in Oceanography*, **58**, I 25–26, 2592-2612, 2011.

Provost C., A. Renault, N. Barré, N. Sennéchael, V. Garçon, J. Sudre et O. Huhn, Two repeat crossings of Drake Passage in austral summer 2006 : Short-term variations and evidence for considerable ventilation of intermediate and deep waters, *Deep Sea Research Part II : Topical Studies in Oceanography*, **58**, Issues 25–26, 2555-2571, 2011.

Maji S. K., H. Yahia, O. Pont, T. Fusco, V. Michau et J. Sudre, A multiscale approach to phase reconstruction for Adaptive Optics, *IEEE 2011 10th International Workshop on Electronics, Control, Measurement and Signals (ECMS 2011)*, 1-4, DOI : 10.1109/IWECMS.2011.5952381, 2011.

Maes C., J. Sudre et V. Garçon, Detection of the Eastern Edge of the Equatorial Pacific Warm Pool Using Satellite-Based Ocean Color Observations, *Scientific Online Letters on the Atmosphere*, **6**, 129-132, DOI : 10.2151/sola.2012-033, 2010.

Yahia H., J. Sudre, C. Pottier et V. Garçon, Motion analysis in oceanographic satellite images using multiscale methods and the energy cascade, *Pattern Recognition*, **43**, 3591-3604, DOI 10.1016/j.patcog.2010.04.011, 2010.

Tew Kai E., V. Rossi, J. Sudre, H. Weimerskirch, C. López, E. Hernández-García, F. Marsac, et V. Garçon, Top marine predators track lagrangian coherent structures, *Proceedings of the National Academy of Sciences*, **106(20)**, 8245 – 8250, DOI :10.1073/pnas.0811034106, 2009.

Rossi V., C. López, E. Hernández-García, J. Sudre, V. Garçon, et Y. Morel, Surface mixing and biological activity in the four eastern boundary upwelling systems, *Nonlinear Processes in Geophysics*, **16(4)**, 557–568, 2009.

Sudre J. et R. Morrow, Global surface currents : a high-resolution productfor investigating ocean dynamics, *Ocean Dynamics*, **58**, 101-118, DOI 10.1007/s10236-008-0134-9, 2008.

Rossi V., C. López, J. Sudre, E. Hernández-García, et V. Garçon, Comparative study of mixing and biological activity of the benguela and canary upwelling systems, *Geophysical Research Letters*, **35**, L11602, DOI :10.1029/2008GL033610, 2008.

Luschi P., S. Benhamou, C. Girard, S. Ciccione, D. Roos, J. Sudre, et S. Benvenuti, Marine turtles use geomagnetic cues during open-sea homing, *Current Biology*, **17(2)**, 126–133, DOI :10.1016/j.cub.2006.11.062, 2007.

Girard C., J. Sudre, S. Benhamou, D. Roos, et P. Luschi, Homing in green turtles chelonia mydas : oceanic currents act as a constraint rather than as an information source, *Marine Ecology Progress Series*, **322**, 281–289, DOI :10.3354/meps322281, 2006.

Conférences internationales

Garçon V., J. Sudre, H. Yahia, B. Dewitte, S. Illig, I. Montes, A. Paulmier, I. Dadou, A. Butz et C. Garbe, Towards super resolution of air-sea CO2 fluxes at

the air-sea interface in the EBUS, Air-sea Gas Flux Climatology ; Progress and Future Prospects Science Workshop, Brest, France, 24 - 27 Sept 2013.

Sudre J., H. Yahia et V. Garçon, Analyse multirésolution opérée sur des exposants de singularité en formalisme microcanonique : détermination de la dynamique océanique et des échanges océan/atmosphère submésoéchelle, XXIVe Colloque Gretsi - Traitement du Signal et des Images, Brest, France, 3 au 6 Sept 2013.

Sudre J., H. Yahia, O. Pont, C. Pottier, C. Maes et V. Garçon, Validation of high and super resolution ocean dynamics products, European Spatial Agency (ESA) Conference, "Ocean surface currents : towards future mission concepts", Noordwijk, Pays-Bas, 6-8 May 2013.

Maji S. K., O. Pont, H. Yahia et J. Sudre, Inferring Information across Scales in Acquired Complex Signals, European Conference on Complex Systems, ECCS'12, Brussels, Belgique, 2012.

Maji S. K., H. Yahia, O. Pont, J. Sudre, T. Fusco et V. Michau, Towards Multiscale Reconstruction of Perturbated Phase from Hartmann-Shack Acquisitions, IEEE NASA/ESA Conference on Adaptive Hardware and Systems (AHS-2012), Erlangen, Allemagne, 25-28 Juin 2012.

Garbe C., V. Garçon, A. Butz, H. Yahia, J. Sudre, B. Dewitte, A. Paulmier et I. Dadou, Climatically-active gases in the Eastern Boundary Upwelling and Oxygen Minimum Zone (OMZ) systems, IEEE International Geoscience and Remote Sensing Symposium (IGARSS), Munich, Allemagne, 22-27 Juil. 2012.

Garbe C., V. Garçon, A. Butz, H. Yahia, J. Sudre, B. Dewitte, A. Paulmier et I. Dadou, Climatically-active gases in the Eastern Boundary Upwelling and Oxygen Minimum Zone (OMZ) systems, European Geophysical Union General Assembly, Vienna, Autriche, 22-27 Avr. 2012.

Sudre,J., H. Yahia, O. Pont, C. Pottier, C. Maes et V. Garçon, Towards high-resolution mapping of ocean dynamics : multiscale fusion between low-resolution altimetry and high resolution sst, Globcurrents, Needs for Ocean Surface Current Data from Space, ESA DUE , Brest, France March 7-9 Mar. 2012.

Yahia H., J. Sudre, V. Garçon et C. Pottier, High-Resolution Ocean Dynamics from Microcanonical Formulations in Nonlinear Complex Signal Analysis, European Geophysical Union General Assembly, Vienna, Autriche, 22-27 Avr. 2012.

Maji S. K., H. Yahia, O. Pont, T. Fusco, V. Michau et J. Sudre, A multiscale approach to phase reconstruction for Adaptive Optics, IEEE 2011 10th International Workshop on Electronics, Control, Measurement and Signals (ECMS 2011), liberec République Tchèque, 1-3 Juin 2011.

Sudre J., H. Yahia, O. Pont, C. Pottier et V. Garçon, Inferring fluid motion at submesoscale from high resolution remotely sensed data, Ocean Surface Topography Science Team Meeting, San Diego, Etats-Unis, 17-21 Oct. 2011.

Gutknecht E., I. Dadou, B. Le Vu, G. Cambon, J. Sudre, V. Garçon, et E. Machu, Nitrogen transfers in the Upwelling off Namibia within the Oxygen Minimum Zone : a 3-D model approach, EUR-OCEANS Conference Ocean deoxygenation and implications for marine biogeochemical cycles and ecosystems, Toulouse, France, 24-26 Oct. 2011.

Le Vu B., E. Gutknecht, E. Machu, I. Dadou, A. Paulmier, J. Veitch, J. Sudre et V. Garçon, Physical and Biogeochemical processes maintaining the Oxygen Minimum Zone in the Benguela Upwelling System using an eddy resolving model, EUR-OCEANS Conference Ocean deoxygenation and implications for marine biogeochemical cycles and ecosystems, Toulouse, France, 24-26 Oct. 2011.

Sudre J., H. Yahia, V. Garçon et C. Pottier, Evaluation de la dynamique océanique à haute résolution satellitaire SST par fusion de données à différentes échelles spatiales, Atelier sur la fusion de données Météo France, Toulouse, France, 18 Oct. 2011.

Garçon V., C. Garbe, J. Sudre, B. Dewitte, H. Yahia, A. Paulmier, et I. Dadou, Climatically-active gases in the Eastern Boundary Upwelling and Oxygen Minimum Zone (OMZ) systems, SOLAS-IGAC France join open meeting ; Chemistry, Transport and Biogeochemistry feedback : Frontiers in Chemistry, Physics and Biology, Paris, France, 29-30 Juin 2011.

Gutknecht E., I. Dadou, B. Le Vu, G. Cambon, J. Sudre, V. Garçon et E. Machu, Nitrogen transfers in the Upwelling off Namibia within the Oxygen Mi-

nimum Zone : a 3-D model approach, Advances in Marine Ecosystem Modelling Research Symposium (AMEMR), Plymouth, Grande-Bretagne, 27-30 Juin 2011.

Le Vu B., E. Gutknecht, E. Machu, J. Sudre, I. Dadou, J. Veitch et V. Garçon, Physical and Biogeochemical processes maintaining the Oxygen Minimum Zone in the Benguela Upwelling System using an eddy resolving model, Advances in Marine Ecosystem Modelling Research Symposium (AMEMR), Plymouth, Grande-Bretagne, 27-30 Juin 2011.

Yahia H., J. Sudre, V. Garçon et C. Pottier, High-resolution ocean dynamics from microcanonical formulations in non linear complex signal analysis American Geophysical Union Fall Meeting, San Francisco, Etats-Unis 5-9 Dec. 2011.

Sudre J., V. Garçon, V. Rossi, et H. Yahia, Apport des courants de surface pour la caractérisation des systèmes d'upwelling, Faculté des sciences de Rabat, Rabat, Maroc, 07 Juin 2011.

Sudre J., C. Maes et V. Garçon, How useful are satellite-based ocean color observations to detect the eastern edge of the equatorial Pacific warm pool?, American Geophysical Union Fall Meeting, San Francisco, Etats-Unis 13-17 Dec. 2010.

Sudre J., O. Pont, C. Pottier, H. Yahia et V. Garçon, Comparison of two remote sensing methods for the evaluation of ocean dynamics, Ocean Surface Topography Science Team Meeting, Lisbonne, Portugal, 18-20 Oct. 2010.

Sudre J., O. Pont, H. Yahia, C. Pottier et V. Garçon, Optimal decomposition for the evaluation of ocean dynamics Ocean Surface Topography Science Team Meeting, Lisbonne, Portugal, 18-20 Oct. 2010.

Sudre J., O. Pont, H. Yahia, C. Pottier et V. Garçon, Evidencing of multiplicative cascading and intermittency in real/synthetic oceanographic signals : application to the evaluation of ocean dynamics, Ocean Surface Topography Science Team Meeting, Lisbonne, Portugal, 18-20 Oct. 2010.

Sudre J., E. Tew-Kai, V. Garçon et H. Yahia, Importance de la méso et subméso-échelle sur la distribution spatiale des tortues et oiseaux marins, Ecologie 2010, Montpellier, France, 2-4 Sep. 2010.

Sudre J., H. Yahia, C. Pottier et V. Garçon, Inferring fluid motion at submesoscale from high resolution remotely sensed data, Orflow10, Trends in Complex Systems, International Workshop on Living Organisms in Flows : From Small-scale Turbulence to Geophysical Flow, Palma de Majorca, Espagne, 2010.

Garçon V., J. Sudre, S. Benhamou, C. López et E. Hernández-García, Island-finding ability of green sea turtles : the role of the LCSs ? Orflow10, Trends in Complex Systems, International Workshop on Living Organisms in Flows : From Small-scale Turbulence to Geophysical Flow, Palma de Majorca, Espagne, 2010.

Hernández-García E., J. H. Bettencourt, V. Garçon, I. Hernández-Carrasco, C. López, V. Rossi, J. Sudre, V. Garçon et E. Tew-Kai, Biological Impact of Ocean Transport : A Finite-Size Lyapunov Characterization, 3rd Conference on Nonlinear Science and Complexity, Ankara, Turquie, 28-31 Juil. 2010.

Sudre J., V. Garçon, C. Maes et C. Provost, GEKCO : Geostrophic and Ekman Courant Observatory, Western Pacific Geophysics Meeting, Taipei, Taiwan, 22–25 Juin 2010.

Le Vu B., E. Gutknecht, J. Sudre, E. Machu, G. Cambon, I. Dadou, P. Penven, et V. Garçon, The Benguela upwelling system, Preliminary coupled bio-physical simulations, MEECE sciences meeting, Heraklion, Crète, 1-5 Fév. 2010.

Yahia H., J. Sudre et V. Garçon, Determination of geostrophic vector field on high resolution SST images from the energy cascade, Ocean Surface Topography Science Team Meeting, Seattle, Etats-Unis, 22-24 Juin. 2010.

Gutknecht E., I. Dadou, G. Cambon, J. Sudre, and V. Garçon, Air-sea CO2, O2 and N2O fluxes in the Namibian Upwelling System : a modelling approach, European Geophysical Union General Assembly, Vienna, Autriche, 2-7 Mai 2010.

Rossi V., C. López, E. Tewkai, E. Hernández-García, J. Sudre et V. Garçon, Influence of ocean circulation and horizontal stirring on marine ecosystem dynamics, from phytoplankton to top predators, Séminaire interne the Ocean Institute, University of Western Australia (UWA),Perth, Australie, Mai. 2010.

Rossi, V., C. López, E. Tewkai, E. Hernández-García, J. Sudre et V. Garçon, Influence of ocean circulation and horizontal stirring on marine ecosystem dynamics, from phytoplankton to top predators, Séminaire interne au Laboratoire d'Océanographie de Villefranche/Mer (LOV – CNRS/UPMC), Villefranche/Mer, France, Nov., 2009.

Submesoscale circulation and top marine predator behaviors : Contribution of multiscales and multisensors analyses

Auteur : Joël Sudre
Directeurs de thèse : Véronique Garçon and Hussein Yahia
Discipline : Physical oceanography, nonlinear signal processing, animal behavior
Lieu et date de soutenance : OMP December 20th 2013
Laboratoire : LEGOS, UMR 5566 CNRS/CNES/IRD/UPS

Abstract

The ocean is governed by complex movements at all spatio-temporal scales. Within an mean and global circulation exists a secondary circulation inhabited by fronts, meanders, narrow jets, eddies, named mesoscale circulation. Observation with satellites allows a description and a synoptic evaluation of this dynamics at mesoscale by using altimetric and scatterometric data. This evaluation was the first objective of the thesis and allowed to develop a product distributed to the international scientific community : the GEKCO product.
However, the description of submesoscale processes at finer resolution requires the use of super-resolution data (like ocean color or sea surface temperature) which have the ability to represent all the complexity of an ocean in fully developed turbulence. A method between physical oceanography and "science of the complexity" using the microcanonical formulation of the multiplicative cascade, the GEKCO product and sea surface temperature images was the topic of the second part of this manuscript.
The ocean dynamics being the keystone of all marine ecosystems, the last part of this thesis was dedicated to the meso and submesoscale impact of the ocean dynamics to the trophic chain by focusing on its two extremities. Study of the flow at submesoscale allowed to show that it plays a preponderant role on the marine biomass ; role of activator in open ocean and role of inhibitor in the east boundary upwelling systems. Various studies on top marine predator paths demonstrated the necessity of taking into account the ocean dynamics to interpret their navigational behavior.

Keywords : mesoscale circulation ; submesoscale circulation ; surface currents ; ocean dynamics, singularity exponent ; microcanonical formulation, multiplicative cascade, satellite imagery, physical/biological interactions, top marine predators.

Circulation submésoéchelle et comportements des prédateurs marins supérieurs : Apport de l'analyse multi-échelles et multi-capteurs

Auteur : Joël Sudre
Directeurs de thèse : Véronique Garçon et Hussein Yahia
Discipline : Océanographie physique, traitement non-linéaire du signal, comportement animal
Lieu et date de soutenance : OMP le 20 Décembre 2013
Laboratoire : LEGOS, UMR 5566 CNRS/CNES/IRD/UPS

Résumé

L'océan est le siège de mouvements complexes à toutes échelles spatiales et temporelles. Au sein d'une circulation moyenne et globale existe une circulation secondaire peuplée de fronts, de méandres, de jets étroits, de tourbillons, que l'on nomme circulation à mésoéchelle. L'observation spatiale permet une description et une évaluation synoptique de cette dynamique à mésoéchelle au moyen de l'altimétrie et la diffusiométrie. Cette évaluation a été le premier objectif de cette thèse et a permis de développer un produit distribué à la communauté scientifique internationale : le produit GEKCO.
Cependant la description des processus submésoéchelle à plus fine résolution nécessite l'utilisation de données à super-résolution (couleur de l'eau, température de surface) qui ont la possibilité de représenter toute la complexité d'un océan en régime de turbulence pleinement développée. Une méthode à la croisée de l'océanographie physique et de la "science de la complexité" utilisant la formulation microcanonique de la cascade multiplicative, le produit GEKCO et des images de température de la mer, a fait l'objet de la seconde partie de ce manuscrit.
La dynamique océanique étant la clef de voûte de tout le monde marin du vivant, la dernière partie de cette thèse s'est intéressée à l'impact de la circulation à mésoéchelle et à submésoéchelle sur la chaîne trophique marine en se focalisant sur ses deux extrémités. L'étude de la circulation à submésoéchelle a permis de montrer qu'elle joue un rôle prépondérant pour la biomasse marine ; un rôle d'activateur en océan ouvert et un rôle d'inhibiteur dans les systèmes d'upwelling de bord Est. Différentes études sur les trajets de prédateurs marins supérieurs ont démontré la nécessité de prendre en compte la dynamique océanique pour interpréter leur comportement de navigation.

Mots clés : circulation à mésoéchelle ; circulation à submésoéchelle ; courants de surface ; dynamique océanique ; exposant de singularité ; formulation microcanonique ; cascade multiplicative ; imagerie satellitaire, interactions physique/biologie, prédateurs marins supérieurs.